WORLD METEOROLOGICAL ORGANIZATION

WORLD WEATHER RESEARCH PROGRAMME

WWRP 2010 - 4

2nd WMO International Workshop on Tropical Cyclone Landfall Processes (IWTCLP-II)

Shanghai, China, 19-23 October 2009

WMO/TD-No.1548

Foreword

Severe calamities and fatalities have arisen from landfalling tropical cyclones (TC) around the world in recent years, such as Morakot (August 2009) in western North Pacific, Nargis (May 2008) in Bay of Bengal, Gonu (June 2007) in North Arabian Sea, Bilis (July 2006) in western North Pacific, Katrina (August 2005) in Gulf of Mexico, and Catarina (March 2004) in South Atlantic etc. Transferring the advancements from the research community to operational forecast centers in NMHSs would be helpful for improving the landfalling tropical cyclone (LTC) forecasts and for mitigation of high-impact tropical cyclone disasters.

The Second International Workshop on Tropical Cyclone Landfall Processes (IWTCLP-II) will focus presentations and discussions on the period around TC landfall, which includes approach of the storm to the coast and the storm moving across the coast. Key issues include TC structure and intensity rapid changes over coastal waters, sudden changes in motion direction and speed (slow down/speed up), high-impact events (heavy rain, high winds, storm surge, etc), effects of topography and land surface differences on storm rainfall, extratropical transition processes, energy budgets of landfalling tropical cyclones, forecast techniques for tropical cyclone landfall, and observations and field programs, including T-PARC and TCS08 that were carried out during August-September 2008.

IWTCLP-II will bring forecasters and researchers together to evaluate the state-of-the-art of landfalling tropical cyclone research and forecasting and to discuss the new developments since the last session of the meeting, which was held in Macao, China during 2005. The workshop will interact with local programs on landfalling tropical cyclone research, forecasting, and an early warning system to serve the EXPO-2010 in Shanghai.

This extended abstract volume contains invited keynote lectures and contributed presentations. Sincere appreciation is extended to all of the contributors to preparing this valuable volume. We also would like to extend our genuine gratitude to the Shanghai Meteorological Bureau, Chinese Academy of Meteorological Sciences, Chinese Natural Science Foundation, and the 973 Typhoon Research Program under Chinese Ministry of Science and Technology for their support of this workshop. Thanks are also extended to the Local Organizing Committee (LOC) for their enthusiasm, generosity, and high efficiency in hosting and supporting the meeting.

Lianshou Chen
Chair
Working Group on Tropical
Meteorology Research and IWTCLP-II

Overview of Second International Workshop on Tropical Cyclone Landfall Processes (IWTCLP- II)

Russell L. Elsberry
Co-Director, IWTCLP-II

The first International Workshop on Tropical Cyclone Landfall Processes (IWTCLP-I) was held in Macao, China during 21-25 March 2005. As is the case for the second workshop (IWTCLP-II), the primary sponsor is the WMO Commission on Atmospheric Science (CAS) World Weather Research Program (WWRP) Working Group on Tropical Meteorology Research (WGTMR). The co-sponsor of IWTCLP-II is the WMO World Weather Watch (WWW) Tropical Cyclone Program (TCP), which is perhaps better known to the National Meteorological and Hydrological Services since WWW/TCP works directly with operational tropical cyclone forecasters. It is with this additional funding that we were able to invite forecasters to participate in this workshop.

The WGTMR, which is chaired by Prof. Lianshou Chen, was previously called the Tropical Meteorology Research Program. In 2007, the WGTMR was established under two panels: Tropical Cyclone Panel for which I am the Chair, and the Monsoon Panel that is chaired by Prof. Chih-Pei Chang. Under the Tropical Cyclone Panel is a new expert team on tropical cyclone landfall processes, which is being organized in conjunction with this workshop and will be planning its future activities. The WGTMR will be meeting on Friday morning to plan its future activities.

The presentations and discussions of this workshop will contribute to the planning of the activities of the Tropical Cyclone Panel. Three outcomes of the IWTCLP-II were: (i) Opportunities for collaborative field experiments; (ii) Possibility of a Forecast Demonstration Project; and (iii) Joint efforts in socio-economic impacts research. The first outcome led to the combined Tropical Cyclone Structure (TCS08) and THORPEX Pacific Asian Regional Campaign (T-PARC) during late July to early October 2008. The TCS08 has been extended to the 2010 typhoon season (thus termed TCS10) in conjunction with the Interacting Typhoon-Ocean Program (ITOP). The second outcome of IWTCLP-I was a Forecast Demonstration Program for the Philippines. Although this program was one of only 10 programs briefed at the Third Early Warning System Conference, funding was not obtained. Although the need for more study of socio-economic impacts was also presented at the Sixth International Workshop on Tropical Cyclones in Costa Rica during November 2006, this type of activity has not been well developed.

The local host for IWTCLP-II is the Shanghai Meteorological Bureau, who is tasked to provide weather support for the Shanghai World EXPO 2010. For this reason, several presentations at the workshop will be directed at the potential threat of tropical cyclone landfall and its impacts near Shanghai during EXPO 2010. Possible collaboration with the China National program on tropical cyclone landfall, or collaboration with a proposed Forecast Demonstration Project using the THORPEX Interactive Grand Global Ensemble (TIGGE), will be explored.

The first session of IWTCLP-II will be on the tropical cyclone landfall impacts. Here the definition of landfall includes any tropical cyclone that has the potential of bringing damaging winds, heavy precipitation, etc. during the forecast period, even if the center (eye) does not cross the coast. In the second session, a panel of forecasters will describe the status of tropical cyclone landfall forecasting and what research is required to improve the guidance for the forecasters. The third and fourth sessions will summarize some recent advances in observations and modeling for improved guidance. The fifth session will focus on the Shanghai EXPO 2010 and related programs. The final sessions will include contributed papers that address the various aspects of tropical cyclone landfall.

It is our expectation that IWTCLP-II will both provide direction for future activities of the Tropical Cyclone Panel and inform the Shanghai Meteorological Bureau of the latest developments in observing, forecasting, and research in tropical cyclone landfall.

CONTENTS

An overview on the study of Tropical Cyclone Rainfall and Intensity Change in Different Phases

Lianshou Chen

Chinese Academy of Meteorological Sciences

Extended Abstract

1. Introduction

There are three critical issues for the operational forecast centers making a correct prediction on landfalling tropical cyclone (LTC) behavior. These also are the problematic areas for tropical cyclone research community around the world. Actually LTCs are including those approach of the storm to the coast and the storm moving coastal accrossing. These problems are sudden change of motion direction or speed when TC approaches the continent, rapid change of structure and intensity when TC is over coastal water, reinforcement of heavy rainfall when the TC remnant revives over land. The calamities from TC landfall will be aggravated due to the erroneous forecast. The later two critical problems will be discussed in this paper.

Tropical cyclone landfall processes can be categorized into three phases, namely before landfall (over coastal water), after landfall (moving over land surface) and return to ocean from the land. Landfall tropical cyclone will have a greatest structure change in this three phases.

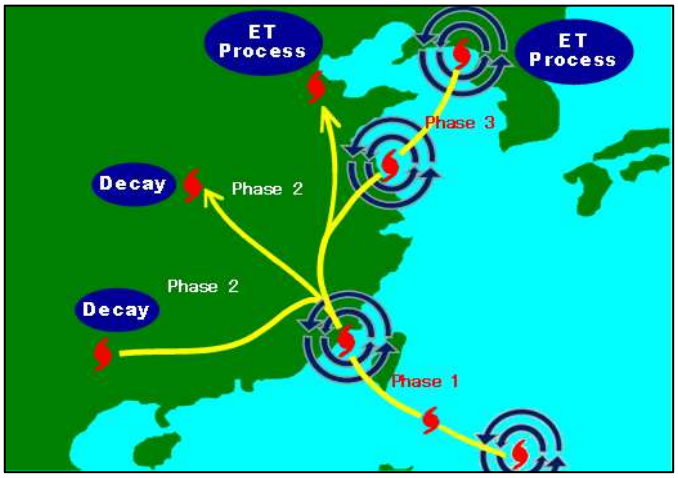

Fig.1 The three phases of landfalling tropical cyclone

2. Intensity rapid change in coastal water

When tropical cyclones approach to the land, most of them will decrease its intensity, only 12.6% of them will intensify rapidly over the coastal water (Zhu, 2009). Meso scale system merge with a typhoon is

an important process for intensity increase rapidly. Numerical simulation (Fig.2) shows that the tropical cyclone central sea level minimum pressure decrease greatly with a meso scale vortex merged with it (Chen and Luo, 2004). Numerical study (Yu ei al, 2008) also shows that the coastal TC will be intensified when positive vorticity bulk or cloud cluster is drawn into the TC.

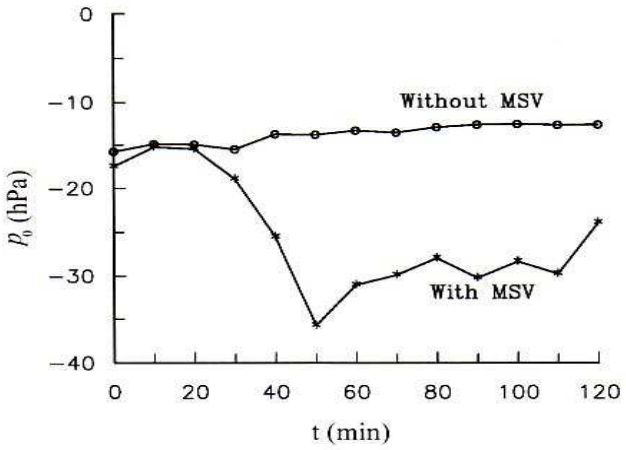

Fig.2 Tropcal cyclone central sea level minimum pressure variation with and without mesoscale vortex merge with

Water vapour transport is an another key process to make the tropical cyclone intensification over the coastal sea.There are two group TC with intensifying cases and decaying cases respectively. Comparison study shows that major characteristic for intensifying group is connected with a water vapor channel of high flux, and decaying group is without such a channel.

Latent heat transfer from the boundary layer will be a favorable process for tropical cyclone rapid intensification over coastal water. One of the target storm Vongfong (0214) of the field program-CLATEX was intensified before landfall. The study (Yan etal, 2005) indicated that Vongfong intensified rapidly right before it made landfall are arisen from the increase of the latent heat upward transfer.

Other mechanism processes such as sea surface temperature (SST), upper level divergence or outflow, vertical wind shear etc. will also affect tropical cyclone intensity rapid change over the coastal sea.

TC structure would has a great change due to the multi-interactions. Meso and micro systems could occur frequently in this stage such as squall line in front of TC, tornadoes, shear lines (Li et al., 2009), inverted trough, small vortex etc. within TC. Those interactions as well as topographic effect will change the TC intensity obviously.

3. Remnant revival over land

Mostly typhoon will be decaying or wither away gradually after it made landfall due to energy dissipation of the ground friction. But few of them are unexpected that a remnant from landfalling typhoon could be revival and reinvigorate rapidly under certain environmental conditions, The rainfall of the revival remnant will possibly exceed the rainfall produced by typhoon in its landfall phase.

The landfall tropical cyclones could reinvigorate if they gain the energy from the environment over

land. Statistical shows (Dong et al., 2009) that the revival TC usually take two tracks, namely moving north or northwestward(T_N) and west or southwestward(T_W) (Fig.3). The rainfall reinforcement are usually coincident with the process of remnant revival.

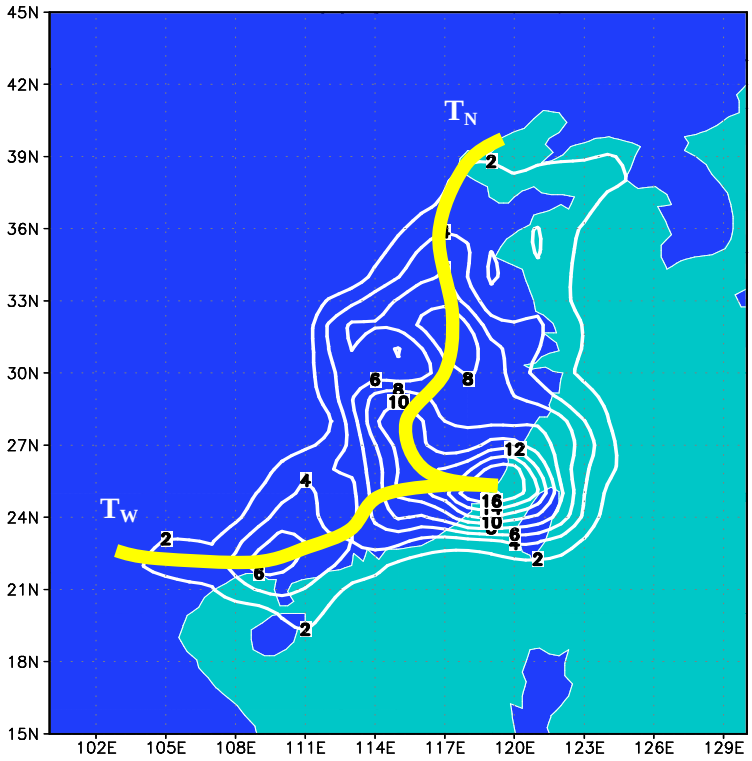

Fig.3 Track frequency of LTC associated with rainfall reinforcement (1949-2006, %)

(Dong et al. 2009)

- Track T_N When LTC or its remnant moves north or northwestwards approaching mid-latitude, they would gain baroclinic energy from mid-latitude systems, especially from the interaction between LTC and westerly trough. Case study shows that the remnant gain baroclinic potential energy from westerly trough and transferring to kinetic energy in lower layer to increase the wind velocity. According to atmospheric adaptation process, central pressure of the remnant will decrease and the system be intensified.

- Track T_W When LTC or its remnant moves west or southwestwards, they may encounter monsoon activities. The remnant interacting with monsoon surge will gain large amount of water vapour and latent heat which will make remnant sustainable and reinvigorated.Water vapour will transfer to latent heat in upper level which is a important energy source to intensify the remnant. Heavy rainfall will be produced accordingly.

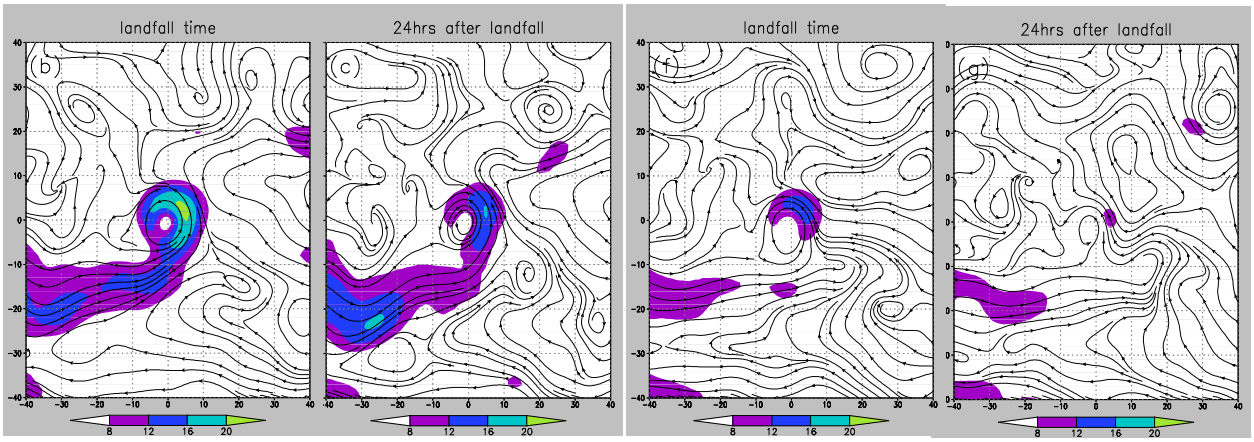

Fig.4 Flow field and vapor flux of two groups of LTC with composite data in 850 hPa (Cheng et al.).(a,b: Strong rainfall group in landfalling time and 24 h after landfall; c,d: Weak rainfall group in landfalling time and 24 h after landfall)

- Water vapour continuous supply to the LTC is a crucial factor to enhance the revived remnant. There are two groups of LTCs with and without heavy rainfall respectively in their landfall period. Composite data analysis shows that the prominent feature for heavy rain group is a water vapour channel connected with the LTC (Fig.4a-b) and the vapour channel is dissipated for the another group(Fig.4c-d).

China is a monsoon country, LTC and its remnant interact with the monsoon surge to maintain the remnant and to enhance the rainstorm which is the distinguishing feature in this region which differ from other regions.

4. LTC return to ocean

Most of tropical cyclones will intensify when they move to ocean from land, because of decrease of energy dissipation due to land friction and roughness as well as high sea surface temperature, such as tropical cyclone from Florida moves to Gulf of Mexico or from Philippines moves to South China Sea. When LTC moves from mainland China to East China Sea, Yellow sea and Bohai sea (Fig.5). It could attack the Shandong and Liaodong Peninsulas as well as Korea Peninsula if the remnant intensified. But the circumstances in those ocean areas are quite different from the other regions. Statistics (Guo, 2009) show that most of the LTC would not increase its intensity, only 49% LTC could intensify when they move to those ocean areas. The major cause could be the low sea surface temperature which is an unfavorable condition for the intensification. Most of the intensification in this sea area arise from the interaction between LTC and mid-latitude systems such as westerly trough. This is a frequent phenomenon for remnant increase its intensity in the mid-latitude.

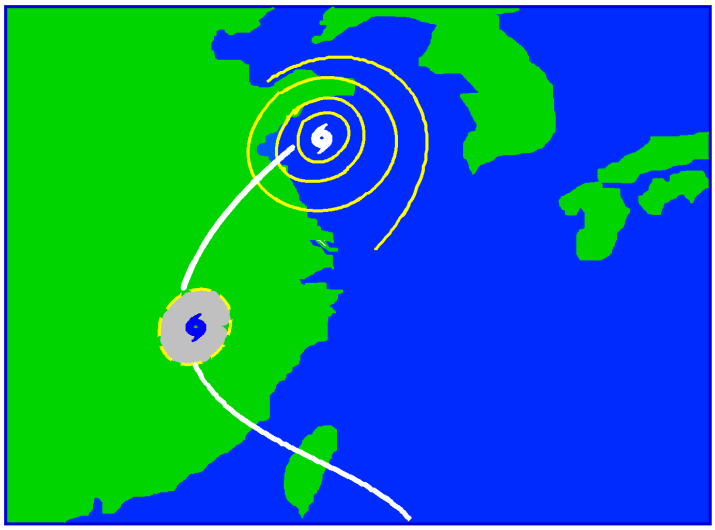

Fig.5 LTC returning to ocean from land

References

Chen Lianshou and Luo Zhexian, 2004: Interaction of Typhoon and Mesoscale Vortex. Advances in Atmospheric Sciences, Vol. 21, No.4, 515-528.

Dong Meiying. 2009: A study on the Mechanism of rainfall reinforcement associated with landfalling tropical cyclones. Doctoral thesis. Chinese Academy of Meteorological Sciences.

Li Ying, Chen Lianshou, Qian Chuanhai, et al. Study on Formation and Development of MesoscaleConvergence Line within Typhoon Circulation, ACTA METEOROLOGICAL SINICA, wait press in 2009

Yan Jinghua, Ding Weiyu, Chen Zitong. Simulation study on the intensification of Vongfong around the off Shore Water. 2004: The 13th National Conference on Tropical Cyclone Science． Daishan China, 10-14 April, 2004.

Yu Yubin. 2008: The theoretical study on tropical cyclone sudden change over the costal waters of China. Doctoral thesis. Chinese Academy of Meteorological Sciences.

Zhu Xiaojin. 2009: Post doctoral Thesis. Chinese Academy of Meteorological Sciences.

Practices and Experiences on Multi-hazard Early Warning System:

---With Emphasis on Typhoon Early Warning

Tang Xu

Shanghai Meteorological Bureau

1. Overview

The Chinese government attaches great importance to the concept of Multi-Hazard Early Warning Systems (MHEWS). On 27 June 2008, Mr. Hu Jintao, President of China, declared that China needs to develop a sustainable MHEWS with a focus on multi-agency coordination and cooperation at all levels of government, to develop a regional joint response capability, and to build an optimum multi-hazard monitoring and emergency response warning process by actively involving multi-agency participation in the decision-making process. This process should also encourage active public participation in response to climate change. According to President Hu Jintao's requirements, the China Meteorological Administration (CMA) is determined to accelerate development of China's public weather service. Following the CMA's instruction, the Shanghai Meteorological Bureau (SMB) enhanced its efforts on the establishment of a complete weather disaster prevention management system under the leadership of the Shanghai Municipal Government (SMG).

As a WMO demonstration project, the CMA and SMG jointly support the Shanghai Multi-Hazard Early Warning System (MHEWS) with 'Multi-agency Response' as the core. The project integrates diversified advanced technologies into a multi-hazard warning process advancing greater multi-agency coordination and cooperation through a multi-link communication platform with responsible emergency response and rescue agencies. This platform is the primary mechanism for information exchange for Shanghai's urban emergency prevention and mitigation system.

The MHEWS is organized around its '4+1'technical platforms and 3-level standard system on multi-agency coordination and cooperation. The '4+1' technical platforms are: Multi-Hazard Detection & Monitoring Platform, Forecast & Warning Information Generation Platform, Multi-agency Coordination and cooperation Support Platform, Dissemination and User Application Platform, and the Multi-Hazard Information Database. The 3-level standard systems on multi-agency coordination and cooperation are: Multi-agency Coordination and Cooperation Standard System, Safety Community Standard System and Regional Joint Defense Standard System.

Multi hazard Early Warning System is a new weather service methodology that integrates inputs for a wide range of weather related threats. It operates not only during emergencies but during normal states as well and can be used to support events of significant importance. Through the multi-hazards early warning system, information can be shared effectively and be disseminated in a timely fashion. In addition, weather service will be able to do more to aid the management of government disaster prevention and mitigation system.

The MHEWS provides technical support to the Shanghai Emergency Response Platform, and has been introduced into the Emergency Response Headquarters of the SMG, providing forecast and warning services to the SMG's emergency response command centre, which is responsible for public emergency response actions and delivery of emergency related information.

2. Recent Progress

Remarkable progress has been made in the Shanghai MHEWS project. At the technical level, the dissemination platform has entered the testing stage; the forecast & warning Information generation platform and multi-agency coordination and cooperation support platform are in the later development stages, and some modules have been put into operation. Early warning subsystems such as city traffic safety, heat wave and human health, power and energy security, As well as bacterial food poisoning are now operational.

Significant progress has been made in extending warning messages to the grass-root level, for instance, early warning information has been integrated into the city grid management system.

Breakthroughs have been made in multi-agency coordination and cooperation. Procedures, mechanisms, and rules for multi agency coordination and cooperation have been basically laid down. For example the DPM related master plans titled 'The emergency response planning of Shanghai Municipality disposing rain, snow and freezing weather disasters', and 'The emergency response planning of Shanghai Municipality disposing heavy fog disasters' have been distributed by the general office of SMG.

A specialized MHEWS for Expo 2010 is under development, and will be fully operational in time to provide emergency response services to Shanghai Expo2010. It and will be one of the most important technical services of the Expo Weather Office and will be supported by the Shanghai MHEWS Operation centre After the Expo2010, the World Meteorological Organization (WMO) will conduct an assessment on the Shanghai MHEWS.

3 Typhoon early warning in MHEWS

Shanghai, a mega-city in east China, is one of the most densely populated cities in the world with a population of 17 million in an area of 6 340 km^2.The urban population density is three times that of Tokyo and 1.74 times that of Paris. With its rapid urbanization and population growth, Shanghai has become more vulnerable to natural hazards such as typhoons, heavy rain, strong winds, tornadoes, storm surge, tide, and floods, which have caused loss of life, extensive property damage and disruption of socio-economic activities.

Typhoons are the most disastrous hazard in Shanghai, and east China, the most economically developed areas in nation. There will be 8.5 typhoons which have obvious influence on east China on average. Shanghai has suffered from typhoons almost every year; during 1949-2002 186 tropical cyclones affected Shanghai with strong winds, heavy rains, storm surges and other disasters. The disastrous catenation effects of such events are magnified by the rapid development of society and economic infrastructure.

With the implementation of MHEWS, Shanghai as well as east China's capacity in typhoon disaster prevention and mitigation Shanghai has been enhanced. A seamless prediction system for typhoons was established by utilizing general circulation information of the atmosphere and ocean, real time satellite and radar data, historical typhoon data as well as numerical model output. Regional cooperation mechanisms on typhoon disaster prevention and mitigation such as joint regional consultation and warning information sharing were established.

The warning coverage was widened by enhancing information dissemination capabilities. The readiness for typhoon related hazards was perfected according to the characteristics of typhoon disasters impacts in developed areas. Following the principle of early briefing, early warning and early dissemination, taking the multi-agency cooperation as core, the impact of typhoon and typhoon related

disasters was effectively minimized.

4. Experience summary

As a new concept of PWS delivery concerning handling high impact weather and benefiting departments of high sensitivity has been developed through the successful practices in Shanghai. The experiences can be summarized into the following aspects:

1) Utilizing standardized mechanisms on multi-agency response to minimize the time for response and deployment to high impact weather, the 'early joint response' and 'early deployment' can be achieved. It is essential to establish work teams and an operations platform suitable to both routine and emergency response.

2) Early warning for multi-hazards such as landfall typhoon should reflect the disaster's characteristics, and needs to be supported at both the management and technical levels. Specialized products such as typhoon risk mapping, ensemble prediction and potential typhoon genesis analysis are crucial to early warning. For example, the ensemble forecast makes warnings which include spatial distribution patterns possible.

3) An integrated MHEWS aims to enhance the capacity of DPM as well as provide timely and refined decision-making support service to the Emergency management system as a whole. The emphasis of system implementation should focus on multi-agency coordination mechanism and timely dissemination of warnings for high impact weather.

4) MHEWS should be integrated into the emergency management system and connected to other systems, and deliver targeted service for social and economic activities, which is the key to sustainable development of MHEWS.

Unusual Variation of Landfall Tropical Cyclone Behavior and Associated Physical Mechanism

---- A National Basic Research Program of China (2009 - 2013)

Yihong DUAN[1] Hui YU[2]

[1]National Meteorological Center/China Meteorological Administration, Beijing 100081, China

[2]Shanghai Typhoon Institute/China Meteorological Administration, Shanghai 200030, China

ABSTRACT

As frequently landed by tropical cyclones (TCs), China is deeply suffered from relevant disasters. Over 2/3 of the country has ever been affected and over 500 million people are influenced annually by TCs. The direct economic losses have an annual mean of 29 billion RMB. The mean life losses reach 475 per year. Improvements in forecast accuracy of TC have contributed significantly to efficient disaster prevention and preparedness. However, landfall TC is still a great challenge to forecasters and decision makers. During the landfall process of a TC, it sometimes shows abnormal behavior as affected by complicated underlying ocean/land condition and complex atmospheric environment. For example, some TCs intensify rapidly and some others disappear suddenly right before landfall. Some TCs turn away oddly as approaching the land. Some TCs landfall with a speed much quicker than over the open ocean and some others stagnate near the coast. Tornado and meso-scale thunderstorm appear in some landfall TCs, which bring about lasting heavy rainfall or catastrophic wind. The forecast ability of these abnormal behavior is very low at present as a result of poor understanding, and can not meet the needs of efficient disaster prevention and preparedness.

To tackle this problem, a 5-year project entitled “Unusual Variation of Landfall Tropical Cyclone Behavior and Associated Physical Mechanism” is funded by the National Basic Research Program of China from 2009 to 2013, aiming to improve the forecast ability of landfall TC by studying the mechanism of unusual change of landfall TC behavior, including track, intensity, high wind and heavy precipitation. Leading institute of the project is Shanghai Typhoon Institute/CMA and it is collaborated by Chinese Academy of Meteorological Sciences/CMA, National Meteorological Center/CMA, Institute of Tropical and Marine Meteorology/CMA, Institute of Atmospheric Physics/CAS, Nanjing University, Beijing University and Nanjing Information Science and Technology University.

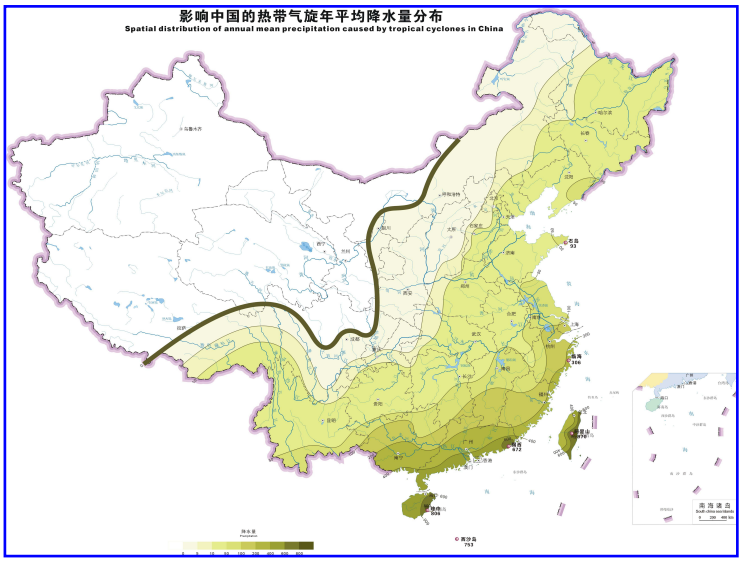

Fig. 1 Spatial distribution of annual mean precipitation caused by TCs in China
(Cited from Climatology Atlas of Tropical Cyclones Affecting China)

1. Main goals

The TCs making landfall in China or those very close to the coast (light blue area in Fig.2) will be studied in this project. The main goals are to: (1) reveal the ocean-land-atmosphere interaction characteristics during the landfall process of TC; (2) understand the role of ocean-land-atmosphere interaction in resulting in unusual change of landfall TC behavior included the its track, intensity and torrential rain; (3) develop an ocean-land-atmosphere coupled TC model and ensemble TC prediction system; (4) improve the theory and model for landfall TC prediction, including the landfall point, intensity change, high-wind and heavy precipitation and related disasters; (5) set up a high resolution four dimensional analyses system for the fine structure of landfall TC and provide a set of high-quality re-analyses data for typical landfall TCs.

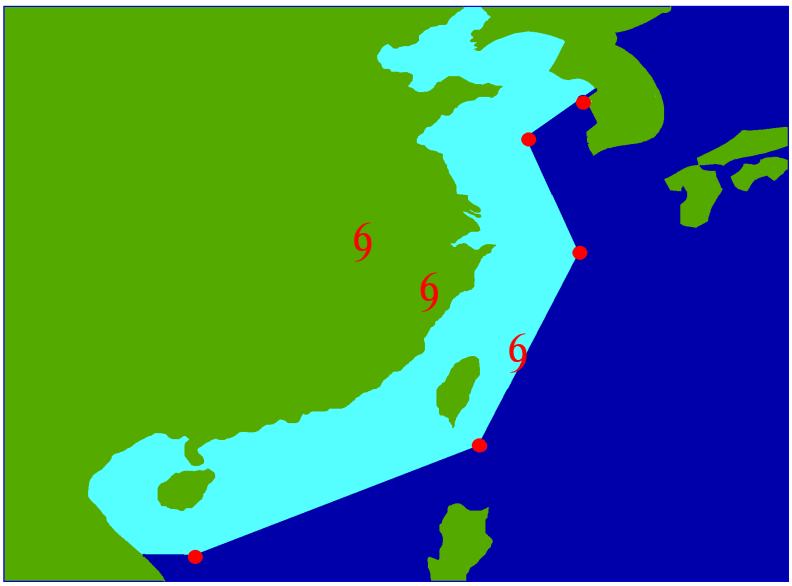

Fig. 2 Sketch map of the TCs which are to be studied in the project,
including those making landfall in China and those over the light blue part of the ocean.

2. Key scientific issues to be studied

The key scientific issues to be studied include: features of main factors (the atmospheric environment, ocean and land condition, and mesoscale systems inside TC) leading to the abnormal variation of landfall TCs, physical mechanism of the ocean-land-atmosphere interaction related to the abnormal variation of landfall TCs and the quantitative application of satellite and radar data in landfall TC analyses and prediction.

The findings on the key scientific issues will be applied to advance the operational TC prediction model, which will be assessed in a test-bed for TC prediction. An ocean-land-atmosphere coupled TC model will also be set up to be used in both the scientific study and operational forecast of landfall TC. Special field experiments are designed to obtain the air-ocean/land surface fluxes and boundary layer parameters of landfall TC for the ocean-land-atmosphere interaction study.

3. Missions of the project

Six missions as shown in Fig.3 are scheduled to fulfill the goals of the project.

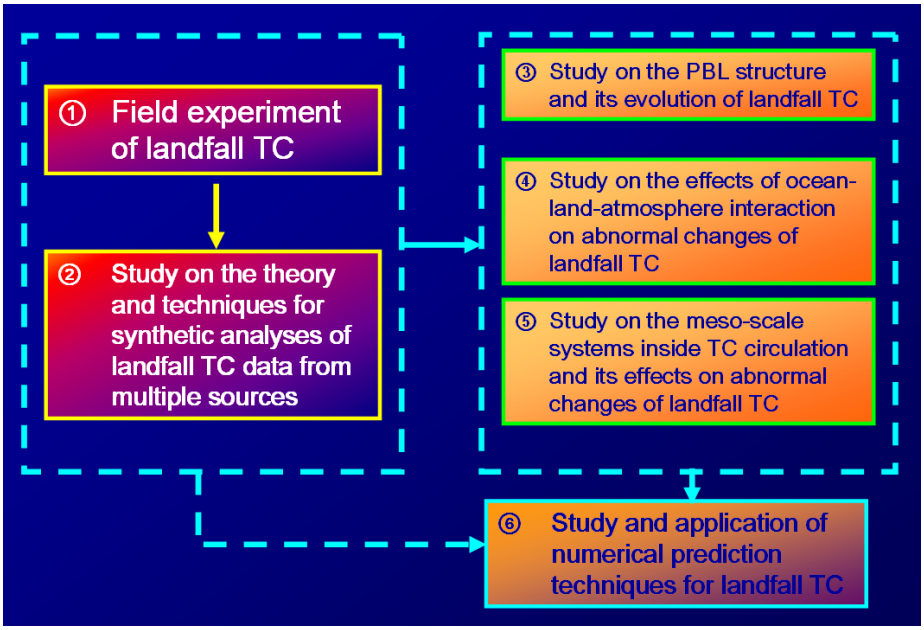

Fig.3 Six missions of the project and their relations

Field experiment of targeted landfall TC is going to be carried out with emphases on obtaining the air-ocean/land surface fluxes and boundary layer parameters of landfall TC for the ocean-land-atmosphere interaction study. Data quality control techniques will be studied and the databank of field experiments will be set up for landfall TC.

The data acquired in field experiments will be used combined with routine reconnaissance data, such as satellite, ground-based radar, AWS, and so on, in the synthetic analyses system for landfall TC. The system will be based on advanced analyses techniques for data from multiple sources and will provide high resolution re-analyses data of targeted landfall TC.

Based on the field experiment, study will be carried out on the PBL structure and its evolution, the exchange of heat, momentum and mass between air and ocean/land. Especially, the PBL parameterization scheme suitable for landfall TC will be explored and tested in the operation system.

Special focus will be placed on the effects of ocean-land-atmosphere interaction and meso-scale system on abnormal changes of landfall TC. The following scientific topics will be studied: (1) the role of

coastal ocean heat status, orientation of coast line, coastal topography and island in resulting the abrupt change in pre-landfall track, meso-scale structure, rapid intensification or sudden disappear of landfall TC; (2) the effects of complex topography and land surface condition (lake, city cluster, etc.) on post-landfall abnormal track, meso-scale structure and abrupt intensification of wind and precipitation; (3) interaction between TC and mid-/low- latitude system and its contribution to long-live TC after landfall; (4) evolution of meso-scale structure of landfall TC and main factors affecting the meso-scale structure; (5) interaction among multi-scale systems inside TC circulation and its effects on abnormal changes of landfall TC; (6) effect of meso-scale system on abnormal track in weak environmental flow; (7) interaction between meso-scale system and remnant of post-landfall TC; (8) structure of meso-scale system related to strong wind and heavy precipitation; (9) meso-scale and fluctuation feature of wind field and the impact on heavy precipitation.

Above missions will provide data and scientific bases for improving the operation numerical TC prediction system. Specially, vortex initialization technique and PBL parameterization scheme for landfall TC will be improved and an ocean-land-atmosphere coupled TC model will be set up to be used in both the scientific study and operation forecast. Pertinent ensemble forecast technique will also be studied. Application demonstration platform of the improved system is going to be set up in both South and East China regional centers.

Changes in Track and Structure Associated with Tropical Cyclone Landfall

Johnny C L Chan

Guy Carpenter Asia-Pacific Climate Impact Centre, School of Energy and Environment

City University of Hong Kong
Email: johnny.chan@cityu.edu.hk

1. Introduction

As a tropical cyclone (TC) makes landfall, the underlying surface and the atmospheric conditions associated with the TC circulation changes. These include changes in friction (both due to changes in roughness and topography), heat and moisture fluxes as well as moisture availability. All such changes will therefore modify the dynamic and thermodynamic properties of the TC, and subsequently the track and structure of the TC. In this paper, we will present results from observational studies and numerical simulations to understand such changes.

2. Track changes

Wong and Chan (2006) performed numerical simulations on an *f* plane of an idealized TC-like vortex near an area in which the underlying surface has a substantially larger roughness as the rest of the domain to simulate the effect of friction on the vortex. The result shows that the vortex drifts towards land (i.e. the part of the domain with larger roughness). The average drift speed is about 1 m s^{-1}, and the track contains oscillations (Fig. 1). Such a drift is present whether the "land" in the model has the same amount of moisture as the sea or has only 5% of the moisture of the sea. If only the land moisture is reduced but the roughness is the same as that of the sea, the vortex does not exhibit any significant motion deviations (see Fig. 1 of their paper). These results suggest that it is the discontinuity in roughness that causes the vortex to drift towards the land.

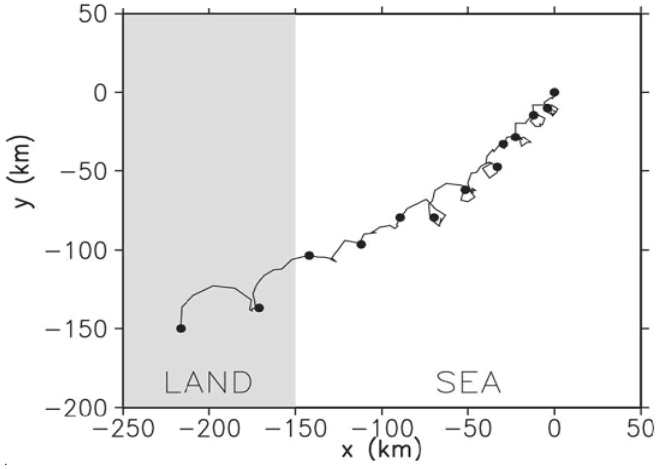

Fig. 1. Track of the TC surface center on an *f* plane with the land (gray shaded) having a much larger roughness than the sea. The dots denote 12-hourly TC positions. The origin is the location of the domain center (re-drawn from Wong and Chan 2006).

Wong and Chan (2006) explained this drift in terms of the modification of the near-surface winds by the rough land surface. Reduction of winds over land leads to a large-scale asymmetric convergence/divergence along the coast. The large-scale boundary-layer asymmetric divergence/convergence induces an asymmetry in vertical motion. An asymmetric flow also develops in the lower troposphere because of the creation/reduction of asymmetric vorticity by the divergence term in the vorticity equation. Adjustment of the atmosphere to these changes in vorticity then generates a pair of "gyres" that steer the TC towards the coast (Fig. 2). Such changes also lead to changes in convection, and hence to the diabatic contributions to the PV tendency (Chan et al. 2002). A combination of the horizontal advection, vertical advection, and the diabatic heating terms then results in the drift of the vortex towards the coast, which is evident in the PV budget calculations (not shown).

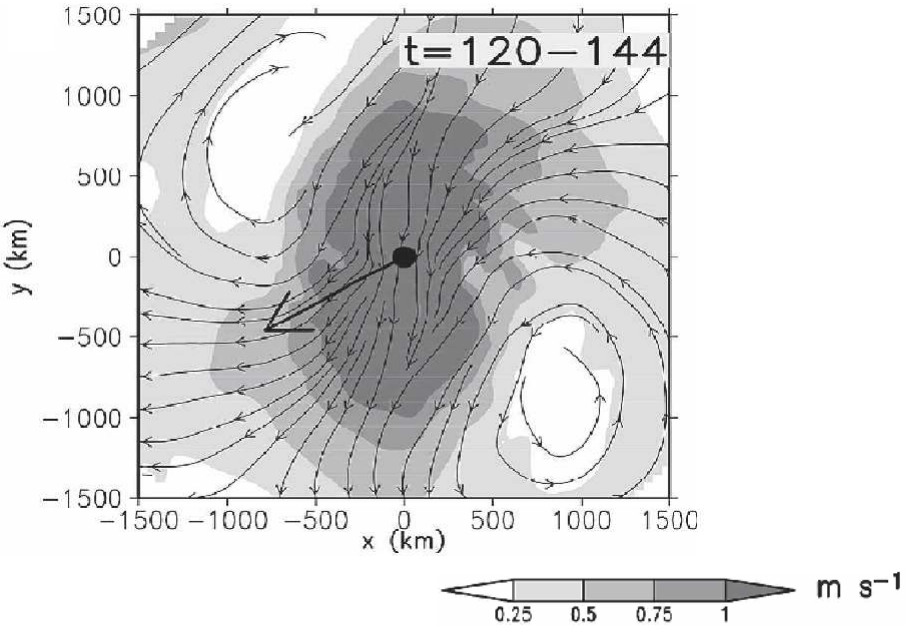

Fig. 2. Time composite between 120 and 144 h of the asymmetric component of the lower tropospheric (about 900 to 550 hPa) flow of the experiment shown in Fig. 1. The TC center is marked by a dot at the origin and the big arrow, magnified by a factor of 10 such that a length equal to 1000 km on the horizontal axis represents an actual distance of 100 km, indicates the overall movement of the center during this period. The shading indicates the wind speed with the grades shown in the bar below (re-drawn from Wong and Chan 2006).

These results suggest the existence of another "inherent" motion of a TC when it encounters a discontinuity in roughness such that a TC is "attracted" towards the area of higher roughness. To study whether such an inherent effect is still present in a more realistic situation, Szeto et al. (2009) performed similar experiments on a beta plane. Under such conditions, a pair of counter-rotating gyres will form and the vortex experiences an inherent northwestward movement (in the Northern Hemisphere). Because the axis of this pair of gyres is southwest-northeast, the flow associated with these gyres is likely to

interact differently with the land surface for different orientations of the coastline. Two experiments are therefore carried out, one with a north-south (NS) oriented coastline and another east-west (EW) oriented. While the dominant motion of the vortex is still towards the northwest, the discontinuity in roughness between the land and the sea results in the vortex deviating from this predominant motion, with the vortex deviating to the right of the beta-induced track (Fig. 3a) in the NS experiment by about 30 km and to the left in the EW experiment by about 15 km (Fig. 3b) at landfall. Because the grid resolution of the simulations is 5 km, such deviations are likely to be real.

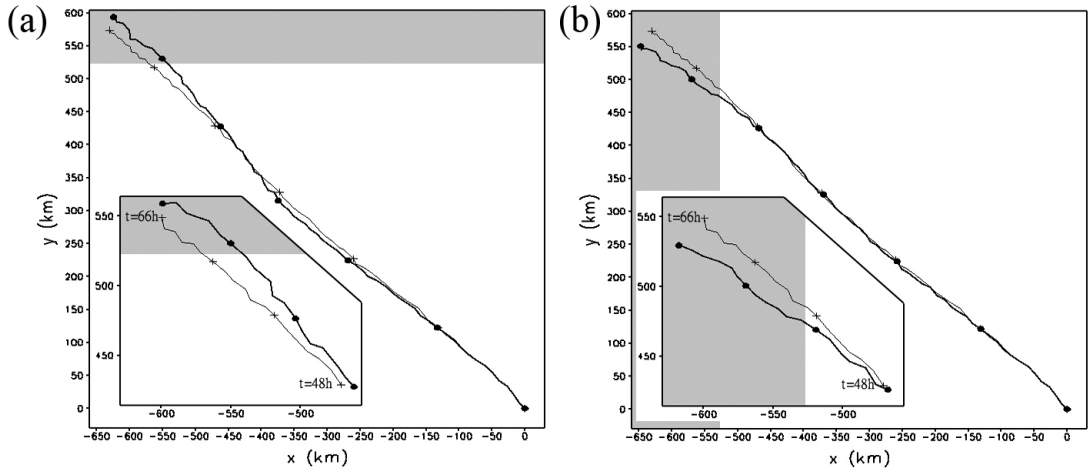

Fig. 3. Track (thick solid) and 12-hourly positions (dots) of the TC surface center in the experiment with (a) an east-west oriented and (b) a north-south oriented coastline on a beta plane. The thin line in each figure denotes the track and 12-hourly positions of the TC in a control experiment with no land. Land surface is shaded and the origin is the position of TC at the initial time (t = 0 h). The inset on the lower-left of each figure shows the enlarged area near landfall (from Szeto et al. 2009).

Szeto et al. (2009) explained this deviation by examining the differences in the flow patterns with and without the land. Because of the different orientations of the coastline, the superposition of the two inherent effects (the beta gyre circulation and the land-induced circulation) leads to different "net" flows (Fig. 4), and hence different convergence/divergence patterns near the land surface in the NS and EW experiments, which leads to different advection and convection patterns. Applying arguments similar to those in Wong and Chan (2006), they explained why such differences in the deviations occur.

The experiments in Wong and Chan (2006) and Szeto et al. (2009) all have uniform roughness in half of the domain. What if the roughness is different along the land mass, such as a river delta or urban vs. rural areas? To address this question, Au Yeung (2009) performed numerical simulations of the movement of an idealized vortex under differential roughness situations. She found that the vortex tends to be attracted towards the area with a higher roughness (Fig. 5), which again results from the modifications of the inherent gyres found by Wong and Chan (2006) so that the advection and convection patterns are modified. In the nSsR case (Fig. 5b), the deviation is so much that the vortex never makes landfall.

To summarize, in the presence of a roughness or moisture discontinuity, which is the case as a TC is about to make landfall, the track of a TC could be very different from that specified by the large-scale steering flow and the beta effect due to the development of a secondary circulation (the inherent gyres found by Wong and Chan 2006) that advects the TC differently and of asymmetric convection, both of

which modify the PV tendency caused by the large-scale processes. Unfortunately, such results are difficult to be verified with observations because all such factors are present in real TC situations and isolating one of the effects is difficult, if not impossible.

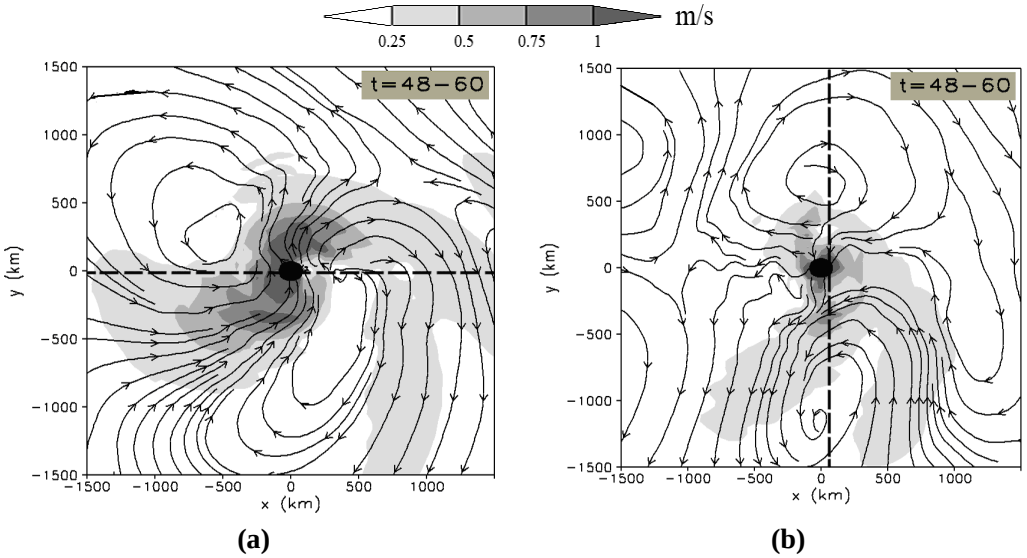

Fig. 4. Time composite during the 48-60 h period of the lower tropospheric (about 900-550 hPa) flow in the beta plane experiments with (a) an east-west oriented and (b) a north-south oriented coastline relative to the control experiment (without land). The TC center is denoted by a dot at the origin. Coastline is denoted by thick dashed line, with the land being to the north in (a) and west in (b) of the line. Shading indicates speed of the flow with the scale on the top of the figure (re-drawn from Szeto et al. 2009).

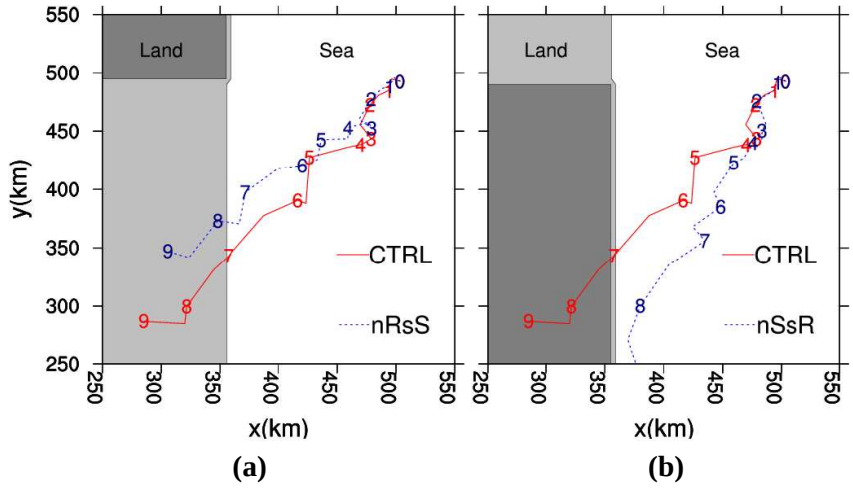

Fig. 5. Track of the TC surface centre (with 12-hourly TC positions) in the different experiments on an *f* plane with differential roughness over land. dark grey represents land with roughness length 0.5 m, light grey for 0.1 m and white area is the sea. (a) land rougher to the north (nRsS) and 9b) land rougher to the south (nSsR). CTRL (red) is the control experiment, i.e. uniform roughness over land. Numbers on the tracks are numbers of the days of integration. (re-drawn from Au Yeung 2009).

3. Changes in convection

Chan et al. (2004) examined radar echoes from four TCs that made landfall near Hong Kong and found that convection appears to be enhanced over the ocean in the offshore side of the TC. An example of this is shown in Fig. 6 for the case of Typhoon Sam. Such a result seems to "verify" the numerical simulation of Chan and Liang (2003) that an idealized vortex with the land moving towards it has more convection on the offshore side (Fig. 7). They explained this result in terms of the changes in atmospheric stability associated with the advection of dry air from the land surface. Note from Fig. 7, however, that after landfall, the maximum convection appears to be on the onshore side. A similar numerical result was obtained by Wong and Chan (2006). Liu et al. (2007) further analyzed cloud-top brightness temperatures of 12 TCs that made landfall in South China and obtained similar results (not shown). However, in a few cases, maximum convection was found to be on the onshore side and they attributed these to a strong vertical wind shear over the TC.

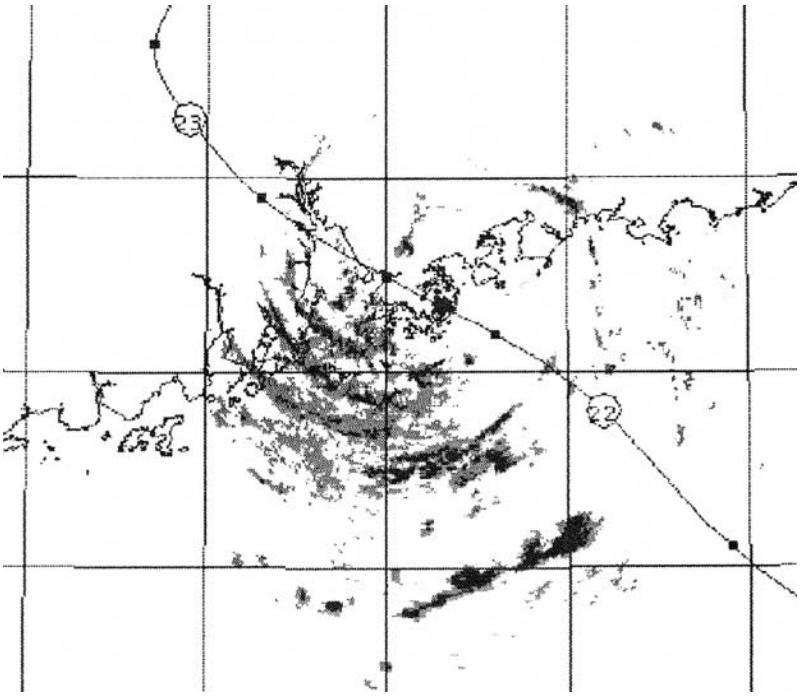

Fig. 6. CAPPI radar image (only reflectivity >36 dB is shown) of Typhoon Sam near Hong Kong at 0900 UTC 22 Aug 1999. Each dot is the 6-hourly position and the number indicates the position at 00UTC. The lat/lon grid is 1^o x 1^o (extracted from Chan et al. 2004).

Very recently, Fung (2009) analyzed hourly data from rain gauges in southern China during the times when a TC was 100, 50 km from the coastline and when it made landfall, and compared the average precipitation rate in the left and right front quadrants of the TC, with the division of the two quadrants being a perpendicular line to the coastline. She found that in most cases, the rainfall was more abundant in the right front quadrant (Table 1), irrespective of the distance of the TC from land, which is again consistent with previous modeling results.

All the numerical studies performed do not have any topography in the land portion of the domain, while the observational studies are for South China that has some mountain ranges with maximum heights of around 1.5 km. Recently, Wong and Chan (2009) examined radar imageries of typhoons that made landfall in Taiwan and found that for those that made landfall in northern part of Taiwan, maximum rainfall over the ocean was also on the offshore side. An example of this is shown in Fig. 8. However, those making landfall in the southern part have slightly different convection distributions (not shown). In these cases, changes in buoyancy associated with the downslope flow from Central Mountain Range may play a part, a hypothesis verified by Wong and Chan (2009) through numerical simulations. With the mountain topography removed, no such asymmetry was obtained.

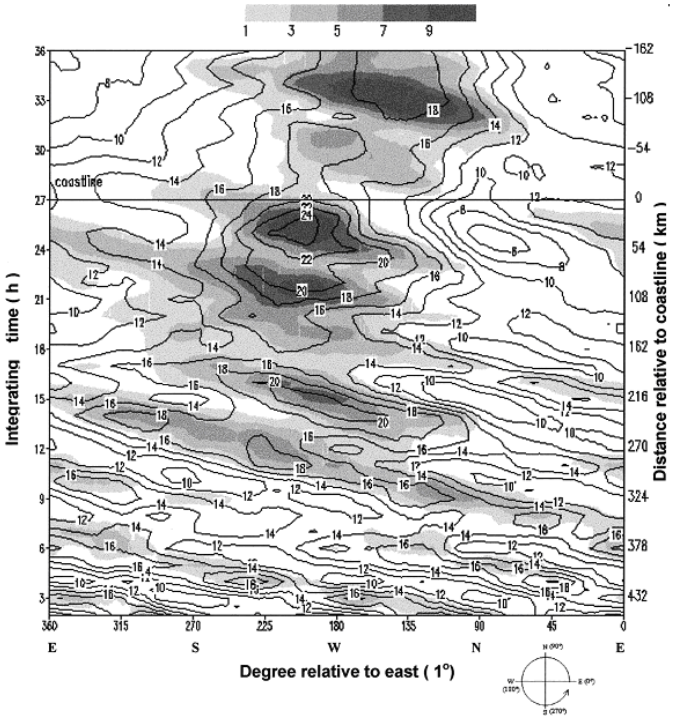

Fig. 7. Total hourly rainfall within 300 km at each azimuth of an experiment in which friction is enhanced and moisture flux turned off over land relative to the control run with no such changes. The shaded area is the amount of increase in rainfall (values indicated in the shaded bar at the top of the figure; unit: cm) compared with the control run. The horizontal line at 27 h indicates the time when the coastline meets the vortex center. Only contours of ≥ 6 cm are plotted (from Chan and Liang 2003).

Table 1. Average precipitation rate and standard deviation (mm h^{-1}) in the left-front and right-front quadrants of 22 TCs that made landfall in South China (from Fung 2009).

	Mean	Standard Deviation
Left Front Quadrant	16.31	15.16
Right Front Quadrant	31.05	21.93

To summarize, differences in roughness and moisture availability as well as topography also cause asymmetries in convection. However, vertical wind shear can modify the convection distribution as well so that in real situations, whether maximum convection occurs in the onshore or offshore side over the ocean and land will depend on all these factors.

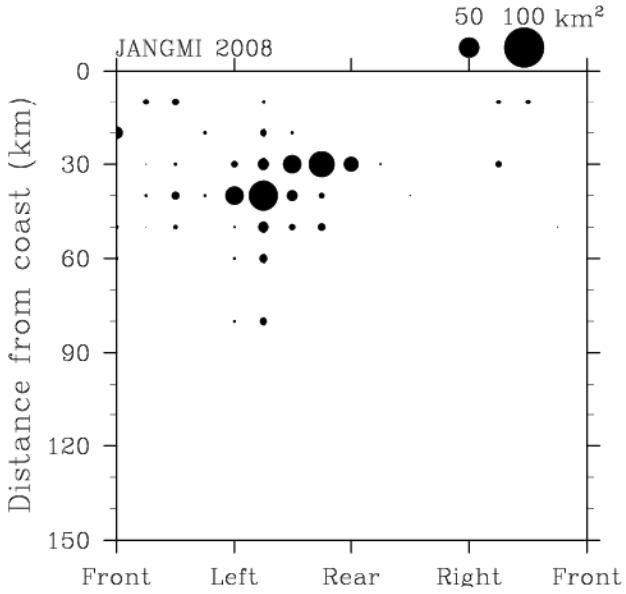

Fig. 8. Areas of strong radar echoes (composite reflectivity >= 55 dBZ) within 75 km from the centre of Jangmi as a function of distance from the coastline and azimuth direction (re-drawn from Wong and Chan 2009).

4. Summary and discussion

This paper reviews results from recent observational and numerical studies on changes in track and convection associated with TC landfall. They point to significant modifications of both the track and the convection distribution as a result of changes in friction and moisture availability, as well as topography. These results highlight the importance of correct representation of the boundary layer and topography in the real-time numerical prediction of TC track and convection.

Acknowledgments. The results presented here are compiled from papers and theses of various researchers and students from City University of Hong Kong, and are supported by the following research grants: CityU 100203 from the Research Grants Council of the Hong Kong Special Administrative Region Government, and 7001042, 7001994, 7002296 and 9610021 from City University of Hong Kong.

References

Au-Yeung, A. Y. M., 2009: The effect of a river delta and coastal roughness variation on a landfalling tropical cyclone. *M. Phil. Thesis*, City Univ. Hong Kong, 73pp.

Chan, J. C. L., F. M. F. Ko and Y. M. Lei, 2002: Relationship between potential vorticity tendency and

tropical cyclone motion. *J. Atmos. Sci.*, **59,** 1317-1336.

Chan, J. C. L. and X. Liang, 2003: Convective asymmetries associated with tropical cyclone landfall. Part I: F-plane simulations. *J. Atmos. Sci.*, **60,** 1560-1576.

Chan, J. C. L., K. S. Liu, S. E. Ching and E. S. T. Lai, 2004: Asymmetric distribution of convection associated with tropical cyclones making landfall along the South China coast. *Mon. Wea. Rev.*, **132,** 2410-2420.

Fung, K. Y., 2009: Rainfall distribution over land associated with tropical cyclone landfall in South China. *Forthcoming M. Phil. Thesis*, City Univ. Hong Kong.

Liu, K. S., J. C. L. Chan, W. C. Cheng, S. L. Tai and P. W. Wong, 2007: Distribution of convection associated with tropical cyclones making landfall along the South China coast. *Meteor. Atmos. Phys*, **97**, 57-68.

Szeto, K. C., M. L. M. Wong and J. C. L. Chan, 2009: Structure and track changes of tropical cyclones during landfall: Beta-plane simulations. *Submitted to Adv. Atmos. Sci.*

Wong, M. L. M. and J. C. L. Chan, 2006: Tropical cyclone motion in response to land surface friction. *J. Atmos. Sci.*, **63,** 1324-1337.

Wong, M. L. M. and J. C. L. Chan, 2009: Convection asymmetries associated with tropical cyclone prior to landfall over Taiwan. *Submitted to J. Geophys. Res.*

Terrain Effects on the Tropical Cyclone Rainfall over Taiwan

Tian-Chiang YEH[1], AND Chih-Pei CHANG[2]

[1]Pacific Science Association, c/o Naval Postgraduate School Code MR/Cp, Monterey, CA USA

[2]Department of Meteorology, Naval Postgraduate School, Monterey, California, USA

I. **Introduction**

Among natural disasters, tropical cyclones cause the most losses in Taiwan. The losses were mainly due to flooding, mudslides, and debris flows induced by the heavy rainfall of the tropical cyclones. In an analysis of a 20-year surface station dataset from 1971 to 1990, Chang et al. (1993) found that the mountainous terrain of Taiwan played a very important role on the modification of the surface structure and the rainfall distribution of tropical cyclones. A leeside low pressure center or trough was usually observed when a TC was near Taiwan. Rainfall was enhanced on the upslope facing the cyclonical flow and was depressed on the leeside. Due to the dominance of the terrain effects they were able to find the principle modes of the TC surface structure as a function of the geographic location of a TC center. The data set used in their study was based on 22 SYNOP stations and did not include the many automatic rain gauges installed since the late 1980s. This sparsely distributed station network not only was unable to show the details of the rainfall distribution over the complex terrain of the Taiwan Island, it contained no station over the large mountain areas in the northern and southern parts of Taiwan. It would be interesting to know whether and how major features of the terrain effect on tropical cyclones reported by Chang et al (1993) may change when more cases after 1990 are analyzed, and when data of the automatic rain gauges are included. This study extended Chang et al's study by using a 28-year data set starting from 1991 and includes the rainfall reports from 287 rain gauges over Taiwan (Fig. 1).

II. **Data**

In the first part of this study, empirical orthogonal function (EOF) pressure modes obtained from Chang et al. are compared with the EOF pressure modes of the TC cases in 1991-2008. Here the procedure to select cases follows Chang et al. They defined a domain of 19-27°N, 117-125°E and a TC was selected if the center based on the best track of JTWC was located inside the domain. All cases of the TC were included starting from 14 hours prior to the first occasion that its center entered the domain and ended 2 hours after its center left the domain. The data for these cases are the synoptic observations at 3 hours intervals in the selected period.

III. **Results and Discussions**

The first EOF pressure mode is a basic state of the low pressure system over Taiwan. Figure 2 compares the 2nd EOF pressure mode from Chang et al. (1993), shown on the left panel, and that computed from the 1991-2008 case, shown on the right panel. With the exception that patterns shown are in opposite phase, the results are very similar to each other. The isobars are mostly oriented

north-northwest to south-southeast with an out-of-phase distribution between the northeast and southwest parts of Taiwan. Similar similarities are found for the other leading EOF pressure modes and rainfall modes between the two studies. Thus there are no significant differences between the earlier and recent cases and the terrain effects on the structure and rainfall distribution of TCs over Taiwan discussed by Chang et al. (1993) are robust.

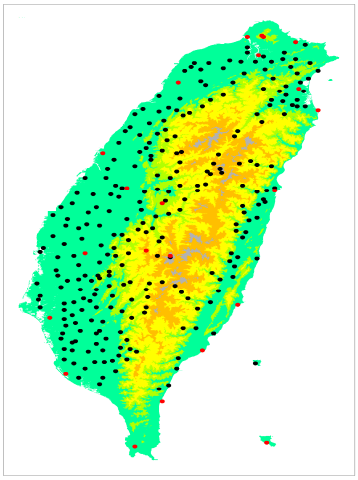

Figure 1. Distribution of the rainfall stations (dots) in Taiwan.

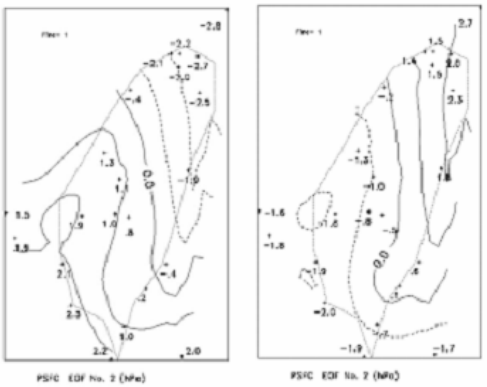

Figure 2. 2nd EOF pressure modes for cases of 1971-1990 (left) and 1991-2008 (right).

Chang et al. showed the averaged tropical cyclone rainfall over Taiwan is relatively small when the centers of the tropical cyclones are more than two degrees away from the coast. Therefore, only the rainfall of cases of TC centers inside the domain of 21°N to 27°N, 119°E to 123°E were examined. The domain is shown as the background map of Figure 3 with the coastal line of Taiwan appearing in the center to provide a geographic reference. The 24 panels in Figure 3 are arranged geographically in the 4° longitude x 6° latitude grids of this background map with a resolution of 1°x1°. Each of the panels shows the horizontal distribution of averaged rainfall rate (mm/h) when the center of a TC moves into the 1°x1° grid sub-domain where the panel is located. For example, the panel at the left-bottom corner of Figure 3 shows the averaged rainfall rate of TCs moving into the grid domain of 21°N to 22°N, 119°E to 120°E. These rainfall distributions gives much greater detail compared to

those shown by Chang et al.

To identify the 24 grid sub-domains, we use a coordinate system such that the notation SD(I,J) represents the I^{th} sub-domain from the left and the J^{th} sub-domain from the bottom, and RR(I,J) represents the rainfall rate distribution of the I^{th} panel from the left and the J^{th} panel from the bottom. For example, RR(4,4) is the averaged rainfall rate of the TCs that moved into the sub-domain of 24°N to 25°N, 122°E to 123°E. It shows that intense rainfall occurs over northern and northwestern Taiwan when TCs moved to the northeastern coast of Taiwan. The terrain effect is quite conspicuous: instead of heavy rainfall occurring near the center of the TC, it occurred on the upslope where the cyclonic flow encounters the mountains. Another rainfall rate maximum center is located in central Taiwan, east of the highest peak of the Central Mountain Range. The four small non-shaded areas in this and other panels need be treated as data-missing areas as rainfall stations installed in them are sparse and probably not representative.

Similar re-distribution of tropical cyclone rainfall was found from other panels of Figure 3. For TCs moving westward from SD(4,4) to SD(3,4), the intense rainfall is shifted from northern Taiwan southward to southwestern Taiwan. Again, the area of intense rainfall was over the upslope of the Central Mountain Range facing the cyclonic flow. The rainfall over southwestern Taiwan continues when TC moves further northwestward to north of the Taiwan Strait. This is the result of strengthened southwesterly winds, often occurring during the southwest monsoon season, that are induced by the TCs.

The distribution of the rainfall rate in Figure 3 can provide a climatology background to estimate the rainfall over Taiwan when a TC is invading. For example, Figure 4 shows the rainfall rates (mm/h) at 00 LST (left panel) and 18 LST on 8 August 2009 when Typhoon Morakot invaded Taiwan. The pattern of rainfall rate at 00 LST, with intense rainfall over northeastern and southwestern Taiwan, resembles RR(3,3) in Figure 3 when the center of Typhoon Morakot was in SD(3,3). At 18 LST, when Typhoon Morakot moved northwestward, the intense rainfall was over southwestern Taiwan. The rainfall rate pattern resembles RR(2,4).

For operational TC forecasts, factors that may cause deviation from the climatology have to be considered to provide a more accurate rainfall forecast. The rainfall rate of Typhoon Morakot and total accumulation were much larger than the climatology average. More discussion on the Taiwan terrain effects on TCs and the issue of applying climatology to TC rainfall forecast will be presented in the Workshop.

Reference

Chang, C.-P., T.-C. Yeh, and J. M. Chen, 1993: Effects of terrain on the surface structure of typhoon over Taiwan. *Mon. Wea. Rev.*, **121**, 734-752.

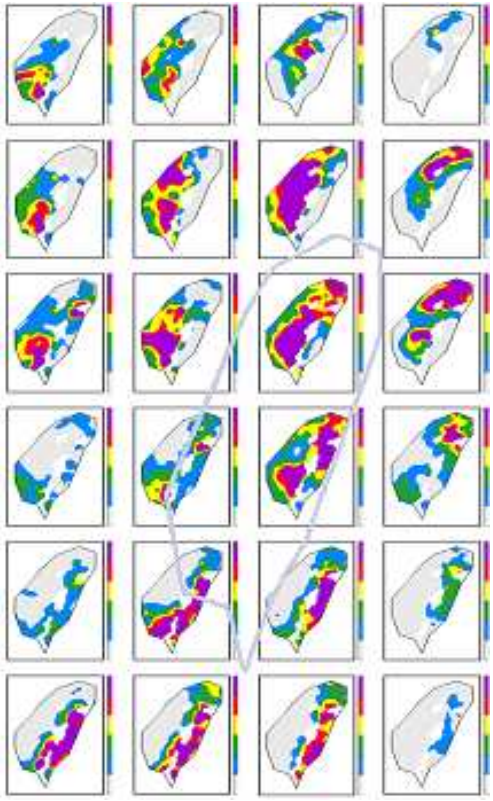

Figure 3. Each sub-diagram is the averaged tropical cyclone rainfall rate (mm/h) over Taiwan. Details see text.

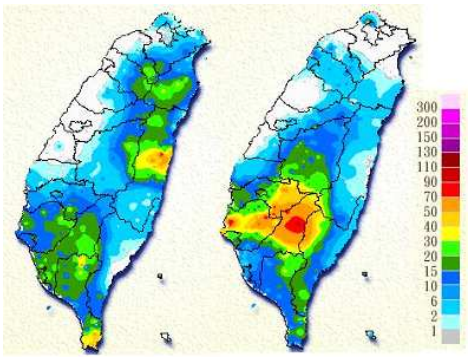

Figure 4. Hourly rainfall distribution in Taiwan during Typhoon Morakot at 00LST (left) and 18LST (right), 8 August, 2009.

Hydrological Perspective on Tropical Cyclone Forecasts

Jinping Liu

Hydrologist

UNESCAP/WMO Typhoon Committee Secretariat

Avenida de 5 de Outubro, Coloane, Macao, China
jpliu@typhooncommittee.org

ABSTRACT

Tropical Cyclone may cause severe heavy rainstorm and meanwhile may bring valuable water resources. The former frequently poses catastrophic flood disaster to human being including urban flood and waterlogging, flash flood and sediment disasters, etc. The latter could brilliantly benefit to human being especially in the water-scarce regions. This paper describes the main challenges faced by hydrological forecasting for the purposes of water resources management and flood risk management at present and introduces the achievements of concluded and on-going projects of Working Group on Hydrology of Typhoon Committee in recent years on flood forecasting and flood disaster prevention and reduction. Accordingly the paper discusses the requirement of hydrological forecasting and flood control on the forecasts of the trajectory and intensity of tropical cyclone and the associated precipitation for various purposes. Finally, the paper points out that direct communications among meteorological service, hydrological service and flood control department should be engaged in real time for hydrologists and decision makers to understand the probability of tropical cyclone forecasts and for meteorologists to understand the requirements of hydrological and decision-making issues.

1. Introduction

Because of the concomitant high intensity rainstorm, strong wind and high tide-surge, typhoon (tropical cyclone) may usually cause severe natural disaster, such as urban flood and waterlogging, devastating gustiness, catastrophic river flood, flash flood, sediment disaster including mud-flow, landslide and debris flow, which may cause huge damage to people's life and property.

On the other hand, the water resource has increasingly becoming a key and conditionality factor to the economic and social development in the most regions of the world, especially in Asia Pacific region. Because of the impact of climate change, extreme weather events, e.g. food (too much water) and drought (too less water), have been getting more and more frequent than before. The drought disasters may be occurring in the affected area and/or somewhere else when typhoon is approaching and landing. The rain brought by typhoon could become valuable water resource in the water-scarce regions.

In order to deal with water scarcity, "Rainwater Harvesting" has been internationally widely accepted as an effective measure to fully use rainwater for human well-being. The performance targets are expected to achieve (1) rainfall capture for the frequent small storms, (2) runoff control for infrequent storms and (3) flood risk management for rare extreme storms.

In this context, aiming to tropical cyclone related disaster reduction and floodwater utilization, hydrologists are expected to provide different forecasting products based on both observed rainfall and forecasted rainfall to the decision-making departments for the different purposes of water resources management and flood risk management, including discharge, water stage and runoff yield in the typhoon affected rivers, reservoirs and cities.

2. River Flood Forecasting and Warning

There are a number of hydrological models available for real-time operational flood forecasting at present, including lumped models, distributed models and semi-distributed models. Invariably, the basic structure of a hydrological forecasting system involves data inputs, model's response and product outputs (figure 1). For the outputs aiming to the especial purposes, the requirements to the data inputs may be variable on the spatial and temporal scale.

In addition to the dynamic precipitation data, the GIS-based hydrological model requires additional static geospatial data. The base model data consists of elevation, hydrological connectivity, channel cross-sections, permeable/impermeable surfaces, soils permeability, and drainage channels.

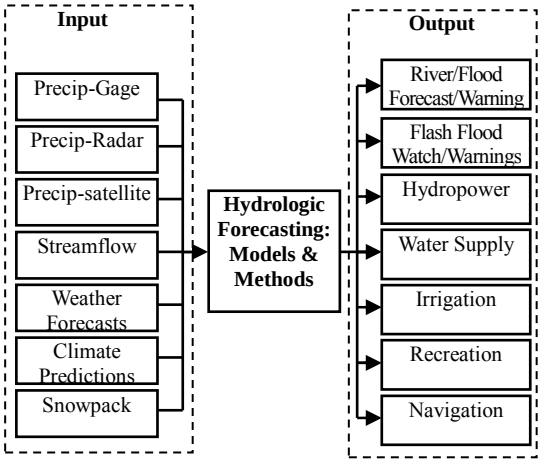

Fig. 1 Basic structure of hydrological forecasting system

2.1 Space Scale

As traditional hydrological model, the lumped hydrological models are commonly used as main approaches in the real time operational flood forecasting, in which where the catchment behavior is described by catchment scale parameters as a unit. The spatial resolution is linked to the schematization of the basin, which can be considered as a single element or an ensemble of sub-basins. In order to get the model's parameters matching the catchment's characteristics and insure the flood forecasting accuracy, the large river basin is usually divided into several or decades forecasting catchments based on the feature of topographic and geographic, type of soil, vegetation, the distribution of rainfall and hydrological observation stations, and the river system in the basin. The magnitude of the catchment area is usually variable from 10^1 to 10^3 km^2.

Figure 2 shows sketch map of forecasting catchments dividing in Hai River basin of China as an example. The total area of Hai river basin is 317800km^2. It is divided into 283 sub-basin as forecasting catchments. The smallest catchment is 30.6km^2 and the largest is 3100km^2.

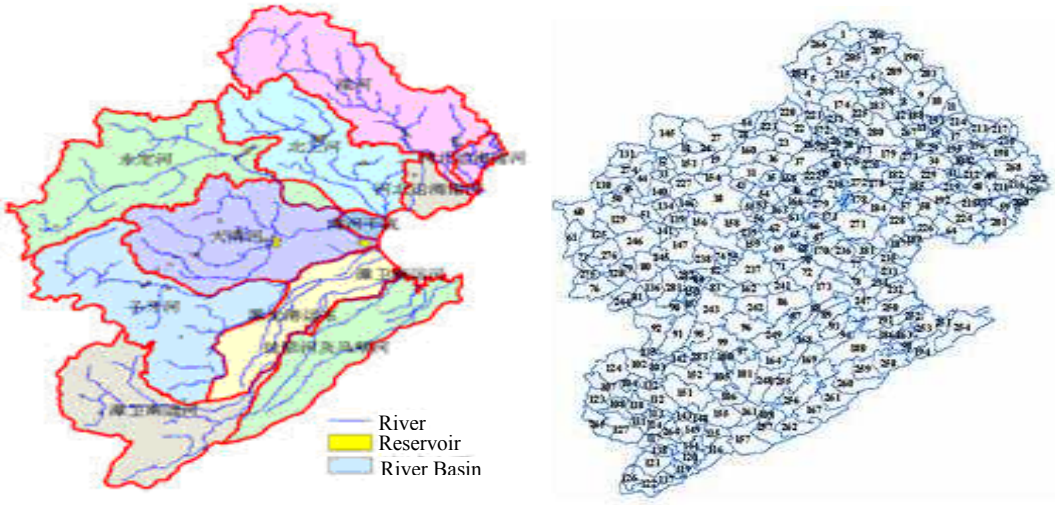

Fig. 2 Lumped hydrological model's forecasting catchments dividing in Hai River Basin of China

The distributed and semi-distributed hydrological models describes the hydrologic processes at small scale and then adding these up and routing the flows through the landscape by taking an explicit account of spatial variability of processes, input, boundary conditions, land use and wathershed characteristics provided by Digital Elevation Models (DEM). The scale of model grid can vary from 10^1m x 10^1m up to 10^3 m x 10^3m with the catchment area and the purpose of modeling. Considering the limitation of DEM and the computing speed, the solution of 1km x 1km ~ 4km x 4km is usually adopted in the real-time operational flood forecasting.

2.2 Time Scale

The time resolution depends on the objective of the forecasting and on the time scale of the catchment response. In the most cases, 6-hourly rainfall values are sufficient, but in rapidly responding catchments where an accurate representation of the peak is required, rainfall input must have a finer resolution. Considering the rapid flow concentration in mountainous catchments, hourly rainfall is required. In the flat catchments daily rainfall might be sufficient. It is strongly suggested to use data in hourly resolution for distributed hydrological models.

2.3 Desired Lead Time

The lead time of flood forecasting varies with the size of catchment and the availability of forecasted rainfall. Without the rainfall forecasting, theoretically, the maximum lead time is the concentration time of flow in the river basin after precipitation falls on the ground. For the decision makers, the desired forecasting lead time may be from several hours to several days according to the decision targets.

(1) Forecasting for early warning. hydrologists are required to provide river flood prediction products with lead time of 3 days at least to decision makers for flood disaster preparedness including warning issuing, dweller evacuation from flood prone area, material redeploying for flood defense and etc. In some main rivers, the lead time might be expected up to one week for some key points in downstream.

(2) Forecasting for real-time flood control. Based upon real-time observed rainfall and river stream flow and the operation of water projects, hydrologists are required to provide continual flood forecasting to the whole river system from upstream to downstream with lead time of 1 day at least or nowcasting for flood fighting, water dispatching and water projects operation.

(3) Forecasting for flood disaster rehabilitation. In order to meet the demands of promoting what is beneficial and abolishing what is harmful, hydrologists are required to provide the recession prediction up to 30 days in advance.

2.4 Meteorological Data Requirements

The basic meteorological data are rainfall and potential evapotranspiration. If snow melt has to be represented, temperature and radiation (optional) data are required. Based on the above discussion, there are some special requirements for meteorological data including Quantity Precipitation Estimated (QPE) and Quantity Precipitation Forecasts (QPF) in the future:

(1) As input of the lumped hydrological models, the 6 hourly observed and forecasted precipitation with the desired catchment-scale (10^2~10^3 km^2) are required.

(2) As input of the distributed hydrological model, temperature and precipitation data should be hourly. It is possible to use different precipitation input data type as radar data, satellite data or their combinations, and forecasted rainfall maps. All the data maps must have the same working region and resolution (less than 10^1km x 10^1km).

(3) As input of hydraulic flood routing model, forecasted storm surge at river mouth is required as model's lower boundary conditions. The time step of hydraulic model usually adopts several minutes so that to ensure the model's stability. Therefore, hourly water level forecasts at coast area suffered by storm surge would be sufficient for hydraulic river flood routing models.

Since the precipitation falling in various area (catchment) will cause the totally different flood situation and the totally flood control response, rainfall forecasts aiming to the river basin or catchment are strongly expected to hydrologist and decision makers of flood control.

3. Sediment Disaster and flash flood forecasting and Warning

Due to increased intensity and variability of rainfall, the risk of sediment disaster including flash flood, mudflow, debris flow, landslide, occurred in mountainous terrain area is trending to increase rapidly. As a result, the mortality risk in mountain area is getting much higher than before. The recent findings of the WMO shows that, where of the 139 countries responding to the WMO country-level disaster prevention and mitigation survey, 105 indicated that flash floods were among the top two most important hazards around the world and require special attention. Typhoon may be a major contributor to this situation.

With the promoting of the capacity of integrated disaster prevention and reduction, the observed absolute mortality in flash flood triggered by short-duration strong precipitation is getting down, but it is still approximately four times higher than other death in flood disaster. In China, for example, the proportion of the life losses caused by flash flood and sediment disaster to the total death caused by flood disaster is increased from 25% in early of 1990's to more than 80% at present.

3.1 Sediment Disaster Forecasting and Warning

Typhoon Committee (TC) Working Group on Hydrology (WGH) conducted a project named "Sediment Disaster (including debris flow and landslide) Forecasting and Warning System", led by Japan. This project provides a forecasting method of occurrence of rainfall-triggered sediment disaster to TC Members.

It is considered that sediment disaster does not occur only due to rainfall but terrain, geology and forest are involved complicatedly and optimum rainfall index will vary from a region to another. In the method, Critical Line (CL), Warning Standard Line (WL) and Evacuation Standard Line (EL) are set up based on historical record (figure 3 and figure 4).

In figure 7, with rainfall intensity (normally 10-minute, 30-minute, 1-hour rainfall, etc.) on the ordinate and total rainfall on the abscissa, and with occurrence rainfall and non-occurrence rainfall plotted by symbols ⊙ and ×, respectively, they can be grouped by a straight line or curve sloping (CL) down to the right. The lower left side to this CL is a safety area where sediment disaster will not occur and the upper right side is a dangerous area where sediment disaster may occur. CL in the method indicates an integrated index colligating the intensity and quantity of precipitation, geographic and topographic features and forest condition in the region of sediment disaster events.

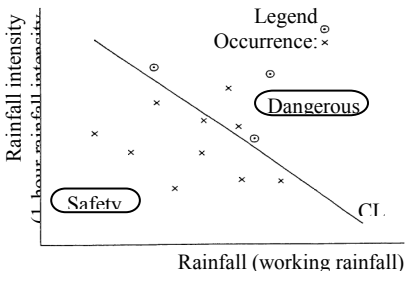

Fig. 7 Setting of sediment disaster

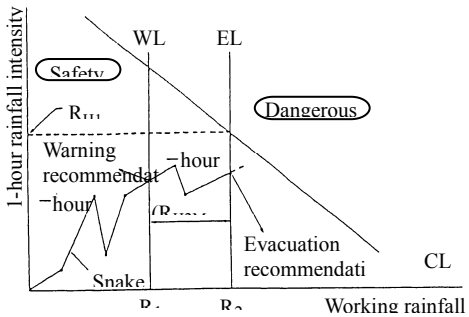

Fig .8 General Expression for EL

In practice, a warning recommendation and an evacuation recommendation can be issued when real-time rainfall data plotted at certain intervals cross WL and EL (R_{H1M} and R_{H2M} are the Maximum precipitation in the preceding one hour and two hours, respectively). The line connecting these plotted points is called a snake curve. About a minute is desirable as plotting time intervals in view of the warning and evacuation system.

In this method, short-time (normally 10-minute, 30-minute, 1-hour rainfall, etc) observed and forecasted rainfall value or QPE and nowcasting or QPF are expected. Even though hours lead time (nowcasting products) would play very important role in sediment disaster reduction, especially mortality risk reduction.

3.2 Flash Flood Forecasting and Warning

A flash flood can be defined as: "a flood that rises and falls quite rapidly with little or no advance warning, usually as a result of intense rainfall over a relatively small area". Flash floods are distinguished from other types of flooding by the short timescales over which flood-producing rainfall occurs (generally less than 6 hours) and the small spatial scales (generally less than 1000 km^2) of drainage basins in which flooding occurs. Most flash floods occur at night and, as would be expected, produce the most damage in urban areas. Aside from intense rainfall and small net storm motion, factors that contribute strongly to flash flooding are low permeability or saturated soils, impervious ground surfaces, and steep slopes. Failure of small to medium-sized dams, including debris dams, contributes significantly to the fatalities and damage associated with flash floods.

The purposes of flash flood forecasting are to provide flash flood watch and warning. Flash flood watching is to (1) inform the public of hydro-meteorological conditions which may cause flooding when the flooding is neither certain nor imminent; (2) provide advance notice on flooding possible within 36 hours; and (3) enable decision makers to monitor conditions more closely and elevate flood mitigation resources to a higher state of readiness.

Flash flood warning is to (1) issue when flooding is imminent; (2) provide advance notification of short-fused flood events which require immediate action to protect lives and property; (3) allow customers and partners to take immediate mitigation actions such as evacuation to higher ground.

The physical processes causing flash floods and river floods are not much different; however, predictive uncertainties tend to be greater for flash floods than for river floods. This is partly due to errors in rainfall data which tend to average out over the larger spatial and temporal scales associated with river floods. In addition, predictive models for river floods can be calibrated using streamflow observations at forecast points. Most regions where flash flood predictions are required do not have streamflow gages, even rain gages. The historical sediments disaster and flash flood events and their corresponding rainfall record are also hard to collect.

Both lumped and distributed models can be used in hydrological modeling of flash flood. Due to averagely Mean Area Precipitation (MAP), the high peak is very hard to be predicted by lumped models. With increasing of availability of geographic data and radar rainfall data, distributed or semi-distributed hydrological models are adopted widely in practice.

The precipitation data requirements for flash flood prediction includes (1) improved quality of precipitation estimates; (2) accurate high–resolution seamless multi-sensor gridded precipitation estimates (QPE); (3)nowcasting; (4) 3-days short-term (0-1 hour) high quality seamless QPF.

QPE and nowcasting are very important for flash flood warning. They refer to the estimation of rainfall up to the current time using multiple sensors (radar, rain gauges, satellite estimates) and the forecasting of rainfall out to 1-3 hours in the future based heavily on current observed data.

For flash flood forecasting and warning, it is expected that the precipitation analyses in a "basin world", which means all calculations are done over the areas of small basins. The spatial scale of precipitation estimates and forecasts is expected to be at 1km x 1km grid resolution. This gridded

precipitation is then converted to an Mean Area Precipitation (MAP) for a predefined set of watershed boundaries.

The coupled meteorological–hydrological nature of flash floods is becoming more and more evident. Prediction of flooding events will require interactive meteorological and hydrological models that introduce the new weather radar data and include feedbacks from the near-surface soil water to the atmosphere. Coupled hydrological–meteorological models should be constructed in a manner that permits prediction of the time and space distribution of both the rainfall and the resultant flooding.

4. Reservoir Flood Forecasting and Operation

A reservoir is a necessary infrastructure and plays a vital role in water supply, flood control, power generation, navigation, recreation, and environmental requirements, etc. Some reservoirs might serve for single purpose, but the most reservoirs serves for multi-purposes. Reservoir operators consider many factors simultaneously when making water release decisions to accommodate competing objectives. Reservoir regulation manuals provide the operator with guidance or "rules" for release decisions that are often based on conditions of reservoir inflow, pool elevation, and downstream flow rates, etc.

To enhance the capacity of reservoir operation, Typhoon Committee finalized a cooperation project in 2008 named "Guideline for Reservoir Operation in Relation to Flood Forecasting", led by Republic of Korea. Since flood control policies by reservoir operation can not be separated from more general, integrated, water management and planning, this guideline in public participation in reservoir operation will open. Such achievements indeed form a critical basis for any water related expert practitioner, decision maker, research, or representative of the civil society, considering to involve the general public and stakeholder in decision-making processes related to flood control by reservoir operation.

Reservoir regulation in flood season has to put the security of dam itself and flood security in downstream of the dam at the first priority, and then take into account the floodwater capture for water supply, power generation and agriculture irrigation, etc. The key variables governing the operation of flood control reservoirs are: (1) the available storage capacity, (2) the expected volume of inflow from an incoming flood, and (3) predicted precipitation in future. Although the residual storage is always known, the uncertainty regarding the expected inflow volumes and predicted precipitation makes reservoir regulation a challenging task.

There are many optimization models available for single- or group-reservoir regulation. The fundamental of reservoir regulation is the principle of water balance:

$$\begin{cases} \left(\dfrac{Q_t + Q_{t+1}}{2} - \dfrac{q_t + q_{t+1}}{2} \right) \times \Delta t = V_{t+1} - V_t = \Delta V \\ q = f(V) \end{cases}$$

in which, Q_t, q_t, V_t are respectively the inflow, outflow and reservoir storage at time t, and Q_{t+1}, q_{t+1}, V_{t+1} are respectively the inflow, outflow and reservoir storage at time $t+1$, with unit of V in m^3 and units of Q, I in m^3/s. Evaporation is usually neglected and is only considered for runoff calculation procedure during flood events. Δt is the time interval between time t and $t+1$, with unit in hour.

The inflow (Q) forecasting may use the same hydrological models and methods with river catchments forecasting. The space scale also may be the same.

The time interval (Δt) may vary with the variety scope of inflow. 1~6 hours may be acceptable for the reservoirs with small and steep catchment, and 12~24 hours for the reservoirs with large and flat catchement.

ΔV is the floodwater volume which will be remained in reservoirs after flood regulation. Multi-purpose reservoirs can be operated according to prioritized goals representing tradeoffs among flow and storage objectives. How much water should be released before the heavy rain to ensure enough

available storage for incoming flood without meaningless water-releasing, and how to operate the dam to release stably before rainstorm and during the flood to ensure the endurable flood risk in downstream is a real challenge to reservoir operators. That needs hydrologists to provide the precise forecasts with long enough lead time.

The estimation of the expected inflow volume is one of the major products of the methodologies. Ultimately, the regulation schedules are defined based on this volume, and thus, the adopted procedure for its estimation has great influence over the results. The stored water in reservoir may has to be pre-released if the inflow volume is predicted too much. The outflow process is decided by shape of forecasted inflow hydrograph.

Consequently, observed precipitation and QPE, QPF (intensity and total amount of precipitation) within the lead time of hydrological forecasting are essential and vital for the purpose. One-day lead time might be sufficient for small-scale reservoirs, but 1~3 days, even one-week lead time would be required for medium- and large-scale reservoirs.

5. Conclusions

In real time flood forecasting there are three main sources of uncertainty: the input measurements; the precipitation forecast; and the hydrological model. The most significant improvements needed are without doubt to improve the spatial and temporal distribution of rainfall intensity during tropical cyclone landfall, which is one of the most crucial parts for successful flood forecasts especially for basins characterized by a complex topography. Moreover, given the time steps used by the meteorological models in terms of model time resolution and time interval of forecast issue, aggregation or disaggregation procedures are necessary to fit an appropriate time step from a hydrological point of view.

Hydrologists need forecasts of the trajectory of typhoons and the associated precipitation for various purposes. The required horizontal resolution, temporal resolution and lead time of the precipitation forecast depend on the specific purpose as well as the scale of the river catchment. The precipitation forecast in the time scale of 1 day with the lead time of 3 days is required for the purpose of water resources management, drought relief and flood control for large basins. On the other hand, rainfall forecasts with intervals of 6 hours or less are required for flash floods, landslides, sediment disasters, and other hydrological requirements.

Direct communications between meteorologist and hydrologist should be engaged in real time for hydrologists to understand the probability of TC forecasts and for meteorologists to understand and the requirements of hydrological issues.

References

1. Typhoon Committee, Report on UN ESCAP/WMO Typhoon Committee Members Early Warning System, WMO/TD-No. 1475, 2009
2. UN ESCAP. Statistical Yearbook for Asia and the Pacific 2008, ST/ESCAP/2531
3. FFMPA User's Guide: http://www.weather.gov/mdl/ffmp/
4. Bull. Amer. Met.Soc. Prediction and Mitigation of Flash Floods. adopted by AMS Council, 2000.
5. Jinping LIU, Olavo Rasquinho, Derek Leong. Innovative Strategies for Effective Flood Management Focusing on Disaster Risk Reduction in TC Area. UN ESCAP/WMO Expert Meeting on Innovative Strategies Towards Flood Resilient Cities in Asia-Pacific. 2009

Forecasting Surface Impacts of wind, wave and storm surge

Bruce Harper BE PhD

Systems Engineering Australia Pty Ltd, Brisbane, Australia

Introduction

Land-falling tropical cyclones are capable of delivering devastating impacts in the near-coastal environment due to the effects of damaging surface winds, waves and storm surge combined with rapidly growing coastal populations, and set against a background of potential climate change influences.

While the ultimate defence against disaster is mitigation through long-term strategic planning and resilient design, accurate forecasting and warning remains an essential tactical component of emergency management to help reduce risks to life and property (Figure 1).

This paper provides an overview and summary of the relevant impacts, assesses present observational practice, predictive capabilities and procedures and considers future research needs and initiatives.

Figure 1 Schematic of tropical cyclone impacts.

Near-Surface Winds

For effective use by emergency managers (land or sea) and for boundary forcing of ocean (wave, surge) models, gridded surface wind swaths are essential products in a land-falling tropical cyclone scenario. Within this context, mean and gust winds are separately required.

Near-surface extreme winds are subject to a wide variety of influences that affect the ability to make reliable measurements and to effectively forecast local conditions (Figure 2). Also accurate surface wind measurements provide essential feedback to the forecasting and modelling environments (whether in operational or research modes). While there is a comprehensive WMO standard for wind measurement (e.g. WMO 2008; Chapter 5) it would seem that the recommendations therein are rarely fully implemented.

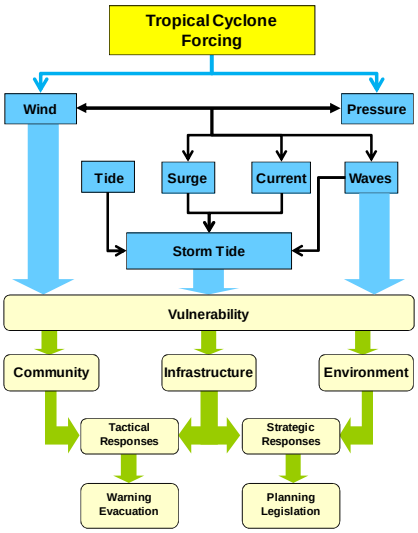

This may be because of physical limitations due to historical siting of instruments, urban development, cost of maintenance and calibration and the like, but also to a lack of appreciation of how significant some influences can be on the actual measurement of the wind in the near-surface land boundary layer.

The advent of remotely sensed near-surface winds over the ocean .e.g. by satellite (QuikScat, ASCAT, HIRAD) and aircraft (dropwindsonde and SFMR etc) and land-based Doppler radar introduces additional considerations in regard to sampling and averaging.

Observations

There are three essential aspects to be considered in respect of near-surface wind observations:

1. Instrument type and response
   - o A fast response is desirable (low inertia, quality bearings) with a "response length" < 5m.
   - o Cup and propeller sensors can suffer from over-speeding, sonic, hot-film and semi-conductor sensors may be rain-affected, buoys may be inertia and motion affected.
   - o Ruggedness and reliability is required for surviving extreme conditions.
   - o Maintenance and calibration requirements.
2. Sampling and processing
   - o Instrument response, sampling and processing define the "*measurement chain*", whereby each component acts as a series of filters.
   - o Sampling of at least 4Hz is required for accurate measures of turbulence and gust detection
   - o 10-min mean is the WMO standard synoptic metric to filter out high frequency turbulence and be more representative of numerical models.
   - o Shorter averages are described as "*gusts*" and "*lulls*" relative to the mean and typically described by the standard deviation or coefficient of variation (*turbulence intensity* in this context).
   - o The "*peak gust*" is the maximum (averaged over some duration) within a stated period of observation and so is a high-biased estimate of the true mean wind.
   - o The 3-sec peak gust is typically used in wind engineering design to represent forces on (static) structures such as typical buildings and houses.
   - o 1-min "*sustained*" winds used in tropical cyclone contexts are long peak gusts that overestimate the true mean.
3. Exposure
   - o Surface wind observations are made in the lowest part of the boundary layer where vertical shear is high, and the height of the sensor above local ground level is a critical parameter; the WMO standard height over land being 10m.

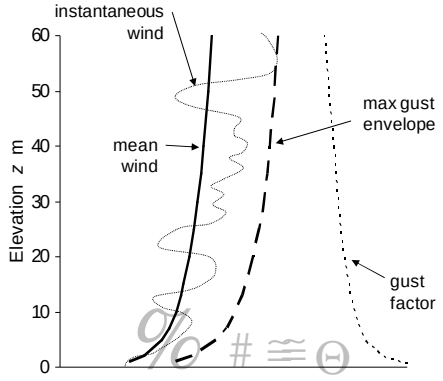

- On land, "o*pen terrain*" is a basic requirement for the immediate siting of instrumentation to avoid upstream aerodynamic effects. WMO (2008) defines open terrain as an area where the distance between the anemometer and any obstruction is *at least* 10 times the height of the obstruction.
- At sea, avoidance of local flow distortions (bridges, funnels, towers, cranes) should take precedence over standard height (it is difficult to remove localized effects from ship obs).
- Floating buoy measurements should be made at the highest possible elevation dependent on the diameter of the buoy (10m preferably).
- When sensors are located on the side of masts, they should be placed on booms with a length of at least three mast widths to avoid local blocking effects. Sensors placed on top of buildings or similar bluff bodies should be raised at least one building width above the top and data adjusted for non-standard height if necessary (likewise cliff-top locations should be particularly avoided).
- Obstacle and vegetation locations, height and terrain elevation changes should be documented on a map within a 2km radius and changes over time monitored to facilitate adjustments.
- Measured winds should be adjusted to account for site exposure, considering adjustments for azimuthally varying surface roughness and topographic effects (e.g. Powell et al. 1996). Analytic procedures are available and wind tunnel testing may be advisable in some circumstances.

For an up-to-date overview of the many specific observation platforms (land and sea) available for tropical cyclones and the associated uncertainties in their measurements, the reader is referred to Powell (2009).

Issues:

- The majority of surface wind observing stations are unlikely to meet the WMO guidelines in terms of response, sampling and exposure (Wieringa 1996). Airports are the most reliable sub-set.
- Changes over time in instrumentation, sampling and processing can introduce undetected biases and inconsistencies into wind observing networks.
- Manufacturers often do not publish detailed response characteristics of sensors.
- Definitions of how gusts are determined can appreciably affect the magnitudes (e.g. Miller 2007).
- WMO regional association documents presently do not adequately or consistently define mean and gust wind speed metrics and there has traditionally been lack of good guidance (Harper et al. 2006).
- Use of 1-min "sustained" winds in a mean wind context will overestimate ocean response (waves, storm surge) and total energy unless magnitudes or drag coefficients are reduced.
- Doppler radar-measured winds must be attenuated to obtain near-surface winds.
- Tropical cyclone wind turbulence characteristics appear essentially similar to extra-tropical.

Figure 2 Schematic of the vertical wind profile in a built environment.

Forecasting and Modelling

Outside of the Atlantic Basin, the Dvorak method remains the principle means of assigning the peak intensity of surface winds in a tropical cyclone, although there are many variants in detail that are regionally applied (e.g. Velden et al. 2006). Even with targeted direct surface wind measurements in the Atlantic (e.g. aircraft transects, dropwindsondes, SFMR, QuikScat if applicable), the Dvorak method influences intensity estimates through a variety of "model" pathways.

Critically, there is seemingly an attraction to the use of a *Vmax* as the single intensity estimate of a tropical cyclone for simplifying what is an otherwise extremely complex phenomenon. However, it is always necessary to also describe the spatial structure of the storm to obtain meaningful impact information of use

to emergency managers and to provide boundary conditions for ocean (wave and surge) models.

Accordingly, many agencies provide graphical representations of areas likely to be impacted by surface winds of various strengths. These are typically banded by Beaufort-scale descriptions of "gale", "storm" and "hurricane" force winds, aligned with forecast advisories based on largely symmetric wind radii and in some cases with probability contours. The way in which these products are prepared, however, seems to have remained largely undocumented and proprietary within agencies. One suspects therefore, that few if any of the present graphical wind structure products have an underlying robust "model" of the wind structure.

The graphical surface wind products could, for example, be underpinned by full 3D numerical modelling (e.g. MM5, HWRF, GFM etc albeit at generally crude resolution), diagnostic numerical boundary layer models (3D: e.g. Kepert 2001, 2002; depth-averaged or "slab" models e.g. Shapiro 1983, Thompson and Cardone 1996, Vickery et al. 2000), parametric modelling (e.g. Harper and Holland 1996, Willoughby at al. 2005), statistical best tracks data, real time observations, simply approximations or perhaps a subjective combination of the above. In some cases, allowance of decay of winds over-land might also be explicitly applied (e.g. Kaplan and DeMaria 1995, DeMaria et al 2006).

H*Wind, the sophisticated NOAA/AOML data assimilation tool (e.g. Powell 2009) is capable of fine scale depiction of surface winds over land and sea but remains experimental in an operational context, perhaps due to its apparently limited prognostic capabilities. Nevertheless it has much appeal for post-event impact assessments and the development underpinning H*Wind addresses the many complicating aspects of wind observations listed earlier.

Issues:

- The basis of the Dvorak *Vmax* representing a peak 1-min gust is weak; conversions to 10-min mean are also (historically) inappropriate for open sea.
- The traditional tendency to assign a single wind speed metric to a tropical cyclone is of limited practical value in a landfall situation, where detailed spatial and temporal information is essential for emergency management and also for ocean model boundary conditions.
- Warning products typically do not enforce the spatial context as a "wind scale", which can lead to public misunderstanding.
- "Wind scales" remain non-standard globally due to varying intensity intervals, descriptors and wind-averaging practices.
- Graphical wind speed products seem not to be underpinned by a "model" of the storm structure
- Impact models (wind, wave and surge) require tropical cyclone structure information and are generally "reconstructed" for that purpose outside of the mainstream intensity forecast process.
- Prognostic numerical models need to ingest winds that are consistent with their spatial and temporal scale (observation/data assimilation issues).
- Structural damage models are based largely on empirical calibration against actual events, which vary greatly for a range of regional and demographic reasons.

Possible Initiatives

The foregoing development in regard to forecasting of near-surface land-falling wind impacts suggests a range of possible initiatives (research and operational) for providing future improvements:

- Standardise wind nomenclature across WMO regions and national agencies.
- Standardise wind-scales to reduce public confusion (e.g. use of internet resources).
- Fully adopt WMO (2008) recommendations in regard to instrumentation, sampling and exposure. This should lead to detailed wind-tunnel or meso-scale modelling of some key compromised measurement sites to ensure they are calibrated to standard exposure. Software GIS-based tools could be developed to assist in analytical anemometer adjustment for less complex sites.
- Ensure all measured surface winds ingested by numerical models are standard exposure.
- Apply consistent exposure-based wind-averaging conversion factors (e.g. Harper et al. 2006).
- Regularly revisit and revise WMO guidelines on exposure, height adjustments and gust factors to keep pace with scientific developments.
- Ensure instrument reliability in extreme conditions.
- Increased density of surface land and sea wind sensors. Consider mobile instruments for research (e.g. Masters et al. 2005; Schroeder et al. 2009) or developing low cost mesonets.
- Cross-calibration of wind sensors to account for response, spatial and temporal averaging, matching with Doppler winds and identified coherent features such as boundary layer rolls.
- Utilise mesoscale data assimilation (e.g. H*Wind)
- Develop standardized models of wind structure (wind-pressure, scale, asymmetry, gradient to surface, surface roughness) to provide uniformity of descriptors, accumulate storm statistics and provide prognostic impacts guidance.
- Wind damage, economic and insurance loss models need significant investment to reduce uncertainties and assist in justifying mitigation efforts

Near-Shore Waves

Ocean waves are generated during the transfer of momentum from the wind to the sea. The growth of wave height is most rapid for higher wave frequencies (shorter periods or wavelengths) and when the wind speed matches the wave speed. As the wave field grows, complex wave-wave mechanisms then act to transfer the energy derived from the wind towards lower frequency (higher period or longer wavelength) components. If a constant wind speed persists for long enough, the wave growth process becomes self-limiting because wave breaking (e.g. white caps) prevents the sea from absorbing any more energy at that specific transfer frequency. This equilibrium condition is known as a *fully-arisen* or *fully-developed* sea and most commonly occurs under broad frontal storm conditions in open ocean environments at higher latitudes. In tropical waters, this condition may also occur during monsoons, periods of persistent trade winds or extra-tropical transition. Fully-developed seas are rarer close to the centre of tropical cyclones because of the constantly varying wind speed and direction in the inner vortex.

In the near-shore environment, the local coastal topography (capes, bays) typically limits the available *fetch* (or distance acted on by the wind) available for generating waves from some directions. Wave growth may be *fetch-limited* by the presence of barrier reefs, island chains and large sand shoals. Where the fetch is not physically limited, the wave height growth is termed *duration-limited*. Large, slow moving tropical cyclones, particularly in association with high-pressure ridges poleward, can create such conditions. Also, in fast moving extra-tropical transition settings the related effect of *fetch-trapping* can amplify wave heights in a resonance-like situation (e .g. Bowyer and McAfee 2005)

Individual ocean waves are dispersive, propagating through and away from the area of wind generation at speeds dependent upon their wavelength and the local depth, and at the mean angle of the wind. Traditionally the term *sea* is given to the shorter period (younger) wave, and *swell* to the longer period

(older) wave. These two wave components exist together, the swell propagating from a remote wave generating system, the sea being generated locally, relative to the swell component. Because of these differing sources, the mean direction of the two (or more) components is often also different, especially in tropical cyclones (refer Figure 3).

Because wave speed depends on depth of water, any wave that approaches contours of changing depth at an angle will experience *refraction*, whereby embayments tend to experience *divergence* of energy and headlands experience *convergence*. This is accompanied by *shoaling* resulting in a change in the height of the wave relative to its original deepwater condition. *Diffraction* is an additional process whereby energy is transferred laterally along a wave crest after experiencing a sharp (normally man-made) disturbance.

As a wave enters increasingly shallow water wave breaking will occur where the water particle velocity at

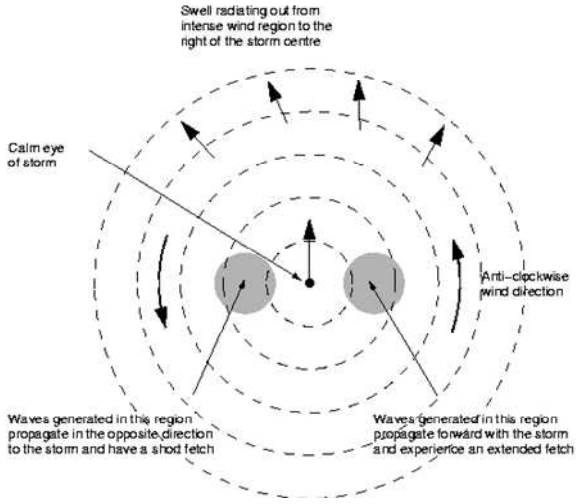

the crest begins to exceed the wave speed. Ultimately much of the energy of the wave is dissipated through turbulence and heat during the breaking process but the forward momentum flux or radiation stress within the surf zone can result in a quasi-steady superelevation of the local water level above the still water level. This phenomenon is termed *breaking wave setup* (Hanslow and Nielsen 1996). Coral reef cays and atolls can be especially susceptible to breaking wave setup effects (Gourlay 1996) in conjunction with tides. In swampy regions or when a coastal area is fully inundated and wave energy dissipates mainly through bottom friction, breaking wave setup diminishes. Likewise deep river entrances or channels may not experience or transfer wave setup. Wave setup is also often modulated by irregular wave height groupings, termed *surf beat*.

In addition to wave setup, any residual energy of individual waves is manifested as vertical *wave runup* of the upper beach face (Nielsen and Hanslow 1991). This allows some waves to attack at higher levels than the setup level alone or cause intermittent dune overtopping. Setup and runup influences are typically complementary whereby beaches having a low slope experience the majority of the energy dissipation as setup while very steep beaches experience higher levels of runup. In deepwater regions with sheer coastal cliffs, wave runup can become extreme and explosive, reaching elevations of twice the wave height (e.g. Cyclone *Heta* 2004, Niue).

Observations

Wave data is collected in a variety of forms but, due to the statistical nature of the sea state and its

near-linear characteristics, is normally used in directional spectral energy format, with the most common scalar parameters being the (equivalent) significant wave height Hs and peak spectral period Tp. Much of the global wave observation network has been established for commercial purposes (marine operations, oil and gas etc) but these also typically feed into the meteorological networks, together with atmospheric and ocean parameters. National wave data buoy systems have become increasingly established since the 1980s (e.g. NOAA NDBC, UK WaveNet, Australian State Governments etc) with the majority now offering directional information derived from pitch-roll-buoys, the latest using GPS rather than the more fragile accelerometer sensors.

Figure 3 Schematic showing the generation of waves in a translating hurricane (after Young 1999).

Some of the first insights into the complex wave fields in tropical cyclone conditions were obtained by aircraft mounted side-scan radars in 1978 and the NASA/SRA instrument is widely used in the USA (e.g. Walsh et al. 2002). Several countries also operate HF radar facilities (e.g. NOAA, UK/OSCR, AUS/COSRAD) that can provide spatial wave height information in addition to surface winds and currents, typically out to about 300km offshore. Wave staffs and pressure gauges are also utilised for non-directional measurements and velocity-pressure instruments for directional data. Satellite altimetry (e.g. Topex /Poseidon) can also provide wave height and derived wind speeds on polar orbiting transects that can be useful for model verification. Drifting wave buoys are also increasingly used for targeted deployments.

Issues:

- Wave height, period and direction observations in deep water are relatively routine and reliable, with well-established processing standards. Data are available around a variety of developed nations but the networks are still relatively sparse
- Point-measured wave data often differs from spatially derived (e.g. remotely sensed) data due to sampling and averaging techniques.
- Shallow water wave measurements in specific locations are relatively limited.
- Measurements of breaking wave properties (setup, runup and swash) are exceedingly rare and normally only obtained from brief periods of experimentation at specific sites.
- Post-storm surveys of beach debris levels are significantly affected by localised wave setup, runup and wind stress components.

Forecasting and Modelling

Numerical wave models used for generation and propagation are spectrally based and consider the evolution of the directional energy spectrum in time and space propagating under the action of a variety of source and dissipation terms. To select the most appropriate model requires an understanding of the relative importance of the various physical processes active in each domain. A modified form of classification presented by Battjes (1994) appears in Table 1, which divides wave prediction into four physical process domains.

Models can then be divided into two general classes: *phase resolving*, which predict both the amplitude and phase of individual waves, and *phase averaging* models which predict average quantities such as the spectrum or its integral properties. Should phase averaged properties vary rapidly (order of a few wavelengths) then a phase resolving model, with significant computational overheads, may be required. If not, then phase averaging models are adequate. These are then described by their treatment of the complex source terms into 1st, 2nd or 3rd generation models, each requiring increased computational effort.

Wave models should be selected on the basis of their suitability to a specific region rather than their absolute complexity, as there are many factors affecting their practical use. For example, 1st generation models can still be well suited to some enclosed or directionally limited near-shore regions (SWAMP Group 1985). Likewise many 2nd generation models (e.g. Sobey and Young 1988) continue to prove particularly accurate in many tropical cyclone situations. Where highly accurate wave height estimates are required close to the region of maximum winds, 3rd generation models (e.g. WAM, WAMDI (1988); WAVEWATCH, Tolman (1991); SWAN, Booij et al.(1996)) are recommended due to their ability to better cope with the rapidly changing wind directions and high stress regions (e.g. Jensen et al. 2006). Importantly though there are different variants for deep and shallow water situations or especially targeted versions for reef regions (e.g. Hardy et al. 2003).

Notwithstanding the capabilities of the available complex numerical wave models there is reliance on empiricism in regard to near-shore wave impacts, and analytical wave setup and runup formula (e.g. Nielsen and Hanslow 1991, Gourlay 1996, Stockdon et al 2006) are essential adjuncts to full model solutions. Also, for some open ocean forecasting purposes there is good skill and utility in simpler parametric models (e.g. Young and Burchell 1996, Bowyer and McAfee 2005).

Table 1 Relative importance of various physical processes in numerical wave modelling

Physical Process	**Deep Oceans**	**Shelf Seas**	**Shoaling Zone**	**Harbours**
Diffraction	⊗	⊗	°	∗
Depth refract./shoaling	⊗	•	∗	•
Current refraction	⊗	°	•	⊗
4 wave interactions	∗	∗	°	⊗
3 wave interactions	⊗	°	•	°
Atmospheric input	∗	∗	°	⊗
White-capping	∗	∗	°	⊗
Depth breaking	⊗	°	∗	⊗
Bottom friction	⊗	∗	•	⊗

⊗ - negligible; ° - minor importance; • - significant; ∗ - dominant (after Battjes 1994).

Issues:

- Spectral wave models have over time been empirically calibrated against specific and limited sets of wind and wave data.
- Recent measurements of drag coefficients in high winds suggesting saturation around 30 m/s are conceptualised in some models but not others (e.g. Moon et al. 2008).
- Wind averaging assumptions are of a similar order of magnitude effect to possible drag coefficient changes.

- Accurate wave modelling requires good wind structure representation up to 10 times *Rmax*
- Observed values of wave setup can vary greatly over short distance and in different environments
- Numerically modelled wave setup tends to significantly underpredict observed values
- Wave runup is a very localised phenomenon that requires knowledge of beach slope, dune elevations, vegetation and strata etc
- There is very little information on wave effects on domestic structures during storm tide inundation events (e.g. Kraus and Lin 2009)

Possible Initiatives:

While numerical wave modelling has proven quite accurate in deepwater situations, and propagation within shallow areas is well developed, the following issues remain of research and operational interest for land-falling tropical cyclones:

- The influence of the drag coefficient as it relates to relative wave age (steepness), wind-wave angle and wind speed
- Wind-wave and wave-current coupling effects
- Increasing the density of wave buoy networks
- Accurate bathymetry in coastal waters
- Accurate wind structure out to *Rgales*
- Overland dissipation due to vegetation and effects by and on the built environment
- Assimilation of future higher resolution satellite wind and wave data

Storm Tide

The term *storm tide* is used here in preference to the generic *storm surge* when describing the impact of a land-falling tropical cyclone. Importantly, surge is the *long wave* component magnitude related to the energetics of the storm, its size, track and speed and the specific coastal interactions. Then storm tide is the combination of that with the pre-existing astronomical tide and localised breaking wave setup component. Accordingly, storm tide refers to an absolute sea level elevation that can be related to land elevation and hence is applicable to assessing impacts (Figure 4).

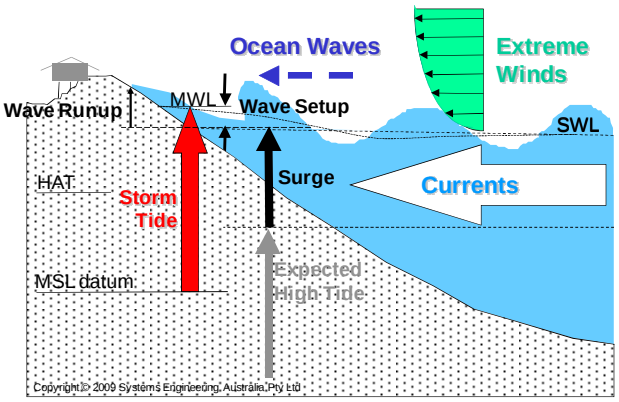

Figure 4 Schematic diagram of the components of storm tide. (after Harper 2001); MSL is the mean sea level, HAT is the highest astronomical tide level, SWL is the still-water level in the absence of surface waves, MWL is the beach-face mean water level due to breaking wave setup influence, wave runup elevation is normally referenced to the SWL.

The storm surge (or meteorological tide), is an atmospherically forced transient long wave ocean response caused by the extreme surface winds and low surface pressures. Severe tropical cyclones (<980 hPa) on or near the coast are capable of producing a dangerous storm surge (>3m), which can increase coastal water levels for periods of several hours and significantly affect over 100 km of coastline (Harper 2001, Dube et al. 2009). In regions with a significant tidal range, the phasing of the peak of the surge with the astronomical tide on the day normally dictates the degree of likely impact. Close to the position of the peak surge level, which is normally close to the region of maximum winds, the rate of increase in water height can at times be quite rapid, e.g. several metres in one hour and bores are possible.

Storms that are more remote from a coast but with large circulations may also generate synoptic scale responses of generally low magnitude (<1m) but that can persist for several days and likely interact with many high tide sequences. Depending on the specific environment these may manifest as coastally-trapped edge-waves (e.g. Kelvin-like, Yankovsky 2009), or basin-wide responses and seiching. These situations can readily cause widespread beach erosion and encroachment, and in conjunction with heavy rainfall may raise river tail-water levels and exacerbate near-coastal flooding.

The potential magnitude of the surge is affected by many factors - principally the intensity of the tropical cyclone, its size and forward speed. In deep water far from the coast the main contribution comes from the so-called *inverted barometer* effect - which is broadly a mirror image of the cyclone's own surface pressure profile in the underlying ocean. The local magnitude is about 10 mm per hPa of pressure deficit, relative to the ambient surface pressure far removed from the storm centre. Consequently, a Category 5 cyclone (e.g. 910 hPa) would produce a maximum pressure-induced surge component of about 1m directly below the eye in deep water. Islands with narrow continental shelves and in deep water away from the coast normally only experience the static effects of the pressure-induced surge. In such situations, breaking wave setup may represent the greater component of increased water levels. In shallow waters, the pressure surge component interacts with the bathymetry and coastal forms, and may become dynamically amplified at the coastline to levels approximately twice the offshore levels.

By contrast, the influence of the severe surface wind shear on surge levels is confined largely to the shallower waters of the continental shelf. The wind-induced surge component is depth dependent, increasing with decreasing water depth and normally responsible for the greater proportion of surge height at the coastline. Flat, shallow and wide continental shelf regions are therefore much more effective in assisting the generation of large storm surges than are narrow, steep shelf regions. Storm surge magnitude can often be regarded as linearly proportional to the intensity for a given coastal site but can be highly site specific due to local factors. The relative horizontal scale (e.g. *Rmax*) of the cyclone is also important in determining the length of affected coastline.

When normally dry land becomes inundated during a severe storm tide episode, the sea begins to quickly flood inland as an intermittent wave front, driven by the initial momentum of the surge, products of wave setup and runup and the local surface wind stress. This flow then reacts to the local ground contours and the encountered hydraulic roughness due to either natural vegetation or housing and other infrastructure. It will continue inland until a dynamic balance is reached between the applied hydraulic gradients, wind stress and the land surface resistance or until it becomes constrained by elevation. As the storm abates or the tide reduces, an ebb flow is created that is often responsible for observed coastline scouring after such events.

Observations

Storm tides are most reliably recorded by permanently located and continuously operated water level gauges optimised for recording tides and not subject to breaking wave influences. While this ensures accurate detection of the broadscale tide+surge component it does not measure the wave setup that may be significant elsewhere. As previously mentioned, measuring of wave setup is extremely difficult because of its localised effects. Remote sensing (aerial and satellite imagery) is especially useful in mapping impacts and debris lines after an event and may become of increasing use in forecasting where significant aerial monitoring capability exists (e.g. NASA/SRA).

Issues:

- Tide gauge network density is often inadequate to detect the peak of a coast-crossing storm.
- Gauges not designed for the likely storm surge magnitudes may be damaged and data lost.
- Real-time gauges provide important feedback to forecasters of pre-cursor water levels that may not be fully represented in a model.
- Beach debris levels will include locally complex influences of wave setup and runup.
- Inland inundation heights may include local wind stress effects that can raise water levels above oceanic levels.

Forecasting and Modelling

Numerical modelling of storm surge over large spatial domains has been successfully undertaken for the past 30 years (Bode and Hardy 1993, Harper 2001, Dube et al. 2009) and is well established. The most common approach is to numerically solve the 2D depth-integrated shallow water equations (i.e. barotropic) at scales appropriate to the applied forcing and the coastal features. Normally Coriolis, bed friction (with some empiricism) and advective components are included. While 3D barotropic and baroclinic models are also widely available, they are more complex to initialize, more expensive to operate, and normally only applied in response to specifically identified regional sensitivities. The choice of numerics (FD or FE, implicit, explicit), discretisation (regular, spherical, or triangular), and transition (nested or coupled) vary according to needs and preferences. Many models implement wetting and drying (although this can be problematical in terms of numerical stability) and “constant volume” models are becoming more popular in this context.

Tides are increasingly fully modelled due to the availability of global constituents but this can prove difficult in some complex areas where bathymetric data is poor and if measured constituents are available for specific high impact sites they may be preferable. In such cases linear addition is often acceptable but should be verified by numerical experimentation and a non-linear interaction factor can be devised for operational purposes if necessary. This will often be <10% effect and will likely attenuate peak levels relative to the assumption of independence.

In regions of significant coastal waterways and riverine environments with good data and potentially high impacts, very sophisticated models can now be developed that show high levels of accuracy (e.g. < 0.3m, Westerink et al. 2008). However, in most areas of the world, and especially the high-risk developing nations, suitably good data is typically unavailable. Nevertheless, with careful consideration of the environments, accuracy of the order of 0.5<1.0m for forecasting are not necessarily unrealistic aims.

Coupled surge-wave models have become more popular, incorporating consideration of the wave radiation stress (responsible for wave setup) in the momentum flux. However, the correct coupling extends to

bottom stress and surface stress to make the models especially complex. When properly calibrated, this results in a new balance of still empirically-dependent assumptions.

In spite of the ready availability of numerical ocean models for storm surge prediction, many agencies appear not to have fully embraced their use, and empirical (e.g. Nickerson 1971) are apparently still widely used. This likely reflects the level of resources available to implement operational products and the traditional separation of numerical atmospheric and ocean expertise. However it may also reflect forecaster preferences for simplified hands-on approaches of similar utility to the Dvorak method for intensity estimation. Accordingly there remains a place for parametric or hybrid approaches to storm tide forecasting that provide a significant increase in warning capability with relatively low overhead and can incorporate powerful Monte Carlo ensembles. Australia, for example, with its extensive and complex tropical coastline, has adopted such techniques with benefit (Harper 2001, Harper et al. 2009).

Issues:

- Model domains and physics must be constructed to address the regional coastal scales, oceanic and meteorological influences.
- Accurate bathymetry in shallow water (<50m) or reef areas where bed friction is important.
- Tide plus surge in conjunction with accurate land elevations are required to estimate impacts.
- Storm surge model accuracy is a function of the supplied wind forcing and its inherent uncertainty, which should be transferred into the storm tide prediction via ensemble simulations.
- In the face of data limitations (tide, bathymetry, land elevation, wind structure and air/sea observations) overly complex models will likely be counter-productive.
- Accurate winds within 12 hr of landfall and within 5 to 7 *Rmax* are essential for surge modelling.
- Calibration and verification of storm tide models remains an essential factor in their development.

Possible Initiatives

Lack of quality data (atmospheric, bathymetric and topographic) is the principal barrier to accurate storm tide forecasting, combined with limited agency resources. Some possible initiatives in this area are:

- Capacity building in developing nations at highest risk, especially increased understanding of the regional contributions to storm tide risk and emergency management options.
- Risk studies could be done as a first-pass assessment of impacts allowing concentration on identification of the primary storm tide components in specific regions and targeting of data to address those needs.
- Development of simplified forecasting tools suited to local needs. While these might involve numerical modelling in various ways, the operational tool need not be complex or onerous.
- The availability of forecast gridded wind fields (as previously discussed) would greatly facilitate improved forecasting of storm tide impacts.
-

References

Battjes J.A. 1994: Shallow water wave modelling. Proc. Int. Symp.: Waves - Physical and Numerical Modelling, Vancouver, 1-23.

Bode L. and Hardy T.A., 1997: Progress and recent developments in storm surge modelling. *J Hyd Engin*, 123, 315–331.

Bowyer P.J., and A.W. MacAfee, 2005: The Theory of Trapped-Fetch Waves with Tropical Cyclones—An Operational Perspective. *Weather and Forecasting*, 20, 229–244.

DeMaria M., Knaff J.A. and Kaplan J., 2006: On the Decay of Tropical Cyclone Winds Crossing Narrow Landmasses. *J. Appl. Meteor. Climatol.*, 45, 491–499.

Dube S.K, Murty T.S., Feyen J.C., Cabrera R., Harper B.A., Bales J.D. and Amer S. (2009) Storm surge modeling and applications in coastal areas. In Chan J. (Ed.) Global Perspectives on Tropical Cyclones, *World Scientific*, (in press).

Gourlay M.R. 1996: Wave setup on coral reefs. 1. Set-up and wave-generated flow on an idealised two dimensional horizontal reef. *Coastal Engineering*, 27,161-193.

Hanslow D.J. and Nielsen P. 1993: Shoreline setup on natural beaches. *J Coastal Res*, Special Issue 15, 1-10.

Hardy T.A., McConochie J.D. and Mason L.B., 2001: A wave model for the Great Barrier Reef. *Ocean Eng*, 28 (1), 45-70.

Harper B.A. and Holland G.J. 1999: An updated parametric model of the tropical cyclone. Proc. 23rd Conf. Hurricanes and Tropl Met, *AMS*, 10-15 Jan.

Harper B.A. (ed.), 2001: Queensland climate change and community vulnerability to tropical cyclones - ocean hazards assessment - stage 1, Systems Engineering Australia Pty Ltd in association with James Cook University Marine Modelling Unit, *Queensland Government*, March, 375pp.

Harper B.A., Kepert J. and Ginger J., 2008: Wind speed time averaging conversions for tropical cyclone conditions. 28th Conf Hurricanes and Trop Met, *AMS*, Orlando, 4B.1, April.

Harper B.A., Hardy T.A. and Mason L.B. 2009: Developments in storm tide modelling and risk assessment in the Australian region. Proc. WMO/IOC JCOMM 1st Scientific and Technical Symposium on Storm Surges, Seoul, Korea, 2-6 Oct, 2007. *Natural Hazards*, Vol 51, 1, Oct, 225-238.

Jensen R.E., V.J. Cardone and A.T. Cox, 2006: Performance of Third Generation Wave Models in Extreme Hurricanes. 9th International Wind and Wave Workshop, *ASCE*, Sept 25-29.

Kaplan J. and DeMaria M., 1995: A simple empirical model for predicting the decay of tropical cyclone winds after landfall. *J. App. Meteor.*, 34, No. 11, 2499-2512.

Kepert J.D. 2001: The dynamics of boundary layer jets within the tropical cyclone core - part I: linear theory. *J. Atmos. Sci.*, 58, 2469-2484.

Kepert J.D. 2002: The impact of landfall on tropical cyclone boundary layer winds. Proc. 25th Conf Hurricanes and Tropical Meteorology, *AMS*, San Diego, 335-336.

Kraus N.C. and Lin L., 2009: Hurricane Ike along the upper Texas coast: an introduction. *Shore & Beach*, Vol 77, 2, 3-8.

Masters F., Reinhold T., Gurley K. and Powell M. 2005: Gust factors observed in tropical cyclone landfalls. Tenth Americas Conference on Wind Engineering, *ASCE*, Baton Rouge.

Miller C. 2007: Defining the effective duration of a gust. Proc. 12th Intl. Conf. Wind Engin., ICWE12, Intl. Asoc. for Wind Engin., *IAWE*, July 2-6, Cairns, 759-766.

Moon I.J., I. Ginis, and T. Hara, 2008: Impact of the reduced drag coefficient on ocean wave modeling under hurricane conditions. *Mon. Wea. Rev.*, 136, 1217–1223.

Nickerson J.W. 1971: Storm surge forecasting. Navy Weather Research Facility, Tech Report 10-71.

Nielsen P. and Hanslow D.J. 1991: Wave runup distributions on natural beaches. *J Coastal Res*, Vol 7, No 4, 1139-1152.

Powell M. D., S. H. Houston, and T. A. Reinhold, 1996: Hurricane Andrew's landfall in South Florida. Part I: Standardizing measurements for documentation of surface wind fields. *Weather and Forecasting*, 11, 304–328.

Powell M.D. 2009: Near-surface-based observations of tropical cyclones. In: Chan J. (Ed.) Global Perspectives of Tropical Cyclones, *World Scientific* (in press).

Schroeder J.L., Edwards B.P and Glammanco I.M., 2009: Observed tropical cyclone wind flow characteristics. *Wind and Structures*, Vol 12, 4, 349-381.

Shapiro L.J., 1983: The asymmetric boundary-layer flow under a translating hurricane. *J. Atmos. Sci.*, 40, 1984 - 1998.

Sobey R.J. and Young I.R. 1986: Hurricane wind waves -- A discrete spectral model. *J. Waterways Port Costal Ocean Eng.*, 112, 370-389.

Stockdon H.F., Holman R.A., Howd P.A. and Sallenger A.H. Jr., 2006: Empirical parameterization of setup, swash, and runup. *Coastal Engineering*, Vol 53, 7, May, 573-588.

SWAMP Group, 1985: Ocean wave modeling. *Plenum Press*, New York, 256pp.

Thompson E.F. and Cardone V.J. 1996: Practical modeling of hurricane surface winds. *J. Waterway, Port, Coastal and Ocean Eng.,* 122: 195–204.

Vickery P.J., Skerjl P.F., Steckley A.C., Twisdale L.A. 2000: Hurricane wind field model for use in hurricane simulations. *J. Engineering Structures,* 126, 1203–1221.

Velden C., Harper B., Wells F., Beven J.L., Zehr R., Olander T., Mayfield M., Guard C., Lander M., Edson R., Avila L., Burton A., Turk M., Kikuchi A., Christian A., Caroff P. and McCrone P. 2006: The Dvorak tropical cyclone intensity estimation technique: a satellite-based method that has endured for over 30 years. *Bulletin American Meteorological Society*, Vol 87, Sept, 1195-1210.

Walsh E.J. et al, 2002: Hurricane Directional Wave Spectrum Spatial Variation at Landfall. *J. Phys. Ocn.*, 32, 1667–1684.

Westerink J.J., R.A. Luettich, J.C. Feyen, J.H. Atkinson, C. Dawson, H.J. Roberts, M.D. Powell, J.P. Dunion, E.J. Kubatko, and H. Pourtaheri, , 2008: A basin- to channel-scale unstructured grid hurricane storm surge model applied to Southern Louisiana. *Mon. Wea. Rev.*, 136, 833–864.

Wieringa J. 1996: Does representative wind information exist? *J. Wind Engineering and Industrial Aerodynamics*, 65, 1-12.

Willoughby H.E., Darling R.W.R. and Rahn M.E., 2005: Parametric representations of the primary hurricane vortex. Part II: A new family of sectionally continuous profiles. *Mon. Wea. Rev.*, 134, (4), 1102-1120.

WMO 2008: Guide to meteorological instruments and methods of observation. WMO-No. 8, 7th Ed, 681pp.

Yankovsky A.E. 2009: Large-scale edge waves generated by hurricane landfall, *J Geophys Res*, 114, C03014.

Young I.R. and Burchell G.P. 1996: Hurricane generated waves as observed by satellite. *Ocean Eng,* 23, 761-776.

Young I.R. 1999: Wind generated ocean waves. *Elsevier Sciences Ltd.*, 306pp.

Air-Sea Interactions in Tropical Cyclones

Lynn K. Shay

Rosestiel School of Marine and Atmospheric Science

University of Miami，Miami, Florida, 33157, U.S.A.

nshay@rsmas.miami.edu

1. Introduction

Significant progress has been made in the area of upper ocean response and air-sea interaction during tropical cyclone (TC) passage over the global oceans. Here, we will review progress in this topical area as described in Shay (2009) over the past two decades since Ginis (1995). One theme that has resurfaced is the idea of integrated thermal structure on TC intensity. Briefly, Leipper and Volgenau (1972) demonstrated that the 26°C isotherm depth and the upper ocean's thermal structure, known as oceanic heat content (OHC), has important implications on TC intensity variations:

$$\mathrm{OHC} = c_p \int_0^{D26} \rho\left[T(z) - 26\right]\, dz,$$

where c_p is specific heat at constant pressure, D26 is the 26°C isotherm depth, and OHC is zero when SST decrease to less than 26°C. While their ship-based measurements were not acquired under directly forced TC conditions, post-pre OHC differences demonstrated the importance of this integrated ocean thermal energy.

The most apparent effect of TC passage is the marked SST cooling, and by proxy the OML temperature response, of typically 1 to 6 °C occurring to the right (left) of the storm track by 1-2 radii of maximum winds (Rmax) in the northern (southern) hemispheres. These larger *biases* of the maximum SST decreases and OML depth increases of 20 to 40 m are usually due to entrainment mixing of the cooler thermocline water with the warmer OML (see Fig. 1) associated with vertical shear of the horizontal currents across the OML base. Ocean mixing and cooling are principally a function of wind-forced currents and their associated shears ($\partial v/\partial z = S$). These wind-forced currents are often associated with near-inertial response (periods close to f^{-1}, where f is the local Coriolis parameter). While the forced current structures have large vertical scales, near-inertial shears across the OML base tend to be associated with shorter vertical wavelengths (e.g., higher order baroclinic modes) that reduce the Richardson numbers (defined as the ratio of buoyancy frequency (N^2) and (S^2)) to below criticality values (Price *et al.* 1994; Shay et al. 1998; Sanford *et al.* 2005; Jacob *et al.* 2003; Shay 2009). Other physical processes are associated with the OML heat budget through surface enthalpy flux (sensible and latent heat :Q_o)
, upwelling of colder isotherms from the thermocline processes and advection by the horizontal current field.

Parameterizations of momentum, heat and moisture transfers are further complicated by sea state, sea spray and the complexities of the upper ocean. There is a level of mutual dependence of the air-sea transfer processes of heat, moisture and momentum as suggested in idealized model simulations (Emanuel 1995) that intensity is sensitive to the ratio of enthalpy and drag coefficients (c_k c_d^{-1}, where c_k is the bulk enthalpy coefficient and c_d is the surface drag coefficient). The conclusion that this quantity probably lies within a rather limited range ($\leq$1.5) is commensurate with the observation that most TCs do not usually reach their maximum potential intensity (MPI).

2: Oceanic States

Coupled models to predict hurricane intensity change are being used to issue forecasts to the public who increasingly rely on the most advanced weather forecasting systems to prepare for landfall (Marks and Shay 1998). Oceanic models will have to include realistic initial conditions to simulate not only the oceanic response to hurricane forcing (Sanford *et al.* 2007; Price *et al.* 1994; D'Asaro 2003, Jacob and Shay 2003; Black *et al.* 2007; Shay and Uhlhorn 2008; Jaimes and Shay 2009), but also to simulate the atmospheric response to oceanic forcing (Bender and Ginis 2000; Bao *et al.* 2000; Shay *et al.* 2000; Hong *et al.* 2000; Walker *et al.* 2005; Lin *et al.* 2005,2009 ; Wu *et al.* 2007; Ali *et al.* 2007, Manielli *et al.* 2008; Shay and Brewster 2009). The atmospheric response is related to the level of feedback from the oceanic responses.

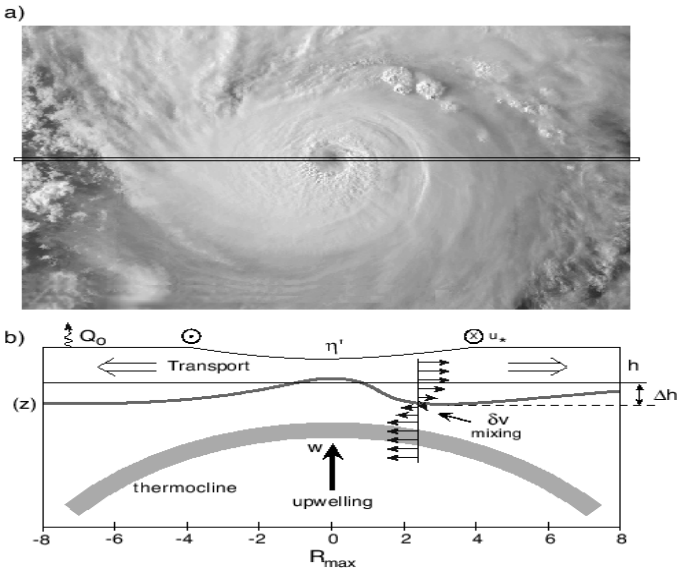

Figure 1: a) TC image and b) a cartoon depiction of basic physical processes forced by hurricane winds such as shear-induced mixing and OML deepening, upwelling due to transport away from the center, and surface heat fluxes from the ocean to the atmosphere, all of which may contribute to ocean cooling during TC passage (from Shay 2009).

Assimilative ocean modeling efforts and feature based model initialization are effective methods for providing initial boundary conditions to the oceanic and coupled TC prediction models (Falkovich *et al.* 2005; Halliwell *et al*. 2008; 2009). It is now fairly clear that the ocean model used in forecasting must be initialized so that surface height anomaly (SHA) features are in the correct locations and temperature and salinity profiles, and hence the OHC and OML depths are realistic. For example, ocean forecast systems based on Hybrid Coordinate Ocean Model were evaluated in the northwest Caribbean Sea and Gulf of Mexico for Sept 2002 prior to TCs Isidore and Lili, and for Sept 2004 prior to TC Ivan (Halliwell *et al.* 2008). In the NW Caribbean Sea, the thermal structure hindcast followed

the September climatology but does not reproduce the larger OHC value found in the observed profiles (Shay and Uhlhorn 2008).

The OML heat budget and ensuing air-sea fluxes are influenced by the choice of entrainment mixing parameterizations across the OML base. Contrasting viewpoints on this entrainment mixing topic have been focused on documenting the differences between 1-D and 3-D responses to TC passage (Jacob *et al*. 2000; Jacob and Shay 2003; Yablonsky and Ginis 2009; Halliwell *et al*. 2008, 2009). Away from strong oceanic fronts, the 1-D approach seems to be valid in that advective tendencies by weak background currents are considered to be nonessential in modeling efforts especially for moderate to fast moving TCs (Price *et al*. 1994; Schade and Emanuel 1999). The modified 1-D column approach follows from this approach except that the domain is initialized with differing thermal structure. In the horizontal plane, temperature (and hence density) gradients have to geostrophically adjust prior to turning on the TC forcing. If the ocean is not in geostrophic balance, simulations (i.e. levels of SST cooling) will be unrealistic due to a mass field imbalance. The adjusted, steady-state ocean currents are small compared to a translation speed of most TCs (e.g., Froude number). In regimes where strong pressure gradients exist, the bulk Richardson number instability, which is at the core of the "1-D assumption", remains at critical levels only for a short period (Uhlhorn 2008) that limits SST cooling and OML deepening. In a 3-D ocean model with realistic ocean conditions for the Gilbert case, Jacob and Shay (2003) simulated OML temperatures and compared with observed profile data and found that the three higher-order turbulent mixing schemes lead to a more accurate ocean response simulation with a WCR present. However, in most basins, strong fronts and currents are often located very close to the coast (Kuroshio, Gulf Stream, etc) and must be accounted for in forecasting landfalling TCs as they represent an additional TC energy source (Marks and Shay 1998).

3: Oceanic Response

During TC Gilbert (1988), the sampling strategy was designed to measure the momentum and thermal structural variations from pre, during and two cold-wake experiments in a quiescent area of the western GOM (Shay *et al.* 1998). Temperatures and OML depths revealed that Gilbert induced an SST decrease of 3.5^{o}C to the right of the storm track associated with deeper OML of up to 70 m. The spatial evolution of the response indicated a near-inertial, wave-like pattern. Jacob *et al.* (2000) assessed the various contributions to the observed OML heat and mass budgets during and subsequent to Gilbert's passage. Advection of temperatures by the background currents accounted for 5% of the heat budget near the track and up to 15% of the budget in the WCR, whereas the wind-forced current advection was much weaker. Estimated surface fluxes contributed 10% to the heat balance between the track and 3 Rmax. In this quiescent ocean, cooling in the wake was dominated by entrainment heat flux induced by the shear at the OML base by forced near-inertial currents behind the eye. In front of the storm, the wind stress accounted for a similar fraction of cooling for the asymmetric based on Powell and Houston (1996) winds. More recently, measurements from TC Frances revealed an SST decrease of 2.3^{o}C based on drifter and float measurement deployed during the CBLAST experiment (Black *et al.* 2007).

The ocean's momentum response is classified into two regimes: the directly-forced or near-field; and the evolving 3-dimensional wake or far-field. In the near-field, the cyclonically-rotating wind stress field of a TC causes OML currents of about 1 to 1.5 m s^{-1} to diverge from the storm track

starting within one-quarter of an inertial wavelength (Λ) which is the product of the storm translation speed (U_h) and the local inertial period (IP) as noted above. This current divergence causes the upwelling of cooler water underneath the storm track, thereby decreasing the OML depth. Over the next half of the inertial cycle, OML currents converge towards the storm track, causing an increase in the OML depth as warmer water is downwelled into the thermocline. This alternating cycle of upwelling and downwelling of the isotherms (and isopycnals) occurs over distances of Λ and establishes horizontal pressure gradients that couple the OML to the thermocline as part of a spreading 3-dimensional wake (Price et al. 1994; Shay *et al.* 1998, 1992; Zedler *et al.* 2001; D'Asaro 2003; Sanford *et al.* 2007). In this context, the near-inertial wake response has been fairly well observed and modeled during TC passage. Observations of the ocean current response to TC passage have been generally sparse over the global oceans as the community has had to rely on fortuitous encounters with buoys and moorings deployed in support of other experiments or ships crossing TC wakes (Teague *et al.* 2007, Zedler *et al.* 2001). Surface currents have also been shown to impact the direction of the surface wind stress which may be important in high wind conditions (Drennan and Shay 2006) and affect the wind-forced surface waves (Sanford *et al.* 2007).

For forced near-inertial motions, currents rotate anticyclonically with depth in the northern hemisphere in time as energy propagates downward into the thermocline while the phase propagates upward . This has been observed in current profilers in Gilbert (Shay et al. 1998), moored ADCP measurements in Ivan (Teague *et al.* 2007), and EM/APEX floats deployed in Frances during CBLAST (Sanford *et al.* 2005, 2007). Gilbert current profiles revealed a predominance of the anticyclonic-rotating energy where the average ratio of the anticyclonic to cyclonic energies was 3.6 (e.g., preference for downward energy propagation from the OML). The corresponding vertical energy flux indicated an average value of ~2 ergs cm^{-2} s^{-1} (Shay and Jacob 2006).

4: Global Monitoring:

The thermal structure is affected by the momentum response during TC passage. However, the level of ocean cooling depends crucially on the initial OML and the 26°C isotherm depths and the strength of the stratification (N) across the base of the OML as noted. In many basins, the 26°C isotherm depth is located near the OML base. Integrated thermal energy reflects the vertical distribution of the thermal energy in the OHC estimation. Since the amount of work done on the OML scales as the surface friction velocity (u_*^3), the deeper the layer (e.g., 26°C isotherm), the higher the stress-induced turbulent mixing is needed to redistribute OML properties through shear-induced instabilities. In this framework, high OHC (100 kJ cm^{-2}) values, strong buoyancy frequencies (N~20 cph), and lower latitudes (10 to 20°) affect the thermal structure and that decrease the negative feedback during TC passage. This is one reason why no cold wakes are apparent in the Eastern Pacific warm pool regime (Shay and Brewster 2009).

Global ocean monitoring for isotherm depths, thermal structure and OHC given the relative paucity of *in situ* profiler measurements with perhaps the exception of the global ARGO float network. Thus, satellite remote sensing offers the optimal approach to infer isotherm depths and OHC variations . Measurements from radar altimeter missions of the SHA field from NASA TOPEX, Jason-1 and 2, U.S. Navy Geosat Follow-On-Mission (GFO), Envisat and ERS-2 (Cheney *et al.* 1994; Scharroo *et al.* 2005) and SSTs are used in a reduced gravity model (e.g., Goni *et al.* 1996) with hurricane season climatology (Mainelli –Huber 2000). Since mesoscale ocean features only move a

few km d^{-1}, altimeter-derived SHA locates warm (cold) features that are usually identified as positive (negative) values as observed during TC's Opal (Shay *et al.* 2000), Ivan (Walker *et al.* 2005; Halliwell *et al.* 2008), Katrina and Rita in the Gulf of Mexico (Mainelli *et al.* 2008 ; Shay 2009), Maemi (Lin *et al.* 2005, Wu *et al.* 2007), Chaba and Songda (Wada and Usui 2007) in the western Pacific Ocean basin, and cyclones in the Bay of Bengal (Jena *et al.* 2006; Ali *et al.* 2007).

In the western Pacific Ocean, Lin *et al.* (2005) analyzed remote sensing imagery prior and subsequent to the passage of TC Maemi in 2003 where intensity increased by 36 m s^{-1} over an eddy-rich oceanic regime where SSTs exceeded 29.5°C. Based on results from the Coupled Hurricane Intensity Prediction System (Emanuel 2003), the WCRs acted as an insulator between TCs and the deeper thermocline water (Wu *et al.* 2007). Lin *et al.* (2009) argue that there needs to be translational speed dependence on the available OHC and the 26°C isotherm depth for TCs to reach category-5 status. Based on temperature data from ARGO floats (Lin *et al.* 2008), specific isotherm depths ranges and OHC values were determined for differing TC speeds. Another example of this impact was observed during TC's Katrina and Rita as they both deepened to a Cat-5 TC over a bulging, lobe-like structure along the LC's western flank (Scharroo *et al.* 2005; Shay 2009; Jaimes and Shay 2009). There was a one-to-one correlation between TC intensity (surface pressure decreases) and OHC values exceeding 100 kJ cm^{-2} in the LC. Background SSTs of more than 30°C were nearly uniformly distributed in this regime, and did not reveal the complex LC and bulging WCR structure in the central Gulf of Mexico (Shay 2009). Mainelli *et al.* (2008) input OHC into the SHIPS (DeMaria *et al.* 2005) and found that OHC is a better indicator of TC strength than just SST alone.

5. Air-Sea Interface:

Due to limited observations at the air-sea interface in high-wind conditions, the understanding has not progressed nearly enough to significantly improve the parameterization of momentum and energy transfers between the two fluids. The relationships of the transfer processes of small-scale roughness (Charnock 1955) and stability are understood under moderate-wind conditions (Large and Pond 1981), but additional phenomena not typically observed such as the sea state maturity (Donelan et al. 2004; Moon *et al.* 2004a,b) and sea spray (Wang *et al.* 2001; Andreas and Emanuel 2001) have been shown to modulate the heat and momentum exchange.

Surface winds in TC's have been estimated remotely using the Stepped-Frequency Microwave Radiometer from aircraft (Uhlhorn *et al.* 2007). They developed a new emissivity and wind speed model function based on comparisons with direct measurements of surface winds in hurricanes by GPS dropwindsondes. This function eliminates a previously-documented high bias in moderate SFMR-measured wind speeds (10 to 50 m s^{-1}), and additionally corrects an extreme wind speed (>60 m s^{-1}) systematic underestimate in the past cases. The model function behaves differently below and above the hurricane wind speed threshold (32 m s^{-1}).

Enthalpy (heat and moisture) fluxes across the interface and into the atmospheric boundary layer are critical elements to TC's (Emanuel 1995). Momentum transfer between the two fluids is characterized by the variations of wind with height and a c_d that is a function of wind speed and surface roughness. Using GPS sondes (Hock and Franklin 1999) deployed in the TC boundary layer, Powell *et al.* (2003) found a logarithmic variation of mean wind speed in the lowest 200 m, a maximum speed at 500 m, and a gradual weakening with height to 3 km. From these estimates, the

surface stress, roughness length, and neutral stability drag coefficient determined by the profile method suggest a leveling of the surface momentum flux as winds increase above hurricane-force and a slight decrease of the drag coefficient with increasing winds.

Donelan *et al.* (2004) described a series of tank experiments and found a "saturation" of the drag coefficient does appear once the wind speed is ~ 33 m s^{-1}. Beyond this speed, the surface does not become any rougher. The saturation level for c_d is ~0.0025, corresponding to a roughness length of 3.35 mm from the laboratory results. Powell *et al.* (2003) found a "saturation" of the drag coefficient at 0.0026 at about 35 m s^{-1} that decreased at higher wind speeds using wind profiles normalized by a mean boundary layer wind. Shay and Jacob (2006) found a "saturation" wind speed at 30 m s^{-1} of 0.003 where c_d began to leveled off at surface wind speeds up to 38 m s^{-1}. A similar approach was used from the TC Ivan data set (Teague *et al.* 2007). Jarosz *et al. (*2007). found a peak value of 0.0026 at 32 m s^{-1} before decreasing. Sanford *et al.* (2007) estimated the volume transport per unit of width based on velocity profiles in TC Frances using surface drag coefficients of Powell *et al.* (2003) and Large and Pond (1981) formulations. Numerical simulations from a mixing model embedded in the 3-D ocean model (Price *et al.* 1994) indicated consistent results for the volume transport and SST cooling values at two of the three floats to the right of the storm track. Along the track, however, differences differed by about 15 to 20%. As Sanford *et al.* (2007) point out, an azimuthal dependence in the surface drag coefficient due to surface waves (Wright *et al.* 2001) must be included in the models.

The momentum flux is parameterized with a non-dimensional surface roughness (Charnock's equation) and the stability correction based on similarity theory. Moon *et al.* (2004a,b) investigated the Charnock coefficient under TC conditions using a coupled wind-wave (CWW) model. In the CWW model, the surface wave directional frequency spectrum near the spectral peak is calculated using the WAVEWATCH III (Tolman 2002) model and the high frequency part of the spectrum was parameterized using the theoretical model of Hara and Belcher (2002). The wave spectrum is then introduced to the wave boundary layer model of Hara and Belcher (2004) to estimate the Charnock coefficient at differing wave evolution stages. The regression lines between the wave age and the Charnock coefficient have a negative slope at low wind speeds but have a positive slope at higher wind speeds. This slope change occurs between 25 and 35 m s^{-1} consistent with these saturation estimates above.

Direct turbulent flux measurements were carried out in the hurricane boundary layers using a research aircraft instrumented with fast-response turbulence sensors (Black *et al*. 2007).The wind speed range for momentum and enthalpy fluxes and exchange coefficients has been extended by over 50% compared to that in previous studies. The drag coefficient (c_d) increase linearly with 10 m wind speed up to 22 m s^{-1} then level off at higher wind speed (French *et al.* 2007). The Dalton number (c_E) is nearly constant with 10 m wind speed up to 30 m s^{-1} (Drennan *et al.* 2007). Combining the sensible and latent heat flux measurements, Zhang (2007) derived the enthalpy flux and the exchange coefficient for enthalpy transfer (c_k) showing that there is no evidence of an increase of c_k with wind speed, in good agreement with the Humidity Exchange over the Sea (HEXOS) result (DeCosmo *et al.* 1996) . The ratio of c_k/c_d versus wind speed for the flux runs with both momentum and enthalpy flux measurements. The average of the c_k/c_d values is 0.63 well below the 0.75 threshold for TC development (Emanuel 1995).

Acknowledgments: The author gratefully acknowledges support from the NSF, NASA Hurricane Science Program, MMS and NOAA JHT program. Several scientists shared material for the review book chapter to be published in GPTC-II. Dr. Jeff Kepert provided an insightful review and the patience of the Editors Drs. Johnny Chan and C. P. Chang is acknowledged. WMO kindly provided travel support.

References:

Ali, M. M., P. S. V. Jagadeesh, and S. Jain, 2007: Effects of eddies on Bay of Bengal cyclone intensity, *EOS,* **88**, 93,95.

Andreas, E. and K. A. Emanuel, 2001: Effects of sea spray on tropical cyclone intensity. *J. Atmos. Sci.*, **58,** 3741-3751.

Bao, J.-W., J. M. Wilczak, J. K. Choi, and L. H. Kantha, 2000: Numerical simulations of air-sea interaction under high wind conditions using a coupled model: A study of hurricane development. *Mon. Wea. Rev.*, **128**, 2190-2210.

Bender, M. and I. Ginis, 2000: Real-time simulation of hurricane-ocean interaction. *Mon. Wea. Rev.*, **128,** 917-946.

Black, P. G., E. A. D'Asaro, W. Drennan, J. R. French, P. P. Niiler, T. B. Sanford, E. J. Terrill, E. J. Walsh, and J. Zhang, 2007: Air-sea exchange in hurricanes: synthesis of observations from the Coupled Boundary Layer Air-Sea Transfer experiment. *BAMS,* **88**, 357-384.

Bosart, L., C.S. Veldon, W.E. Bracken, J.Molinari, and P.G.Black, 2000: Environmental influences on the rapid intensification of hurricane Opal (1995) over the Gulf of Mexico. *Mon. Wea. Rev.*, **128**, 322-352.

Braun, S. A. and W.-K. Tao, 2000: Sensitivity of high resolution simulations of hurricane Bob (1991) to planetary boundary
layer paramterizations. *Mon. Wea. Rev*., **128**, 3941-3961.

Chen, S., J. F. Price, W. Zhao, M. Donelan, and E. J. Walsh, 2007: The CBLAST Hurricane program and the next generation fully coupled atmosphere-wave-ocean models for hurricane research and prediction., *BAMS*, **88**, 311-317.

D'Asaro, E. A., 2003: The ocean boundary layer under hurricane Dennis. *J. Phys. Oceanogr*., **33**, 561-579.

DeCosmo, J. B., K. B. Katsaros, S. D. Smith, R. J. Anderson, W. A. Oost, K. Bumke, and H. Chadwick, 1996: Air-sea exchange of water vapor and sensible heat: The Humidity Exchange over the Sea (HEXOS) results. *J. Geophys. Res*., **101**, 12,001-12,016.

Donelan, M. A., B. K. Haus, N. Reul, W. J. Plant, M. Stiassine, H. Graber, O. Brown, and E. Saltzman, 2004: On the limiting aerodynamic roughness of the ocean in very strong winds. *Geophys. Res. Letters*., 31L18306,doi:1029/2004GRL019460.

Drennan, W. M. and L. K. Shay. 2006: On the variability of the fluxes of momentum and sensible heat. *Bound. Layer Meteor.,* **119(1)**, 81-107.

Drennan, W. M., J. A. Zhang, J. R. French, C. McCormick, and P. G. Black, 2007: Turbulent fluxes in the hurricane boundary layer, Part II: Latent heat flux. *J. Atmos. Sci.,* **64,** 1103- 1115.

Emanuel, K A., 1986: An air-sea interaction theory for tropical cyclones Part 1: Steady-State maintenance**.** *J. Atmos. Sci.***, 43,** 585-605.

Emanuel, K A., 1995: Sensitivity of tropical cyclones to surface exchange and a revised steady-state model incorporating eye dynamics**.** *J. Atmos. Sci.* **, 52,** 3969-3976.

Falkovich, A., I. Ginis, and S. Lord, 2005: Implementation of data assimilation and ocean initialization for the coupled GFDL/URI hurricane prediction system. *J. Atmos. and Ocean. Tech*., **22**, 1918–1932.

French, J. R., W. M. Drennan, J. A. Zhang, and P. G. Black, 2007: Turbulent fluxes in the hurricane boundary layer. Part 1: Momentum flux. *J. Atmos. Sci.*, **64,** 1089-1102.

Gill, A. E., 1984: On the behavior of internal waves in the wakes of storms. *J. Phys. Oceanogr*., **14**, 1129-1151.

Ginis, I., 1995: Interaction of tropical cyclones with the ocean. *In Global Perspective of Tropical Cyclones,* Chapter 5, Ed. R. L. Elsberry, **Tech. Document WMO/TD 693**, World Meteorological Organization, Geneva, Switzerland, 198-260.

Halliwell, G., L. K. Shay, S. D. Jacob, O. Smedstad, and E. Uhlhorn, 2008: Improving ocean model initialization for coupled tropical cyclone forecast models using GODAE nowcasts. *Mon Wea Rev*, **136 (7)**, 2576–2591.

Halliwell, G., L. K. Shay, J. Brewster, and W. Teague, 2009: Evaluation and sensitivity analysis of an ocean model to hurricane Ivan in the northern Gulf of Mexico. *Mon. Wea. Rev*. **(Submitted)**

Hara, T., and S. E. Belcher, 2004: Wind profile and drag coefficient over mature ocean surface wave spectra. *J. Phys. Oceanogr*., **34,** 2345-2358.

Hock, T. J., and J. L. Franklin, 1999: The NCAR GPS dropwindsonde. *BAMS*, **80**, 407-420.

Hong, X., S. W. Chang, S. Raman, L. K. Shay, and R. Hodur, 2000: The interaction of hurricane Opal (1995) and a warm core ring in the Gulf of Mexico. *Mon. Wea. Rev*., **128,** 1347-1365.

Jacob, D. S., L. K. Shay, A. J. Mariano, and P. G. Black, 2000: The three-dimensional mixed layer heat balance during hurricane Gilbert. *J. Phys. Oceanogr*., **30**, 1407-1429.

Jacob, S. D., and L. K. Shay, 2003: The role of oceanic mesoscale features on the tropical cyclone- induced mixed layer response. *J. Phys. Oceanogr*., **33**, 649-676.

Jaimes, B. and L. K. Shay. 2009: Mixed layer cooling in mesoscale eddies during Katrina and Rita. *Mon. Wea. Rev*. **(In Press),** doi: 10.1175/2009MWR2849.1, 20pp.

Jarosz, E., D.A. Mitchell, D.W. Wang, and W.J. Teague, 2007: Bottom-up determination of air-sea momentum exchange under a major tropical cyclone. *Science*, **315**, 1707.

Jena, B., M. V. Rao and B. K. Sahu, 2006: TRMM-derived sea surface temperature in the wake of a cyclonic storm over the central Bay of Bengal. *Inter. J. of Rem. Sens*., **27(14),** 3065-3072.

Large, W.G., and S. Pond, 1981: Open ocean momentum flux measurements in moderate to strong winds. J. *Phys. Oceanogr*., **11,** 324-336, 1981

Leipper, D., and D. Volgenau, 1972: Hurricane heat potential of the Gulf of Mexico. *J. Phys. Oceanogr.*, **2,** 218-224.

Lin, I.-I., C.-C. Wu, K. A. Emanuel, I.-H. Lee, C.-R. Wu, and I.-F. Pun, 2005: The interaction of supertyphoon Maemi (2003) with a warm ocean eddy. *Mon Wea. Rev*., **133**, 2635-2649.

Lin, I-I., I.-F. Pun and C.-C. Wu, 2009: Upper ocean thermal structure and the western north Pacific Category 5 typhoons. Part II: Dependence on translation speed. *Mon. Wea Rev*., **137**, (In Press).

Mainelli-Huber, M., 2000: On the role of the upper ocean in tropical cyclone intensity change. M.S. Thesis, RSMAS, University of Miami, Miami, FL, 73 pp.

Mainelli, M., M. DeMaria, L. K. Shay and G. Goni, 2008: Application of oceanic heat content estimation to operational forecasting of recent category 5 hurricanes. *Wea. and Forecast,* **23***, 3-16.*

Marks, F., and L.K. Shay, 1998: Landfalling tropical cyclones: Forecast problems and associated research opportunities: Report of the 5th Prospectus Development Team to the U.S. Weather Research Program, *BAMS,* **79**, 305-323.

Moon, I., I. Ginis, and T. Hara, 2004a: Effect of surface waves on Charnock coefficient under tropical cyclones. *Geophys. Res. Lett.*, **31**, L20302.

Moon I.-J., I. Ginis, and T. Hara, 2004b: Effect of surface waves on air–sea momentum exchange. II: Behavior of drag coefficient under tropical cyclones. *J. Atmos. Sci.*, ***61,*** 2334–2348.

Powell, M. D., and S. Houston, 1996: Hurricane Andrew's landfall in South Florida. Part II: surface wind fields. *Wea and Forecasting*., **11**, 329-349.

Powell, M.D., P.J. Vickery, and T.A. Reinhold, 2003: Reduced drag coefficient for high wind speeds in tropical cyclones. *Nature*, **422,** 279-283.

Price, J. F., R. A. Weller, and R. Pinkel, 1986: Diurnal cycling: Observations and models of the upper ocean response to diurnal heating, cooling and wind-mixing. *J. Geophys. Res.*,**7,** 8411-8427.

Price, J. F., T. B. Sanford, and G.Z. Forristall, 1994: Observations and simulations of the forced response to moving hurricanes. *J. Phys. Oceanogr*., **24**, 233-260.

Sanford, T B., J. F. Price, J. Girton, and D. C. Webb, 2007: Highly resolved observations and simulations of the oceanic response to a hurricane. *Geophys. Res. Lett.*, **34,** L13604, 5 pp.

Schade, L., and K. Emanuel, 1999: The ocean's effect on the intensity of tropical cyclones: Results from a simple ocean-atmosphere model. *J. Atmos. Sci.*, **56**, 642-651.

Scharroo, R., W.H. Smith, and J.L. Lillibridge, 2005: Satellite altimetry and the intensification of Hurricane Katrina. *EOS,* **86,** 366-367.

Shay, L.K., A.J. Mariano, S.D. Jacob, and E.H. Ryan, 1998: Mean and near-inertial ocean current response to hurricane Gilbert. *J. Phys. Oceanogr.*, **28**, 858 – 889, 1998.

Shay, L. K., G. J. Goni, and P. G. Black, 2000: Effects of a warm oceanic feature on hurricane Opal. *Mon. Wea. Rev.,* **128**,
1366-1383.

Shay, L. K, and S. D. Jacob, 2006: Relationship between oceanic energy fluxes and surface winds during tropical cyclone
passage (Chapter 5). Atmosphere-Ocean Interactions II, *Advances in Fluid Mechanics*. Ed. W. Perrie, WIT Press,
Southampton, UK, 115-142.

Shay, L. K., and E. W. Uhlhorn, 2008: Loop Current response to Hurricanes Isidore and Lili. *Mon Wea. Rev.,* **136**, 3248-3274

Shay, L. K., and J. Brewster. 2009: Eastern Pacific oceanic heat content estimation for hurricane forecasting. *Mon. Wea. Rev*, **(Submitted).**

Shay, L. K., 2009: Air-Sea Interactions in Tropical Cyclones (Chapter 4). In *Global Perspectives of Tropical Cyclones*, 2nd Edition, Eds. Johnny C. L. Chan and C. P. Chang, *World Scientific Publishing Company: Earth System Science Publication Series,* London, UK, 45 pp (Accepted, Revised and Resubmitted).

Teague, W.J., E. Jarosz, D.W. Wang, and D.A. Mitchell, 2007: Observed oceanic response over the upper continental slope and outer shelf during Hurricane Ivan. *J. Phys. Oceanogr.*, **37**, 2181-2206.

Tolman, H. L., 2002: User manual and system documentation of WAVEWATCH-III version 2.22. NOAA/NWS/NCEP/OMB Tech. Note 222, 133 pp.

Uhlhorn, E. W., P. G. Black, J. L. Franklin, M. Goodberlet, J. Carswell and A. S. Goldstein, 2007:Hurricane surface wind measurements from an operational stepped frequency microwave radiometer. *Mon. Wea. Rev*., **135,** 3070-3085.

Uhlhorn, E. W., 2008: Gulf of Mexico Loop Current mechanical energy and vorticity response to a tropical cyclone. *PhD Dissertation.* RSMAS, University of Miami, Miami, FL 33149, 148 pp.

Wada, A., and N. Usui, 2007: Importance of tropical cyclone heat potential for tropical cyclone intensity and intensification in the western north Pacific. *J. of Oceanography*, **63**, 427-447.

Walker, N., R. R. Leben, and S. Balasubramanian 2005: Hurricane forced upwelling and chlorophyll a enhancement within cold core cyclones in the Gulf of Mexico. *Geophys. Res. Letter,* **32**, L18610, doi: 10.1029/2005GL023716, 1-5.

Wang, D.W., D.A. Mitchell, W.J. Teague, E. Jarosz, and M.S. Hulbert, 2005: Extreme waves under Hurricane Ivan. *Science*, **309**, 896.

Wang, Y., J. D. Kepert, and G. J. Holland, 2001: The effect of sea spray evaporation on tropical cyclone boundary layer structure and intensity. *Mon. Wea. Rev*., **129**, 2481-2500.

Wright, C. W., E. J. Walsh, D. Vandemark, W. B. Krabill, A. W. Garcia, S. Houston, M. Powell, P. Black, and F. D. Marks, 2001: Hurricane directional wave spectrum spatial variations in the open ocean. *J. Phys. Oceanogr.,* **31**, 2472-2488.

Wu, C.-C., C.-Y. Lee, and I-I Lin, 2007: The effect of the ocean eddy on tropical cyclone intensity. *J. Atmos. Sci.,* **64(10)**, 3562-3578.

Yablonsky, R. M, and I. Ginis, 2009: Limitation of one-dimensional ocean models for coupled hurricane-ocean forecasts. *Mon. Wea. Rev*., DOI 10.1175/2009MWR2863

Yin, X., Z. Wang, Y. Liu, and Y. Xu., 2007: Ocean response to typhoon Ketsana traveling over the northwest Pacific and a numerical model approach. *Geophys. Res. Lett.*, **34**, doi:10.1029/3007GL031477.

Zedler, S., T. Dickey, S. Doney, J. Price, X. Yu, and G. Mellor, 2001: Analyses and simulations of the upper ocean's response to hurricane Felix at the Bermuda Testbed Mooring site: 13-23 August 1995. *J. Geophys. Res,* **107**, 3232.

Impact of Storm Surge from Tropical Cyclone Beni, Vanuatu

David Gibson

Forecasting and Services, Vanuatu Meteorological Service, Port Vila, Vanuatu

Email: dgibson@meteo.gov.vu

1 Abstract

On average, two to three cyclones per cyclone season either cross or come close to Vanuatu's vicinity, an island nation in the south west Pacific. The peak period is January and February in any given season. Its geographical location enables it to have a fair share of tropical cyclones occurring in the South West pacific, be it a La Nina, El Nino or a Neutral period. Tropical cyclones bring with it heavy rainfall, damaging winds, flooding, coastal flooding, inundation, landslide, as well as very rough and phenomenal seas to Vanuatu as it approaches its shores. In recent years, storm surge has gain recognition for being exceptionally dangerous during cyclones as developments continues to spread along coastal areas.

Because of the size of the islands within Vanuatu, the impacts of a tropical cyclone 25 kilometers from the island are no different from that making landfall. Having a better understanding of the direction in which the cyclone is approaching the island, the topography of the island, and other vital meteorological variables observed during the period of the approaching cyclone may help in providing a better warning service.

A recent example of how a tropical cyclone can cause considerable damage through storm surge and wind waves without even making landfall is tropical cyclone Beni. This paper will examine the effects of storm surge and wind wave in Vanuatu during Beni and the storm surge model currently available for use by the Vanuatu Meteorological Service. Additionally, the paper will examine the shortfalls on storm surge and wind wave forecasting in Vanuatu and areas for improvement.

2 Formation and Evolution of TC Beni

A Tropical depression developed south of Solomon Islands, and on Saturday the 25th of January 2003, the tropical depression was named TC Beni. Beni, at its initial stages, had a good 250hPa outflow. Beni deepened and became organized on the 26th. It had a complex route in its initial stage, as on the 27th, it made a clockwise loop before turning south, then later southeast. Most global models agree on a movement through the southern part of Vanuatu.

On the 28th at 0500UTC, Beni turn southeastward at 8 knots with gale winds affecting the northern and central parts of Vanuatu. Beni continues to maintain its southeast track, and at 0300UTC, on the 30th, it was 50 nautical miles west of Tanna island, the southern part of Vanuatu. At that time, winds close to the center were estimated at 95 knots, with the system moving at 14 knots. Winds 45 to 55, gusting to 60 knots affected Tanna and later Aneityum.

At 0500UTC on the 30th of January 2003, Beni was 40 nautical miles northwest of Aneityum, while maintaining its southeast track. At 1200UTC, the cyclone was about 70 nautical miles southwest of Aneityum Island. At 2000UTC, 30th of January, TC Beni moved further south southwestwards away from Vanuatu, and weakened further.

3 Damages

At 1500UTC, 29th of January, Beni was located at about 200 kilometers west of Efate Island. Strong to gale force winds started to affect Port Vila by 2100UTC 29th of January. Storm surge was evident in Port Vila harbor by 0000UTC on the 30th. At the sea front park, sea came inshore by about 35 to 40 meters. The sea front park was totally damaged. Around 3 coastal resorts were flooded. 3 dwellings along coastal area of Mele Bay were also flooded.

In the central and southern parts of Vanuatu, a coastal village was completed inundated, causing 15 families to be homeless.

Figure 1 Sea Front Park, Port Vila during the passage of Tropical Cyclone Beni, 30th January 2003

4 Storm Trak Model

In 2003, a storm surge model, STORMTRAK, was developed for Vanuatu, Tuvalu, Fiji and Samoa under the AusAID-funded South Pacific Sea Level and Climate Monitoring Project (SPSLCMP). The model was developed to assist the Pacific Island Nations in storm surge forecasting. The functions of the model include "cyclone wind and storm tide modeling." (Mclnnes, Oliver, Hubbert, 2004) Although Vanuatu composed of 83 islands, the model focused on Efate, the main island, one of a few islands in Vanuatu with topography and bathymetric data.

The STORMTRAK model run from Beni produced 0.5 to 0.6m surge (high tide included) (Figure 2), however observations indicate inundation of about 20 to 40 meters onshore. Inundation was generated mostly by the wind wave, as the Port Vila harbor is on the western side of the island, and well exposed to the westerly winds.

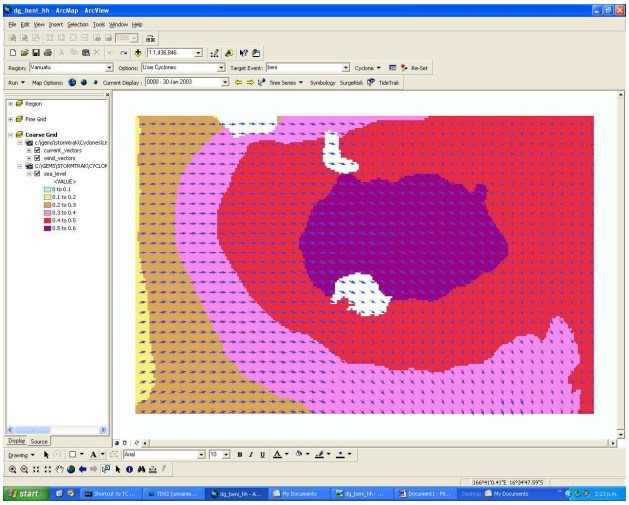

Figure 3, STORMTRAK Model run, TC Beni, 0000UTC, 30 January 2003

5 Comparisons between TC Beni and TC Ivy

TC Ivy travel from the north of Efate, and made landfall on the island on the 26th of February 2004. Despite this, the storm surge observed from the Cyclone was minimal compared to Beni.

6 Topography and the Direction of the approaching cyclone

Storm surge and wind waves, the later being the main driving force behind waves moving inland, can inflict considerable damage to developments along coastal areas. Almost all coastal areas around Efate are prone to the effects of storm surge and wind wave. However, the topography and the direction of the approaching cyclone plays a significant in role to the severity of the impacts of both the storm surge and wind waves.

Past cyclones indicated that those traveling from the northwest of Vanuatu and towards the central islands may generate waves and surge that can cause considerable damage to coastal developments compared to those coming directly from the north, east or northeast, including those making landfall.

7 Conclusions

Tropical Cyclone Beni was an exceptional system in that although it was about 200 KM from Efate, the impacts of storm surge was greater compared to other cyclones that made landfall. The main reason was that it occurred during the peak tide as well as approach from the northwest, with the westerly winds driving the waves inland. The topography of Port Vila harbor also played a significant role in the magnitude of the inundation.

In the southwest pacific, storm surge alone is not the main driving force behind flooding and inundation of coastal areas. As experienced by Beni, although the surge is 0.5 meter, the inundation was about 20 to 50 kilometers. Wind wave is one of the main causes of coastal flooding in the south west pacific, yet it is not well captured in storm surge models. This can sometimes lead to an underestimation of the severity of storm surge and wind waves in advisories and warnings.

Reference

Mclnnes K, Oliver S, and Hubbert G. 2004, *Evaluating the Storm Threat for Pacific Island Countries*, International Conference on Storms, Victoria

A Statistical Analysis of Unusual Tracks Characteristics of Tropical Cyclone Closed to Taiwan Island

A.-M. Liu, Y. Lin, X.-Y. Wu, and Z.-G. Huang

Meteorological Observatory of Fujian Province, Fuzhou 350001 China

1 INTRODUCTION

The topography of Central Mountains on Taiwan Island, altitude more than 3.4km, impact particularly on tropical cyclone motion when TC approximates to Taiwan. In addition to its structure, the TC motion would be altered due to the topographic forcing, resulting in unusual tracks - sharp turn, bounding or looping, which make trouble for predicting where and when TC would make landfall mainland. LUO Zhe-xian explained that topographic forcing of Taiwan island make the maximum wind velocity region constrict to core, which probably make TC deflect to the right of it's tended path[1]. Model simulation indicate a small vortex that forms at the opposite of island as TC approximating Taiwan, may intensified under appropriate conditions, and would replace the older core to be a new center of TC eventually [2]. CHEN Lian-shou explained that orographic effect is a important factor in modulating TC motion, in addition to inner structure and interaction between systems different scale [3].

In this paper, the temporal and spatial distributions of all sorts of unusual TC tracks, which intrude upon Taiwan and nearby area, are represented through statistical analyzing cases for the 60-year period, 1949~2008. Appropriate explanations for unusual tracks are also discussed, aimed at offering a climatic reference of irregular tracks and enhancing forecast accuracy.

2 CLASSIFICATION & DISTRIBUTION

Taiwan island and nearby sea area are chosen to be Target region: 21-26 degree north latitude, 118-124 degree east longitude. 323 TCs entered the target region for 60-year period, among which 115 TCs, take up more than 35% of total numbers, are attributed to unusual tracks and classified into 5 sorts:

(1) Left-deflection
(2) Right-deflection
(3) Zigzagging
(4) Induced-depression
(5) Looping

Table 1 gives monthly distribution of unusual tracks within target region. Table 1 indicates TCs with unusual track are more active in July to September. All sorts of unusual tracks have relations with topography and atmospheric circulation.

Tab.1 Monthly distribution of TC unusual tracks within target region

	MAY	JUN	JUL	AUG	SEP	OCT	NOV
Left-defel(47)	0	4	17	17	9	0	0
Right-defel(25)	0	4	7	4	9	1	0
Inflection（9）	0	0	4	2	3	0	0
Indu-depre（24）	1	0	10	9	2	0	2
Looping（10）	0	1	2	2	4	1	0
Total（115）	1	9	40	34	27	2	2

3 ANALYSIS

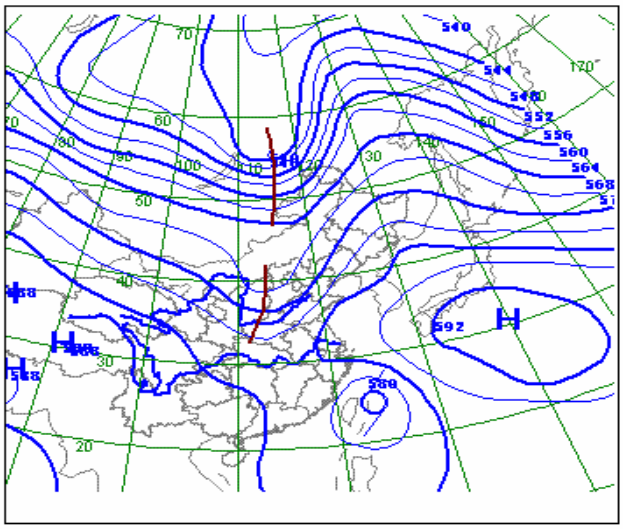

Fig.1 Typical 500hpa height deflects TC to left. Typhoon Wipha, 08:00(BJT), 18 Sep. 2007

3.1 Left-deflection: Track deflected to the left and mean azimuth difference exceeds 30 degree. This sort takes up more than 40% of total cases. Left-deflection may result from pressure gradient asymmetric distribution caused by topographic forcing, switch of different environmental steering, or interaction between TC and ambient cloud clusters [5]. Fig.1 gives a typical 500hp height pattern when Left-deflection occurred. Under this synoptic situation, most points of deflection concentrate on northeast offshore of Taiwan Island. The poleward-moving TC was blocked by the extended subtropical high, thus isobars became denser at the northeast of TC. Moreover, Topographic friction of Taiwan Island strengthened the asymmetry of pressure field, which increase west component of movement, so favored Left-deflection. While a few left-deflection occurred in southeast offshore of Taiwan, probably induced by change of environmental steering and Fujiwhara effect.

3.2 Right-deflection: Track deflected to the right and mean azimuth difference exceeds 30 degree. The factors caused right-deflection include: Topographic trough induced by interaction between easterly wind and topography, retreat and weakening of subtropical high, or easterly wave. Fig.2 shows topographic trough make TC deflected to right when TC moves over the ocean of southwest of Taiwan Island.

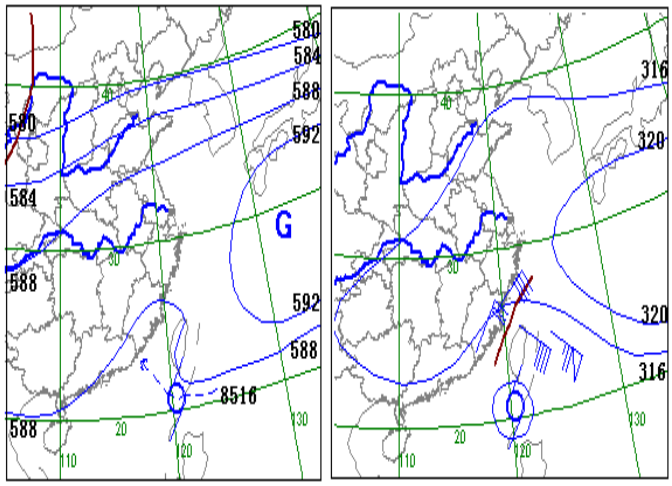

Fig.2 Topographic trough deflect TC to right

Left: 500hpa Right: 700hpa

3.3 Zigzagging: Track deflected to left as TC approaching to the island and to right as getting across the island to ocean surface again. Zigzagging track illustrate the impact of different underlying surfaces on TC motion.

3.4 Induced-depression: A small orographic depression occurred as TC close to Taiwan Island in 20.7% cases. Most induced-depressions formed on the west side of Taiwan Island or in the strait, only several cases show the depression occurred on the east side. Approximate 1/3 amount of depressions intensified to be new core of TC replacing former center, which exhibited bound-effect. Studies indicate three circumstances are favored induced-depression: (1) in weak environmental steering; (2) airflow in the right front of TC perpendicular to the Central Mountains; (3) TC moves northwestward and make landfall the southeast of Taiwan.

3.5 Looping: Less than 10% cases exhibited looping phenomena in weak environmental steering. Under this circumstance, the topographic forcing played a more important role in modulation of TC motion, resulting in asymmetric structure. Fig.3 gives the contrast of circulation pattern (500hpa height) between looping track and smooth track.

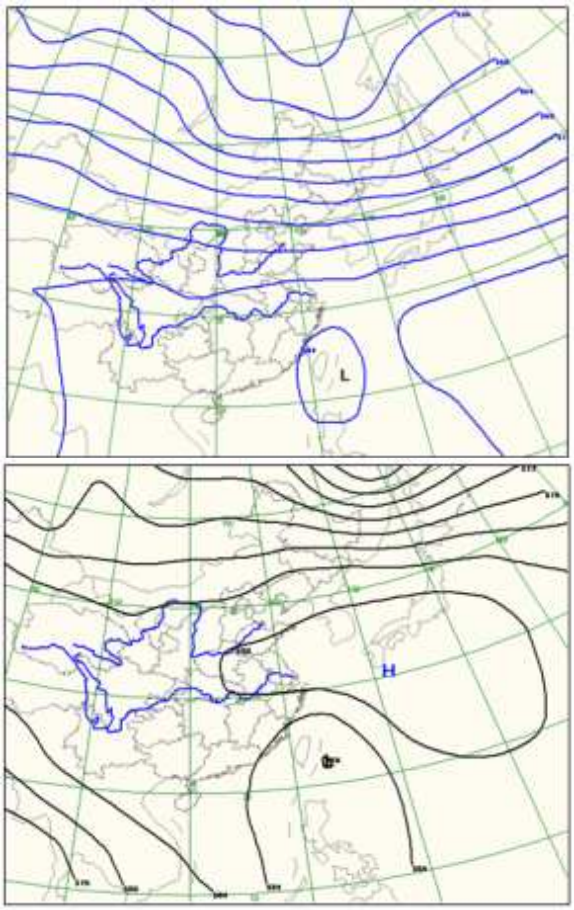

Fig.3 500hpa mean-height field contrast.

Top: looping tracks across Taiwan Island. Bottom: smooth tracks across Taiwan Island.

4 SUMMARY

4.1 Probability of unusual track occurrence is more than 1/3, among which 2/3 made landfall mainland. So it is very important to predict unusual tracks accurately.

4.2 Left-deflection points mainly concentrate on the north part of Taiwan island or near the northeast offshore, where topography have more impact on TC motion than environmental steering do.

4.3 Right-deflection points concentrate on the west side of Taiwan island, caused by impact from topographic trough or induced-depression.

4.4 Induced-depression mainly formed in the strait, most of which lasting 12-24 hours. Track intends to right-deflect (left-deflect) when induced-depression occurred on the north (south) of TC.

4.5 Most looping TCs make landfall to north of Hualian of Taiwan Island. In weak environmental steering, β-effect and topographic forcing make TC motion more complex and hard to predict. Studies indicate that high potential energy, instability and strong updraft present at left front of TC [6].

REFERENCES:

[1] LOU Zhe-xian, CHEN Lian-shou. Effect of the Orography of Taiwan Island on Typhoon Tracks [J]. SCIENTIA ATMOSPHERICASINICA, 1995, 19(6):701-706.

[2] MENG Zhi-yong, XU Xiang-de**.** Mechansism of the Impact of the Cyclone System Induced by the Taiwan Island Topography on Tropical Cyclone Unusual Motion [J]. SCIENTIA ATMOSPHERICASINICA,1998,22（2）:156-168**.**

[3] 陈联寿. TC运动研究和业务预报的现状和发展[C]//台风会议文集(1985). 北京：气象出版社, 1987: 6-30.

[4] 陈瑞闪.台风[M].福建科学技术出版社,2002:106-119.

[5]LIU Ai-ming. Study of sudden left-deflection of tropical cyclone track in China Seas [J]. Journal of Oceanography in Taiwan Strait, 1996, 12(2):113-119.

[6] LIU Ai-ming, LIN Yi, LIU Ming. Analysis of Track of Typhoon Landing on Taiwan Island in 2005 [J]. Meteorological, 2006,32(6):38-44.

Ocean Surges And Climigration: A Case Along Nigeria Coastline

Ediang O A,Ediang A. A,Sholademi M.O(Mrs),Ekhameye P.O

Nigerian Meteorological Agency

Pmb1215 Oshodi Lagos，Nigeria.

+2347033466011
ediang2000@yahoo.com

Climigration has been coined as a word to describe this type of displacement.

Climigration occurs when a community is no longer Sustainable exclusively because of climate-related events and permanent relocation is required to protect people.

This study portrayed the connection between ocean surges and Climigration along Nigeria Coastline as a Resource-Hazard Twin Paradox.

The Paper presents a review works that the entire Coastline of Nigeria is a scene of active flooding and erosion, partly from Storm Surges.

The Paper finally discuses that, Twenty Seven occurrence of ocean surge events Over the beach of the Victoria island in Nigeria were recorded between 1994 to 2008 and each with its devastating consequences resulting from the massive flooding and erosion and displacement of coastal dwellers.

Research Needs and Opportunities for Improved Forecasting of U.S. Landfalling Tropical Cyclones

Robert Rogers

U.S. Department of Commerce

National Oceanographic and Atmospheric Administration

Atlantic Oceanographic and Meteorological Laboratory

Hurricane Research Division，Miami, FL 33149， USA

Robert.Rogers@noaa.gov

1. Motivation

The risk to life and property from U.S. landfalling tropical cyclones continues to escalate in coastal areas. Population continues to increase in this area, with about 50% of the U.S. population now living within 50 miles of the coast. The value of coastal infrastructure and economic activity continues to rise as well. It is estimated at over three trillion dollars, or nearly one-third of annual U.S. gross domestic product. In addition to saving lives, more accurate hurricane forecasts and warnings can reduce response and recovery costs by providing fewer false alarms and reducing the warning footprint.

A concerted effort is needed to improve forecasts of landfalling tropical cyclones (TCs). That is the goal of NOAA's Hurricane Forecast Improvement Project (HFIP). This project is intended to provide decision makers and the public accurate and reliable forecasts up to 7 days in advance. Such forecasts will provide advance notice of both the location and severity of the impacts of landfalling TCs. Societal benefits include a reduction in the loss of lives, more confidence in the forecasts, an elimination of unnecessary evacuation costs, and a reduction in economic loss that results from better preparations. The goals of the HFIP are to:

- improve forecast accuracy – including the impact areas, which require an improvement in track forecasts by 50% in 10 years; the severity of the impacts, which require an improvement in intensity forecasts by 50% in 10 years; and improved predictions of storm surge impact locations and severity
- extend forecast reliability out to 7 days
- quantify, bound, and reduce forecast uncertainty to enable risk management decisions to be made

The current capabilities of the hurricane forecasting system include a reduction in track error by ~50% since 1990, but little progress in reducing intensity error (Fig. 1). Progress in the prediction of storm size is difficult to measure due to inadequate observations. Storm surge forecasts are currently accurate within ±20% when the track, intensity, and size are known. Modest annual improvements to the precipitation forecast have been realized, with the forecast patterns matching the observations when the track error is low. Social and behavioral science research for landfalling TCs are still in its infancy.

2. Operational priorities and research needs

The current forecast capabilities and goals have driven the development of priorities from the operational forecasting community. Table 1 shows a list of operational priorities provided by the National Hurricane Center (NHC) in Miami, FL. Fourteen priorities are identified, with the highest priority focusing on providing guidance for TC intensity change, in particular rapid intensity change (both intensification and weakening). Improved capabilities for observing the TC and its environment to support forecast analysis and model initialization and statistically-based guidance for track, intensity, and precipitation are also high priorities. Improved guidance for coastal inundation and TC track are next on the list, followed by TC genesis guidance, guidance for changes in TC size and wind structure, and guidance for TC precipitation.

With these operational priorities in mind, the U.S. TC community has developed a list of topics that need to be addressed by the research community in order to address the priorities. This list of research needs, provided in Table 2, is divided into two broad categories, basic research (termed "general research" here) on the physical processes governing TC structure, intensity change, formation, track, precipitation, and storm surge; and applied research that falls under the categories of "Model Development" and "Observations and Observing Strategies." Model development subtopics include data assimilation, global and regional model development and improvement, physical parameterization development, verification and diagnostics development, and probabilistic guidance development. Observations and observing strategies include developing new observing platforms and strategies for observing the TC and its environment and providing these observations for model initialization, diagnostics, and development. More detail is provided in Table 2.

3. Research gaps and sufficiency

The research activities from each of the major U.S. agencies engaged in TC research (NOAA, NASA, National Science Foundation (NSF), and the U.S. Navy) are mapped onto the topics in Table 2. This is a comprehensive mapping that provides a snapshot of all of the TC research activities being supported by the U.S. TC research agencies in 2008. The total amount of man-years and dollar amount devoted by each agency to TC research is shown in Fig. 2. For 2008, roughly the same number of man-years was devoted from each agency, with NOAA devoting the most at 79 man-years and NASA devoting the least of the four major agencies at 44 man-years. In terms of dollar amounts, NOAA committed the most in 2008 at $13.7 million, followed by the Navy at $9.6 million, NSF at $6 million, and NASA at $4.6 million.

The distribution of agency-funded research by topic area is shown in Fig. 3. The greatest amount of research for the combined agencies is in TC intensity/structure, TC formation/genesis, model development, and observations. When separated by agency, though, differences emerge. The bulk of the efforts from NOAA are in the applied research topics, i.e., model development and observations (with a small amount for TC intensity/structure). The other agencies are concentrated in the basic research area. NASA and NSF both have significant research efforts dedicated to TC formation and intensity/structure, while the Navy is concentrated in intensity/structure and model development. Comparatively little effort is dedicated to TC track, QPF, and storm surge.

Each of the research efforts shown in Table 2 were then mapped onto the operational priorities in Table 1. This mapping showed how specific research efforts contributed to the operational goals and allowed an assessment of which operational goals were being addressed more than others. Figure 4 shows this mapping for the NHC priorities. The operational priorities most-addressed (> 30 man-years in 2008) by the research efforts are TC size/structure (priority #9), genesis/formation (#7), and intensity change (#1). Significant efforts are also being made in the collection of observations (#2) and performing surface wind analyses (#8). Comparatively little effort is being made toward statistical aids (#3) and the comparison of model resolution vs. ensembles (#10). (Little effort is also being made toward improving forecaster efficiency (#4), but this is not primarily a research but a logistics topic.)

4. Summary and the way ahead

From this evaluation it is clear that the #1 operational priority, improved forecasts for TC intensity change, is one of the top research topics. In fact, when combined with structure changes, 35% of the total research efforts are being directed toward these two operational priorities. By contrast, little emphasis is being made toward developing statistical models combining the various guidance products (so-called "guidance on guidance"), as well as comparisons of deterministic vs. ensemble-based approaches to forecasting. These topics merit further attention by the research community.

An obvious question that arises from this analysis is determining the appropriate research levels for each operational priority. For example, is 33 man-years for intensity change research enough? What about for track forecasting? These values will need to be quantified before definitive statements about sufficiency can be made. As this analysis matures and is expanded, it will allow for a direct application of research investments to desired operational capabilities. It will also provide a baseline for establishing the "next generation" strategic objectives. It does highlight the importance of the verification capability and the quantitative assessment of sufficiency, though, as mentioned above. Finally, this database needs to be updated regularly to relate research efforts toward achieving strategic objectives.

TPC/ NHC Priority[1]	JTWC Priority[1]	Operational Need[1]	Linkage to Research Needs
1	**1**	Guidance for tropical cyclone intensity change, with highest priority on the onset, duration, and magnitude of rapid intensification events. Similar guidance is also needed on when rapid over-water weakening (such as had been observed in recent Gulf of Mexico hurricanes) will occur.	A1a-f, B1, B2, B3a-e, B6, B7
2	**2**	Improved capability to observe the tropical cyclone and its environment to support forecaster analysis and model initialization.	B1, C1-C3
3	**5**	Statistically-based real-time guidance on guidance for track, intensity and precipitation (e.g., multi-model consensus approaches), provided to forecasters in probabilistic and other formats.	B5,B6
4	**6**	Enhancements to the operational environment to increase forecaster efficiency, by expediting analysis, forecast, coordination, and/or communication activities.	C1c
5	**7**	Additional operational guidance on coastal inundation (e.g., storm surge and waves).	A4, A5, B2, B3, B6
6	**8**	Improved and extended track guidance. Identification, and then reduction of, the occurrence of guidance and official track outliers, focusing on both large speed errors (e.g., accelerating recurvers and stalling storms) and large direction errors (e.g., loops), and on specific forecast problems, including interactions between upper-level troughs and tropical cyclones, track forecasts near mountainous areas, and extratropical transition.	A2, B1-B3, B5-B6
7	**3**	Guidance for tropical cyclone genesis that exhibits a high probability of detection and a low false alarm rate, and/or provides probability of genesis.	A3, B1-B3, B5-B7
8	**9**	Operational analysis of the surface wind field (including maximum sustained winds) in tropical cyclones. This also includes methods for forecasting the wind field over elevated terrain and high-rise buildings.	B1, B2, C1-C3
9	**4**	Guidance for changes in tropical cyclone size/wind structure and related parameters, including combined sea heights.	A1a-g, B1-B7
10	**10**	Guidance on the operational utility and relative merits of high-resolution model output compared to lower resolution ensemble model output.	B6, B7
11	**11**	Guidance for tropical cyclone precipitation amount and distribution.	A4, B1-B7
12	**12**	Improved utility of microwave satellite and radar data in tropical cyclone analysis.	B1, C1c
13	**13**	Improved techniques for estimating the intensity of tropical cyclones passing over and north of sea-surface temperature gradients (e.g., in the eastern North Pacific Ocean and the Atlantic Gulf Stream).	C1
14	**14**	Quantitative guidance tools for seasonal tropical cyclone forecasts for the Atlantic and North Pacific basins, using statistical and/or dynamical methodologies.	A6,B2, B6

Table 1. Prioritized list of needs identified by U.S. National Hurricane Center and Joint Typhoon Warning Center. "Linkage to research needs" indicates which research topics shown in Table 2 address that operational need.

Research Topics	Type of Research B = Basic; A =Applied
A. General Research	
1. Intensity and Structure Changes. a. Environmental scale processes (e.g., dry air, midlevel easterly jet, and suspended mineral dust from Saharan Air Layer; vertical shear of horizontal wind; easterly wave disturbance; TUTT and monsoon trough influences). b Vortex scale processes (e.g., eyewall replacement and rainband development, vortex mixing and resilience). c. Convective scale processes (e.g., convective bursts, vortical hot towers). d. Turbulent and microphysical scales (e.g., momentum and enthalpy fluxes; cloud microphysics; radiation; e. Upper ocean processes and structure (e.g., oceanic heat content; currents; waves; SST; mesoscale features). f. Landfall effects (e.g., surface flux changes; topographic and land surface effects). g. Extratropical transition. h. Predictability limits.	B,A
2. Track. a. Convective and vortex structure (e.g., asymmetries) b. Land interaction. c. Multi-vortex interactions. d. Predictability limits.	B,A
3. Tropical cyclone formation. a. Convective processes. b. Mesoscale processes (e.g., stratiform precipitation, vorticity structure). c. Environmental processes. d. Tropical transition.	B,A
4. Precipitation. a. Environmental interaction. b. Microphysical processes (hydrometeor production and conversion, fallout, aerosol impacts). c. Topographic effects.	B,A
5. Coastal and inland inundation (i.e., surge, waves, flooding). a. Surge wave and ocean bottom interaction. b. Wave breaking and set up.	B,A
6. Predictability of seasonal tropical cyclone activity.	B,A

Table 2. List of TC research topics being pursued by U.S. TC research community.

Research Topics	Type of Research B = Basic; A =Applied
B. Model Development Topics	
1. Data assimilation (e.g., technical approach, high resolution data, new data sources/instrument, vortex initialization, atmosphere and ocean initialization; techniques to evaluate the uncertainty and representativeness of observations and use of observations for initializing NWP models).	A
2. Global and regional model development/improvements (e.g., resolution, nesting, coupling to ocean; coupling with hydrology/inundation models).	A
3. Relative importance of physical processes in global and regional models on track, intensity and structure, and precipitation. a. Atmosphere-ocean boundary layer for coupled air-sea-wave problem; momentum (wave-induced drag) and enthalpy fluxes (sea spray complexity). b. Upper ocean processes and structure (e.g., oceanic heat content; currents; waves; SST; mesoscale features). c. Land surface coupling: sensitivity of Land Surface Model, radiation. d. Microphysical processes (e.g., hydrometeor production and conversion, fallout, aerosol impacts, radiation). e. Convective processes (e.g., latent heating, momentum transfer, mixing).	B, A
4. Verification for three dimensional, high-resolution regional models for all phases of the tropical cyclone life cycle; varying atmosphere/ocean environment.	A
5. Diagnostic techniques to further increase the utility of global and regional models in forecasting tropical cyclone track, intensity structure, precipitation, and genesis.	A
6. Development of advanced, probabilistic guidance (e.g., ensembles); optimal ensemble construction and configuration; value of high-resolution deterministic forecasts vs. ensembles.	A
7. Studies to optimize resolution and scale dependent parameterization.	B, A
C. Observations and Observing Strategies	
1. Observing strategies/capabilities to improve analyses and forecasts of tropical cyclones (e.g., formation, track, intensity, structure, inundation). a. Where to take observations for initialization of tropical cyclone vortex and environment. b. Alternatives and tradeoffs for observing tropical cyclone and their environment (OSE, OSSE, cost/benefit). c. Information systems (e.g., data fusion, visualization).	A
2. Required observations to support model diagnostics and verification (e.g., IFEX, TCS-08, CAMEX III/IV. TCSP, RAINEX, NAMMA).	A
3. New and/or improved observational technologies.	B,A

Table 2. (continued)

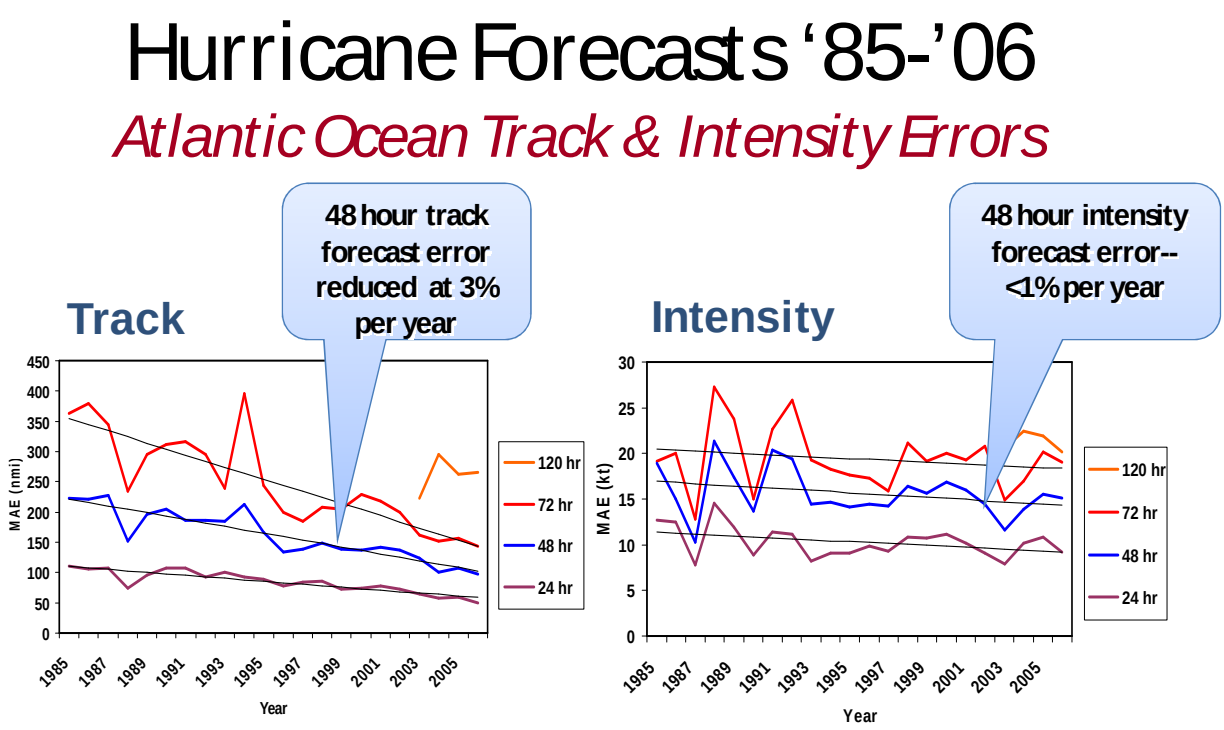

(a) (b)

Figure 1. Trends in operational (NHC) forecasting errors for tropical cyclone track and intensity at various lead times for the 1985-2006 time period.

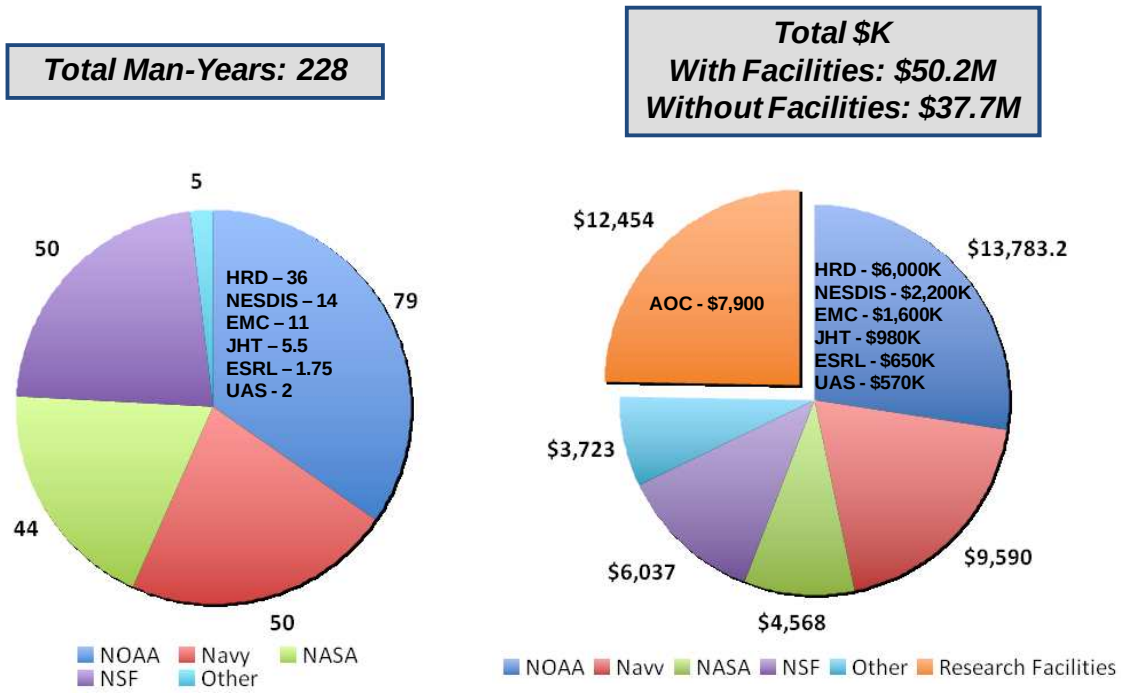

(a) (b)

Figure 2. (a) Total number of man-years devoted to TC research in 2008 separated by agency; (b) total number of dollars devoted to TC research in 2008 separated by agency.

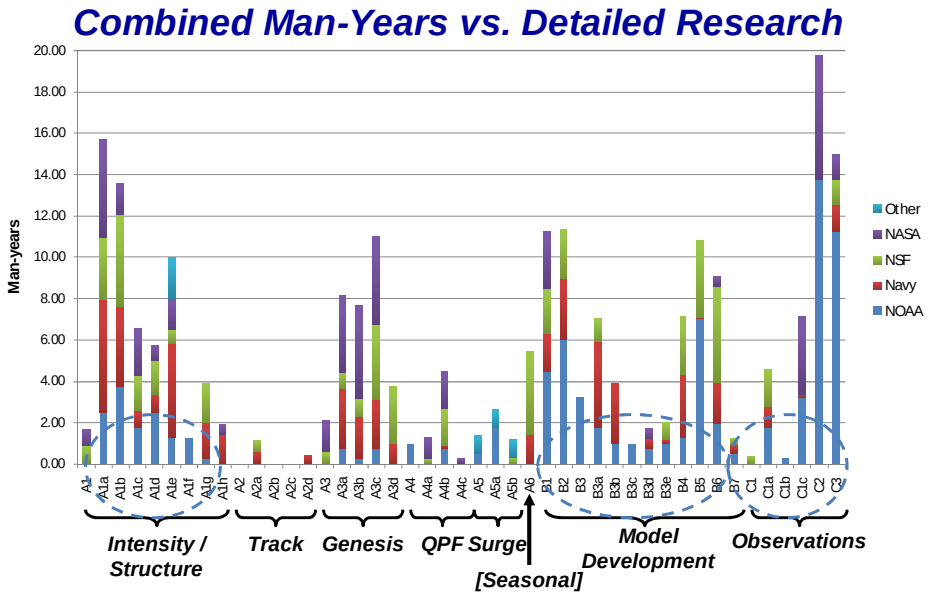

Figure 3. Combined research efforts (in man-years) and which research topics they address for 2008.

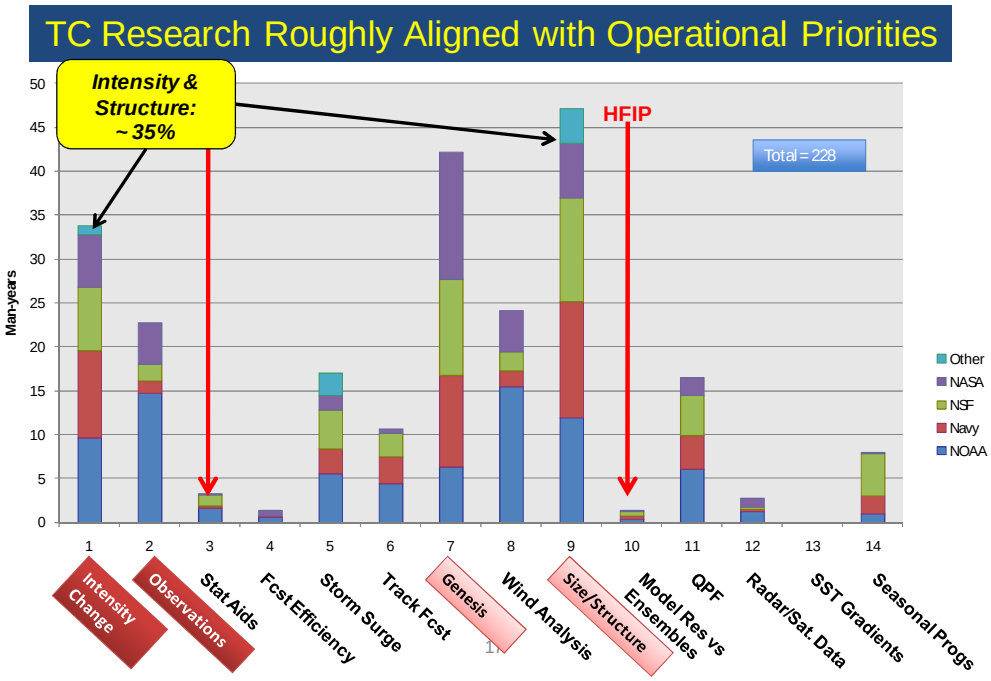

Figure 4. Mapping of research efforts (in man-years) onto operational priorities for 2008.

Tropical Cyclone Information and Products at the Japan Meteorological Agency "Present Status and Challenges for the Future"

Kiichi Sasaki

Japan Meteorological Agency

1. Introduction

The Japan Meteorological Agency (JMA) is the Regional Specialized Meteorological Center (RSMC) for the western North Pacific Basin designated by the World Meteorological Organization (WMO). It routinely monitors tropical cyclones (TCs) in the western North Pacific and the South China Sea and issues track forecasts up to 120 hours ahead and intensity forecasts up to 72 hours ahead as the RSMC TC advisory for National Meteorological and Hydrological Services (NMHSs) of Typhoon Committee Members.

In addition to these track and intensity forecasts, JMA provides domestic users with a variety of TC information and products such as hourly TC information and 50kt wind probability when a TC of tropical storm (TS) intensity or higher is approaching Japan. Present status and future challenges of TC information and products at JMA are presented.

2. Operational Forecast and Warning

Since an average of 10.8 TCs of TS intensity or higher affect Japan (approach within 300km) every year, issuing accurate and timely TC forecasts and warnings is one of the most important roles of JMA. TC information and products at JMA are outlined in Figure 1. We will review present status of them focusing on track, intensity, precipitation and storm surge forecasts.

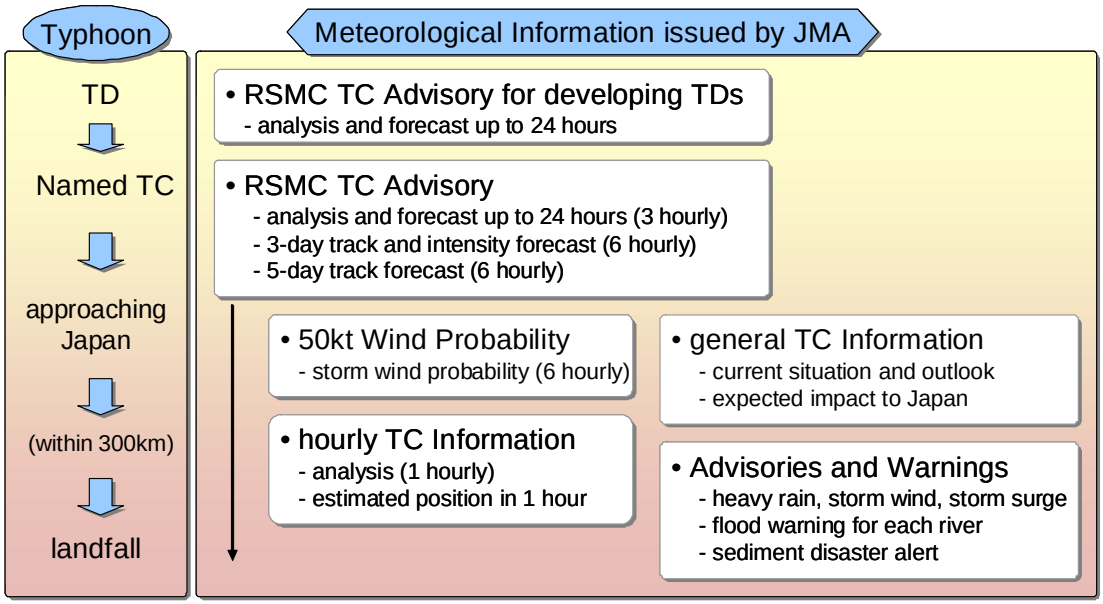

Figure 1. Outline of TC information and Products at JMA.

2.1 Track forecast

Among TC forecast and warning variables, the track forecast is the most essential one to issue appropriate TC information. Figure 2 shows that JMA's operational track forecasts have been improving steadily, but still have certain position errors of about 100km for 24-hour forecasts, about 200km for 48-hour forecasts and 250 or more for 72-hour forecasts. To indicate such forecast uncertainties, JMA uses 70% probability circle; a circular area within which a TC will be located with a probability of 70% at each forecast time. The size of the circle is determined statistically depending on the movement direction and speed of a TC.

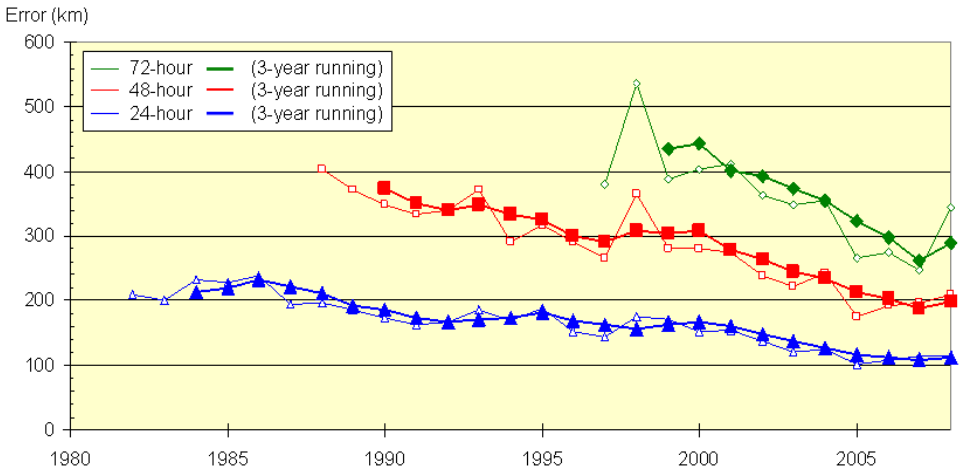

Figure 2. Annual mean position errors of 24-, 48- and 72-hour operational track forecasts.

Position errors of operational track forecasts from 2003 to 2008 were verified by categorizing them in each TC grade and area. Position errors of track forecasts for typhoons (TYs) tend to be smaller than those for TSs and severe tropical storms (STSs). Figure 3 indicates mean position errors for 24-hour forecasts in respective TC grades (TY, STS, TS) and areas. Their position errors were about 90km to 100km for TYs, about 115km to 130km for STSs and about 140km to 150km for TSs.

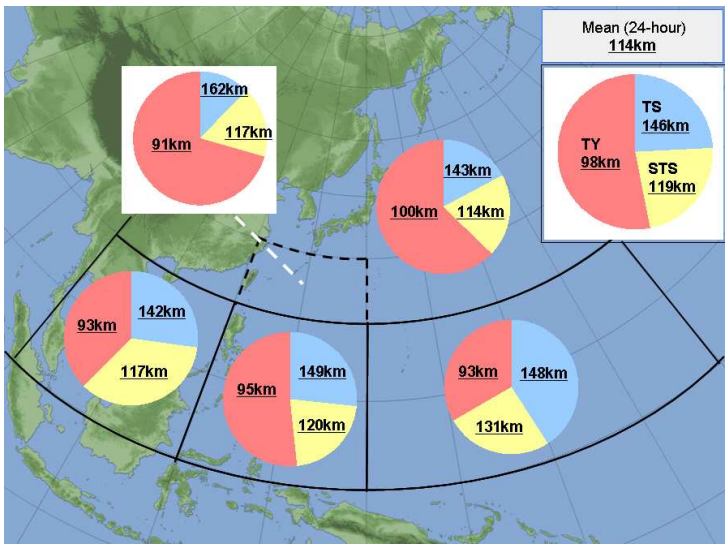

Figure 3. Mean position errors of 24-hour operational forecasts from 2003 to 2008 in respective TC grades (TY, STS, TS) and areas.

From April 2009, JMA has started issuing 5-day track forecasts. Radii of 70% probability circles for 96-hour and 120-hour forecasts are determined based on reliability information obtained from JMA's Typhoon Ensemble Prediction System (TEPS), which became operational in February 2008. Figure 4 shows the 5-day track forecast for TS Morakot (0908) issued at 00UTC 4 August 2009 and corresponding TEPS predictions. Further enhancement of 5-day track forecasts using ensemble prediction results is one of our challenges for the future.

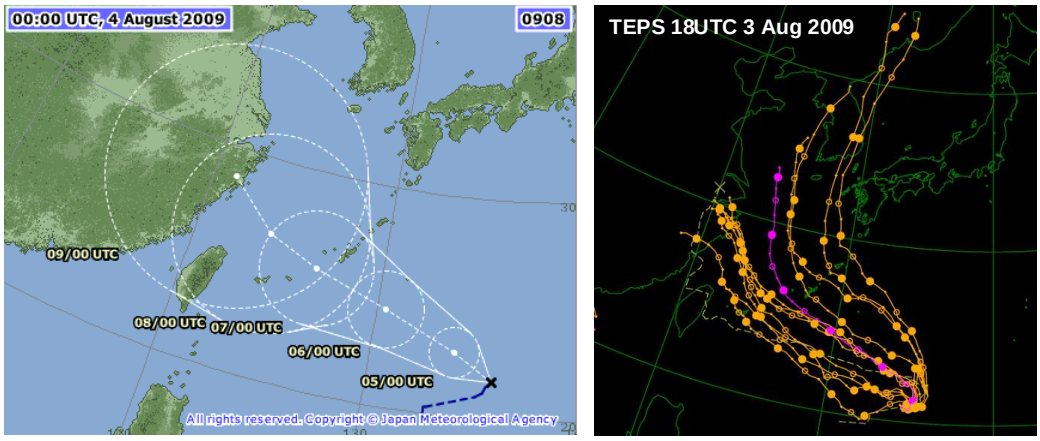

Figure 4. 5-day track forecast for TS Morakot (0908) issued at 00UTC 4 August 2009 (left) and TEPS predictions of 18UTC 3 August 2009 initial (right).

2.2 Intensity forecast

Compared to the track forecast, there is little improvement in the intensity forecast for years. For example, central pressure forecasts are particularly difficult in case that a TC is developing or weakening rapidly with a change of 30hPa or more in 24 hours as shown in table 1. With recent increase of rapid change case-ratio (changes more than 30hPa in 24 or 72 hours), annual mean RMSEs of central pressure forecasts for 24- and 72-hour forecasts are almost the same in the past several years as shown in Figure 5.

24-hour C-Pressure Forecast

pressure change	num. cases	RMSE (hPa)
<10hPa	1297	8.2
<15hPa	630	8.0
<20hPa	456	10.1
<25hPa	325	13.3
<30hPa	220	15.6
<35hPa	148	19.4
<40hPa	99	22.7
<45hPa	53	27.2
45hPa=<	61	29.6
total	3289	12.1

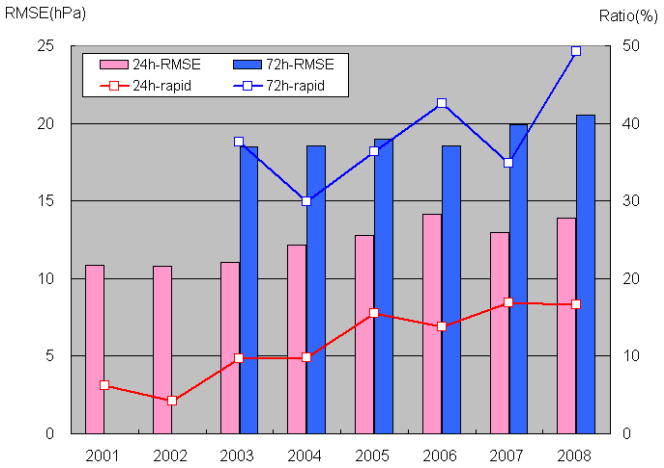

Table 1. RMSEs of 24-hour operational central pressure forecasts from 2001 to 2008 in respective categories of pressure changes during 24-hours (left).
Figure 5. Annual mean RMSEs of 24- and 72- hour operational central pressure forecasts and annual rapid change case-ratios (right).

Figure 6 presents verification results of central pressure change predictions for TCs in 2008 by the high resolution Global Spectral Model (GSM; TL959L60) of JMA, which became operational in November 2007. Although GSM still has a certain bias in central pressure predictions, it captures a intensification tendency of TCs in their developing stages, while it sometimes suggests development of TCs in their weakening stages. Further progress of numerical weather prediction techniques for TC intensity predictions is desired to improve operational central pressure and maximum sustained wind forecasts.

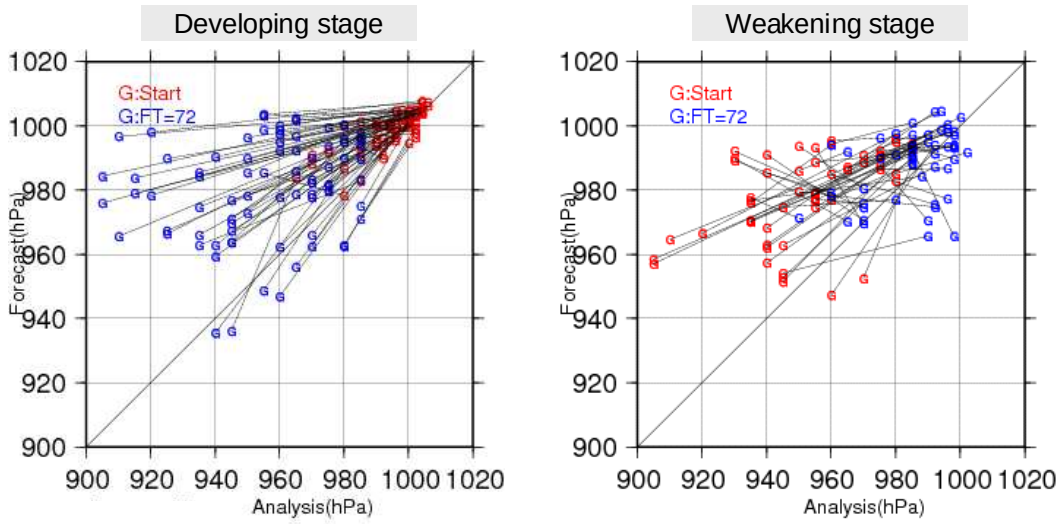

Figure 6. Verification results of central pressure change predictions by the high resolution GSM (TL959L60) for TCs in 2008.

2.3 Precipitation

Heavy precipitation associated with a TC often causes flood and landslide damage in every part of Japan and JMA is requested to provide appropriate precipitation-related information when a TC is approaching Japan. Since possible heavy precipitation areas and their expected precipitation amounts are closely dependent on the TC track, we have to make a rough expectation of them to some extent at present. Figure 7 shows ensemble track predictions for TY FITOW (0709) by JMA's one-week ensemble prediction system (one-week EPS) at 12UTC 3 September 2007 initial and accumulated precipitation amounts at a point (36N, 139E) corresponding to respective forecast tracks. They suggested that the typhoon might bring heavy precipitation of 300mm or more in the vicinity of the point if it passed over the region on 6 or 7 September 2007.

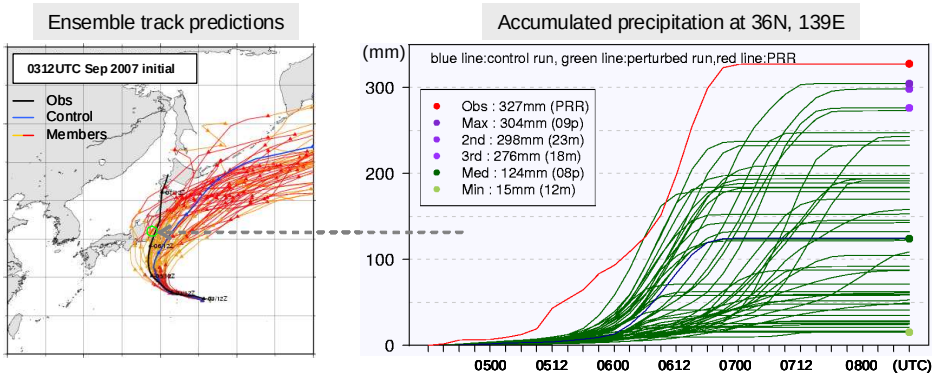

Figure 7. Ensemble track predictions by one-week EPS for TY FITOW (left) and accumulated precipitation at 36N, 139E (right).

Considering several likely scenarios suggested by one-week EPS or TEPS, duty forecasters provides domestic users with heavy precipitation information on possible areas and expected precipitation amounts. Figure 8 shows examples of detailed TC forecasts in 3-hour intervals up to 24 hours ahead and heavy precipitation information issued by JMA in the morning of 6 September 2007 about 15 hours before the landfall of TY FITOW (0709).

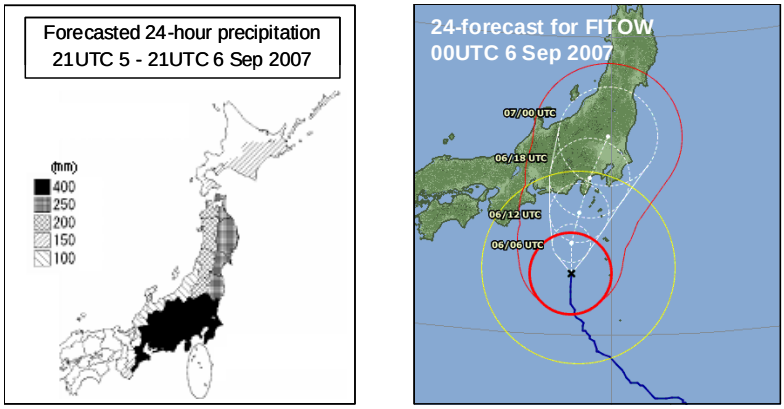

Figure 8. Examples of heavy precipitation information (left) and a detailed 24-hour TC forecast for TY FITOW (0709) issued at 00UTC 6 September 2007 (right)

The occurrence of a flood or a landslide is closely related to accumulated precipitation around a river or a region concerned. Therefore providing not only forecast information on heavy precipitation but also observed information is important for disaster-prevention activities. JMA provides a variety of observed precipitation information and products including statistical information on a real time basis through the Internet and disaster-related warnings such as flood forecast for each river (Figure 9).

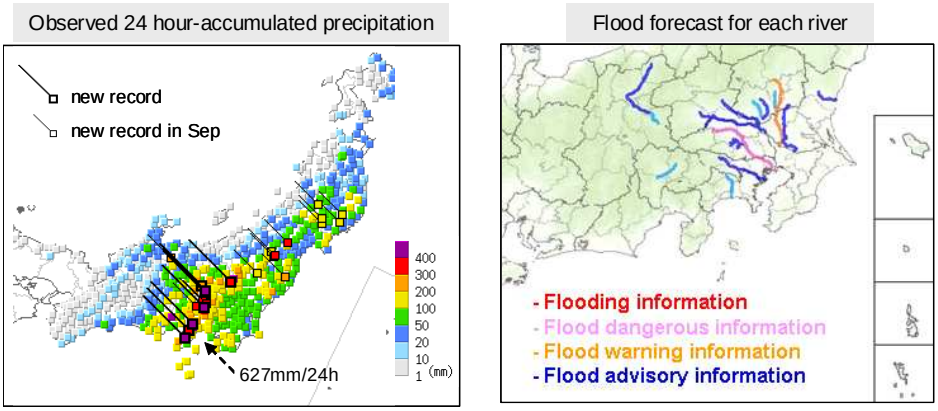

Figure 9. Examples of observed 24-hour accumulated precipitation with statistical information (left) and flood forecast for each river (right) during the passage of TY FITOW (0709).

2.4 Storm surge

NMHSs are required to issue timely storm surge warnings when an intense TC is approaching. However forecasting the occurrence of storm surges associated with a TC is very difficult because it strongly depends on the TC track and intensity. Although position errors of track forecasts have significantly reduced recently, an average of about 100km in 24-hour forecasts is still large to predict storm surges properly at a certain point. Considering present forecast uncertainties, JMA makes storm surge predictions for several possible TC tracks and provide forecasters with storm surge guidance for about 290 coastal points.

Figure 10 is an example of storm surge predictions calculated by JMA storm surge model when TY FITOW (0709) was just to make landfall to Kanto Region of Japan on 6 September 2007. Storm surges associated with TY FITOW (0709) were calculated for five possible paths of the forecast circle (1: center, 2: fastest, 3: rightmost, 4: slowest, 5: leftmost). In this case, as TY FITOW (0709) moved nearly along the center path of the forecast circle which passed near Tokyo, predicted storm surges for the center path showed close agreement with observational data at the Tokyo tide station. Storm surge warnings are issued based on these ensemble prediction results.

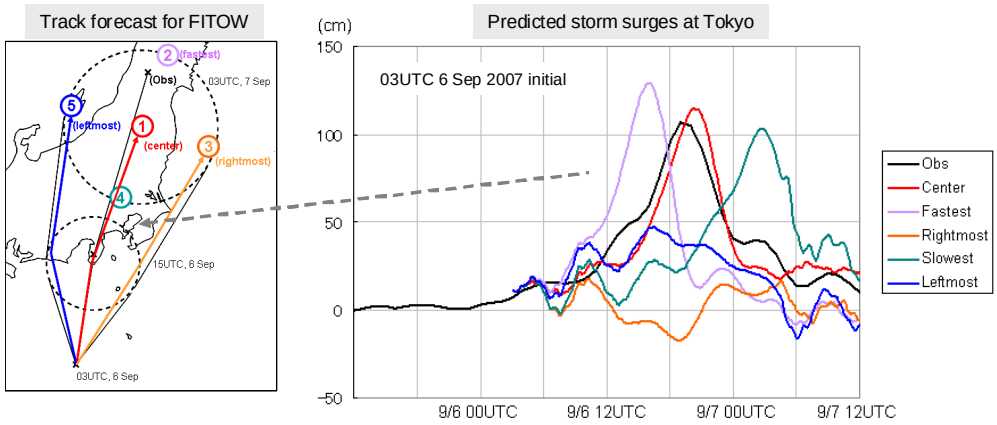

Figure 10. Track forecast for TY FITOW (0709) issued at 03UTC 6 September 2007 (left) and predicted storm surges at Tokyo for five different tracks (right).

3. Tropical Cyclone Research

In recent years TC forecasts have considerably improved thanks to the progress of numerical weather prediction techniques and various observation networks including microwave satellites observations. However, JMA is requested to issue more accurate and timely TC information and products to further contribute to TC related-disaster prevention activities in Japan. In this point of view, our operational needs for TC research are summarized as follows:

- Improvement of the TC ensemble prediction system to provide forecasters with more appropriate information on track forecast reliability.
- Comprehensive real-time track and intensity forecast guidance using multi center model predictions including ensemble predictions in forecaster-friendly format.
- NWP model-based forecast guidance for TC intensity change, particularly for rapid developing TCs.
- Development of techniques to estimate TC intensity using microwave satellite data such as TMI, AMSR-E, AMSU and SeaWinds.
- Quantitative guidance on forecasting precipitation amounts, maximum winds and storm surge heights associated with a TC.
- Operational guidance on the occurrence of TC-related disasters such as floods, landslides and storm surges.

4. Summary

Present capability of TC forecasting and warning at JMA is reviewed focusing on track, intensity, precipitation and storm surge forecasts. Although TC forecasts have considerably improved recently and a variety of TC information and products are now provided promptly to users, forecasters are still requested to issue more appropriate TC information to support disaster prevention activities. In this point of view, some challenges for the future such as further improvement of TC information using ensemble prediction results are discussed.

A Brief Overview of Operational Tropical Cyclone Forecast in Taiwan

Tien-Chiang Yeh

Pacific Science Association

c/o Department of Meteorology
Naval Postgraduate School Code MR/Cp
Monterey, CA 93943 USA

I. Introduction

Taiwan is located in the main paths of the western North Pacific tropical cyclones (TC). About one third of the named TC in the basin affected Taiwan and nearby ocean areas. On average, 4 TCs made center landfall at the island each year. With damaging wind and the heavy rainfall, TC is the major hazardous weather system in Taiwan. The operational service, CWB, is responsible for issuing warnings. and providing TC forecast information, which are the Bureau's most important job when a tropical cyclone is ,approaching. A, brief overview of the operation of the tropical cyclone forecast at the CWB is given below. Requirements to provide better service were discussed.

II. Tropical cyclone forecast

To provide accurate rainfall and wind speed distributions over Taiwan is the main goal of the TC forecast of the weather service. Both rainfall and winds distributions depend heavily on the location of the center of the cyclone, therefore the track forecast is the number one variable of TC forecast. Particularly, the 24-h track forecast. The numerical model prediction results are the major guidance for the TC track forecast. CWB operates a global numerical model (CWBGFS), and two limited area numerical models (NFS and CWBWRF). Lower resolution grid fields are also obtained from the forecasts of the global models of NCEPS, ECMWF, JMA, and UKMET through FTP or from the Global Telecommunication System. The annual averaged TC track forecast center position errors were shown in Figure 1. The CWB was able to improve their forecast skill by reducing the 24/48-h track forecast error from 170/325 km in year 2000 to about 100/170~190 km after year 2005. Better forecast from numerical models and the application of ensemble technique through CWB's TAFIS system contributed to the improvement of the forecast skill.

A Typhoon Aid Forecast Information System (TAFIS) was developed to help forecasters to do TC forecast. The TAFIS has the capability of determining, the center of each model forecast, displaying the track of each model forecast and of each official forecast available, calculating the error of each forecast, and deriving the ensemble results from different model forecasts. Different track forecast guidances with their errors are all integrated on TAFIS that can help the forecasters to examine vast amount of information and make their decision in TC track forecast.

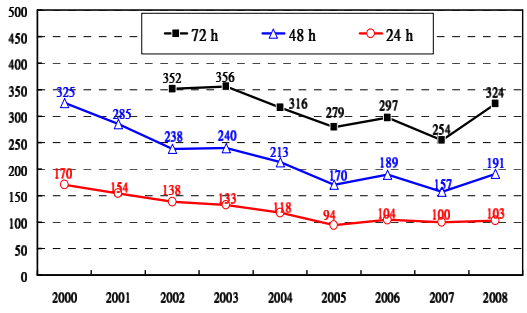

Figure 1: The CWB annual averaged TC position errors (km) from 2000 to 2008.

CWB has collected complete historical weather observational data when TC invaded Taiwan. Based on the observations, Wu and Chi (1973) shown that TC rainfall over Taiwan is correlated with the locations of the TC center. Analog approach and climatology forecast method were then developed and implemented to be the operational forecast aid for TC rainfall forecast at CWB (Wang et al. 1986; Wu and Shieh 1990; Yeh et al. 2000). Although complete verification of the score of the forecast has not been provided, Yeh (2002) shown the correlation coefficient of the observed and forecasted 6-h accumulated rainfalls at each SYNOP observation station when TC nearby is larger than .65 in most of the area. Smaller numbers were found at offshore islands where mountain effect is smaller. For observing more detailed distribution of the rainfall, CWB installed an automatic surface observation network which includes about 400 rain gauges. A climatology model based on the high density rain gauges then was developed by Lee et al. (2006) and implemented at CWB. Based on the rainfall of the analog TC cases selected and the statistical model forecasts, ranges of the total accumulated rainfall for the whole period of TC warning and the 24-h accumulated rainfall at every county were issued at the CWB every 3 hours. Figure 2 displayed the time sequence of the accumulated rainfall observed at a village in Kaohsiung County when Typhoon Morakot invaded in 2009. The corresponding CWB forecast rainfall ranges were also shown in the figure. The maximum accumulated rainfall of 800 mm was first forecast at the 0601 LST (01 AM of 06 August). The forecast value was updated to 1,400 mm at 0719 LST when the observed amount reached 500 mm. With exceptional large and long extending rainfall, the updating of the forecast values had been more gradual. However, CWB was able to warn the public at least 10 hours before the rainfall amount reached the forecasted value. The total accumulated rainfall due to Typhoon Morakot at the village in Fig. 2 reached 2,872 mm in the 4-day period from 0601 LST to 1000 LST.

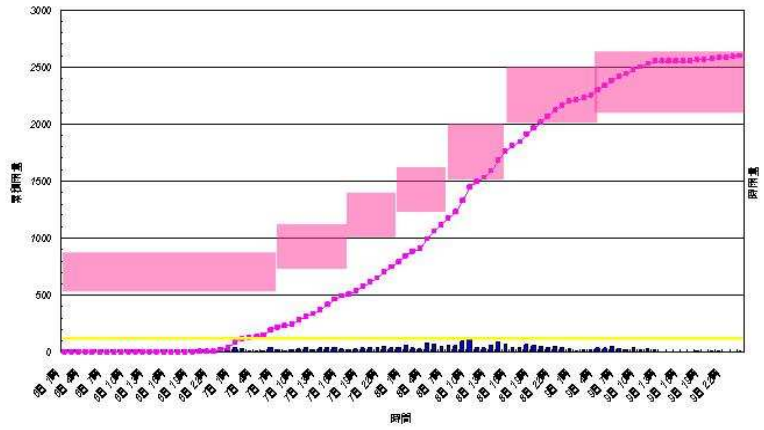

Figure 2: Curve is the accumulated rainfall (mm in vertical axis) observed at a village in Kaohsiung County, Taiwan from 1 AM 6 Aug to 1 AM 10 August, 2009 (horizontal axis). Shaded boxes are the CWB forecasted rainfall ranges for the area.

Similar to TC rainfall forecast procedure, climatology approach was used for TC wind speed distribution forecast. Figure 3 displays the distribution of the average gust wind speed, in Beaufort scale, at Taipei when TC centers were in the map domain. The average was calculated for cases whose TC center locations were similar. Different from a station in plane area or over the ocean, the figure shown the wind speeds at Taipei did not reach its maximum when TC centers moved close to Taipei (at a distance within the radius of maximum wind speed). But the wind speed reached the maximum when TC centers were located either northeast or southwest of Taipei. Yeh et al. (2004) explained that this is the result of the topography. They also showed, that, based on the climatology forecast methods, the correlation coefficient between the observation and the forecast of the maximum gust wind speed in Beaufort scale for the next 24 hours is near 0.50. And, the equitable threat score is near 0.20 with the threshold of the wind speed equals Beaufort scale 10.

During operations, forecasters at CWB determine and forecast the TC intensity change subjectively by referring to satellite observations, SST distribution, depth of the warm ocean layer, vertical wind shear, synoptic environment, and land and topography effect. When TC moved closer to Taiwan, additional observations from radar, and occasionally from dropsonde soundings, provided better estimation of the TC structure. The results were issued in terms of current tropical cyclone central pressure, maximum wind speed, radius of the maximum wind speed, and the radii of the wind speeds equal Beaufort scale 7 and 10. The intensity changes were provided only in a qualitative way, indicating whether the TC was going to intensify/weaken or expend/shrink in the next few hours. For the wind speed forecast over Taiwan, the forecasters will consider the current TC structure, the potential intensity change, and the local modification of the wind speeds at a forecast location. The forecast parameters issued to the public are the potential maximum substantial and gust wind speeds, in Beaufort scale, for each county or city for the next 24 hours in intervals of 6 hours. The process is repeated every 3 hours when warning was issued.

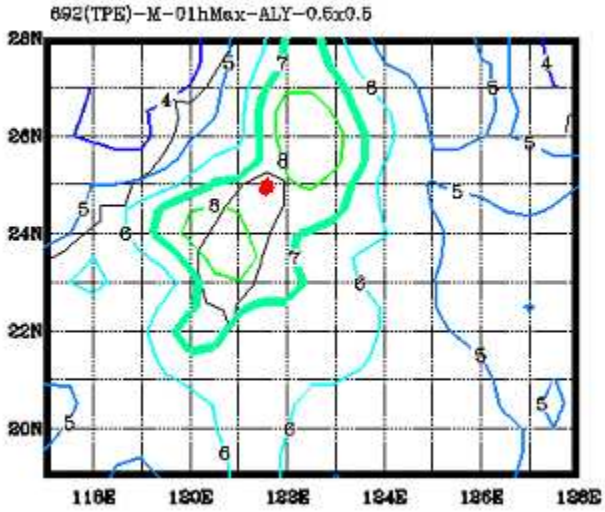

Figure 3: The averaged wind speeds (in Beaufort scale) at Taipei (dot) according to TC center positions.

III. **Requirement to improve the service**

In the past decade, the improvement of the numerical models has significantly reduced the TC track forecast error. However, this improvement still is often not adequate. Because a slow down or speed up or looping or rightward or leftward shift of the center in upstream of Taiwan when TC approached is important to know in advance for a good wind and rainfall forecast over Taiwan, and the model results usually did not provide such details. Larger diverse of the track were also noticed from different model forecasts in downstream of Taiwan. Because the high mountains affect the TC structure, and different processes in the model lead to different TC structure and different topography effects. Therefore studies on improvement of the model and on the topography effect on the movement and the structure of TC are the top priority for CWB.

Improvement of the quantitative rainfall forecast is the most urgent task in Taiwan. In the rainfall case of Typhoon Morakot, some numerical model did predict more than 2,000 mm of rainfall. However, more systematic verification of the model rainfall forecast is needed before the guidance can be confidently applied to the operation. How to better use the radar observation to provide guidance for quantitative rainfall forecast is also suggested for research studies.

Wind speed information of a TC has already been included in the TC bulletin. The maximum wind speed, radius of the maximum wind, and the size of the storm were relatively easy to obtain from most of the warnings issued by the operational centers. However, the rainfall information of a TC has not yet been

provided. Since some observations from satellites operated by the leading centers aere not available to public in real time, a suggestion is for the leading TC operation centers n the western North Pacific to provide information of the TC rainfall rate, or some sorts of TC rainfall parameters. The information will benefit TC rainfall forecast over land.

Statistical forecast methods have been proven useful for TC rainfall and wind speeds forecast over Taiwan area. More studies are suggested to improve the models' accuracy, particularly to integrate the structure information observed from satellite or radar into the models.

The record-breaking rainfall of Typhoon Morakot induced devastating floods, mudslides and debri flows in Taiwan. Hundreds of lives and billions of dollars of damages were lost, causing criticisms and resentment from the public and the press towards the weather service. Thus, it is important to have publics know the limite of the current skill of the TC forecast. Unrealistic expectation on TC forecast will minimize the usefulness of the forecast information on hazard mitigation, in some cases wrong expectation on the forecast may actually have a negative impact on hazard mitigation process. A suggestion is for the working group or WMO to provide a statement for the publics and the government officials to know the current limitation and the skill of the TC track, rainfall, wind speeds and storm surge forecasts.

References.

Lee, C. S.; Huang, L. R.; Shen, H. S.; Wang, S. T., 2006. A climatology model for forecasting typhoon rainfall in Taiwan, Natural Hazards, 37(1-2), 87-105.

Wang, S.-T., C.-L. Yeh, G. T. Chen, and S.-L. Shieh, 1986: The characteristics of typhoon precipitation and the prediction methods in Taiwan area (III) (in Chinese). Hazards Mitigation Program Technical Report 74-51, Taipei, 152pp.

Wu, T.-Y., and S.-L. Shieh, 1990: On the application of scientific results in meteorological research to typhoon forecast operation (III) (in Chinese). Research Report, NSC79-0414-P052-01B, Taipei, 137pp.

Yeh, T.-C., 2002: Typhoon rainfall over Taiwan area: The empirical orthogonal function modes and their applications on the rainfall forecasting. TAO, 13, 449-468.

Yeh, T.-C., S.-L., Shieh, and S.-C. Wu, 2000: A study of typhoon rainfall statistics forecast over Taiwan area. PartII: Spatial distribution of the forecasts (in Chinese). Atmos. Sci., 28, 263-279.

Yeh, T.-C., S.-L., Shieh, and S.-C. Wu, 2004: A study on the typhoon strong wind forecast over Taiwan area (III) (in Chinese). Research Report, NSC92-2625-Z052-004, Taipei, 178pp.

International Workshop on Tropical Cyclone Landfalling rocesses II, Shanghai China, October 2009

Jim Davidson

Bureau of Meteorology, Australian

1. Summary

This Workshop paper endeavours to encapsulate the outcomes of IWTCLP-I (2005), IWTC-VI (2006) and recent contributions from the 3 Australian TCWCs (personal communication) – where they are applicable to the TC forecasting challenge. It was considered that the best approach was to build on the fine achievements of participants at IWTCLP-I and IWTC-VI.

As was discussed at IWTC-VI (and still relevant today), prospects for further improvements in quantitative forecasts of TC landfall appear to largely rest on greater access to multi-model consensus and single-model ensemble (EPS) forecasts of not only track and intensity but also storm tide and precipitation. Substantial gains can also be realised through the continuing development and distribution of parametric models for forecasting landfall hazards. Remote sensing data, especially from weather satellites, will remain critical to the forecast process.

One of the major recommendations from IWTC-VI (and an ongoing priority) is for greater effort to be directed by the research community into intensity and structure prediction, which continues to be a serious deficiency in forecasting landfall hazards. Importantly, this does not imply that studies into improving track forecasting should be given a low priority as small deviations in the path of a TC do have an immense bearing on the distribution of impacts.

A need is known to exist for improved specification of meteorological forcing for storm surge models. Another prominent weakness is forecasting the spatial and temporal distribution of rainfall from a landfalling TC, coupled with consequential flooding. An even greater universal challenge is modelling the combination of TC storm surge, wave action and riverine flooding.

With a focus on the TC landfall phase, the highest operational priority from the Australian TCWCs perspective are advanced techniques for optimising NWP EPS and consensus output for track and intensity forecasts, storm surge, waves and precipitation. For a TC approaching the coastline, a full suite of probabilities for the various landfall hazards is highly desirable eg the probability that (1) the TC will make landfall between A and B, (2) it will be a Category 4 system at landfall, (3) that it will produce a storm surge > 3 metres – and so on.

2. Tropical Cyclone Landfall Hazards (to be considered in this paper)

Wind (includes tornadoes)
Storm Tide – Waves
Rainfall – Flood — Landslips, Mudslides, Debris Flows
Note in particular that 5 of the 6 TC landfall hazards are water related.

3. Established Facts (from IWTC-VI)

- Landfall hazard prediction is highly dependent on the TC's track. At a particular location, even small deviations in track can result in vastly different impacts from wind, storm tide, precipitation and flooding.
- Most deaths in TCs are caused by flooding, landslips, mudslides and debris flows.
- With the steady growth in coastal population and infrastructure, we are witnessing what amounts to a quantum leap in vulnerability (and therefore risk) in many TC prone areas, irrespective of trends in TC numbers and intensities. Not surprisingly, evacuation times have increased accordingly.
- TC speed at landfall is quite critical in terms of potential wind and flood damage. The faster a TC is moving, the lower the risk of significant wind and flood damage.

4. Priorities identified at IWTCLP-I

Participants gave the following priority ranking in regards to improving TC landfall forecasts:

1. Further improvements in track landfall forecasts;
2. Improved predictions of TC-related precipitation (both temporal and spatial) following landfall;
3. Advances in understanding and predictions of structure and intensity during and following landfall, and from tropical storm stages to extra-tropical transition: and
4. Further application of storm surge models, including improved specification of the meteorological forcing.

5. Forecasting Strengths and Weaknesses identified at IWTC-VI

Relative Strengths

- Track forecasting (but small deviations in track do matter)
- Storm surge modelling (but also dependent on meteorological inputs)
- Hydrological modelling (but also dependent on meteorological inputs)
- NWP (including mesoscale/nested/coupled models)
- Remote sensing data (eg satellite, scatterometer, Doppler radars)
- Dvorak technique (although with some qualifications/reservations)

Relative Weaknesses

- Forecasting intensity, structure, structural change
- Forecasting spatial and temporal rainfall distribution
- Modelling wave action (including vicinity of small islands)
- Modelling the combination of "riverine flooding + storm surge + waves"
- Forecasting landslips, mudslides and debris flows
- Defining Wind-Pressure relationships (which are TC dependent)
- Forecasting fine-scale wind features upon landfall
- Estimating the wind decay rate in the transition over land
- Surface and upper air observations networks in many regions
- Quality of topographic and bathymetric data available for modelling

6. As an overlay, a selection of forecaster requirements agreed to at IWTC-VI is reproduced below. Most if not all the statements remain valid today.

EPS – Consensus Forecasts – Parametric Models - Probability Forecasts

- EPS (single-model) and Consensus forecasts (multi-model) are seen to complement Deterministic NWP forecasts. The continuing availability of high-resolution deterministic NWP modelling output is seen to be critical in the forecast process.
- EPS, Consensus and Parametric modelling applications can and should be developed for most if not all TC parameters and hazards (eg genesis, track, intensity, storm surge, waves, precipitation and maybe floods). A suite of parametric models would be especially useful for small NMHSs – but also of value as "first guess" guidance in RSMCs/TCWCs.
- Probabilities can be derived from all 3 techniques (EPS, Consensus and Parametric).
- "What if" scenarios can be operationally tested in real-time using parametric models.
- The full data set from EPS and Consensus runs should be made available to forecasters, so that the implications of different forecast scenarios for the various TC hazards can be examined. Forecaster training in the use of EPS and Consensus forecasts is essential.
- Consensus forecasts should be closely evaluated to identify: (1) the minimum number and optimal combination of forecast members that adds value to the forecast process; and (2) strategies to deal with situations when the consensus forecast does not work.
- A demonstrated need exists for a single password-protected repository for all global NWP forecast tracks and intensities, including where available EPS and Consensus forecasts. See for example: **http://www.bom.gov.au/bmrc/projects/THORPEX/TC/index.html**

Track Forecasts

- Track forecasts are most important at longer lead-times but intensity/structure forecasts are nearly as important at shorter lead-times near landfall.
- The causes of large forecast errors should be systematically investigated through a comprehensive examination of all relevant potentially linked elements: observations, data assimilation and vortex specification techniques for initial conditions, model resolution and physical processes representations. Document synoptic patterns likely to be associated with large forecast errors including identification of model biases and weaknesses.
- The continuing development of high-resolution models should be encouraged. Because they better resolve orography, they may well assist in improving track and intensity prediction of TCs near landfall (including wind and rainfall distribution).

Intensity and Structure Forecasts

- The continuing development of dynamical models and statistical-dynamical models is encouraged with the aim of improving the skill in intensity and structure prediction (and resulting wind and rainfall fields).
- More research needs to be undertaken in improving our understanding of genesis, intensification, size changes, and extra-tropical transition and weakening processes.
- More research should be conducted (both numerical and statistical) in improving TC vortex specification and initialisation (eg bogussing), via data assimilation (down to mesoscale), parameterisation, and inclusive of the inner core and outer core regions.

Wind Forecasts

- The Dvorak technique needs to be recalibrated for all basins, with the application of remote sensing advances.
- A public domain parametric wind field model is required, which includes assymetries. This could then be used in conjunction with scatterometer data and the Dvorak technique to determine an individual TC's wind and pressure profile.
- Further studies are required into the asymmetry in TC structure at landfall, including developing a greater understanding of fine-scale and transient features such as mesovortices, boundary layer wind streaks and roll vortices.

Rainfall - Floods – Storm Surge – Wave Action

- Improved rainfall forecasting techniques should be developed, including ones that are EPS-based. See for example: **http://www.ssd.noaa.gov/PS/TROP/etrap.html**.
- A parametric precipitation model for landfalling TCs should be developed and evaluated.
- QPF for landfalling TCs is required at greater spatial and temporal resolution.
- Even an indication of a "dry", "average" or "wet" landfalling TC is considered useful.
- Continued development of a very short-range rainfall forecasting technique is required, with extrapolation for the first 0-3 hours followed by mesomodelling out to about 6 hours.
- Greater availability of near real-time radar-rainfall accumulation techniques is required, especially for short lead times such as in flash flood, landslip and mudslide situations.
- Better modelling is required of the combined effects of storm surge, wave action and riverine flooding (using higher resolution topographic and bathymetric data).
- Further studies are required in to wave setup and techniques developed for providing more reliable operational estimates. Wave setup can often be an important component of storm tide. Wave runup is also significant in some locations and warrants further investigation.
- Another major requirement is improved operational hydrological flood modelling through tighter coupling with meteorological and tidal modelling outputs. The best results are likely to be achieved through meteorological forcing by high-resolution NWP output.
- Allowance should be made for gridded rainfall inputs to hydrological models to take advantage of improved spatial and temporal rainfall analyses from high-resolution NWP models. Hydrological model domains are best digitised to enable gridded rainfall inputs.

Partnerships – Communication – Community Response

- It is important to develop stakeholder partnerships, especially with the media, disaster managers and local government.
- Social scientists should be employed or utilised by NMHSs to improve the communication of TC warnings. For example, a continuing trend is evident towards more probability-type forecasts. Media specialists and social scientists should be closely involved in the creation of effective warning formats involving probabilities, keeping in mind that communicating RISK is not the same as communicating PROBABILITY.
- The availability of radar and satellite images on the Internet and TV, more graphical warning products, the inclusion of "recommended response actions" in warnings, and the use of a Category system have improved the chances of a threatened community better understanding the threat and responding appropriately. In pictorial displays, TCs are best represented as envelopes of damaging/destructive winds – and not just a singular point.

7. Australian TCWCs response to the 3 topics to be specifically addressed during the Workshop session

A. Summarize present capabilities and deficiencies of your NMHS by describing what TC landfall forecast variables or impacts are being adequately provided and where requirements are not being met.

Capabilities:

- An efficient forecasting process well supported by systems (software (TCModule), observations networks, satellite, radar, access to NWP). Very competent TC forecasters.
- Each of the 3 TCWCs has strong communication links with key Media and Disaster Management agencies (including participation in regular teleconferences during events).
- A range of products is available for different audiences. For example, the pictorial Forecast Track Map conveys important information in an easy to understand format.
- Track forecast errors have markedly decreased reflecting advances in TC forecasting.

Deficiencies:

- Limited coverage of observations and radars especially in isolated and offshore regions.
- Growing demand for advanced lead time of TC genesis (to seven days) which remains a difficult task.
- Forecasting intensity and structure changes at landfall is still a significant challenge.
- Reliable TC strike probability information is not yet available.
- Storm tide forecasts are relatively imprecise compounded by limited community understanding of the risk.
- A significant gap continues today in the transfer of new satellite monitoring and intensity forecasting techniques into TCWC operations.
- The challenge in maintaining adequate TCWC staffing levels for lengthy TC events.

B. What TC research studies would be most helpful to provide better guidance for your NMHS forecasts?

Relevant quote from IWTC-V:

Establish good decisions as the goal of research rather than good predictions, good theories or good models.

Relevant quote from IWTC-VI

There's greater value in focussing resources on researching extreme events (not forgetting though that weak TCs can produce major floods).

See the attached table which has been modified to incorporate the TC research priorities of the Australian TCWCs. Below are specific research studies identified by the TCWCs:

- With a focus on the TC landfall phase, advanced techniques for optimising NWP EPS and Consensus output for track and intensity forecasts, storm surge, waves and precipitation.
- Better "operationalisation" of latest research (eg develop suitable data viewing tools)
- Improved NWP guidance on TC genesis (eg Okubo-Weiss), intensity and structure.
- Improved conceptual models of both TC genesis and decay after landfall.

- Improved operational systems for storm surge forecasting.
- Improved wave guidance through coupling of ocean wave model with TC NWP.
- Improved temporal and spatial rainfall forecasts for landfalling TCs.
- Improved TC database to enhance the capabilities of risk assessments.
- Improved observational systems/platforms within the TC and its environment.

C. Comments about issues or requirements about improving public response to TC landfall warnings are encouraged.

- The pre-season disaster mitigation campaign in TC-prone areas is a joint undertaking by the Bureau of Meteorology, Emergency Management and now partnered by ABC Local Radio (the emergency broadcaster in Australia).
- The introduction of regular teleconferences during TC events with disaster managers has proven to be a great success in ensuring that important information is shared and that a consistent message is relayed by trusted authorities to a threatened community.
- Regular radio and TV interviews during TC events are a key link in the warning chain.
- "Recommended response actions" provided by disaster managers are clearly articulated in TCWC warnings and are generally understood by a threatened community.
- The suite of warning services satisfies a range of needs with graphical products (eg the Forecast Track Map) considered the best means of conveying key messages.
- In Australia's far northern remote indigenous communities, there is a need for more effective public education initiatives, action plans and enforcement of preparation and mitigation activities.

The **Standard Emergency Warning Signal** (SEWS) – a distinctive siren - has been used in Australia for many years on radio and TV to introduce a warning where a significant threat exists. Later this year, a **National Early Warning System** (NEWS) will be introduced to alert communities by telephone where a threat is both very significant and very imminent (short-fuse). The trigger for the NEWS was the disastrous Victorian bushfires early in 2009.

As a general guide only, the following 4 factors would normally be present for the use of the SEWS and/or NEWS to be considered by authorities:

SEWS	NEWS
1. Potential for loss of life and/or a major threat to a significant number of properties or the environment. Usually the threat/impact would be the lead item in local news bulletins.	1. Potential for loss of life and/or a serious threat to a significant number of properties. Usually the threat/impact would be the lead item in state news bulletins.
2. A significant number of people need to be warned.	2. A significant number of people need to be warned and maybe evacuated.
3. Impact is expected within 12 hours – or is occurring at the time.	3. Impact is expected within 6 hours – or is occurring at the time.
4. One or more phenomena are classified as "destructive".	4. One or more phenomena are classified as "very destructive/very dangerous".

8. Australian TCWCs Highest Operational Priority

With a focus on the TC landfall phase, advanced techniques for optimising NWP EPS and Consensus output for track and intensity forecasts, storm surge, waves and precipitation. For a TC approaching the

coast, a full suite of probabilities for the various landfall hazards is highly desirable eg the probability that (1) the TC will make landfall between A and B, (2) it will be a Category 4 system at landfall, (3) that it will produce a storm surge > 3 metres – and so on.

9. Operational Needs of TC Forecast and Warning Centres

TPC/NHC	JTWC	Australia TCWCs	Operational Need
1	**1**	**2**	Guidance for tropical cyclone **intensity change**, with highest priority on the onset, duration, and magnitude of rapid intensification events.
2	**2**	**4**	Improved **observational systems** in the storm and its environment that provide data for forecaster analysis and model initialization.
3	**5**	**1**	**Statistically-based real-time guidance** for track, intensity and precipitation (eg multi-model consensus approaches), provided to forecasters in probabilistic and other formats.
4	**6**	**8**	**Enhancements to the operational environment** to increase forecaster efficiency, by expediting analysis, forecast, coordination, and/or communication activities.
5	**7**	**5**	**Additional operational guidance on coastal inundation** (eg storm surge and waves).
6	**8**	**9**	**Identification, and then reduction of, the occurrence of guidance and official track outliers**, focussing on both large speed errors and large direction errors, and on **specific forecast problems**, including interactions between upper-level troughs and tropical cyclones, track forecasts near mountainous areas, and extra-tropical transition.
7	**3**	**3**	Guidance for **tropical cyclone genesis** that exhibits a high probability of detection and a low false alarm ratio, and/or provides probability of genesis.
8	**9**	**10**	**Operational analysis of the surface wind field** in tropical cyclones. This also includes methods for forecasting the wind field over elevated terrain and high-rise buildings.
9	**4**	**7**	Guidance for **changes in tropical cyclone size/wind structure** and related parameters, including combined sea heights.
10	**10**	**12**	Guidance on the operational utility and relative merits of **high-resolution model output compared to lower resolution ensemble model output.**
11	**11**	**6**	Guidance for **tropical cyclone precipitation amount and distribution.**
12	**12**	**11**	Improved utility of **microwave satellite and radar data** in tropical cyclone analysis.

Targeted Observation of Tropical Cyclones

Chun-Chieh Wu

PSA

cwu@typhoon.as.ntu.edu.tw

ABSTRACT

The advance in targeted observations of tropical cyclone movement is reviewed in this article. The targeted observations from DOTSTAR (Dropwindsonde Observations for Typhoon Surveillance near the Taiwan Region) in understanding and improving the tropical cyclone track predictability is highlighted, along with the progress of the field program of THORPEX-PARC in the summer of 2008. The impact of the dropwindsinde data from DOTSTAR has been demonstrated. A specific targeted method (Adjoint-Derived Sensitivity Steering Vector) for tropical cyclone motion has been proposed. Intercomparison of all targeted observation guidance products for western North Pacific typhoons have also been conducted.

1. Introduction

Over the past 30 years, persistent and steady progress on the track forecasts of TCs have been well demonstrated through the improvement of the numerical models, the data assimilation system, and the new data available to the forecast system (Wu 2006). In addition to the large amount of satellite data, the special dropwindsondes data deployed from the surveillance aircraft have also provided significant added values in improving the track forecasts.

In order to optimize the limited aircraft resources, targeted observations in the critical areas which have the maximum influence on numerical weather forecasts of TCs are of great importance. Therefore, targeted observing strategies for aircraft missions must be further developed. And it is the prerequisite for the device of observing strategy to identify the sensitive areas that have the greatest influence in improving the numerical forecast, or minimizing the track forecast error.

To make use of the available data or the potentially new data, it is important to evaluate the potential impact and to test the sensitivity of the simulation and prediction of TCs to different parameters. This understanding can be of great use in designing a cost-effective strategy for targeted observations of TCs (Morss et al. 2001; Majumdar et al. 2002a, b; Aberson 2003; Wu et al. 2005).

In this section, three issues related to the author's works are addressed: first, the impact of the DOTSTAR data; second, results from a set of Observation System Simulation Experiments (OSSEs); and third, an innovative development of the new targeted observation strategy, Adjoint-Derived Sensitivity Steering Vector (ADSSV).

2. Impact of dropwindsonde data on TC track forecasts in DOTSTAR

Since 2003, the research program of "Dropwindsonde Observations for Typhoon Surveillance near the Taiwan Region" (DOTSTAR, Wu et al. 2005, 2007b) has continuously conducted dropwindsonde observations of typhoons in the western North Pacific (Fig. 1). Three operational global and two regional models were used to evaluate the impact of the dropwindsonde on TC track forecasting (Wu et al. 2007b). Based on the results of 10 missions conducted in 2004 (Wu et al. 2007b), the use of the dropwindsonde data from DOTSTAR has improved the 72-h ensemble forecast of three global models, i.e., the Global Forecasting System (GFS) of National Centers for Environmental Predictions (NCEP), the Navy Operational Global Atmospheric Prediction System (NOGAPS) of the Fleet Numerical Meteorology and Oceanography Center (FNMOC), and the Japanese Meteorological Agency (JMA) Global Spectral Model (GSM), by 22% (Fig. 2).

Wu et al. (2007b) showed that the average improvement of the dropwindsonde data made by DOTSTAR to the 72-h typhoon track prediction in the Geophysical Fluid Dynamics Laboratory (GFDL) hurricane models is an insignificant 3%. It is very likely that the signal of the dropwindsonde data is swamped by the bogusing procedure used during the initialization of the GFDL hurricane model. Chou and Wu (2008) showed a better way of appropriately combining the dropwindsonde data with the bogused vortex in the mesoscale model in order to further boost the effectiveness of dropwindsonde data with the implanted storm vortex.

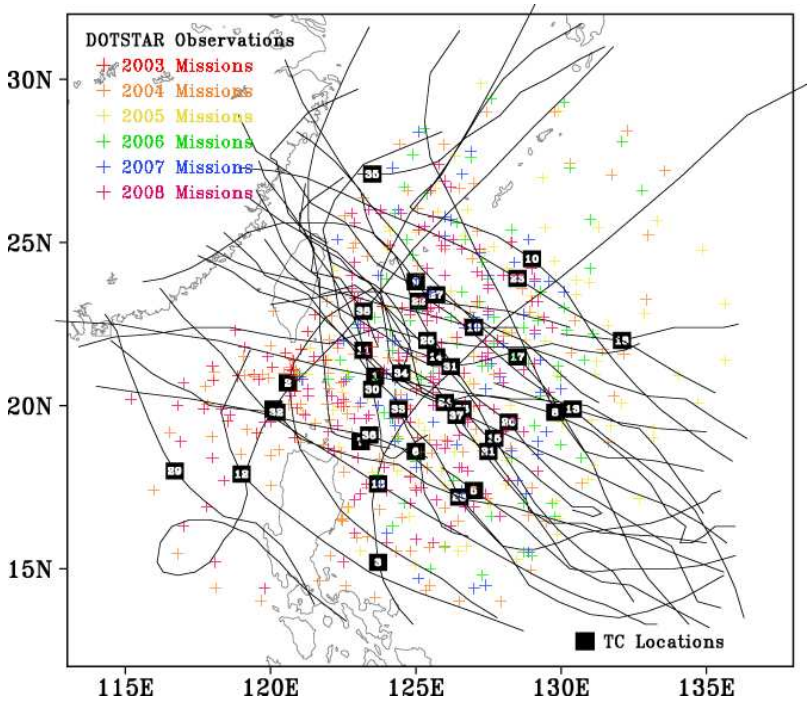

Figure 1. Best tracks of the 31 typhoons with 38 DOTSTAR observation missions from 2004 to 2008. The squares indicate the storm locations when the DOTSTAR missions were taken. The numbers on the squares represent the sequence of the missions. (From Wu et al. 2007b)

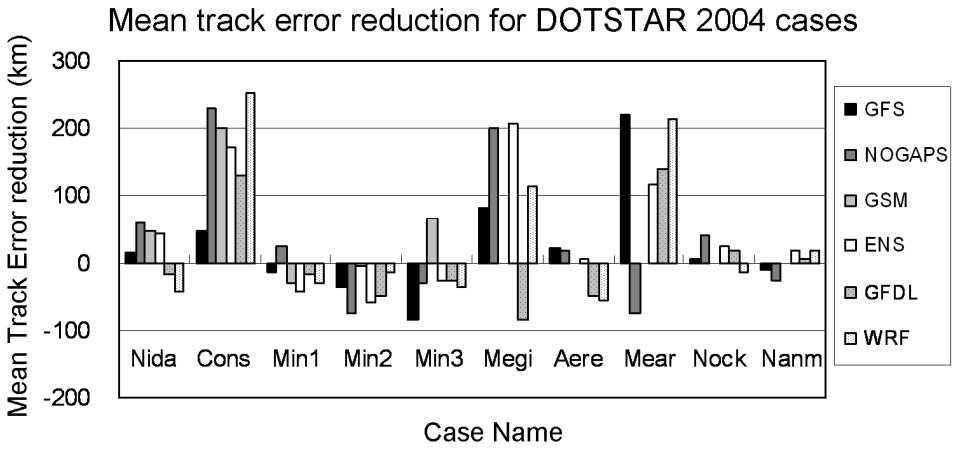

Figure 2. This represents 6-72-h mean track error reduction (in km) after the assimilation of the dropwindsonde data into each ten models. The storm name is abbreviated by its first four alphabets, while Min1, Min2 and Min3 stands for the first, second, and third cases in Mindulle. (From Wu et al. 2007b)

3. OSSE study (Wu et al. 2006)

As the conventional observations usually have far less degrees of freedom than the models, the four-dimensional variational data assimilation (4DVAR) has become one of the most advanced approaches in combining the observations with the model in such a way that the initial conditions are consistent with the model dynamics and physics (Guo et al. 2000). Based on 4DVAR, a bogus data assimilation method had been developed by Zou and Xiao (2000) to improve the initial conditions for TC simulation.

A set of Observation Systems Simulation Experiments (OSSEs) have been performed to identify the critical parameters and the improved procedures for the initialization and prediction of TCs. A control experiment is carried out to create the imaginary "nature" data for Typhoon Zane (1996), using the fifth-generation Pennsylvania State University-National Center for Atmospheric Research Mesoscale Model (MM5). Then the initial data from the control experiment is degraded to produce the new initial condition and simulation, which mimics typical global analysis that resolves the Zane circulation. By assimilating some variables from the initial data of the control experiment into the degraded initial condition based on 4DVAR, the insight into the key parameters for improving the initial condition and prediction of TCs is attained (Wu et al. 2006).

It is shown that the wind field is critical for maintaining a correct initial vortex structure of TCs. The model's memory of the pressure field is relatively short. Therefore, when only the surface pressure field is assimilated, due to the imbalance between the pressure and wind fields, the pressure field adjusts to the wind field and the minimal central sea-level pressure of the storm rises quickly.

It is well demonstrated that taking the movement of the TC vortex into consideration during the data assimilation window can improve the track prediction, particularly in the early integration period. When the vortex movement tendency is taken into account during the bogus data assimilation period, it can partially correct the steering effect in the early prediction and the simulation period (Fig. 3). This concept provides a

new and possible approach to the improvement of TC track prediction.

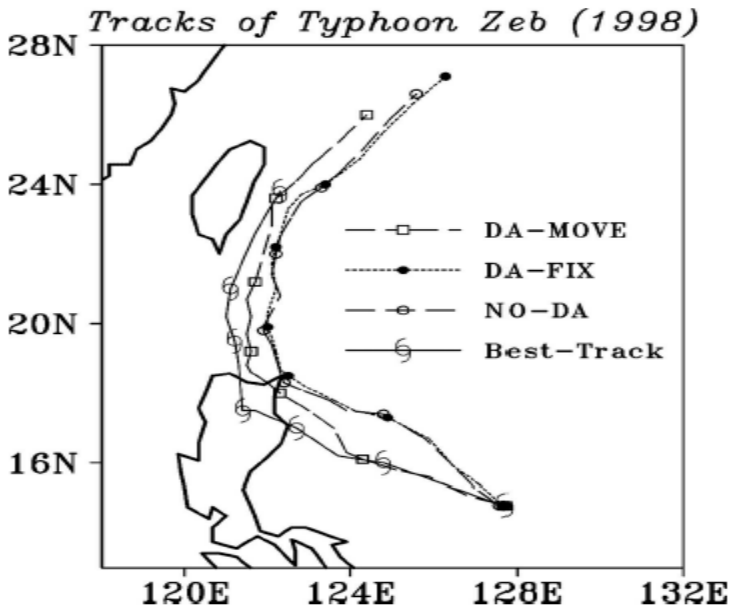

Figure 3. The 72-h JTWC best track (indicated with typhoon symbol) and the simulated storm tracks from experiments NO-DA, DA-FIX and DA-MOVE for Typhoon Zeb (1998), shown for 12-h intervals from 0000 UTC 13 Oct. to 0000 UTC 16 Oct. 1998. NO-DA: a standard MM5 simulation with an initial bogused vortex following Wu et al. (2002) without data assimilation. DA-FIX: experiment assimilated the above bogused vortex (fixed in location) based on a 30-min window 4DVAR data assimilation. DA-MOVE: experiment in which the vortex is assimilated with the same initial data except it moved in 3-h window assimilation. (From Wu et al. 2006)

4. Targeted observations for TCs

(1) Adjoint-Derived Sensitivity Steering Vector (ADSSV) (Wu et al. 2007a, 2009a)

By appropriately defining the response functions to represent the steering flow at the verifying time, a simple innovative vector, Adjoint-Derived Sensitivity Steering Vector (ADSSV), has been designed (Wu et al. 200a) to clearly demonstrate the sensitive locations and the critical direction of the typhoon steering flow at the observing time.

Because the goal is to identify the sensitive areas at the observing time that will affect the steering flow of the typhoon at the verifying time, the response function is defined as the deep-layer-mean wind within the verifying area. A 600 km by 600 km square area centered on the MM5-simulated storm location is used to calculate the background steering flow as defined by Chan and Gray (1982), and two response functions are defined: R_1, the 850-300 hPa deep-layer area average (Wu et al. 2003) of the zonal component (u), along with R_2, the average of the meridional component (v) of the wind vector, i.e.,

$$R_1 \equiv \frac{\int_{850hPa}^{300hPa}\int_A u \quad dxdydp}{\int_{850hPa}^{300hPa}\int_A dxdydp} \quad \text{, and} \quad R_2 \equiv \frac{\int_{850hPa}^{300hPa}\int_A v \quad dxdydp}{\int_{850hPa}^{300hPa}\int_A dxdydp}. \qquad (1)$$

By averaging, the axisymmetric component of the strong cyclonic flow around the storm center is removed, and thus the vector of (R_1, R_2) represents the background steering flow across the storm center at the verifying time. To interpret the physical meaning of the sensitivity, a unique new parameter, ADSSV, is designed to relate the sensitive areas at the observing time to the steering flow at the verifying time. The ADSSV with respect to the vorticity field (ς) is

$$ADSSV \equiv \left(\frac{\partial R_1}{\partial \varsigma}, \frac{\partial R_2}{\partial \varsigma}\right) \quad , \qquad (2)$$

where the magnitude of ADSSV at a given point indicates the extent of the sensitivity, and the direction of the ADSSV represents the change in the response of the steering flow due to a vorticity perturbation placed at that point. For example, an increase in the vorticity at the observing time would be associated with an increase in the eastward steering of the storm at the verifying time, given the ADSSV vector at one particular grid point aims to the east at the forecast time.

The ADSSV, based on the MM5 forecast (Fig. 4), extends about 300-600 km from the north to the east of Typhoon Meari (2004). The directions of the ADSSVs indicate greater sensitivity in affecting the meridional component of the steering flow.

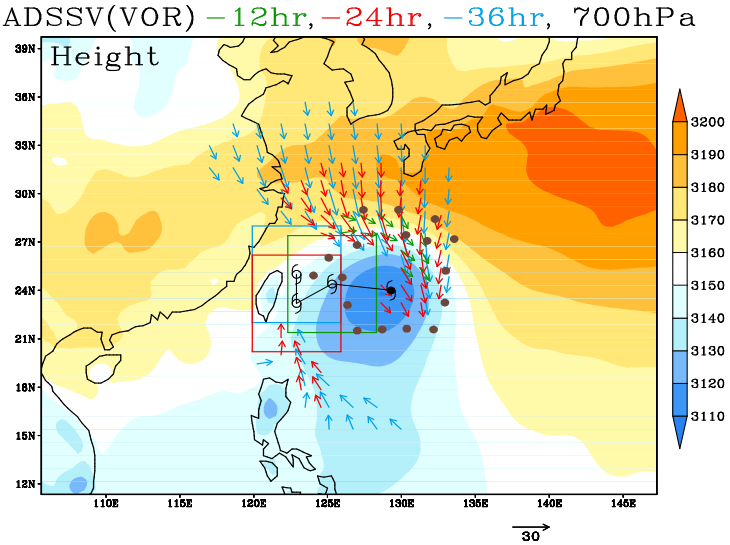

Figure 4. ADSSV with respect to the vorticity field at 700 hPa at 12 (in green), 24 (in red) and 36 h (in blue) as the verifying time, superposed with the geopotential height field (magnitude scaled by the color bar to the right, unit: m) at 700 hPa and the deployed locations of the dropsondes in DOTSTAR. (Brown dots) The scale of the ADSSV vector is indicated as the arrow to the lower right. (Unit: m) The 36-h

model-predicted track of Meari is indicated with the typhoon symbols in red for every 12 h. The three square boxes represent the verifying areas at three different verifying times. (From Wu et al. 2007a)

In Wu et al. (2009a), the ADSSV is calculated from the nonlinear forecast model of the fifth-generation Pennsylvania State University–National Center for Atmospheric Research (PSU–NCAR) Mesoscale Model (MM5) and its adjoint to interpret the dynamical processes in the interaction between Typhoon Shanshan (2006) and the midlatitude trough. The ADSSV results imply that high-sensitivity regions affecting the motion of Typhoon Shanshan are located at the edge of the subtropical high and the 500-hPa midlatitude trough over northern central China. These ADSSV signals (Fig. 5) are in very good agreement with the quantitative evaluation based on the potential vorticity (PV) diagnosis. The vertical structure of the ADSSV is also shown for more physical insights into the typhoon–trough interaction. The maximum ADSSV occurs at 800–500 hPa to the southeast of Shanshan (associated with the subtropical high), while distinct ADSSV signals are located upstream of the storm center at about 500–300 hPa (associated with the mid- to upper-tropospheric midlatitude trough). Overall, it is demonstrated that the ADSSV features can well capture the signal of the large-scale trough feature affecting the motion of Shanshan, which can also be well validated from the PV analysis.

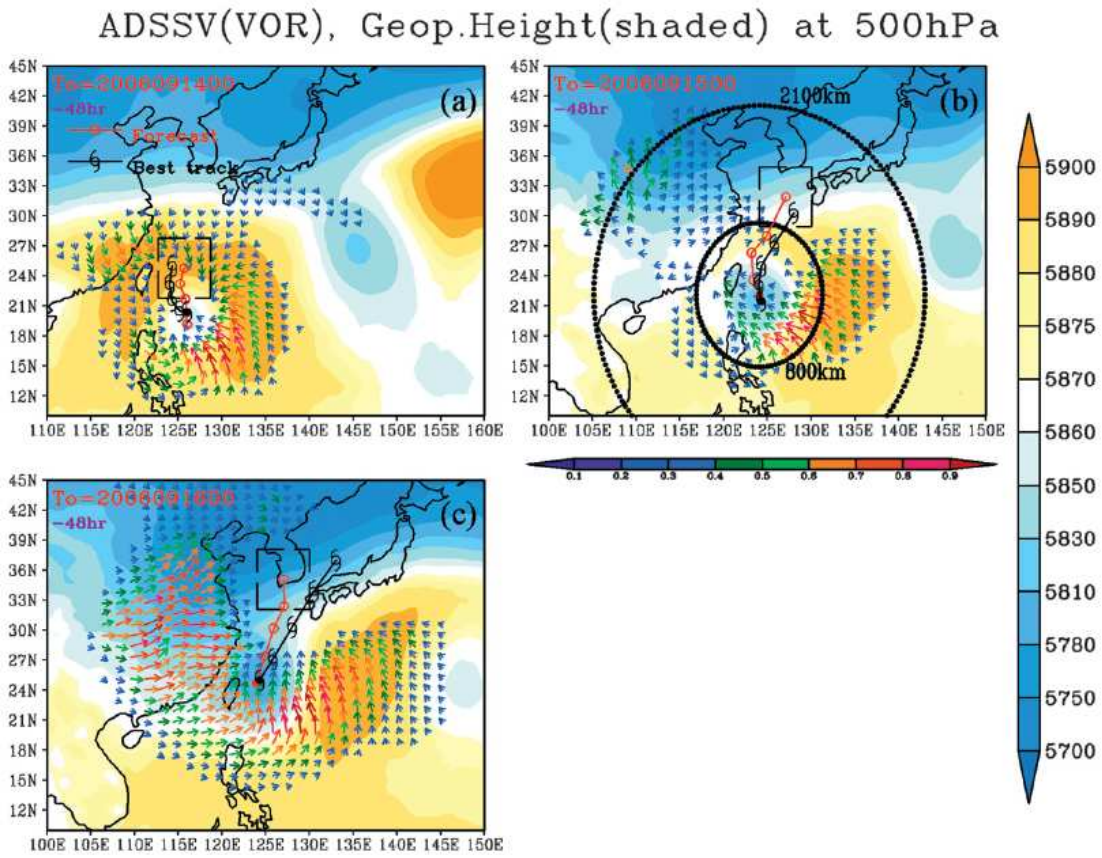

Figure 5. ADSSV with respect to the vorticity field at 500 hPa at the observing time, superposed with the geopotential height (magnitude scaled by the color bar to the right; m) at 500 hPa for (a) EXP1, (b) EXP2, and (c) EXP3. The magnitude of the ADSSV is normalized by the maximum value in the domain (the value smaller than 0.25 is omitted). The best track from CWB analysis and 48-h model-predicted track are indicated with the black typhoon symbols and the red circles for every 12 h, respectively. The dashed square box represents the verifying area at the verifying time. (From Wu et al. 2009a).

(2) Recent techniques for targeted observations of TCs

To optimize the aircraft surveillance observations using dropwindsondes, targeted observing strategies have been developed and examined. The primary consideration in devising such strategies is to identify the sensitive areas in which the assimilation of targeted observations is expected to have the greatest influence in improving the numerical forecast, or minimizing the forecast error. Since 2003, four objective methods have been tested for operational surveillance missions in the environment of Atlantic hurricanes conducted by the National Oceanic and Atmospheric Administration (NOAA) (Aberson 2003) and DOTSTAR (Wu et al. 2005). These products are derived from four distinct techniques: the ensemble Deep-Layer Mean (DLM) wind variance (Aberson 2003), the ensemble-transform Kalman-filter (ETKF, Majumdar et al. 2002), the total-energy singular vector (TESV) technique (Peng and Reynolds 2006), and the Adjoint-Derived Sensitivity Steering Vector (ADSSV) (Wu et al. 2007a). The above techniques have been applied in a limited capacity to identify locations for aircraft-borne dropwinsondes to be collected in the environment of the TCs. For the surveillance missions in Atlantic hurricanes conducted by NOAA Hurricane Research Division (HRD; Aberson 2003) and the DOTSTAR (Dropwindsonde Observations for Typhoon Surveillance near the Taiwan Region; Wu et al. 2005), other than the ADSSV method shown above, three other sensitivity techniques have also been used to determine the observation strategies:

(i) Deep-Layer Mean wind variance

Based on the deep-layer mean (DLM; 850-200-hPa averaged) steering flows from the NCEP Global Ensemble Forecasting System (EFS; Aberson 2003), areas with the largest (DLM) wind ensemble spread represent the sensitive regions at the observing time. The DLM wind ensemble spread is chosen because TCs are generally steered by the environmental DLM flow, and the dropwindsondes from the NOAA Gulfstream IV sample this flow.

(ii) Ensemble Transform Kalman Filter (ETKF)

This ensemble transform Kalman filter (ETKF) (Bishop et al. 2001) technique predicts the reduction in forecast error variance for a variety of feasible flight plans for deployment of targeted observations based on the 40-member NCEP EFS (Majumdar et al. 2006). That is, the ETKF uses the differences among ensemble members to estimate regions for observational missions. The ETKF takes the approach of DLM wind variance further. While DLM wind variance indicates areas of forecast uncertainty at the observation time, it does not correlate initial condition uncertainty with the errors in the forecasts. The ETKF explicitly correlates errors at the observation time with errors of the forecasts and identifies ensemble variance that impacts the forecasts in the verifying area at the verifying time.

(iii) Singular Vector (SV) technique

The SV technique maximizes the growth of total energy or kinetic energy norm (e.g., Palmer et al. 1998; Peng and Reynolds 2006) using the adjoint and forward-tangent models of NOGAPS (Rosmond 1997; Gelaro et al. 2002), along with the ensemble prediction system (EPS) of JMA and the Singular Vector products from European Center for Medium Range Forecast (ECMWF). Peng and Reynolds (2006) have demonstrated the capability of the SV technique in identifying the sensitive regions suitable for targeted observations of TCs.

The above techniques have been applied in a limited capacity to identify locations for aircraft-borne dropwinsondes to be collected in the environment of the TCs. To gain more physical insights into these

targeted techniques, studies to compare and evaluate the techniques have been conducted by Majumdar et al. (2006), Etherton et al. (2006), and Reynolds et al. (2007).

(3) Intercomparison of the targeted teniquues (Wu et al. 2009b)

Wu et al. (2009) compares six different guidance products for targeted observations over the northwest Pacific Ocean for 84 cases of 2-day forecasts in 2006 and highlights the unique dynamical features affecting the tropical cyclone (TC) tracks in this basin. The six products include three types of guidance based on totalenergy singular vectors (TESVs) from different global models, the ensemble transform Kalman filter (ETKF) based on a multimodel ensemble, the deep-layer mean (DLM) wind variance, and the adjointderived sensitivity steering vector (ADSSV). The similarities among the six products are evaluated using two objective statistical techniques to show the diversity of the sensitivity regions in large, synoptic-scale domains and in smaller domains local to the TC. It is shown (Fig. 6) that the three TESVs are relatively similar to one another in both the large and the small domains while the comparisons of theDLM wind variance with other methods show rather low similarities. The ETKF and the ADSSV usually show high similarity because their optimal sensitivity usually lies close to the TC. The ADSSV, relative to the ETKF, reveals more similar sensitivity patterns to those associated with TESVs. Three special cases are also selected to highlight the similarities and differences among the six guidance products and to interpret the dynamical systems affecting the TC motion in the northwestern Pacific. Among the three storms studied, Typhoon Chanchu was associated with the subtropical high, Typhoon Shanshan was associated with the midlatitude trough, and Typhoon Durian was associated with the subtropical jet. The adjoint methods are found to be more capable of capturing the signal of the dynamic system that may affect the TC movement or evolution than are the ensemble methods.

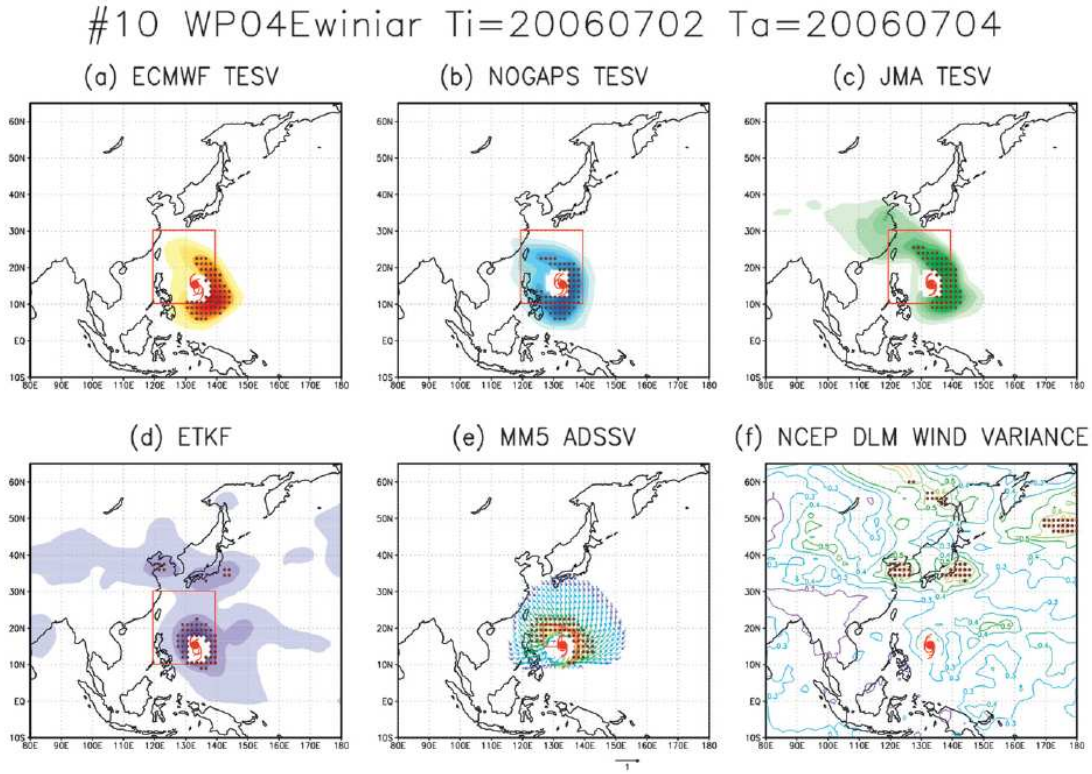

Figure 6. The large-domain common targeted location comparison of (a) ECSV, (b) NGPSV, (c) JMASV, (d) ETKF, (e) ADSSV, and (f) NCVAR for case 10, Typhoon Ewiniar, at ta = 0000 UTC 2 Jul 2006 and tv = 0000

UTC 4 Jul 2006. Except for (f), the verifying areas of the other five methods are indicated by the red squares. The JTWC best track and each model forecast of case 10 valid at ta are denoted by the solid and empty typhoon symbols, respectively. The brown dots represent X =63 grid points with the highest value. (From Wu et al. 2009)

Summary

DOTSTAR, a TC surveillance program using dropwindsondes has been successfully launched since 2003. To capture the sensitive areas which may influence TC track, a newly-designed vector, ADSSV, has been proposed (Wu et al. 2007a). Aside from being used to conduct research on the impact of targeted observations, the DOTSTAR's tropospheric soundings around the TC environment may also prove to be a unique dataset for the validation and calibration of remotely sensed data for TCs in the Northwest Pacific region.

Five models (4 operational and 1 research models) were used to evaluate the impact of dropwindsonde data on TC track forecasts during 2004. All models, except the GFDL hurricane model, show positive impacts from the dropwindsonde data on TC track forecasts. In the first 72 h, the mean track error reductions in the three operational global models, NCEP GFS, NOGAPS and JMA GSM, are 14, 14, and 19%, respectively, and the mean track error reduction of the ensemble of the three global models is 22%.

Along with the development of ADSSV in DOTSTAR, an important issue on the targeted observations based on various techniques have been studied (Wu et al. 2009). The THORPEX-PARC (T-PARC) program had been successfully carried out in the summer of 2008, where DOTSTAR participated the international T-PARC initiative under World Meteorological Organization (collaborating with the Japanese program, Typhoon Hunting 2008, TH08, as well as Tropical Cylcone Structure 2008, TCS-08). Joint flights among DOTSTAR, Falcon (DLR), P3 (NRL) and C130 (USAF) for Typhoons Nuri, Sinlaku, Hagupit, and Jangmi have been successfully conducted during T-PARC in the summer of 2008. The unprecedented data obtained would provide a great opportunity for the advance of the research on TC genesis, structure change, targeted observation, recurvature, and extratopical transition.

Acknowledgements: The author thanks all the helpful inputs from collaborators in DOTSTAR and T-PARC.

References

Aberson, S. D. (2003), Targeted observations to improve operational tropical cyclone track forecast guidance. *Mon. Wea. Rev.*, **131**, 1613–1628.

Bishop, C. H., and Z. Toth (1999), Ensemble transformation and adaptive observations. *J. Atmos. Sci.*, **56**, 1748-1765.

Chan, J. C.-L., and W. M. Gray (1982), Tropical cyclone movement and surrounding flow relationship. *Mon. Wea. Rev.*, **110**, 1354-1376.

Chou, K.-H., and C.-C. Wu (2008), Development of the Typhoon Initialization in a Mesoscale Model -

Combination of the Bogused Vortex and the Dropwindsonde Data in DOTSTAR. *Mon. Wea. Rev.*, **136**, 865-879.

Etherton, B., C.-C. Wu, S. J. Majumdar, and S. D. Aberson, (2006), A comparison of the targeting techniques for 2005 Atlantic tropical cyclones. Preprints, 27th Conf. on Hurricanes and Tropical Meteorology, Monterey, CA, Amer. Meteor. Soc.

Gelaro, R., T. E. Rosmond, and R. Daley (2002), Singular vector calculations with an analysis error variance metric. *Mon. Wea. Rev.*, **130**, 1166-1186.

Guo, Y.-R., Y.-H. Kuo, J. Dudhia, D. Parsons, and C. Rocken (2000), Four-dimensional variational data assimilation of heterogeneous mesoscale observations for a strong convective case. *Mon. Wea. Rev.*, **128**, 619–643.

Majumdar, S. J., C. H. Bishop, R. Buizza and R. Gelaro (2002a), A comparison of ensemble-transform Kalman-filter targeting guidance with ECMWF and NRL total-energy singular-vector guidance. *Q. J. R. Meteorol. Soc.*, **128**, 2527–2549.

___, ___, B. J. Etherton and Z. Toth (2002b), Adaptive sampling with the Ensemble Transform Kalman Filter. Part II: Field program implementation. *Mon. Wea. Rev.,* **130**, 1356-1369.

___, S. D. Aberson, C. H. Bishop, R. Buizza, M. S. Peng, and C. A. Reynolds (2006), A comparison of adaptive observing guidance for Atlantic tropical cyclones. *Mon. Wea. Rev.*, (in press)

Morss, R. E., K. A. Emanuel, and C. Snyder (2001), Idealized adaptive observation strategy for improving numerical weather prediction. *J. Atmos. Sci.*, **58**, 210-232.

Palmer, T. N., R. Gelaro, J. Barkmeijer, and R. Buizza (1998), Singular vectors, metrics, and adaptive observations. *J. Atmos. Sci.*, **55**, 633-653.

Peng, M. S., and C. A. Reynolds (2006), Sensitivity of tropical cyclone forecasts. *J. Atmos. Sci.,* **63**, 2508-2528.

Reynolds, C. A., M. S. Peng, S. J. Majumdar, S. D. Aberson, C. H. Bishop and R. Buizza (2007), Interpretation of adaptive observing guidance for Atlantic tropical cyclones. *Mon. Wea. Rev.,* **135**, 4006-4029.

Rosmond, T. E. (1997), A technical description of the NRL adjoint model system, NRL/MR/7532/97/7230, Naval Research Laboratory, Monterey, CA, 93943, 62 pp.

Wu, C.-C., P.-H. Lin, S. D. Aberson, T.-C. Yeh, W.-P. Huang, J.-S. Hong, G..-C. Lu, K.-C. Hsu, I-I Lin, K.-H. Chou, P.-L. Lin, and C.-H. Liu (2005), Dropwindsonde Observations for Typhoon Surveillance near the Taiwan Region (DOTSTAR): An Overview. *Bulletin of Amer. Meteor. Soc.,* **86**, 787-790.

_____(2006), Targeted observation and data assimilation for tropical cyclone track prediction. Proc., 6th International Workshop on Tropical Cyclones, WMO/CAS//WWW, San Jose, Costa Rica, November 21-28, 409-423.

___, K.-H. Chou, Y. Wang, and Y.-H. Kuo (2006), Tropical Cyclone Initialization and Prediction Based on Four-Dimension Variational Data Assimilation. *J. Atmos. Sci.*, **63**, 2383-2395.

___, J.-H. Chen, P.-H. Lin, and K.-H. Chou (2007a), Targeted Observations of Tropical Cyclone Movement Based on the Adjoint-Derived Sensitivity Steering Vector. *J. Atmos. Sci*., **64**, 2611–2626.

___, K.-H. Chou, P.-H. Lin, S. D. Aberson, M. S. Peng, and T. Nakazawa (2007b), The impact of dropwindsonde data on typhoon track forecasts in DOTSTAR. *Wea. Forecasting*, **22**, 1157–1176.

___,, S.-G. Chen, J.-H. Chen, and K.-H. Chou (2009), Interaction of Typhoon Shanshan (2006) with the Mid-latitude Trough from both Adjoint-Derived Sensitivity Steering Vector and Potential Vorticity Perspectives. *Mon. Wea. Rev.*, **137**, 852-862.

___, J.-H. Chen, S. J. Majumdar, M. S. Peng, C. A. Reynolds, S. D. Aberson, R. Buizza, M. Yamaguchi, S.-G. Chen, T. Nakazawa , and K.-H. Chou (2009), Inter-comparison of Targeted Observation Guidance for Tropical Cyclones in the North western Pacific. *Mon. Wea. Rev.*, **137**, 2471-2492.

Airborne deployment of expendable platforms for mitigation of TC landfall impacts: Examples from TPARC/TCS08

Peter G. Black

Science Applications International Corporation, Inc., Monterey, CA USA

Email: peter.black@nrlmry.navy.mil

INTRODUCTION

The TPARC/TCS08 project deployed numerous expendable platforms into Tropical Cyclones (TCs) at various stages of their life cycle from the US Air Force Reserve aircraft, WC-130J during the period from 1 August to 27 September, 2008. These platforms were GPS dropsondes for measuring atmospheric vertical profiles of temperature, humidity and wind, AXBTs for measuring the ocean vertical temperature profile to 300- or 900- m (depending upon type) and drifting buoys of two types: Adaptive Ocean Observing Platform (ADOS) and Minimet. The ADOS drifting buoys contained surface pressure sensors and temperature sensors at 10-m intervals to 140m while the Minimet contained surface pressure, surface wind speed and direction, and sea surface temperature. Deployments of 12 buoys each were conducted prior to typhoons Hagupit and Jangmi on 20 and 26 September, respectively, the later about 36 hours prior to landfall in Taiwan. This paper examines the potential for mitigating landfall impacts through improved observations from air-deployed sensors ahead of and within landfalling TC's.

LONG-TERM GOALS

Major goals for this project are two-fold: 1) provide new observations simultaneously, both within the TC itself as well as the ocean below, to a developing NRL coupled TC modeling effort (COAMPS-TC) and 2) utilize Tropical Cyclone Structure 2008 (TCS-08) field program data sets to improve understanding of TC life cycle, especially Rapid Intensification (RI) mature stage episodes associated with oceanic environmental changes.

OBJECTIVES

Specific objectives are four-fold:

1) Coordinate an airborne program for observation of Western Pacific Tropical Cyclones (WPAC TCs) that will lead to improved understanding and prediction of TC structure, intensity and track from genesis through mature and Extratropical Transition (ET) stages of TC life cycle.
2) Utilizing enhanced WC-130J GPS dropsonde observations, flight level and surface wind and thermal observation and airborne radar images, develop an analysis scheme for the monsoon and storm scale circulation features that would:
    a. Define large-scale context for detailed mesoscale observations from companion NRL P-3 aircraft in selected storm quadrants, including specification of surface radius of gale, storm and typhoon force winds over time.

   b. Provide initial thermal and kinematic data for couple COAMPS-TC model development during TC life cycle.
   c. Improve characterization of TC vertical structure by radius and storm quadrant for TC boundary layer and lower troposophere inner core regions.
3) Determine TC structure change by co-location of storm scale kinematic analyses with satellite vis, ir and microwave satellite data to study the dynamics of inner and outer eyewall/rainband evolution in time, especially eyewall replacement cycles.
4) Assist with validate current and advanced satellite intensity estimation schemes, such as SATCON, and evaluate proposed new composite intensity estimation schemes, with observations of peak surface winds observed by the Stepped Frequency Microwave Radiometer (SFMR).

APPROACH

The approach used to undertake the field observing phase of the TCS08 project was to define a series of flight plans targeted at observing the 3D environmental structure during TC mature stage and to observe intensity and structure at the surface and mid-levels. To this end, a series of flight patterns were designed to be flown either east or west of the operating base, and are shown in Fig 1. In addition, a communications scheme between scientists at various other operation centers, especially the main operations center in Monterey and with the two aircraft and the Guam operations center. A schematic of this communications plan is shown in Fig. 2 together with the WC-130J flight track as it was displayed in real time.

Once this plan was in place, the objective was to select a case that would demonstrate the usefulness of simultaneous TC atmospheric and oceanic observations. Such a case was TC Hagupit followed less that one week later by Super-typhoon Jangmi.

DISCUSSION AND PRELIMINARY RESULTS

As mentioned earlier, 12 drifters were deployed in front Hagupit and 12 more were deployed ahead of Jangmi. All drifters fell to the sea on parachutes and deployed properly. The deployment was described in Black (2005), in the first IWTCLP volume. Fig. 3 shows the deployment pattern for Jangmi superimposed on the buoy positions from the Hagupit deployment. Coincidentally, the tracks of the two storms were nearly parallel allowing observations in Jangmi from nearly 24 drifters. The drifter observations showed a cold eddy along the track of Jangmi which was verified by satellite observations (Fig. 5 and by AXBTs (Fig. 6). The surface manifestation of the cold eddy only became visible after the intense mixing took place in the region by the high winds ahead of Jangmi. Note in Fig 5 that the cold region produced by Hagupit and the southern boundary of this same cold eddy is still visible to the left of Jangmi's track. The region of deepening mixed layers produced by the storm, in excess of 100 m as well as the relatively shallow mixed layers over the cold eddy is shown in Fig. 6.

As the storm moved across the boundary between the warm and cold eddies within the Southern Eddy Zone on 27 Sept, the rapid deepening that produced a minimum pressure of 902 mb and super-typhoon status abruptly halted and was replaced by rapid filling over the next 24 hours (Fig. 7), making landfall with 57 m/s maximum winds rather than 77 m/s maximum winds, thus sparing Taiwan a worse catastrophe. Detection of these ocean features thus played a big role in explaining the rapid intensity change, a result that could eventually come into operational use in the future.

The dramatic change in the structure of Jangmi is shown in Fig. 8 with a rapid drying and thinning of the rainbands in the NW quadrant as the storm approached Taiwan. Coincidentally, this region of rain band decay is just downwind from the cold SST anomaly produced by the storm.

Fig. 9 shows the wind structure of Jangmi at its peak intensity based on analysis by airborne SFMR surface winds compared with the incomplete and rain-affected observations from Quikscat satellite scatterometer. Without the aircraft observations or satellite intensity estimates, the true knowledge of the high winds in the eyewall would not be fully known. Fig. 10 shows Jangmi's eyewall structure from the WC-130J airborne weather radar.

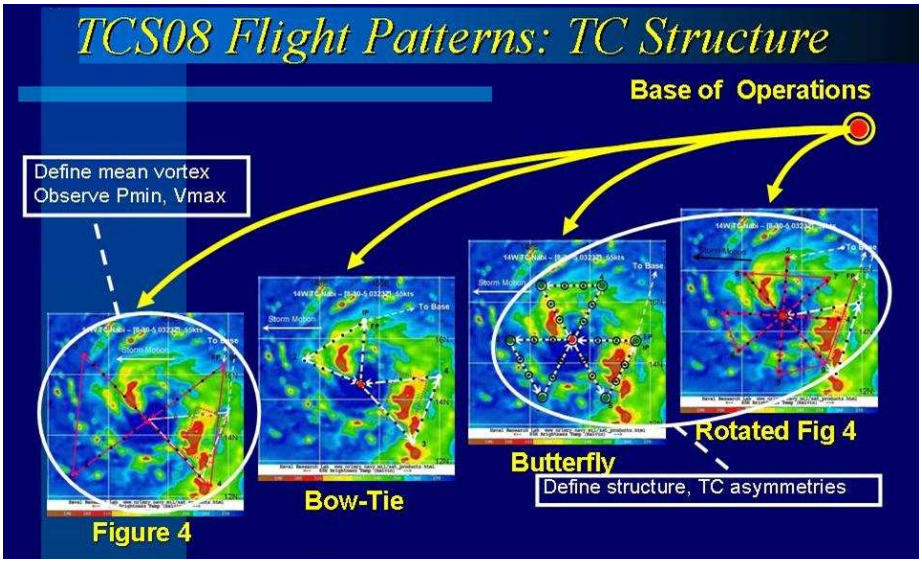

Figure 1. Types of flight patterns flown in mature TC's during TCS08.

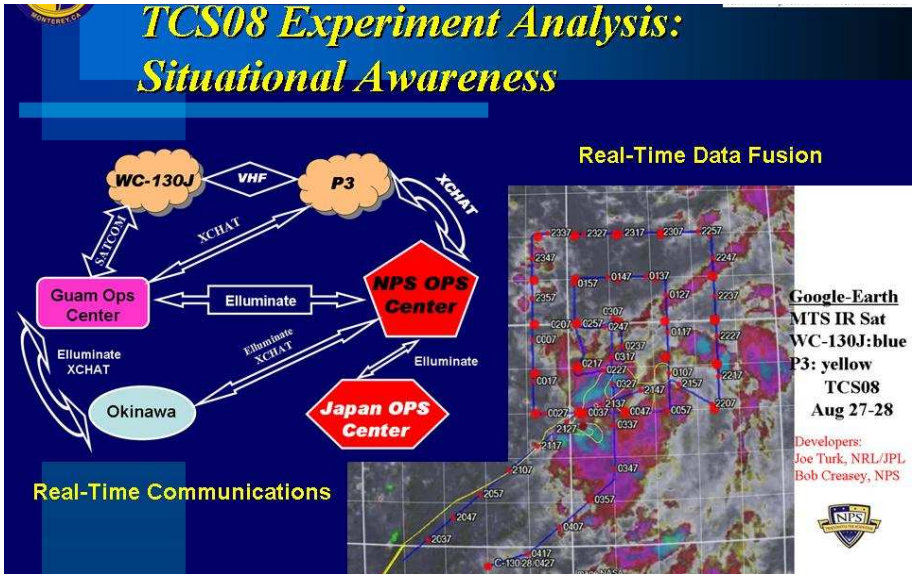

Figure 2. Communication flow between Guam operations center, Monterey operations center and the aircraft used for real-time situational awareness. Right panel shows display of WC-130J track on MTSAT IR imagery displayed in Google Earth with P3 track shown in yellow.

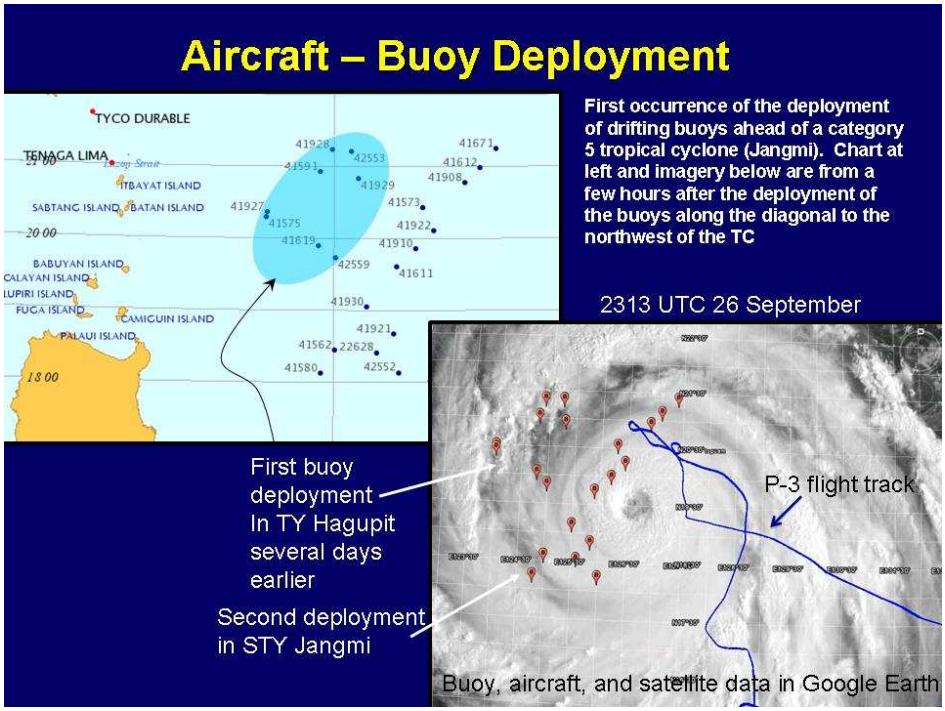

Figure 3. Drifting buoy locations in front of TC Jangmi shortly after deployment. Data and positions were transmitted via satellite (Service Argos).

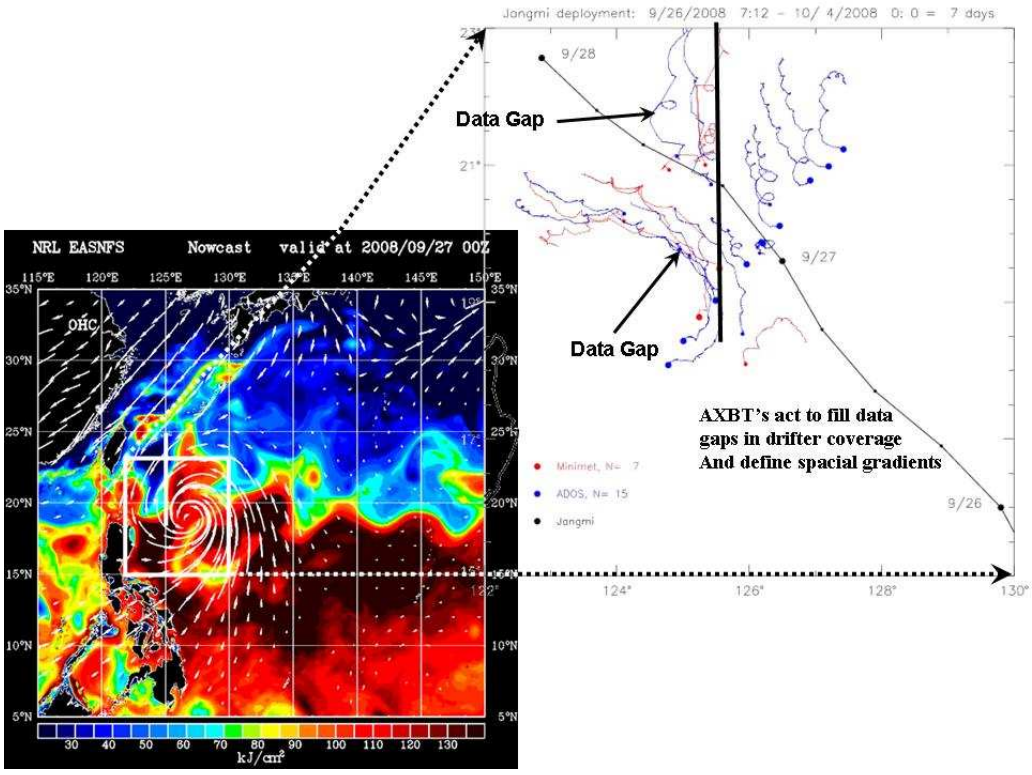

Figure 4. Ocean Heat Content from NRL Stennis ocean model (left) together with drifter trajectories relative to storm track and boundary between cold, cyclonic and warm eddies.

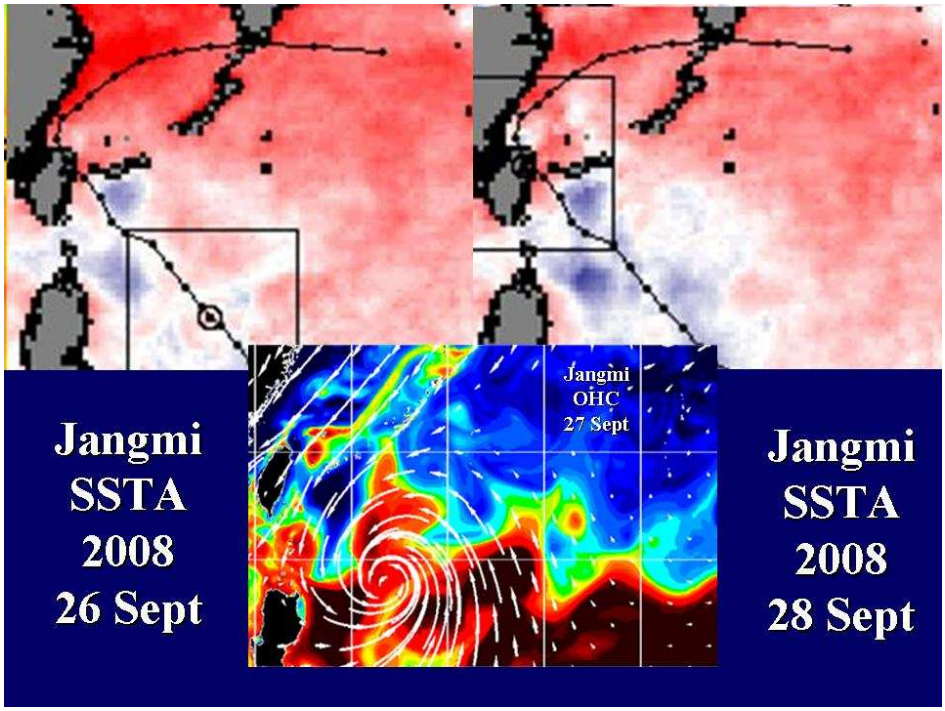

Figure 5. SST anomaly observed by IR and microwave sensors (Remote Sensing Systems) for Jangmi on 26 and 28 September together with Stennis Ocean Model OHC for 27 September.

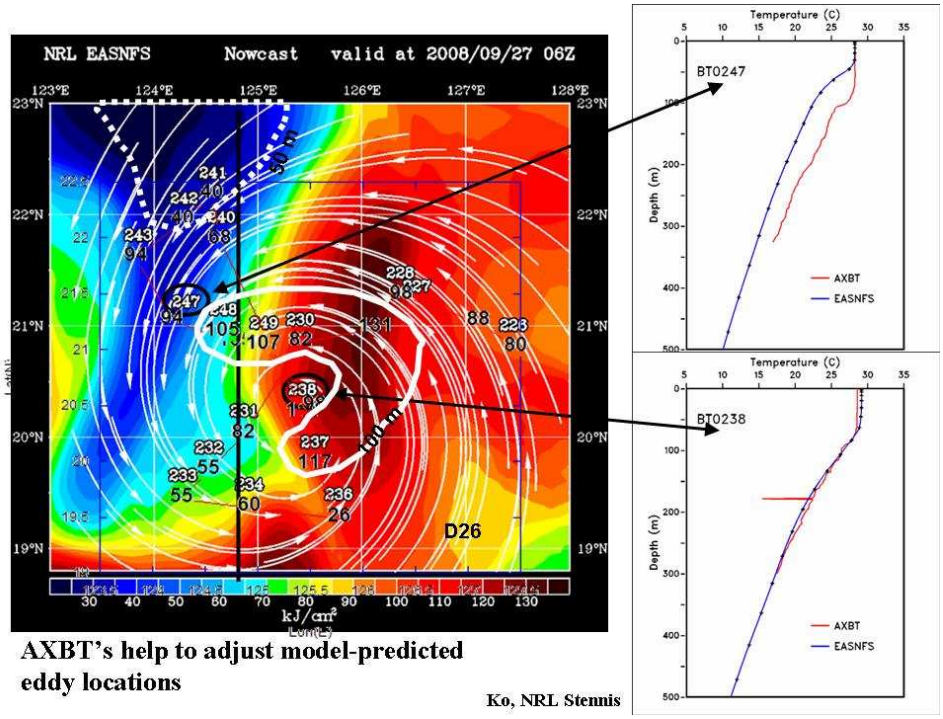

Figure 6. AXBT observations superimposed upon OHC together with 100 m contour (white solid) and 50 m contour (dotted) for the bottom of the ocean mixed layer.

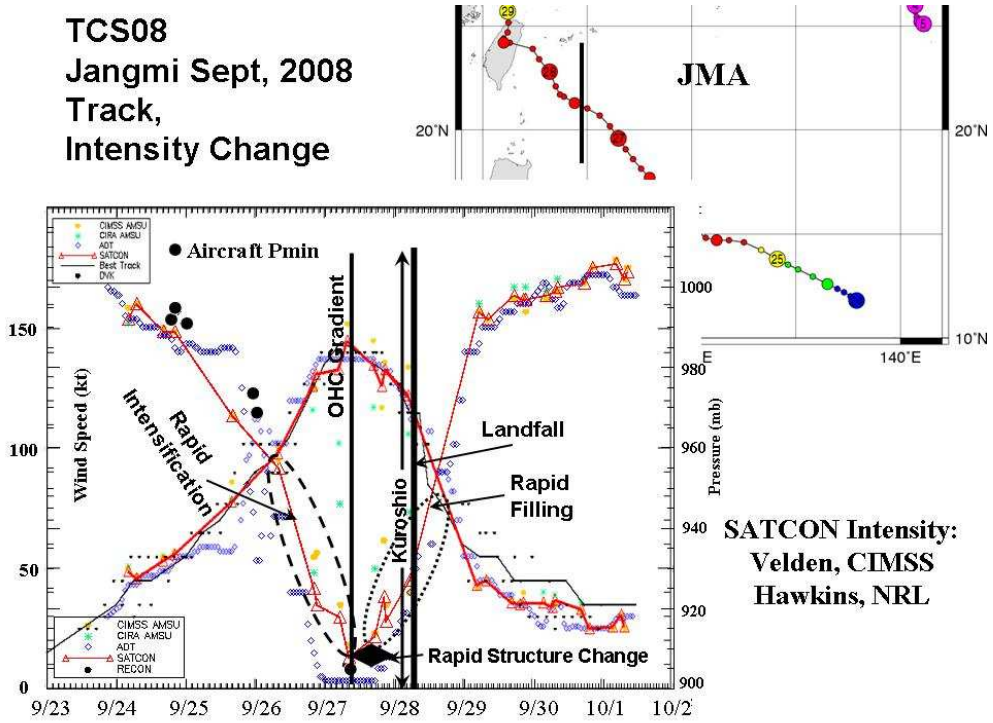

Figure 7. Vmax and Pmin profiles relative to OHC gradient at eddy boundary just offshore from the Kuroshio and landfall on Taiwan. Track in upper left shows eddy boundary (solid black line).

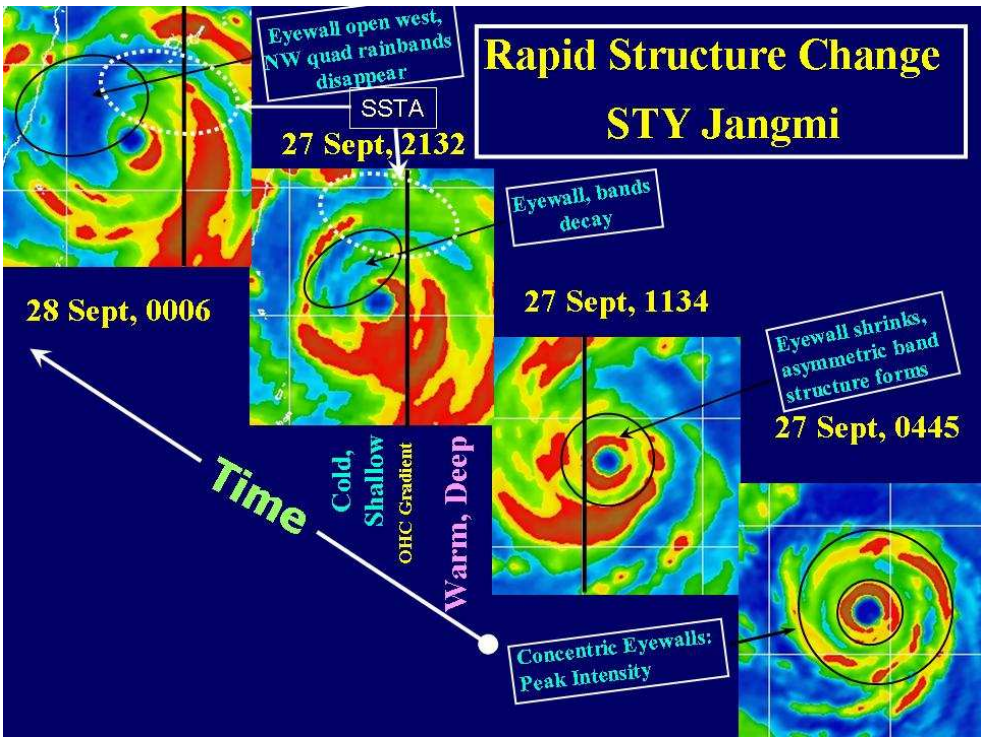

Figure 8. Rapid change in Jangmi structure while passing eddy boundary, shown by solid black line. Thin black oval shows region of rainband decay downstream from maximum SST anomaly shown by dotted white oval.

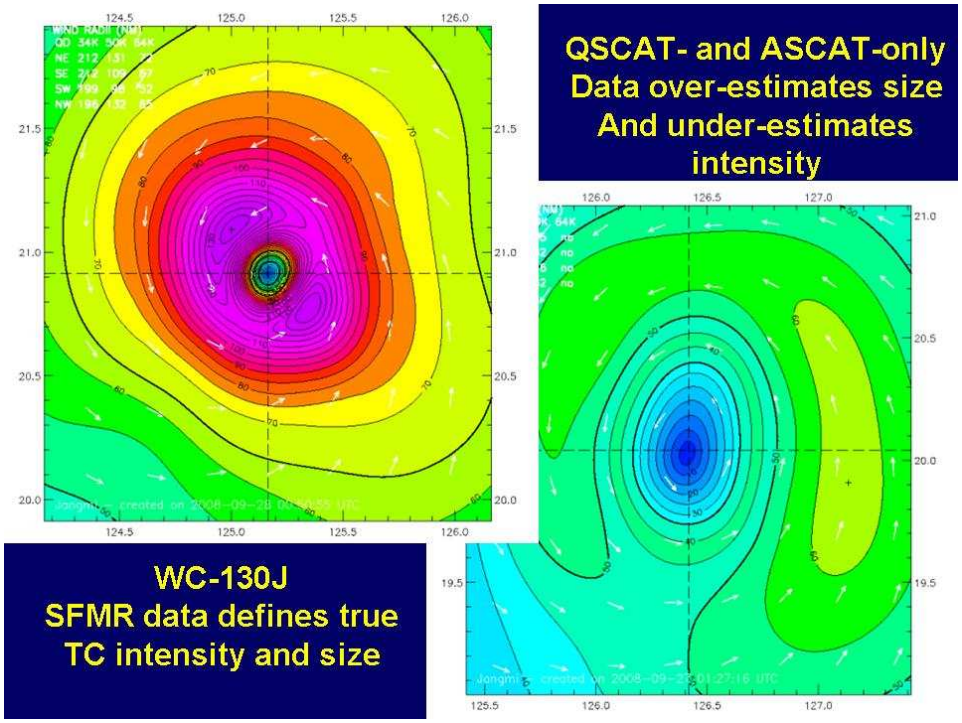

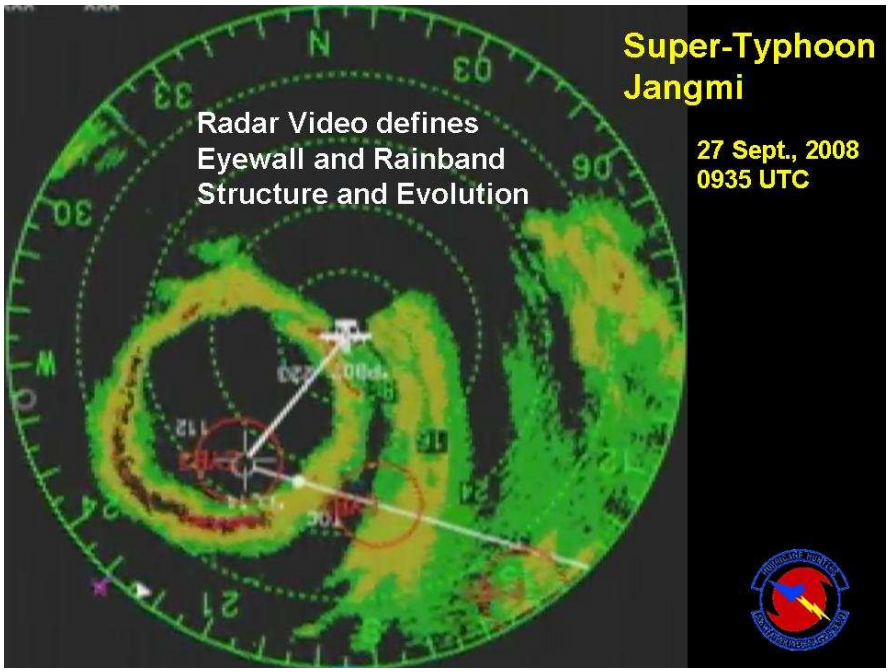

Figure 9. Surface wind field in Jangmi from airborne SFMR (upper-left) compared with windfield derived from satellite scatterometer measurements (upper-right). Lower panel shows airborne radar display of eyewall structure (north is up) taken as the aircraft prepares to enter the eyewall.

Some Recent Studies Related to Tropical Cyclone Wind Structure Changes

Russell L. Elsberry
Department of Meteorology
Naval Postgraduate School
Monterey, California 93943 USA

Abstract

The focus in this paper is on the outer wind structure and structure changes in tropical cyclones, which are important for the location and timing of warnings of the onset of gale-force winds, and affect tropical cyclone motion via the beta-effect propagation effect. Deviations from a simple tangential wind profile with radius will occur when secondary eyewalls form, and a recent high-resolution numerical simulation by Terwey and Montgomery suggests large increases in the radius of 50 kt (R_{50}) and 34 kt (R_{34}) winds as a result of a secondary eyewall. Creation of the conditions for an annular hurricane would also imply a large increase in R_{50} and R_{34}.

A single model that an intensifying (weakening) tropical cyclone will be accompanied by an increase (decrease) in outer wind structure is tested with a unique set of H*Wind analyses of the surface wind in the Atlantic during the 2003-2005 season. Whereas a small set of H*Wind analyses during the formation stage has the expected increases in R_{34} values, a considerable percentage of R_{34} decreases occur during the intensification stages when only increases would be expected. Similarly, a considerable percentage of R_{34} increases are observed during the decay phase when decreases would be expected, although a forecaster rule-of-thumb is that the tropical cyclone circulation expands during the decay stage.

Lee et al. (2009) categorized 73 typhoons into small, medium, and large sizes based on radius of 15 m s^{-1} (R 15) winds. Whereas many of the small TCs form from an easterly wave synoptic pattern, the monsoon-related formation patterns are favorable for forming medium to large size TCs. Most (67% of small, 50% of medium, and 72% of large) of these 73 TCs stay in the same size category during intensification, which implies specific physical mechanisms for maintaining TC size in the basin. The conclusion is that it is the environment that determines the difference between large and small size storms directly during formation and indirectly by its effect on the convective distribution during intensification.

1. Introduction

Whereas much of the recent tropical cyclone structure research has focused on the intensity, the focus in this paper is on the outer wind structure of tropical cyclones. A brief review of some studies of the wind structure and wind structure changes will be presented. Some preliminary results from a study of the most comprehensive data set on the surface wind distributions in Atlantic hurricanes will be given.

In the U.S., the emergency management community requires warnings of when sustained (one-minute average) surface winds exceeding gale force (here ≥ 34 kt) will arrive at a location in

advance of a tropical cyclone. That is, the objective is to give the public sufficient time to complete all disaster preparedness activities prior to when gale-force winds (usually accompanied by heavy precipitation) arrive, so that these activities (including evacuation or moving to a secure shelter) are completed safely. In addition, warnings are to be provided to ships to sortie from ports and/or divert around the region with surface winds exceeding 35 kt (usually accompanied by ocean waves greater than 12 feet). The storm surge prediction community has often used empirical wind relationships tied to the central surface pressure. Recent hurricanes such as Katrina during 2005 have illustrated the importance of the outer wind structure in accounting for the high storm surge along the Gulf of Mexico coast well to the east of the landfall position. Accurate warning of how far inland damaging winds will occur requires not just the maximum intensity of the storm, but also the wind structure at various radii must be forecast.

In the past, the uncertainty in the time of arrival of gale-force winds was so dominated by the large track forecast errors, as compared to the uncertainty due to the wind structure, that little attention has been given to outer wind structure. The inability to observe the surface wind distribution in tropical cyclones over the water also contributed to the deficiency in wind structure forecasting. However, the Japan-U.S. Quikscat and other scatterometer observations have provided some surface wind observations, at least in those outer regions of the tropical cyclone without significant rain scattering problems.

In contrast to the empirical wind profiles that have been previously used to describe the wind structure, more complex outer wind profiles associated with secondary eyewalls and annular tropical cyclones will be described in section 2. The implications of empirical wind profiles and idealized numerical models for wind structure change are described in section 3. A simple wind structure change model tied to intensification and decay phases is tested in section 4 and found to not explain many observed changes. Finally, some conclusions are made in section 5.

2. Complex outer wind profiles

a. Secondary eyewalls

Willoughby et al. (1982) [References and figures labeled ES- are as in: Elsberry, R. L., and R. A. Stenger, 2008: Advances in understanding of tropical cyclone wind structure. *Asia-Pacific J. Atmos. Sci.* **44**, 11-24] described secondary eyewalls in which a concentric ring of convection develops at an outer radii, and these convective regions have an associated wind maximum that is not included in simple profiles as in ES-Fig. 1. Rather, a profile as in ES-Fig. 1 outward from the radius of maximum wind would adjust to another relative wind maximum at the radius of the secondary eyewall with a decreasing wind with radius profile farther outward from that maximum. Because the secondary eyewalls in the cases described by Willoughby et al. (1982) tended to contract inward, progressively larger wind speeds evolved at smaller radii as in the modified Rankine vortex ($v\ r^x$ = constant). Meanwhile, the maximum wind speed (i.e., the intensity) in association with the inner eyewall decreased such that it became smaller than the wind speed associated with the secondary eyewall. This evolution has been termed an *eyewall replacement cycle*, although it is not clear that the inner eyewall cloud band always disappears. A more general characterization by Elsberry et al. (2007) of the life cycle intensity changes used below is a decay and re-intensification cycle (Stage IIa).

Based on microwave imagery during 1997-2005, Hawkins et al. (2006) observed that 80% (70%, 50%, 40%) of the tropical cyclones in the western North Pacific (Atlantic, eastern North Pacific,

Southern Hemisphere) with maximum winds exceeding 120 kt had one or more secondary eyewall formations.

One may expect the outer wind speeds would increase, and the radius of 34-kt winds would increase, if an external physical mechanism that led to the secondary eyewall had a wind profile as in ES-Fig. 1 with the same exponent $x = 0.4$. Alternately, an internal mechanism might create the secondary eyewall wind maximum and simultaneously "spin-up" the wind speeds at outer radii along a profile as in ES-Fig. 1.

A high-resolution numerical simulation by Terwey and Montgomery ("Secondary eyewall formation in two idealized, full-physics modeled hurricanes," manuscript submitted to *J. Geophys. Res. Atmos*.) led to an intense vortex (87 m s^{-1}) at a relatively small radius (30 km) that was then followed by a secondary eyewall formation. As shown in ES-Fig. 2, the inner wind maximum decreased until around Hour 180 the outer wind maximum at 80 km was stronger (65 m s^{-1}), which would be designated as an eyewall replacement cycle. Terwey and Montgomery do not display the outer wind profiles before and after the secondary eyewall formation and eyewall replacement cycle. To demonstrate the potential magnitude of the outer wind structure changes, a modified Rankine vortex with an exponent $x = 0.5$ was assumed. Given the two wind maxima and corresponding radii in ES-Fig. 2 (and given above), the 50-kt wind radius would increase from 360 km to 541 km, and the 34-kt wind radius would increase from 783 km to 1171 km. These (likely excessive) outer wind radii increases from before to after an secondary eyewall formation and eyewall replacement cycle suggest large outer wind structure modifications during such events. Another possible implication of such an event occurring as the tropical cyclone was approaching the coast would be a sudden decrease in the disaster preparation time needed before gale-force winds would be reaching the coast.

b. Annular tropical cyclones

Knaff et al. (2003) defined a subset of tropical cyclones they called annular hurricanes that had: (i) a larger than average eye size; (ii) symmetrically distributed low cloud-top brightness temperatures in the eyewall; and (iii) few or no rainband features. Knaff et al. (2003, Fig. 3) demonstrate that these annular tropical cyclones are significantly stronger, maintain their peak intensity longer, and weaken more slowly than the average tropical cyclone. Furthermore, Knaff et al. (2003) state that annular hurricanes develop and are sustained in environmental conditions with: (i) relatively weak easterly or southeasterly vertical wind shear; (ii) easterly winds and lower than average temperatures at 200 mb; (iii) sea-surface temperatures (SST) in the range of 25.4°C – 28.5°C; and (iv) absence of interaction with adjacent troughs that would cause eddy momentum flux convergence.

Because Knaff et al. (2003) found that the formation of annular hurricanes appeared after an asymmetric mixing of the eye and eyewall components via mesovortices, it is assumed here that prior to becoming an annular hurricane, the storm was quite intense. Indeed, the discriminant analysis technique proposed by Knaff, Cram, Schumacher, Kossin, and DeMaria ("Objective identification of annular hurricanes," manuscript submitted to *Wea. Forecasting*) for objectively identifying an annular hurricane in the Atlantic and eastern North Pacific performs best if all hurricanes with intensities ≤ 84 kt are first eliminated. For the six (eight) Atlantic (eastern North Pacific) annular hurricanes that they identified during 1995-2006, the minimum intensity was 100 kt (90 kt). Annular typhoons also exist, but it is unknown if the same SST, minimum intensity, and other thresholds apply.

Given that annular tropical cyclones form a secondary eyewall during an intense stage, it will be

assumed that a similarity exists with the secondary eyewall formations discussed in subsection 3a above. For the 14 annular hurricanes during 1995-2006, the mean radius of the lowest azimuthally-averaged cloud-top temperatures (i.e., eyewall radius) was 81 km, with a minimum of 62 km, and a maximum of 128 km. With a minimum intensity of 90 kt at such large radii, the outer wind speeds would likely be larger than for an average hurricane. The differences are assumed to be: (i) annular tropical cyclones form from an *internal* mechanism following an eyewall mixing event in which the intense inner wind maximum is diminished; and (ii) the outer (secondary) eyewall is stable to radial deflections (rather than contracting) due to special environmental conditions listed above.

The relevance to outer wind structure changes is similar to that in subsection 2a, i.e., forming an intense outer wind maximum in an annular tropical cyclone is likely to increase the 34-kt wind radius.

3. Idealized tropical cyclone structure changes

The implication from an empirical wind profile such as in ES-Fig. 1 is that the outer- and inner-core wind structure vary together. That is, physical processes that increase/decrease the intensity would have a corresponding increase/decrease in the entire wind structure. In this simple model, the outer winds would increase during the intensification stage and would decrease during the weakening stage of the tropical cyclone life cycle.

In the idealized axisymmetric models of the intensification stage, a similar scenario occurs with outer wind speed increases following the spin-up of the inner core. In the Emanuel (1995a, b) model, the temperature profile is assumed to be moist-neutral at each radius, so that the entire vertical profile is known given the temperature and moisture near the surface, and from hydrostatic equation the surface pressure is known. Given an initial cyclonic vortex (typical maximum wind speed of 10 m s^{-1} at a radius of 150 km), the frictional forces lead to an inflow, and the air parcels acquire heat and moisture from the warm ocean as they approach the center. The purpose of the model is to estimate the intensity from the thermal and moisture conditions that are predicted to exist at the bottom of the eyewall cloud. However, the assumption of a moist-neutral atmosphere tied to the near-surface temperature and moisture radial profile provides the radial profile of the pressure field at all levels as well, and thus the outer wind structure.

As in the case of the empirical wind profile in ES-Fig. 1, the outer wind increases in the axisymmetric model will be directly correlated with the intensity increases, which in the idealized model are determined by the sea-surface temperature and upper-tropospheric temperatures at which the outflow is assumed to occur. Except for the imposed temperature and moisture profiles at large radius, the outer conditions are tied to the inner core prediction – the values of wind or momentum at the outer boundary are assumed to not be important.

4. Actual structure changes

If the tropical wind structure changes are driven by the inner-core processes, the implication from empirical wind profile reasoning or the idealized, axisymmetric models would be that the outer winds would increase during the intensification stage and decrease during the decaying stage. Whereas the forecaster rules of thumb are compatible with the idea of increasing outer winds during the intensification stage, the general expectation (e.g., Merrill 1984) is that the tropical cyclone size expands (i.e., outer winds at a radius would be increasing) during the decay or extratropical transition stage. Especially in the case of extratropical transition in which the tropical cyclone is moving into the

midlatitude westerlies, the apparent expansion may be due to the circulation being superposed on an environment with stronger winds.

a. Data set of surface wind analyses

These simple conceptual ideas of outer wind structure changes are tested by applying the tropical cyclone life cycle intensity change definitions of Elsberry et al. (2007) displayed in ES-Fig. 4. The Elsberry et al. (2007) formation Stage I is limited to V_{max} less than 34 kt. Storm intensification from 34 kt to the first intensity peak (or end of this stage) is defined as Stage II. After the first intensity peak, if the storm intensity decays by at least 10 kt and then re-intensifies by at least 10 kt, it is defined as a decay and re-intensification cycle that is labeled as Stage IIa. If the re-intensification criterion of Stage IIa is not met, the storm is decaying and classified as Stage III. In addition, Stage II is subdivided into rapid or non-rapid intensification, and Stage IIa is subdivided into a decay followed by either a rapid or a non-rapid intensification. Rapid intensification is defined here as an increase equal to or greater than 15 kt in 12 h. A 12-h interval was selected to better capture rapid intensification events during storm intensity cycles and exclude intensity fluctuations that occur over shorter periods of time. Details of the data set used to examine the wind structure are given in Elsberry and Stenger (2008).

A total of 564 H*Wind analyses contain dropsonde data in 508 analyses, aircraft flight-level reduced data in 470 analyses (hereafter referred to as "aircraft FLR data"), and 135 analyses with SFMR data. Dropsonde data were generally absent from eastern North Pacific tropical cyclones and for weak storms. Dropsonde, aircraft FLR, and SFMR data were simultaneously available in 55 of the H*Wind analyses. However, most analyses contain a combination of dropsondes and aircraft FLR data, or dropsondes and SFMR data.

Those H*Wind analyses that include the SFMR observations are considered to have the most reliable representation of the surface wind fields because of the continuous profiles along the radial flight paths of the aircraft. Due to the limited number of analyses with SFMR data, it was necessary to include surface wind analyses that were primarily based on the reduction of aircraft flight-level winds (usually flown at 700 mb). A comparison of the time evolution of R_{34} and R_{50} for Hurricane Ivan (2004) using mutually exclusive analyses that contain SFMR data versus aircraft flight-level reduction is given in ES-Fig. 5 for different quadrants of the storm. The differences between these wind radii derived from H*Wind analyses based primarily on these two data sources are within the range of variability depicted by the aircraft FLR data. Other storm cases have a similar agreement as in ES-Fig. 5.

b. Observed outer wind structure changes during life cycle

Histograms of 12-h axisymmetric outer wind structure changes in terms of R_{34} values are shown in ES-Figs. 6-8. These calculations of axisymmetric wind structure are computed along 24 equally-spaced radial legs at consecutive rings spaced every 6 km from the center of the tropical cyclone. It is important to note that all quadrants in which land intersects the 34-kt wind radii are eliminated from the calculations, but no fewer than two quadrants or 13 radial legs are used in the calculation at any analysis time. After eliminating all cases that involve landfall, or where insufficient analyses are available to compute the 12-h structure change, 400 cases remained to evaluate R_{34} structure variability during the 2003-2005 Atlantic tropical cyclone seasons.

Without consideration of the life cycle stage, the histogram for the all-sample of 12-h changes in R_{34} approximates a Gaussian distribution (ES-Fig. 6, dashed line). A bias toward positive 12-h R_{34} changes is evident in this sample that includes all stages. Outer wind structure changes in terms of

12-h R_{34} values between ± 10 km were deemed as steady state, and the clustering of values in this range appears to be justified by the distribution, if not a little conservative. Note that the changes in the axisymmetrical radial structure in the entire sample can be quite large over a 12-h period, with values as large as ± 135 km. For a hurricane approaching a coastline at 5 m s^{-1}, an undetected 12-h expansion of the gale-force wind radius by 135 km would decrease the preparation time by about 8 hours.

Only a very small sample of H*Wind analyses are available for the Formation Stage I as defined in ES-Fig. 4. Thus, the histogram of 12-h R_{34} changes for Stage I in ES-Fig. 6b should be viewed as tentative. This limited sample of R_{34} change values does seem to indicate a general tendency toward an expansion in size during the formation stage. It is noteworthy that one expansion of 120 km in 12 h was documented. Given the limitations of this sample, it seems unlikely that a larger sample will make the distribution more Gaussian. The tendency for positive increases in R_{34} in the formation stage is consistent with the expectation of the empirical profiles as in Fig. 1 and the axisymmetric models discussed in section 3.

The histograms for 12-h R_{34} changes during rapid (Fig. ES-7a) and non-rapid (ES-Fig. 7b) intensification during Stage II suggest a tendency for more increases (54% and 56%, respectively) than decreases (32% and 28%) in outer wind speeds. The non-rapid intensification following a decay in Stage IIa has similar percentages (ES-Fig. 7d) of positive (54%) and negative (26%) 12-h R_{34} changes. For the rapid intensifications following a decay in Stage IIa (ES-Fig. 7c), the percentages of positive (44%) and negative (33%) 12-h R_{34} changes are more nearly balanced, and with a large percentage of steady-state (± 10 km) conditions (23%). The relatively large number of decreases in the R_{34} values for the intensification Stages II and IIa does not agree with the expectations from the empirical wind distribution or the axisymmetric models that would suggest an increase in outer winds (R_{34}) during intensification. Thus, further study is required to understand the physical processes that lead to a decrease in R_{34} during intensification.

The histogram for 12-h R_{34} changes during the Decay Stage III (ES-Fig. 8b) indicates a tendency for more negative (49%) than positive (26%) values, with a considerable fraction of steady-state conditions (± 10 km). Approach to land may account for some shift toward negative R_{34} changes in the distribution during the Decay Stage III, whereas storms such as Hurricane Ophelia during 2005 shrunk in size while at higher latitudes with little or no intensity change, no significant land interaction, and under weak vertical wind shear conditions. By contrast, the 12-h R_{34} changes during the decay stage of the Stage IIa decay and re-intensification cycle (ES-Fig. 8a) has proportionally more increases (51%) than decreases (37%), and has a distribution that approaches Gaussian centered on + 20 km increase in R_{34} over 12 h. Recall that a decrease in R_{34} values during the decay stage might be expected from the empirical wind profile in Fig. 1, and from subsequent solutions of the axisymmetric model to fit a decreasing intensity. By contrast, the forecaster rule-of-thumb is to expect an increase in the size during the decay of tropical cyclones (Merrill 1988). Again, further study is required to understand the physical processes that lead to both decreases and increases in the outer winds when the tropical cyclone intensity is decreasing either in the Stage IIa decay or the final decay in Stage III.

The histograms for R_{50} and R_{64} changes (not shown) have similar distributions for the different life cycle stages in ES-Figs. 6-8. Steady states for R_{50} and R_{64} changes over 12 h have been defined as ±7 km and ±3 km, respectively. These definitions were based on examination of the histograms of all

analyses compared to a Gaussian distribution. Structure changes reflected by these radii can also be quite large over a 12-h period. For example, the 12-h R_{50} changes can be as large as ±99 km.

In summary, a significant fraction of R_{34} changes over 12 h during the intensification or re-intensification phases are decreases rather than the increases that would be expected from the simple conceptual models discussed in Section 5a. Similarly, a significant fraction of R_{34} increases over 12 h are found during the decay phases when decreases might have been expected from the simple conceptual model. However, Merrill (1984, 1988) had suggested that the radii of outer closed isobars increase during the decay phase and Knaff et al. (2007) model has a latitudinal dependence that may predict R_{34} increases at latitudes greater than 25°N where decay is expected. Thus, these axisymmetric (and quadrant-by-quadrant, not shown) R_{34} changes are more complicated than the simple conceptual model that directly correlates R_{34} changes to intensity changes.

These life cycle histograms may indicate two possibilities: (i) structure change is random and unpredictable; or (ii) identifiable internal and external mechanisms exist that lead to the observed structure changes. Through analysis of individual storm cases as in ES-Fig. 2, structure change mechanisms are being studied to prove the second possibility applies in the majority of the cases with large changes. Through examination of tropical cyclones that undergo similar structure changes, it may be possible to isolate the most probable mechanism(s) that lead to the changes observed. Individual storm analysis is currently in progress by examining cases of large R_{34} and R_{50} changes that may be explainable in terms of the internal or external mechanisms that have been proposed for structure changes.

5. Size evolution in relation to formation

The focus of the Lee et al. (2009) study is on how TC size is maintained during its evolution, i.e., why do some large TCs remain large throughout their lifetime and similarly for small TCs? For this purpose, size for each TC is determined from the formation stage (prior to tropical storm intensity) until the mature stage (reaching typhoon intensity) with respect to a synoptic pattern classification scheme such that differences in the origin of large and small TCs are revealed.

Oceanic winds retrieved from the QuikSCAT satellite during the 2000-2005 seasons in the WNP are obtained. Best tracks of the TCs are obtained from the Joint Typhoon Warning Center (JTWC), which consists of 6-hourly positions of the 145 TCs that occurred in the basin during 2000-2005. The synoptic environment associated with these TCs is examined using the National Centers for Environmental Prediction (NCEP)-Department of Energy (DOE) Reanalysis 2 dataset with 2.5° lat./long. horizontal resolution and 6-h temporal resolution. In addition, convective patterns within these TCs are monitored by the hourly imagery from the Geostationary Meteorological Satellite-5 (GMS-5) and Geostationary Operational Environmental Satellite-9 (GOES-9) infrared channel-1 (IR1) cloud-top temperatures with 5-km resolution and spatial coverage of 20°S-70°N, 70°-160°E.

The Lee et al. (1009) the sample is limited to the 73 storms that intensified to typhoon during their lifetimes. Azimuthal average R15 values at the first sampled time period during the tropical storm (34 kt or 17.5 m s^{-1}) stage are designated at R15-TS and during typhoon stage as R15-TY. Then these 73 TC storms are categorized as small, medium, and large according to the 33% and 67% percentiles within the R15-TS and R-15 TY distributions. These tercile values are 1.1°lat. and 1.8°lat. at the TS stage, and 1.8° lat. and 2.6° lat. at the TY stage.

During the early stage intensification, systematic increases in the boundaries of the R15 size categories during intensification from tropical storm to typhoon in Table 1 imply a natural mode of spinup of the vortex may be maintenance of the axisymmetric radial profile of the tangential wind as the intensity increases. The 0.7° lat. (0.8° lat.) increase in R15 for the threshold value of small (large) typhoon versus a small (large) tropical storm in Table 1 is consistent with this mode of vortex intensification.

Most of tropical storms stay in the same size category when they become typhoons. Specifically, 67% of the small tropical storms remain small, and the corresponding percentages for medium and large tropical storms are 50% and 72%, respectively (Table 1). For those small tropical storms that do increase in size, 21% become medium-size typhoons, and only 12% become large typhoons. By contrast, all of the large tropical storms that decreased in size as a typhoon only became medium-sized typhoons (i.e., none became small typhoons). This asymmetry in size evolution is because a substantial decrease in size of a large typhoon would require a mechanism for decreasing the angular momentum of the outer-core region, or the near-surface angular momentum would have to be dissipated at a high rate. In the later case, surface friction would need to have an important role (if no exceptionally large vertical transport occurs). However, TCs are mostly over the ocean during their TS-to-TY intensification stage and an explanation for a sudden increase in surface friction in the outer region is not evident.

Notice that the rare transition from a small size tropical storm to a large typhoon requires a large spinup of the outer winds since the R15 must increase from <1.1° lat. to > 2.6° lat. Interestingly, a medium size tropical storm that does change size as a typhoon is twice as likely to become a small typhoon (8 out of 24) than a large typhoon (4 of 24). Since a small size typhoon has a R15 < 1.8° lat., and the medium size tropical storm must have an R15 < 1.8° lat., this situation means absolutely no increase in outer winds during the intensification. Recall that all of these medium-size tropical storms are all intensifying to become a typhoon, so the maintenance

Table 1 Definitions of small, medium, and large size (unit: degree latitude) TCs during the TS stage (first column) and TY stage (first row). Number in parentheses is the number of TC cases in each category. The other table entries are the proportion (percentages in parentheses) of cases that change from one TC size category to another during the intensification from TS to TY, and the diagonal entries (bold) indicate cases with no change in TC size category.

TS \ TY	Small [< 1.8° (24)]	Medium [1.8° – 2.6° (24)]	Large [> 2.6° (25)]
Small [< 1.1° (24)]	16 / 24 (67%)	5 / 24 (21%)	3 / 24 (12%)
Medium [1.1° – 1.8° (24)]	8 / 24 (33%)	12 / 24 (50%)	4 / 24 (17%)
Large [> 1.8° (25)]	0 / 25 (0%)	7 / 25 (28%)	18 / 25 (72%)

or decrease in outer winds can not be attributed to the storm being in a decay stage. By contrast, a large spinup of the outer winds must occur if the medium size tropical storm is to become a large typhoon, which requires a R15 > 2.6° lat.

In summary, the R15 values for TCs in the WNP tend to remain in the same size category during their intensification from TS to TY. Implication of this tendency is that physical mechanisms have to

be present to maintain the size of large TSs, and to keep the R15 small for small TSs (i.e., to inhibit significant strengthening of outer-core winds). Before these physical mechanisms are explored, it is of interest to examine the origins of small and large TCs.

Lee et al. (2008) identified six synoptic patterns for TC formation in the WNP based on the low-level wind flow and surge direction: easterly wave (EW), northeasterly flow (NE), coexistence of northeasterly and southwesterly flow (NE-SW), southwesterly flow (SW), monsoon confluence (MC), and monsoon shear (MS). This synoptic pattern classification is applied to the TC cases in this study for which R15-TS can be determined with QuikSCAT data during their formation. In the monsoon-related patterns (MC, MS, SW and NE-SW), formation of medium size to large size tropical storms is favored. In particular, strong southwesterly winds are a common ingredient in the MC, SW, and NE-SW synoptic patterns. The MS pattern has strong easterlies and westerlies (> 5 m s^{-1}) to the north and south of the depression that also contributes to strong winds in the outer-core region, which is somewhat favorable for formation of large-size tropical storms. Most of the tropical storm formations associated with the EW pattern are either small or medium size, which is consistent with the finding in Lee et al. (2008) that convection and possible mesoscale convective systems in the EW-type formations are mostly concentrated within a small radius (about 1^o-2^o lat.) from the system center. Since these episodes of convection tend to be confined to an area of low-level vorticity near the center, formation of a smaller-size tropical storm is favored.

In summary, it is the differences in the environment that determine the differences between persistently large and small TCs directly during formation and indirectly during intensification by its effect on the convection distribution. It should be emphasized that this conclusion is based on examination of low-level flow patterns without consideration of the potential contributions from vertical wind shear and upper-level processes. In addition, the TC size pedigree based on formation patterns as identified here is for the early stage intensification only. Stronger TCs above typhoon intensity can grow in size much more rapidly than the climatological rate under the influence of factors other than those identified in this study.

6. Conclusion

Advances are beginning to be made in the understanding of tropical cyclone outer wind structure changes, which are important both directly for forecasting the time when damaging winds will arrive and indirectly via their effect on beta-effect propagation. Just as a general theory does not exist for tropical cyclone intensification, a general theory does not exist for outer wind structure change. In the simplest wind structure models, an increase in the maximum wind speed is accompanied by an increase in the outer winds due to the radial gradient of column-mean virtual temperature, and thus the radial gradient of surface pressure. Since the intensity change is not necessarily correlated with outer structure changes, such a simple explanation is inadequate.

Knaff et al. (2007) have developed a climatological and persistence technique for predicting the wind radii evolution each 12 h to 120 h. The key step in their technique is the fitting of the wind profile to the operational estimates of the 34, 50, and 64 kt radii. The “forecasts” after these times are essentially a reversion to the climatological profile. Since the climatological profile is a modified Rankine profile tied to the maximum wind and a radius of maximum wind, forecast increases in these values will necessarily result in an increase in outer wind speeds for tropical cyclones at latitudes less than 25°N. For latitudes north of 25°N, the contribution of the increasing latitudinal effect, especially with a

decreasing maximum wind speed, will then broaden the vortex (smaller value of the x-exponent in the modified Rankine vortex).

The simple wind structure model will not account for the frequently observed expansion of the outer wind as the tropical cyclone intensity begins to decrease as it is moving into the midlatitude westerlies, although some of this expansion may simply be due to the zonal wind shear in the environment. The Knaff et al. (2007) forecast technique has a latitudinal variation in the climatological wind structure profiles, so their forecasts will tend toward the climatological profile at each latitude as the cyclone moves poleward.

Neither the simple wind structure model nor the Knaff et al. (2007) forecast technique will address the wind structure or the wind structure changes associated with secondary eyewall formation (or eyewall replacement cycles). These events are considered to be a primary contributor to the outer wind speed increases. Thus, it is necessary to first predict the occurrence of a secondary eyewall formation and then to predict how the outer wind structure will be changed. Although numerical model simulations (e.g., Terwey and Montgomery 2009) are indicating secondary eyewall formations, the operational numerical models have not been shown to predict the timing and magnitude of such events. Whereas statistical techniques (e.g., Kossin group) are being developed for the Atlantic, the accuracy or applicability to other basins needs to be established.

Most of the outer wind structure studies have been in the Atlantic because reconnaissance aircraft measurements are necessary for "ground truth." The recent addition of the SFMR on all of the U. S. Air Force WC-130J aircraft will provide a rich data set for studies of outer wind structure and structure change. Similar observations and numerical simulations studies are needed for tropical cyclones that form in a monsoon trough environment. Some SFMR observations have been obtained during the Tropical Cyclone Structure (TCS08) field experiment, and more will be collected during TCS10. However, more studies such as in Lee et al. (2009) are needed with Quikscat observations.

An optimistic hypothesis is that if an accurate specification could be provided of the initial outer wind structure, then the present mesoscale tropical cyclone models should be capable of predicting the future outer wind structure. This hypothesis needs to be tested to advance the capability to provide improved warnings of the onset of damaging winds associated with tropical cyclones.

Acknowledgments: The participation by R. L. Elsberry is partially supported by the Office of Naval Research Marine Meteorology program. Dr. Mark Powell of HRD is acknowledged for his H*Wind analyses. Mrs. Penny Jones expertly prepared this manuscript.

REFERENCES

Elsberry, R. L., T. D. B. Lambert, and M. A. Boothe, 2007: Accuracy of Atlantic and eastern North Pacific tropical cyclone intensity forecast guidance. *Wea. Forecasting*, **22**, 747-762.

Elsberry, R. L., and R. A. Stenger, 2008: Advances in understanding of tropical cyclone wind structure changes. *Asia-Pacific J. Atmos. Sci.*, **44**, 11-24.

Emanuel, K.A., 1995a: The behavior of a simple hurricane model using a convective scheme based on subcloud-layer entropy equilibrium. *J. Atmos. Sci.*, **52**, 3959-3968.

Emanuel, K. A., 1995b: Sensitivity of tropical cyclones to surface exchange coefficients and a revised steady-state model incorporating eye dynamics. *J. Atmos. Sci.*, **52**, 3969-3976.

Hawkins, J. D., M. Helveston, T. F. Lee, F. J. Turk, K. Richardson, C. Sampson, J. Kent, and R. Wade, 2006: Tropical cyclone multiple eyewall configurations. Paper 6B.1, *27th Hurr. And Trop. Meteor. Conf.*, Monterey, CA, Amer. Meteor. Soc., Boston, MA.

Knaff, J. A., J. P. Kossin, and M. DeMaria, 2003: Annular hurricanes. *Wea. Forecasting*, **18**, 204-223.

Knaff, J. A., C. R. Sampson, M. DeMaria, T. P. Marchok, J. M. Gross, and C. J. McAdie, 2007: Statistical tropical cyclone wind radii prediction using climatology and persistence. *Weather and Forecasting*, **22**, 781-791.

Lee, C.-S., K. K. W. Cheung, J.S.N. Hui, and R. L. Elsberry, 2008: Mesoscale features associated with tropical cyclone formations in the western North Pacific. *Mon. Wea. Rev.*, **136**, 2006-2022.

Lee, C.-S., K.K.W. Cheung, W.-T. Fang, and R. L. Elsberry, 2009: On maintenance of tropical cyclone size in the western North Pacific. Submitted to *Mon. Wea. Rev*.

Merrill, R. T., 1984: A comparison of large and small tropical cyclones. *Mon. Wea. Rev.*, **112**, 1408-1418.

Merrill, R. T., 1988: Environmental influences on hurricane intensification. *J. Atmos. Sci.*, **45**, 1678-1687.

Willoughby, H. E., J. A. Clos, and M. G. Shoreibah, 1982: Concentric eyewalls, secondary wind maxima, and the evolution of the hurricane vortex. *J. Atmos. Sci.*, **39**, 395-411.

Airborne Deployment of GPS Dropsondes from High Altitude for Diagnosis of TC Genesis: Examples from TPARC/TCS08

Peter G. Black

Science Applications International Corporation, Inc., Monterey, CA USA

Email: peter.black@nrlmry.navy.mil

INTRODUCTION

Approximately half of the TPARC/TCS08 WC-130J flights were flown in TC genesis situations in which GPS dropsondes were deployed from an altitude at or near 300 mb. Nearly all of these were flown in the first five weeks of the project from 1 August to 7 September, 2008. These flights were flown into cloud clusters that exhibited a cohesive structure and which various models indicated had development potential. AXBT's were also deployed on these flights for diagnosis of the underlying ocean structure. This paper examines the potential for mitigating landfall impacts through improved observations of the genesis phase of TC development resulting in increase lead times for preparation for potential landfall situations.

OBJECTIVES AND OBSERVATIONAL STRATEGY

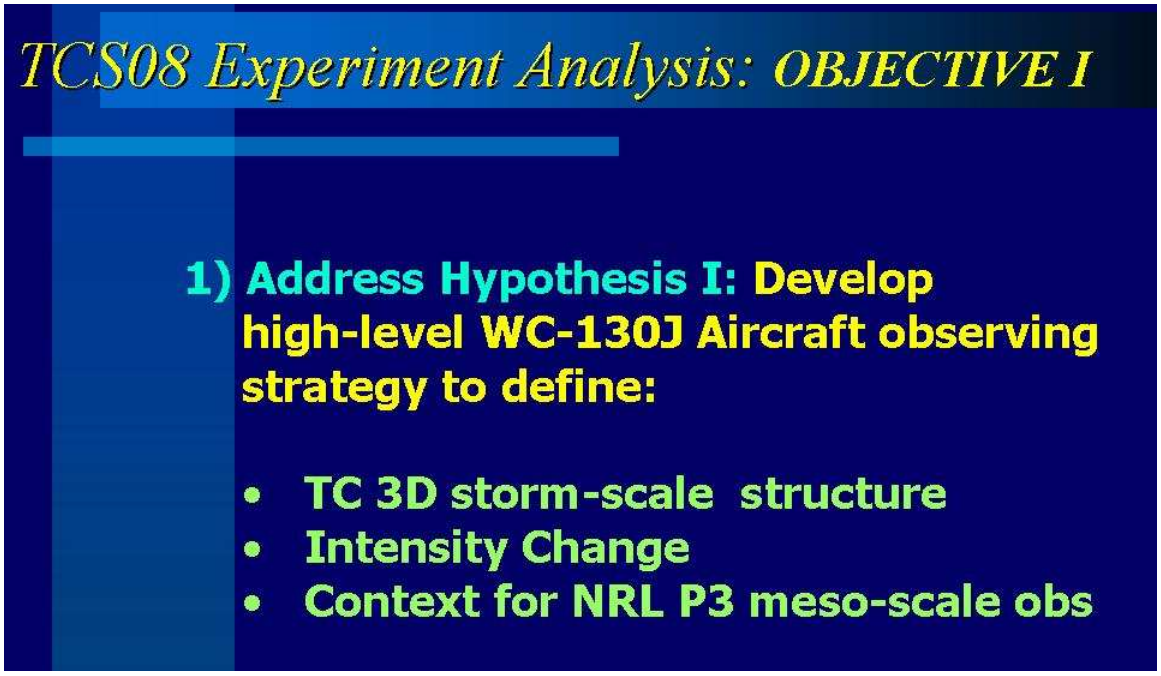

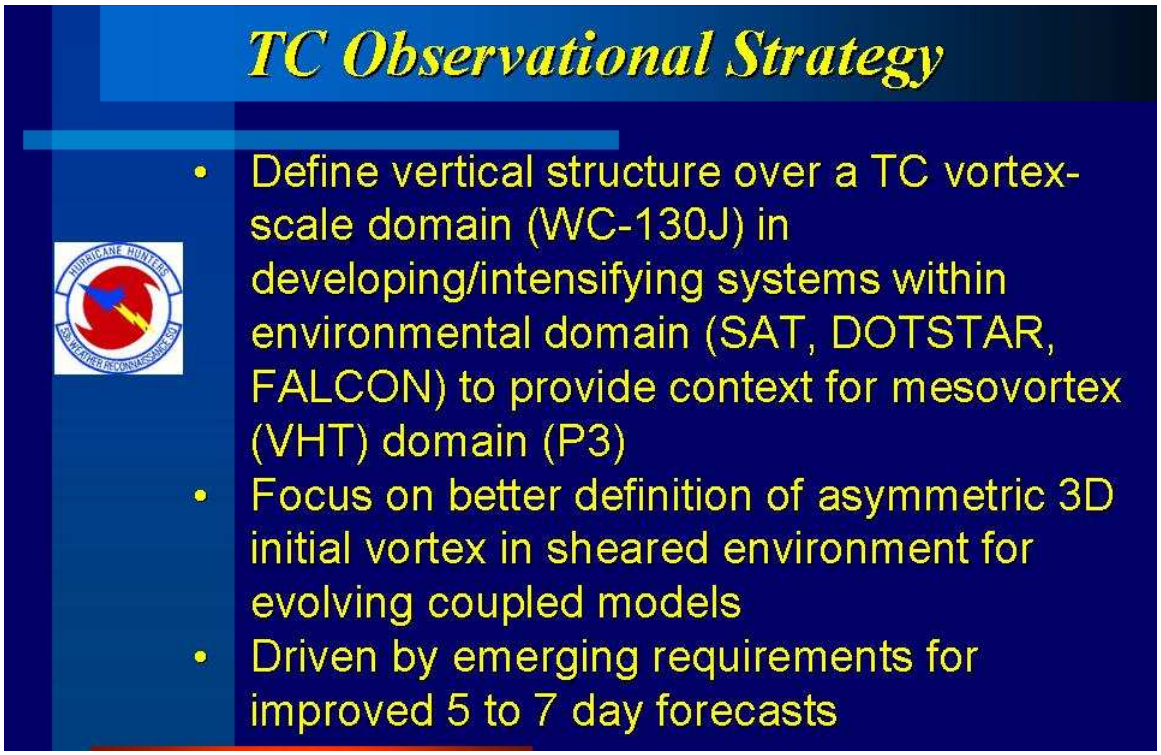

HYPOTHESIS AND RATIONALE

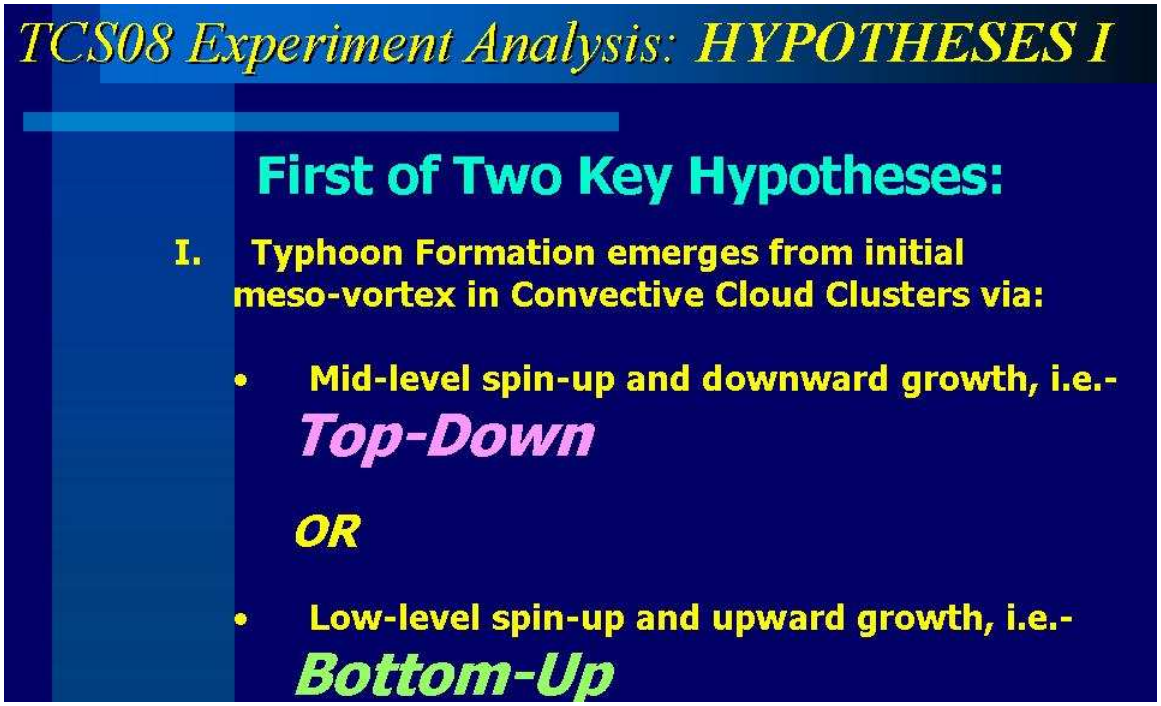

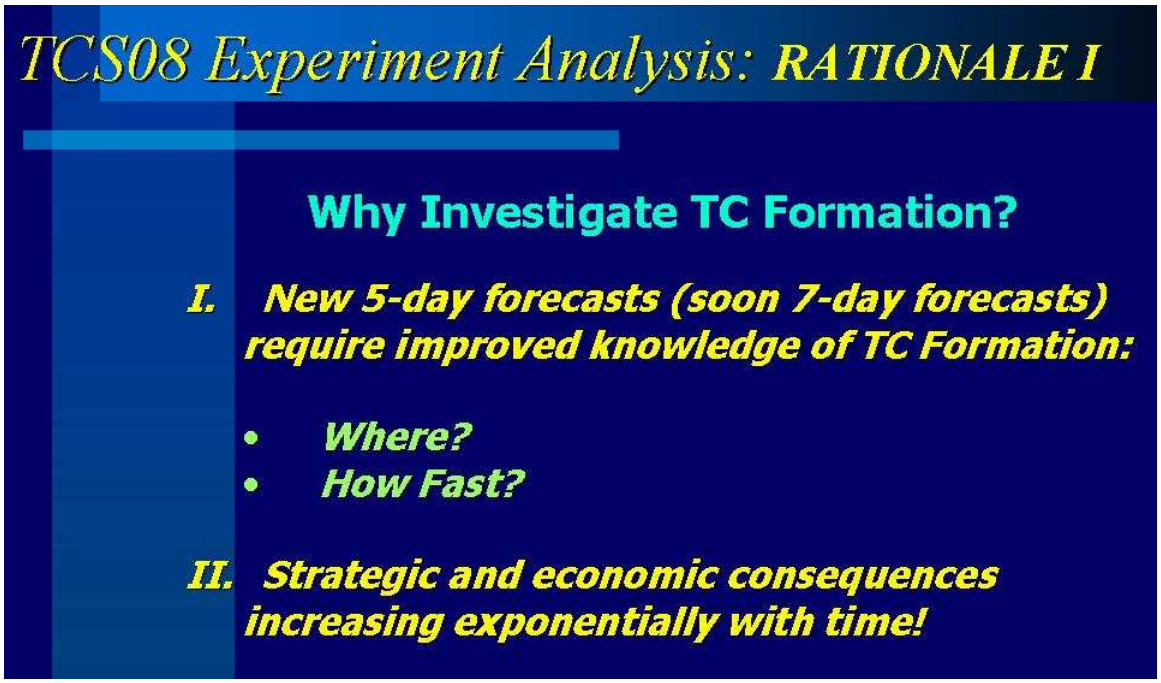

DISCUSSION AND PRELIMINARY RESULTS

During TCS08, flights were made into two disturbances that both exhibited 'vortex pairs' at different altitudes. These systems were labeled TCS25 and TCS37 and were flown with GPS deployment from 300 mb on 27-28 August and 6-7 September, respectively. Both features were propagating westward associated with a tropical wave interacting with an upper level trough. Fig. 1shows near-surface GPS dropsonde derived wind barbs plotted on visible and microwave imagery in the upper left and lower right panels, respectively. These plots show a closed circulation at the surface with a center of circulation entirely in the clear located about 150 km north of a cluster of convective cells. Maximum winds within this circulation were westerly and southwesterly at about 15-18 kt to the southwest and southeast of the circulation center, just upstream and downstream from the convective activity. The upper right and lower left panels show the wind barbs at the 700 mb level. These also show a closed circulation, as do winds in the layer from 750 to 500 mb, but with the center of circulation imbedded within the convective region 120 km south of the surface circulation. Peak winds were westerly at 20 kt just south of the max wind band at the surface and southwest of the center of circulation.

Fig. 2 shows the WC-130J airborne radar image superimposed on the microwave image that illustrates an incipient eye feature in the middle of the curved microwave convective feature. This observation together with the sondes suggest that throughout the middle levels rotation is taking place to the extent that cyclonically curved bands are forming. However, the low level GPS sondes clearly show that no surface circulation exists beneath the mid-level center, but instead is displaced 120 km to the north. TCS25 never developed, but was a trackable entity for 4 days.

TCS37 was a similar situation to TCS25 in that it too exhibit the vortex pair characteristic, but with the mid level vortex located at 400 mb, a somewhat higher level than that in TCS25. In this case the surface and 400

mb vortices were separated by nearly 200 km (Fig. 3) with the surface center west of the 400 mb center which was imbedded within the convective cluster. The surface center was in the clear as was the case for TCS25. The peak winds associated with the surface center were 15 kt southerly winds located east of the center within the convective cluster. Peak 400 mb winds were southwesterly at 25 kt and located along the southern edge of the convective cluster within a region of growing convective clouds. This system also failed to develop, but was trackable for 3 days. Fig 4 shows a strong diurnal signal to the convection with active cluster development during the fist half of the flight followed by rapid dissipation during the second half of the flight.

These two systems are likely typical of many incipient disturbances prior to any development. With an aircraft available to deploy GPS dropsondes within the region, it may be possible to not only diagnose the vortex pair development, but to eventually distinguish the conditions that lead to TC genesis from those that are followed by decay and with a day or two more lead time than is currently possible.

CLOSING COMMENT AND CONCLUSIONS

We are at an historic turning point in history for the improvement of TC genesis and intensity change observation and forecasting where the capability to observe winds over the TC surface and mid-level domain concurrent with subsurface ocean thermal structure matches, or soon will match, the improvements in coupled model capabilities to assimilate and model the total TC environment. This alignment should provide the next best opportunity for improving TC structure and intensity change forecasting.

This study has shown that low/mid level vortex pairs are typical of potential TC formation events. The challenge is now to define conditions for development and decay. A new observing strategy was pioneered that hopefully can be repeated within the ITOP experiment in 2010

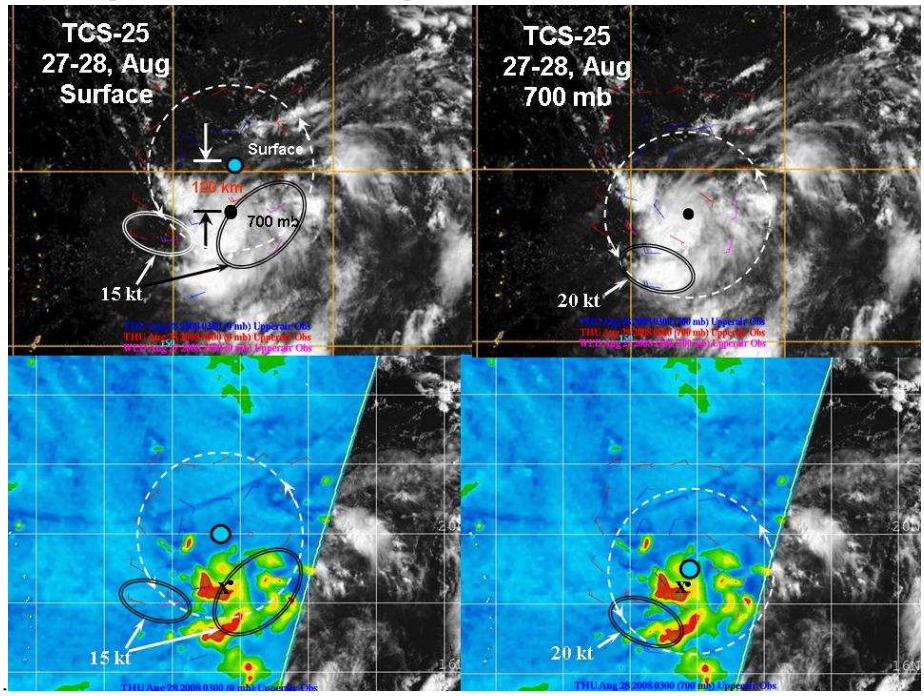

Figure 1. Visible and microwave satellite imagery for TCS25 with GPS dropsonde surface winds plotted in the upper and lower left panels and 700 mb winds plotted in the upper and lower right panels. The ovals

indicate the maximum wind regions, the dashed circle the approximate radius of maximum wind, the blue dot the surface circulation center, the black dot the 700 mb circulation center and the 'x' indicates the airborne radar incipient eye center.

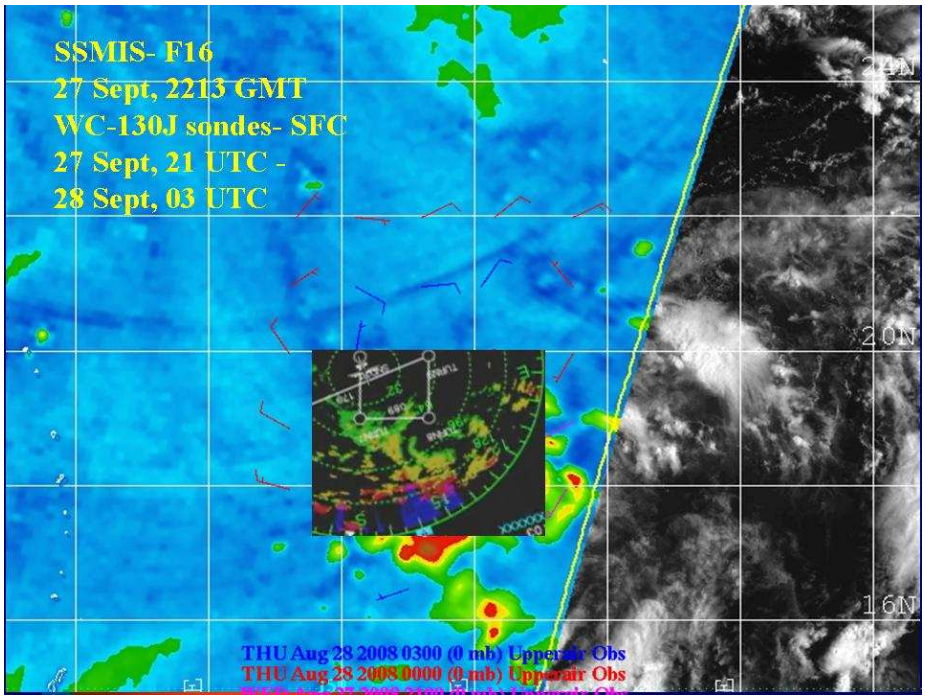

Figure 2. Airborne radar image superimposed upon satellite microwave image and 700 mb GPS dropsonde wind barbs.

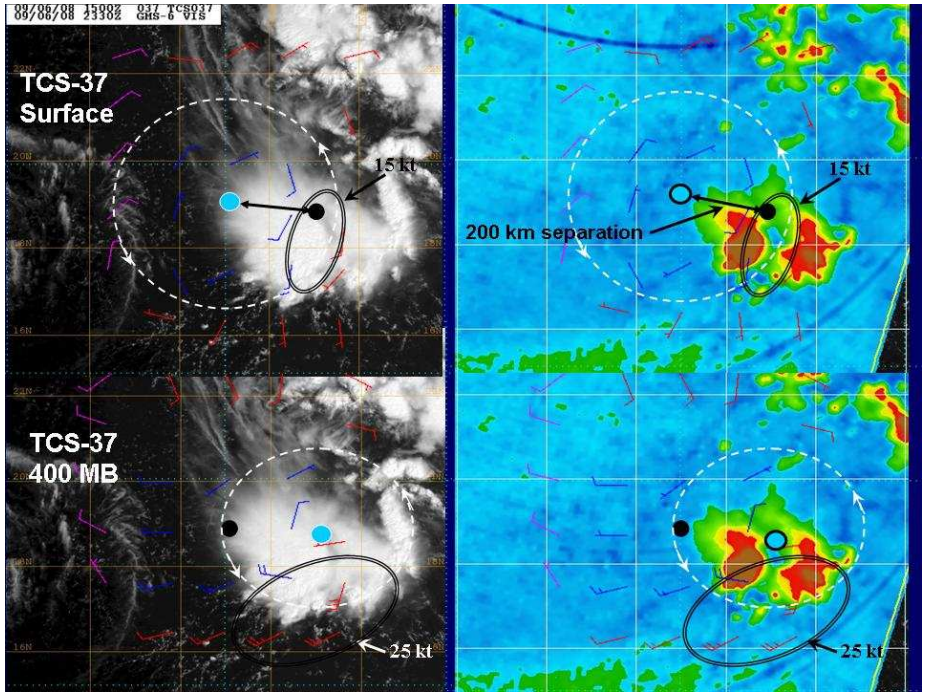

Figure 3. Visible and microwave imagery for TCS37, 6-7 Sept. Upper left and upper right panels show the surface wind barbs. Lower left and lower right show the 400 mb wind barbs. The ovals indicate the wind maxima.

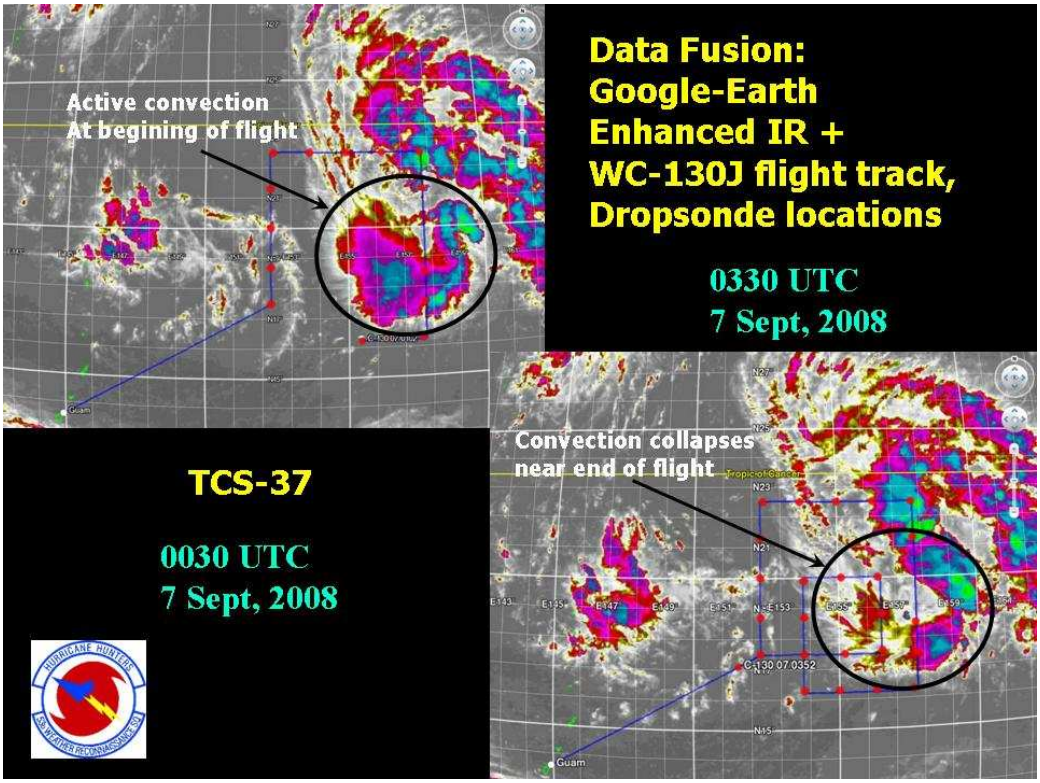

Figure 4. Infrared imagery near the beginning of the TCS37 flight showing and intense convective cluster covering the eastern half of the intended flight track (upper left panel). This is contrasted three hours later by an infrared image showing the convective cluster almost entirely dissipated. Near the end of the TCS37 flight (lower right).

Transition of the Inflow Boundary Layer of Landfalling Tropical Cyclones

Yuqing Wang and Jing Xu

International Pacific Research Center and Department of Meteorology

University of Hawaii at Manoa, Honolulu, HI 96822

1. **Introduction**

The inflow boundary layer of a tropical cyclone (TC) is subject to change from marine boundary layer to continental boundary layer when it makes landfall. This is due to changes of the surface properties, including the contrasts in the surface roughness, wetness, and surface temperature over the ocean and over the land. These surface properties may affect the surface friction, surface heat and moisture fluxes, vertical turbulent mixing, and thus the vertical structure of the inflow boundary layer. Previous studies have mainly focused on the comparison of changes in the storm intensity and asymmetric structure of landfalling TCs, such as the distribution of rainfall, surface winds, etc. (Tuleya et al. 1984; Powell 1987; Marks and Shay 1998; Powell and Houston 1998; Chan and Liang 2003; Wong and Chan 2007; Kimball 2008). In this study, idealized simulations were performed to understand the transition of the inflow boundary layer of landfalling TCs. The experiments were also attempted to examine the effect of land surface temperature on the structure and intensity changes of landfalling TCs.

2. **Model and experimental design**

The model used in this study is the fully compressible, nonhydrostatic tropical cyclone model–TCM4 developed by Wang (2007). A full description of TCM4 can be found in Wang (2007), and its applications to the studies of the inner-core dynamics of TCs can be found in Wang (2008a and b, 2009) and Wang and Xu (2009). The model settings are the same as those used in those previous studies but with higher resolution. The model uses the mass coordinate in the vertical with the lower boundary at a flat surface with the unperturbed surface pressure of 1010 hPa and with its top at about 38 km. The model domain is quadruply nested with two-way interactive nesting and with the inner meshes automatically moving to follow the model storm (Wang 2001, 2002c). The model has 32 vertical levels with relatively high resolution both in the lower troposphere and near the tropopause. The horizontal grid intervals of 54, 18, 6, and 2 km have domain sizes of 251×201, 127×127, 145×145, and 217×217 grid points for the four meshes, respectively.

The model physics include an E-ε turbulence closure scheme for subgrid scale vertical turbulent mixing (Langland and Liou 1996), a modified Monin-Obukhov scheme for the surface flux calculations (Fairall et al. 2003), an explicit treatment of mixed-phase cloud microphysics (Wang 2001), a nonlinear fourth-order horizontal diffusion for all prognostic variables except for that related to the mass conservation equation, a simple Newtonian cooling term to mimic the radiative cooling (Rotunno and Emanuel 1987), and the dissipative heating due to molecular friction related to the turbulent kinetic energy dissipation rate (ε) from the E-ε turbulent closure scheme. As in Wang (2007, 2008a and b, 2009), the same model physics are used in all meshes. Since no large-scale environmental flow is included in this study, convection occurs mainly in both the inner-core region and the spiral rainbands within about 200 km from the TC center and is covered by the finest innermost domain. Therefore, cumulus parameterization is not considered in any mesh in this study.

The experimental design follows Wang (2008a and b, 2009). The model was initialized with an axisymmetric cyclonic vortex on an f–plane of 18oN in a uniform easterly environmental flow of -5 m s-1. The model TC was thus moving westward over the ocean first with a constant sea surface temperature (SST) of 29oC and made landfall over a flat land after about 116-120 h of simulations. The land surface temperature was specified either as the same as the SST (lnd2f) or 1.5oC lower (lnd1f) or 1.5oC higher (lnd3f) than SST. The land has a roughness length for momentum (z0m) of 5 cm and the roughness length for heat and moisture of z0m/4.5. The wetness over the land was given as 0.1 for all landfalling experiments. To show how the land affects the simulated storm structure and intensity, a supplementary experiment (lnd0f) was conducted in which the storm was embedded in a 5 m s-1 easterly flow over the ocean only.

The initial thermodynamic structure of the unperturbed model atmosphere is defined as the western Pacific clear-sky environment given by Gray et al. (1975). The initial cyclonic vortex has a maximum tangential wind speed at the surface of 20 m s-1 at a radius of 80 km that decreases sinusoidally with pressure to vanish at 100 hPa. The mass and thermodynamic fields are obtained by solving the nonlinear balance equation as described in Wang (2001). Namely the initial storm was in hydrostatic and gradient wind balances and the environmental flow was in geostrophic balance.

3. **Storm motion and intensity change**

Figure 1 shows the tracks of storms simulated in all experiments. TCs moved mainly westward following the steering easterly flow but with a motion component to the north or to the right of the steering flow due to the larger surface frictional convergence to the right of the storm than that to the left of the storm center (Wang 1998). Note that all storms with land effects moved slightly to the left of the storm without the land effect. The difference appeared before landfall even about 600 km offshore, implying that the land could have a remote effect on the motion of TCs. Nevertheless, the storm tracks seemed to have a less effect by the land surface temperature except for about 3 hours later of landfall for the storm in the warm land experiment (lnd3f).

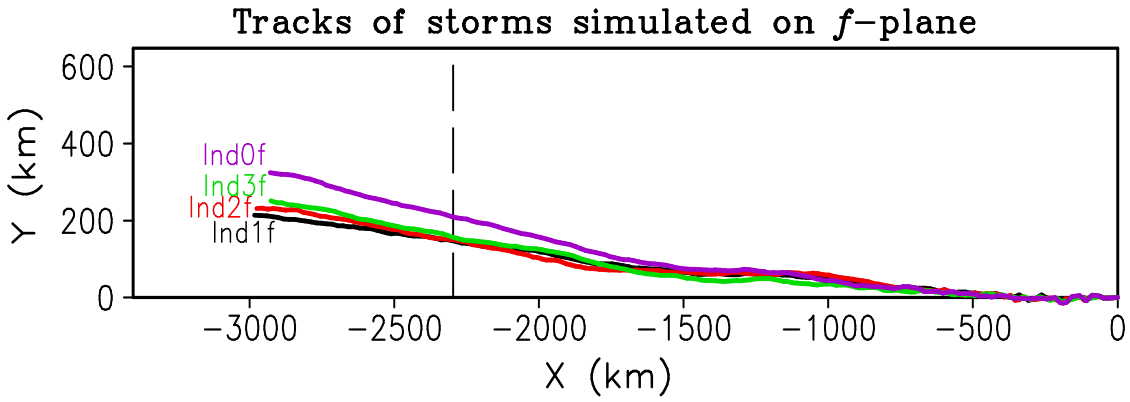

Fig. 1. Storm tracks simulated in all experiments. The dashed vertical line indicates the west coastline of the ocean.

Figure 2 shows the evolution of the maximum azimuthal mean tangential wind speed at the lowest model level and the minimum sea level pressure (MSLP) in all experiments. The model storm in ocean-only experiment reached its maximum intensity after about 108 h of simulation with the MSLP of 910 hPa and the maximum azimuthal mean wind speed of 75 m s^{-1}. Since the landfalls occurred between 116-120 h, storms in three landfalling experiments made landfall after they reached their maximum intensity. As a result, all storms weakened immediately after the storm center moved across the coast. Note that although differences in storm

intensity before landfall were small, significant differences occurred after landfall. The weakening rate of the storm after making landfall was inversely proportional to the land surface temperature. The storms then reached a quasi-steady intensity in about one day after landfall. The storms did not weaken continuously after landfall because our initial sounding for temperature and specific humidity over the land is the same as that over the ocean. Namely, the continental air in our simulation was sufficiently moist to maintain a weak tropical storm. The slower weakening for storm in the warmer land surface experiment was due mainly to two facts: the same land surface wetness implied more soil moisture available for surface latent heat flux for higher land surface temperature and the higher land surface temperature gave rise to higher convective available potential energy (CAPE, Fig. 3). Both favored the active convection and thus the maintenance of the storm intensity in warm land experiment.

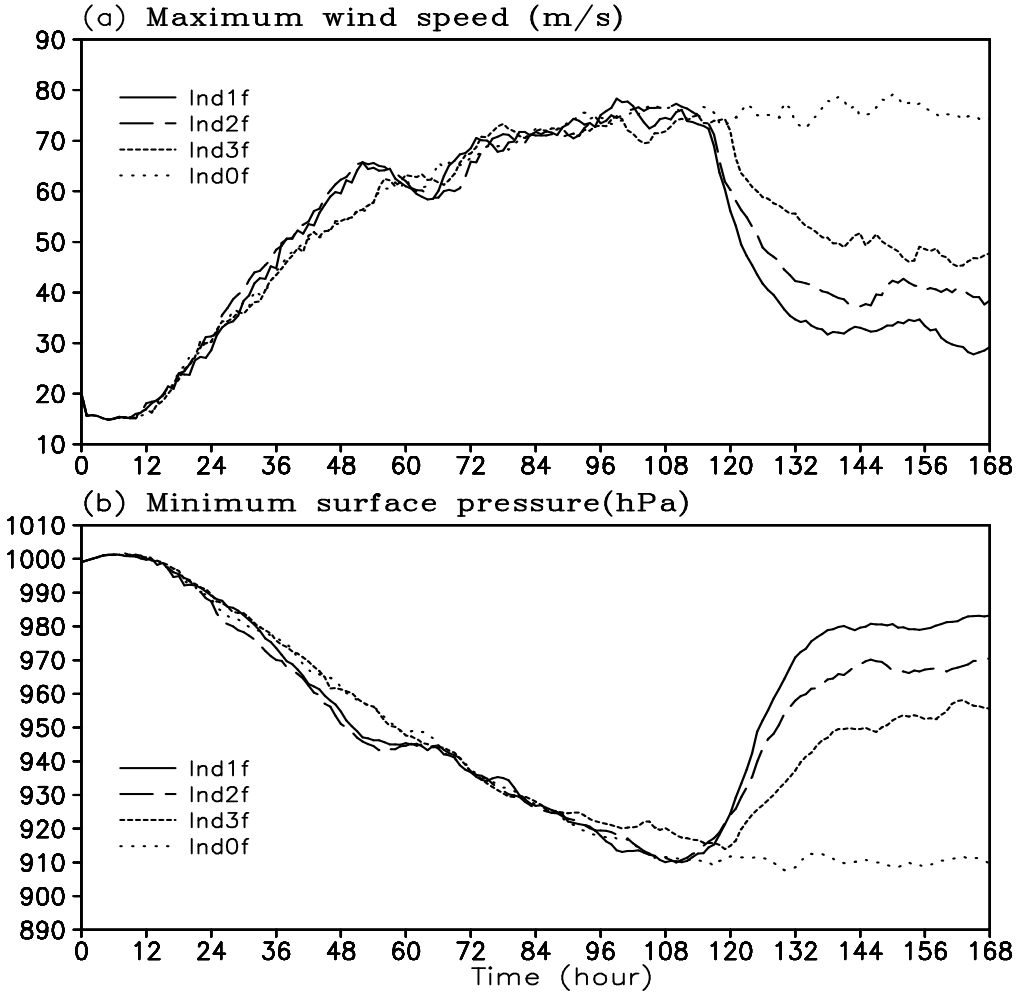

Fig. 2. Time evolution of the storm intensity in the all experiments. (a) The maximum azimuthal mean wind speed (m s^{-1}) at the lowest model level (35 m) above the sea surface and (b) the minimum sea level pressure (hPa).

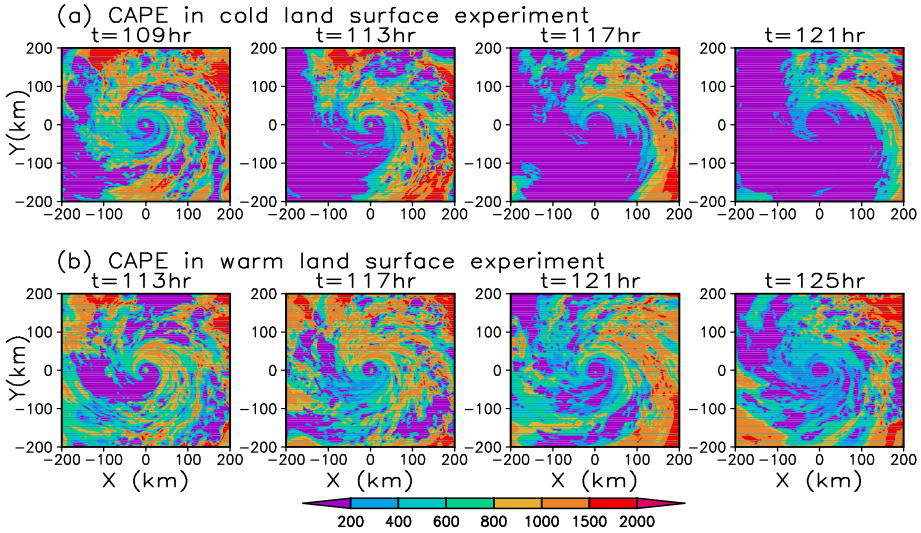

Fig. 3. Convective available potential energy (CAPE) in cold (lnd1f) and warm (lnd3f) land experiments at given times, showing the high CAPE in warm land experiment.

4. **Asymmetric structure of winds and rainfall**

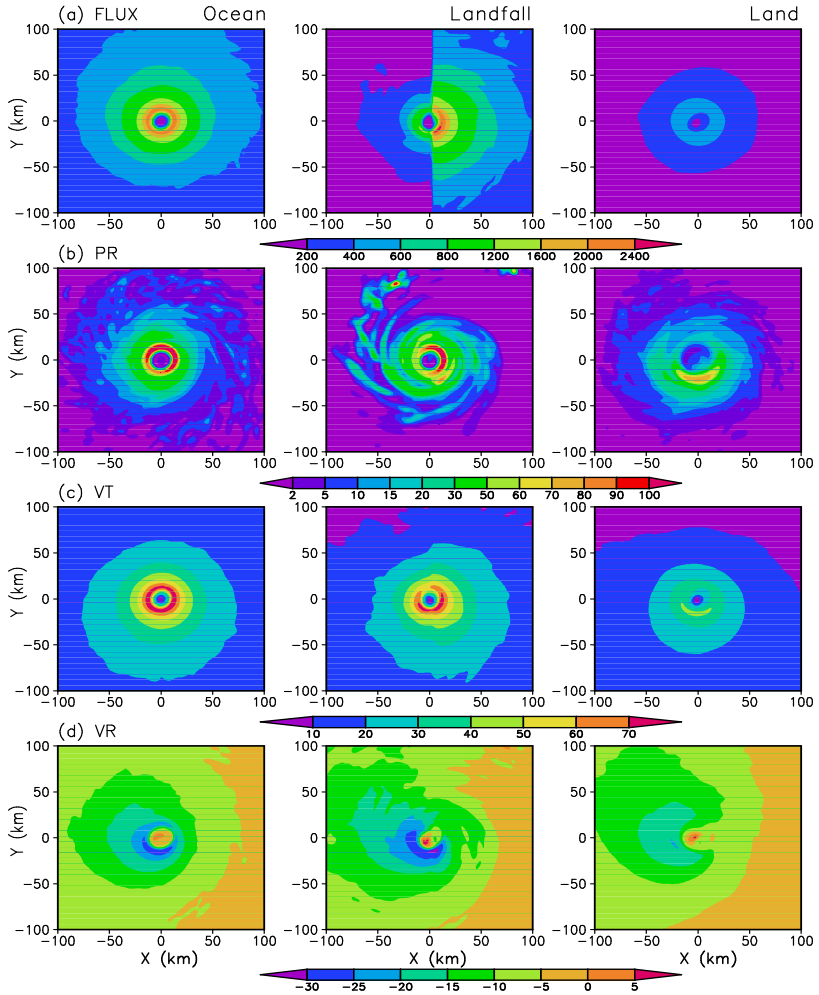

Fig. 4. (a) Surface sensible and latent heat fluxes (FLUX, Wm^{-2}), (b) surface rain rate (PR, mm h^{-1}), (c)

tangential wind speed (VT, ms^{-1}), and (d) radial wind speed (VR, ms^{-1}) at the lowest model level (35 m above the sea surface) in experiment lnd1f for storm over the ocean (averaged between 96-110h), at landfall (at 116h), and over land (averaged between 121-135h).

Figure 4 shows the horizontal distribution of various variables averaged over the ocean and over the land and also at landfall. Surface flux was quasi-symmetric for storms either over the ocean or over the land but largely reduced after landfall. At landfall, surface flux over the land area in the storm core was largely reduced but remained large for the area over the ocean. Rainfall rate was quite axisymmetric when the storm was over the ocean although it was slightly larger to the right in the eyewall. At landfall, rainfall reduced in the left front quadrant over land but remain large for the ocean part of the eyewall. After landfall, rainfall maximum in the eyewall moved to the left of the storm center and largely reduced as the storm weakened significantly. Tangential wind speed was also quite axisymmetric when the storm was over the ocean but became very asymmetric after landfall with maximum values to the left of the storm center. The radial wind was stronger to the front to left front of the storm either over land or over the ocean both in the inner core and outside of the core. However, the asymmetries were considerably enlarged at and after landfall.

5. **Transition of inflow boundary layer at landfall**

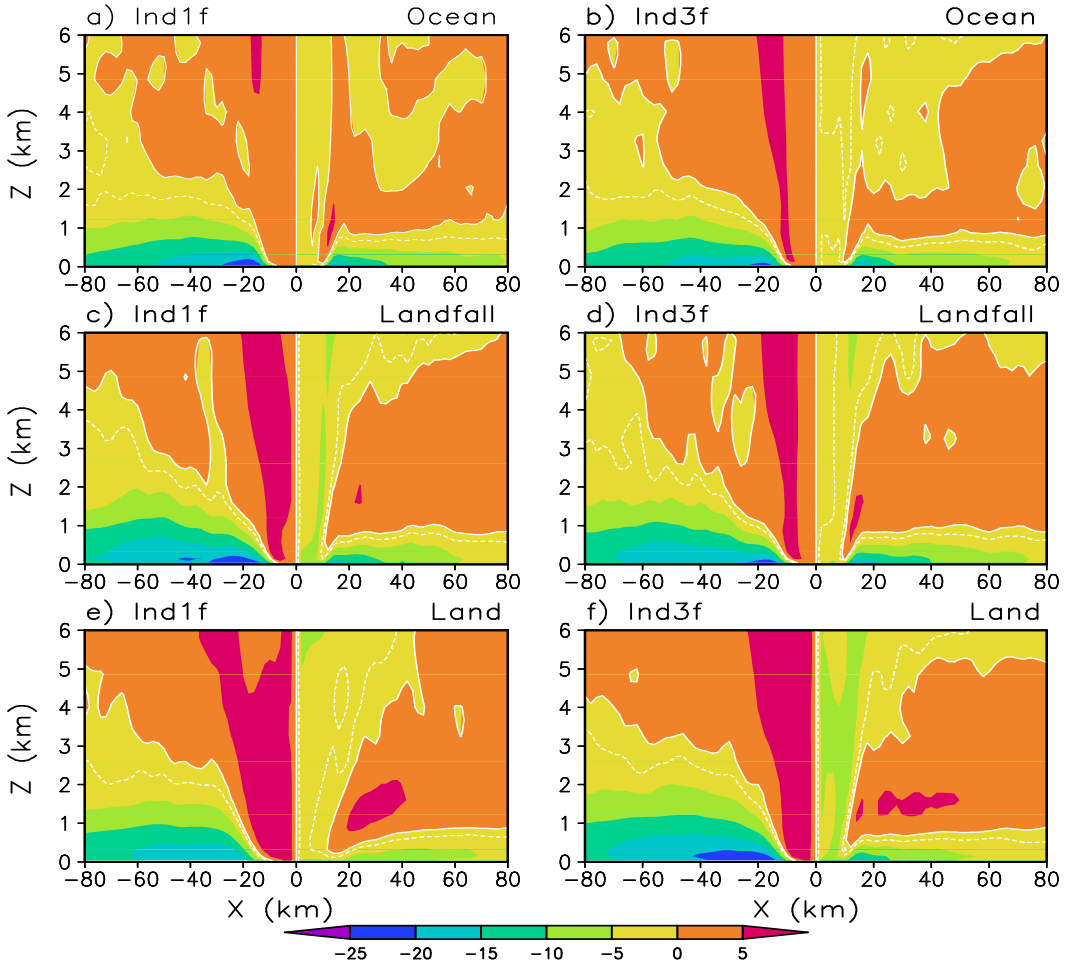

Fig. 5. Zonal-vertical cross-section of radial wind speed through the model TC center in the cold (left) and warm (right) land experiments. Dashed contours show the -2 m s^{-1} radial wind speed and solid contours show 0 radial wind speed. Note that 15 h average was applied to both the land and ocean cases and only a 5 h mean

was applied to the storm about at landfall in two experiments.

The enhanced radial wind asymmetry at the lowest model level after landfall implies the transition of marine inflow boundary layer to the continental inflow boundary layer. As we can see from Fig. 5, inflow boundary layer was much deeper in the front than in the rear of the storm center regardless the storm was over the ocean or over the land or at landfall. Note that although the inflow layer in the rear of the storm center remained almost the same over the ocean, at landfall or over land, the inflow layer deepened considerably in the front quadrant after landfall in all landfalling experiments. The exact deepening however depends on the land surface temperature. The warmer the land surface temperature, the deeper the front inflow boundary layer. This can be easily seen from the -2 m s^{-2} radial wind speed to the west of the storm center (x=0 in Fig. 6). For example, the inflow boundary layer after landfall in lnd3f was about 50% deeper than that over the ocean about 12 h earlier. This is mainly a result of the enhanced vertical mixing due to the large mechanical and buoyant turbulences over the land. In the warm land case, the buoyant turbulent mixing would be strong and enhance the vertical mixing, such as the case of lnd3f in which the land surface temperature was 1.5 K warmer than SST. The large difference in the inflow layer depth between lnd1f and lnd3f may imply that tropical cyclones making landfall during day time could have a deeper inflow boundary layer than the storms making landfall during night time.

6. **Conclusions**

Idealized simulations were conducted to examine the transition of the inflow boundary layer of landfalling TCs and the changes in wind and rainfall distributions for storms making rainfall. Consistent with previous studies, storms over the ocean showed quasi-symmetric inner core structure in rainfall and tangential wind, while the radial winds were stronger in the front quadrant than in the rear quadrant. After landfall, strong asymmetries developed in both rainfall and wind fields. In general, both rainfall and tangential wind speeds became larger to the left than to the right of the storm center over the land. Storms started to weaken immediately when their center making landfall. The weakening rate is found to inversely proportional to the land surface temperature. The depth of boundary layer inflow however is directly proportional to the land surface temperature. The sensitivity of storm structure and intensity changes to the land surface temperature found in this study may have implications to the importance of timing (day or night) of landfalling TCs to the prediction of storm transition at landfall. Further, although this is a preliminary study, our results also suggest that accurate prediction of land surface processes is critical to the accurate prediction of landfalling tropical cyclones (Davis et al. 2008). An extension of this work is to initialize the land area with relatively dry conditions so that the dry air intrusion from land area on storm structure and intensity changes can be examined.

Acknowledgments: This study has been supported by NSF grant ATM-0754039. Additional support has been provided by the JAMSTEC, NASA, and NOAA through their sponsorships of the International Pacific Research Center (IPRC) in the School of Ocean and Earth Science and Technology (SOEST) at the University of Hawaii

References

Chan, J. C. L., and X.-D. Liang, 2003: Convective asymmetries associated with tropical cyclone landfall. Part I: f-plane simulation. *J. Atmos. Sci*., **60**, 1560-1576.

Davis, C. and co-authors, 2008: Prediction of landfalling hurricanes with the advanced hurricane WRF model.

Mon. Wea. Rev., **136**, 1990-2005.

Fairall, C. W., E. F. Bradley, J. E. Hare, A. A. Grachev, and J. B. Edson, 2003: Bulk parameterization of air–sea fluxes: Updates and verification for the COARE algorithm. *J. Climate,* **16**, 571–591.

Gray, W. M., E. Ruprecht and R. Phelps, 1975: Relative humidity in tropical weather systems. *Mon. Wea. Rev.*, **103**, 685-690.

Kimball, S. K., 2008: Structure and evolution of rainfall in numerically simulated landfalling hurricanes. *Mon. Wea. Rev*., **136**, 3822-3847.

Langland, R. H., and C.-S. Liou, 1996: Implementation of an E-ε parameterization of vertical subgrid-scale mixing in a regional model. *Mon. Wea. Rev.*, **124**, 905-918.

Marks, F. D., and L. K. Shay, 1998: Landfalling tropical cyclones: Forecast problems and associated research opportunities. *Bull. Amer. Meteor. Soc*., **79**, 305-323.

Powell, M. D., 1987: Changes in the low-level kinematic and thermodynamic structure of Hurricane Alicia (1983) at landfall. *Mon. Wea. Rev*., **115**, 75-99.

Powell, M. D., and S. H. Houston, 1998: Surface wind fields of 1995 Hurricanes Erin, Opal, Luis, Marilyn, and Roxanne at landfall. *Mon. Wea. Rev*., **126**, 1259-1273.

Rotunno, R., and K. A. Emanuel, 1987: An air-sea interaction theory for tropical cyclones. Part II: Evolutionary study using a non-hydrostatic axisymmetric model. *J. Atmos. Sci*, **44,** 542-561.

Tuleya, R.E., M. A. Bender, and Y. Kurihara, 1984: A simulation study of the landfall of tropical cyclones using a movable nested-mesh model. *Mon. Wea. Rev*., **112**, 124-136.

Wang, Y., 1998: On the bogusing of tropical cyclones in numerical models: The influence of vertical structure. *Meteor. Atmos. Phys*., **65**, 153-170.

Wang, Y., 2001: An explicit simulation of tropical cyclones with a triply nested movable mesh primitive equation model: TCM3. Part I: Model description and control experiment. *Mon. Wea. Rev***., 129,** 1370-1394.

Wang, Y., 2007: A multiply nested, movable mesh, fully compressible, nonhydrostatic tropical cyclone model - TCM4: Model description and development of asymmetries without explicit asymmetric forcing. *Meteor. Atmos. Phys*., **97**, 93-116.

Wang, Y., 2008a: Rapid filamentation zone in a numerically simulated tropical cyclone. *J. Atmos. Sci.*, **65**, 1158-1181.

Wang, Y., 2008b, Structure and formation of an annular hurricane simulated in a fully compressible, nonhydrostatic model–TCM4. *J. Atmos. Sci.*, **65**, 1505-1527.

Wang, Y., 2009: How do outer spiral rainbands affect tropical cyclone structure and intensity? *J. Atmos. Sci.*, **66**, 1250-1273.

Wang, Y., and J. Xu, 2009: Energy production, frictional dissipation, and maximum intensity of a numerically simulated tropical cyclone. *J. Atmos. Sci*., (in press).

Wong, M. L. M., and J. C. L. Chan, 2007: Modeling the effects of land-sea roughness contrast on tropical cyclone winds. *J. Atmos. Sci*., **64**, 3249-3264.

Satellite Digital Data and Products for Tropical Cyclone Studies

J. Hawkins[1], C. Velden[2] and T. Nakazawa[3]

[1] Naval Research Laboratory, Monterey, USA

[2] Cooperative Institute for Meteorological Satellite Studies, Madison, USA

[3] Meteorological Research Institute, Tsukuba, Japan

1. Introduction

One of the objectives of the meeting is to describe advances in observations and numerical modeling systems (including data assimilation) that are expected to improve forecast guidance for tropical cyclone landfall. This document will provide an overview of the current satellite digital data and products for tropical cyclone studies, mainly focusing on microwave radiometers and scatterometers, after the last Macao meeting.

2. Tropical Cyclone Intensity Via Geostationary Digital Data

The well-known Dvorak technique (Velden, et al 2006) is based on the principles of satellite imagery cloud pattern recognition with the amount of organization directly correlated to tropical cyclone (TC) intensity. Trained satellite analysts determine the cloud pattern type and relate it to storm development stages. As satellite IR sensors became more sophisticated in the 1970s, Dvorak expanded his techniques to include special enhancements (Dvorak 1984). Recently, scientists collaborated to automate the Dvorak technique, called the Advanced Dvorak Technique (ADT, Velden et al. 1998b; Olander and Velden 2007). The ADT was designed to minimize human judgment in the cloud pattern typing and rules application stages. This algorithm now operates on both GEO and LEO satellite IR imagery, and is competitive with subjective applications. The ADT is now operational at NOAA/NWS and other global TC centers use the ADT in their analysis procedures.

ADT values have been validated, modified and tested with aircraft reconnaissance (recon) measurements of minimum sea level pressure (MSLP) and maximum sustained winds (max winds) for Atlantic-basin TCs. However, no recon data sets exist to facilitate a similar effort using the current suite of GEO/LEO IR imagers in the western Pacific.

3. Low Earth Orbiting (LEO) Data

LEO data provides a suite of sensors with spectral and spatial capabilities not found on GEO platforms. Multi-channel vis/IR, microwave imagers/sounders and radars use different parts of the electromagnetic spectrum to extract environmental measurements and derived parameters. Each sensor has inherent advantages and disadvantages that will be summarized below to ensure all participants comprehend their capabilities. The operational National Oceanic and Atmospheric Administration's (NOAA) Advanced Very High Resolution Radiometer (AVHRR) and the Defense Meteorological Satellite Program's (DMSP) Operational Linescan System (OLS) are the two operational sensor series, each with multiple satellites currently in operation. Research grade vis/IR imagers augment the operational sensors via the NASA Moderate Resolution Imaging

Spectroradiometers (MODIS) and the Sea-viewing Wide Field-of-view Sensor (SeaWiFS). The two MODIS sensors (Earth Observation System [EOS] Aqua and Terra) and SeaWiFS provide enhanced spatial and spectral sensitivity in comparison to AVHRR/OLS data. Here we show the MODIS and scatterometers, due to the page limitation.

3.1 MODIS

The NASA MODIS (Moderate Resolution Imaging Spectroradiometer) sensor is a key instrument aboard the Terra (EOS AM) and Aqua (EOS PM) satellites. Terra's orbit is keyed to ascending overpasses at ~1030 local, while Aqua is 2.5 hours later at ~1300 local. Both MODIS sensors view the entire Earth's surface every 1 to 2 days, acquiring data in 36 spectral bands. MODIS has the benefit of viewing TCs with its 250 m visible channel, sometimes catching spectacular imagery of cloud-free eyes as illustrated in Fig. 1 for typhoon Man-yi. Eyewall mesovortices have been captured on multiple TCs, providing dramatic information for dynamical simulations/studies on inner core structure. For more information on MODIS, please see: http://modis-atmos.gsfc.nasa.gov/.

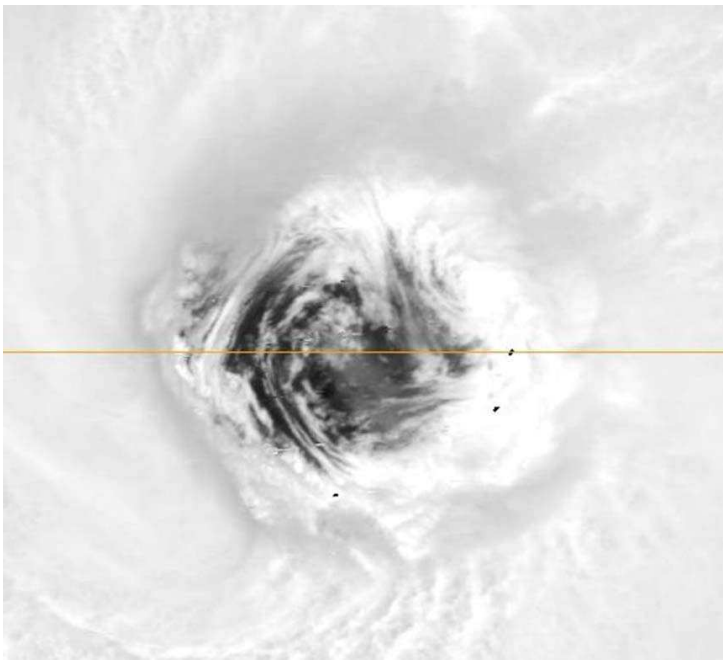

Figure 1. MODIS 250-m visible image of typhoon Man-yi on July 12, 2007 at 0503 UTC while the storm's intensity was ~ 120 kts. MODIS resolution can permit identification of meso-vortices inside cloud free eyewalls.

3.2 Scatterometers: (Quick Scatterometer–QuikSCAT, Advanced Scatterometer (ASCAT))

The SeaWinds instrument on the QuikSCAT satellite is one of the few active microwave radars that measure near-surface oceanic wind vectors (speed and direction). Wind vectors can be derived at multiple resolutions, with accuracy degrading as the resolution increases. Standard 50 and 25 km wind vectors are operationally available from NOAA/Navy and 12.5 and 2.5 km products are experimental via NOAA and Brigham Young University (BYU, Dr. Long). QuikSCAT operates at 13.4 GHz (Ku-band) and has a large 1,800-km swath compared to the 500 km ERS-1/2 scatterometers and the 1100 km MetOp Advanced

Scatterometer (ASCAT) swath, making approximately 400,000 measurements and covering 90% of Earth's surface/day. Current versions of the retrieval algorithm actually do well in rain conditions, unless viewing at the edge of swath where only one polarization is available. Rain flagged data in genesis cases (<35 knots) are problematic and need to be treated with caution.

For more information on QuikSCAT, NOAA-NESDIS real-time products and the BYU high resolution 2.5 km wind vector data sets, please see: http://winds.jpl.nasa.gov/missions/quikscat/index.cfm http://manati.orbit.nesdis.noaa.gov/quikscat/

http://www.scp.byu.edu/data/Quikscat/HRStorms.html

The MetOp ASCAT sensor has a unique swath configuration, with twin 550 km swaths to each side of nadir, separated by a 672 km "hole" or area of no wind retrievals (Fig. 2 below). A NRL TC web page example highlighting one 550 km swath over TC Kamba in the southern hemisphere is shown in the right hand panel of Fig. 2. Routine 50 km oceanic surface wind vectors are being produced now, but 25 km winds are available in an experimental mode. The near real-time digital data set is provided via collaborative agreements with EUMETSAT and NOAA.

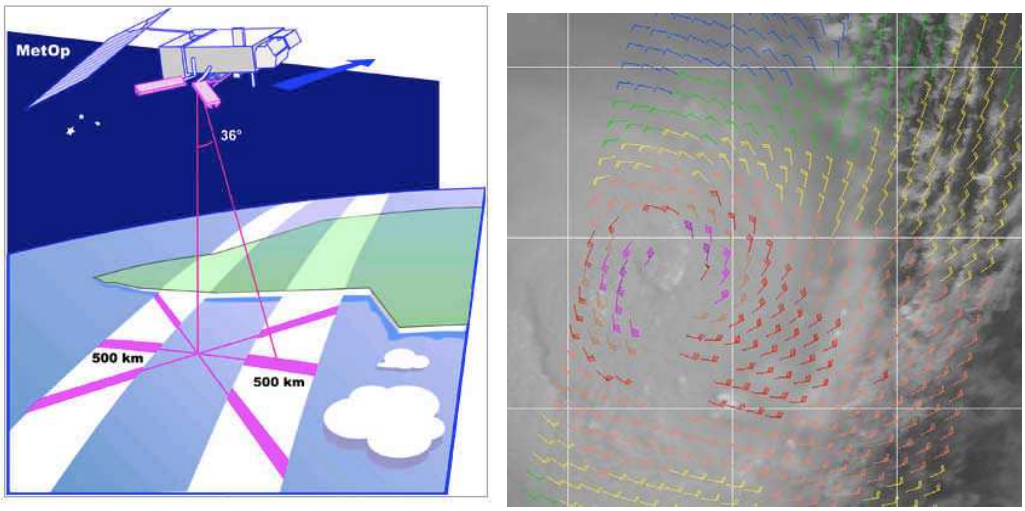

Figure 2. Schematic of the ASCAT twin 550 km swaths with the 672 km non-retrieval zone in the middle (left panel) and an example of ASCAT winds for TC Kamba on March 10, 2008 at 0334 UTC. Wind vectors are color coded by wind speed.

Both QuikSCAT and ASCAT have potential "spatial resolution" issues, since a TC's wind field typically includes high gradient zones that can be a mismatch for large scatterometer footprints. Scatterometers thus can not retrieve the maximum wind values for most TCs, but can represent a "minimum maximum" or the lowest max wind to be used with all other sources (in-situ and remote sensing) in determining the max sustained wind.

4. Passive Microwave Imager/Sounder Data

4.1 Microwave Imagers/Applications:

Passive microwave digital imagery and products have proven to significantly aid the global TC reconnaissance effort as demonstrated by the TC web pages developed by NRL's Marine Meteorology Division

and now operational at FNMOC. These storm-centered, medium-resolution brightness temperature (TB) images display evolving storm rainband and eyewall structure that is critical in monitoring a storm's location, structure and intensity that is not always evident in coincident vis/IR imagery. Subjective Dvorak and Automated Dvorak Technique (ADT) intensity estimates are created for TCs in formative stages, but IR data frequently misses early eyewall structural details due to obstructed views from clouds aloft, while microwave imagers clearly depict eyewall evolutions.

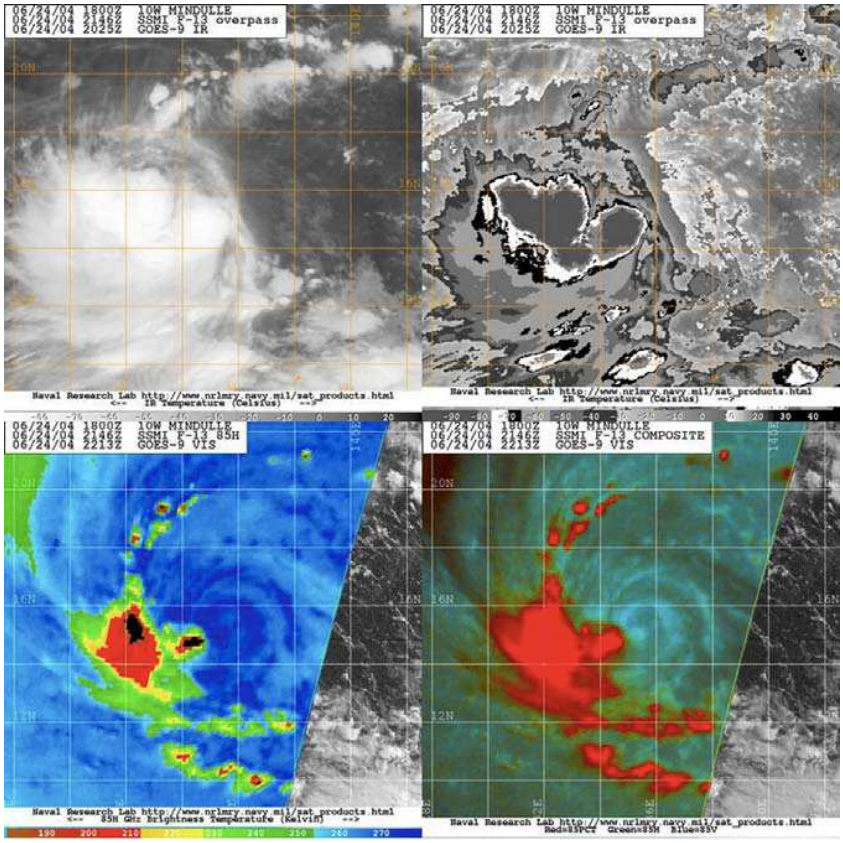

Figure 3. IR and Dvorak IR imagery for typhoon Mindulle on June 24, 2004 at 2025 UTC in the western pacific (top panel) compared with SSM/I microwave products (85 GHz, lower-left) and 85 GHz "color" product (lower-right) from the NRL TC web page, http://www.nrlmry.navy.mil/TC.html.

The ice-scattering channels on most microwave imagers (85-91 GHz) are particularly adept at isolating TC rainband and eyewall structure. These channels react to intense convection by viewing dramatically lowered equivalent blackbody brightness temperatures (TB) caused by scattering from precipitation-size ice hydrometeors (Spencer et. 1989). Fortunately, cirrus canopies, which may cover very large non-raining areas, contain small ice crystals and do not block views of lower-level rain clouds. Figure 3 (lower left panel) depicts one 85 GHz horizontal polarization (H-pol) example and reveals the magnitude of the TB differential between rainbands and the rest of a storm. Satellite analysts can quickly learn how to observe the convective rainband structure of each TC and more precisely locate the storm and infer important intensity information, thus creating a higher fidelity preliminary best track and warning estimates (Hawkins, et al., 2001).

The 85 GHz "color" product highlights cloud liquid water (CLW) and thus details the low-level cloud lines that make up the low-level circulation spiraling into the storm center. The color product is superb in helping detect shear and often reveals reduced convection within storm quadrants or semi-circles in advance of

other wind shear products such as those created using a combination of geostationary winds and numerical weather prediction (NWP) output. Shear can be subtle, but when convection signals are so "stark" in microwave TB values, reduced convective signatures are a tell-tale sign shear is ongoing. In Fig. 3, NE shear has completely removed strong convection from the NE semi-circle, exposing the low-level circulation. All active convection with high cloud tops and frozen hydrometeors are downwind of these strong shear conditions.

4.2 Microwave Satellite Data Sets:

Modest temporal sampling is afforded by the medium size SSM/I swath (1400-km) and slightly large swath SSMIS (1700-km) due to the fact there are currently two (2) SSMIs (F-13 and 15) and two (2) SSMISs (F-16 and 17) flying. F-18 is slated for a Fall 2009 launch. The 85-91 GHz footprints are in the 12 km range and thus are able to sample most TC features, but these sensors can NOT monitor smaller eyewall structures associated with compact and/or small intense systems or western pacific midgets. Some eyewall cycles cannot be adequately monitored via these sensors alone. Additional SSM/I info (http://www.ncdc.noaa.gov/oa/rsad/ssmi/ssmi.html).

DMSP satellites are sun synchronous, thereby imaging the same earth location at the same local time of day (with some drift, thus what is observed one year can be different the next year). There are significant gaps between successive passes, especially in the tropics, limiting storm detection to, at most, twice during a 24-hour period per satellite.

The Tropical Rainfall Measuring Mission (TRMM) microwave imager (TMI) has three times better ice scattering channel imagery due to a combination of its 400 km orbit (versus 850 km for DMSP) satellites and its antenna size. Thus, TMI 85 GHz imagery has 6 km resolution across its 800 km swath (Lee, et al, 2002). This resolution is needed to resolve small TC eyewalls as depicted for hurricane Dean in 2007 (Figure 4). The TMI 85 GHz image (left panel) nicely resolves the main features of an inner and outer eyewall for this average to small size storm. Clear edge of scan details illustrate the fact conical scanners maintain their footprint across the scan swath. The AMSU-B (middle panel) is near the edge of scan and has problems with basically all aspects of storm structure (inner eyewall is ambiguous at best) and the larger outer eyewall is "fuzzy". In contrast the modest resolution SSM/I image (right panel) can monitor both the intense convection surrounding the inner eyewall and the impressive secondary eyewall that is nearly compete.

Note that TRMM is in a 35 deg tropical inclination and thus frequently samples TCs in the 28-38 deg N/S belt and thus makes up in part for its relatively small swath with frequent sampling for some storms. Users should remember that TRMM is NOT sun-synchronous, thus TMI overpasses can occur at anytime during the day/night and often bridge the temporal gaps from the current suite of operational sun synchronous microwave imagers. The TRMM Precipitation Radar (PR) provides a three dimensional rainfall structure in the tropics, including TCs. The PR provides superb 3-D views of moderate to heavy rainfall, adding key vertical structure details not feasible from all other sensors other than CloudSat. Note that the swath of the PR is 200 km with 4 km in horizontal and 500 m vertical resolution. More TRMM info: http://trmm.gsfc.nasa.gov/overview_dir/tmi.html

TMI data is complimented by the Japanese provided Advanced Microwave Scanning Radiometer (AMSR-E) launched onboard the NASA EOS Aqua platform in May 2002 that combines a "huge" 1800 km swath with TMI-like spatial resolution. This research sensor has been a major boon to TC monitoring due to its

resolution and swath attributes and the fact it has a sea surface temperature (SST) capability in addition to an ice scattering channel (89 GHz), 37 GHz and the ability to produce rainrate, total precipitable water and ocean surface wind speeds. When all factors are combined, the AMSR-E is the best microwave imager for TC monitoring within the constellation. More info: http://aqua.nasa.gov/about/instrument_amsr.php

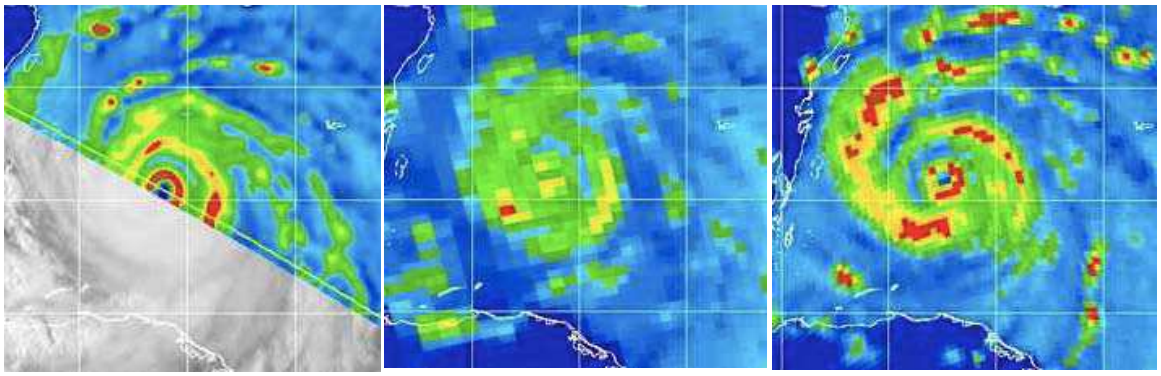

Figure 4. Example of ice scattering channels from TMI, AMSU-B and SSM/I for hurricane Dean on August 20, 2007 at 2140, 2218, and 2356 UTC respectively. All three images have the same scale and projection, with two degree latitude and longitude lines in white and the TMI data is remapped differently (courtesy NRL TC web page).

4.3 Mapping Inner-Core Structure for Intense Tropical Cyclones:

TCs reaching a maximum sustained wind speed greater than or equal to 120 kts often form double or concentric eyewalls as revealed by passive microwave imagery (WMO, 2006a, b, OFCM, 2006, Hawkins, et al, 2006, Velden et al, 2006). These intense TCs can create a single eyewall followed by the formation of a secondary eyewall at a larger radii. The outer eyewall usually constricts the inflow of moisture, mass and momentum into the inner eyewall and the inner eye weakens and/or dies completely. The outer eyewall then becomes the primary eyewall and begins to shrink in size while the storm regains strength. This process can continue several times when favorable environmental conditions exist. Mapping this eyewall replacement cycle (ERC) is vital to understanding inner storm dynamics, short-term intensity trends, modeling simulations and upgrading land falling warnings (see hurricane's Katrina and Rita as prime examples).

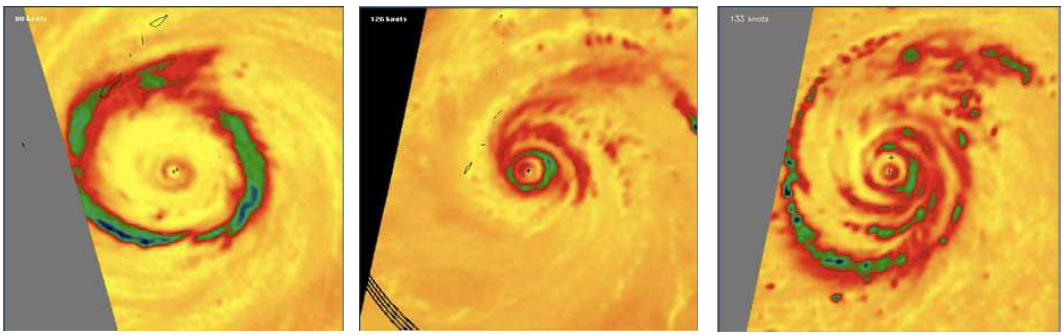

Figure 5. 85 GHz TB imagery for three TCs exhibiting double eyewall (1024x1024 km).

TCs come in all shapes and sizes and this is also true for cases with double eyewalls. Figure 5 displays three TCs, each with very distinct attributes that would impact aircraft flight patterns. Typhoon Winnie (far left) has a very weak and small inner eye and a main eyewall with a diameter of ~ 500 km! Typhoon Paka (center

panel) was a very small intense system whose inner eye was barely captured here while just east of Guam. Typhoon Rosie (right panel) not only has two eyewalls, but is working hard on a third one, which has been verified before via eastern pacific aircraft radar.

Figure 6 depicts how microwave imagery and its ability to discern precipitation and cloud liquid water organization can help monitor each genesis stage system. Typhoon Man-yi in 2001 was sampled by a SSM/I sensor 15 times from late on Aug 1 to mid day Aug. 6. Convective cluster organization is weak in the first three frames, but undergoes a significant upgrade late on 2 Aug as evidenced by the 2234 UTC example. Clear circulation features are in place in all quadrants, hard convection is present near the apparent center, and active banding has formed at a large radii. Within 10 hours, consolidation has occurred, the band has wrapped and contracted significantly and additional convection is near the center. A single small intense eyewall occurs at 0753 UTC on 4 Aug, while it is quickly encircled by an outer eyewall later on the 4th and the inner one slowly decays by the end of 5 Aug such that a single larger diameter eyewall results.

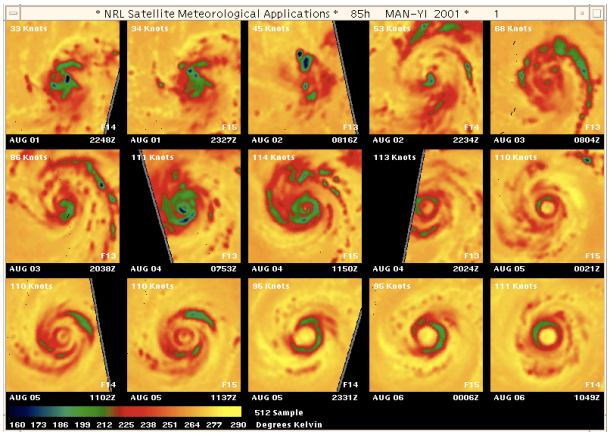

Figure 6. SSM/I 85 GHz H-pol TB readily depict inner storm structure evolution for typhoon Man-yi in 2001. Each image covers 512x512 km per side and are false colored according to the scale in the bottom left. Note that cold convective areas are green/blue in this rendition and ambient conditions are yellow.

4.4 Microwave Sounder Data Sets

Microwave sounder data on the NOAA series of polar orbiters has served multiple functions in the TC monitoring effort; 1) create TB imagery using sounder channels that are similar in frequency to microwave imager channels, 2) utilize temperature sounding capabilities to extract TC intensity estimates, and 3) produce rainfall estimates with multi-channel retrievals. The Advanced Microwave Sounding Unit (AMSU) sensor has been a mainstay on the NOAA operational spacecraft and has channels sensitive to both temperature (AMSU-A1/A2) and moisture (AMSU-B).

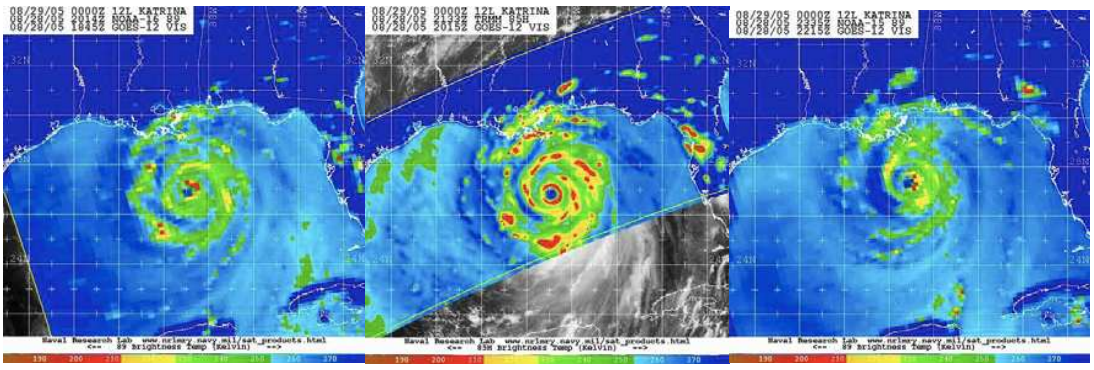

Figure 7 highlights the inherent benefits and weaknesses of AMSU-B TC imagery. The left panel views hurricane Katrina on the left side of the ascending scan which results in blockiness due to the coarse resolution, but the storm is large enough that AMSU-B data is helpful in understanding rainband and even eyewall structure. The right panel AMSU-B overpass is closer to the swath center and shows storm evolution, with decreasing strong convection on the west side as dry air and shear impact the storm. The TMI data in the middle panel clearly depicts an intense single eyewall storm with a very strong secondary band nearing completion to form a concentric eyewall.

Figure 7. Intercomparison of 89 GHz H-pol TB "images" from AMSU-B for hurricane Katrina (left and right most panels) on August 28th within several hours of one another that sandwich a TRMM TMI 85 GHz H-pol image (center panel).

Use of microwave sounder data to estimate TC intensity via the so called "warm core anomaly" method has been around since the 1980s. However, the old microwave sounding unit (MSU) was severely limited by its poor spatial resolution. The AMSU-A temperature sounder has mitigated many of these issues and is now used to demonstrate in near real-time TC intensity retrievals with accuracies approaching RMS errors of 12 MB when validated against Atlantic-based recon measurements.

4.5 Microwave Sounder Intensity Estimates:

The concept of estimating TC structure, intensity, and intensity change using polar-orbiting satellite passive microwave sounder observations, spans over three decades. NOAA series microwave sounder data have been used to map a TC's warm core and via hydrostatic approximations, related to storm intensity. Radiation sensed by oxygen emission in the 55 GHz region is used to derive upper-tropospheric temperatures in the storm core. Several factors including coarse spatial resolution and the changing position of the storm within the instrument swath between observations limited the success of early attempts.

Within the last decade, progress has been made in understanding, treating, and reducing the undesirable effects of instrument-related warm core sampling limitations. This progress has been partially due to advanced microwave sounding instrumentation on the most recent NOAA satellites, starting with NOAA-15's inclusion of the Advanced Microwave Sounding Unit (AMSU-A). The AMSU-A instrument is a cross-track scanning microwave sounder containing 15 channels with frequencies ranging from 23.8 – 89 GHz. Resolution varies from 48-km at nadir to ~ 100-km near the limb. The primary channels used for TC monitoring are the ~55 GHz oxygen band channels 5-8 and the moisture channels 1-4 (AMSU-A) and 16 (AMSU-B). The qualitative relationship between the strength and vertical distribution of the AMSU-A observed warm core and TC intensity is well illustrated by a time series of NOAA-15 AMSU-A observations of Hurricane Floyd from September 8-16, 1999 and near-coincident aircraft reconnaissance sea-level pressure estimates (Figure 8). Floyd's sea-level pressures are at their minimum values (<930 hPa) during periods when the warm core is well defined - particularly when upper-tropospheric temperature anomalies are at their maximum values.

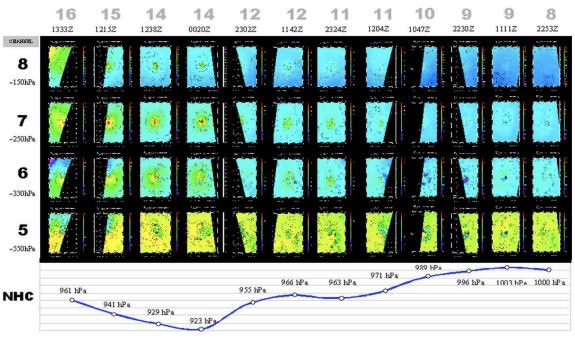

Figure 8. Image-time matrix of AMSU channels 5-8 over a period 8-16 September, 1999 during Atlantic hurricane Floyd. The coincident recon MSLP trace is indicated at the bottom. Floyd's strongest warm core temperature anomalies are illustrated by the yellow/red signatures in channels 6-8 late in the period.

Recent attempts at quantifying this relationship have led to intensity algorithms that are competitive with the IR-based Dvorak technique. These methods rely on the magnitude of the AMSU-A observed warm core (Figure 9). Scientists at the Cooperative Institute for Research in the Atmosphere (CIRA) have developed an algorithm that utilizes the retrieved vertical temperature structure from the multispectral AMSU-A radiances, that are then combined with a number of additional AMSU-A based predictors to derive MSLP and maximum sustained wind (MSW) estimates (Demuth, et al 2006).

Another algorithm developed at the CIMSS uses the raw AMSU radiance anomalies along with corrective measures for AMSU footprint size and offsets to estimate MSLP (Velden, et al, 1989). Limb corrections are applied to the AMSU data to compensate for decreasing TBs as the viewing angle increases from nadir. Eye size is used as a proxy for the warm core dimension, and is derived by the ADT algorithm for "clear eye" cases, or from the radius of maximum winds estimated by operational forecast centers in other cases. Hydrometeor contamination problems decrease effective TBs, requiring a correction using AMSU-A channels 2 and 15. A two-channel difference can determine if TBs are being depressed due to hydrometeor scattering. A correction is then applied to the raw TBs resulting in a new set of regression coefficients (Wacker et al, 2004). Improved performance was validated and transitioned for real-time use in 2003 (Herndon, 2004). Both the CIMSS and CIRA AMSU intensity techniques have NOT been routinely validated in the western since recon flights ceased in 1987, but TCS-08 results have provided a small sampling of intercomparisons.

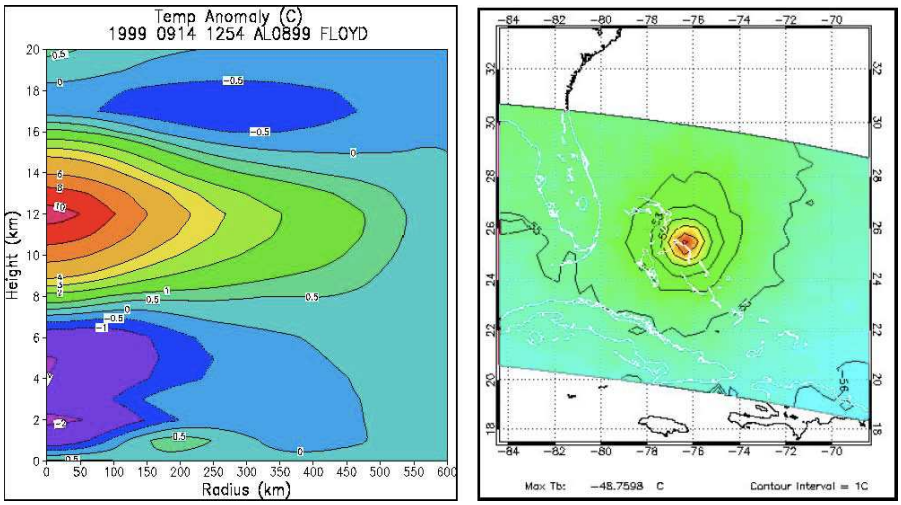

Figure 9. Representation of AMSU-A retrieved vertical temperature anomaly from CIRA (left) and horizontal raw TB anomaly for channel 8 (~150 hPa) from CIMSS (right) for Hurricane Floyd on September 14, 1999.

4.6 CloudSat Cloud Radar:

CloudSat is a NASA Earth System Pathfinder mission that utilizes a millimeter wavelength cloud radar with the goal of advancing our understanding of cloud abundance, distribution, structure and radiative properties. CloudSat's radar is 1000 times more sensitive than existing weather radars and enables it to detect small particles of cloud liquid water (CLW) and ice within clouds that can NOT be seen by ground-based radars. Thus, CloudSat's 4 GHz (3 mm) nadir-viewing radar (2.5x1.4 km spot) and it's 500 m resolution (interpolated to 240 m) provides us with a 1st ever capability to map the 3-D profile of CLW and ice and

compliments the heavy to mid-range precipitation sensing handled by the TRMM PR. CloudSat was purposely placed in the "A"-train orbit that includes nearly coincident measurements by the EOS Aqua spacecraft (MODIS and AMSR-E), the Cloud-Aerosol Lidar and Infrared Pathfinder Satellite Observations (CALIPSO) lidar, Aura and Parasol. Vertical cross sections of radar reflectivity are created at NRL via post processing and a graphic is created that includes the CloudSat overpass on top of coincident GEO, MODIS vis/IR imagery, and AMSR-E 89 GHz TB (Mitrescu et al, 2008). Figure 10 illustrates the wealth of detail CloudSat provided for TC Ileana.

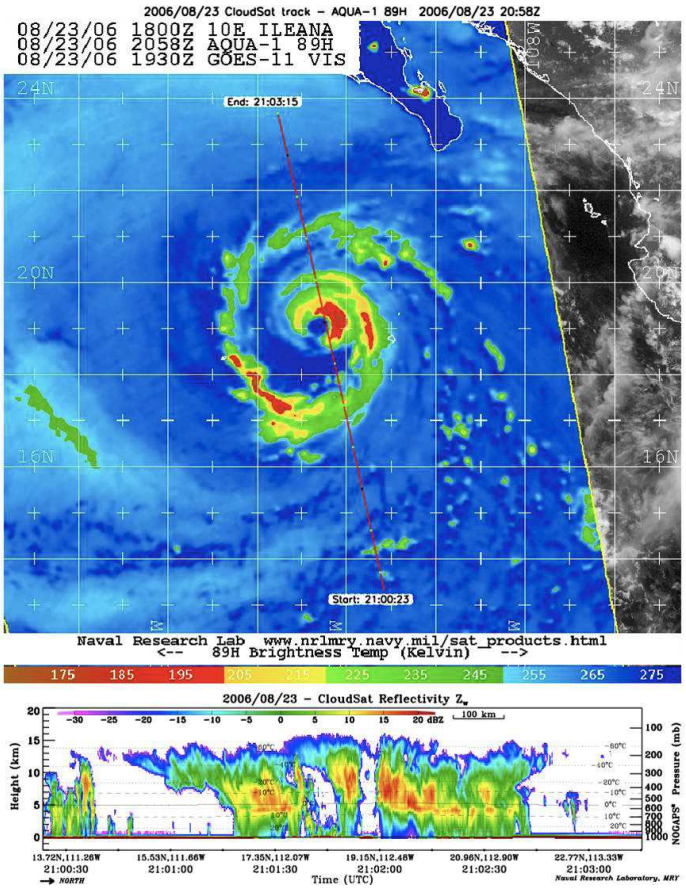

Figure 10. CloudSat cloud radar reflectivity vertical cross section (altitude scale 0-20 km) for transect through hurricane Ileana in the eastern pacific on Aug. 23, 2006 at 2058 UTC. CloudSat ground track is overlain on coincident AMSR-E 89 GHz TB image. The radar overpass goes from south to north and intersects both the rainbands and eyewalls

REFERENCES

Demuth, J.L., M. DeMaria, and J.A. Knaff, 2006: Improvement of advanced microwave sounding unit tropical cyclone intensity and size estimation algorithms. J. Appl. Meteor., 45, 1573-1581.

Gaiser, P.W., K.M. St. Germain, E.M. Twarog, G.A. Poe, W. Purdy, D. Richardson, W. Grossman, W. L. Jones, D. Spencer, G. Golba, M. Mook, J. Cleveland, L. Choy, R.M. Bevilacqua, and P.S. Chang, 2004, "The WindSat space borne polarimetric microwave radiometer: sensor description and early orbit performance",

IEEE Trans. Geosci. Remote Sensing, Vol 42, 11, 2347-2361.

Goerss, J., C. Velden, and J. Hawkins, 1998: The impact of multispectral GOES-8 wind information on Atlantic tropical cyclone track forecasts in 19910. Part II: NOGAPS forecasts. Mon. Wea. Rev., 126, 1219-1227.

Goerss, J., and T. Hogan, 2006: Impact of satellite observations and forecast model improvements on tropical cyclone track forecasts. Preprints, 27th Conf. on Hurricanes and Tropical Meteorology, Monterey, CA,

Hawkins, J. D., M. Helveston, T. F. Lee, F. J. Turk, K. Richardson, C. Sampson, J. Kent and R. Wade, 2006, Tropical cyclone multiple eyewall configurations, 27th AMS Conf. on Hurricanes and Tropical Meteorology, CD-ROM.

Hawkins, J. D., F. J. Turk, T. F. Lee, and K. Richardson, 2008, Observations of tropical cyclones with SSMIS, Special SSMIS issue of IEEE Trans. Geosci. Remote Sensing, April Issue.

Hawkins, J. D., T. F. Lee, K. Richardson, C. Sampson, F. J. Turk, and J. E. Kent, 2001, Satellite multi-sensor tropical cyclone structure monitoring, Bull. Amer. Meteor. Soc., Vol. 82, 4, 567-578.

Herndon, D.C., and C. S. Velden, 2004: Upgrades to the UW CIMSS AMSU-based Tropical Cyclone Intensity Algorithm, 26th AMS Conf. On Hurricanes and Tropical Meteorology.

Kossin, J. P., J. A. Knaff, H. I. Berger, D. C. Herndon, T. A. Cram, C. S. Velden, R. J. Murname, and J. D. Hawkins, 2007, Estimating hurricane wind structure in the absence of aircraft reconnaissance, Weather & Forecasting, Volume 22, Issue 1, 2007, 89-101.

Lee, T. F., F. J. Turk, J. D. Hawkins, and K. A. Richardson, 2002, Interpretation of TRMM TMI images of tropical cyclones, Earth Interactions E-Journal, 6, 3.

Mitrescu, C., S. Miller, J. Hawkins, T. L'Ecuyer, J. Turk, P. Partain, and G. Stephens, 2008: Operational applications of CloudSat data, J. Appl. Meteor., In press.

Mohr, K. I., and E. J. Zipser, 1996, Defining mesoscale convective systems by their 85-GHz ice-scattering signatures, Vol. 77, 6, 1179-1189. June

Negri, A. J., R. F. Adler, and C. D. Kummerow, 1989, False-color display of Special Sensor Microwave/Imager (SSM/I) data, Bull. Amer. Meteor. Soc., Vol. 70, 2, 146-151.

OFCM-NOAA, 2007, Interagency strategic research plan for tropical cyclones: The way ahead, Available via OFCM web site.

Olander, T. and C.S. Velden, 2006: The Advanced Dvorak Technique (ADT) -- Continued development of an objective scheme to estimate TC intensity using geostationary IR satellite imagery. Weather and Forecasting, 22, 287-298.

Olander, T.L. and C.S. Velden, 2007: The Advanced Dvorak Technique: Continued development of an objective scheme to estimate tropical cyclone intensity using geostationary infrared satellite imagery, Weather & Forecasting, 22, 287-298.

Turk, F. J., S. DiMichele, and J. D. Hawkins, 2006, Observations of tropical cyclone structure from WindSat, IEEE Trans. Geosci. Remote Sensing, 44, 3, 645-6510.

Turk, J., S. Miller, J. Hawkins, K. Richardson, 2007: Dynamically updated environmental satellite data in Google Earth: An application to tropical meteorology, AGU Fall Meeting, San Francisco, Dec.

Wacker, R.S., C.S. Velden, and G.W. Petty, 2004: Toward a correction for precipitation scattering effects in satellite-based passive microwave tropical cyclone intensity estimation, 26th AMS Conf. on Hurricanes and Tropical Meteorology.

Wimmers, A. J. and C. S. Velden, 2007: 'MIMIC': A new approach to visualizing satellite microwave imagery of tropical cyclones, Bull. Amer. Meteor. Soc., 88, 1187-1196.

Velden, C., et al 2005: Recent innovations in deriving tropospheric winds from meteorological satellites. Bull. Amer. Meteor. Soc., 86, 205-223.

Velden, C. S., 1989: Observational analysis of North Atlantic tropical cyclones from NOAA Polar-orbiting satellite microwave data. J. Appl. Meteor., 28, 59-70.

Velden, C. S., T. L. Olander and S. Wanzong, 1998a, The Impact of multispectral GOES-8 Wind Information on Atlantic Tropical Cyclone Track Forecasts in 19910. Part I: Dataset Methodology, Description, and Case Studies, *Mon. Wea. RevÄi0., 126, 1202-1218.*

Velden, C. S., T. Olander, and R. M. Zehr, 1998b: Development of an objective scheme to estimate tropical cyclone intensity from digital geostationary satellite imagery. Wea. and Fore., 13, 1720186.

Velden, C., et al 2006: The Dvorak Tropical Cyclone Intensity Estimation Technique: A Satellite-Based Method that has Endured for over 30 Years. Bull. Amer. Meteor. Soc., 87, 1195-1210.

Velden, C., J. Simpson, W. T. Liu, J. Hawkins, K. Brueske, and R. Anthes: Chapter 11: The Burgeoning Role of Weather Satellites, Äi0Hurricane! Coping with Disaster, American Geophysical Union Publication, Robert Simpson, Editor, 2003.

WMO/IWTC Report: Tropical cyclone inner core dynamics, 2006a, 6th International Workshop on Tropical Cyclones, Co-author.

WMO/ITWC Report: Tutorial on the use of satellite data to define tropical cyclone structure, 2006b, 6th International Workshop on Tropical Cyclones, Co-author.

Tropical cyclones landfalling in the mainland, Hainan and Taiwan of China and their interrelations

Ren Fumin[1], Wang Xiaoling[1], Chen Lianshou[2]

[1.] National Climate Center, Beijing 100081, China

[2] Chinese Academy of Meteorological Sciences, CMA, Beijing 100081, China

In consideration of the fact that the position data of landfalling tropical cyclone (TC) in China includes only place names, using the Northwest Pacific TC dataset and landfalling TC dataset during 1951 - 2004 from Shanghai Typhoon Institute of CMA, a computerization scheme for landfalling TC information is developed. The scheme consists of four aspects: 1) approximation of coastal line. As Fig. 1 shown, the approximation of the coastaline of China is consisted of discrete points which are selected from 0.5*0.5 degree grid points and closest to the coastaline. 2) calculation of landfalling position. A landfalling position is defined as a point of intersection of the coastaline and the track of a TC, in which the coastaline here is defined as a line segment between two adjacent discrete points. 3) calculation of other parameters for the landfalling point such as the TC landfalling intensity and the landfalling time. 4) error correction. This includes two steps. First, according to a comparison analysis with observation, errors in number of landfalling times for each landfalling TC case can be corrected. Second, after a comparison analysis, big differences in landfalling time which are equal to or larger than 5 hours can be corrected using true landfalling information by hand, with statistics showing there are 27 TC cases at all.

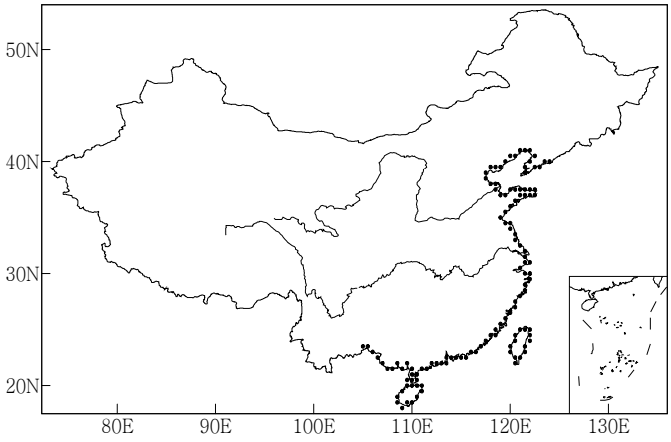

Fig.1 approximation for the coastline of China

Then, assessment of the computerized data shows that the results of landfalling information computerization is satisfactory.For the time difference of landfalling information computerization, Figure 2 shows that during 1951-2004 there are 490 landfalling cases with 593 times of landfalls. Compared with observation, time differences for the 593 times can be divided into 0(same as observed), 1, 2, 3 and 4 hours, with 184, 259, 97, 48 and 5 times, respectively，and the average time difference is 1.04hrs, with corresponding distance difference of

about 26km in landfalling position which is much less than the average positioning difference of about 54.4 km between CMA and JTWC datasets(Lei, 2001).

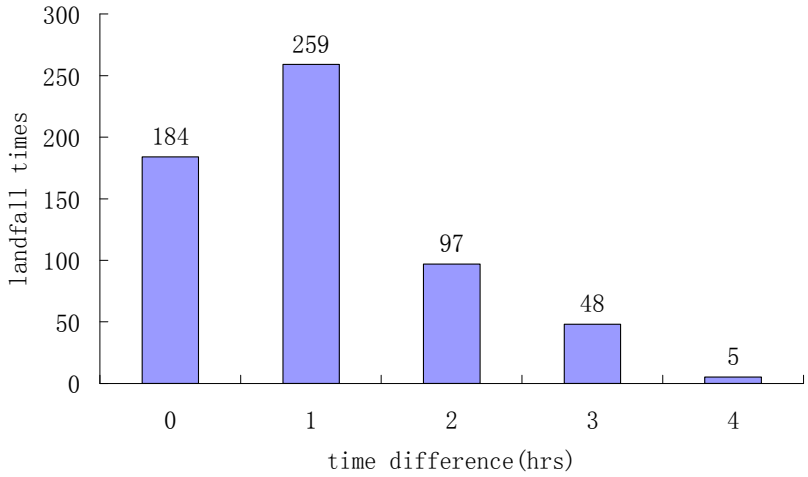

Fig. 2 statistics of the time difference in landfalling information computerization for China during 1951-2004

Based on the above computerized data , climatic characteristics of landfalling TCs in China are investigated with a focus on three sorts of TCs landfalling in the mainland , Hainan and Taiwan and their interrelations. The results include the following six aspects.

Firstly, regions most frequently affected by landfalling TCs were the eastern coast of Hainan, the eastern coast of Taiwan and the coastal region from Fujian Province to Leizhou Peninsula, with the largest number of landfalling TCs being 40 in Wanning of the Hainan Island. Figure 3 shows the frequency distribution of landfalling TC points for China during 1951-2004.

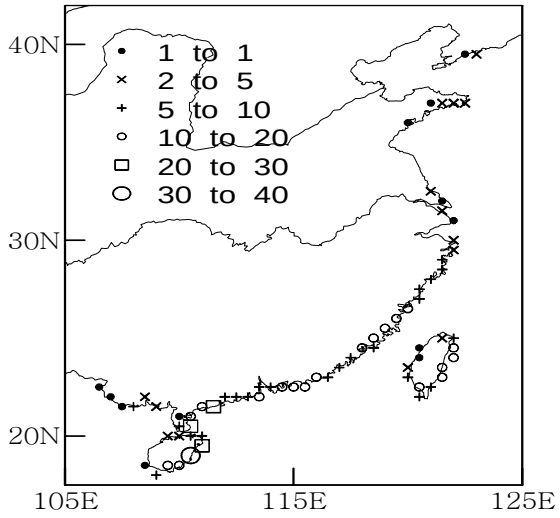

Fig. 3 frequency distribution of landfalling TC points for China during 1951-2004

Secondly, the eastern coast of Taiwan and parts of the coastal Zhejiang Province saw the strong landfalling TCs

and their average intensity reached the typhoon level, with the strongest landfalling TCs up to strong typhoon level in the southernmost of Taiwan. For the extreme cases during 1951-2004, Taiwan, Hainan and the mainland of China experienced the maximum intensity of 78.1 ms^{-1}, 60.0 ms^{-1} and 54.8 ms^{-1} respectively, with the mainland Zhejiang province experienced a more intense landfalling Super Typhoon Samei with a new record landfalling intensity being 60.0 ms^{-1} in 2006.

Thirdly, the TC landfalling season for China was from May to November, especially between July and September, with the highest frequency in August. Frequent intensity levels of landfalling TCs were mainly between tropical depression and typhoon, with the most frequent ones being strong tropical storm and typhoon. For the first-landfall and last-landfall tropical cyclones (Fig. 4), results show that the date of first-landfall showed an obvious interdecadal change and a long-term delaying trend, while the date of last-landfall displayed no long-term trend, which implies that the period of landfall season decreases during the past 54 years. Further analysis reveals that the long-term delaying trend in the date of first-landfall might be because of the southward movement and westward extension of the Northwest Pacific High in May during the period.

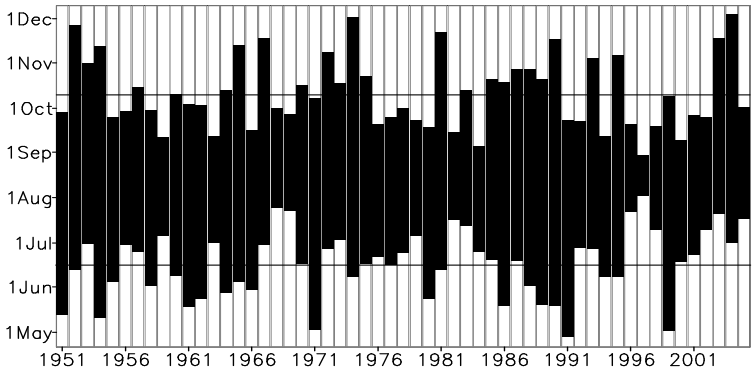

Fig. 4 changes of the dates of first-landfall and last-landfall tropical cyclones for China

Fourthly, although frequencies of landfalling TCs for the whole China, the mainland, Hainan and Taiwan all showed to different extents decreasing trends during the past 54 years, only the decreasing trend of landfalling TCs for Hainan is significant with the significant level being 95%, while no obvious increasing or decreasing trend is found in frequencies of strong landfalling TC (TS) with an intensity level of tropical storm or above (Fig. 5). Fig. 5 also shows that the rates of landfalling TS in the mainland, Hainan and Taiwan are much different, with values being 77.3%, 61.1% and 86.8% repectively.

Fifthly, generally the mainland had the highest frequency of landfalling TCs, the earliest date of the first landfall, the last date of the last landfall, and thus the longest landfalling season, while Taiwan had the lowest frequency of landfalling TCs, the last date of the first landfall, the earliest date of the last landfall, and thus the shortest landfalling season.

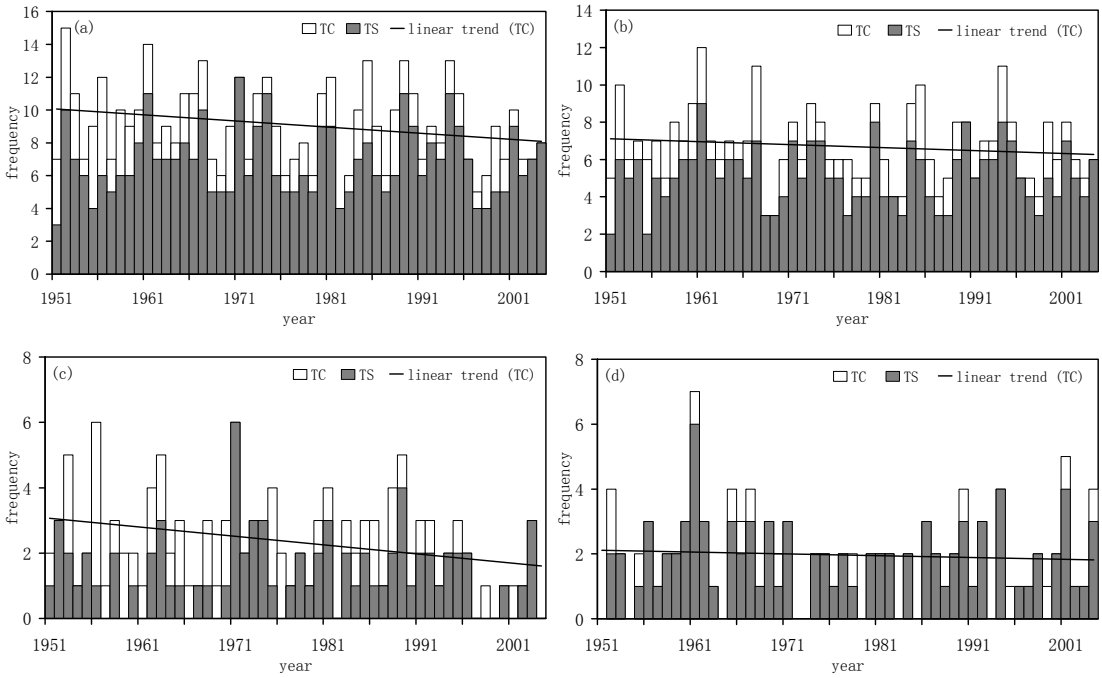

Fig. 5 changes of frequencies of landfalling TCs
(a) the whole China, (b) the mainland of China, (c) Hainan and (d) Taiwan

Table 1 statistics of TC frequencies of different landfalling China ways during 1951-2004★

landfalling frequency / TC track / landfalling ways	mainland		Hainan		Taiwan		total
	↓ Hainan	↓ Taiwan	↓ mainland	↓ Taiwan	↓ mainland	↓ Hainan	
landfall	360(6.6)		126(2.3)		107(1.6)		490(8.8)
first landfall	262		121		107		
landfall in 1 region	258		97		33		388
landfall in 2 regions	4	0	24	0	73	0	101
landfall in 3 regions	1						1

★ values in round brackets are averages for 1971-2000

Finally, viewing from an angle of the way of landfall(Table 1), TCs landfalling in one region were the most frequent (79. 2 %), those in two regions the next (20. 6 %), and only one TC made landfall in three regions. Among the TCs landfalling in two regions, those with a track from Taiwan to the mainland had the highest frequency(73) and weakened most quickly in intensity, those with a track from Hainan to the mainland had the second highest frequency(24) and weakened slowly, and those with a track from the mainland to Hainan had the third largest frequency(4) and weakened quickly, while no TC had a track from mainland to Taiwan, from Hainan to Taiwan or from Taiwan to Hainan.

Refernces

Chen Lianshou, Luo Zhexian and Li Ying. Research advances on tropical cyclone landfall process. Acta Meteorologica Sinica, 2004, 62(5): 541~549

Chen Lianshou and Ding Yihui. An introduction to tropical cyclones in the western North Pacific. Science Press, 1979, 22~26pp

Dong Keqin and Li Zengzhong. A study on the topography effect of Hainan island on landfall typhoons. Chinese Journal of Atmospheric Sciences, 1980, 4(3):288~292

Wu Hui. Climatic features of tropical cyclone in Hainan Island and its relationship with ENSO. Meteorological Monthly, 2005，31(12):61-64

Chen Min, Zheng Yongguang and Tao Zuyu. An analysis on tropical cyclones' climatic feature in the western north Pacific for 1949-1996. Journal of Tropical Meteorology, 1999, 15 (1) :10~16

Yu Hui. Climatic analyses on intensity change of tropical cyclone making landfall on China coast. Extended Abstract Collectoin of the 12th Session of National Workshop on Tropical Cyclones. Beijing: 2002, 33-35

Li Ying, Chen Lianshou and Zhang Shengjun . Statistical characteristics of tropical cyclone making landfalls on China. Journal of Tropical Meteorology, 2004, 20(1):14-23

Yu Hui and Duan Yihong. A statistical analysis on intensity change of tropical cyclone over northwestern Pacific. Acta Meteorologica Sinica, 2002 ,60 (6) :680～687

Lei Xiaotu. The precision analysis of the best positioning on WNP TC. Journal of Tropical Meteorology, 2001, 17(1): 65~70

Landfalling Tropical Cyclones: Forecasting System of the Future

Robert Rogers

U.S. Department of Commerce

National Oceanographic and Atmospheric Administration

Atlantic Oceanographic and Meteorological Laboratory

Hurricane Research Division

Miami, FL 33149

Robert.Rogers@noaa.gov

1. Motivation

The risk to life and property from U.S. landfalling tropical cyclones (TCs) continues to escalate in coastal areas as population continues to increase in this area. A concerted effort is underway to improve forecasts of landfalling TCs through NOAA's Hurricane Forecast Improvement Project (HFIP). The goals of this effort are to improve forecast accuracy (track and intensity forecast improvements of 50% in 10 years and improvements to storm surge impact locations and severity); extend forecast reliability out to 7 days; and quantify, bound, and reduce forecast uncertainty to enable risk management decisions to be made. While success in recent years has been realized for improving track forecasts, much less success has occurred for intensity forecasts (Fig. 1). This remains an ongoing challenge for both the operational and research communities.

2. Research approach for improving forecasts

Progress toward overcoming these challenges requires a multifaceted research approach. This approach involves the use of both improved models and improved observations. Working synergistically, these components can be used to test and develop new theories on TC evolution that will lead to improved understanding and, ultimately, improved forecasts.

Improved models include running deterministic models at higher resolution than is currently the case to better resolve the physical processes important in TC structure and evolution. For example, new global models will need to be run on horizontal grid lengths of < 5 km, and ultimately at 1 km, while regional models will need to be run on grid lengths initially of 1 km, and ultimately on the order of 100's of m. In addition to deterministic runs, an ensemble framework will provide significant value to the forecast. Ensemble members can be generated by varying the initial conditions or the physical parameterizations, and they can provide an indication of the forecast spread (Fig. 2). They can also be used for forecast guidance and for data assimilation. Multiple models can also comprise an ensemble, providing further information for the forecaster.

Improvements in the observations are also a vital component in improving TC forecasts. These improvements include the use of existing as well as planned observing systems in modeling systems through

data assimilation and model diagnostics and evaluation. Observations will be obtained from a variety of existing and new platforms, including aircraft (both manned and unmanned), satellite, and in situ measurements. TC intensity change and formation is a multiscale process, involving physical processes that operate at scales ranging from the environment, vortex, convective, turbulent, and microphysical scales. As such, an observing and model evaluation system is required that functions at all of these scales.

A key element in the synergistic interaction between models and observations is an improved use of observations in the modeling system. This can primarily occur through both data assimilation and model diagnostics and evaluation. Figure 3 shows an example of using real-time airborne Doppler radar observations to generate initial conditions for a 1.5-km mesoscale model using an ensemble Kalman filter (EnKF) approach. A series of flight legs were flown into Hurricane Ike (2008), from which thinned observations (superobs) of radar-derived velocities were obtained. An ensemble of 4.5-km model runs were performed to generate covariance matrices for the ingestion of the superobs that were transmitted from the aircraft in realtime and used to initialize the 1.5-km run. The resulting run showed an improvement in the track forecast, particularly at landfall in Texas (Fig. 4). This technique has the potential to significantly improve the representation of TC's in numerical models and the subsequent forecasts of both track and intensity.

Another example of the use of observations in modeling systems is through model evaluation. Robust techniques for evaluating model performance are critical to assess the ability of a model to accurately depict the physical processes occurring in the TC. They can be used to test aspects of the model configuration such as variable physical parameterizations and variable horizontal resolution. As mentioned previously, a multiscale approach to model evaluation is a key component of this process. Figures 5 and 6 show examples of two methods for evaluating numerical models using observations at the convective and the turbulent scales. The data used in the comparisons of convective-scale structures are the airborne Doppler radar-derived fields of horizontal and vertical velocity and vorticity (Fig. 5), while the data used for the evaluation of turbulent-scale structures shown in Fig. 6 are dropsondes released from ~ 2 km altitude and turbulence probe measurements collected from the aircraft flying between 0.1 and 0.4 km altitude. The improvement in the depiction of strong updrafts and vorticity cores as a function of horizontal resolution is evident in Fig. 5, while the impact of varying assumed ocean mixed layer depth on the mean boundary-layer profiles and sensible heat fluxes are evident in Fig. 6.

3. Summary

In summary, the forecasting system of the future will require both improved models as well as improved observations. Global and regional models, run in both deterministic and probabilistic mode, will be required. Multiscale observations, both in situ and remotely-sensed, and both manned and unmanned, will be required. Crucially, though, these components will have to work together to fully realize the improvements required in today's TC forecasting environment. This interaction between observations and models will involve both advanced data assimilation techniques such as EnKF as well as advanced multiscale diagnostic evaluations. With this interaction, new and existing theories of TC evolution will be tested, leading to a better understanding and prediction of tropical cyclones.

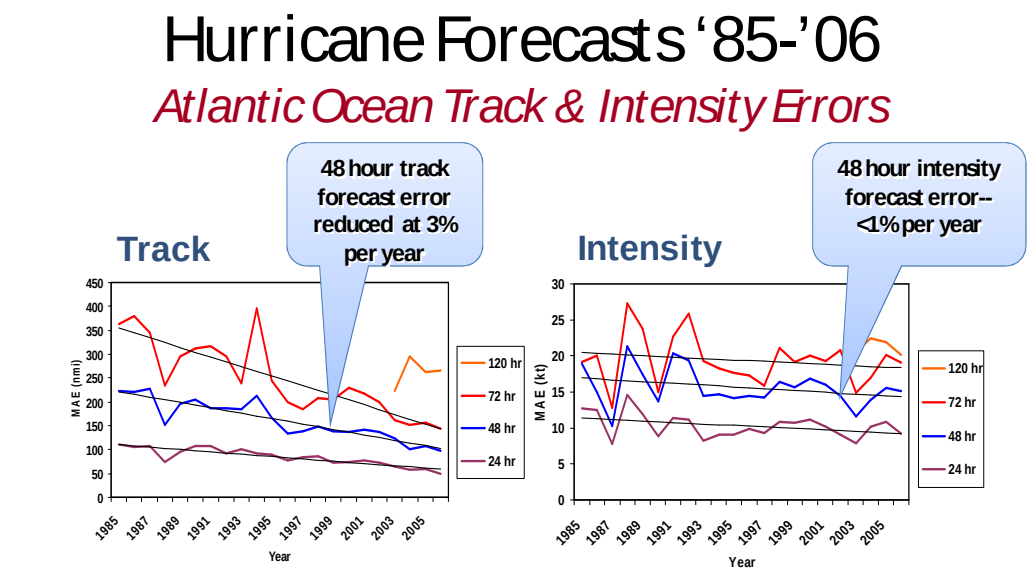

(a) (b)

Figure 1. Trends in operational (NHC) forecasting errors for tropical cyclone track and intensity at various lead times for the 1985-2006 time period.

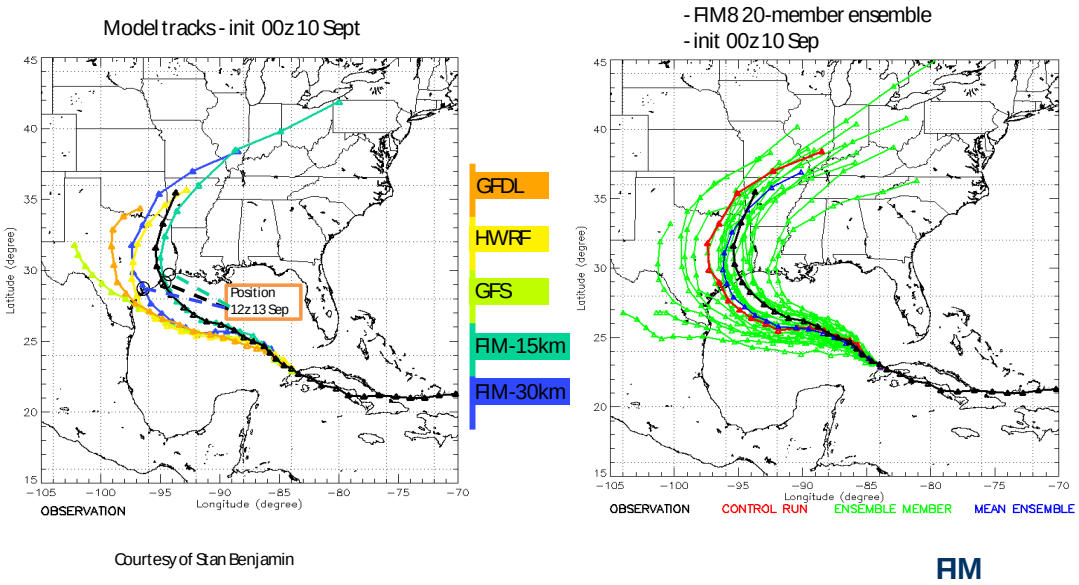

(a) (b)

Figure 2. (a) Forecast tracks for Hurricane Ike (2008) for various models initialized at 00 UTC 10 September 2008. (b) Forecast tracks for Hurricane Ike (2008) for individual ensemble members (green), a deterministic control run (red), the ensemble mean (blue) and the observed track (black) for the NOAA/ESRL FIM model initialized at 00 UTC 10 September 2008.

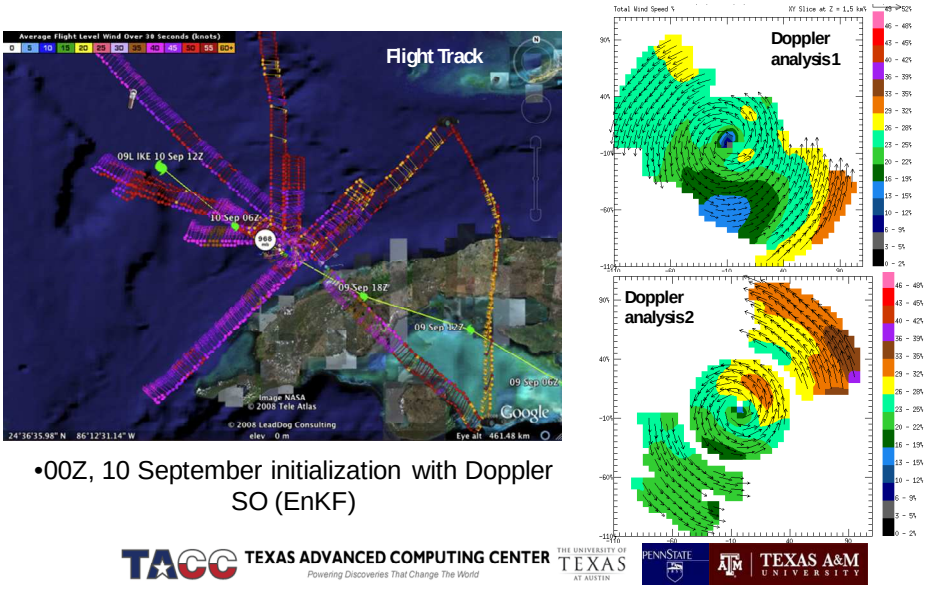

Figure 3. Flight track and flight-level winds (left panel, barbs, kt) for NOAA P-3 mission into Hurricane Ike on 10 September 2008. Right panels show wind speed (shading, m/s) and direction at 1.5 km altitude for two radar legs.

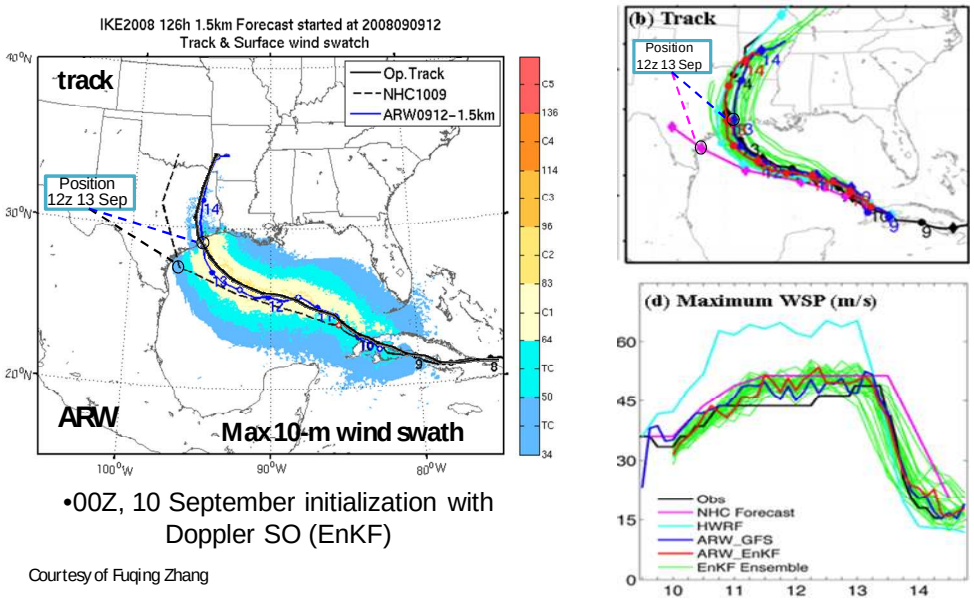

Figure 4. Left panel shows plot of observed (black), NHC forecast (dashed), and forecast track produced by 1.5-km WRF-ARW model initialized using airborne Doppler data shown in Fig. 3 for Hurricane Ike (2008). Shading shows wind swath (kt) from WRF run. Right panel shows comparisons of NHC forecast, individual ensemble members used in the EnKF, and the forecasts from the 1.5-km ARW run using the EnKF for the track (top right) and peak surface winds (bottom right) for Ike.

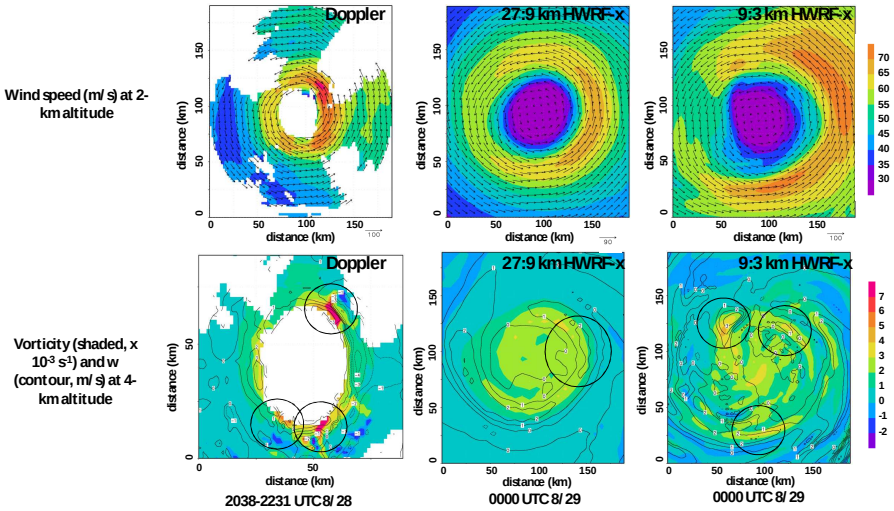

Figure 5. A comparison of wind speeds and directions (top row; m/s) at 2-km altitude for Hurricane Katrina (2005) from airborne Doppler data (top left) and 27-9 and 9-3 km runs of the HWRF-x regional model (top center and right). Bottom row shows vorticity (shaded, x 10^{-3} s^{-1}) and vertical motion (contour, m/s) at 4-km altitude from Doppler data and 27-9 and 9-3 km HWRF-x runs. Circled areas in bottom row denote areas of high vorticity and upward motion.

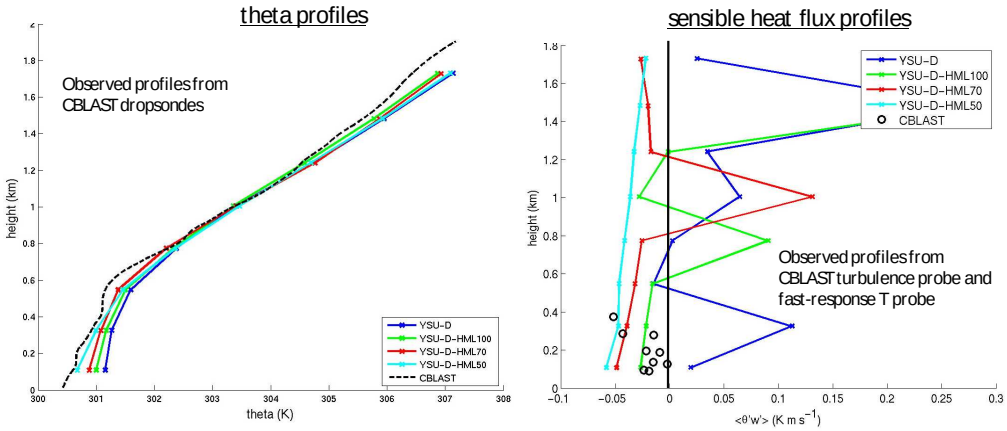

(a) (b)

Figure 6. (a) Profiles of equivalent potential temperature from dropsondes (denoted by "CBLAST") and different configurations of the YSU boundary layer scheme in WRF-ARW simulations from Hurricane Isabel (2003). (b) Profiles of sensible heat flux derived from CBLAST turbulence probe (black circles) and different configurations of YSU boundary layer scheme for Isabel simulations.

Practices in Public Weather Service
Typhoon Early Warnings and Disaster Mitigation

Tang Xu and Jonathan Wakrat

Shanghai Meteorological Bureau

1. Philosophy of Shanghai PWS

Accurate and timely forecasting have always been the standards by which the weather services has been judged. Great efforts have been made over the last century to that effect. Increasingly powerful technology, more refined methodology and steady advances in oceanic and atmospheric science and predictive modeling have advanced the accuracy of such forecasting to a degree that would have been difficult to imagine a generation ago. Globalization and International cooperation in the global meteorological community have also helped improve the international standard of meteorological forecasting. Despite such steady advances, it has become apparent in recent years that practices in public weather service delivery have not always kept pace with refinements in meteorological science.

In recent years the Shanghai Meteorological Bureau has taken steps to upgrade the service delivery. The first step in the process is to identify problem areas requiring improvement. The Met service is essentially an organization dominated by scientists, who work to make sense of large volumes of data. As a result of this unique scientific focus a gap developed between the weather services and the users of it's data. This disconnect was evident in aspects of service delivery such as a lack of user specific quantitative data which was often delivered in entirely too general or "raw" form and a lack of standard operational procedures (SOP's) to deliver the service, inadequate coordination with relevant departments, unsatisfactory interaction with end users, and so on.

Besides the standard of forecasting accuracy, the success of Public Weather Service (PWS) should be judged by its level of service delivery. Essentially we need to introduce another standard of success, namely, how well we can benefit society by providing the right information to the right people at the right time and place, thereby mitigating adverse effects brought upon by the weather.

One of the biggest challenges PWS have faced is translating the technical terms and figures into actionable language that can be used effectively by the partners and the user community, then delivering the right information to the right stakeholders at the right time.

The effort to overhaul the service delivery component of PWS provided several key lessons:

- Real and effective cooperation with users of weather related information is critical to better service delivery.
- Understanding the needs of users of users and tailoring products to those specific needs helps bridge the gap between users and provider.
- The development of mutual standard operating procedures for multi-agency cooperation and coordination is a very effective technique for mitigating the effects of severe weather
- Partnership between NMHSs and agencies plays an important role in the process and should be enhanced.
- Communication needs to be strengthened through a variety of means

- The creation of service delivery professionals and a service delivery platform separate from the more scientific forecasting platform is an effective technique to upgrade the PWS
- Feedback from users is important and a system for generating and acting upon such inputs needs to be put into operation.

2. PWS Practices in Shanghai: A brief overview

The Typhoon warning hazard and related prevention and mitigation is only one component of a much larger Operations system that recently began operations at the SMB. The response to a tropical cyclone flows through the same integrated Multi-Hazard Early Warning System Operations Centre as other weather related events. The Operations Centre uses inputs from the forecasting platform, which includes the Regional Typhoon Warning centre. The two platforms work in tandem, providing not only more accurate forecasts, but better service delivery as well.

At the SMB, a MHEWS Operations center and Standard Operating Procedures (SOPs) have been established by creating a new position, Chief Service Officer (CSO), to ensure better service delivery. The CSO is now the core of the multi-agency procedure and the PWS Platform. All future weather related emergencies, including those from tropical cyclones will flow through this Operation Centre., which is a vital supporting facility of the Shanghai Municipal Government Emergency Response System.

In 2006，the Chief Service Officer centered service delivery procedure was established at the SMB. The CSO is the coordinator/advisor in charge of establishing service delivery and organizing internally. As a service delivery professional, separate from the Forecasting Platform, the CSO is responsible for dealing with daily comprehensive data flows, collecting the detail requirements of the agencies and providing the specialized information to the right people at dozens of agencies across the mega-city.

The platform is a fast, efficient, and unified meteorological service delivery operation system supported by the Forecasting Platform. The functions of the platform include service delivery, decision-making support, multi-agency coordination, disasters information collecting, interaction with users, Etc.

A key component of the platform is public dissemination of weather warning information. The PWS platform dissemination mechanism includes the multi agency response component, coordinated by the CSO.

A key test of the upgraded PWS will be at the EXPO 2010 Shanghai, where the SMB will be open a dedicated Expo Weather office in the WMO/CMA Meteorological themed pavilion. An onsite observatory is being built on the bank of the Huangpu River to provide better and more accurate weather forecasting as well as early warning information to participants, visitors, and EXPO park management. The Expo Weather Office will be supported by the Shanghai MHEWS and comes equipped with broadcast and special dissemination facilities.

3. PWS Case Study: Typhoon Matsa

Typhoon Matsa, (麥莎) was one of eight Pacific tropical cyclones to make landfall on China during 2005 striking the neighbouring Chinese province of Zhejiang on August 5. The typhoon dropped heavy precipitation on China, and in combination with strong winds destroyed about 59,000 houses and damaged more than 20,000 km² of croplands. Throughout the country, Matsa caused 25 direct deaths and 18 billion CNY ($2.23 billion 2005 USD) in damage.

In shanghai winds reached 147 km/h, the highest wind gust ever recorded in the city. The storm produced heavy amounts of rainfall, causing record-breaking river flooding and 84 city streets; in some

locations insufficient water drainage left a total of 20,000 homes and apartments flooded, The flooding also closed the city subway system for a few hours. Strong winds downed 2,700 trees and 400 power lines in the city. Throughout the city an estimated 15,000 houses were destroyed. In addition, four people were electrocuted as a result of the flooding caused by Matsa. In Shanghai alone, damage totaled $1.33 billion CNY ($164.5 million USD) A total of seven people died in the city.

Although severe, the effect of Typhoon Matsa could have been much worse if enhanced disaster prevention and mitigation actions had not been taken. Cooperation among regional weather bureaus provided enhanced accuracy. Wind speed and storm duration were accurate while rainfall was slightly short of the prediction. The SMB delivered its forecast with 24 hour warning, immediately triggering a chain of previously established coordinated multi-agency responses. During the storm, updated "nowcasts" and medium term forecasts of storm intensity, direction and wind speeds were delivered every two hours.

In terms of Typhoon warning dissemination there was coordination with local television, radio, web and print news services.

In addition timely typhoon early warning information and typhoon forecast and warning was disseminated through mobile phone messages, (420,000 at a time with daily totals over 1,000,000) and 8000 electronic public screens enabling unprecedented penetration to every area of the cities including the most vulnerable groups. The SMB's dedicated phone lines also received 100,000 inquiries.

Deputy mayor Yangxiong signed the 'Shanghai typhoon emergency alarm' in the early hours of August sixth the multi-agency response mechanism began taking joint-actions in response to the threat. These city wide DPM actions were supported at the decision making level by the MHEWS Operations Team and the entire PWS platform. In shanghai alone 100,000 people were mobilized at the community level. In the neighboring province of Zhejiang hundreds of thousands of people were evacuated from the coast. Response teams from various departments were mobilized in anticipation of landfall.

The weather service provided continual monitoring of the weather and received reports of inundations and disasters through its telephone service. SMB Vehicles were dispatched to investigate and the information was passed to the Municipal Emergency Management center, of which the PWS is a supporting facility.

Landfall Typhoon Forecast Evaluation and Assessment Demonstration Project (LtfeaDP)

Shanghai Meteorological Bureau

East China Regional Meteorological Center

The World Expo 2010 will be held in Shanghai from May to October, 2010, when it is just the major raining season of Shanghai and East China. During this period, climatologically, about five typhoons make landfall in the coastal regions of East China. It is almost certain that those landfall typhoons will have tremendous impact on the exhibition and related activities.

To provide a better service of landfall typhoon forecast for the Expo 2010, and to enhance the ability of forecasters and decision-makers to effectively use products of the most advanced typhoon forecasting techniques in the world, a TMRP(Tropical Meteorology Research Program)/WMO demonstration project: "Landfall Typhoon Forecast Evaluation and Assessment Demonstration Project (LtfeaDP)" is proposed.

Unlike on-going WMO forecast demonstration projects "Shanghai MHEWS" which is focused on the coordination of multi-agency's response to weather- or climate-related hazards, and "WENS" which is concentrated on providing a better service of nowcasting (0-6h) of high impact weather, the LtfeaDP will place the emphasis on evaluation and assessment of the performance of longer-term (0-72h) landfall typhoon forecasts. Specifically, based on the TIGGE database, the LtfeaDP will develop techniques to evaluate accuracy of forecast for landfall location and time, gale distribution, and torrential rain, calculate forecast errors of various systems and make a comprehensive analysis of their performance, evaluate the reliability of the forecasts; and finally produce probabilistic predictions and assessment of their social and economic impacts, which is absent or lacking in operational forecast as well as in "Shanghai MHEWS" and "WENS".

Through close international collaborations, the LtfeaDP will demonstrate and quantify the benefits of end-to-end forecast and service of landfall typhoon which are made by using the latest science and technology. The LtfeaDP, as a means of forecasting experience exchange，a platform for application of typhoon forecast technology, and a bridge to connect forecast and public service, is expected to promote the implementation of the most advanced landfall forecast techniques in East China and to largely benefit WMO members as well.

Key words：WMO Demonstration Project，Landfall Typhoon，Evaluation and Assessment，EXPO 2010

Tropical Cyclone Structure (TCS10) and Other 2010 Experiments

Russell L. Elsberry
Department of Meteorology
Naval Postgraduate School
Monterey, California

1. Introduction

Several field experiments to be conducted in 2010 may be directly or indirectly related to understanding potential tropical cyclone-related threats to the Shanghai 2010 World Expo. The directly related field experiment is the Tropical Cyclone Structure (TCS10) experiment, which is an extension of the TCS08 field experiment. The TCS10 is in conjunction with a major United States and Taiwan oceanographic experiment in the western North Pacific called Interacting Typhoon and Ocean Program (ITOP). Another major combined field experiment will be held in the Atlantic during 2010. Whereas the actual field experiment will be too late in 2010, the "dry run" during 2009 in preparation for this experiment may provide new insights that would assist in forecasting and warnings for the Shanghai 2010 Expo.

As indicated above, the TCS10 is an extension of the TCS08 in the sense that two U. S. Air Force WC 130J (so-called Hurricane Hunters) aircraft will again be stationed in the western North Pacific during (tentative dates) 20 August to 20 October 2010. Although their primary mission will be in support of the ITOP objectives, they will be making valuable observations in tropical storms and typhoons that will be available in real-time to support analyses and forecasts by the Shanghai Meteorological Bureau and other forecast/warning centers in Asia and the western North Pacific. A review and some early results from TCS08 will be presented in section 2 to provide an indication of the objectives of TCS10. In section 3, a brief introduction to the 2010 Atlantic experiments will be given to indicate related tropical cyclone research initiatives.

2. Tropical Cyclone Structure (TCS08)

The TCS08 was carried out in conjunction with the THORPEX Pacific Asian Regional Campaign (T-PARC). This multi-nation field campaign included other national programs:

- Typhoon Hunter-2008 (TH-08) [Japan];
- Predictability and Observation Experiment (PROBEX) [South Korea];
- Tibetan Plateau Experiment [China];
- The South China Sea Experiment [China];
- Dropsonde Observations for Typhoon Surveillance near the Taiwan Region (DOTSTAR) [Taiwan]

The combined TCS08.T-PARC addressed the shorter-range dynamics and forecast skill of high-impact weather events in one region (Eastern Asian and the western North Pacific) and the downstream impact on the medium-range dynamics and forecast skill of another region (in particular, the eastern North Pacific and North America). Although many significant weather events occur over eastern Asia and the western North Pacific, the focus of TCS08/T-PARC was on various aspects of typhoon activity, which include formation, intensification, structure change, motion, and extratropical transition.

The combination of observational platforms and collaborative experiments is set such that the experimental design for TCS08/T-PARC addressed three primary components: (1) A tropical measurement strategy is designed to examine circulations of the tropical western North Pacific monsoon environment as they relate to tropical cyclone formation, tropical cyclone intensification, and tropical cyclone structure change. (2) The measurement strategy for the extratropical transition (ET) and downstream impacts was based on the poleward movement of a decaying tropical cyclone and the resulting intense cyclogenesis that results from its interaction with the midlatitude circulation. (3) The third measurement strategy focused on identification of regions in which extra observations may reduce numerical forecast error growth. The T-PARC targeted observations were aimed primarily at reducing errors associated with forecasts of tropical cyclone track over the western North Pacific. This component of T-PARC will be described by Professor Chien-Chieh Wu.

a. Field program summary

During the field program period of 1 August – 4 October 2008, four typhoon, four tropical storms, and four tropical depressions occurred over the western North Pacific. In addition to these circulations for which official forecasts were issued by the Regional Specialized Meteorological Center (RSMC, Tokyo), a separate set of 51 tropical circulation systems were identified by the T-PARC/TCS08 research team. These systems were defined as tropical cloud clusters, low-level waves, or subtropical circulations of interest to the project.

During the period, 500 aircraft mission hours were flown during a total of 76 missions. The missions were flown into 4 typhoons, one tropical depression, and 5 tropical cloud clusters. Overall, 72% of the flight missions were flown into the four typhoons. A significant number of flight hours were dedicated to each objective listed above. The final quality-controlled T-PARC data set is nearly complete. Observation data that had never before been obtained in the environment of the western North Pacific include dropwindsondes from 13 driftsondes, the ELectra DOppler RAdar (ELDORA) radar, Twin Otter Doppler Wind Lidar (TWODL) on the NRL P-3, the Stepped Frequency Microwave Radiometer (SFMR) on the USAF 53rd Weather Squadron WC-130J, the DLR Doppler Wind Lidar, and the DLR Differential Absorption Lidar (DIAL). In addition to the *in situ* observations, comprehensive sets of remotely-sensed observations have been archived. Finally, a complete set of operational and experimental deterministic and ensemble numerical analyses and forecasts have been archived from a variety of operational forecast centers.

b. Early stage tropical cyclone objectives

An early TCS08 result is the validation of two subjective and four objective satellite-based tropical cyclone estimation methods with in situ aircraft observations in four typhoons (provided by C. Velden): (i) Significant spread was found in the subjective estimates among the three operational agencies and five independent analysts. (ii) Objective techniques based on microwave and on infrared imagery are very competitive with the subjective techniques. (iii) The satellite consensus (SATCON) improves the accuracy over all methods.

A unique set of oceanographic observations was obtained in TCS-08 from two deployments of drifting buoys in advance of two typhoons—including the first-ever deployment in advance of a Category 5 tropical cyclone. Since the second typhoon followed the first typhoon within a week, the second deployment resulted in about 20 drifters to observe the ocean response. Several research groups are studying this data set as part of the planning for a large ocean response to typhoons field experiment during 2010 called ITOP. The follow-on TCS08 field experiment called TCS10 will also be conducted in

conjunction with the ITOP.

As one example of several research modeling efforts related to the TCS08/T-PARC experiment, the NRL—Monterey regional model COAMPS-TC has been revised and improved based on the TCS08/T-PARC cases. An improved vortex initialization technique, plus revisions in the shallow convection, microphysics, and boundary layer representations, have led to a new COAMPS-TC version that is in beta test for western North Pacific implementation during 2009, and participation in the Hurricane Forecast Improvement Program in the Atlantic.

The performance of the ECMWF, UKMO, GFS, and NOGAPS models in predicting tropical cyclone formation has been evaluated (i) An experienced analyst is able to define individual model characteristics and tendencies related to the pre-tropical cyclone seedling to tropical cyclone transition. (ii) When all four global model forecasts are in agreement as to position and evolution, high confidence can be given to the prediction scenario with few false alarms. (iii) The consensus technique was most successful for those seedlings that will later become tropical storms or typhoons, but was not successful for weaker systems.

For the first-time, the WC-130J deployed from 31,000 feet dropwindsondes and air-deployed expendable bathythermographs, and still could make surface wind estimates from the SFMR. This set of aircraft observations in combination with geostationary and polar-orbiting satellite observations will be used by many research teams for years.

c. Extratropical transition and downstream impacts

During the field phase of T-PARC, several tropical disturbances moved poleward to undergo a transition into the midlatitudes. The character of these disturbances included a weak circulation associated with widespread deep convection, a midget tropical cyclone, a typhoon, and a super typhoon. Corresponding to the variety of tropical disturbances was a wide range of forecast and actual structural changes and downstream developments, which provide a broad spectrum of forcing and downstream impacts to be investigated.

A three-aircraft mission was conducted into what was thought to be a weakening TY Sinlaku. However, during the mission convection increased rapidly and the ELDORA observations identify some of the deepest convection observed during the T-PARC/TCS-08 period. Sinlaku re-intensified to a typhoon and then began ET 24 h later. This period represents a source of a large amount of variability in deterministic and ensemble forecast fields from a variety of operational forecast centers. The measurement strategy associated with the case of TY Sinlaku was defined to observe the important physical mechanisms associated with the ET process that influences predictability downstream. TY Jangmi also provided a source of reduced predictability, but this was related to modification of the midlatitude jet stream due to outflow from Jangmi rather than increased convection and downstream ridge building.

During the field phase, a variety of poleward-moving tropical circulation were observed by a wide range of instruments designed to observe the complex physical processes associated with the poleward movement of a tropical cyclone. These observations will provide a basis for examining the impact of the tropical circulations on the region of the midlatitudes into which they are moving and their downstream impacts through a variety of physical mechanisms.

3. Atlantic field experiments during 2010

Recent years have seen several field campaigns aimed at understanding the dynamics of tropical cyclone formation. These include the NASA Tropical Cloud Systems and Processes (TCSP) in 2005, the NASA AMMA project in 2006, serendipitous observations of the early development of Hurricane Ophelia in RAINEX, and occasionally from reconnaissance aircraft. This collection of studies has sampled only pieces

of a large and complex scientific puzzle. The U. S. National Science Foundation (NSF) PREDICT (PRE-Depression Investigation of Cloud-systems in the Tropics) 2010 experiment is focused on the formation of a tropical depression, which is a necessary meteorological precursor that results, in most cases, in the subsequent formation of a tropical cyclone.

The PREDICT 2010 is a new effort to study formation in the Atlantic for several reasons. (1) The problem of tropical depression formation remains unanswered and is one of the great remaining mysteries of the tropical atmosphere. Perhaps the greatest shortcoming of previous campaigns is the limited sampling, both in space and in time. (2) It is difficult to piece together snapshots of tropical disturbances taken at different times. "Genesis" (the formation of a tropical depression-strength vortex at sub-synoptic scales) often occurs between sampling times, or after disturbances move out of range. (3) Very few observations exist for both precursors to genesis and the ensuing tropical cyclone formation process. The limited range of previous projects has also meant a limited phenomenological scope, in terns of precursors to genesis and the multi-scale interactions needed for TC formation. In tropical cyclone formation, the synoptic-scale precursors take many forms (tropical waves, monsoon troughs, upper-tropospheric PV features, etc.). Although Dunkerton et al. (2008) argued that the genesis process should be relatively invariant on mesoscale and sub-synoptic scales in spite of these differences in synoptic precursor patterns, this hypothesis needs to be verified. (4) The marsupial paradigm of tropical cyclogenesis proposed by Dunkerton et al. (2008) embodies several unifying hypotheses that must be tested to confront the issues raised above. (5) Finally the combination of observational resources for PREDICT 2010 is unprecedented.

A key ingredient in the marsupial paradigm is the role of rotating deep moist convection and how convective organization in a rotating environment differs from that of typical mesoscale convective systems in the tropics. Differences in cloud systems arising from the unique nature of the proto-vortex environment imply a different pathway of dynamical evolution than what might otherwise occur in the absence of this environment. A unique cloud system structure and dynamical evolution, and a key role of precursor waves, contribute to the early stages of tropical cyclones. The mesoscale aspects of this structure and evolution remain poorly understood.

To address limitations of previous campaigns, the proposed PREDICT aims to dramatically increase the spatial and temporal sampling of tropical disturbances prior to, and during, genesis. The PREDICT experiment is envisioned as a close collaboration between the United States NSF, the National Oceanic and Atmospheric Administration (NOAA), and the Naval Postgraduate School in Monterey, California. The primary research tools are the NCAR G-V aircraft, with altitude and range advantages over previous aircraft, and two NOAA WP-3D aircraft each equipped with a tail Doppler radar, a lower fuselage (weather surveillance) radar, and the standard suite of flight-level and dropwindsonde observations that accompany normal hurricane and pre-hurricane reconnaissance. The NCAR G-V aircraft will be double-crewed for a portion of the field phases to allow sampling disturbances for as much as 16 out of 24 hours. The project will cover the majority of the Atlantic sector, including the Caribbean, and therefore will be able to observe many forms of precursor disturbances and observe the physical processes of genesis on the mesoscale. Finally, the project will integrate the plethora of satellite data and derived products now available to coordinate the aircraft missions to maximize the total data coverage and physical interpretation.

Diagnostic methods for evaluating precipitation forecasts for land-falling tropical cyclones

Barbara G. Brown

National Center for Atmospheric Research

Boulder CO USA

Abstract

Traditional methods for evaluation of heavy precipitation forecasts, such as may accompany a land-falling tropical cyclone, have typically relied on simple measures of "matching" between forecast and observed grids. These methods do not provide diagnostic information regarding characteristics of the precipitation areas that are relevant for warning the public or assessing flood risk – such as the location of storm regions or the precipitation intensity associated with the predicted precipitation areas. In addition, precipitation verification for land-falling tropical cyclones are often restricted to storm total precipitation, an approach that neglects to consider temporal/spatial attributes of the precipitation that may be important for formulating warnings. Several new spatial, diagnostic methods that have recently been developed to evaluate precipitation forecasts can lead to enhanced information about the performance of predictions associated with land-falling hurricanes. These methods include "object-based" approaches that provide information about performance in the context of particular storm attributes, such as location, intensity, and spatial extent. The application of object-based verification approaches for the evaluation of hurricane precipitation forecasts is demonstrated. In addition to precipitation forecasts, these methods may also be beneficial for evaluating the performance of wind forecasts for land-falling tropical cyclones.

Impact of South China Sea Monsoon on Post LandFalling Typhoons – A Case Study

Peter J. Sousounis, Mélicie Desflots, and Jason Butke

AIR Worldwide Corp., Boston, MA

Inland flooding is a significant insured risk from typhoons in China because of the relatively high frequency of typhoon landfalls, the slow multi-day circuitous paths that typify many of the storms that affect the mainland, and the lack of adequate flood defences in high-exposure regions.

The heavy amounts of precipitation that accompany mainland China typhoons are also a complicated result of significant orographic as well as regional climatic effects. Typhoon Bilis 2006 is a prime example of a typhoon that extensively flooded a significant region of inland China. Bilis made landfall in Fujian Province with tropical storm force winds but as it moved slowly southwestward over the next few days caused significant flooding well inland. Bilis caused an estimated 35 B RMB in economic loss. It was the third costliest tropical cyclone in China's History behind Herb 1996 and Winnie 1997 – both of which were Super Typhoons.

The South China Sea Monsoon, which is a branch of the South East Asia Monsoon, is believed to have played a significant role in Bilis' hydrological longevity. A detailed synoptic analysis, numerical modeling results, and conceptual model of the post-landfall evolution of Bilis that highlights the impact of the South China Sea Monsoon will be provided at the workshop.

Study on the Impact of Landfall Tropical Cyclones in China

Qinghong Zhang(张庆红) Qing Wei(韦青)

Department of Atmospheric Science, School of Physics, Peking University, Beijing, China, 100871

Lianshou Chen(陈联寿)

Chinese Academy of Meteorological Science, Beijing, China, 100081

Abstract The impact of Tropical Cyclones (TCs) on developing countries can be very significant. The purpose of this study is to build an impact index correlated with both the strong wind and heavy rainfall (flood) damage of TCs in China. Considering the radius of TC, Total Destructiveness Index (TDI) and Total column water Vapor Index (TVI) are defined, and the economic loss is used to represent the impact of landfall TCs. The analysis based on 30 landfall TCs from 2001-2007 indicate significant correlation between the impact of landfall TCs and TVI (TDI). Further study shows that landfall TCs with higher TVI would bring heavier rainfall, and make more economical loss over land in China. A TC impact index is defined as a function of TVI and TDI. The correlation between TC impact index and economical loss are significant(r=0.769). Tropical storm Bilis 2006 is a landfall TC with the highest impact index from 2001-2007. Using system cluster analysis method, 30 landfall TCs in this study are graded into 5 categories according to their impact index.
Key Words: topical cyclones; impact index; water vapor; economic loss.

1. Introduction

Tropical cyclones (TCs), regionally known as hurricanes, typhoons, or cyclones; influence societies around the globe. Landfall TCs are high-impact weather systems in China. Heavy rainfall, strong wind and storm surge are associated with TCs and make loss of life and damage to properties (Chen and Ding 1979). The intensity of TCs is graded based on their maximum surface wind velocity both in China and United States. TCs in China are: tropical depression (10.8-17.1 m/s), tropical storm (17.2-24.4 m/s), sever tropical storm(24.5-32.6 m/s), typhoon(32.7-41.4 m/s), sever typhoon (41.4-51.0 m/s) and super sever typhoon(>51.0 m/s). The Saffir-Simpson Hurricane Wind Scale is a 1 to 5 categorization based on the hurricane's intensity at the indicated time in United States. The scale provides examples of the type of damages and impacts in the United States associated with winds of the indicated intensity. Category One Hurricane (64-82 kt), Category Two Hurricane (83-95 kt), Category Three Hurricane (96-113 kt), Category Four Hurricane (114-135 kt), and Category Five Hurricane (>135 kt). All these scales are based on the wind intensity and may represent the damage caused by strong wind, but other impact, like flood caused by heavy rainfall and storm surge are ignored. The damage caused by heavy rainfall is a main component in damage agent of TCs in China (Chen and Ding 1979). For example, Tropical storm Bilis 2006 brought continuous heavy rainfall that caused flood and hill-creep for 5 days after it made landfall over the Southern China. The total economic loss of Bilis is 45.9 billion RMB. Saomei is another Super typhoon that made landfall over China in 2006. Although, the maximum surface wind velocity when Saomei made landfall is 72 m/s, which is much higher than that of Bilis(23.1 m/s). Saomei dissipated rapidly after its landfall and its total economic loss is 25.87 billion RMB,

which is half of that of Bilis. The intensity, which is the maximum surface velocity, can not represent the economic impact of TC. There is a need to introduce another category scale that include the heavy rainfall damage, as well as wind damage in the operational forecast system.

2. description of data and analysis scheme

The data used in this study include: 1) The economic loss of TCs obtained from the Ministry of Civil Affairs（Zhang et. al. 2009）and be normalized using the inflation and GDP from 2001 to 2007[1]; 2)Total column water vapor derived from SSM/I satellite observation[2]; 3) QuickScat sea surface wind velocity over the ocean[3]; 4)CMORP（Climate prediction center MORPHing method）precipitation data with 3-h interval[4]; 5)Best track and radius of TCs from JTWC（Joint Typhoon Warning Center）.

An objective analysis scheme is used to separate TC precipitation from CMORP precipitation (Ren et. al. 2001; Wei 2008). System cluster analysis and multiple linear regression methods are used in this study. The potential destructiveness of tropical cyclone was defined by Emanual 2005. The Power Dissipation Index as: (PDI):

$$PDI = \int_0^{\tau} V_{\max}{}^3 \, dt \qquad (1)$$

where Vmax is the maximum sustained wind speed at the conventional measurement altitude of 10 m. Since radius is ignored in PDI, and the damage caused by high wind is highly corresponding to the radius of typhoon, we define total destructiveness Index (TDI) as sum of PDI of each observing point in the radius of TC. TDI only indicate the thread of strong wind in TCs, the destructiveness caused by heavy rainfall is also important. Former study showed that rainfall and column-integrated water vapor are closely related in the tropics (Muller et. al. 2009). The Total Column water vapor Index (TVI) is defined as the sum of column water vapor (CWV) of each point inside the radius of TC in this study.

$$TDI = \sum_{i=1}^{n} V_i{}^3 \qquad (2)$$

$$TVI = \sum_{i=1}^{n} CW\ V_i \qquad (3)$$

V is detected surface wind from QuickScat, and CWV is column water vapor from SSM/I. n is the total grid number inside the radius of tropical cyclone. If there are grid points whose CWV or V is missing, their values are considered as the area mean of other all available observations. The Influence Time (IT) is defined when TC outer cloud band first reach the coast line. Due to the limitation of observation frequency of orbit satellite, the most nearest observation with IT are chosen. Table 1 gives name, normalized economic loss, influence time, location of typhoon at IT, radius, TVI, TDI of 30 landfall TCs whose data are available from 2001 to 2007.

3. Correlation between normalized economic loss and TVI (TDI)

[1] http://www.econstats.com

[2] http://www.ssmi.com/ssmi/ssmi_description.html

[3] http://www.ssmi.com/qscat/qscat_browse.html

[4] http://www.cpc.ncep.noaa.gov/products/janowiak/cmorph_description.html

The correlation between the normalized economic loss and the minimum sea level pressure at IT is low as -0.341, and so is the maximum surface wind (0.34) and PDI (0.327). So neither the maximum surface wind, nor the minimum sea level pressure can be used to evaluate the economic impact of TCs. If we compare the distribution of CWP of Bilis and Saomei 2006 at their IT (Figure 1), the 62 mm contour of Bilis 2006 has covered more area than that of Saomei 2006. Also TVI of Bilis 2006 is 69013 mm, which is much more than that 28303 mm of Saomei 2006.The relative intensive Samei 2006 is a relative dry TC, but the relative weak tropical storm Bilis 2006 is a relative moist one. The TVI of other 28 landfall TCs are also calculated in table 1. The TVI of Bilis 2006 is the highest in the 30 TCs, and that of Matsa 2005 is the second highest one. The similarity of Bilis 2006 and Masta 2005 is the huge radius, heavy precipitation, long duration after their landfall, as well as their relative more economic loss.

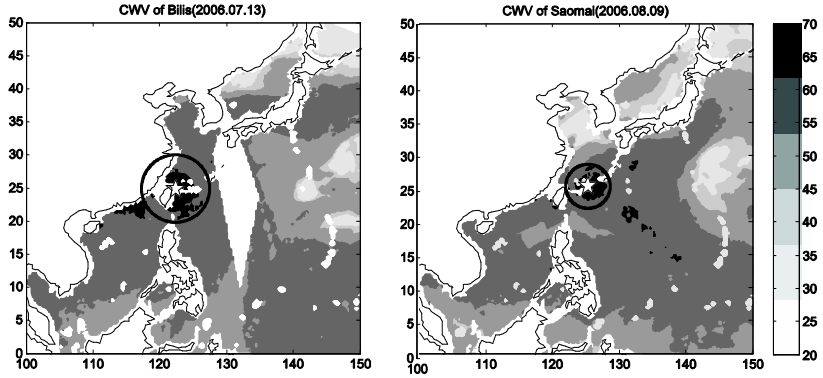

Figure 1 CWV(mm) detected by SSM/I of Bilis 2006 and Saomei 2006. Star represents the center of TC, dark circle indicate the radius of TC.

The correlation between TVI (TDI) and economic loss is 0.751 (0.59) with 99% significance. So TVI, and even TDI has higher correlation with economic lost than that of PDI. The TC radius should not be ignored and the TVI is a good indicator to evaluate the damage of landfall TCs. There are 2 reasons for that the economic lost of tropical storm Bilis 2006 is much more than that of super typhoon Saomei 2006. One is the radius of Bilis 2006 is 3 times of that of Saomei 2006. Another one is CWV in Bilis 2006 is 2 times of that of Saomei 2006 (Table1).

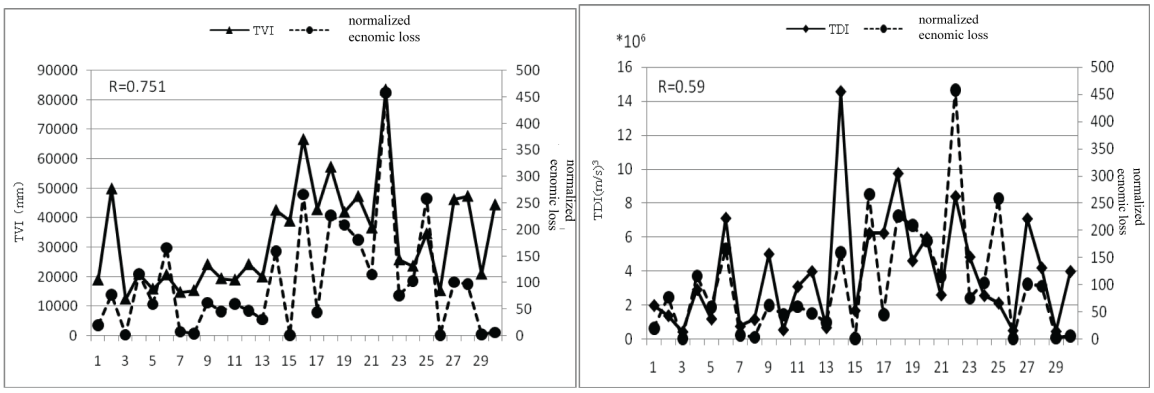

Figure 2. TVI, TDI and normalized economic loss of 30 landfall TCs at their IT.
(x coordinate is TCs order given in table 1)

It is interested that why the economic lost of landfall tropical cyclone has high correlation with the TVI before their landfall. As we all know, the damage of rainfall caused by tropical cyclone depends on the intensity and the duration of precipitation, a rainfall parameter L is defined as：

$$L = \sum_{i=1}^{m} \sum_{t=1}^{n} l_{i,t} \qquad (4)$$

In which

$$l_{i,t} = \begin{cases} 1 & 10\ mm \geq x_{i,t} \geq 5\ mm \\ 2 & 20\ mm > x_{i,t} \geq 10\ mm \\ 3 & x_{i,t} > 20\ mm \end{cases} \qquad (5)$$

x is the accumulated TC precipitation at a given grid point in every 3 hour; n is the total observed times of precipitation (8 times in a day), m is the number of grid point with TC precipitation in a given time. Using the objective analysis scheme and CMORPH satellite data, L is calculated for the 30 TCs. The correlation of TVI at IT and L of landfall TCs is 0.526 with 99% significance. Furthermore, the correlation of L and normalized economic loss is 0.586 with 99% significance. The more water vapor carried by TCs before their landfall, the heavier rainfall they brought and the more economic loss they make over land.

4. Impact index of TC

Here we defined an impact index of tropical cyclone I, in which TDI and TVI are considered.

$$I = 1.499 * 10^{-6} TVI * L + 6.657 * 10^{-6} TDI - 49.732 \qquad (6)$$

L=2501.6 J/g , which is the latent heat vaporization of water under the temperature of 0°C. The correlation between I and normalized economic lost is 0.769, which is higher than that of TVI and TDI. Bilis 2006 is the TC with the highest impact index among the 30 landfall TCs, and Matsa 2005 is the second one. Saomei 2006 is the first rank in term of intensity, but 14th rank in term of impact index among the 30 landfall TCs. Bilis 2006 is the 22th rank in term of intensity but the 1st rank in term of impact index. 5 categories are classified using system cluster analysis scheme.

300＜I	categories 5
200＜I≤300	categories 4
120＜I≤200	categories 3
60＜I≤120	categories 2
I≤60	categories 1

Among the 30 landfall TCs, category 5, which is the highest grade, include only 1 TC, which occupies 3% of the total TCs, category 4 include 3 TCs, which occupies 10% of the total landfall TCs, category 3 and 2 include 7 TCs each, which occupies 23% of the total landfall TCs, category 1 include 12 TCs, which occupies 40% of the total landfall TCs.

Reference

Chen L., Y. Ding, 1979: An introduction to Western Pacific Typhoon, pp. 2-7, *Science Press*, Beijing.

NHC, 2009: The Saffir-Simpson Hurricane wind scale (Experimental). (http://www.nhc.noaa.gov/aboutsshs.html)

Emanuel K. 2005: Increasing destructiveness of tropical cyclones over the past 30 years. *Nature*, 436: 686-689.

Zhang Qiang，Liguang Wu，Qiufeng Liu. 2009: Tropical Cyclone Damages in China:1983-2006. *Bulletin of the American Meteorological Society,* 90: 489-495.

Ren, Fu-Min, Byron Gleason, David Easterling, 2001: A Numerical Technique for Partitioning Tropical Cyclone Precipitation, *Journal of Tropical Meteorology, Vol.17, No.3,* 308-313(in Chinese).

Wei Q. 2009: Study on the precipitation and impact of tropical cyclone over Western Pacific Ocean. Master Thesis. Peking University.

Muller, C. J., L. E. Back, P. A. O'Gorman, and K. A. Emanuel, 2009: A model for the relationship between tropical precipitation and column water vapor. *Geophys. Res. Lett.*, **36**, L16804, doi:10.1029/2009GL039667.

A study on the Tropical Cyclones Torrential Rain Over Liaodong Peninsula

Liang Jun[1] ，Chen Lianshou[2]，Li Ying[2] Zhang Caifeng[1]

([1] Dalian Meteorological Observatory, Dalian 116001, China；[2] Lasw /Chinese Academy of Meteorological Sciences, Beijing, 100081, China)

1. Introduction

Heavy rainfall in the Liaodong Peninsula is mostly induced by tropical cyclones which move northward after their landfall and pass through Huanghai Sea and Bohai Sea（fig. 1）. The tropical cyclones moving northward gain the baroclinic energy from the cold air in middle-latitude, its structure and intensity would be changed, the mesoscale convective systems (MCS) often occur in the extratropical transition (ET) processes of tropical cyclones. The high impact weather, such as heavy rainfall and high winds, would be occurred in the Liaodong Peninsula when those tropical cyclones approached. Sometimes damage may arise from ET processes more severe than it in landfalling stage.

This paper will focus on the heavy rainfall in the Liaodong Peninsula associated with typhoons turning to Bohai Sea and Northern Yellow Sea after landfall, including rainfall distribution and intensity.

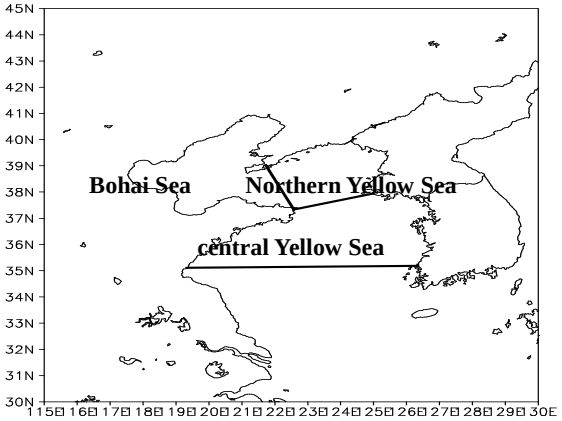

Fig.1 Distribution of the Yellow Sea and Bohai Sea (including the Bohai Sea and the northern and central Yellow Sea)

2. Data and typhoon cases

Convectional data and Tropical Cyclone Year Book published by Chinese Meteorological Press, and objective analysis data of wind/temperature/humitidy from T106 with horizontal grid mesh of 1.125°×1.125° and vertical resolution of 17 layers are used in this study. The conventional observation of surface and upper level sounding are taken from the Micaps system. The satellite digital data are taken from MRI/JMA and FY-2C. The global grid point data with the horizontal resolution of 1°×1° from NCEP are used as well.

The PSU/NCAR MM5V3 model and relevant bogussing techniques were employed in the numerical simulation in this paper.

The case selected for the interaction with sea surface temperature (SST) was typhoon Polly (9216) which moved northward after its landfalling, and induced heavy rainfall in the Liaodong Peninsula. The case

selected for topography effect was typhoon Winnie（1997) turning to Bohai Sea after landfall. In order to study ET processes between typhoon and mid-latitude cold airs, the case seleced was typhoon Matsa(0509), which caused heavy rainfall process in Shandong Peninsula and Liaodong Peninsula during 8—9 August，2005.

3. Results

Numerical simulations are conducted to investigate the effect of sea surface temperature (SST) on the track, intensity, lower layer convergence and moisture flux as well as precipitation of the typhoon Polly. Figure 2 shows an example of tracks and precipitation comparison of typhoon Polly (9216), which are different with SST in northern Yellow Sea changed in the sensitive experiments. Increase of SST drives the tropical cyclone tracking towards or deflecting to a warm SST area (Fig.2a), and leads to significant intensification of lower layer convergence and moisture transport, and therefore notable enhancement of precipitation (Fig.2b).

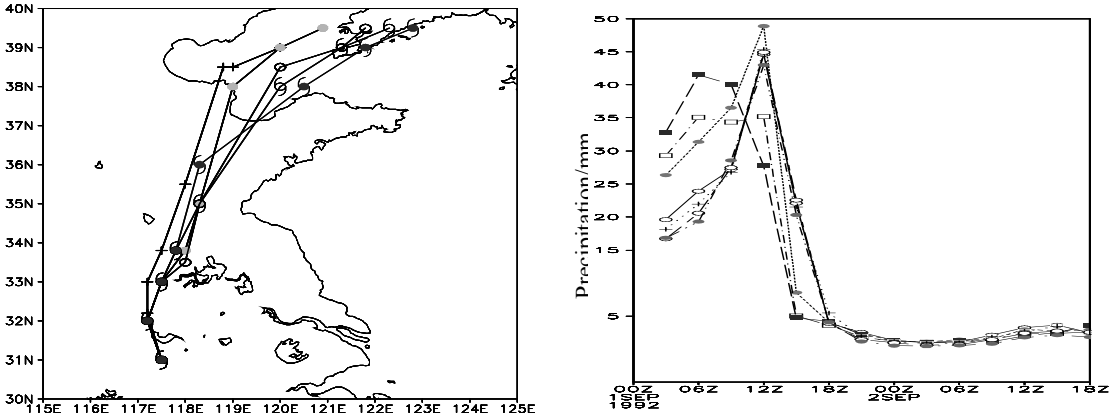

Fig.2 Polly's tracks with 6-h internal (a) and time evolutions of 3-h precipitation (b) in the sensitive experiments and the control experiment(CE). In (a), cross line denotes the CE, lines with blackened circle, open circle, open typhoon mark,blackened typhoon mark denote SST rising 1 ℃ , 2 ℃ , 4 ℃ , 5 ℃ ,respectively. In (b),

The maximum SST in Bohai is normally in June, and in northern Yellow Sea it is normally in August. From April to July, especially July, SST in northern Yellow Sea is low, typhoon moves eastward, it plays little roles in precipitation over the Liaodong Peninsula.

Figure 3 is a diagram of precipitation per 3 hours in Dalian and the precipitation associated with typhoon Winnie（1997). Topography forcing of Liaodong Peninsula and its vicinities were simulated and its meso-scale structures was analyzed based on Temperature of Block Body (TBB), disturbed streamline field and vertical velocity. Results show that the storm rainfall over Liaodong peninsula is closely related to mesoscale convective system (MCS) and topographic effect. The distributions of TBB display a clear mesoscale structure of convective cloud. Mesoscale cyclonic vortex systems are continuously generated and transported to the south of Liaodong peninsula which is favorable to sustain tropical cyclone (TC) intensity and induce heavy precipitation. Heavy rainfall areas are corresponding to convergence zone. The local vertical circulations in north and east of Liaodong peninsula are favorable for intensification of upward movement in vertical. According to this diagram, topography played important roles in precipitation increment. The precipitation cell intensity are increased with the topographic effect. Contrarily, the precipitation cell intensity is decreased without topographic effect.

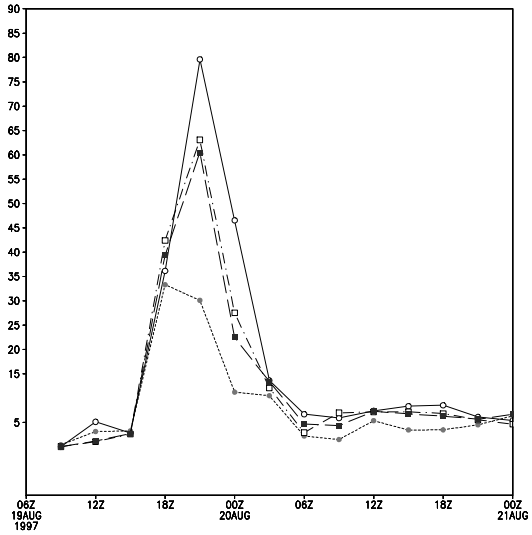

Fig.3 Time evolutions of 3-h precipitation in Dalian in the Winnie simulation experiments
（solid line is CE, dashed line is Expt1, dot dash line is Expt2, long dash line is Expt3. unit：mm）

Furthermore, dynamical and diagnostic analyses were employed with two landfalling typhoons (the revival and dissipation). The results exhibit that ET effect on revival of the tropical cyclone is related to frontogenesis over Liaodong Peninsula. Several sets of numerical simulations are performed to study the impact of cold air on the rainfall of landfalling tropical cyclone in Liaodong Peninsula with typhoon Matsa(0509). The results indicate that the intensity of convective cloud and upward velocity as well as precipitation in Liaodong Peninsula has obvious difference when the cold air invades the external part of tropical cyclone. Both of the weak cold air in lower and middle troposphere (Fig.4a) and severe cold air in upper troposphere (Fig.4b) can lead to notable intensification in radar reflectivity and ascending motion in Liaodong Peninsula, that is favorable to enhancement of precipitation there. The latter effect is more significant than the former one. Without the impact of cold air in lower and middle troposphere (Fig.4c), the heavy rainfall center would occur in the north to Liaodong Peninsula. The severe cold air in lower and middle troposphere (Fig.4d) can result in the weakening of vertical velocity and TC circulation over Liaodong Peninsula, thus TC rainfall decreases remarkably in that area.

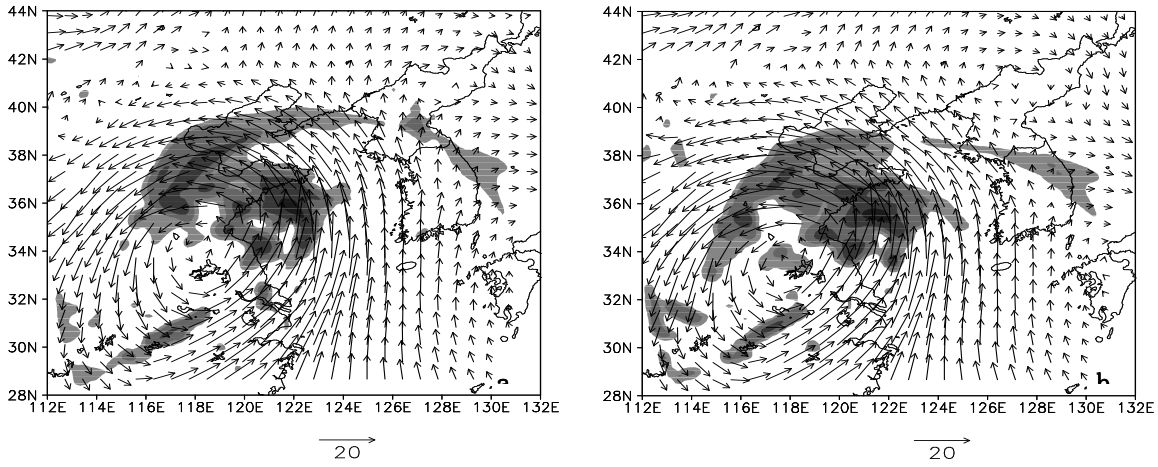

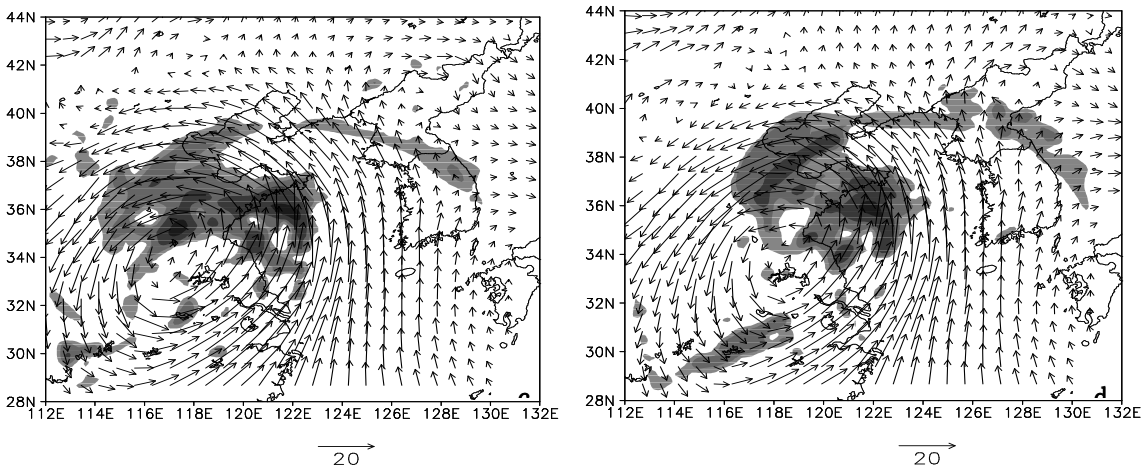

Fig.4 Simulated 850-hPa wind (vector) fields and radar reflectivity intensity distribution (only≥10dBZ shaded) in the sensitivity experiments: (a) Exp1; (b) Exp2; (c) Exp3; (d) Exp4

4. Summary

Many results have been found in this study. Some of them are useful for the operational forecasting. The main part of them is summarized as follow.

Heavy rainfall in the Liaodong Peninsula is associated with the environmental fields when the tropical cyclones move northward. The steady subtropical high about 125ºE results in that the typhoon moves northward and approaches a baroclinic frontal zone, thus fails to move eastward into sea while it is reinvigorated. Superposition between the upper layer divergence and the lower layer convergence, and the non-zonal upper level jet located in north of 35°N are favorable for intensification of upward movement in vertical and northward tracking of the tropical cyclone. During the tropical cyclone passing through the Liaodong Peninsula where there exists a convergence moisture transportation by lower level jet, the baroclinic frontal zone in middle latitudes traverses the tropical cyclone, and energizes it with baroclinic energy, and it is favorable for reducing heavy rainfall in Liaodong Peninsula.

Increase of SST in north of the Yellow Sea drives the tropical cyclone tracking towards or deflecting to a warm SST area, and leads to significant intensification of lower layer convergence and moisture transportation, and therefore enhance the precipitation remarkably.

Topography plays important roles in precipitation increment. The rainfall over the upwind slopes of the mountains and the precipitation cell intensity are increased with the topographic effect. Contrarily, the precipitation cell intensity is decreased without topographic effect.

The intensity of convective cloud and upward velocity as well as precipitation in Liaodong Peninsula has obvious difference when the cold air invades the external part of tropical cyclone. The impact of weak cold air in lower and middle troposphere and severe cold air in upper troposphere lead to notable intensification of radar reflectivity and ascending motion in Liaodong Peninsula, and it is favorable for increase of precipitation in Liaodong Peninsula. The latter effect is more significant than the former one.

References:

[1] Chen Lianshou, Ding Yihui. Introduction of the Western Pacific Typhoon(in Chinese). Beijing: Science Press, 1979. 399～428

[2] Zhu Peijun, Zheng Yongguang, Tao Zuyu. Analysis of the Extratropical Transition of Tropical Cyclone over Mainland of China. Journal of Tropical Meteorology, 2003, 19(2): 157～162

[3] Niu Xuexin, Du Huiliang, Liu Jianyong. The Numerical Simulation of Rainfall and Precipitation Mechanism Associated with Typhoon Sinlaku (0216). Acta Meteorologica Sinica(in Chinese). 2005，63(1)：57～68

[4] Li Ying, Chen Lianshou, Xu Xiangde. Numerical Experiments of the Impact of Moisture Transition on Sustaining of Landfalling Tropical Cyclone and Precipitation.*Chinese Journal of Atmospheric Sciences* (in Chinese), 2005，**29**(1)：91～98

[5] Ji Chunxiao, Xue Yuangen, Zhao Fang, et al. The Numerical Simulation of Orographic Effect on the Rain and Structure of Typhoon Rananim During Landfall. Chinese Journal of Atmospheric Sciences,2007，31(2)：233～244

[6] Meng Zhiyong, Xu Xiangde, Chen Lianshou. Mesoscale Characteristics of the Interaction between TC TIM (9406) and Mid-Latitude Circulation. Acta Meteorologica Sinica(in Chinese). 2002，60(1)：31～39

[7] Li Ying, Chen Lianshou, Zhang Shengjun. Statistical Characteristics of Landfalling Tropical Cyclone. *Journal of Tropical Meteorology* (in Chinese), 2004, **20** (1): 14～23

[8] Tao Zuyu, Tian Baijun, Huang Wei. Asymmetry structure and torrential rain of landing Typhoon 9216. *Journal of Tropical Meteorology* (in Chinese), 1994, **10** (1): 69～77

[9] Duan Yihong, Qin Zenghao, Gu Jianfeng. The Numerical Study of the Effect of SST on Tropical Cyclone Intensity(I)—the numerical simulation of TC intensity and SST experiments. On Science, Operational Experiments and Dynamics of Typhoon. Volume 3(in Chinese). Beijing: China Meteorological Press, 1996. 129～134

[10] LI Qingcai, Wang Chengshu, Cao Gangfeng. A Mechanism Study of Torrential Rain Intensifying due to Landing Typhoon. *Chinese Journal of Atmospheric Sciences* (*Scientia Atmospherica Sinica*) (in Chinese), 1998，**22** (2): 199～206

Cuban Experience in Tropical Cyclone Landfall Forecast for an Effective Warning System

José Rubiera *

Cuban Meteorological Service

Abstract

The Atlantic basin has being living a period of high tropical cyclone activity that began in 1995. In the 15 years that have passed by, Cuba had 17 landfall of tropical cyclones of any category, namely, 6 Tropical Storms, 5 Minor Hurricanes (SS Category 1 and 2) and 6 Mayor Hurricanes (SS Categories 3, 4 and 5). Only 42 lives have been lost in these 15 years, averaging 3 per season. These results are direct consequences of an effective Early Warning System, but such a system would not be possible without an effective forecast of meteorological variables at landfall.

The forecast of the behavior of meteorological variables such as winds, wind gusts, storm surge and coastal flooding, as well as rainfall is a must to modulate the response actions to the intensity and duration of those variables, in order to get a more effective use of financial and material resources, making only the evacuations that are considered necessary to protect lives.

In this work, a review is made of the tools for forecasting wind field, storm surge and rainfall at tropical cyclone landfall in Cuba, with an emphasis in the established facts that cause shortcomings and difficulties, which lead to errors in these variables at landfall.

In Cuba's experience, the most important fact is the errors in tropical cyclone tracks forecast, which directly leads to great errors, because small deviations in track can result in great differences in the wind, storm surge and precipitation forecast. Another factor is the amount of time in which the tropical cyclone is impacting land, for winds, storm surge and rainfall will have less impact in a fast moving storm.

Landfall hazards are also discussed according to what Cuba has experienced in these 15 years of high tropical cyclone activity, as well as some of the strengths and weaknesses that have been identified in our experience.

José Rubiera is the Director of the National Forecast Center of the Institute of Meteorology, Cuban Meteorological Service. Hurricane specialist and forecaster, he has a Ph. Degree and a Senior Researcher Category. Dr. Rubiera has also the category of Senior Professor at the School of Meteorology in Havana University. He is also Vice Chairman of the WMO RA IV Hurricane Committee and also Vice Chair of the WMO CBS Expert Team on Communication, Outreach and Public Education Aspects of Public Weather Service.

Experiments on a Statistical Prediction Scheme of Tropical Cyclone Intensity Forecast in Western North Pacific Based on Partial Least Square Regression

Li-na BAI[1], Jin-jie SONG[1], Yuan WANG[1], Lian-shou CHEN[2], Pei-yan CHEN[2]

[1.] Key Laboratory of Mesoscale Severe Weather, Department of Atmosphere Sciences, Nanjing University, 210093; [2.] National Climate Center, 100081; 3. Shanghai Typhoon Institute, 200030.

Abstract

Operational track forecasts have shown considerable improvement over the past several decades, while intensity forecast remains a difficult task in all tropical cyclone (later TC for short) basins. For TC intensity forecast in the western North Pacific, the most skillful models are the Climatology and Persistence model (CLIPER), in which the potential predictors are those related to climatology, persistence and trends of intensity, such as TC initial intensity and latitude; and the Statistical Typhoon Intensity Prediction Scheme (STIPS), which includes storm environmental conditions (vertical wind shear, etc.) in addition to climatology and persistence.

Shanghai Typhoon Institute of the China Meteorological Administration produces intensity forecasts through 72 h using STI-CLIPER since 2004. The predictands in STI-CLIPER are the intensity changes from the initial forecast time at 12 h intervals of all TCs. Potential predictors include current intensity, location, the 12 h and the 24 h change in intensity and location. STI-CLIPER uses the multinomial regression of ordinary least-square method (hereafter OLS) to establish the regression equation between predictands and predictors to predict TC intensity changes.

The OLS model can hardly choose the right independent variables objectively in the process of modeling, when there is a high degree of collinearity among the potential predictors, which makes the model miss some important variables and debases the accuracy and reliability of the model as a result. The correlation coefficients between predictands in PLS-CLIPER are calculated. It is found that there are marked collineartities between them. For example, the correlation coefficients between initial latitude and 12 h (24h) change in latitude is 0.306 (0.347), which are proved to be significant on a 0.05 level by applying a t-test. To overcome the collinearities of predictands, the partial least-squares regression method (hereafter PLS) is put forward, which is considered as the second generation statistic regression method. The PLS method combines the multi-linear regression analysis and canonical correlation analysis, as well as the principal-components analysis.

The present work adopts PLS in order to establish a statistic intensity forecast model (hereafter PLS-CLIPER) with high accuracy and credibility. To compare the forecast skill with STI-CLIPER, PLS-CLIPER uses the same predictors and predictands. The history track and intensity information during 1970-1999 used to develop these two models come from Typhoon Year-books produced by the China Meteorological Administration (CMA). PLS-CLIPER differs from OLS-CLIPER in two important ways. Firstly, the regression methods are different; Secondly, the dependent samples used to establish the regression equations are different. Historical TCs occurring in the current month every year are selected as samples to develop the equation by STI-CLIPER model. To the contrast, historical TCs occurring in the interval of 30

days, which chooses the current day as a midpoint, are selected by PLS-CLIPER model.

The forecast results of both schemes are analyzed from 2004 to 2007. The forecast capabilities of both models in terms of mean absolute error (MAE) and trend consistence ratio (TCR) can be estimated. If MAE from a model is smaller and TCR is larger than those from another model, then this model is considered to be more skillful. The skills of both models are reduced from 12 h to 120 h, since MAE is shown to increase and TCR is reduced gradually. In addition, MAE from PLS-CLIPER is smaller and TCR is larger than those from OLS-CLIPER through the 72 h forecast period, which means PLS-CLIPER is superior to STI-CLIPER for intensity forecasts. This advantage decreases gradually as the extension of forecast time. For example, the MAE from PLS-CLIPER is smaller than that from OLS-CLIPER by 1.8 m/s at 12 h, but the values at 72 h are nearly the same; The TCR from PLS-CLIPER is larger than that from OLS-CLIPER by 10% at 12 h, but reduced to 1% at 72 h.

PLS-CLIPER is not affected by the TC position and intensity at initial time, as well as TC intensity change and storm motion speed in the last 12 hours. The great improvement is for TCs: 1) weaker than 50m/s, 2) increasing or maintaining their intensities in the 12 hours, 3) locating at 15~20°N, or east of 170°E, and 4) faster moving. Typhoon 'Wipha' is chosen to demonstrate the forecast skills of OLS-CLIPER and PLS-CLIPER for single TC. Results show that PLS-CLIPER is more skillful in forecasting intensity change than OLS-CLIPER not only for the whole samples, but also for single TC.

After 72hr, PLS-CLIPER and OLS-CLIPER are not applicable because of large errors. To overcome this shortcoming, PLS-STIPS is developed by combing the statistical methodology with environmental predictors. The potential predictors used in PLS-STIPS development can be divided into two basic categories: 1) those related to climatology, persistence of intensity, which are the same as used in PLS-CLIPER; 2) Those related to current environmental conditions, which are divided into three categories, namely those related to the SST, those related to the moisture fields, and those related to the wind fields. SST values are determined at the storm center by interpolating from the grid SST data, while moisture and wind-related predictors are area averaged around the center.

The forecast results of both schemes are analyzed in 2006. Results show that PLS-STIPS is more skillful than PLS-CLIPER. This advantage increases gradually as the extension of forecast time. For example, the MAE from PLS-CLIPER is smaller than that from OLS-CLIPER by 0.04 m/s at 12 h, but increases to 2.07 at 120 h. The great improvement is for TCs: 1) with initial intensity of 15~30m/s, 2) with intensity change of -6 ~ 2m/s in the past 12 h, 3) locating north of 25°N, or east of 130°E, and 4) moving at the speed of 1~2°/12 h.

In this work, the environment data used in PLS-STIPS come from the daily NCEP reanalysis data, so PLS-STIPS is just an experiment, but not an operational model. When PLS-STIPS will be used to forecast TC intensity operationally, the data should be replaced by the outputs of a real-time prediction model.

The effects of the vortex intensity to the forecast tracks of typhoon "Fengshen"

Suhong Ma Anxiang Qu

National Meteorological Center, China

1. Introduction

Typhoon Fengshen in 2008 (19 Aug. 2008-25 Aug. 2008) has larger forecast track errors for the longer time forecasts both in subjective and in numerical forecasts especially in the Global numerical Model for TC Track Prediction (GMTTP) in NMC (shown in Fig. 1). All the forecast tracks from GMTTP have obviously north-ward bias especially for the later track forecasts (after 18UTC 20 August).

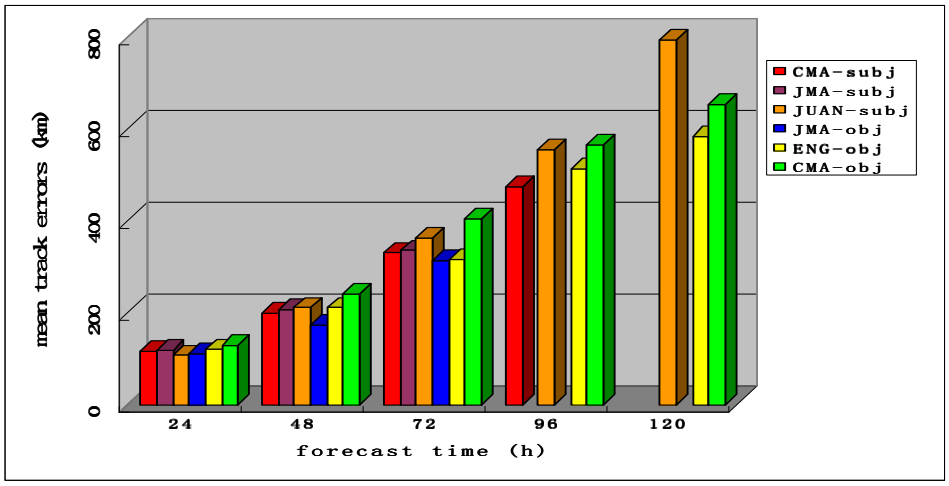

Fig.1 mean track errors for Typhoon Fengshen in 2008. CMA-subj: subjective forecast of CMA; JMA-subj: subjective forecast in JMA; JUAN-subj: subjective forecast in GUAN; JMA-obj: global model forecast in JMA; ENG-obj: global model forecast in England; CMA-obj: global model forecast in CMA

2. General information of GMTTP in CMA

GMTTP has been running in operation since 2004. This system was set up based on global Spectral model T213L31 and Optimal interpolation, the BOGUS vortex technique was used in the initialization of TC vortex. GMTTP was upgraded in the following two aspects in 2008: (1) the data assimilation system was upgraded from OI to 3DVR (SSI) and the satellite data could be assimilated directly; (2) the vortex relocation technique was applied in the new system. The two above improvements greatly reduced the mean track errors of GMTTP system. Fig2 was the mean track errors from the old version and new version of GMTTP system in 2007, where 27.7% reduction for 24h, 25.1% for 48h and 30.6% for 72h.

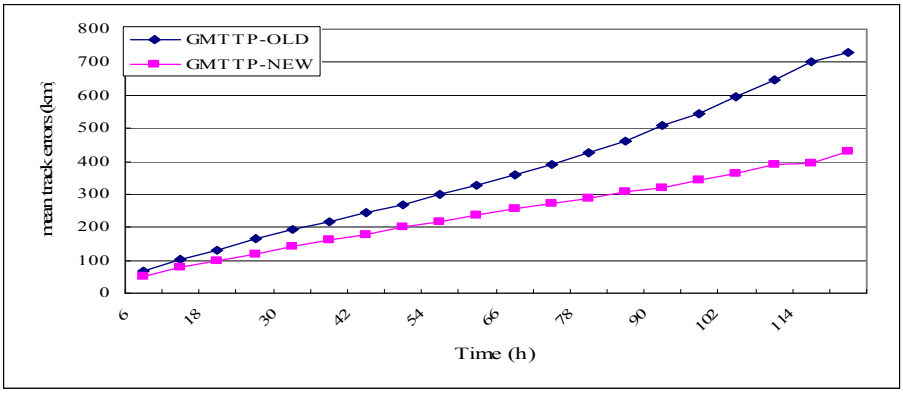

Fig.2 Mean track errors from new and old version of GMTTP in 2007;

3. Configuration of experiments

Three experiments were carried out in order to analyze the reasons for the larger track errors. (1)Using the analyses from the GMTTP system as the initial condition (noted as EXP1); (2)Removing the shallow vortex from the analyses(noted as EXP2);(3)Adding Bogus vortex to the analyses after removing the shallow vortex （noted as EXP3. The differences of geopotential height in the initial condition at 12UTC 21 Aug. 2008 are shown in fig3a-3f for the three experiments.

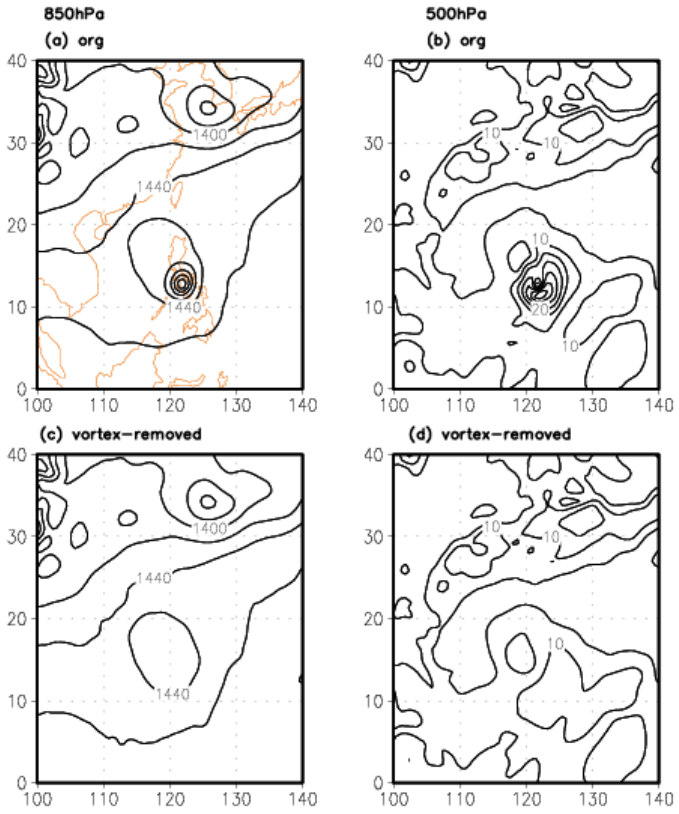

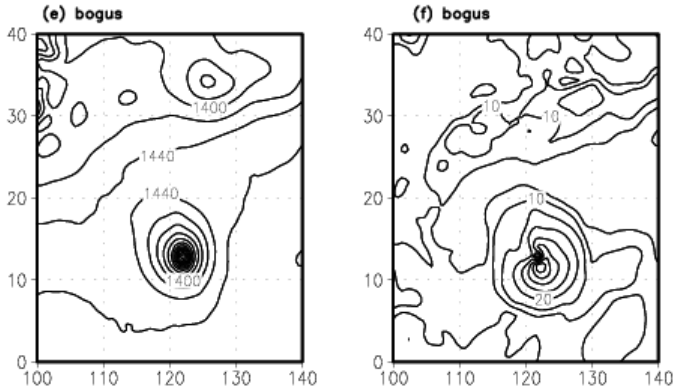

Fig.3 Initial geopotential heights for the three experiments. Where: org for EXP1; vortex-removed for EXP2 and bogus for EXP3.

4. Results

Fig.4 are the differences of the geopotential height (color-shaded) at 850hPa and 500hPa from EXP1 and EXP2 superimposed by the geopotential height of EXP1 (contour) for time 00h,24h,48h and 72h. It could be found that in the initial time the only differences in the geopotential height at 850hPa and 500hPa are the TC vortexes as shown by the color-shaded areas. The differences started to spread to the east and north east ward after 24h(as shown in Fig 4c-g). The differences are larger at 850hPa. The results show that the intensity of the vortex has positive effects on the subtropical high to the East and north-east side of Fengshen: the deeper the initial vortex the stronger the subtropical high.

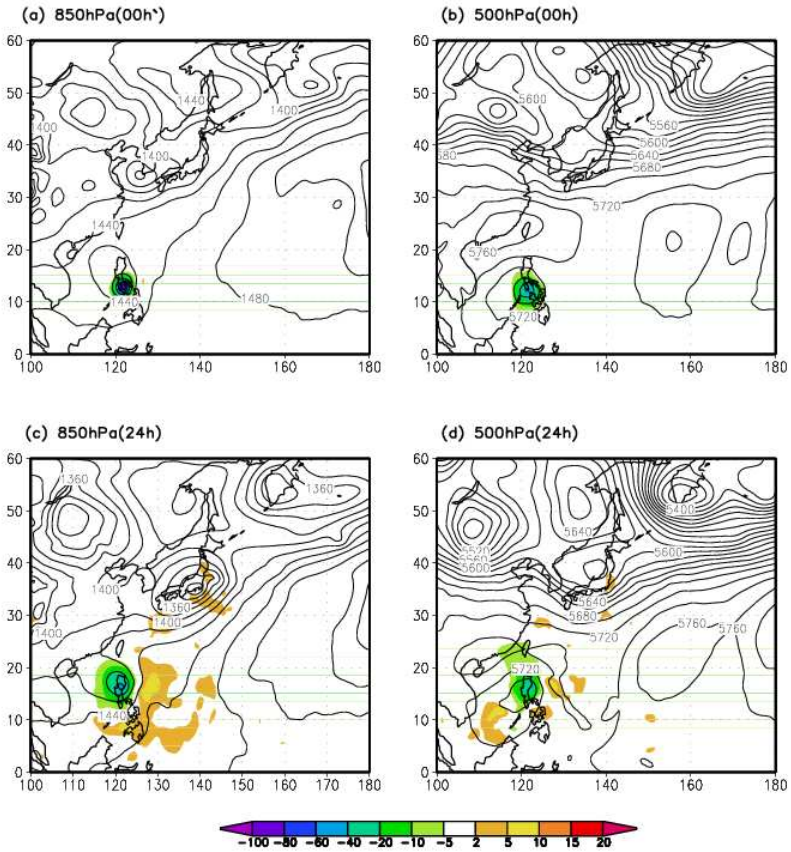

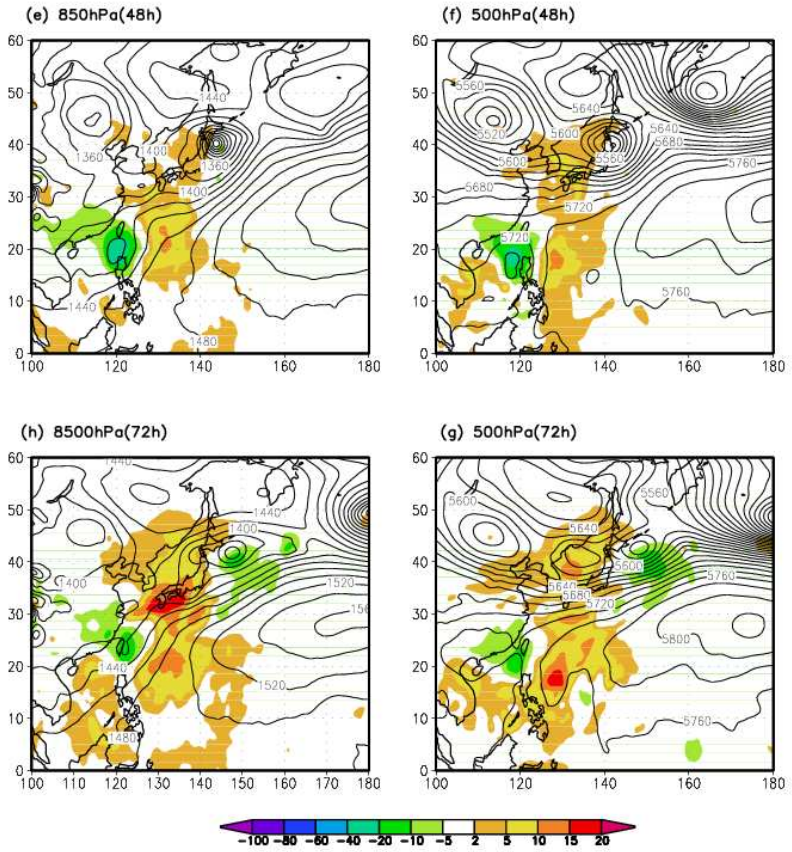

Fig.4 the differences of geopotential height at 850hPa and 500hPa for EXP1 and EXP2 (color shaded) superimposed by the geopotential height form EXP1(contour)

The patterns of the differences from EXP1 and EXP3 are almost the same as these from the Exp1 and EXP except that the differences from EXP1 and EXP3 are larger since the differences in the initial time from EXP1 and EXP3 are larger because the bogus vortex was added in the initial fields of EXP3. The results also indicate that vortex of Fengshen has positive effects on the subtropical height to the east and north-east side of it and the stronger of the subtropical higher could effectively reduce the north bias of the forecast tracks.

Fig5. shows the mean track errors for EXP1 and EXP2 from 00UTC 21 Aug. to 12UTC 24 Aug. 2008 with 12h interval. It could be found that the track errors are obviously reduced since the stronger vortexes are added.

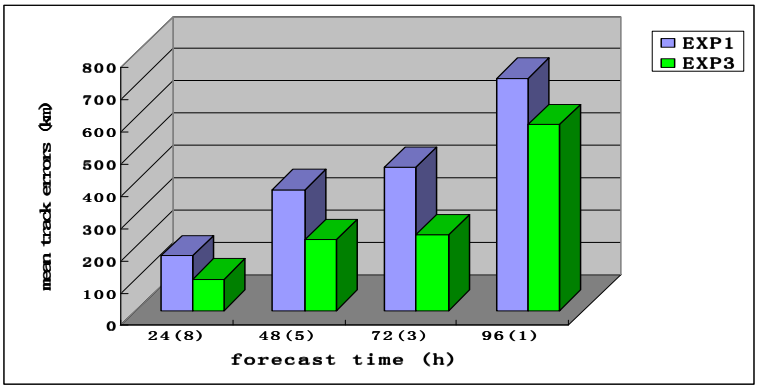

Tropical Cyclone Landfall Processes

Evan Thompson

Weather Branch Head

Meteorological Service, Jamaica

The Meteorological Service in Jamaica is responsible for monitoring weather conditions over and around Jamaica and for issuing reliable and timely weather and climate services relevant to the needs of respective client groups. They also facilitate the country's preparation for tropical cyclones affecting the Caribbean area and the issuance of forecasts and warnings in respect of these tropical cyclones.

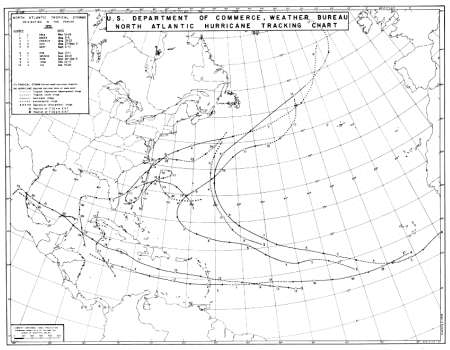

The recent history of Jamaica does not include many instances of the island being directly hit by significant tropical storms or hurricanes. The population is able to clearly recall the events of Hurricane Charlie in the year 1951 and Hurricane Gilbert in 1988. In each case, the centres of these tropical cyclones carved tracks across the island. More recently, there are vivid recollections of similar systems making 'close calls' on the country with the land mass escaping the full extent of the storms' furious effects on each occasion.

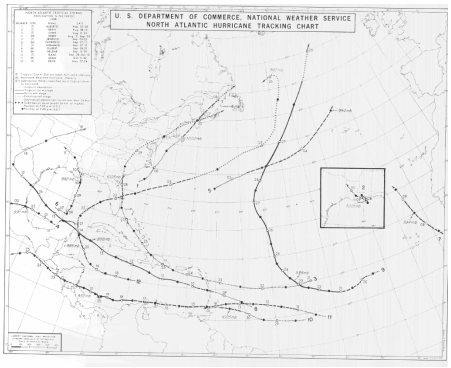

Since the beginning of the current decade, Jamaica has experienced annual threats of tropical cyclone landfall activity; including one direct hit and at least three "miraculous" misses. In most of these cases, specifically in the years 2002, 2003, 2006, 2007 and 2008, wind speeds associated with the systems were within the tropical storm range, while hurricanes approached the island's waters in 2001 (Michelle), 2004 (Ivan), 2005 (Dennis & Emily) and 2007 (Dean).

During this period, Tropical Storm Gustav in 2008, reported to be just seven kilometres shy of being declared a hurricane, was the only tropical cyclone that actually made landfall with its surface-level centre intersecting the island's eastern coastline on August 28 of that year. This occurred after the official forecast track derived from forecast models projected its passage just north of the island during the preceding day, and was updated during the night to a path along the southern coastline.

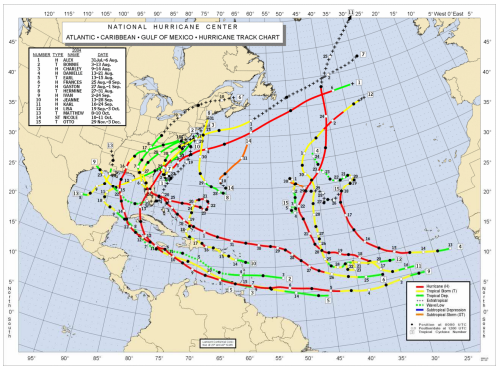

Hurricane Ivan provided a sense of mystery and intrigue

during its approach to the island on September 10, 2004. With all forecast models, and even layman intuition, expecting a direct hit of the hurricane based on its antecedent northward movement, a dramatic backing of the track kept its centre just off the southern coastline until its departure on September 11. As early as September 7, the models were projecting that Ivan would pass over Jamaica within three days. This forecast was maintained through the 8th, 9thand 10th; however, the script was rewritten during the pre-dawn hours of September 11 as the system weakened slightly and changed its forward direction while located less than 40 kilometres from the mainland.

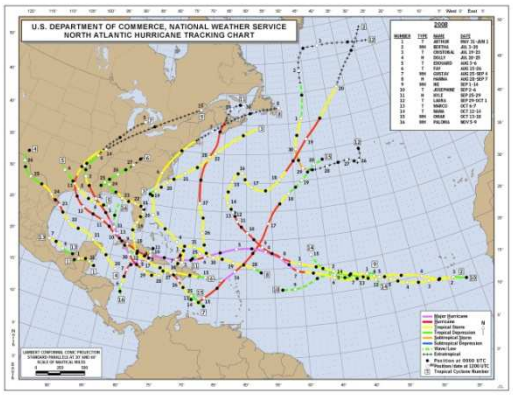

The general belief of Jamaicans is that the location and orientation of the Blue Mountain range, extending as high as 2,256 metres into the troposphere approximately 30 kilometres from the southeastern coastline, was responsible for the sharp change in direction. The interaction of the swath of upper-level winds associated with the hurricane and the rugged orography is felt to have held the key to the system being steered westward. There was also another school of thought, which suggested that the hurricane itself was responsible for modifying the environment into which it was moving, and created more conducive conditions to the left of its prior path.

One of the unfortunate deficiencies of the operations of Jamaica's Meteorological Service during the threat of tropical cyclone landfall is the inability of the organization to determine the storm surge potential of the systems moving over adjacent waters. There is, currently, no capacity to run storm surge models developed for the local situation when posed with a threat.

In the event of Hurricane Ivan in 2004, the organization was able to make contact with meteorologists at the regional training institute, the Caribbean Institute for Meteorology and Hydrology in Barbados, and requested that forecast models be run in respect of the developing conditions. There was full cooperation, and the Service was able to provide warnings with the benefit of the scientific information available from storm surge forecasts. This was considered essential to alerting the country's vulnerable populations about landfall risk.

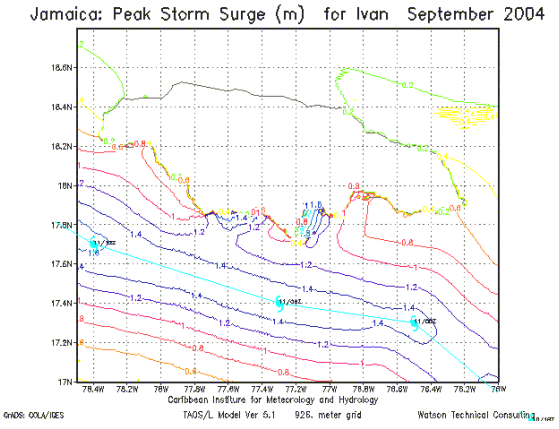

Adiabatic Rearrangement of Potential Vorticity Hollow Towers

Eric A. Hendricksa*and Wayne H. Schubertb

aNational Research Council, Monterey, California

bColorado State University, Fort Collins, Colorado

1. Introduction

One of the important forecasting challenges with tropical cyclones is rapid variability in structure and intensity. This is especially important when an intense hurricane is approaching a densely populated land mass. Such an event occurred in 2008, when Hurricane Dolly was approaching the Texas coast (see Fig. 1 for a radar reflectivity image). Shortly after the time of this radar image, the National Hurricane Center best track intensity estimate was 80 kts and 976 mb (valid at 1200 UTC on July 23, 2008). Note the azimuthal variability of the inner core structure, and in particular the wavenumber-4 pattern in the eyewall and the appearance of both straight line segments and mesovortices. Because of the high correlation of radar reflectivity and vorticity (e.g., Fig. 1 of Kossin et al. 2000), it can reasonably be concluded that the radar image of Dolly has captured the barotropic instability of a thin vorticity ring. The barotropic or combined barotropic-baroclinic instability of hurricane-like vorticity rings and subsequent vorticity mixing has been the subject of a number of recent theoretical, numerical, observational and experimental studies (Schubert et al., 1999; Kossin and Schubert, 2001; Kossin and Eastin, 2001; Montgomery et al., 2002; Terwey and Montgomery, 2002; Kossin et al., 2002; Nolan and Montgomery, 2002; Nolan and Grasso, 2003; Kossin and Schubert, 2004; Rozoff et al., 2009; Hendricks et al., 2009). In the present work, we examine the dynamic instability of a three-dimensional hurricane-like potential vorticity (PV) hollow tower, and examine the role of PV mixing between the eyewall and eye in regulating tropical cyclone structure and intensity change.

*Corresponding author address: Eric Hendricks, National Research Council, Monterey, CA 93943; e-mail: eric.hendricks.ctr@nrlmry.navy.mil

2. Model Description

2.1 Governing Equations

We consider a compressible atmosphere constrained by quasi-hydrostatic motions on an f-plane. The isentropic vertical coordinate primitive equations in rotational form are shown below. The horizontal momentum equations can be cast in either momentum form or vorticity-divergence form. In momentum form, for a horizontal velocity vector $\mathbf{u} = (u, v)$, the equations for zonal and meridional momentum are

$$\frac{\partial u}{\partial t} + \dot{\theta}\frac{\partial u}{\partial \theta} - mPv + \frac{\partial}{\partial x}(M + K) = F_u, \quad (1)$$

$$\frac{\partial v}{\partial t} + \dot{\theta}\frac{\partial v}{\partial \theta} + mPu + \frac{\partial}{\partial y}(M + K) = F_v. \quad (2)$$

By taking the curl ($\mathbf{k} \cdot \nabla_\theta \times$) and divergence ($\nabla_\theta \cdot$) of $\partial \mathbf{u}/\partial t$, the equations in vorticity-divergence form are

$$\frac{\partial \zeta_\theta}{\partial t} + \frac{\partial}{\partial x}\left(\dot{\theta}\frac{\partial v}{\partial \theta}\right) - \frac{\partial}{\partial y}\left(\dot{\theta}\frac{\partial u}{\partial \theta}\right) + \frac{\partial (mPu)}{\partial x} + \frac{\partial (mPv)}{\partial y} = F_\zeta, \quad (3)$$

$$\frac{\partial \delta_\theta}{\partial t} + \frac{\partial}{\partial x}\left(\dot{\theta}\frac{\partial u}{\partial \theta}\right) + \frac{\partial}{\partial y}\left(\dot{\theta}\frac{\partial v}{\partial \theta}\right) + \frac{\partial (mPu)}{\partial y} - \frac{\partial (mPv)}{\partial x} + \nabla^2 (K + M) = F_\delta. \quad (4)$$

The hydrostatic, continuity, and thermodynamic equations are the same for both formulations:

$$\frac{\partial M}{\partial \theta} = \Pi, \quad (5)$$

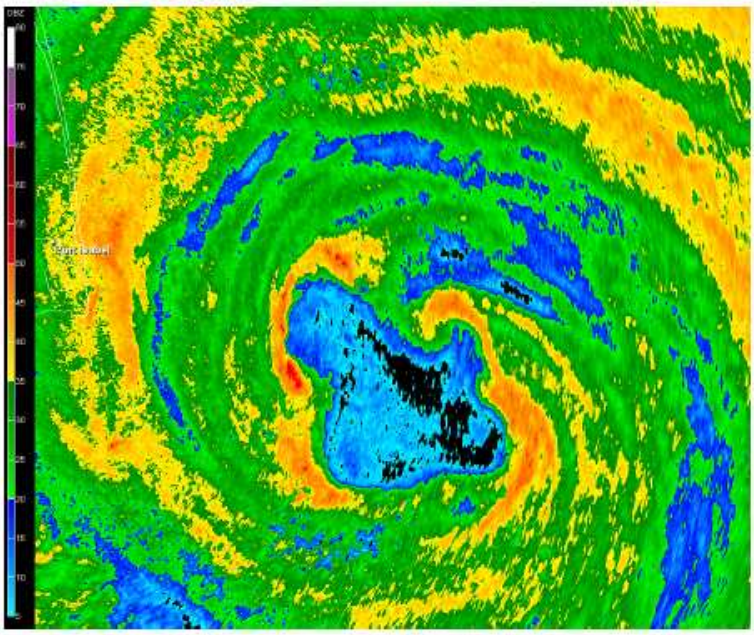

Figure 1: Base reflectivity from the Brownsville, TX National Weather Service radar at 1052 UTC on July 23, 2008. At this time Hurricane Dolly was approaching the coast and asymmetries, including eye mesovortices and straight line segments, were observed in the inner-core.

$$\frac{\partial m}{\partial t} + \frac{\partial (mu)}{\partial x} + \frac{\partial (mv)}{\partial y} + \frac{\partial (m\dot{\theta})}{\partial \theta} = 0, \quad (6)$$

$$\dot{\theta} = \frac{Q}{\Pi}. \quad (7)$$

Here, u is the zonal momentum, v is the meridional momentum, $K = (u^2 + v^2)/2$ is the kinetic energy per unit mass, $\Pi = c_p(p/p_0)^\kappa$ is the Exner function, $\Phi = gz$ is the geopotential, $M = \theta\Pi + \Phi$ is the Montgomery potential, F_u and F_v are momentum sources and sinks, Q is a heat source or sink, $\eta_\theta = f + \partial v/\partial x - \partial u/\partial y$ is the isentropic absolute vorticity, $\zeta_\theta = \partial v/\partial x - \partial u/\partial y$ is the isentropic relative vorticity, $m = -\partial p/\partial\theta$ is the pseudodensity, $\dot{\theta}$ is the diabatic heating rate, and $P = \eta_\theta/m$ is the potential vorticity. All variables are functions of x, y, θ, and t, and all horizontal derivatives are taken on isentropic surfaces.

The potential vorticity principle is obtained by combining (3) and (6) while eliminating the isentropic divergence:

$$\frac{DP}{Dt} = \frac{1}{m}\left[P\frac{\partial(m\dot{\theta})}{\partial\theta} - \frac{\partial}{\partial x}\left(\dot{\theta}\frac{\partial v}{\partial\theta}\right) + \frac{\partial}{\partial y}\left(\dot{\theta}\frac{\partial u}{\partial\theta}\right) + F_\zeta\right]. \quad (8)$$

Note that, in the absence of diabatic heating and friction, P is materially conserved.

2.2 *Discretization*

The model uses a doubly-periodic Fourier spectral representation of the state variables in each isentropic layer. In the vertical, the equations are discretized on a Charney-Phillips grid. A third order Adams-Bashforth explicit scheme is used for the temporal integration, with the CFL condition set by the Lamb wave.

The solution is obtained on a doubly periodic domain in the horizontal with 250 × 250 points, and 8 isentropic layers between the levels θ = 300, 307.5, 315,..., 360 K. Ordinary diffusion was used with $\nu = 50$ m^2 s^{-1} on ζ_θ, δ_θ and m. Since internal

gravity waves may be generated during PV mixing, a sponge layer was used near the lateral boundaries with Laplacian damping with a $1/e$-damping time of 0.5 h for the shortest wave. The top and bottom boundaries were rigid. Since the experiment is adiabatic, PV is nearly materially conserved in each insentropic layer. The minor non-conservation of PV occurs because of the addition of diffusion, which is necessary to control spectral blocking. The integration was performed using the the vorticity-divergence prognostic formulation.

3. Unstable baroclinic vortex evolution

The PV field in real hurricanes is complicated due to the nonconvervative effects of diabatic heating and friction, as well as horizontal advection. This study is focused on the advective aspects of the problem. The model was run with an initial condition of an unstable baroclinic vortex, which shall be referred to as a potential vorticity (PV) hollow tower. The radial reversal of PV satifies the Charney-Stern necessary condition for combined barotropic-baroclinic instability (see Montgomery and Shapiro (1995) for a discussion of this theorem as it relates to rapidly rotating vortices). Here we simulate the dry adiabatic rearrangement of PV due to dynamic instability of this hurricane-like PV hollow tower. The initial PV hollow tower was constructed based on observations of intense hurricanes, such as Dolly in Fig. 1. However the field is axisymmetric because we wish to simulate the complete evolution, before the onset of dynamic instability and PV mixing. The vorticity is maximized just above the surface and decays vertically (as in real hurricanes). The initial condition for the isentropic relative vorticity is separable: $\bar{\zeta}_\theta(r,0,\theta) = \bar{\zeta}_\theta(r,0) f(\theta)$, where

$$\bar{\zeta}_\theta(r,0) = \begin{cases} \zeta_1 & 0 \le r \le r_1 \\ \zeta_1 S(\frac{r-r_1}{r_2-r_1}) + \zeta_2 S(\frac{r_2-r}{r_2-r_1}) & r_1 \le r \le r_2 \\ \zeta_2 & r_2 \le r \le r_3, \\ \zeta_2 S(\frac{r-r_3}{r_4-r_3}) + \zeta_3 S(\frac{r_4-r}{r_4-r_3}) & r_3 \le r \le r_4 \\ \zeta_3 & r_4 \le r \le \infty \end{cases} \tag{9}$$

and $f(\theta) = \exp[(\theta-\theta_{ref})^2/(2\sigma)]$. Here, $\zeta_1 = 0.0$ and $\zeta_2 = 0.001$ s^{-1}, $r_1, r_2, r_3, r_4 = 30, 40, 50, 60$ km, $S(s) = 1 - 3s^2 + 2s^3$ is a cubic Hermite shape function that provides smooth transition zones, $\theta_{ref} =$ 305 K, and $\sigma = 5$ K below θ_{ref} and $\sigma = 15$ K above θ_{ref}. The background pseudodensity $m(\theta) = m_0 \exp(-a(\theta-\theta_s)/(\theta_t-\theta_s))$, with $m_0 = 4000$ Pa K^{-1} and $a = 2.5$. A balance initialization is used to determine the balanced mass field associated with the baroclinic vortex. The solution is obtained numerically using the vorticity-divergence formulation with $\zeta_\theta(x,y,\theta,0)$ and $m(x,y,\theta,0)$ defined above, and $\delta_\theta(x,y,\theta,0)$ equal to zero. An unbalanced, weak perturbation is added the basic state vorticity at each isentropic layer of the form $\zeta'_\theta(r,\phi,\theta) = \zeta'_\theta(r,\phi) f(\theta)$ where

$$\zeta'(r,\phi,0) = \zeta_{amp} \sum_{m=1}^{12} \cos(m\phi + \phi_m) \times \begin{cases} 0 & 0 \le r \le r_1, \\ S(\frac{r_2-r}{r_2-r_1}) & r_1 \le r \le r_2, \\ 1 & r_2 \le r \le r_3, \\ S(\frac{r-r_3}{r_4-r_3}) & r_3 \le r \le r_4, \\ 0 & r_4 \le r < \infty, \end{cases} \tag{10}$$

where $\zeta_{amp} = 1.0 \times 10^{-5}$ s^{-1} and $f(\theta)$ is defined as above. The impulse is expected to arise from a wide spectrum of background convection. The simulation was performed on an f-plane with $f = 5 \times 10^{-5}$ s^{-1}.

The adiabatic evolution the PV hollow tower is shown in Figs. 2–5, progressing from $t = 0$ to $t = 48$ h. In each plot, 4 panels are shown. The top panels depict the azimuthal mean PV and tangential velocity, and the bottom panels depict θ slices of PV near the surface and at upper levels. In Fig. 2 (top left panel), note the initially erect PV hollow tower due to the baroclinic vortex. Also note the background PV that increases due to greater static stability near the tropopause in the presence of background rotation.

Progressing to $t = 12$ h in Fig. 3, note that the PV ring on the $\theta = 304$ K surface has become dynamically unstable and is breaking down at azimuthal wavenumber $m = 3$. The lower left panel of Fig. 3 is quite similar to the radar reflectivity image of Fig. 1. However, note that the fastest growing mode is wavenumber $m = 3$, instead of $m = 4$ (as in Fig. 1). This occurs because our PV hollow tower is likely thicker than Dolly's PV hollow tower. Schubert et al. (1999) demonstrated that the fastest growing azimuthal mode is generally at a lower wavenumber in thicker vorticity rings. Note also at this time that the upper level PV ring has not changed. The ring breakdown at lower levels has caused the PV tower to tilt inward slightly (top left panel). Moving forward to $t = 24$ h in Fig. 4, the low level PV ring has broken down completely and PV is

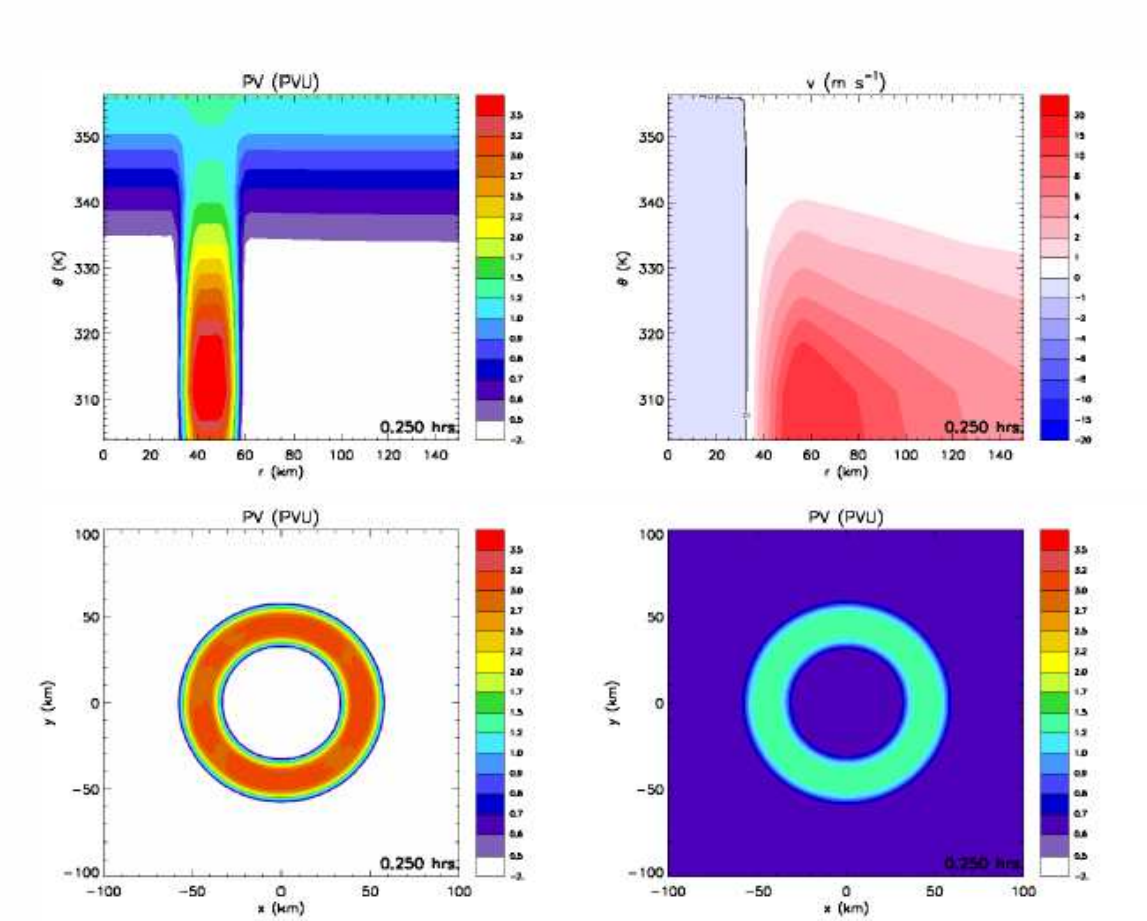

Figure 2: The azimuthal mean PV (PVU) [top left panel], the azimuthal mean tangential velocity (m s^{-1} [top right panel], PV (PVU) on the $\theta = 304$ K surface [bottom left panel], and PV (PVU) on the $\theta = 341$ K surface [bottom right panel]. All fields are shown at $t = 0.25$ h.

being mixed into the eye, while the upper level PV ring is still unchanged. The PV hollow tower is now tilting more significantly below $\theta = 325$ K, but is vertically erect above it. The PV mixing at low levels causes the tangential velocity to increase at lower radii, changing the radial profiles from U-shaped to V-shaped. Finally, at $t = 48$ h (Fig. 5), the low level PV ring has mixed from an annulus into a near monopole. The upper level PV ring is still similar to the initial condition. The PV hollow tower now slopes outward with height, at approximately 50 km per 30 K, or 1.67 km K^{-1}. The tower is now hollow above $\theta = 317$ K and monopolar below $\theta = 317$ K. A "PV bridge" exists at $\theta = 310$ K across the eye. The PV bridge has previously been simulated in a high resolution (2 km), full-physics nonhydrostatic model simulation of Hurricane Andrew (1992) using the PSU-NCAR MM5 model (Yau et al., 2004). We have simulated a similar structure in an idealized model with nearly conservative dynamics. A side-by-side comparison of the azimuthal mean PV in our simulation and the Yau et al. (2004) azimuthal mean PV simulated in Hurricane Andrew (1992) is shown in Fig 6.

Willoughby (1998) has shown that there are two distinct eye regimes separated by a low level inversion. The inversion is typically near 800 hPa. He argued that the air above the inversion has often been in the eye since it formed and is characterized by very weak descent. Below the inversion, the air is moist due to sea surface fluxes, moist frictional inflow, and evaporation of downdrafts. A schematic of the flow regimes in the eye is shown in the bottom panel of Fig. 6. Willoughby (1998) has hypothesized that the eye inversion is caused by subsidence warming. An interesting question is whether it is possible that this inversion is caused dynamically by PV mixing. To illustrate this point, it is useful to go back

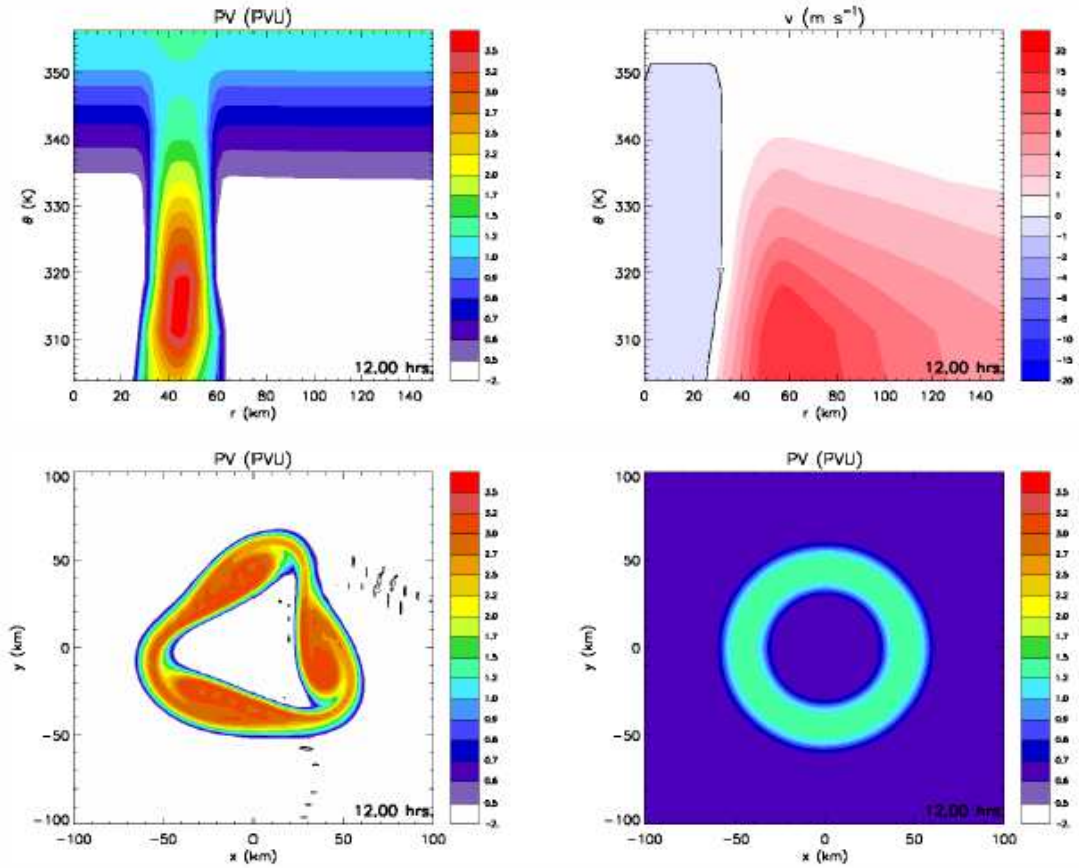

Figure 3: The azimuthal mean PV (PVU) [top left panel], the azimuthal mean tangential velocity (m s^{-1} [top right panel], PV (PVU) on the $\theta = 304$ K surface [bottom left panel], and PV (PVU) on the $\theta = 341$ K surface [bottom right panel]. All fields are shown at $t = 12$ h.

to the PV equation (8). In our simulation the diabatic term is zero and F_ζ is weak, so PV is nearly materially conserved. The hydrostatic PV in isentropic coordinates on an f-plane is $P = (f+\zeta_\theta)/m$, or written another way, $P = -(f+\zeta_\theta)\partial\theta/\partial p$ (where g has been removed for simplicity). Thus P can be viewed as isentropic absolute vorticity $(f + \zeta_\theta)$ multiplied by "static stability" $(-\partial\theta/\partial p)$. Assuming that the evolution is essentially quasi-balanced, a given PV field can be partitioned (by inversion) into each of these components. Since the large PV that exists in the "PV bridge" across the eye was mixed from the eyewall, it is possible that the hurricane eye inversion is dynamically controlled. If this were the case, it may be one of the only lower tropospheric inversions that forms dynamically, rather than by subsidence warming or warm air advection over a cool layer.

Another interesting aspect of this simulation is that the initially erect PV hollow tower evolved into a tilted structure. Is it possible the PV mixing in three-dimensions is one mechanism by which the eyewall slope initially forms? This will be explored in future work.

In order to assess the robustness of the numerical simulation, the temporal evolution of various domain integral quantities were examined. The total mass is defined by

$$R = \iiint \frac{m}{g}\, dx\, dy\, d\theta, \qquad (11)$$

the kinetic energy is defined by

$$K = \iiint \frac{1}{2}\left(u^2 + v^2\right) m\, dx\, dy\, d\theta, \qquad (12)$$

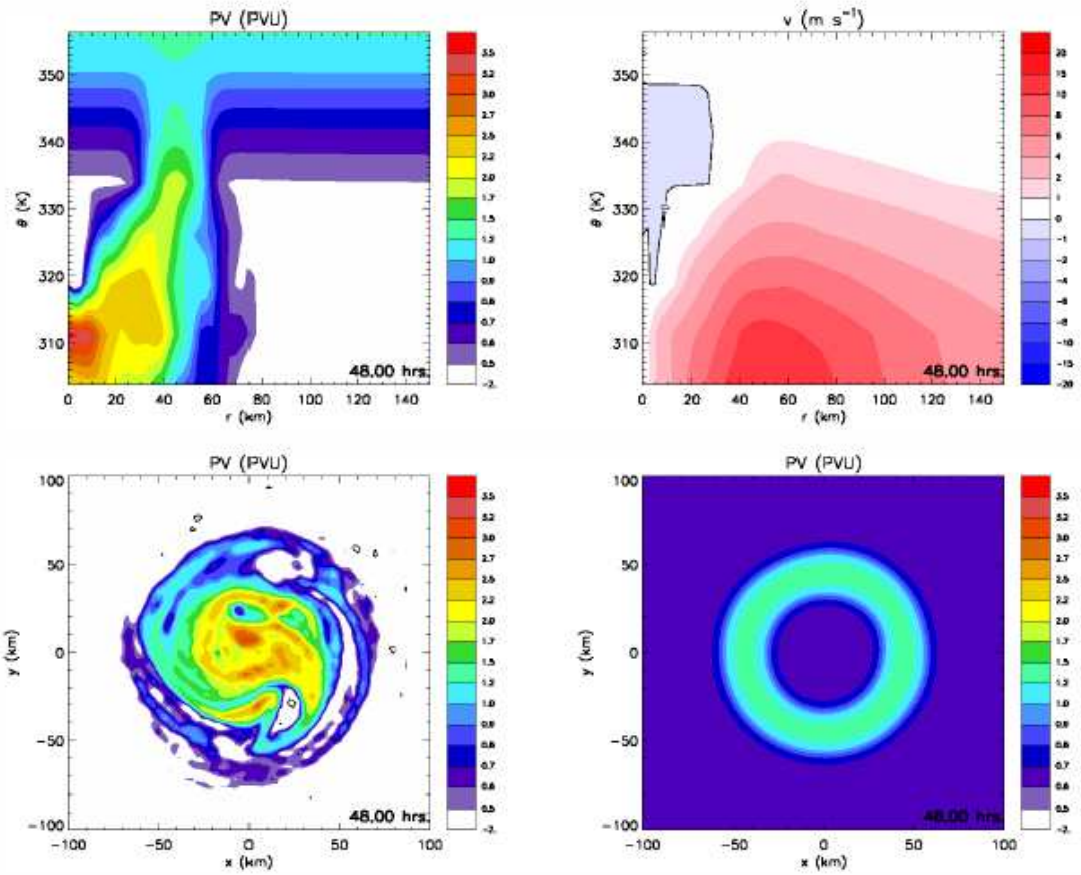

Figure 5: The azimuthal mean PV (PVU) [top left panel], the azimuthal mean tangential velocity (m s^{-1} [top right panel], PV (PVU) on the $\theta = 304$ K surface [bottom left panel], and PV (PVU) on the $\theta = 341$ K surface [bottom right panel]. All fields are shown at $t = 48$ h.

strongest at low levels. Minor mixing occurred at middle levels and virtually no mixing occurred at upper levels. Due to the import of PV into the eye at low levels, the radial profile of tangential velocity became more Rankine-like (instead of U-shaped) there. Additionally, a "PV bridge" formed across the eye, which has been previously simulated in moist full-physics models. It is interesting to note that this feature was simulated in a highly idealized framework. Since, by inversion, a portion of this "PV bridge" is static stability, and thus it is possible that the hurricane eye inversion is dynamically controlled, and as such, it may be one of the only inversions of this sort on Earth. Another interesting aspect of this simulation was that an initially vertically erect PV hollow tower became tilted due to adiabatic PV mixing preferentially at lower levels. Thus it is possible that one mechanism for the formation of the eyewall slope in hurricanes is PV mixing resulting from dynamic instability. This will be explored further in future work. Finally, this study illustrates the utility of examining hurricane evolution in a dynamically clean framework, i.e., by making PV maps on isentropic surfaces.

ACKNOWLEDGMENTS

This research was supported by the National Science Foundation under grant ATM-0837932. A portion of this research was performed while the first author held a National Research Council Research Associateship Award. We are grateful to Dr. Scott Fulton for his comments and assistance.

References

Hendricks, E. A., W. H. Schubert, R. K. Taft, H. Wang, and J. P. Kossin, 2009: Lifecycles of

hurricane-like vorticity rings. *J. Atmos. Sci.*, **66**, 705–722.

Kossin, J. P. and M. D. Eastin, 2001: Two distinct regimes in the kinematic and thermodynamic structure of the hurricane eye and eyewall. *J. Atmos. Sci.*, **58**, 1079–1090.

Kossin, J. P., B. D. McNoldy, and W. H. Schubert, 2002: Vortical swirls in hurricane eye clouds. *Mon. Wea. Rev.*, **130**, 3144–3149.

Kossin, J. P. and W. H. Schubert, 2001: Mesovortices, polygonal flow patterns, and rapid pressure falls in hurricane-like vortices. *J. Atmos. Sci.*, **58**, 2196–2209.

Kossin, J. P. and W. H. Schubert, 2004: Mesovortices in Hurricane Isabel. *Bull. Amer. Meteor. Soc.*, **85**, 151–153.

Kossin, J. P., W. H. Schubert, and M. T. Montgomery, 2000: Unstable interactions between a hurricane's primary eyewall and a secondary ring of enhanced vorticity. *J. Atmos. Sci.*, **57**, 3893–3917.

Montgomery, M. T. and L. J. Shapiro, 1995: Generalized Charney-Stern and Fjortoft theorem for rapidly rotating vortices. *J. Atmos. Sci.*, **52**, 1829–1833.

Montgomery, M. T., V. A. Vladimirov, and P. V. Denissenko, 2002: An experimental study on hurricane mesovortices. *J. Fluid Mech.*, **471**, 1–32.

Nolan, D. S. and L. D. Grasso, 2003: Nonhydrostatic, three-dimensional perturbations to balanced, hurricane-like vortices. Part II: Symmetric response and nonlinear simulations. *J. Atmos. Sci.*, **60**, 2717–2745.

Nolan, D. S. and M. T. Montgomery, 2002: Nonhydrostatic, three-dimensional perturbations to balanced, hurricane-like vortices. Part I: Linearized formulation, stability, and evolution. *J. Atmos. Sci.*, **59**, 2989–3020.

Rozoff, C. M., J. P. Kossin, W. H. Schubert, and P. J. Mulero, 2009: Internal control of hurricane intensity: The dual nature of potential vorticity mixing. *J. Atmos. Sci.*, **66**, 133–147.

Schubert, W. H., M. T. Montgomery, R. K. Taft, T. A. Guinn, S. R. Fulton, J. P. Kossin, and J. P. Edwards, 1999: Polygonal eyewalls, asymmetric eye contraction, and potential vorticity mixing in hurricanes. *J. Atmos. Sci.*, **56**, 1197–1223.

Terwey, W. D. and M. T. Montgomery, 2002: Wavenumber-2 and wavenumber-m vortex Rossby wave instabilities in a generalized three-region model. *J. Atmos. Sci.*, **59**, 2421–2427.

Willoughby, H. E., 1998: Tropical cyclone eye thermodynamics. *Mon. Wea. Rev.*, **126**, 3053–3067.

Yau, M. K., Y. Liu, D.-L. Zhang, and Y. Chen, 2004: A multiscale numerical study of Hurricane Andrew (1992). Part VI: Small-scale inner-core structures and wind streaks. *Mon. Wea. Rev.*, **132**, 1410–1433.

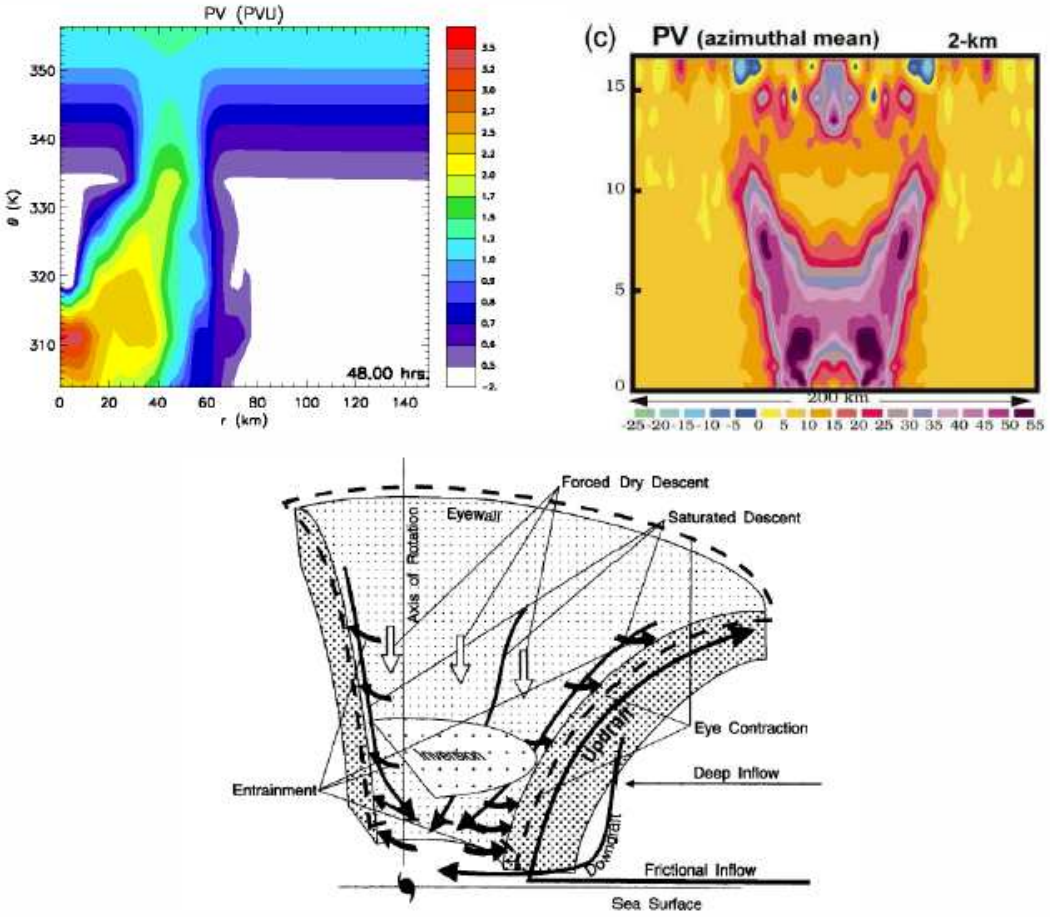

Figure 6: The azimuthal mean PV (PVU) in our ideal model [top left panel] and a cross-section of PV in the (Yau et al., 2004) full-physics nonhydrostatic model simulation [top right panel]. In the right panel, the ordinate is height above sea level in km. A schematic of the secondary flow in the hurricane eye and eyewall is also shown in the bottom panel (reproduced from Willoughby 1998).

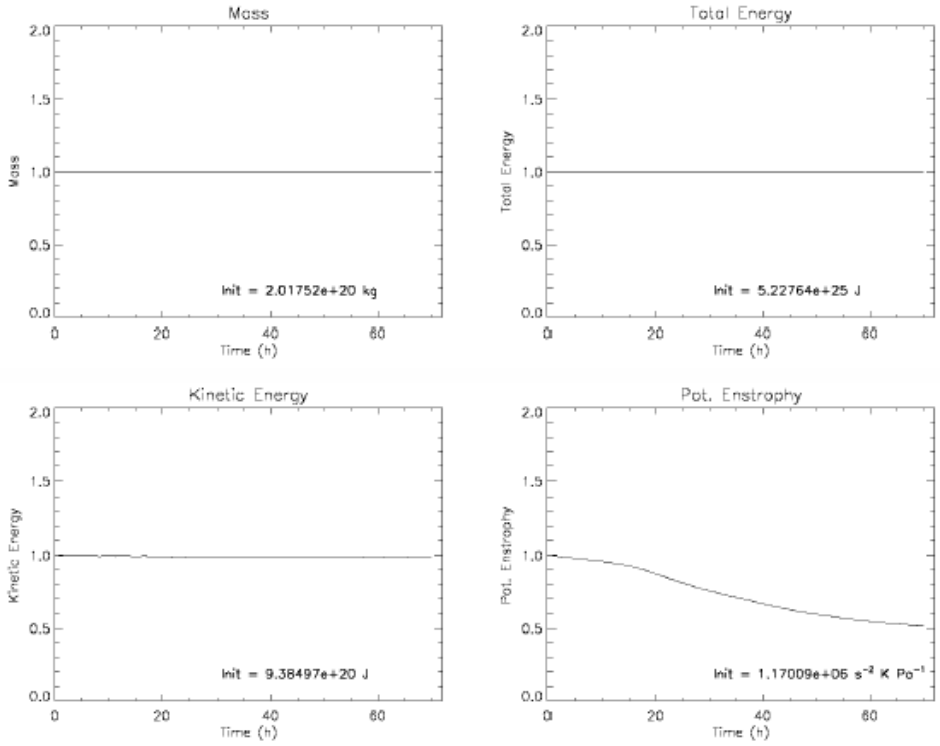

Figure 7: Temporal evolution of the domain integral quantities for the unstable baroclinic vortex simulation. In each panel the values are normalized by the initial value which is shown in the bottom right portion of the plot.

Primary Analyses on Structure and Evolution of Typhoon Khanun (2005) during Its Later Period from Land into Sea

Gang FU*, Na WEI, Qian WANG and Xiaolan LI

Dept. of Marine Meteorology, Ocean University of China, 266100, Qingdao

Abstract

In this paper, the structure and evolution of typhoon Khanun (No.0515) in September 2005 during its later period from land into sea were investigate by using FNL (Final Analysis) data of NCEP. Around 00 UTC 5 September 2005, Khanun formed around (142.3°E, 8.2°N) originally as a weak tropical depression with central pressure of 1006 hPa and the maximum wind speed 12 m/s. Then it moved northwestward with gradually-increased intensity. Around 18 UTC 6, it intensified into a tropical storm. At 12 UTC 7, it developed into a strong tropical storm. At 12 UTC 8, Khanun intensified into a typhoon. Around 0650 UTC 11, Khanun made landing in Taizhou city of Zhejiang Province with central pressure 945 hPa and the maximum wind speed 50 m/s. After landing, the intensity of Khanun decreased gradually when it moved northward, and then northeastward. Around 18 UTC 11, it weakened as a strong tropical storm in Yancheng city of Jiangsu Province. Around 00 UTC 12, Khanun propagated into the western part of the Yellow Sea. Then it transformed into an extra-tropical cyclone. The track of Khanun can be found in Figure 1.

This paper is only focus on Khanun's later period when it moved from land into sea. Firstly, the evolutionary process of typhoon Khanun was documented by using GMS (Geostationary Meteorological Satellite) imagery. Then our analyses are focus on the pressure,

temperature, humidity and potential vorticity at 06, 12, 18 UTC 12 September, respectively. In order to document the three-dimensional structure of Khanun, analyses at 06 UTC (over land) and 18 UTC (over sea) 12 September 2005 were conducted in order to compare the structure change of Khanun during its transformation from land into sea. Moreover, a high-resolution numerical modeling of Khanun's transformation from a tropical cyclone into an extra-tropical cyclone is under consideration.

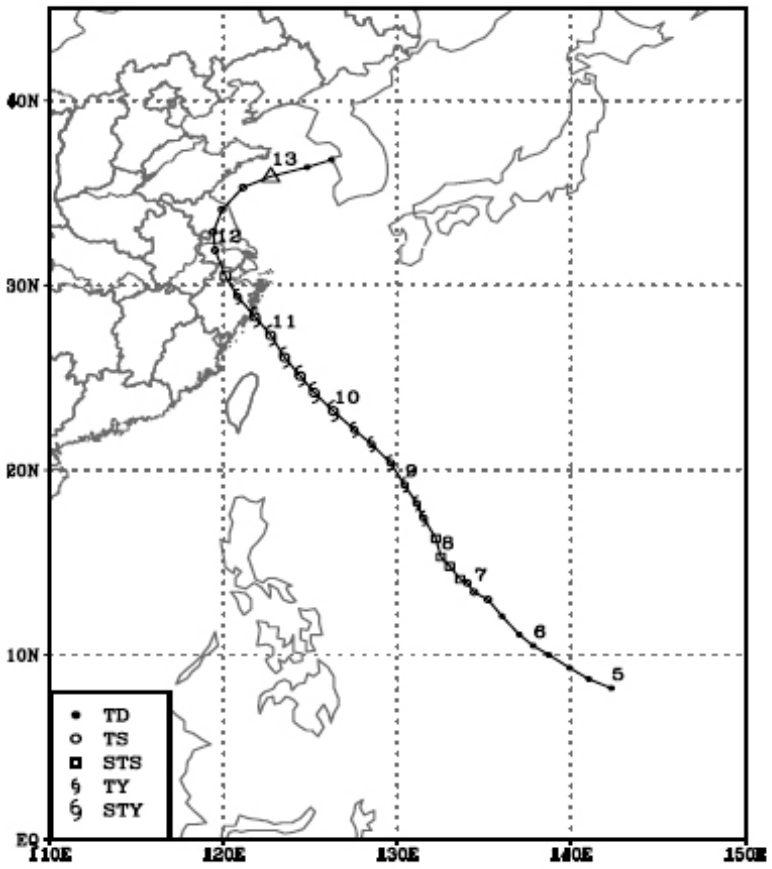

Fig.1: Track of "Khanun" in September 2005. Symbol "Δ" indicates that typhoon has been transformed into extra-tropical cyclone.

Corresponding author: Prof./Dr. Gang Fu, Dept. of Marine Meteorology, Ocean University of China. No.238, Songling Road. Qingdao 266100. China. E-mail: fugang@ouc.edu.cn

Track Information of Typhoon Khanun

Year	Month	Day	UTC	Center Location		Central Pressure	Max. Speed	Grade
				(°N)	(°E)	(hPa)	(m/s)	
	9	5	00	08.2	142.3	1006	12	TD
	9	5	06	08.7	141.0	1004	12	TD
	9	5	12	09.3	139.9	1004	12	TD
	9	5	18	10.0	138.7	1004	15	TD
	9	6	00	10.5	137.8	1004	15	TD
	9	6	06	11.1	137.0	1004	15	TD
	9	6	12	12.2	136.0	1004	15	TD
	9	6	18	13.0	135.2	1000	18	TS
	9	7	00	13.4	134.4	1000	18	TS
	9	7	06	13.9	134.0	998	20	TS
	9	7	12	14.1	133.6	990	25	STS
	9	7	18	14.8	133.0	990	25	STS
	9	8	00	15.3	132.5	985	28	STS
	9	8	06	16.3	132.2	980	30	STS
	9	8	12	17.4	131.5	975	33	TY
	9	8	18	18.2	131.1	960	33	TY
	9	9	00	19.2	130.4	960	40	TY
2005	9	9	06	20.4	129.6	960	40	TY
	9	9	12	21.4	128.5	960	40	TY
	9	9	18	22.2	127.5	960	40	TY
	9	10	00	23.2	126.3	950	45	STY
	9	10	06	24.2	125.2	950	45	STY
	9	10	12	25.1	124.4	945	50	STY
	9	10	18	26.1	123.5	945	50	STY
	9	11	00	27.3	122.7	945	50	STY
	9	11	06	28.3	121.8	945	50	STY
	9	11	12	29.4	120.8	975	33	TY
	9	11	18	30.5	120.1	985	25	STS
	9	12	00	31.9	119.5	995	20	TS
	9	12	06	32.9	119.4	995	20	TS
	9	12	12	34.1	119.9	995	20	TS
	9	12	18	35.3	121.1	995	18	TS
	9	13	00	35.9	122.7	1000	15	TD
	9	13	06	36.4	124.8	1002	15	TD
	9	13	12	36.8	126.2	1004	12	TD

Eyewall evolution of Typhoon Aere (2004)

Qingqing Li

Shanghai Typhoon Institute, and Laboratory of Typhoon Forecast Technique/CMA, Shanghai, China

1. Introduction

Eyewalls are one of the most intricate phenomena observed in tropical cyclones (TCs). Maximum winds and torrential rainfall occur usually in eyewalls. It is generally believed that the various eyewall evolutions are associated with complex thermodynamic and dynamic processes within the TC. Many studies have shown that the eyewall evolution is at least partly responsible for the intensity change of TCs (Black and Willoughby 1992; Blackwell 2000; Zhu et al. 2004). Therefore, the evolution of eyewalls especially due to the interaction between the TC circulation and environment is a very magnetic issue to investigate. Many studies have focused on the impact of terrain on landfalling TCs. It was documented that frictional effect of the landmass and reduction in heat and moisture supply from the ocean are the main causes of the evolution of landfalling TCs. Wu et al. (2003), Wu et al. (2009), and Li et al. (2009) examined the eyewall evolution of TCs making landfall in Luzon, revealing eyewall contraction, breakdown, and reformation. An interesting finding is the reformation of an eye larger than that prior to the landfall. In the current study, the eyewall evolution of Typhoon Aere (2004) is investigated as it is significantly influenced by the Taiwan terrain, and is compared with the eyewall evolution of TCs making landfall in Luzon.

2. Model configuration and preliminary model verification

A triple nested grid Weather Research Model (WRF, NCAR version) is employed to simulated the evolution of Typhoon Aere from 00 UTC 23 to 00 UTC 26 August 2004. The resolution of the finest, intermediate, and outer grid is 2, 6, and 18 km, respectively, and they include 259 × 289, 301 × 301, and 200 × 200 grid points, respectively. All meshes have 48 vertical levels. The Kain-Fritsch scheme (Kain and Fritsch 1993) is applied to the 18-km grids, and no cumulus parameterization is used in the 6- and 2-km domain. Other model physics options include the Morrison mixed-phase microphysics scheme and the MYNN 3rd level TKE boundary layer scheme.

Figure 1 shows the comparison of the simulated and observed track of Aere. The WRF model successfully reproduces the northwestward travel of Typhoon Aere during the period 00 UTC 23 to 06 UTC 24 August 2004., The simulated typhoon moves slightly southwestward before making landfall in Taiwan, and it makes landfall at the northern head of Taiwan. However, the observed typhoon seemingly does not make landfall in Taiwan, just passing by the northern part of Taiwan (Fig. 1). When entering the Taiwan Strait, both the observed typhoon and the modeled typhoon turn to the southwest. The simulated intensity change of the typhoon agrees fairly with that of the observation (not shown).

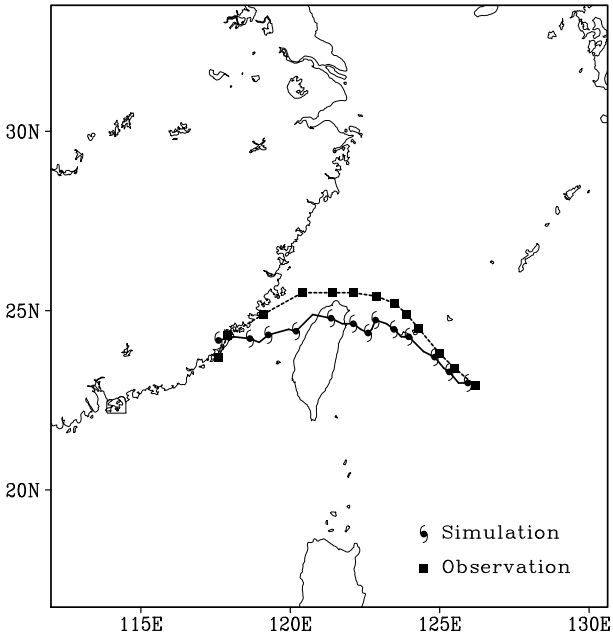

FIG. 1. Comparison of the tracks of the simulated TC (typhoon symbols) and observation (solid squares).

3. Eyewall evolution

Figure 2 depicts the simulated composite radar reflectivity, indicating the eyewall evolution of Typhoon Aere. Before 40 h, the typhoon eye is apparent, accompanied with intense convection in the eyewall. As the TC makes landfall in Taiwan, the eyewall breaks down. After 52 h, the typhoon inters the Taiwan Strait, with the strong and broad convection in the southern part of the system. Unlike the reformation of the large eyes examined by Wu et al. (2003), Wu et al. (2009), and Li et al. (2009), the eyewall of Aere seems not to accomplish the reformation, just exhibiting a partial-eyewall feature. However, the convection in the storm center is enhanced, when the inner core is located in the strait. Through examining the surface latent and sensible heat fluxes, it is found that the breakdown of the eyewall and the weakening of Aere after landfall are mainly due to the great reduction of heat fluxes from the underlying surface, and the recovery of the surface heat fluxes contributes to the development of convection in the inner-core region.

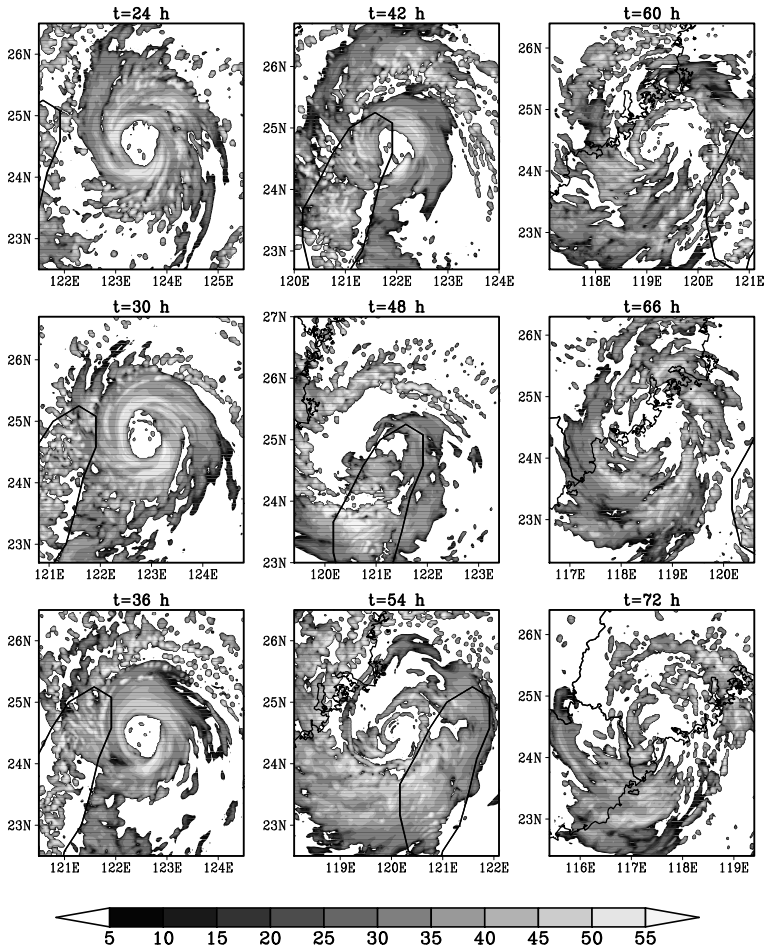

FIG. 2. Composite radar reflectivity (dBZ).

Wu et al. (2009) demonstrated that the formation of a large eyewall results from the formation of the outer eyewall as the storm reenters the water. For the current case, no large eye is observed. When the simulated storm is situated in the Taiwan Strait, a high-PV band is present in the southern sector of the storm (Fig. 3a). Apparently, the diabatic heating is the key factor contributing to the PV generation in the abovementioned high-PV band (Fig. 3d). The cyclonic advection is responsible for the redistribution of the large PV (Fig. 3b) and axisymmetrization which is associated with the formation of the outer eyewall. Looking at the details of Fig. 3b, pronounced PV advection occurs in the western and southern part of the near-core region, with relatively weaker advection in the north. Wang (2008) found that strong horizontal deformation, especially due to shearing deformation, elongates and filaments most of scalars in the rapid filamentation zone, thus axisymmetrizing and stabilizing PV asymmetries. Figure 4 shows the rapid filamentation zone (filamentation time < 45 min) in the west and south of the near-core region where the high-PV band is observed (Fig. 3a). No rapid filamentation zone occurs in the north of the near-core region, making the axisymmetrization of high PV unable to arise herein. Thus, although diabatic heating triggers the generation of high PV, the axisymmetrization of PV cannot accomplish owing to the lack of the rapid filamentation zone in the norther part of the near-core region. The outer eyewall does not form in the simulation.

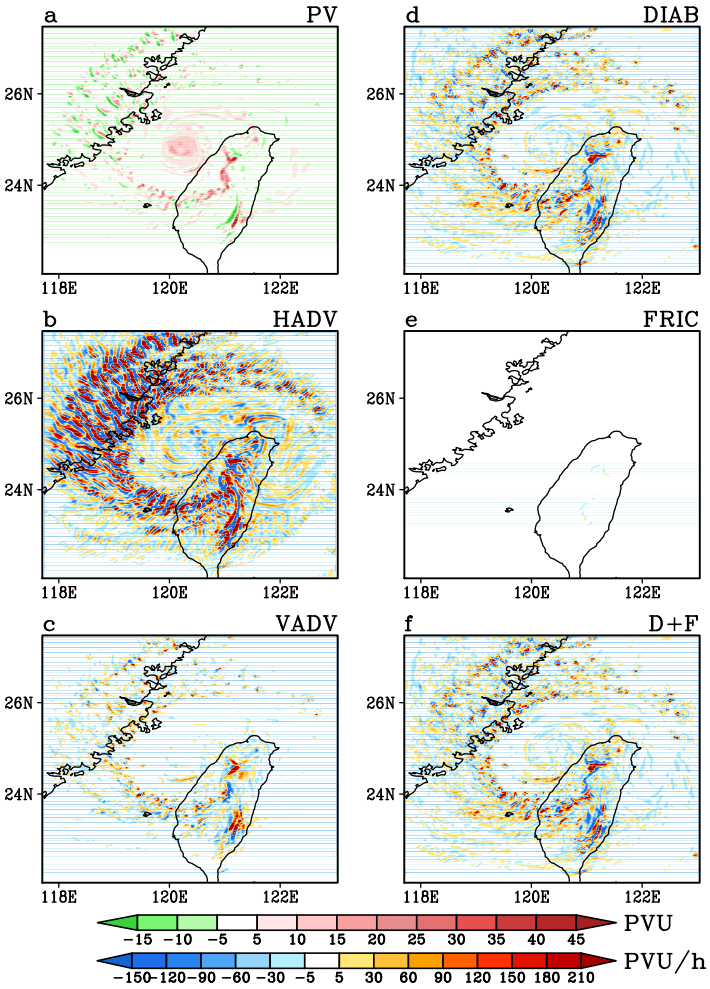

FIG. 3. The local changes of PV at 52 h and at 3 km due to the horizontal (HADV) and vertical (VADV) advection of PV, diabatic heating (DIAB), and friction (FRIC); D + F denotes the sum of diabatic heating and friction.

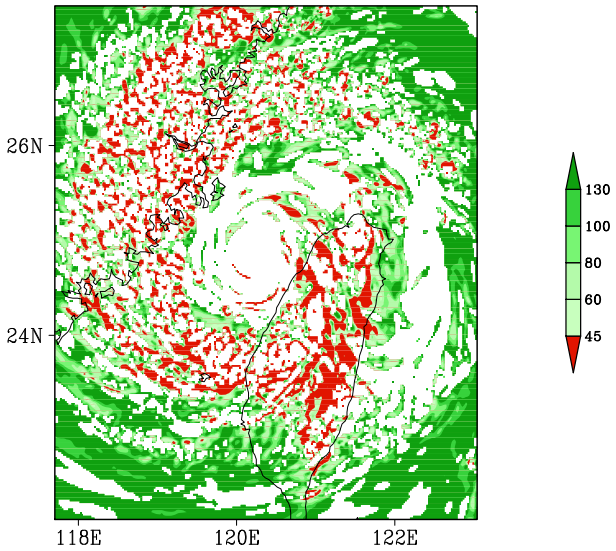

FIG. 4. Filamentation time (min) at 3 km and at 52 h.

References

Black, M. L., and H. E. Willoughby, 1992: The Concentric eyewall cycle of Hurricane Gilbert. *Mon. Wea. Rev.,* **120**, 947–957.

Blackwell, K. G., 2000: The evolution of Hurricane Danny (1997) at landfall: Doppler-observed eyewall replacement, vortex contraction/intensification, and low-level wind maxima. *Mon. Wea. Rev.,* **128**(12), 4002–4016.

Kain, J. S., and J. M. Fritsch, 1993: Convective parameterization for mesoscale models: The Kain-Fritsch scheme. The Representation of Cumulus Convection in Numerical Models, *Meteor. Monogr.,* No. 46, Amer. Meteor. Soc., 165-170.

Li, Q., Y. Duan, G. Fu, and, H. Yu, 2009: Numerical investigation of the eyewall evolution of a tropical cyclone. *Acta Meteorologica Sinica* (in press).

Wang, Y., 2008: Rapid filamentation zone in a numerically simulated tropical cyclone. *J. Atmos. Sci.*, **65**, 1158–1181.

Wu, C.-C., H.-J. Cheng, Y. Wang, and K.H. Chou, 2009: A numerical investigation of the eyewall evolution in a landfalling typhoon. *Mon. Wea. Rev.*, **137**, 21–40.

Wu, C.-C., K.-H. Chou, H.-J. Cheng, and Y. Wang, 2003: Eyewall contraction, breakdown and reformation in a landfalling typhoon. *Geo. Res. Letts.,* **30,** 1887, doi: 10.1029/2003GL017653.

Zhu, T., D.-L. Zhang, and F. Weng, 2004: Numerical simulation of Hurricane Bonnie (1998). Part I: Eyewall evolution and intensity changes. *Mon. Wea. Rev.,* **132**, 225–241.

Gradient-wind Momentum Approximation and Dynamics of Boundary Layer in Tropical Cyclone

Yuan Wang, Yunwu Zhao, Jinjie Song

(Key Laboratory of Mesoscale Severe Weather/Ministry of Education;

and School of Atmospheric Sciences, Nanjing University, Nanjing 210093)

In classic Ekman (1905) pumping theory, the first analytic solutions of the planetary boundary layer (BL) dynamics have been obtained under the balances among the pressure-gradient force, the Coriolic force, and the frictional force. However, classic Ekman theory only includes the geostrophic effects but neglects the ageostrophic ones. Geostrophic momentum approximation (which is also called semi-geostrophic theory) was proposed by Hoskins in 1975, which measures the ageostrophic deviation by the Rossby number (R_O). The small-parameter expansion method was used and first-order approximation of the Rossby number was obtained. Geostrophic momentum approximation partly includes the ageostrophic deviation between the real wind and the geostrophic wind, which is replacing the advected momentum by the geostrophic wind, but retaining the advecting velocities. Wu and Blumen introduced the geostrophic momentum approximation into the boundary layer dynamics in 1982. In their job, four-force balancing is established including the pressure-gradient force, the Coriolis force, the turbulent friction, and the ageostrophic deviation. The hodographs in their job could distinguish the cyclonic systems with the anti-cyclonic ones. The geostrophic coordinates have also been utilized by Blumen and Wu in 1983, which makes the questions of the atmospheric boundary layer under the geostrophic momentum approximation more simplified.

Tropical cyclone (TC), which is an intense storm generated on the tropical ocean, has strong self-rotation whose general centrifugal force (centrifugal force caused by the self-rotation of the TC) is very important and cannot be neglected. On the other hand, although the basic flow should follow the gradient-wind balance, the deviation should also be imposed on the gradient wind.

Dealing problems of the Boundary Layer of the Tropical Cyclone (TCBL) with geostrophic momentum approximation will face two problems: On one hand, the small-parameter expansion method needs the magnitude of the inertial deviation term (R_O) to be no more than 0.4. However the strong rotation in TC makes the magnitude of the general centrifugal force much larger than the Coriolis force, which leads to the unavailability of the condition $R_O \le 0.4$. Therefore, the geostrophic momentum approximation cannot be used directly to deal with TCBL problems. On the other hand, the deviation is measured by the Rossby number in geostrophic momentum approximation. The magnitude of $R_O = \frac{U}{fL}$ will be constant if the characteristic velocity and horizontal spatial scale are certain, which cannot express the inertial deviation changing with different angular velocity in different positions in TCBL. Therefore, corrections should be made on the geostrophic momentum approximation when dealing TCBL problems.

In order to solve the problem above, the basic flow in the tropical cyclone is based on the gradient-wind balance. Consequently, the general centrifugal force is included as a single force. After including the inertial deviation, the similar small-parameter expansion as Hoskins in 1975 could utilized, and the nonlinear terms in the deviation term could be linearized. This process is called GRadient-wind Momentum Approximation, which is replacing the advected momentum by the gradient wind, but retaining the advecting velocities. The gradient-wind momentum approximation partly includes the deviation between the real wind and the gradient wind. In the gradient-wind momentum approximation, a new parameter $\tilde{R}_O = \dfrac{U}{(f+\Omega)L}$ is introduced which measures the magnitude of the deviation from the real wind to the gradient wind, and it could be simply understood as the inclusion of the rotation in the traditional Rossby number. Consequently, two questions mentioned above is solved.

The governing equations in the TCBL with five-force balancing is established, including the inertial deviation linearized by the gradient-wind momentum approximation, the pressure-gradient force, the Coriolis force, the general centrifugal force, and the turbulent friction. The top of the TCBL is the free atmosphere with gradient-wind balance, while the underlying surface is inhomogeneous with topography and different eddy viscosity. The horizontal wind could be obtained after solving the dimensionless equations, while the vertical velocity could be derived by integration of the 3-dimensional non-divergent continuity equation.

Comparisons among the classic Ekman theory, the geostrophic momentum approximation, and the gradient-wind momentum approximation are made. It can be easily seen that the classic Ekman theory is the approximation of the geostrophic momentum approximation when the movement assumed to be stationary and $R_O = 0$. However, the gradient-wind momentum approximation are based on the gradient-wind balance and including the rotation and it is a correction to the geostrophic momentum approximation when applied to the TC systems.

Some simplicities and DeMaria's TC model established in 1992 are applied to simulate the analytic solutions. The repetition of the analytic solutions clearly shows that, the differences between the gradient-wind momentum approximation and the classic Ekman theory are concentrated on the radial wind component, but not obvious on the tangential wind component. The radial wind under gradient-wind momentum approximation is larger than the one under classic Ekman theory at the middle and bottom level of the TCBL. The inclusion of the self-rotational effects makes the strengthening of the surface friction, which leads to the strengthening of the radial wind velocity no matter on the magnitude or extent. However, weak friction at the top level of the TCBL makes no obvious improvement to the radial wind velocity. In gradient-wind momentum approximation, not only the inflow strengthens evidently, but the maxima also tilt outwards with height increasing. However in classic Ekman theory, the maxima retains at the same radius with different height. In the vertical velocity distribution, The ascending velocities has a significant strengthen near the TC's center when compared with classic Ekman theory, the boundary of the ascending and descending motion changes from 200km to 250km. More inflow and lifting is in the TCBL under gradient-wind momentum approximation than the classic Ekman theory. The effects of convergence and lifting have been underestimated under classic Ekman theory due to the neglecting of the rotation.

The vorticity and convergence fields show that, the convergence field has an evident reinforcing, especially at the middle level of the boundary layer. In contrast, the vorticity field on the left panels varies irregularly: the contour of 1×10^{-4} is wider in gradient-wind momentum approximation, while the contour of 2×10^{-4} is narrower. This is because the convergence field is only controlled by the radial velocity, while the vorticity field is also controlled by the tangential velocity. The gradient-wind momentum approximation makes much alteration on radial but little on tangential velocity, which leads to the reinforcing of the

convergence field but irregularity of the vorticity field. The radial velocity of the typhoon 'Nuri' verifies the accuracy of the gradient-wind momentum approximation.

Another improvement is the forecasting of the height of the TCBL. The standard height of the BL in classic Ekman theory is $h_E = \sqrt{\frac{2K}{f}}$. If the eddy coefficient K remains constant, the TCBL's height also remains unchanged. After the inclusion of the angular velocity, the standard height of TCBL changes to $h_E' = \sqrt{\frac{2K}{f+\Omega}} = \sqrt{\frac{f}{f+\Omega}} h_E$, which means a significant decline due to the self-rotation of TC. The larger the angular velocity is, the lower the TCBL's height is. Therefore, the top of the TCBL shapes like a funnel which seems "inner lower, outer higher". If the underlying surface is inhomogeneous, rough surface (large eddy viscosity) will lead to high standard height, and vice verse.

WRFV3.1 is utilized to simulate the height of the typhoon Hagupit, and the simulation proves the validity of the gradient-wind momentum approximation with conclusion above. Three points are chosen along the direction of Hagupit's landfalling to show the differences quantitively, with A over the land, C over the sea, and B at TC's center. The result of gradient-wind momentum approximation fits well with the output of WRFV3.1 over the sea, and both have the trend of ascending with the radius increasing. Because gradient-wind momentum approximation in this study only contains dynamical processes but no thermal ones, mismatch occur on the left side of -30km. As a comparison for classic Ekman theory, the height remains constant on matter over the land or over the sea, which could not reveal the variation of TCBL's height well. Generally speaking, gradient-wind momentum approximation could obtain the height of TCBL more accurately.

In this paper, the gradient-wind momentum approximation is introduced and utilized to solve the problems of TCBL dynamics. Analytic solutions are obtained and simulated by applying the DeMaria TC model, and verified by observation and numerical modeling.

It can be obtained from the simulation, observation and modeling that gradient-wind momentum approximation has a significant improvement on the radial velocity of the TCBL compared with classic Ekman theory. The radial velocity becomes stronger in magnitude and wider in extent at the middle and bottom level of the TCBL, and the maximum center tilts with radius and height. The improvement of the radial velocity will simultaneously influence other relevant variables, such as the vertical velocity, the convergence field, and the stream field. The inclusion of the rotation brings more convergence in the TCBL. gradient-wind momentum approximation also improves the accuracy of the height of TCBL, with lower top at TC's center and higher at TC's edge.

Many assumptions are made in this paper and more studies are needed on the vertically variable angular velocity, eddy viscosity, and horizontal mixing in the future. Including the centrifugal force into the Ekman momentum approximation will bring more accuracy in TCBL dynamics.

The Mechanism of High Precipitation of Morakot : A Preliminary Numerical Test Study

TANG Jie

(Shanghai Typhoon Institute, Laboratory of Typhoon Forecast Technique/CMA, Shanghai, China)

To China mainland, the main precipitation induced by Morakot (0907) continued from 6 Aug to 11 Aug. Most of precipitation distributed in Taiwan,north of Fujian and a majority of of Zhejiang. During the whole, the amount of observation stations that total rainfall amount more than 500mm is much more than 970. In Taiwan, there is 81 stations that more than 1000 mm and 20 stations more than 2000mm. In many station including Tainan and Yushan, this process is a new historic record.

Generally,The main features of the precipitation during Morakot process is including: wide spread**,** high asymmetry, strong rainfall intensity, long duration and extremely high total precipitation amount. While landfall at China mainland, the main body of Morakot showed a distinct hollow **character for more than 48 hour.**

After crossing Taiwan, the center of Morakot stayed for more than 20 hour in the region of Taiwan strait and move quite slowly. During the period,a incompact but large eye occurred in the center of this typhoon(fig2.5).The strong south convective cloud was weakened by the friction of the central mountain in Taiwan island .From 08th 20h ,the south cloud cluster is intensified again. The lowest TBB had reached to -80 degree. Almost with the same time, from 8th14h to 9th 05h,the outer spiral cloud had affected Zhejiang and Fujian duratively.

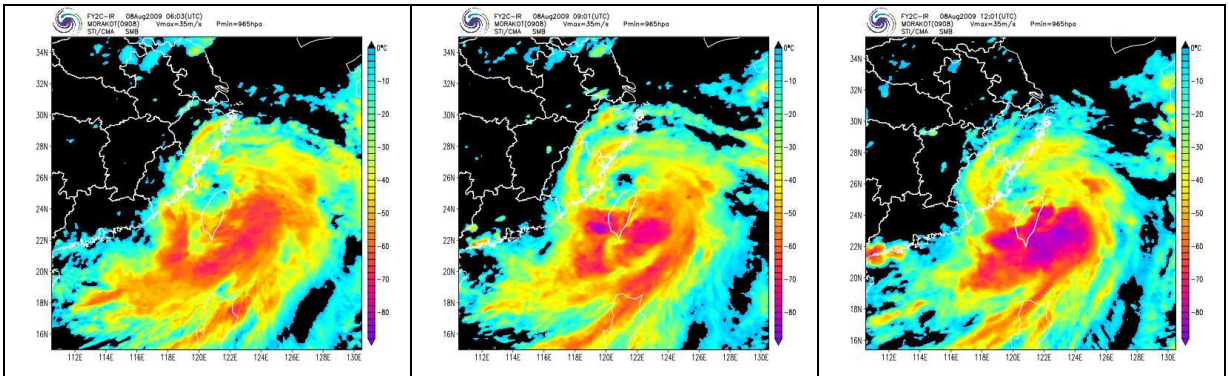

a 08th14h	b 08th17h	c 08th20h

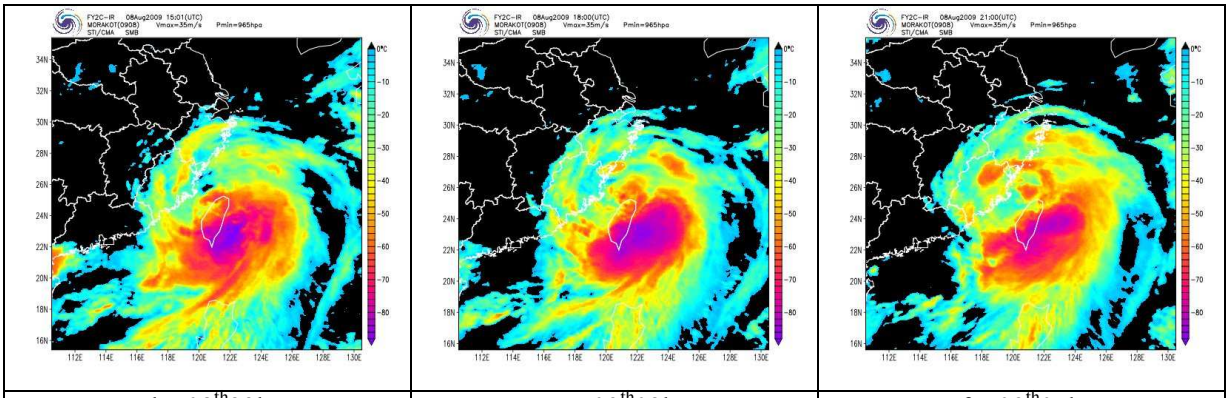

d 08th23h	e 09th02h	f 09th05h

fig 1 TBB of FY2C cloud from 08th14h to 09th05h

By high resolution by WRFv3.0,the high precipitation process of Morakot is reproduced. Hence, we can find that TD Goni(0907) located the north of South Sea during Morakot landfall process(fig2.6a). With Moving to the south along the coast line of Hainan island, Goni reintensifed to be tropical storm. And then ,Goni and Morakot jointly formed a large low pressure system(fig2.6b). While the intensified Goni move the south and east, the humidity flux of the south part of the large low pressure system is increased. After a few hours,the humidity supply of Morakot reached to the peak(fig2.6c,d).

Contrast the variation of Goni intensity,the humidity flux of the east part of Goni and of the south part of Morakot in 700 hPa. The humidity flux of Goni is increased followed the intensification of Goni at 08th00h. And the humidity supply to the south of Morakot reached to the maximum 12 hours after that. At 08th 12h，the center surface pressure of Goni reached the minimum,1006.5hPa,the humidity flux of the east part of Goni and of the south part of Morakot increased again one by one. The story happened twice proved that the intensification of Goni is in favor of the humidity supply of Morakot and also do some help to the consistence high precipitation of Morakot.

To verified the validity of the discussion shown above, a sensitive numerical test that reduced the intensity of Goni is put. Contrast the results, the moist supply of Morakot and Goni is smaller in sensitive test(fig2.7b) than in the control test(fig2.7a). This phenomenon was proved that the increased intensity of Goni can do good to the moist supply of Morakot and to the consistence of the structure of Morakot.

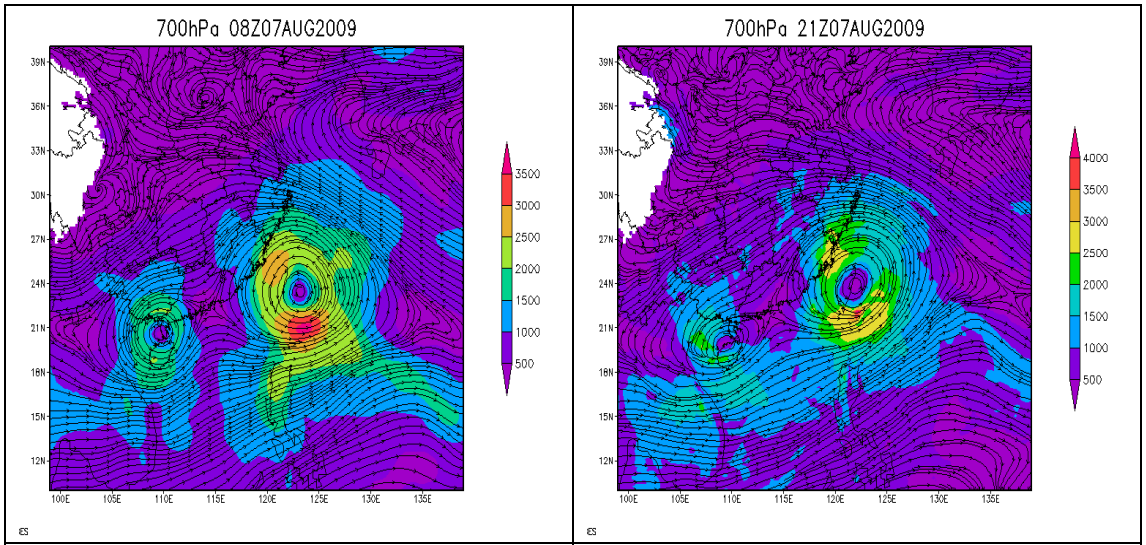

fig.2. a 07th11h 700hPa humidity flux （shaded）and horizontal fluid	fig.2b 08th05h 700hPa humidity flux （shaded）and horizontal fluid

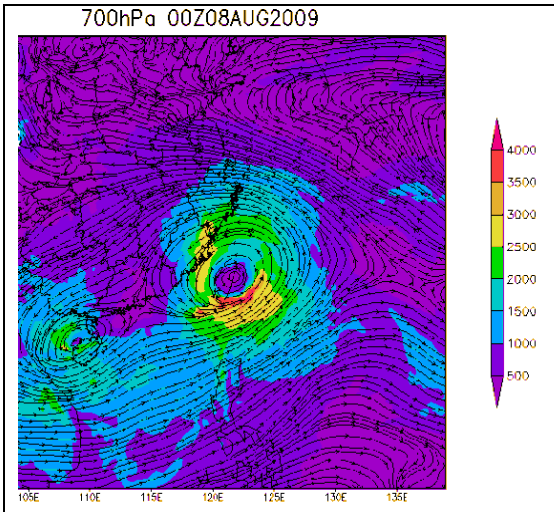

fig.2c 08th08h 700hPa humidity flux （shaded）and horizontal fluid

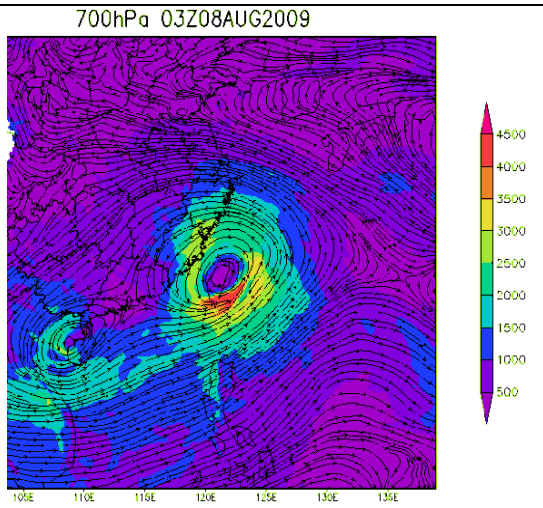

fig.2a 08th11h 700hPa humidity flux （shaded）and horizontal fluid

°

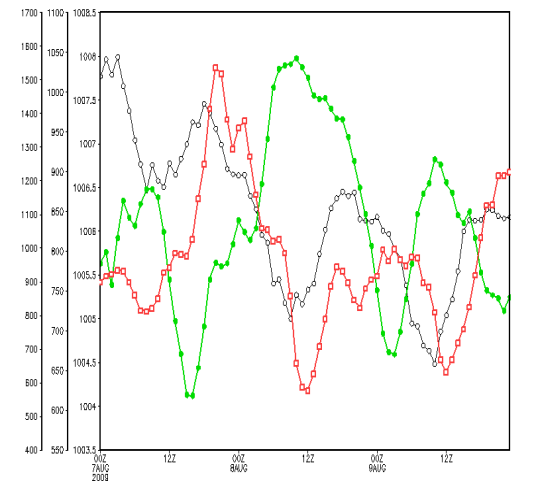

Fig.3a control test
Black thick line:minimum surface pressure of Goni,value showed by the rightmost y axis;
Red thick line:the humidity flux of the east part of Goni,value showed by the leftmost y axis;
Greeen thick line: he humidity flux of the south part of Morakot,value showed by the middle y axis;

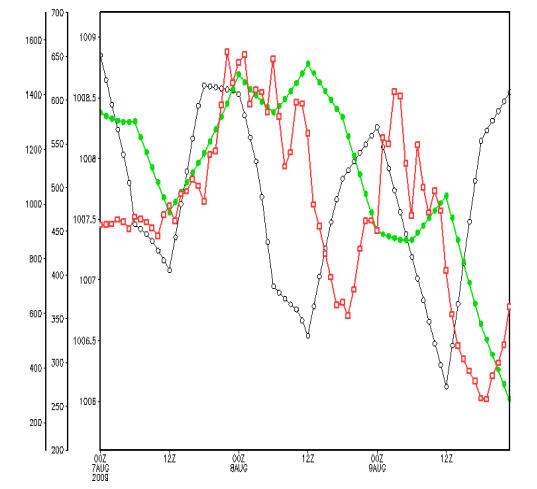

Fig3 b sensitive test by reduce the intensity of Goni
Black thick line:minimum surface pressure of Goni,value showed by the rightmost y axis;
Red thick line:the humidity flux of the east part of Goni,value showed by the leftmost y axis;
Greeen thick line: he humidity flux of the south part of Morakot,value showed by the middle y axis;

Drawing the vertical section of Wenzhou where the extreme precipitation burst (fig4). After gained sufficient humidity from the southwest low level jet, the convection is induced and reached the top of troposphere more than 200hPa. The moist unstable air just located at the low level (lower than 700hPa) of the east region of Morakot but not in the middle level of troposphere. This maybe means the heavy precipitation burst in Fujian and Zhejiang is induced by convective instability originated from the east of Morakot.

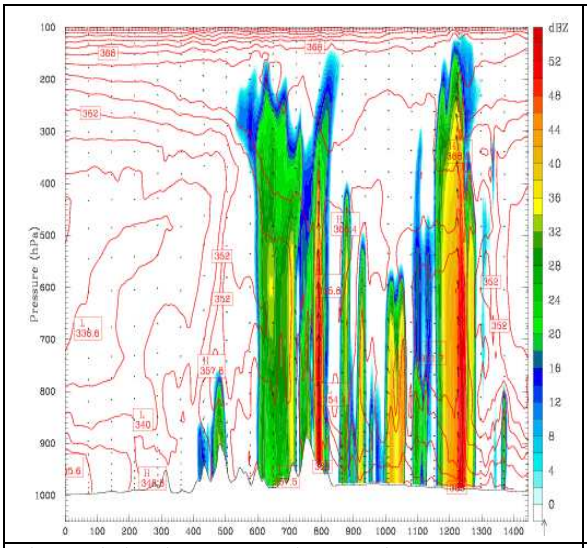

Fig4a vertical section across Wenzhou at 05Z/09
Shaded:simulated radar dbz，
Red thick line:equivalent potential temperature
Wind varb: 3-dimensional wind barb

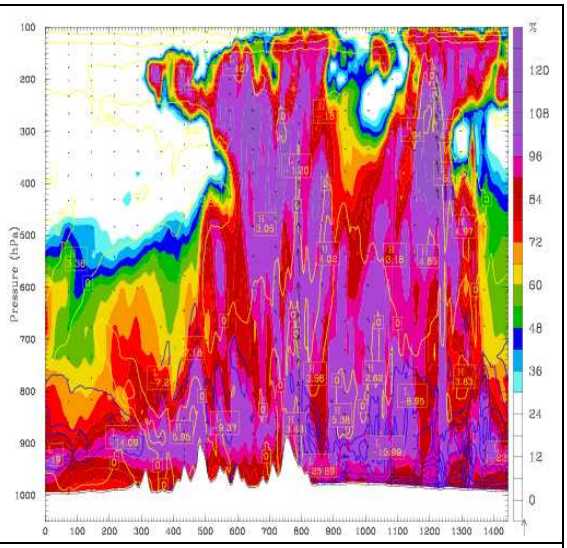

Fig4b vertical section across Wenzhou at 05Z/09，
Shaded: relative humidity
Thickline:convective instability (blue:unstable;yellow:stable)
Wind varb: 3-dimensional wind barb

Generally, the reintensification and southeastward movement of Goni and the incresment of southwest monsoon increased the southwest low lever moist flux. The sufficient energy and humidity from the southwest stream supply the development and consist of the large scale typhoon Morakot that standstilled at Taiwan Straits. Durative humidity supply at low level ,the topography effect and weak steering environment is the key reason of the extremely high rainfall by Morakot.

Acknowledgements

This work was supported by Supported by Major State Basic Research Development Program of China(No. 2009CB421505) , National Natural Science Foundation of China(No. 40875039， No. 40905029). Shanghai Typhoon Foundation Grants (No. 2008ST14）

Climatic Trend of the Tropical Cyclones' Influences on China's Mainland as Revealed by the Wind and Precipitation Observations

Ming YING and Baode CHEN

(Laboratory of Typhoon Forecast Technique, Shanghai Typhoon Institute, China Meteorological Administration, Shanghai, China)

1. Introduction

Severe wind and torrential rain, which are main causes of many nature hazards in China's land areas (Chen and Ding, 1979), are common accompanied phenomena of tropical cyclones (hereafter TCs). Their influences cover almost the second and third Ladder areas as shown in the Chinese topography (Fig. 1a; STI/CMA, 2007). Storm winds associated with TCs are more intense near the coastal areas (Yang and Lei, 2004; STI/CMA, 2007), and heavy rains cover considerable extents. Statistically TC rainfall outweighs more than 10% of the annual precipitation in some areas (Rodgers, et al., 2000; Ren et al., 2006; STI/CMA, 2007). Therefore, understanding climatic trends of influences of wind and rainfall resulted from TCs is very important in assessment of the risk of TC impacts.

2. Data and methodology

The wind and precipitation observed in the period of 1955 to 2007 at 676 stations with the records more than 50 years are used (Fig. 1b), which cover the most of areas that are potentially affected by TCs.

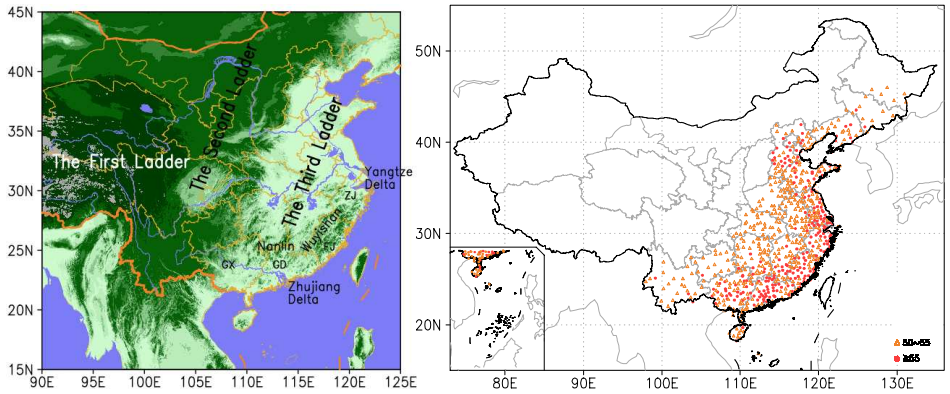

(a) (b)

Fig. 1 The Chinese topography (a), and the distribution of stations with observations more than 50 years (b).

To obtain the climatic trends, quantile regression on medians (Koenker and Bassett, 1978; Koenker, 2005; Barbosa, 2008) is applied to the wind and rainfall observations at each station. Not only has the median an advantage over mean in describing the averaging status, but also is the quantile regression suitable to estimate the conditional quantiles without assuming the form of the probability distribution. Additionally, a bootstrap method with 5000 re-sampling (Xu, 2006) is used to estimate the significant levels of the trends.

3. Results

Figure 2 shows trends of annual days with Beaufort-Scale 8 wind related to the TCs as well as trends of

extreme sustained wind and gust wind. Both the windy days and the extreme winds present significant trends in most coastal areas of China, especially in the southeast coast. Specifically, the decreasing trends of windy days are mostly observed at the stations in the coastal area of Fujian (FJ) Province, while the increasing ones are found in the Yangtze Delta and near Zhanjiang City in Guangdong (GD) Province (Fig.2a). In terms of the maximum sustained winds, the two regions with increasing trends are similar to those in Fig.2a, whereas the stations with decreasing trends scatter more in the coastal area of Guangdong Province than in that of Fujian Province (Fig.2b). As to the extreme gust winds, the significant decreasing trends are clear at most stations in the southeast coast, while the primary regions with increasing trends are still identified in the Yangtze Delta and close to Zhanjiang City (Fig.2c). In general, the main feature of those trends indicates that the coastal severe winds caused by TCs decline significantly in an average sense, which reflects weakening trends of TCs which affected China mainland.

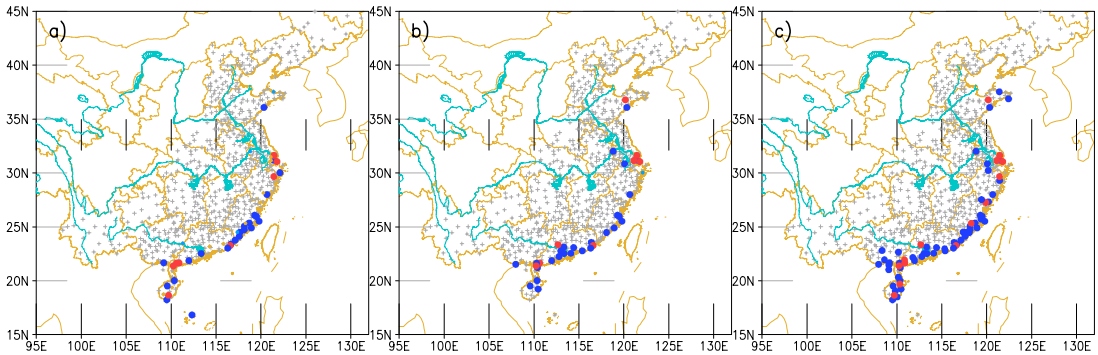

Fig. 2 The significant climatic trends (dots) of the median for station observed TC winds. (a) the annual days of Beaufort wind scale 8 (≥17.2 ms^{-1}), (b) the maximum 2-min sustained winds, and (c) the extreme gust winds. The grey cross marks the locations of stations; the color dots denote increasing (red and orange) and decreasing (blue and light blue) trends, respectively. The significant levels are in proportion to the size of dots, i.e. big and small ones are 95% and 90%, respectively.

On the other hand, the trends of TC rainfall are quite different from those of the winds (Fig. 3). The significant decreasing trends of the annual rainy days are found in the most areas from the tropics to mid-latitudes, although some increasing ones exist (Fig.3a), which are mostly limited to the south of Yangtze River. The distributions of the stations with significant trends are quite similar among the annual total precipitation, the maximum storm precipitation and the maximum daily precipitation (Fig.3b, 3c and 3d). Figures 3a-d show consistent spatial patterns of decreasing trends in the extra-tropical regions demonstrating that the influences of TCs are reduced in the north part of China. However, in the south part of China, the mix-up of stations with different trends seems to be from contributions of local factors.

As regards to the intensity of TC precipitation, it seems that the maximum daily rainfall is rarely changed since the proportion of stations with significant are really small and their locations are separate widely. However, as shown in Figure 3e, the maximum 1 hr precipitation exhibits significant increasing trends in some stations in the southeast area of China while few stations possess decreasing trends, which suggests enhanced intensity of TC rainfall in this area.

Aside from the collective features, the coastal stations possessing significant trends are distributing along the coastline except for the Zhujiang Delta (Fig. 1a). In addition, the stations far from the coastline are mainly located on the windward slopes of the chain of mountains lying in the southeast coastal regions, namely the Nanlin and the Wuyishan (Fig. 1a). These results indicate the essential roles of the terrain in the enhanced trends of the rainfall intensities. And to some extents, the increased rough of the land surface may have similar effects on the trends for stations in the Yangtze Delta and Zhujiang Delta where are flat plains.

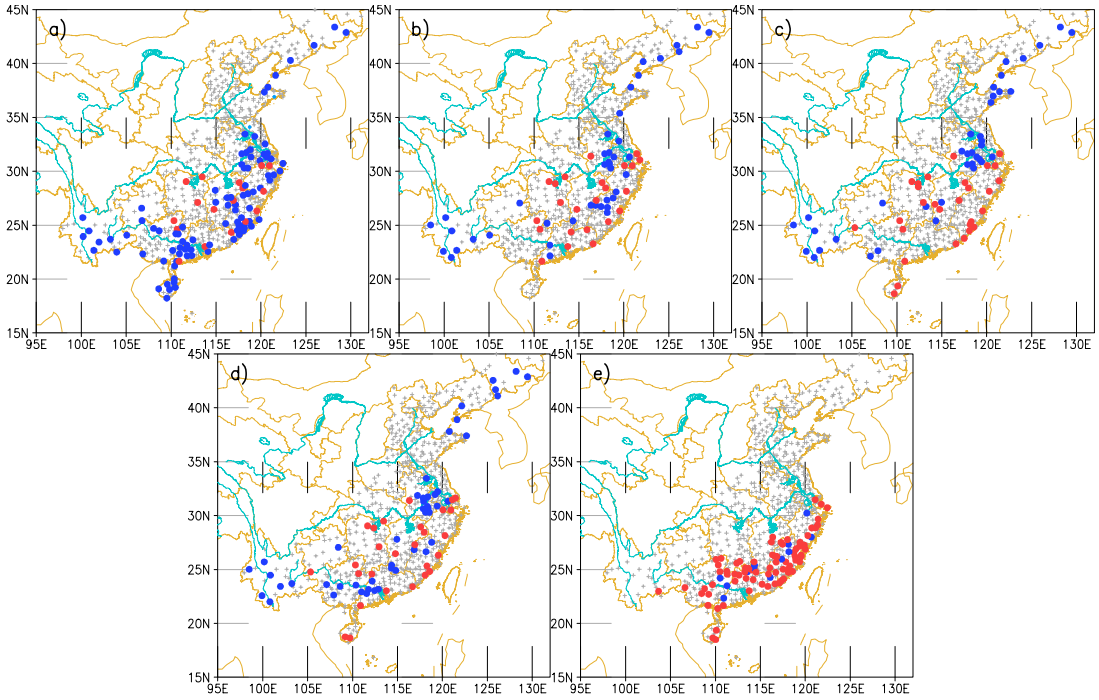

Fig. 3 Same as Fig. 2, but for the TC rainfall. (a) the annual rainy days, (b) the annual total precipitation, (c) the maximum storm precipitation, (d) the maximum daily precipitation, and (e) the maximum 1-hr precipitation.

4. Remarks

Although it is hard to reach a consensus on the issue of TC activity and the climate change, the results described here present evidence for the climatic trends of TCs affecting China. The evidence is primary based on two aspects of TCs that closely related to the general circulation and the hydrologic cycle, namely the storm wind and the storm precipitation, respectively. In a collective sense, the decreasing trends of storm winds observed in the southeast coastal area of China reveal the intensities of TCs affecting China are reducing. However, the increasing trends of the intensity of precipitation measured by maximum 1 hr rainfall demonstrate that the influences of TCs are rising. The discrepancy or inconsistency between the trends of storm wind and precipitation suggest that the manner how the circulation and hydrologic cycle are coupled together could be changing, which is needed to be investigated further in future.

References:

Chen, L., and Y. Ding, 1979: *An Introduction to Western Pacific Typhoons*. Science Press, Beijing, 491pp. (in Chinese)

Koenker, R, and G. W. Basset, 1978: Regression Quantiles, *Econometrica*, 46: 33-50.

Koenker, R, 2005: *Quantile Regression*, Cambridge University Press, New York, 349pp.

Barbosa, S. M., 2008: Quantile trends in Baltic sea-level. *Geophys. Res. Lett.*, 35: L22704, doi: 10.1029/2008GL035182.

Ren, F., G. Wu, W. Dong, X. Wang, Y. Wang, W. Ai, and W. Li, 2006: Changes in tropical cyclone precipitation over China. *Geophys. Res. Lett.*, 33: L20702. Doi: 10.1012/2006GL027951.

Rodgers, E. B., R. F. Adler, and H. F. Pierce, 2000: Contribution of Tropical Cyclones to the North Pacific Climatological Rainfall as Observed from Satellites. *J. Appl. Meteorol.*, 39: 1658-1678.

Shanghai Typhoon Institute of China Meteorological Administration (STI/CMA), 2007: *Climatological Atlas*

of Tropical Cyclones Affecting China. Science Press, Beijing, 177pp.

Xu, K.-M., 2006: Using the Bootstrap Method for a Statistical Significance test of Differences between Summary Histograms. *Mon. Wea. Rev.*, 134: 1442-1453.

Yang, Y., and X. Lei, 2004: Statistics of Strong Wind Distribution Caused by Landfall Typhoon in China. *J. Tropical Meteorol.*, 20(6): 633-642. (in Chinese with English abstract)

Moist Frontogenesis Evolution during the Extratropical Transition (ET) process of the typhoon landfalled at China mainland

TANG Jie

(Shanghai Typhoon Institute, Laboratory of Typhoon Forecast Technique/CMA, Shanghai, China)

1. Introduction

Extratropical transition of TCs have discussed the importance of different factors including preexisting cyclonic system and latent heat release in previous papers (e.g.Browning,1998). Harr et.al (2000) treated the development of frontal characteristics as a manifestation of the physical processes that take place during ET firstly, since the change of frontal features signifies the evolution undergoing ET from a nearly symmetric TC structures to the typical asymmetric extratropical cyclone structure.

Cylonegenesis is always highly related with frontogenesis (Bluestein,1993 pp352). Thus, ET, which is defined by the process from a tropical cyclone to a extratropical cyclone, can be considered as a frontogenesis in some content. The difference between ET and classical Cylonegenesis maybe just is some tropical system character in ET process. This difference may make the evolution of the front during ET more complicate and distinct. If this is true then, detail diagnosis based on the front function is reasonable to understanding ET.

Petterssen (1956) defines frontogenesis as the tendency toward formation of a discontinuity in the density field or the intensification of an existing sloping transition surface. This frontogenesis also can be described by the discontinuity of potential temperature more often nowadays. And vector frontogenesis is defined as the Lagrangian temporal derivative of the horizontal potential temperature gradient (Keyser et al 1988). The vector frontogenetical function is shown in eq(1) and eq(2)

$$\vec{F} = F_n\vec{n} + F_s\vec{S} = -\frac{d}{dt}|\nabla_h\theta|\vec{n} + \vec{n}\cdot\left(\vec{k}\times\frac{d}{dt}\nabla_h\theta\right)\vec{S} \qquad (1)$$

F_n is the scalar frontogenetical function as shown and F_s is the rotational frontogenetical function.

Harr and ELSBERRY(2000) and Kitabatake(2000) diagnosed some ET cases by the vector frontogenetical function shown above respectively. And rotational frontogenesis induced by background circulation was found to be important to the reintensification of ET(Harr and ELSBERRY,2000). Up to now, there is few research discuss the role of frontogenesis during the reintensification process of ET happened in China mainland. Unlike other cases, ET process happened in China mainland always are affected by southwest low level jet with large humidity derive from monsoon. So the contribution of the moist to ET needed to be discussed in detail here.

Some typhoon cases that landfall at China mainland will be transient to have extratropical cyclone characters and be intensified again which is called as ET under the influence of southward and westward air stream. These ET cases with complicate structure always brought severe rainfall disaster. The 0108 typhoon named Toraji landfalled at Fujian on 31 Jul 2001 and finished ET at 00Z/02 02 Aug is such a typical ET case. This paper is to discuss the front evolution of the ET process of Toraji to study the detail story of ET cases happened in China mainland.

A brief model description and verification is introduced in section 2. And then the ET evolution is presented by the TBB figures and model result. The Last section is a preliminary summary.

2. Model description and verification

A nonhydrostatic version of the WRF model (version 3.0.1) is used to simulate ET process of Trojii. The twonested grid (54, 18 km) domains are used (ignore the domain figure) in two-way nesting. There are 31 levels in the vertical for all four nested domains. Total simulation time is 60 h, starting at 1200 UTC 31 Jul and ending at 0000 UTC 03 Aug 2001.

Figure1.a compares the model-simulated track of Toraji to the JMA best-track estimates, using results from the 18-km resolution domain. In general, the WRF simulates Toraji's track very well, especially its ET process moving from Shandong to Liaoning from 1800 UTC 31 Jul, albeit the model result is 3-5 h earlier than the observed track. Figure1.b shows that the 18-km simulated storm intensity, indicated by the minimum sea level pressure of 997.9 hPa, is weaker 4hPa and later about 6 hour than that of the JMA best-track estimates (994hPa) .The weak is maybe is due to the coarse resolution of 18 km.

Generally, this numerical test is similar with the observation. The result of WRF is successfully to repeat the ET process of Toraji.

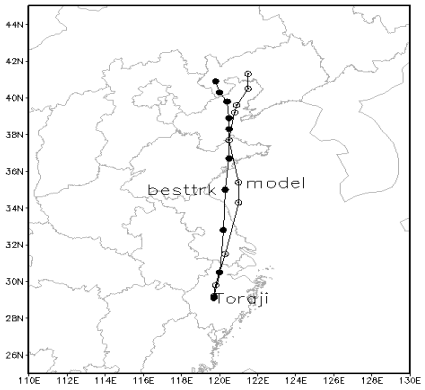

Fig1.a Track contrast:Besttrack vs Model. Black line with triangle is JMA besttrack; Blue thick line with hollow circular plate is model result .

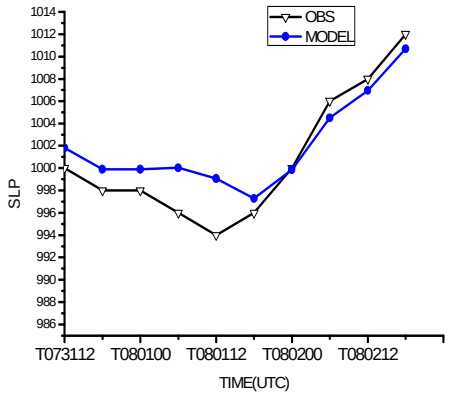

Fig1.b intensity contrast:Besttrack vs Model. Black line with triangle is JMA besttrack; Blue thick line with solid circular plate is model result .

3. Analysis for the front evolution of ET

After landfall, Toraji stalled at the coast of Fujian and Zhejiang more than 20 hours until 12Z/31 Jul. During that period, a middle latitude trough lied in the central China from the northeast to the southwest (Fig2.a). And then, Toraji, moving northwards and close to the trough, began to transform to be an extratropical cyclone (Fig2.b) at 19Z/31 Jul. After several hours, a cloud with more than 500km radius developed (Fig2.c). From 19Z/31 Jul to 08Z/01 Aug, Toraji interacted with the middle trough. Several MCS occurred in the circulation of Toaji,inducing rainstorms from Jiangsu to Liaoning region（Fig2.d）.

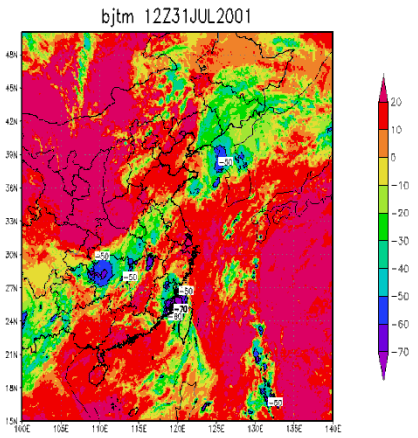

Fig.2a TBB at 1200UTC 31,July

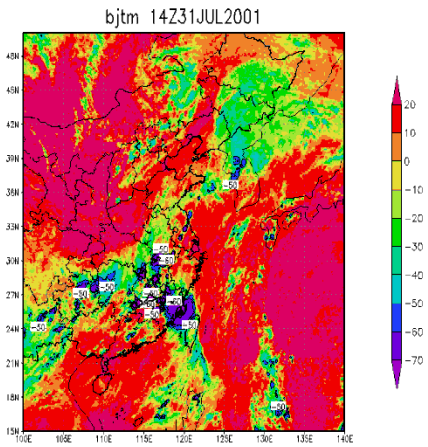

Fig.2b TBB at 1400UTC 31,July

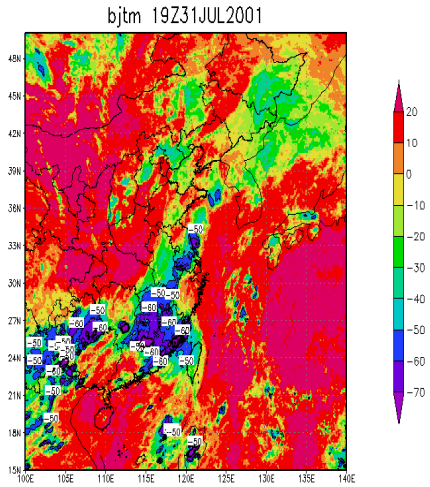

Fig.2c TBB at 1900UTC 31,July

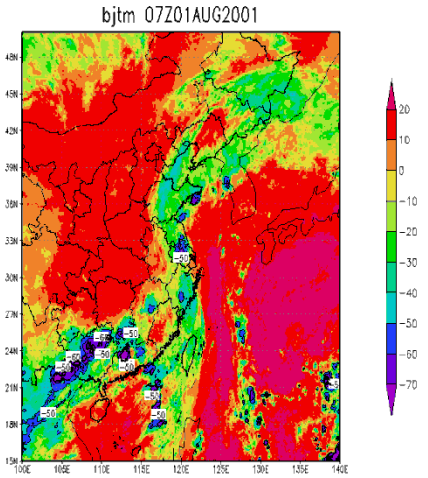

Fig.2d TBB at 0700UTC 1,Aug

To the further discussion of front evolution, extending the 2-dimensional vector frontogenetical function shown in eq(1) to be 3-dimensional vector frontogenetical function

$$\vec{F} = F_n\vec{n} + F_S\vec{S} + F_z\vec{k} = -\frac{d}{dt}\nabla_h\theta_e\vec{n} + \vec{n}\cdot\left(\vec{k}\times\frac{d}{dt}\nabla_h\theta_e\right)\vec{S} + \frac{d}{dt}\left(\frac{\partial\theta_e}{\partial z}\right)\vec{k} \qquad (2)$$

And F_n, F_S, F_z is the frontogenetical function in three direction .They are called as scalar frontogensis, rotational frontgenesis and vertical frontgenesis，shown as below.

$$F_n = -\frac{1}{|\nabla\theta_e|}\left\{\left[\frac{\partial\theta_e}{\partial x}\frac{\partial}{\partial x}\left(\frac{d\theta_e}{dt}\right) + \frac{\partial\theta_e}{\partial y}\frac{\partial}{\partial y}\left(\frac{d\theta_e}{dt}\right)\right] + \frac{\partial\theta_e}{\partial x}\left(-\frac{\partial\theta_e}{\partial x}\frac{\partial u}{\partial x} - \frac{\partial\theta_e}{\partial y}\frac{\partial v}{\partial x}\right) + \frac{\partial\theta_e}{\partial y}\left(-\frac{\partial\theta_e}{\partial x}\frac{\partial u}{\partial y} - \frac{\partial\theta_e}{\partial y}\frac{\partial v}{\partial y}\right) + \frac{\partial\theta_e}{\partial z}\left(\frac{\partial\theta_e}{\partial x}\frac{\partial w}{\partial x} + \frac{\partial w}{\partial y}\frac{\partial\theta_e}{\partial y}\right)\right\}$$

(3)

$$F_s = -\frac{1}{|\nabla\theta_s|}\left\{\left[\frac{\partial\theta_s}{\partial y}\frac{\partial}{\partial x}\left(\frac{d\theta_s}{dt}\right)+\frac{\partial\theta_s}{\partial x}\frac{\partial}{\partial y}\left(\frac{d\theta_s}{dt}\right)\right]+\frac{\partial\theta_s}{\partial y}\left(-\frac{\partial\theta_s}{\partial x}\frac{\partial u}{\partial x}-\frac{\partial\theta_s}{\partial y}\frac{\partial v}{\partial x}\right)-\frac{\partial\theta_s}{\partial x}\left(-\frac{\partial\theta_s}{\partial x}\frac{\partial u}{\partial y}-\frac{\partial\theta_s}{\partial y}\frac{\partial v}{\partial y}\right)+\frac{\partial\theta}{\partial z}\left(\frac{\partial\theta_s}{\partial x}\frac{\partial w}{\partial y}-\frac{\partial w}{\partial x}\frac{\partial\theta_s}{\partial y}\right)\right\}$$

(4)

$$F_z=\frac{\partial}{\partial z}\left(\frac{d\theta_s}{dt}\right)-\left(\frac{\partial\theta_s}{\partial x}\frac{\partial u}{\partial z}+\frac{\partial\theta_s}{\partial y}\frac{\partial v}{\partial z}+\frac{\partial\theta_s}{\partial z}\frac{\partial w}{\partial z}\right) \qquad (5)$$

From fig3.a and fig3.b,there is a obvious warm frontogenesis process on the 3KM height in the north part of Toraji under the effect of the inrush of arid cold air from upper levels Fig3a-b).The warm front, beginning from the north part, extended of Toraji from the southwest to the northeast. At the south of front, a strong low level jet stream supply larg mount of humidity to the front. And vertical section of the front structure shows that the warm front is mainly in the low level troposphere(fig.4.a).This maybe means the warm front is highly related to the south warm air at the leverl lower than 3KM. And the low level warm frontogensis is more due to the vertical frontogenesis,Fz. And fig4a-d also means the genesis of the warm front is induced by scalar frontogensis and vertical frontogensis. Further diagnosis shows that the divergence and adiabatic at low level is the main role in the frontgenesis.

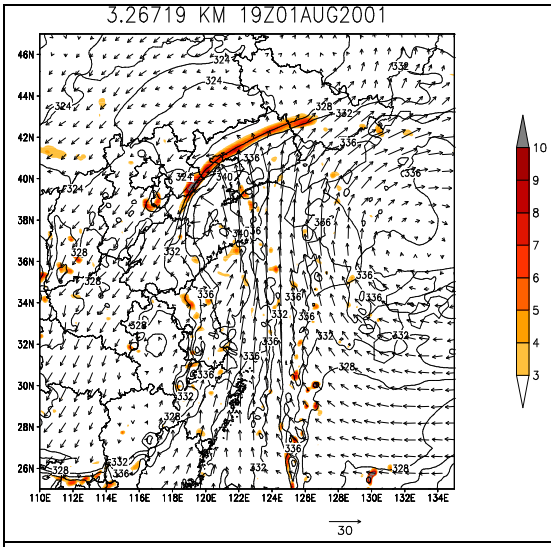

Fig3.a frontogenesis of Toraji on 3KM 19Z01Aug,Color shaded:Moist frontogenesis function on 3KM ;Black thick line: equivalent potential temperature on 3KM ; Black barb:Wind vector on 3KM

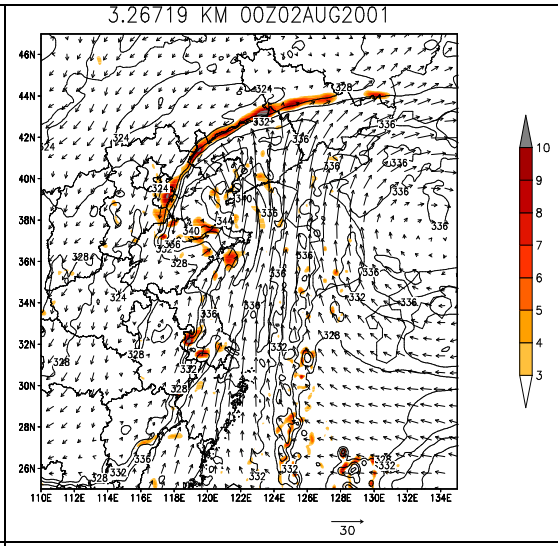

Fig3.b frontogenesis of Toraji on 3KM 00Z02Aug,Color shaded:Moist frontogenesis function on 3KM ;Black thick line: equivalent potential temperature on 3KM ; Black barb:Wind vector on 3KM

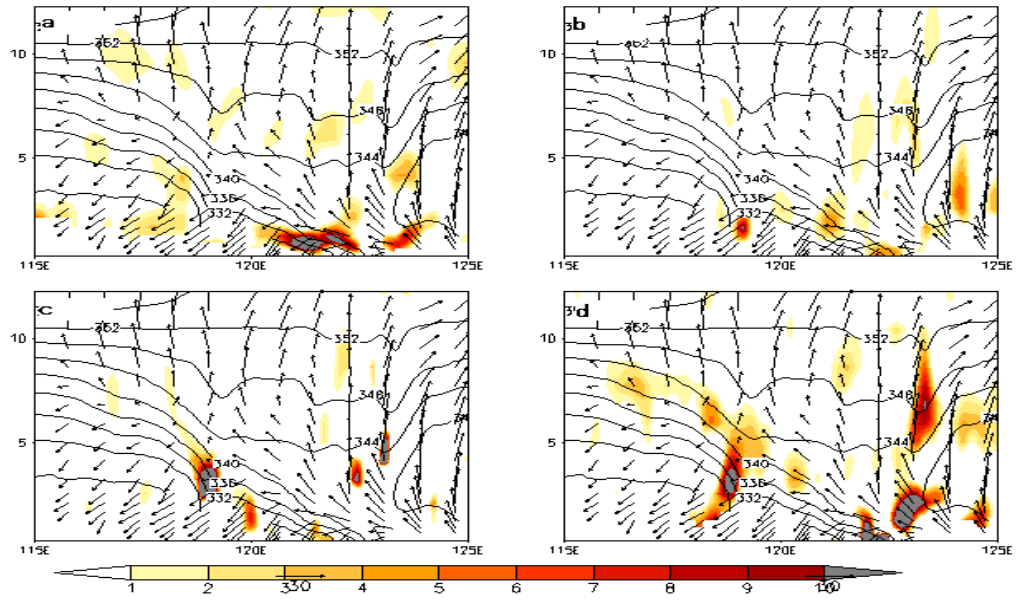

Fig 4 Frontogenesis vertical section along 41°N at 03Z02AUG

a：total moist frontogenesis b:Fs term c; Fn term d:Fz term

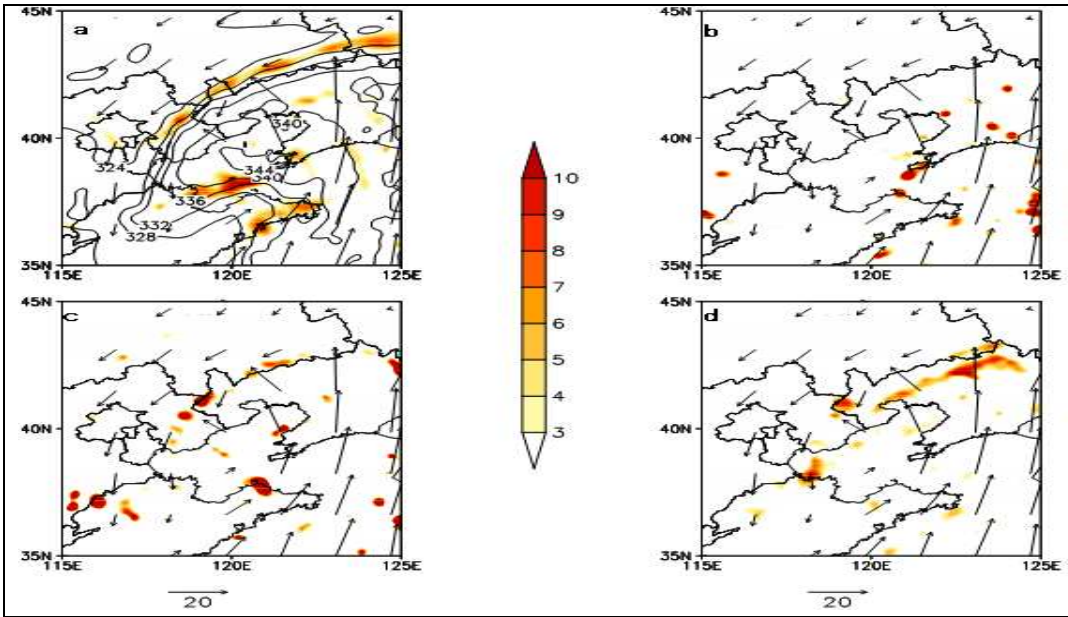

Fig 5 Frontogenesis on 3KM at 02Z02AUG

a：total moist frontogenesis b:Fs term c; Fn term d:Fz term

4 Summary

A numerical resolution is employed to simulate the frontal evolution of tropical cyclone Toraji(0108).By preliminary front diagnosis ,it is found there is a warm front developed in the north part of Toraji. And this low level warm front is related with the low lever jet stream originated in monsoon. During the frontogensis,the divergence and adiabatic in low to middle level is the main role. This maybe means some mechanism relate with adiabatic heating in low-middle level during the ET process of toraji.

More verify and descript work is necessary to judge the importance of different factor of vector Frontgenesis equation in (2)

Acknowledgements

This work was supported by Supported by Major State Basic Research Development Programof China(No. 2009CB421505) , National Natural Science Foundation of China(No. 40875039， No. 40905029). Shanghai Typhoon Foundation Grants (No. 2008ST14）

Reference

Browning,K.A. G. Vaughan, and P. Panagi, 1998: Analysis of an ex-tropical cyclone after its reintensification as a warm-core extratropical cyclone. Quart. J. Roy. Meteor. Soc., **124,** 2329–2356.

Bluestein.H.B.1993:Synoptic-Dynamic Meteorology in Midlatitudes, vol.II Observations and Theory of Weather SYSTEM Oxford Univ. Press, New York

Colle, B.A., 2003: Numerical Simulations of the Extratropical Transition of Floyd (1999): Structural Evolution and Responsible Mechanisms for the Heavy Rainfall over the Northeast United States. *Mon. Wea. Rev.*, **131**, 2905–2926.

Harr, P.A., and R.L. Elsberry, 2000: Extratropical Transition of Tropical Cyclones over the Western North

Kitabatake, N., 2008: Extratropical Transition of Tropical Cyclones in the Western North Pacific: Their Frontal Evolution. *Mon. Wea. Rev.*, **136**, 2066–2090.

Klein, P.M., P.A. Harr, and R.L. Elsberry, 2000: Extratropical Transition of Western North Pacific Tropical Cyclones: An Overview and Conceptual Model of the Transformation Stage. *Wea. Forecasting*, **15**, 373–395.

Pacific. Part I: Evolution of Structural Characteristics during the Transition Process. *Mon. Wea. Rev.*, **128**, 2613–2633.

Targeting Studies for Extra-tropical Transition of Hurricane Fabian: Signal Propagation, the Interaction between Fabian and Midlatitude Flow, and Observation Strategy

Hua Chen and Weiyu Pan

Department of Atmospheric Sciences, Nanjing University of Information Science & Technology, Nanjing, P. R. China

Abstract

This study examines how the impact of targeted observations propagates during the extra-tropical transition (ET) of Hurricane Fabian. Signal (forecast difference between denial experiments and Control experiment) propagation can reveal the interaction between the tropical cyclone (TC) and the midlatitude jet, and the energy dispersion or propagation of the TC undergoing ET also can be found out. The crucial role of an upper-level trough is discussed. Based on this study, a favorable strategy for targeted observations of ET is proposed, and several typical problems regarding the numerical prediction of ET are discussed.

The results show that the greatest signals along with their propagation are associated closely with various types of instabilities. In general, the signal first appears at the location of the TC, and then it propagates to the midlatitude jet through the interaction between the TC and the jet itself. Thereafter, signals propagate downstream along the jet and downward to the lower troposphere at the same time by way of Rossby wave packets - the jet essentially acting as a waveguide. Through the signal propagation and development in the jet, the impact of targeted observations seems sensitive to ET process.

The interaction between the TC and the jet occurs as that high θ (low potential vorticity) air flows out of the TC toward the northeast and into the jet below the tropopause. The interaction may be strengthened by an upstream trough at upper levels. The TC outflow enhances the PV gradient and baroclinity in the jet. Therefore, the jet becomes stronger and more baroclinically unstable. The signal propagation also indicates the energy dispersion of a TC undergoing ET.

The strong southwesterly flow ahead of the upper-level trough steers Fabian to higher latitudes, and strengthens the advection process of low PV air into the jet. Therefore, the development of the upper-level trough and its proximity to the TC are crucial for the interaction between the TC and the jet - and the resulting signal propagation. Small deviates from this synoptic situation may result in great differences in the signal propagation and the ET forecast. The most suitable region for targeting is likely located in a region where crucial synoptic process can magnify initial errors.

Table 1. Description of all experiments

Experiments	Description	Denial area
Control (CT)	All observations used	
Sensitive (SE)	All observations used except in targeted area	Area located within 300km of the TC center at every vertical layer

Random (RD)	All observations used except in random area	A random selected area located at the TC periphery at every vertical layer
Atlantic (AT)	All observations used except in the northern Atlantic Ocean	Entire the northern Atlantic Ocean at every vertical layer

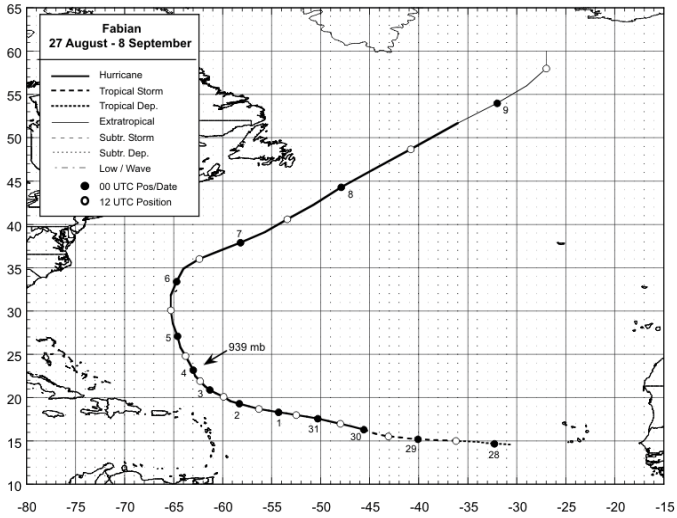

Figure 1. Best track positions for Hurricane Fabian, August/September 2003

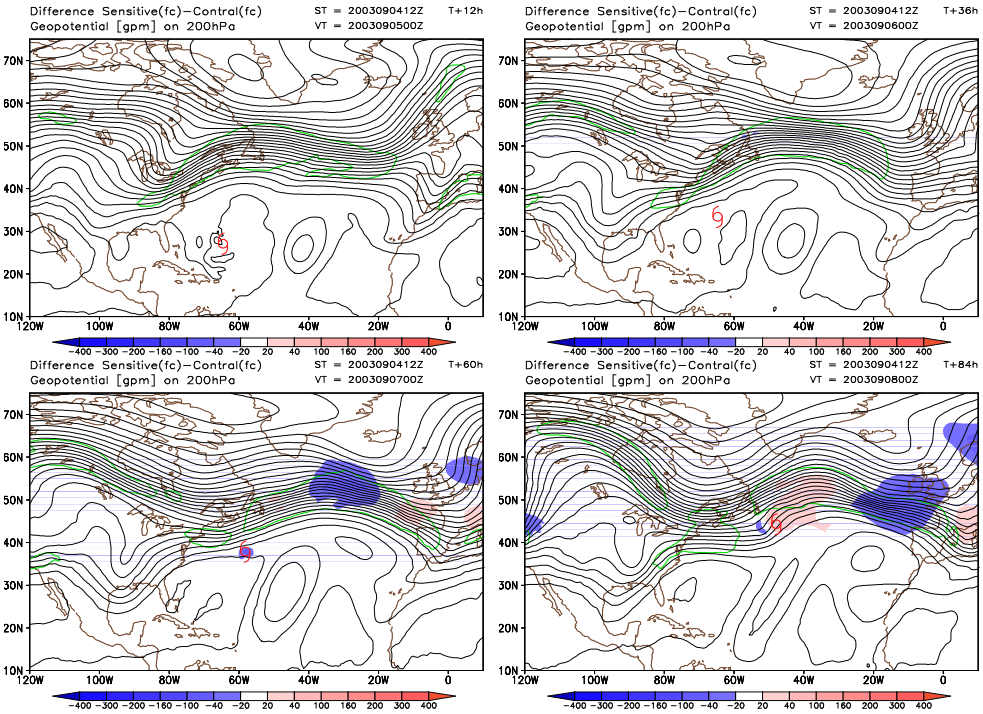

Figure 2. Forecast difference of geopotential height at 200 hPa between SE and CT. ST is the forecast initial time of 1200 UTC 4 September 2003, and VT is the forecast valid time with 24-hour increments. Black lines are the analysis value contour of geopotential height at 200 hPa in CT. Shaded areas represent the signals (Sensitive output minus Control output). Positive areas (red areas) mean that SE has a higher value. The jet regions where wind speed exceeds 40 m s^{-1} are outlined by green solid lines. Fabian is marked by the red symbol.

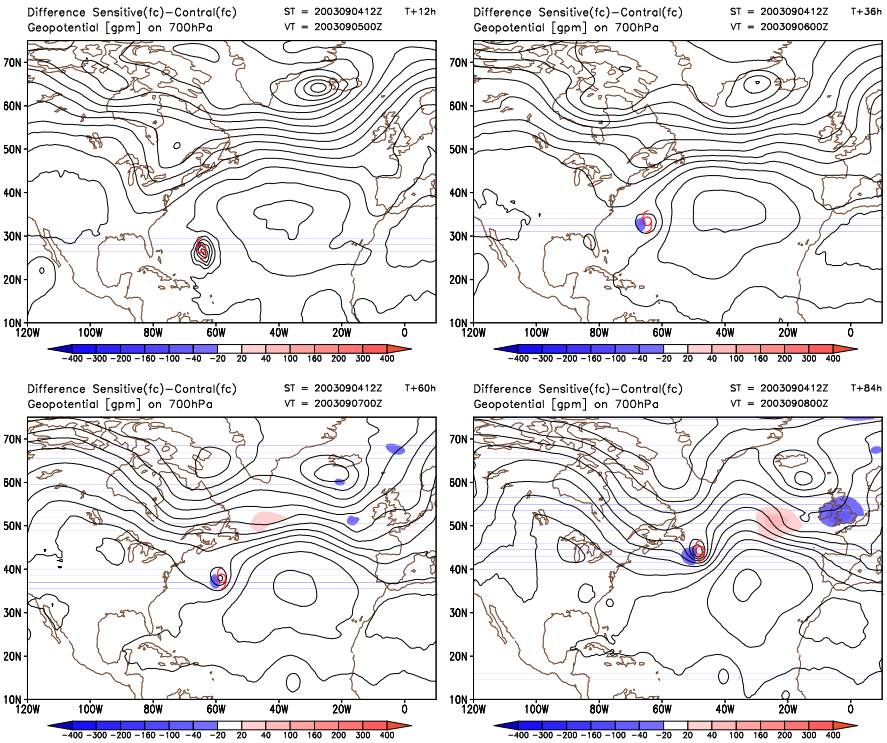

Figure 3. Forecast difference of geopotential height at 700 hPa between SE and CT. Same as Figure 2 except the level is 700 hPa.

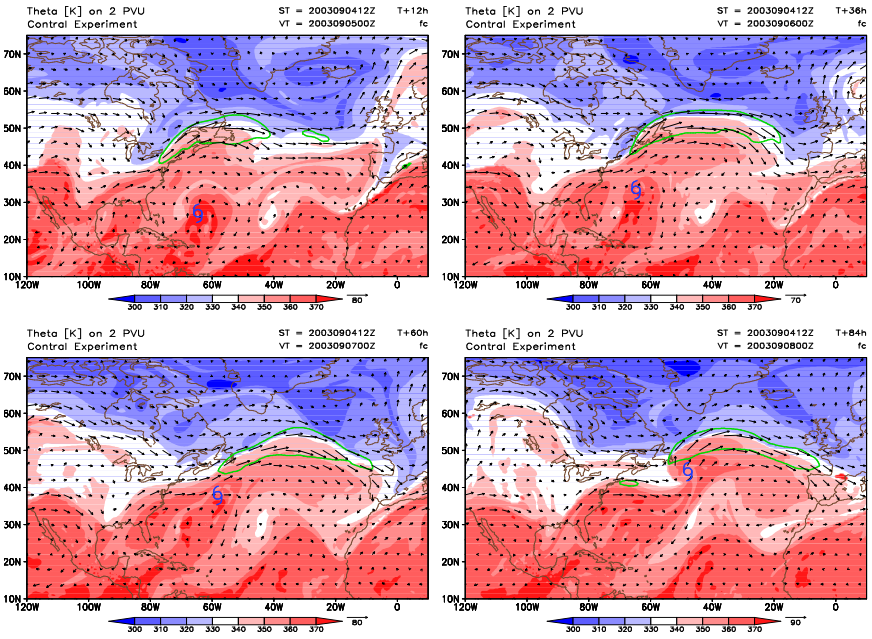

Figure 4. **θ**map on dynamic tropopause in CT. Shaded areas are potential temperature. Black arrows are wind vectors at 200 hPa. The strongest jet regions where wind speed exceeds 50m s^{-1} are outlined by green solid lines. ST is the forecast initial time of 1200 UTC 4 September, and VT is the forecast valid time with 24-hours increments. Both potential temperature and wind data are forecast output of CT.

An Overview on Study in Tropical Cyclone Remote Rainfall

Cong Chunhua[1,2], Chen Lianshou[2], Lei Xiaotu[3], Li Ying[2]

([1.]Shandong Meteorological Observatory,Jinan 250031;[2.]Chinese Academy of Meteorological Sciences ,Beijing 10081;[3.]Shanghai Typhoon Institute, Shanghai 200030)

Abstract

Tropical cyclone (TC) is severe disastrous rainfall weather system which has been studied for a long time by meteorologists. The rainfall related to TC, aside from its personal rainfall ,its remote rainfall which is caused by interaction between TC and mid-latitude weather systems has catch meteorologists' eye. Observations and studies show that the interaction between tropical cyclones and mid-latitude weather systems, such as trough, the Southwest Vortex , the Northwest Vortex , the Northeast Vortex etc, played an important role in the occurrence of tropical cyclone remote rainfall. In those events, plenty of moisture and energy can be transported into mid-latitude region and converge, meanwhile, the mid-latitude weather systems provide large-scale background which benefit the occurrence of TC remote rainfall.

During the decades, with the improvement of the weather monitring network, the upgrade of atmospheric numerical models and rapid development of computer power, the facts of tropical cyclone remote rainfall have been found and the physical mechanism of TCRR are further studied. Some of the achievements relating to tropical cyclone remote rainfall are reviewed in this paper.

Key word: tropical cyclone remote rainfall; mid-latitude weather systems: interaction

Introduction

Tropical cyclone (TC) is a kind of disastrous weather system which has been studied extensively for a long time by meteorologists. Except for heavy rainfall within TC region, at places far away from it, servere rainfall can also be generated by the interaction between TC and mid-latitude weather systems. The latter rainfall events which satisfy two criteria (one is that the rainfall is far from tropical cyclone region, the other is a closely relation between rainfall and TC exists)is called tropical cyclone remote rainfall(TCRR) (Chen Lianshou 2007). Previous research works revealed the close relationship between many famouse rainfalls events in China and TCs far away from rainfall region. For example, the heavy rain happened in August 1963 at Haihe river basin caused by interaction between westerly trough and low-level jet between TC and subtropical high, Severe rainfall event happened in August 1975 at Huaihe river basin and the rainfall event happened in August 1958 at Huanghe river basin (Chen Lianshou 1979).

In resent several decades, with the help of rapidly developing observation networks, and NWP technology, some progresses have been made in the studies on TCRR. Studies show that TC located in low latitude area can lead to cloudburst of mid-latitude area under favorable circulation, in which interaction between TCs and mid-latitude weather systems is happening. TCs have impact on distribution of rain storm not only in Southeast China but also in northern and central China . Statistical research (Zhuo Ga,2000)showed that the remarkable relation exists between the typhoon activity and the annual precipitation on the eastern edge of Tibetan Plateau, aside from North China, the Northeast China and South China. In fact,

TCRR is the product of interaction between TC and mid-latitude weather system, such as westerly trough, the Southwest Vortex, the Northwest Vortex, the Northeast Vortex. TCRR has been a focus of TC studies in recent years, and much progress has been made.

1 Interaction between TCs and mid-latitude weather systems

Observations and studies show that interactions can occur between TC and various mid-latitude weather systems, such as westerly trough, mid-latitude vortex, and bring about remote torrential rain. Studies showed that the landing of TC on the coast of South China can cause heavy rainfall in Shandong province, with southeasterly or southerly low-level jets transporting vapor toward Mainland China from the eastern part of the TC.

1.1 The interaction between TC and westerly trough

Prior to the 1980s, Chinese meteorologists found that the interaction between TC and westerly trough can bring rainstorm in mid-latitude area, and pointed out that deeping trough played an imported role in this process.

Analyses on the TRCC event caused by Typhoon Tim (9406) showed that the interaction between the TC and the westerly trough is apparently manifested with meso scale activities.The distribution of divergence fields at lower and upper levels can have a kind of indication meaning for the rainfall caused by the interaction between mid and low latitude circulations. Furthermore, intensity changes of westerly trough would directly lead to intensity changes of meso scale systems and thus lead to different rainfall. Besides, energy change features of different motion scale are also investigated from energetics point of view. The results show that the maximum and minimum value areas of energy change on meso scale fileds are closely related to the intensity changes of mid and low latitude systems, and have rather good correlation with precipitation changes.

Some studies (Hou Jianzhong,2003)showed that about 87 percent of the torrential rain in Shanxi province were related to the interaction between TC and westerly trough. Sun Jianhua(2003) statistics results indicated that interaction between TC and westerly trough is one of most mechanism of rainfall in the North China plain.

1.2 The interaction between TC and the mid-latitude Vortexes

The mid-latitude synoptic vortexes systems, such as southwest vortex, northeast vortex and northwest vortex, always bringing heavy rains in China, and the rainfall can be greatly enhanced owing to the involving of TC far away.

A serious disastrous rainstorm event occurred in the Sichuan basin during 8-11July1989. Studies showed that the interactions between the TC and the southwest vortex played an important role in this event. Diagnostic analysis revealed the effects of interaction on the evolution of the southwest vortex and the heavy rain. The collision of cold and warm currents at the southeast quardrant of the vortex resulted in moist and high-energy mass convergence and updraft, which triggering the rainstorm.

With NCEP/NCAR reanalysis data and MM5 model, the heavy rainfall event in Sichuan and Chongqing during 3-6 September 2004 caused by a southwest vortex was simulated. The result of simulation showed that the southwest vortex move speed became slow, intensity enhance, and life time extended on the score of implicate of the Sangda typhoon with the heavy rainfall. The convergence and accumulation of warm and damp air from the Sangda typhoon induced the heavy rainfall nearby the southwest vortex. That's to say interaction between the southwest vortex and Sangda typhoon is existent, what's more, the interaction can change the southwest vortex structure and is one of mechanism of the heavy rain.

Ding Yihui(1980)pointed out that the torrential rain of the Northeast China often take place with interaction among two or three weather systems, moreover interaction between TC and the southwest vortex is one of the most form. Sun Jianhua's(2005) studies showed that about 32.2 percent of rainfall in the Northeast China was caused by the interaction.

Our recently studies showed that the TC(0312) prove its importance by reinforcing the rainfall in Shandong province near the northwest vortex. In this case, the TC, landed Gongdong province, is moving westward with a low-level jet, which carried plenty of vapor and warm air to the south of the shear line located right of the northwest vortex, and caused warm frontogenesis. The vertical circulation around the newborn warm-front triggered the heavy rain.

1.3 The interaction between TC and the Subtropical High

As well known, the intensity, position and shape of the subtropical high have decisive impact on the track of TC. The movement and its intensity of mid latitude westerly trough is affected by the variation of the subtropical high which also affects the distribution of rainfall. Some rainstorm case were successfully simulated and the results showed that different typhoon tracks are closely tied to different patterns of the subtropical high. The westward tracks are correspond to strong subtropical high with a zonal form stretching westward; As the tracks recurving, the main body of the subtropical high locates much more east of its normal position. Typhoon can induce barotropic Rossby waves propagating towards the mid and high latitudes. Under different background, wave trains triggered by typhoons of westward and northward tracks are also different, and their effects on the mid and high latitude circulation and the subtropical high are different: compared to the northward tracking typhoon, the westward tracking typhoon is able to induce positive geopotential height anomaly to its north and northwest, resulting in the strengthening and westward stretching of the subtropical. The interaction between TC and the subtropical decide the rainfall intensity and location.

2 Contribution of TC in the TRCC events

According to some study on TRCC, TC play different roles in different TRCC processes. Contribution of TC to the TRCC events can be listed as flowing:

1) TCs transport plenty of water vapor and massive energy to mid-latitude region from low-latitude by the low level jets occurred east of TCs and provide moist and latent heat for TRCCs region.

2) TCs contributes to warm frontogenesis which is always the trigger of TRCCs.

3) The vortex which departs from TC inverse trough provide initial dynamical environment for TRCC.

4) Propagating of the waves generated by TCs provide triggers of TRCC.

3 Contribution of mid-latitude weather systems in the TRCC events

The mid-latitude weather systems also play different role in different TRCC processes. Contribution of mid-latitude weather systems in the TRCC events can be listed as flowing:

Mid-latitude weather systems provide a large-scale favorable background for the occurrence of TRCC.

Mid-latitude weather systems with strong baroclinic energy provide kinetic energy to the development and maintenance of vertical motion which is benefit for the occurring and intensification of TRCC.

The structure of mid-latitude weather systems can affect the intensity and location of TRCC.

4 Distribution of TRCC in China

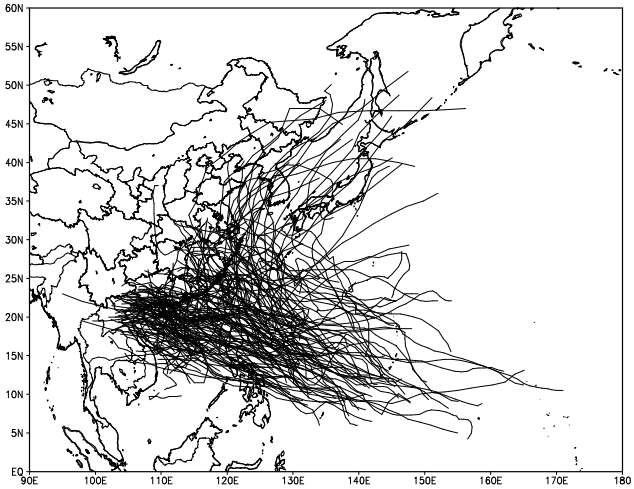

Fig.1 tracks of all TCs related TRCC from 1971 to 2006 in China.

The statistical characteristics of tropical cyclone remote rainfall ,including characteristics of tropical cyclone causing remote rainfall and the climatic features of remote rainfall, are studied based on data of the Tropical Cyclone Yearbooks, daily precipitation of 693 normal meteorological observation stations and NCEP/NCAR reanalysis data from 1971 to 2006 ,. Results indicated that 1.） During the 36 years, the tropical cyclone remote rainfall caused by 169 tropical cyclones spread over 27 provinces of east-central China. 2.)The remote rainfall like best being presence three regions which are juncture of Shandong and Henan province, Hebei and Liaoning ,Shanxi and Sichuan province; 3).The tropical cyclone event has notable interannual change with period of 4-6 year, occurring from June to September every year.4).The tropical cyclone related to remote rainfall show three advantage track.60% of tropical cyclones is the northwest by west track, which is main route. The territorial waters around of the Xisha, the Zhongsha Dongsha and Taiwan are key region through where tropical cyclone is disposed to cause remote rainfall descend on east-central China.

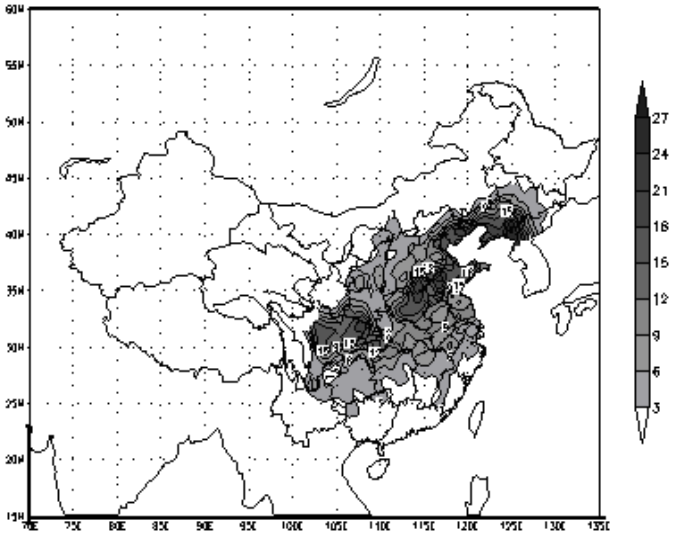

Fig.2 Distribution of TRCC frequency in China

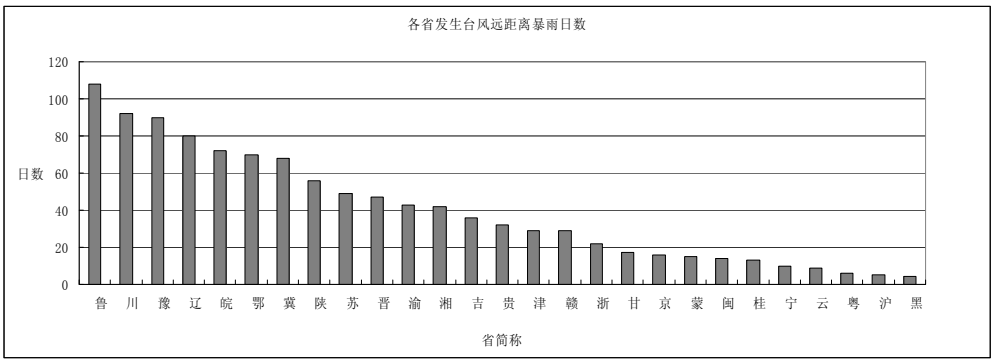

Fig.3 the number of TRCC frequency in 27 province of China

5 Discussion

Although, during the recent decades, us understanding of TRCC has have a progress, confusing about the detail process of interaction between TC and mid-latitude weather systems are still existing. For example, how to interact between TC and mid-latitude weather systems? Are there difference among interaction between TC and different mid-latitude weather systems? What can depend on to forecast TRCC events in real operation.

Reference

Chen Lian-shou, DingYi-hui.. Introduction of West Pacific Typhoons [M]. Beijing: Science Press. 1979 .10-145.

Meng Zhiyong. et al. mesoscale characteristics of the interaction between TC TIM(9406)and mid-latitude circution. Acta Meteor Sinica (in Chinese).2002 .60(1) :31-38.

Chen Lianshou. An overview on the impact of interaction between low-mid latitude circulation on rainfall and tropical cyclone behavior. Paper Presented at the 24th Conference on Hurricanes and Tropical Meteorology , 29 May - 2 J une. Fort Lauderdale. FL. USA. . 2003. 63

Chen Lianshou , Meng Zhiyong. An overview on tropical cyclone research progress in China during the past ten years (in Chinese) .Chinese J Atmos Sci .2001 25 (3) :420-432

Sun Jianhua.et al. A study on severe heavy rainfall inNorth China during the 1990s. Climatic and Environmental Research. 2005.

Chen Zhongming , Huang FuJ un , He Guangbi. A case study of interactions between the tropical cyclone and the southwest vortex. Part l : Diagnostic analysis (in Chinese) . Chinese J Atmos Sci, . 2002.26 (3) : 352-360

Lei Xiaotu , Chen Lianshou. Tropical cyclone landfalling and its interaction with mid-latitude circulation systems. Acta Meteor Sinica (in Chinese) . 2001b 59 (5) :602-615

Sun Jianhua , Qi Linlin , Zhao Sixiong. A study on mesoscale convective systems of the severe heavy rainfall in North China by“9608”typhoon. Acta Meteor Sinica (in Chinese) . 2006. 64 (1) :57-71

Zhu Hongyan ,Chen Lianshou ,Xu Xiangde. A numerical study of the interactions between typhoon and mid2latitude circulation and its rainfall characteristics. Chinese J Atmos Sci (in Chinese) . 2000.24(5) :669-675

Wang Y. Vortex Rossby wave in a numerically simulated tropical cyclone. Part Ⅰ[J] . J . Atmos. Sci. 2002 .59 :1213 - 1238.

Yang Xiaoxia. et al.Study of tropical cyclone remote rainfall in Shandong province. Acta Meteorologica Sinica.2007. 237-250

Zhuo Ga. et al. statistics relationship between Chineseprecipitation and landfall typhoon(J). Plateau meteorology. 2000.19 (2) : 260-264.

Ren Suling.et al. Interactions between typhoon and subtropical anticyclone over westen pactic revealed by numerical experiments. Acta Meteorologica Sinica. 2007. 65(3):329-340.

Li Chunhua. et al. the influence of typhoon on subtropical high location and intensity. Plateau meteorology. 2002.21(6):576-582.

Hou Jianzhong.et al. activity typhoons and extrame rainstorms in Shanxi province.Journal of tropical meteorology. 2006.22(2):203-208.

Chen Zhongming.et al. A case study on interaction between tropical and Shouthwest vortex.(J) Chinesejournal of Atmospheric Science.2002.26 (3):352 – 360.

Chen Zhongming.et al. new advances in Shouthwest China vortex research. Plateau meteorology. 2004.23.Suppl.1-5.

Xu Xiangde.et al.Dyanmic characteristics of typhoon vortex spiral wave and its translation: a diagnostic analysis. Chinese J. Geophys.(in Chinese) 2004.47（1）：33-41.

A Numerical Study of "The Perfect Flood" of Hurricane Floyd 1999

Lian Xie and Qianhong Tang

Department of Marine, Earth and Atmospheric Sciences, North Carolina State University

(email: xie@ncsu.edu)

Abstract

Landfalling tropical cyclones (TCs) often produce heavy precipitation and result in river and flash floods. Such floods can not only cause loss of human lives and properties, but also lead to ecological disasters in the affected watershed areas, estuaries and coastal waters. Approximately 40% of the damages from landfalling TCs in North Carolina could be attributed to inland flooding (Hilderbrand, 2002). This study intends to explore the physical processes of landfalling TC induced flooding from two different perspectives: 1) influence from environmental flow; 2) effect of watershed hydrology. Landfalling TCs such as Hurricane Floyd often interact with large-scale environmental factors to produced enhanced precipitation, and the same amount of precipitation can contribute to different responses of flooding as a result of the different characteristics of watersheds such as land use, soil types, slopes and aspects and ground water hydrology.

In order to better understand the flooding process, a Distributed River Forecast System (DRFS) based on the AnnAGNPS watershed hydrology model (Bingner et al., 2007) has been employed to study the response of the Tar-Pamlico River Basin (Fig. 1) in North Carolina to the landfall of Hurricane Floyd of 1999. AnnAGNPS (Figure 2) is a GIS-driven watershed hydrology and water quality model developed by the US Department of Agriculture (USDA). It is a batch process, continuous-simulation, surface-runoff, pollutant loading (PL) computer model originally designed for simulating watershed hydrology and nonpoint source agricultural water pollution. It simulates loadings of daily river discharge, peak runoff and non-point source pollutants, and operates on a daily time step. It uses the Soil Conservation Service Curve Number method (SCS-CN) to determine overland runoff and the TR-55 method (USDA-NRCS, 1986) to calculate peak flow. The model accounts for lateral subsurface and tile drainage. Runoff in channels is calculated using Manning's equation (Polyakov et al., 2007).

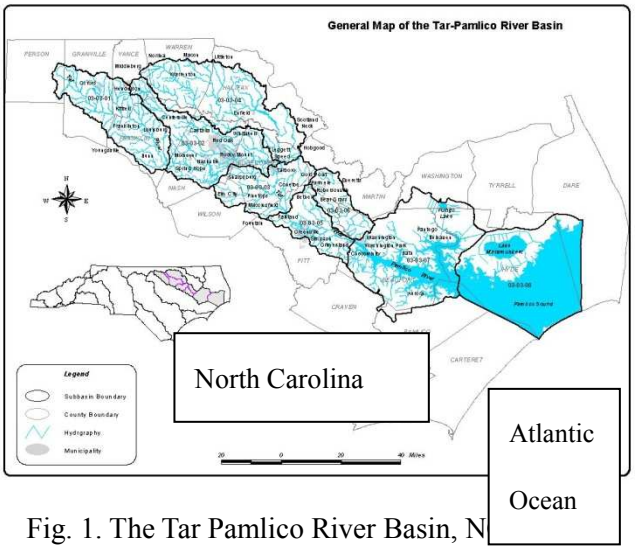

Fig. 1. The Tar Pamlico River Basin, N

The water budget equation (1) in a watershed for a certain period of time (modified from Bingner et al., 2007) is used in the model. Soil moisture change from time t to t+1 equals the sum of precipitation, surface runoff, subsurface lateral flow, evapotranspirition and percolation. For an individual cell, water budget can be presented:

$$SM_{t+1} = SM_t + WI_t - Q_t - q_{lat} - ET_t - PERC_t \quad (1)$$

where

SM_t = soil moisture content (mm) for each soil layer at beginning of time period t;
SM_{t+1} = soil moisture content (mm) for each soil layer at end of time period t;
WI_t = water input (mm) for time period t, consisting of precipitation or snowmelt plus irrigation water;
Q_t = runoff (mm) for time period t;
q_{lat} = subsurface lateral flow and drainage for time period t;
$PERC_t$ = percolation of water (mm) (including infiltration) out of each soil layer during time period t;
ET_t = evapotranspiration (mm) (including evaporation and transpiration) during time period t.

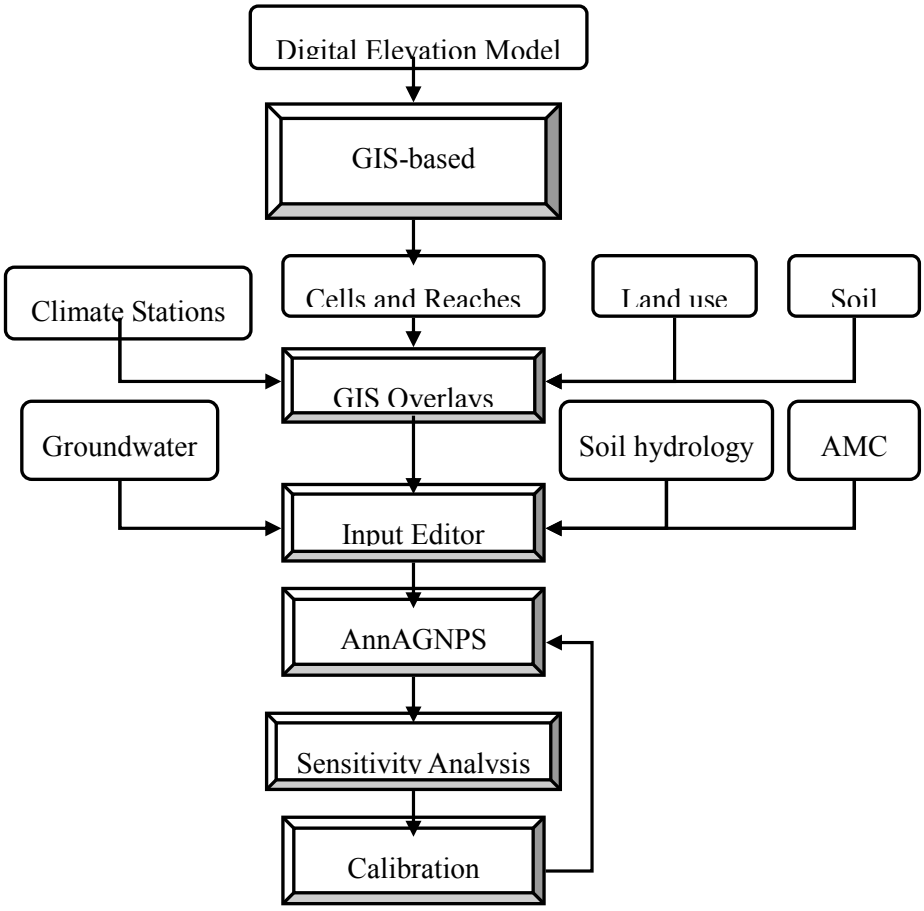

Figure 2. Schematic Diagram of the AnnAGNPS model.

To simulate each of the terms in Equation (1), such as evapotranspiration, surface runoff and percolation, a variety of methods have been applied. The water balance is computed for two soil layers. The first layer is the top 2 meters from surface and is usually treated as the tillage layer. The second layer is from 2 meters to the imperious layer or user defined depth in a soil profile. AnnAGNPS is run at daily time step. The soil moisture (SM) is considered to be valid for the beginning of a day. To assure the accuracy of the initial soil

moisture SM_t, simulation using soil moisture data from the previous three years is conducted in this study to generate initial soil moisture at the beginning of the time step. The runoff (Q_t) is determined using Soil Conservation Service Curve Number method (SCS-CN) (USDA-SCS, 1972). Evapotranspiration (ET_t) is calculated using the Penman equation (Bingner et al., 2007). Subsurface lateral flow and drainage (q_{lat}) is computed by Darcy's equation (Bingner et al., 2007). For the second soil layer, the water input (WI) is the percolation from the first layer (percolation is the downward drainage of soil water into lower layers by gravity), and runoff (Q) is zero.

Scale analysis (Table 1) indicates that precipitation, surface runoff and subsurface lateral flow are more important than evaporation, percolation and soil moisture changes. Distribution of precipitation also affects the total runoff discharge.

Table 1. Scale analysis of water balance equation in a unit area of Tar-Pamlico River Basin

Water Balance Term (mm)	SM_{t+1}-SM_t	WI_t	Q_t	q_{lat}	ET_t	$PERC_t$
Scale for TC event	10^0	10^2	10^2	10^2	10^1	10^1

Hurricane Floyd made landfall near Cape Fear, North Carolina at 0900 UTC 16 September 1999 (09Z/16), as a category 2 hurricane with maximum sustained winds near 50 m/s. Over 50 cm of rain fell in parts of North Carolina, resulting a record flooding. As a result of the extensive flooding, 56 people lost their lives and property damage was estimated at between $3 and $6 billion (more information available online at www.nhc.noaa.gov).

Preliminary results indicate that the model was able to accurately simulate the streamflow (Fig. 3), and the record flooding during the passage of Hurricane Floyd was the results a series of unfortunate events that occurred prior to and during the landfall of storm. In particular, Hurricane Dennis which occurred less than two weeks before the landfall of Floyd played a significant role by pre-conditioning the watershed and coastal ocean. Without Dennis, total river discharge during Hurricane Floyd could have been reduced by over 35%, resulting in a less severe flooding.

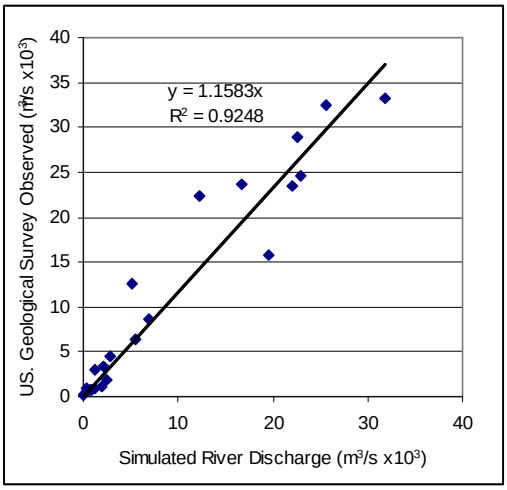

Fig. 3. Simulated vs. observed streamflow

Acknowledgements: This study is funded by NOAA Grant #NA07NWS4680002 and data provided by North Carolina State Climate Office.

References:

Bingner, R. L., F. D. Theurer and Y. Yuan, 2007. AnnAGNPS technical processes. Version 4.0. USDA-ARS documentation.

Hilderbrand, D. C., 2002. Risk Assessment of North Carolina Tropical Cyclones (1925 – 2000). North Carolina State University. MS thesis.

Polyakov, V., A. Fares, D. Kubo, J. Jacobi and C. Smith, 2007. Evaluation of a non-point source pollution model, AnnAGNPS, in a tropical watershed. *Environmental Modelling & Software* 22: 1617-1627.

Performance of a Modified Kain-Fritsch Convection Trigger Scheme in Rainfall Simulation during Typhoon Landfall

Lei-Ming Ma [1,2], and Zhe-Min Tan [2]

[1.] Laboratory of Typhoon Forecast Technique/CMA, Shanghai Typhoon Institute,

Shanghai 200030, P. R.China.

[2.] Key Laboratory of Mesoscale Severe Weather/MOE, Department of Atmospheric

Sciences, Nanjing University, Nanjing 210093, P.R.China.

The objective of this study is to improve the performance of cumulus parameterization (CP) schemes in typhoon prediction with emphasis on convection trigger. We evaluated three of the most popular CP schemes for simulation of typhoons which made landfall on the east coast of China in the year 2006. Sensitivity experiments were designed with different CP schemes (Kain-Fritsch scheme-KF93, Kain and Fritsch 2003; Grell scheme-GR93, Grell 2003; Betts-Miller scheme-BM93, Betts and Miller 1993) for simulation of typhoon rainfall. It is shown that the intensity and coverage of typhoon rainfall, including its subgrid-scale component, is quite sensitive to different choices of CP scheme. For each of the CP scheme, the percentage of subgrid scale rainfall varies substantially for different typhoon cases, which implies that the behavior of the CP in rainfall simulations may be associated closely with specific characteristics of typhoon. Moreover, the GR93 scheme has a significant tendency to underestimate convective rainfall while still producing the most intense typhoon. Equipped with a sophisticated cloud algorithm, the KF93 scheme appears to be more accurate in simulations of rainfall, intensity and track, in comparison with GR93 and BM93.

However, despite its advantages, improvements to KF93 are still possible. For instance, the KF93 scheme has a considerable deficiency when large-scale forcing are weak. The authors assume that this deficiency may bear a close relation to the original trigger function of KF93 for its important role in convection initiation. In particular, the statistical relation between convective temperature perturbation and convergence-determined grid-scale vertical motion is theoretically not quite robust. To avoid this convergence-related controversy, a new formula is proposed in this study to redefine the convective temperature perturbation, in which the particular role of moisture advection is taken into account. Thus, the relationship between environmental forcing (e.g., grid-scale temperature anomaly due to moisture and temperature advection) and local disturbance is explicitly established in this new scheme. Sensitivity experiments were conducted to verify this new algorithm. It is shown that the distribution as well as the intensity of convective rainfall was significantly improved with the new algorithm. The new trigger scheme can reasonably eliminate convective instability under weak synoptic forcing, while change the response of the disturbance in the low troposphere to environmental humidity towards more realistic values.

1. Experiment Design

Numerical simulations were preformed with the nonhydrostatic version of the PSU–NCAR Mesoscale

Model version 5 (MM5; Grell et al. 1994). The initial fields and lateral boundary conditions are derived from the NCEP/GFS Model, the horizontal resolution of which is 1°× 1°. The initial fields are interpolated onto a single computational domain with mesh size of 118 × 118 grid points at resolution of 15 km. This resolution is set to be consistent with the assumptions of the above CP schemes. 28 vertical sigma levels (1.00, 0.99, 0.98, 0.96, 0.94, 0.91, 0.88, 0.84, 0.80, 0.75, 0.70, 0.65, 0.61, 0.57, 0.54, 0.51, 0.48, 0.45, 0.42, 0.38, 0.34, 0.30, 0.25, 0.20, 0.15, 0.10, 0.06, and 0.00) were used. The pressure at the top of the model is 50 hPa. Notice that there is a well-resolved planetary boundary layer (PBL) located below the 850-mb level. PBL processes are treated using the scheme of Hong and Pan (1996) due to its capability for simulating the structure and diurnal variability of the boundary layer over land and ocean. A bogus data assimilation (BDA) scheme (Zou and Xiao, 2000; Xiao et al 2000), which has been verified in simulations of typhoon Danas (2001) (Ma et al. 2006), is introduced in this study to generate a reasonable typhoon vortex at the initial time.

To evaluate the three cumulus parameterization schemes, three special TC cases are chosen, which made landfall on China's eastern coast in 2006. 1) Bilis, the most destructive TC to make landfall in China in the last 50 years; 2) Saomai, which underwent unexpected intensification during landfall; and 3) Kaemi, for which the operational forecast failed to predict its slow westward motion after landfall.

The rainfall datasets used for verification include TRMM/TMI retrieved rainfall rates (Kummerow et al. 1998) and accumulated rainfall observed by the Chinese network of automatic weather stations. The typhoon track datasets were provided by the Joint Typhoon Warning Center (JTWC). A number of 24-hour numerical simulations were conducted for each of the 12 temporal phases to evaluate the performance of BM93, GR93, and KF93. Except for the different options of the CP, identical initialization methods and physics options were used for each of the simulations. For the rainfall accumulation including subgrid scale and grid scale components, it is found that BM93 produced the highest amount, while the GR93 the least. KF93 yields close to the average amount from BM93 and GR93. BM93 and KF93 produce almost identical percentages of subgrid rainfall, both of which start with mainly the subgrid component (more than 90%). This percentage decreases gradually, with the minimum value (70%) at the end of 24h integration (Fig.1). Meanwhile, the GR93 scheme yields the least percentage of subgrid rainfall throughout the simulations. It starts with 74% and ends with 30%. The biggest departure (nearly 50%) for subgrid rainfall percentage between GR93 and BM93 (KF93) appears at the end of integration. Although the KF93 scheme tends to overestimate the coverage of light rainfall (0.1mm/24h) with the Bias score of 1.715, it appears to be the most robust in that it showed no signs of serious systematic failure on skill measures of medium (10.0mm/24h) to heavy rainfall (25.0mm/24h).

2. Modification of the Convection Trigger Scheme

Despite the advantages shown above, KF93 scheme is urged to be improved. A common criticism of the KF scheme was that it sometimes produced widespread light precipitation in marginally unstable environments (Warner and Hsu 2000; Colle et al. 2003). This weakness is also identified in this study. For example, within the Taiwan straits where large scale forcing is very weak, the surface rainfall rate is evidently overestimated by KF93, in comparison with the observations from TRMM/TMI. This deficiency of KF93 in weak environments may close relation to the parameterized convective triggering mechanism for its particular role in convection initialization and deserves to be examined. KF93 estimates the instability available for cloud growth with a largrangian parcel method (Simpson and Wiggert 1969). The first task in KF93 is to identify updraft source layers for parcels with a trigger function. Starting from the surface, vertically adjacent model layers are mixed until the depth of the mixture exceeds a threshold (i.e., 60hPa). A temperature perturbation (δT_{vv}), which was originally defined as a function of grid-resolved vertical motion

given that convection tends to be favored by background vertical motion (Fritsch and Chappell, 1980), must be added to the parcel to drive it upward. Obviously, the definition of δT_{vv} is crucial in determining the prerequisite for a parcel to move upward and to trigger convection. The original assumption of temperature perturbation by vertical motion was given by Fritsch and Chappell (1980) based on the understanding of the role of convergence in destabilizing and moistening the atmosphere (Chen and Orville, 1980). Unfortunately, the effect of convergence in convection development has received much criticism (Arakawa, 2004, Emanuel 1986). For instance, Arakawa (2004) emphasized the importance of moisture advection instead of convergence in determining the boundary layer specific humidity, which fuels convection.

It is noticed that only in the area plenty of moisture, the spatial temperature anomaly shows a close correlation with that of vertical motion in coverage and magnitude. This can be understood through a thermodynamic equation given below:

$$c_p \frac{dT}{dt} - \frac{ART}{p}\frac{dp}{dt} = Q - L\frac{dq}{dt} \tag{1}$$

where c_p is the specific heat at constant pressure, *R* the gas constant for dry air, *L* the latent heat of condensation, *A* the energy constant (0.23885 Cal/J). Other variables assume their usual meaning.

Note in Eq.(1) that the rate of change of temperature change ($\frac{dT}{dt}$) is closely related to $\frac{dq}{dt}$, which is determined by moisture advection as argued by Arakawa (2004). To avoid the convergence controversy, the effect of moisture advection is used to define the temperature perturbation.

The new algorithm is given by $\delta T_{vv} = R_h \cdot \delta T_{vvh} + R_v \cdot \delta T_{vvv}$ (2)

where δT_{vvh} is the temperature spatial anomaly for each local grid point against the horizontal environmental temperature average (average over 9 closest grid points surrounding the target grid point), δT_{vvv} the temperature anomaly at LCL of each of the grid point against the vertical environmental temperature average (average of three sigma levels, i.e., LCL-1, LCL, LCL+1). R_h and R_v are the normalized horizontal and vertical moisture advections, respectively. The normalization algorithm is given below:

$$R_{h,v} = \frac{\vec{v}_M \cdot \nabla q_M - Min(\vec{v}_M \cdot \nabla q_M)_{h,v}}{Max(\vec{v}_M \cdot \nabla q_M)_{h,v} - Min(\vec{v}_M \cdot \nabla q_M)_{h,v}}. \tag{3}$$

where $Min(\vec{v}_M \cdot \nabla q_M)_{h,v}$ and $Max(\vec{v}_M \cdot \nabla q_M)_{h,v}$ are calculated within the same grid boxes as that of δT_{vvh} and δT_{vvv}.

Notice that both R_h and R_v are non-dimensional variables with the magnitude between 0 and 1. In each of the grid boxes, bigger (smaller) R_h or R_v is associated with stronger (weaker) moisture advection and temperature perturbation. The maximum magnitudes of R_h and R_v yield the maximum temperature perturbation. This new algorithm explicitly establishes the positive relationship between grid scale temperature anomaly (represented by the effect of environmental forcing) and locally forced convective disturbance.

3. Performance of the new Trigger Scheme

Performance of the original (KF93) and new trigger algorithm (hereafter KFML) in rainfall simulation is evaluated by sensitivity experiments. The simulation of Bilis with KFML scheme shows consistency with the TRMM/TMI observation. KFML reduced the area coverage of intense subgrid-scale rainfall (greater than 10mm h^{-1}) generated by KF93. In particular, over the area of weak environmental forcing produced by KFML, the distribution as well as the intensity of subgrid-scale rainfall agrees well with that retrieved by TRMM/TMI. The improvement in the subgrid-scale rainfall simulation with KFML is also indicated in the simulations of Kaemi and Saomai. Simulated rainfall regions most clearly affected by the modification of the algorithm are indicated by thick circles. It is seen that the new algorithm considerably reduces the subgrid-scale rainfall intensity over the moisture transportation channel, which has been overestimated in KF93. KFML reduces the subgrid-scale rain by about 10%, irrespective of the different situations of the TC cases. Meanwhile for various TC cases, the simulated grid-scale rainfall by KFML shows negligible difference with that of KF93. Note from statistical verification for total rainfall accumulation that, for light (i.e., less than 10 mm/24h) and medium rainfall (i.e., greater than 10 mm/24h), KFML increases the threat score by about 30% and 25%, respectively, in comparison with KF93 (Fig. 2a). Bias scores also give the consistent results (Fig. 2b), which indicate that KFML can reduce the overestimation of KF93.

An unstable situation under weak environmental forcing is also analyzed. The most unstable region prior to the time of observed convective rainfall is characterized by the warm tongue of equivalent temperature extending upward from the surface, accompanied by strong ascent transporting moisture and energy upward. Before and after the time of observed convective rainfall, the height (700hPa) that the warm tongue of 365K air reaches shows negligible change in KF93. Whilst in the KFML experiment, the height that the 365K isotherm extends descends from 700hPa to 900hPa. Similar results can also be drawn from the TlogP plot, in which the CAPE energy calculated at the grid point with maximum observed convective rainfall is more efficiently consumed in the experiment KFML in comparison with that of KF93. In the KFML experiment the CAPE value is 1103 J kg^{-1} and 678 J kg^{-1} prior to and after the time of convective rainfall respectively, with nearly 38% energy being consumed. However in the KF93 experiment, the exhausted CAPE is only about 17%.

Meanwhile, for the marginally unstable area beside the warm tongue, the energy of instability is barely consumed by KFML, and is significantly less than that of KF93. This accounts for the overall reduction of subgrid rainfall.

The sensitivity of cumulus convection to humidity in the troposphere has been broadly recognized by pervious observational and modeling studies (i.e., Derbyshire et al, 2004; Raymond and Zeng, 2000). In comparison with the original scheme, it is seen that the same amount of relative humidity is associated with reduced latent heat flux in the KFML experiment, which damps the activity of convection (Fig. 3a-b). The weakened convection then reduces the upward transportation of moisture from low troposphere (Fig. 3c-d), and accounts for the reduction in convective rainfall that is overestimated by the KF93 scheme. The reduction of latent heat flux due to the modification of the trigger algorithm is more evident in high relative humidity environments. For example, for the moist environment with relative humidity of 88% and 92%, the reduction of latent heat flux is about 10 and 20W m^{-2}, respectively.

This study has provided convincing evidence of the advantages of the new trigger algorithm in rainfall simulation of the landfalling typhoon. However, detailed examination is still required to extend the understanding of the physics behind the scheme.

Acknowledgements. This study was jointly supported by the national 973 project No. 2009CB421500 and National Natural Science Foundation (No. 40705024) of P. R. China.

References

Arakawa A., 2004: The Cumulus parameterization problem: Past, present, and future. *J. Climate*, **13**, 2493-2525.

Kain J. S., and J. M., Fritsch, 1993: Convective parameterization for mesoscale models: The Kain–Fritsch scheme. The Representation of Cumulus Convection in Numerical Models, *Meteor. Monogr.*, **46**, Amer. Meteor. Soc., 165-170.

Ma, L. -M., Z. Qin, Y. Duan, X. Liang, and D. Wang, 2006: Impacts of TRMM SRR assimilation on the numerical prediction of tropical cyclone. *Acta Oceanologica Sinica*, **25**, 14-26.

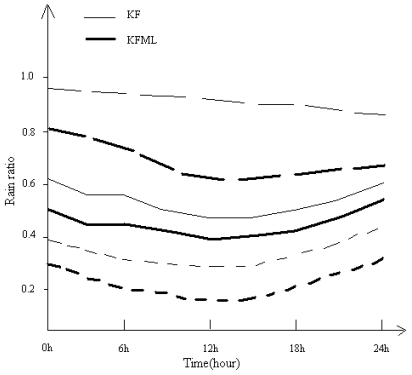

Fig. 1. Temporal evolution of the ratio of subgrid-scale rain in total rain simulated by experiment KF93 (KF) and KFML; solid line for Bilis(2006), short dashed line for Kaemi(2006), and long dashed line for Saomai(2006).

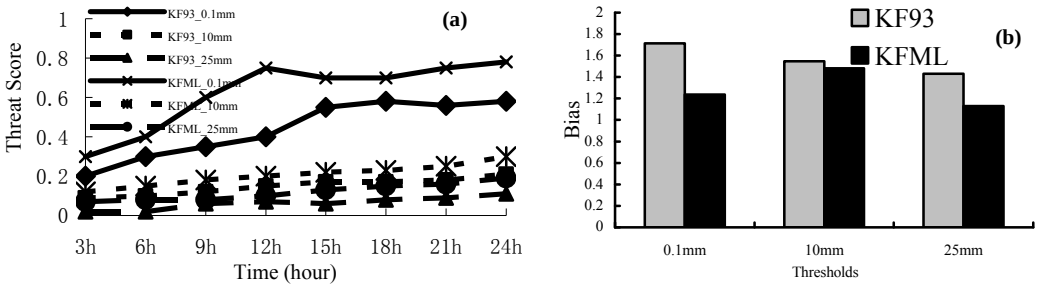

Fig. 2. (a) Threat Score for case-averaged 0- 24h rainfall simulation at 3-h intervals, and (b) bias of case-averaged 24-h accumulated rainfall simulation in experiments KF93 and KFML at the thresholds of 0.1mm/24h, 10mm/24h and 25mm/24h.

.

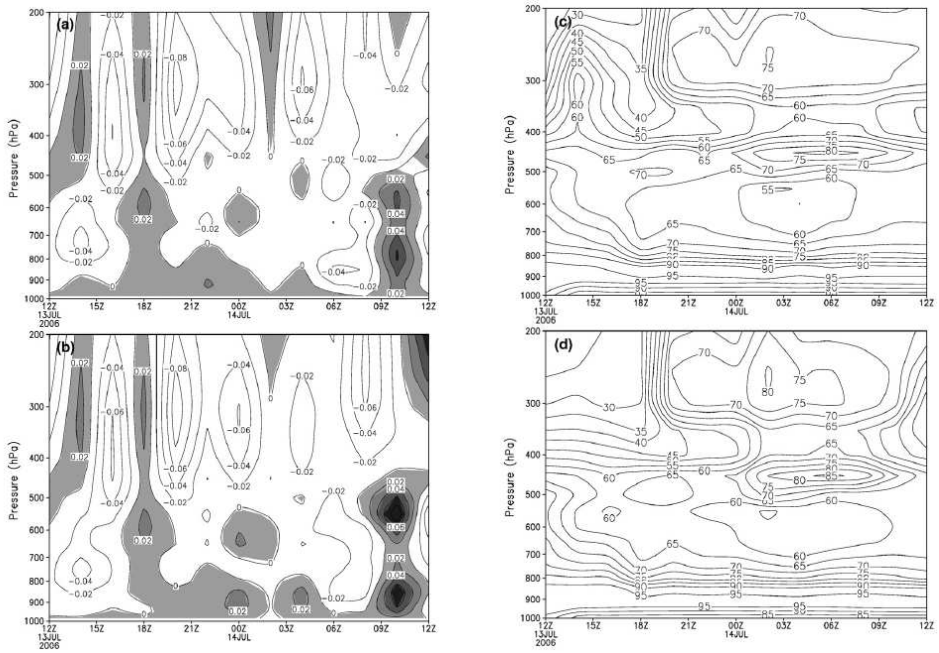

Fig. 3. Temporal evolution of the domain-averaged vertical velocity (m s^{-1}) (a: KFML, b: KF93) and relative humidity (c: KFML, d: KF93) generated by KFML and KF93 for typhoon Bilis during 12 UTC 13 July – 12 UTC 14 July, 2006 over the most unstable region for convection.

Convective Asymmetries Associated with Tropical Cyclone Landfall: β-Plane Simulations

Wei Huang, Xudong Liang

Shanghai Typhoon Institute, China Meteorological Administration 166 Puxi Road, Shanghai 200030

Abstract

In idealized TC-landfall modeling studies, Tuleya and Kurihara (1978) and Tuleya et al. (1984) reported the development of considerable convective asymmetries due to asymmetric surface fluxes. Chan and Liang (2003; hereafter CL03) simulated TC landfall on an f-plane using the Pennsylvania State University–National Center for Atmospheric Research (PSU–NCAR) Mesoscale Model version 5 (MM5), investigating the effects of sensible heat flux, moisture flux, and increased roughness over land on an f-plane on distribution of convection. Their results suggest that moisture supply is the dominant factor in modifying the convective structure, whereas the sensible heat flux has little effect. Prior to landfall, maximum precipitation was found in the front and left quadrants of the TC, but after landfall (when surface moisture flux was turned off and surface roughness increased) it occurred in the front and right quadrants. In their paper, a conceptual experiment, in which moisture supply only occurs over the ocean, showed that dry air over land was advected upward and around such that atmospheric stability was reduced at some locations. The results of more realistic numerical experiments demonstrate that convective instability is indeed greatest immediately upstream of the maximum rainfall. In other words, a change in moisture supply affects the convection distribution during TC landfall via modification of the moist static stability of the atmosphere.

The simulation described in CL03 was performed on an f-plane. Because the β-effect contributes toward wind asymmetry and even convective asymmetry (e.g., Kurok and Chan 2005), it is important to study the asymmetric structure of a TC during landfall on a β-plane to test the validity of the mechanism that modification of the moist static stability plays a key role on distribution of convection of TC proposed in CL03. The objective of the present study is to investigate convective asymmetries during the landfall of a TC on a β-plane, as a follow-up work to that of CL03.

The numerical model used for this study is Version 3 of the fifth-generation Pennsylvania State University-Mesoscale National Center for Atmospheric Research Model 5 (MM5; Dudhia 1993; Grell et al. 1994). The model employs the Betts–Miller cumulus parameterization (Betts and Miller 1993; Janjic 1994), a simple ice scheme (Duhdhia 1989), and the high-resolution Blackadar planetary boundary layer (PBL) scheme (Blackadar 1979; Zhang and Anthes 1982). The horizontal resolution is 15 km and there are 301 grid points in the x and y directions, yielding an experimental domain of 4500 × 4500 km. Sixteen full σ-layers (1.0, 0.99, 0.97, 0.94, 0.90, 0.85, 0.79, 0.71, 0.61, 0.49, 0.37, 0.27, 0.18, 0.10, 0.04, and 0.00) are used in the vertical. This setup is the same as in CL03, thereby enabling a comparison of the results of the two studies.

The control experiment is run with ocean planetary boundary layer (PBL) conditions over the entire domain, similar to the control run in CL03. To simulate the effect of land on the distribution of convection, three experiments are performed with different PBL parameters. Experiment 1 is similar to experiment 3 of CL03, where latent heat flux over land is turned off. The roughness length over land is set 0.25 cm in experiment 2, the same as in experiment 4 in CL03. In experiment 3, moisture supply and roughness length are

increased over land. In all experiments, land use at each grid point is set as "water body." In other words, the land in each experiment is not real land but merely an area over which one parameter is changed. This approach enables us to isolate the effect of surface moisture flux from land areas and the effect of friction on momentum transfer in the two experiments. Given that sensible heat flux showed a negligible effect on convection, we do not describe the experiment in which sensible heat flux was turned off over land.

On the beta-plane, the maximum rainfall was located from southeast to northeast in the control experiment. When cutting off the moisture supply over land, the rainfall maximum shifted to the right-front quadrant of the TC. Compared with rainfall in the control experiment, positive rainfall was located mainly in the front quadrant of the TC, and rotated anti-cyclonically, similar to that in CL03. When the roughness length was increased over land, the rainfall distribution showed little change before landfall. After landfall, the rainfall maximum moved to the right-front quadrant of the TC. Compared with the control experiment, before landfall, positive rainfall was located in the left-front quadrant of the TC. After landfall, positive rainfall was located in the entire front quadrant of the TC. The cutting off of moisture supply over land suppressed convection in the air mass, while increased friction resulted in increased precipitation in the TC, especially after landfall. When these two factors were combined, the total rainfall in the TC was similar to that in the control experiment.

The cutting off of moisture flux altered the moisture structure of the TC. The drier air occupied a large area at low and intermediate levels in the TC; at the same time, a wetter area occurred in the 80°–45° quadrant of the TC. At high levels, this quadrant was drier than that in the control experiment. The vertical structure of moisture altered the distribution of instability. Subsequently, positive CAPE upstream of the TC caused positive precipitation in downstream areas. The difference between the present results and those in CL03 is high instability resulting from the combination of drier air at high levels and related wetter air at low and intermediate levels.

The distribution of precipitation in experiment 2 is consistent with the distribution of CAPE before landfall. This finding suggests that the main factor that determines rainfall distribution may be the suppression of evaporation via reduced wind strength. After landfall, precipitation in experiment 2 was stronger than that in experiment 1, whereas CAPE was similar between the two experiments. A strong negative divergence occurs throughout the front quadrant of the TC, consistent with the distribution of precipitation. It implies that increasing convergence caused by the increasing friction may be another factor in this experiment especially after landfall.

The results of the present study reveal that even if the beta-effect is taken into account and the TC moves by itself to make landfall, the most important effect remains a reduction in moisture flux. The dry air from over land and wet air from the sea act to change the distribution of instability around the TC center, as seen in the distribution of CAPE. Subsequently, positive CAPE upstream of the TC results in positive precipitation in downstream areas. Because the extra-tropical transition process (DiMego and Bosart, 1982) is related to baroclinic instability, related in turn to the distribution of cold and warm air, the instability related to dry and wet air during TC landfall is here defined as the landfall transition process. The contrast in instability caused by wet and dry air is defined by CAPE. The change in instability (CAPE) leads to thermodynamic asymmetry and consequently precipitation asymmetry (data not shown). This process is expected to occur in most TCs upon landfall because of the contrast in latent heat flux between the land and sea surface.

A Study on Formation and Development of Mesoscale Convergence Line within Typhoon Circulation

LI Ying*[1]（李英） CHEN Lianshou[1]（陈联寿） QIAN Chuanhai [2]（钱传海）

[1]State Key Laboratory of Severe Weather, Chinese Academy of Meteorological Sciences, Beijing 100081

[2]National Meteorological Center, Beijing 100081

1. Introduction

Typhoon is a phenomenon at the synoptic scale. However, it brings up mesoscale convective systems (MCS) within its circulation. MCS not only triggers up rainstorm directly, but also has an extremely asymmetric spatial and temporal distribution in typhoon circulation, which in turn affects typhoon structure/intensity and its change. A typhoon usually decays after its landfall. However, it would keep an active MCS (mesoscale vortex, or mesoscale convergence line) within its circulation, due to the effects of terrains and mid-latitude weather systems, encouraging a sudden increase of typhoon rainfall, and resulting in a secondary disaster pounding the inland areas (Chen et al., 2004).

Many previous studies have examined the mechanism of MCS activities in landfalling typhoons. Results show that convergence effects of underlying mountain terrain can generate strong convection and vortex systems at small and mesoscale within typhoon circulation, leading to heavy rainfall or high wind in the affected area In addition, interaction between landfalling typhoons and mid-latitude troughs can speed up the development of MCS, which in turn induces a noticeable change of rainfall rate and distribution (Meng et al., 2002). Some studies analyze the features and propagation of mesoscale disturbance using the wave theory (Luo et al., 2003; Lu et al., 2004). Unfortunately, understanding on the structure of typhoon's inner MCS and the interaction between MCS and typhoon circulation remains insufficient, as such activities are complicated in nature.

In this paper, we examine the formation and development of MCS in typhoon Rananim, and explore the interactions between the MCS and typhoon circulation, based on surface observation data, hourly satellite images, historical typhoon data of the Central Meteorological Observatory, and four times a day 20×20 km regional spectral model data from the Japan Meteorological Agency (JMA).

2. Mesoscale convective system activities in typhoon circulation

2.1 Activities of mesoscale convective cloud clusters

Fig. 1 displays satellite infrared images on August 13, 2004. At 0100 UTC August 13 (Fig.1a), Rananim was traveling across the hilly area in the west part of Zhejiang, without a noticeable rainfall in Jiangxi in the past 24 hours. At the noon (0400 UTC) of August 13 (Fig.1b), convective cloud clusters (indicated by arrow) began to form in a patch 2 latitudinal degrees northwest of the typhoon center, from Anhui to the northern part

* Email:liying@cams.cma.gov.cn

of Jiangxi. Two hours later (Fig.1c), the convective cloud clusters boomed up rapidly, forming up a convective band stretching from the north to south, containing 6 to 7 convective cells of about 200 km in size, at a β— mesoscale level.After that, convective cloud clusters went on with merge and development, and turned themselves into two large convective cloud clusters at 1200 UTC August 13, approaching the remnant center of Rananim in the south (Fig.1d and e). Convective cloud clusters went deeper into the remnant center in the following 12 hours. Meanwhile, the remnant center was moving northwestwards heading for the patch where convective cloud bands were developing, which enhanced the remnant clouds. Cloud image at 0000 UTC August 14 shows that the entire Jiangxi was dominated by the dense depreesion clouds(Fig.1f). From 0000 UTC August 13 to 0000 UTC August 14, a heavy rainfall center of 200 mm appeared in the northern part of Jiangxi.

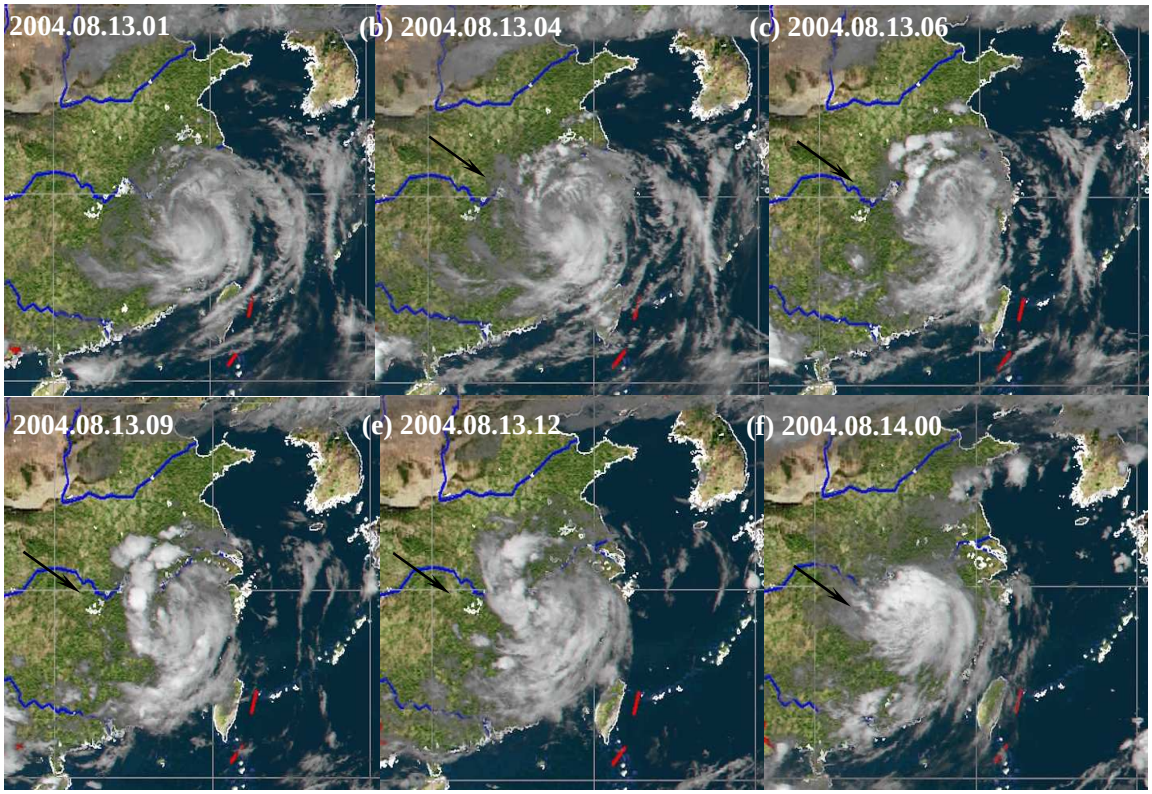

Fig.1. Satellite infrared images from 0000 UTC August 13 to 0000 UTC August 14 August 13, 2004 (number indicating year.month.day.hour, the same below).

2.2 Activities of mesoscale convergence line

Viewing the distribution of surface wind vectors and 6 h accumulated rainfall in future, from 1800 UTC August 12 to 0000 UTC August 14, 2004 (Fig. 2), it is apparent that at 1200 UTC August 12, or 6 hours after Rananim landfall, a depression appeared over the hilly areas of Zhejiang, with a relatively intact and isolated vortex circulation (Fig. 2a). Rainfall in the future 6 hours mainly occurred in the coastal areas near the remnant center of typhoon. At this time, the mid-latitude northerly cold air remained distant from the remnant, with its front positioned at 35°N northwest to the remnant. At 0000 UTC August 13 (Fig. 2b), the northerly airflows

approached 29°N southwardly along 115°E, and formed a convergent region (denoted by symbol C) over Jiangxi where the basin terrain in trumpet form allowed the cold air to stay together. Easterly warm wet airflows from China coastal water on the northern side of the remnant moved westwards along with the vortex circulation, with its front entering the Jiangxi basin, where it joined with cold air to form up a weak mesoscale convergent line (double dashed line). Rainfall in the future 6 hours mainly occurred along the line and under the remnant clouds. At 0600 UTC August 13 (Fig. 2c), the easterly warm wet airflows and the northerly cold airflows intensified and produced a remarkable MCL in the northwest part of the remnant. The MCL located on a region two longitudinal degrees away from the remnant center, in a south-to-north strip over 3 to 4 latitudinal degrees, basically consisting with the position where strong convective cloud clusters formed and developed, as shown in satellite images. Rainfall in the future 6 hours took place in the warm air part near MCL, with two heavy rainfall centers in the south and north. Heavy rainfall clusters reached a scale of 200 km, with a maximum rainfall of 100 mm in 6 hours. At 1200 UTC August 13 (Fig. 3d), the MCL intensity decreased, with smaller wind vectors, resulting in a greatly reduced rainfall near the MCL in the future 6 hours.At 1800 UTC August 13 (figure omitted), wind vectors at both flanks of the previous northwest MCL became much weaker in magnitude and evener in direction, indicating the disappearance of the MCL.

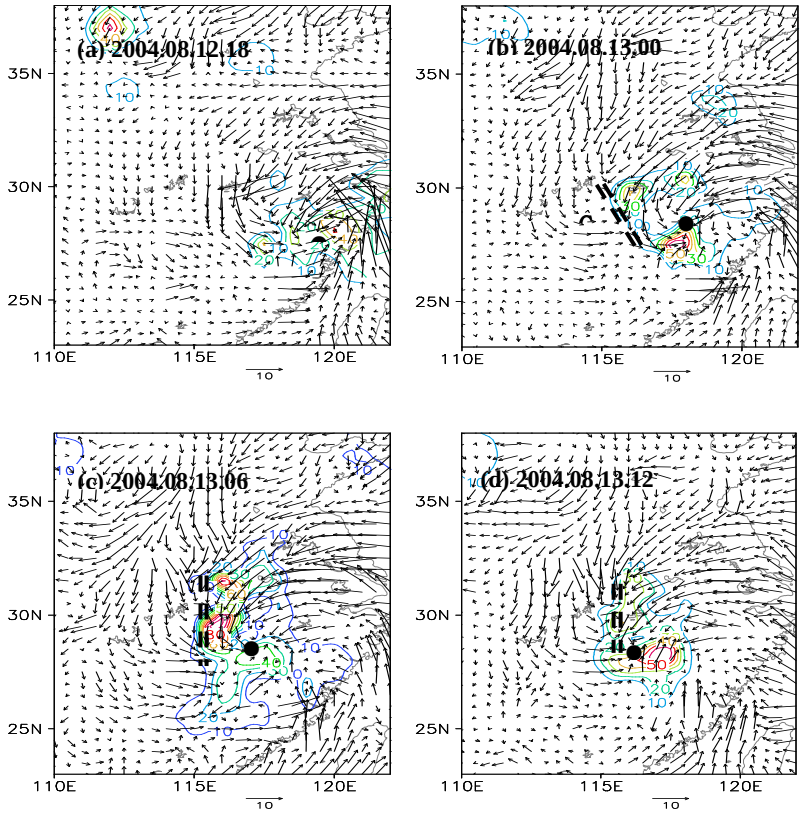

Fig.2. Surface wind vectors and 6 h accumulated rainfall (isoline ≥ 10 mm) in future, from 1800 UTC August 12 to 0000 UTC August 14, 2004 (double dashed lines denote convergence lines, and dots indicate typhoon remnant centers).

2.3 MCL Structure

The aforesaid analysis shows that Rananim induced heavy rainfall over the inland is closely associated with the activities of MCLs within its circulation. However, the most remarkable effect on rainfall is thrown by the MCL in the northwest part of typhoon circulation. We analyze the structures of the said MCL using Lagrangian coordinates (averaged moving speed of the remnant center on August 13, 2004 is used, namely u_0 ＝－3.5m/s，v_0＝1.2m/s) in order to better understand its activity mechanism, and its effects on rainfall.

Fig. 3 shows disturbance wind fields at 925 hPa, 850 hPa, 700 hPa, and 500 hPa at 0600 UTC August 13, 2004. The MCL (double dashed lines) at 925 hPa located in a patch 160 km northwest of the typhoon center (Fig. 3a), the one at 850 hPa 200 km away (Fig. 3b), and at 700 hPa 280 km away, or 80 km further west compared with the one at 850 hPa, or 120 km further west compared with the one at 925 hPa (Fig. 3c). The MCL at 500hPa was not obvious, with a position like that at 700 hPa (Fig. 3d). It indicates that the MCL exists remarkably in lower layer and inclined westwards along with height. At the 300 hPa (figure omitted), there exists a divergence zone over the MCL, desirable for the sustaining of a convergent and ascending movement in lower layer. The figure also shows some mesoscale divergence centers (D) within 100 km of the MCL, which may imply the vertical motion features of mesoscale convective system.

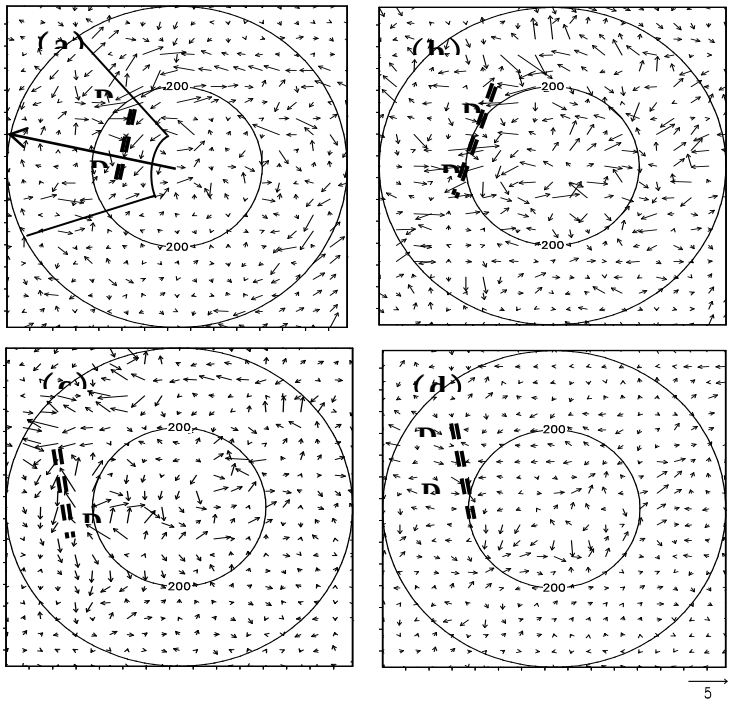

Fig.3. Disturbance wind vectors at （a）925 hPa, （b）850 hPa, （c）700 hPa, and （d）500 hPa at 0600 UTC 13 August 2004 (circle indicates the distant in kilometer away from the typhoon center. D represents the divergence center, long arrow denotes 280-degree wind direction for vertical profiles, and sector indicates averaged area in following text).

2.4 Instability

The vertical velocity section shows（figure omitted) that below 700 hPa, there is a slantwise ascending motion above the MCL, 160 km away from the remnant center at lower level and 200 km at higher level in the west. The updraft reaches the 300 hPa level, with the strongest ascending movement seen near 700 hPa. There is a narrow downdraft patch 250-300 km away from the typhoon center. Both the updraft and downdraft may form up a radial vertical circulation across the MCL. The corresponding potential temperature section (figure omitted) shows that both the low and high levels above the MCL are featured with warm wet air, and the low and middle level with relatively dry and cold air, allowing a convective instability below 900 hPa, and a deep convective stability above the level.

Under a given condition, the criterion for the existence of CSI in vortex atmosphere shall be that the moist potential vorticity (q_w) is less than zero. From the vertical sections of the moist potential vorticity (q_w) along the wind direction of 280 degree averaged on 0000-1800 UTC 13 August 2004 (figure omitted) , we find a shaded area (q_w <0) over the MCL between 700 hPa and 900 hPa, indicating a conditional symmetric instability. It is apparent that convective instability goes along with symmetric instability at MCL, facilitating the development of the convection.

3. Interactions between MCL and typhoon circulation

Assuming physical quantity A is:

$$A = A^* + A'$$

Where, A^* is the background field of A, and A' the disturbance field.

The horizontal and vertical conversion terms of kinetic energy can be as follows:

$$(V^* \cdot I^*)_H = -\{u^*[\frac{\partial}{\partial x}((uu)^* - u^*u^*) + \frac{\partial}{\partial y}((uv)^* - u^*v^*)] + v^*[\frac{\partial}{\partial x}((uv)^* - u^*v^*) + \frac{\partial}{\partial y}((vv)^* - v^*v^*)]\}$$

$$(V^* \cdot I^*)_V = -\{u^*[\frac{\partial}{\partial p}((\omega u)^* - \omega^*u^*)] + v^*[\frac{\partial}{\partial p}((\omega v)^* - \omega^*v^*)]\}$$

$V^* \cdot I^*$ indicates the conversion of kinetic energy between disturbance field and background field, and the subscript H and V denote the horizontal and vertical term respectively. Positive value means disturbance field providing kinetic energy to background field, while negative value implies acquiring kinetic energy from background field.

The horizontal and vertical conversion terms of vorticity conversion are then:

$$I_\zeta^H = -\{\frac{\partial}{\partial x}[(\zeta u)^* - \zeta^*u^*] + \frac{\partial}{\partial y}[(\zeta u)^* - \zeta^*u^*] + \frac{\partial}{\partial x}[(\zeta v)^* - \zeta^*v^*] + \frac{\partial}{\partial y}[(\zeta v)^* - \zeta^*v^*]\}$$

$$I_{\zeta}^{v} = -\frac{\partial}{\partial p}[(\zeta\omega)^{*} - \zeta^{*}\omega^{*}]$$

I_{ζ} indicates the conversion of vorticity between disturbance field and background field, and the superscript H and V denote the horizontal and vertical term respectively. Here, $I_{\zeta} > 0$ indicates that the interactions between two scales lead to disturbance field providing positive vorticity to background field. Oppositely it gets positive vorticity from background field.

We calculate the kinetic energy and vorticity conversions averaged on the MCL area, which is defined as a region between 250-330 degree direction, and 100-400 km away from the remnant center.

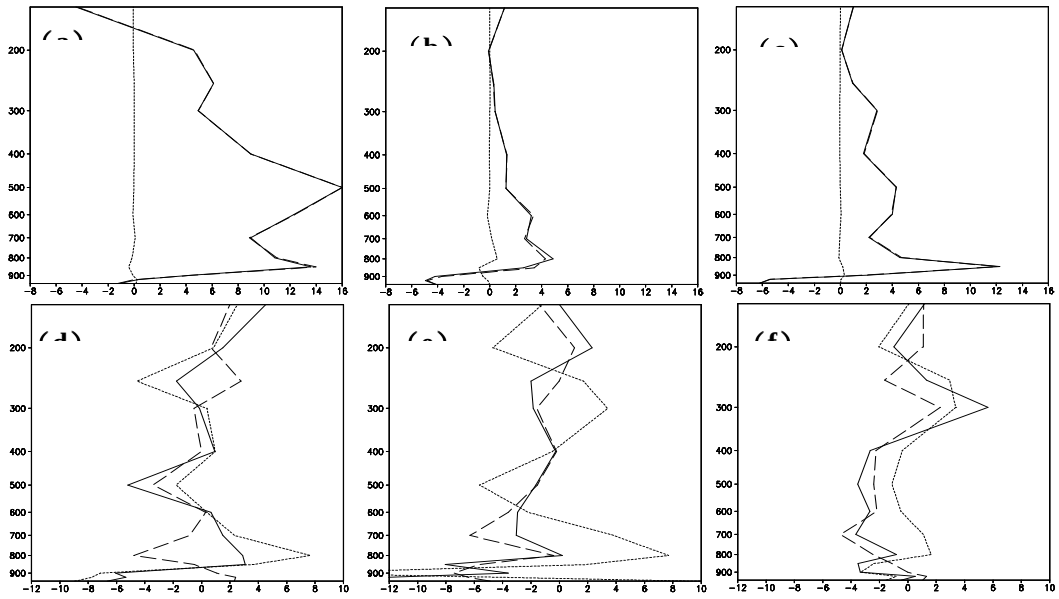

Fig. 4. The mean conversions of kinetic energy（a,b,c，10^{-3} W • kg^{-1}）and vertical vorticity（d,e,f，10^{-10} s^{-2}）on MCL area at 0000 UTC(a)(d), 0600 UTC(d)(e) and 1200 UTC(c)(f) in 13 August 2004 (dotted line represents vertical conversion, broken line horizontal conversion, and solid line the sum of the two).

Fig.4 shows the conversions of averaged kinetic energy (Fig.4a,b,c) and vorticity (Fig.4d,e,f) in the development process of MCL. In the context of kinetic energy conversion (Fig.4a-c), MCL obtains kinetic energy from lower troposphere below 900 hPa, and provides kinetic energy for typhoon circulation at higher levels. Horizontal conversion (broken line) is a key factor, with vertical motion (dotted line) offering a very limited contribution. It could be concluded that the MCL may gain convective unstable energy from lower layer of the remnant background for further development. Meanwhile, the development of MCL can convert baroclinic energy at higher level into kinetic energy for the remnant background. In the early development of MCL (Fig.4a, 0000 UTC 13 August), the kinetic energy provided by mesoscale disturbance is most noticeable. In the late development of MCL (Fig.4b and c), the kinetic energy provided is reduced, which may be associated with the gradual release of unstable energy.

Vorticity conversion makes a different result (Fig.4d-f). MCL obtains positive vorticity from background field (negative value) in lower layer, while provide positive vorticity (positive value) to the background at

upper level. As a whole, MCL obtains positive vorticity from the remnant circulation, especially in its development period (Fig.4e, 0600 UTC, August 13). However, the vorticity output is enhanced at 300hPa in the late period (Fig. 4f, 06h August 13), that may compensate the decay of the remnant.

4. Conclusions

1) The original formation of MCL in typhoon remnant circulation is associated with the cold air. The cold airflow intrudes the remnant and meet the easterly warm wet airflow in lower layer, which leads to the formation of MCL. β－mesoscale convective cloud clusters occur and develop near the MCL before merging into the remnant clouds. The MCL exists obviously below 700 hPa, accompanied by outreaching slantwise updraft and vertical circulation.

2) The increase of atmospheric baroclinicity is responsible for the occurrence of CSI in slantwise updraft. CSI jointed with vertical convective instability in MCL creates a desirable condition for the development of convection.

3) MCT facilitates its own development with kinetic energy and positive vorticity acquired from typhoon remnant in lower layer, while the development of MCL provides kinetic energy and positive vorticity to typhoon circulation at higher level, that may slows down the decay of typhoon.

Acknowledgements : *This work is financed by the National Key Basic Research Program Project of China (Grant No. 2009CB421504) and National Natural Science Foundation of China (Grant Nos. 40730948 and 40675033)*

References

Chen, L. S., H. B. Luo, and Y. H. Duan, 2004: An Overview of Tropical Cyclone and Tropical Meteorology Research Progress. *Adv. Atmos. Sci.*, 21(3),505-514.

Lu, H. C., J. W. Kang, and Z. Kou et al., 2004: The dynamic characteristic of meso-scale mixed waves in typhoon. *Progress in Natural Sci*.,14(5),514-546. (in Chinese)

Luo, Z. X., and L. S. Chen, 2003: Impacts of topography on Rossby waves. *Progress in Natural Sci.*, 13(4),372-377. (in Chinese)

Meng, Z. Y., X. D. Xu, and L. S. Chen, 2002: Mesoscale characteristics of the interaction between TC Tim (9406) and mid-latitude circulation. *Acta Meteor Sinica*, 2002,60(1),31-39. (in Chinese)

Effect of Tropical SST Forcing on the Regional Circulation in East Asia

Sung-Dae KANG, Seong-Hee WON, Tae-Ryong KIM

National Typhoon Center

Korea Meteorological Administration, Seoul, Korea

sdkang@kma.go.kr

ABSTRACT

Tropical sea surface temperature (SST) forcing influences the regional circulation of East Asia by propagating Rossby wave from equatorial region to middle latitude in summer (Kang and Kimura, JMSJ 2003). The propagation can be classify into two types; one is the typical type propagating meridionally, and the other is the atypical type propagating zonally from equatorial region. The authors found linearity between the strength of free Rossby wave propagation and the magnitude of the tropical SST forcing for the typical type. Nonlinearity increases if there is a tropical depression, or typhoon in the North Western Pacific region. However, what determines the types of free Rossby wave propagation was not studied, yet.

To investigate the main factor that determines the types of free (or forced) Rossby wave propagation excited by tropical SST forcing (or mountain drag), two approaches are adopted; one is a numerical approach (NCEP GSM and NCAR MM5), and the other is an analytic approach (linearized shallow water equation) for free and forced Rossby waves, respectively. The two approaches need different triggers to excite the propagation of each Rossby wave. Baroclinic instability (i.e., vertical shear) caused by tropical SST forcing and barotropic instability (i.e., horizontal shear only) caused by mountain drag are the triggers for free and forced Rossby waves, respectively.

According to the main results of the two approaches, the direction of background inflow at the upstream region of each trigger (tropical SST forcing, mountain drag) commonly determine the types of both Rossby wave propagations. The agreement of the two approaches indicates that the dynamics of baroclinic free Rossby wave propagation can be explained by the dynamics of barotropic forced Rossby waves.

Specifically, the numerical approach shows the following results. The meridional component of the background inflow (low-level jet) at the upstream region of the tropical SST forcing domain (around the Philippine Islands) is the main factor that determines the type of free Rossby wave propagation. The type (or, direction) of free Rossby wave propagation is determined by the direction of the background inflow at the upstream region of the tropical SST forcing domain. The change from the typical type to the atypical type occurs when the direction of the background inflow changes from the meridional to the zonal direction, and vice versa. The free Rossby wave can propagate more effectively under favorable conditions such as strong SST forcing and inflow at forcing domain. The shape and location of the triggers in the models are secondary important which determine the direction of free Rossby wave propagation. The linearity of free Rossby wave propagation found by the RCM results (Kang and Kimura, 2003) still exists in the GCM results. This finding reconfirms that the linearity comes only from tropical SST forcing in the RCM domain, and atmospheric circulation anomalies (including the SST anomaly) outside the lateral boundary do not affect the linear response of free Rossby wave propagation against the linear increase of SST forcing around the Philippine Islands.

According to the analytic approach results, the type of forced Rossby wave propagation is the same as the numerical approach results. The inflow direction at the upstream topography region is the main factor that determines the type of forced Rossby wave propagation. Similar to the free Rossby wave, the direction of the forced Rossby wave propagation follows the background inflow direction. The shape of the mountain is of secondary importance when determining the propagation type.

Key Word: Tropical SST, Rossby Wave Propagation, Tropical Depression, Regional and Global Models

Wave Activity Associated with a Landfalling Typhoon

Lingkun Ren

Institute of Atmospheric Physics, Chinese Academy of Science, China

Chungu Lu

NOAA Earth System Research Laboratory, and Colorado State University, USA

1. Introduction

A tropical cyclone can often be viewed as a set of cloud/rain bands superimposed upon a vortex core. From a dynamic point view, this structure may manifest the interaction of waves (disturbances) and basic flows (basic-state vorticity) (Schubert 1985; Chen 2003). In this sense, wave activity associated with a tropical cyclone may well be correlated with rainbands generated by convective processes. When making a landfall, a typhoon (tropical cyclone) typically experiences decreasing rainfall and dissipating spiral cloud/rain bands. Can this change of a landfalling typhoon structure be reflected in its dynamics? It must be, because the dissipating rainbands imply the change of heating structure of a tropical cyclone, the forcing of the dynamics inside the cyclone. Based on the above conjecture, wave activity should display a direct response to the rainfall change due to a landfalling process.

Put the issue in the context of predictability of rainfall resulting from a tropical cyclone. Rainfall is a very difficult field to predict, especially from a landfalling tropical cyclone. The intensity and variability of rainfall from a landfalling cyclone can be affected by various synoptic environments as well as many subscale processes, such as topography and microphysical conditions. However, if one can deduce a dynamic variable that tracks rainfall variability consistently, this variable may be used as an important diagnostic and prognostic reference for tropical cyclone rainfall. As we conjectured above, wave activity may just provide such a role in a tropical cyclone.

In this study, a wave-activity equation is derived within a most general dynamic and thermodynamic framework. This wave-activity law is a generalization of its quasigeostrophic version from the classic theory dated back as early as Elliassen (1952), Edmon et al. (1980), and Andrew (1983, 1987). Applying the derived wave-activity law to the landfalling typhoon “Rananim” over southeast China in 2004, we show that the wave activity tracks the typhoon rainfall remarkably well. The physical processes responsible to the development of such waves (or disturbances) are also analyzed.

2. The generalized wave-activity law

Haynes (1988) and Scinocca et al. (1992) defined wave activity as a conservative perturbation quantity that was quadratic (or of higher-order) in disturbance fields in small-amplitude limit. The wave activity generally satisfies the following wave-activity relation

$$\frac{\partial A}{\partial t}+\nabla\cdot\mathbf{F}=S \qquad (1)$$

where A and $\mathbf{F}$ are the wave-activity density and the divergence of wave-activity flux, respectively, both of which are quadratic or higher-order perturbation quantities, and S is the source or sink of wave-activity density. When S vanishes takes a local conservative form. The wave-activity density in nature is a kind of perturbation energy, which varies as the disturbed fields evolve. In this sense, wave-activity density is capable of representing the strength of disturbance, and therefore the wave-activity relation (1) can be used to evaluate the time change of the disturbances.

One of the difficulties in using such a simple dynamic equation to diagnose or even predict the development of atmospheric disturbances is to obtain a wave-activity relation for a most general dynamic system. Previously derived wave-activity laws were mostly based on some simplified dynamic systems using quasigeostrophic or semisgeostrophic assumptions. In order to overcome this problem, Momentum-Casimir and energy-Casimir methods that were early used by Arnol'd and others to prove stability theorems for some conservative flows were widely employed to investigate wave-basic flow interaction (McIntyre and Shepherd 1987; Shepherd 1990; Scinocca and Shepherd 1992; Magnusdottir and Haynes 1996; Durran 1995; Murray 1998; Ren 2000; Chen 2003). Haynes (1988) derived wave-activity relations using both momentum-Casimir and energy-Casimir methods. Ran and Gao (2007) used the Momentum-Casimir method to derive a three-dimensional wave-activity relation for a pseudomomentum in Cartesian coordinates. Since a Casimir function is generally defined without a specific expression, it is difficult to evaluate the wave-activity relations in practice.

Water vapor is one of the most essential atmospheric elements in moist dynamics. It plays an important role in the development of tropical cyclones, which often result in heavy precipitation. Most of the previous wave-activity theories were only applicable to large-scale atmospheric motions and did not involve the effect of moisture. Little is known about the dynamical role of moisture in wave-basic flow interaction.

In an effort to address the above two problems, in this paper we have derived a three-dimensional wave-activity relation with an inclusion of a moist effect in the following form:

$$\frac{\partial J}{\partial t}+\nabla\cdot\mathbf{F}=\nabla\cdot\left(\boldsymbol{\omega}_e S_{\theta_e^*}\right), \qquad (2)$$

where J and $\mathbf{F}$ are generalized wave-activity density and flux, respectively, and the term on the right-hand-side of (2) is a source/sink term for the wave-activity density. The generalized wave activity is given, through the derivation,

$$J=\boldsymbol{\omega}_e\cdot\nabla\theta_e^*, \qquad (3)$$

where $\boldsymbol{\omega}_e=\nabla\times\mathbf{v}_e$ is the perturbation vorticity, and θ_e^* is the perturbed generalized potential temperature (Gao et al. 2004). Therefore, it is readily seen that this generalized wave-activity density function is simply a generalized moisture potential vorticity substance (GMPVS). The wave activity flux has four components, which are expressed

$$\mathbf{F}_1=\mathbf{v}_0 J, \qquad (4)$$

$$\mathbf{F}_2 = \left[\mathbf{v}_e \left(\boldsymbol{\omega}_0 \cdot \nabla \theta_e^* \right) - \boldsymbol{\omega}_0 \left(\mathbf{v}_e \cdot \nabla \theta_e^* \right) \right], \quad (5) \qquad \mathbf{F}_3 = \boldsymbol{\omega}_e \left(\mathbf{v}_e \cdot \nabla \theta_0^* \right), \quad (6)$$

$$\mathbf{F}_4 = \left(\nabla p_0 \times \nabla \frac{\rho_e}{\rho_0^{\,2}} - \nabla p_e \times \nabla \frac{1}{\rho_0} \right) \theta_e^* . \quad (7)$$

The four terms respectively represent the transport of GMPVS by mean velocity, the generalized heat flux, the generalized momentum flux, and solenoidal forcing term.

3. Case overview and analysis data

A heavy-rainfall event associated with the landfalling typhoon "Rananim" occurred over the southeast coast of China during 12UTC 12 - 00UTC15 August 2004. The Typhoon Rananim can be tracked back to a tropical disturbance with an organized deep convection about 1000 km east of Manila in the Philippines Sea, over a warm water with the sea surface temperature 29°C. It was categorized as a tropical depression by the Joint Typhoon Warning Center (JTWC) at 00UTC 7 August. At 00UTC 8, the system was strengthened into the Tropical Storm Rananim with the minimum sea level pressure (MSLP) 997 hPa. Rananim continued to intensify and reached the MSLP of 963 hPa with the maximum surface wind (MSW) 40 m s^{-1} by 00UTC 11. Rananim made a landfall at approximately 12UTC 12 August in China (Fig 1a). After that, Rananim moved westwards and brought heavy rainfall along its track (Fig 1b). Further weakening occurred as Rananim progressed farther west into inland China. At 00UTC 16, Rananim completely dissipated and the associated heavy-rainfall event stopped.

Grid analysis data was employed to calculate wave activity density and fluxes associated with Rananim. The grid analysis data was produced by ADAS [*ARPS* (Advanced Regional Prediction System) Data Analysis System] combining the NCEP/NCAR final analysis data (1°×1°, 26 vertical pressure levels and 6-hour interval) with the routine observations of surface and sounding. The ARPS model is a nonhydrostatic and fully compressible regional atmospheric prediction system. The model domain used here was configured with a center at (38.5°N, 116.5°E) and the horizontal grids 177×177 with 27 km horizontal grid resolution in both zonal and meridional directions. The vertical domain was divided into 43 unequal layers with the mean grid mesh of 500 m. The analysis data on grid was output on regular height level at a 6-hour interval. Using these data, we can diagnose wave-activity density and flux associated with the Typhoon Rananim. We neglect diabatic heating term, so that the source/sink term in the generalized wave-activity relation vanishes. In this study, we only calculate absolute value of the wave-activity density.

4. Wave activity associated with the landfalling typhoon

4.1 Horizontal structure of vertically integrated wave-activity density

As shown in Fig. 2, at 00UTC 12 August, since the main body of typhoon was still at the sea and its small portion over land, the center of wave-activity density matched with the typhoon. The northwest edge of this wave-activity density overlapped the local weak rainfall region in the southeast China (Fig. 2a). As the typhoon gradually landed, the area of surface rainfall generated by the typhoon increased and was located in the main area of wave-activity density. After 12UTC 12 August, the wave-activity density showed similar horizontal distribution patterns as the heavy-rainfall regions (Fig. 2b-i). The collocation of large-valued

wave-activity density and rainfall implied that the dynamic and thermodynamic properties of the atmosphere over the heavy-rainfall region were significantly disturbed. The figure also shows wave activity associated a synoptic frontal rainfall in northeast China.

4.2 Propagation characteristics of wave-activity density

In the temporal-latitudinal cross section (Fig. 3), both the high-value wave-activity density and rainfall area displayed a westwards propagation component with time. The wave-activity density and surface rainfall was so strikingly collocated as they moved westwards together. The analysis implies that the wave-activity density was consistent with the observed rainfall in the temporal variation tendency.

4.3 Vertical structure of wave-activity density

The above diagnosis demonstrates that the wave-activity density shares similar horizontal distribution patterns and temporal evolution trends with those of observed 6-h accumulative rainfall. The consistence between wave-activity density and surface rainfall suggests that there exists atmospheric wave (namely, disturbance) activity over the landfalling typhoon regions. In other words, the wave described by wave-activity density present a strong dynamic signal over the heavy rainfall region in the landfalling typhone.

The vertical structure of wave-activity density (thin contours) over heavy-rainfall region associated with the landfalling typhoon (thick curve) is examined and is presented in Fig. 4. As it was shown, the observed 6-h accumulative frontal rainfall is mainly located in the northern latitudes belt between 38-43^{o}N at 06UTC 12 August 2004. At this time, a weaker wave-activity density centralized at 2 km level near 28 ^{o}N, corresponds to the light rains of typhoon Rananim at initial-landfalling stage (Fig. 4a). After that, the rainfall from the landfalling typhoon increased gradually, while the rainfall from the frontal system was diminishing. Note that the typhoon clearly displayed multi-spiral rainbands around the typhoon center (Fig. 4b-f). The wave-activity density below 6.5-km level over the two weather systems varied with the similar phase to rainfall, exhibiting multiple-maximum centers.

4.4 Forcing by divergence of wave-activity fluxes

In order to analyze the dynamic processes responsible for the variation of wave-activity density, we calculate the four terms of wave-activity flux divergence (4), (5), (6), and (7). In Figs. 5, one can see that the term $\nabla \cdot \mathbf{F}_2$ exerted dominative influence in the middle and lower troposphere. The term $\nabla \cdot \mathbf{F}_4$ made almost no contribution to the wave-activity density. This suggests that moist and heating process (driving heat fluxes) is the most important process feeding energy into landfalling-typhoon disturbances, while the solenoidal forcing plays almost no role in the development of these disturbances in typhoon, at least in this particular case. The latter is clearly consistent with the dominant barotropicity of typhoon dynamics. The importance of $\nabla \cdot \mathbf{F}_2$ suggested that the interaction between the basic-state cyclonic circulation of the typhoon and mesoscale disturbance due to moist-heating process dominated the variation of mesoscale waves embedded in landfalling typhoon. Note that all the forcings (divergence of all four terms) are collocated with rainfall region in the landfalling Rananim.

5. Conclusion

In this study, we have derived a wave-activity equation for the most general dynamic system with the inclusion of moisture process. The quadratic perturbation of GMPVS can be interpreted as some type of

disturbance energy. The wave-activity fluxes contain four terms, two of which shear some analogy to the heat and momentum fluxes in the classic wave-activity relation. The other flux terms involve the transport of wave-activity density by the basic-state velocity and solenoidal forcing.

Using this derived wave-activity relation, we diagnosed the development of disturbances in a landfalling typhoon occurred in southeastern China. The vertically-integrated wave-activity density showed strong signals in locations where surface rainfall existed. The wave activity density also displayed propagation characteristics, which is in phase of rainfall from the landfalling typhoon. These results suggest that the generalized wave activity can be very useful not only in diagnosing tropical cyclone rainfall, but also in predicting the rainfall location as well as intensity. Further diagnoses of the development of wave activity associated with a landfalling typhoon indicated different roles of dynamic processes played in the development of disturbances. The generalized momentum flux and solenoidal forcing seem to contribute very little to the wave-activity density in the landfalling typhoon, while the generalized heat flux seems to play a dominant role.

REFERENCES

Andrews, D. G., 1983: Finite-amplitude Eliassen-Palm theorem in isentropic coordinates. *J. Atmos. Sci.,* **40**, 1877-1883.

Andrews, D. G., 1987: On the interpretation of the Eliassen-Palm flux divergence. *Q. J. R. Meteorol. Soc.,* **113**, 323-338.

Chen, Y., G. Brunet, and M. K. Yau, 2003: Spiral Bands in a Simulated Hurricane. Part II: Wave Activity Diagnostics. *J. Atmos. Sci.,* **60**, 1239–1256.

Durran, D. R., 1995: Pseudomomentum diagnostics for two-dimensional stratified compressible flow. *J. Atmos. Sci.,* **52**, 3997-4008.

Edmon, H. J., B. J. Hoskins, and M. E. McIntyre, 1980: Eliassen-Palm cross sections for the troposphere. *J. Atmos. Sci.,* **37**, 2600-2616.

Eliassen, A., 1952: Slow thermally or frictionally controlled meridional circulation in a circular vortex. *Astrophys. Norv.,* **5**, 19-60.

Gao, S., X. Wang, and Y. Zhou, 2004: Generation of generalized moist potential vorticity in a frictionless and moist adiabatic flow. *Geophys. Res. Lett.*, *31*, L12113, doi:10.1029/ 2003GL019152.

Haynes, P. H., 1988: Forced, dissipative generalizations of finite-amplitude wave activity conservation relations for zonal and nonzonal basic flows. *J. Atmos. Sci.,*
45, 2352-2362.

Magnusdottir, G., and P. H. Haynes, 1996: Application of wave-activity diagnostics to baroclinic-wave life cycles. *J. Atmos. Sci.,* **53**, 2317-2353.

McIntyre, M. E., and T. G. Shepherd, 1987: An exact local conservation theorem for finite amplitude disturbances to non-parallel shear flows, with remarks on Hamiltonian structure and on Arnol'd 's stability theorems. *J. Fluid. Mech.*,**181**, 527-565.

Murray, D. M., 1998: A pseudoenergy conservation law for the two-dimensional primitive equations. *J. Atmos. Sci.,* **55**, 2261–2269.

Ran, L., and S. Gao, 2007: A three-dimensional wave-activity relation for pseudomomentum. *J. Atmos. Sci.,* **64**, 2126-2134.

Ren, S., 2000: Finite-amplitude wave-activity invariants and nonlinear stability theorems for shallow water semigeostrophic dynamics. *J. Atmos. Sci.,* **57**, 3388-3397.

Schubert, W. H., 1985: Wave, mean-flow interactions, and hurricane development. Preprints, *16th Conf. on Hurricanes and Tropical Meteorology,* Houston, TX, Amer. Meteor. Soc., 104-141.

Scinocca, J. F. and T. G. Shepherd, 1992: Nonlinear wave-activity conservation laws and Hamiltonian structure for the two-dimensional anelastic equations. *J. Atmos. Sci.,* **49**, 5-27.

Shepherd, T. G., 1990: Symmetries, conservation laws, and hamiltonian structure in geophysical fluid dynamics. *Adv. Geophys.,* **32**, 287-338.

Figure 1

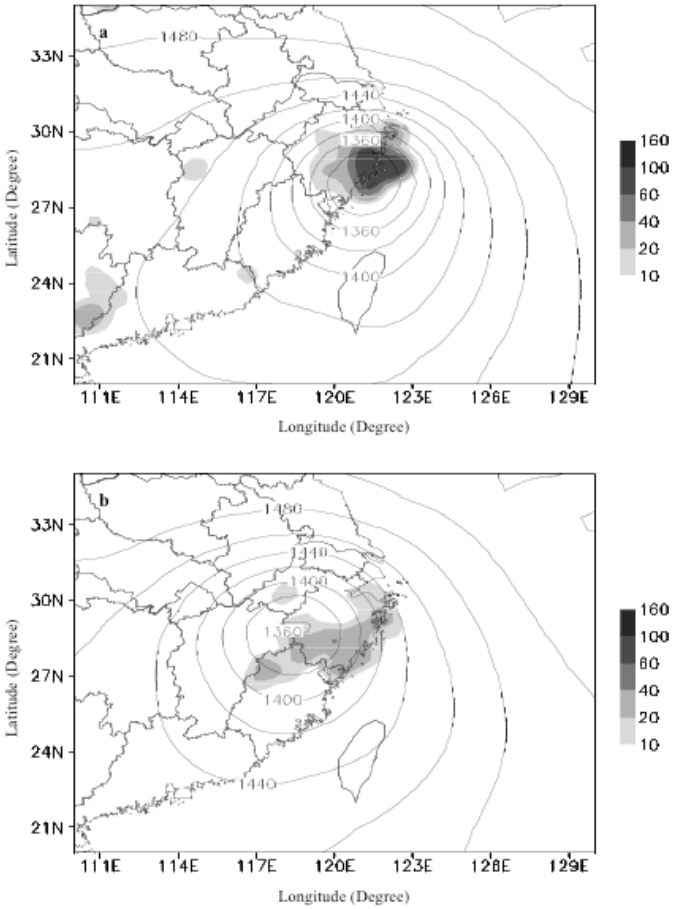

Figure 1. The horizontal distributions of the geopotential height (solid contour, Unit: gpm) on 850 hPa level and the observed 6-h accumulative surface rainfall (gray shade, Unit: mm) at 12 UTC 12 (a) and 00 UTC 13 (b) August 2004.

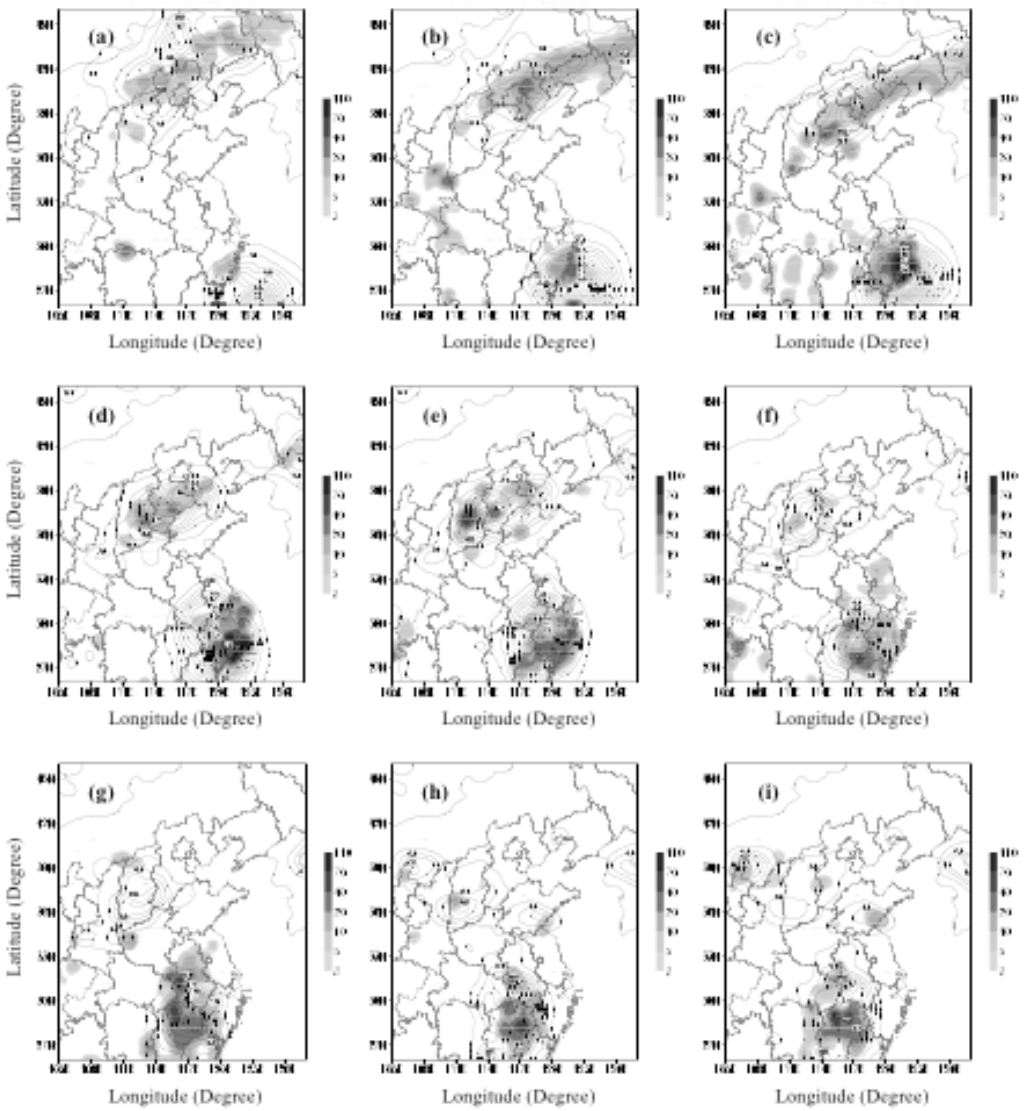

Figure 2: The horizontal distributions of vertically integrated wave-activity density at (a) 00 UTC, (b) 06 UTC, (c) 12 UTC, (d) 18 UTC of 12 August, (e) 00 UTC, (f) 06 UTC, (g) 12 UTC, (h) 18 UTC of 13 August, and (i) 00 UTC 14 August 2004 (contours, in unit: 10^{-3} K s^{-1}). The gray shade denotes the observed 6-h accumulated surface rainfall (Unit: mm).

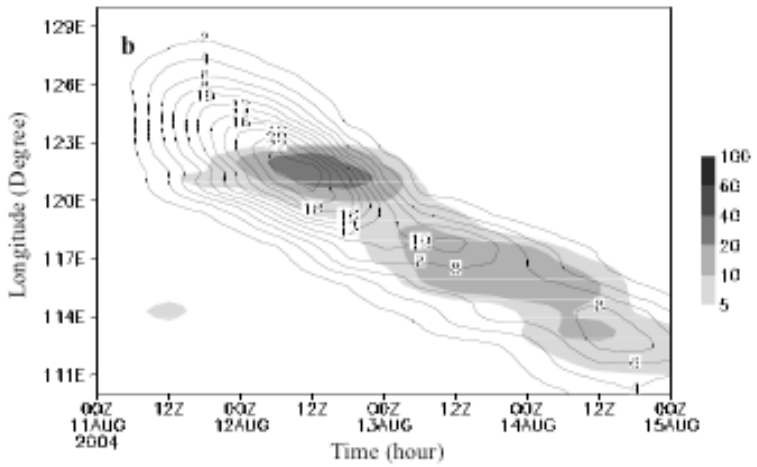

Figure 3: The temporal-longitudinal cross sections of wave-activity density vertically integrated and averaged over the latitude belt of 25-30°N during 00 UTC 11 - 00 UTC 15 August 2004 (Unit: 10^{-4} K s^{-1}). The gray shade denotes the 6-h accumulated surface rainfall (Unit: mm).

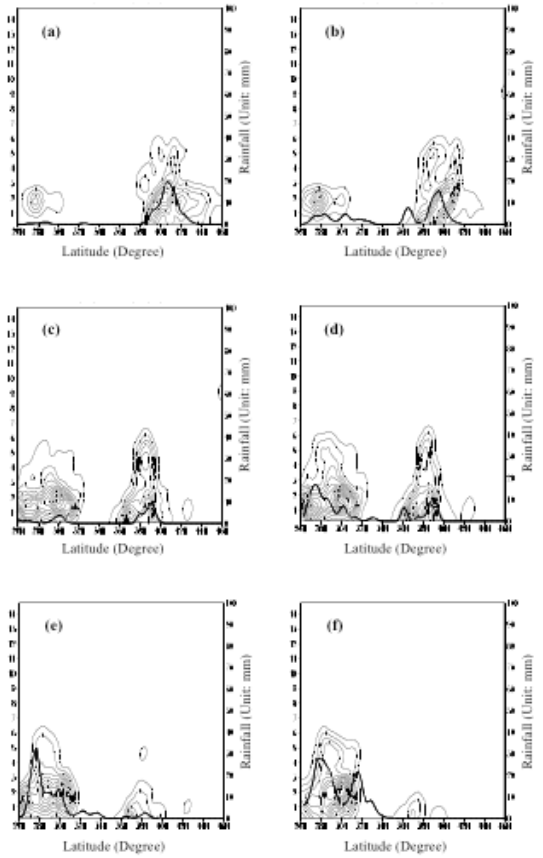

Figure 4: The vertical-latitudinal cross sections of wave-activity density averaged over the longitude belt of

116-119°E at 06 UTC 12 (a), 12 UTC 12 (b), 18 UTC 12 (c), 00 UTC 13 (d), 06 UTC 13 (e) and 12 UTC 13 (f) August 2004 (Unit: 10^{-7} K m^{-1} s^{-1}). The thick solid line denotes the 6-h accumulated surface rainfall (Unit: mm).

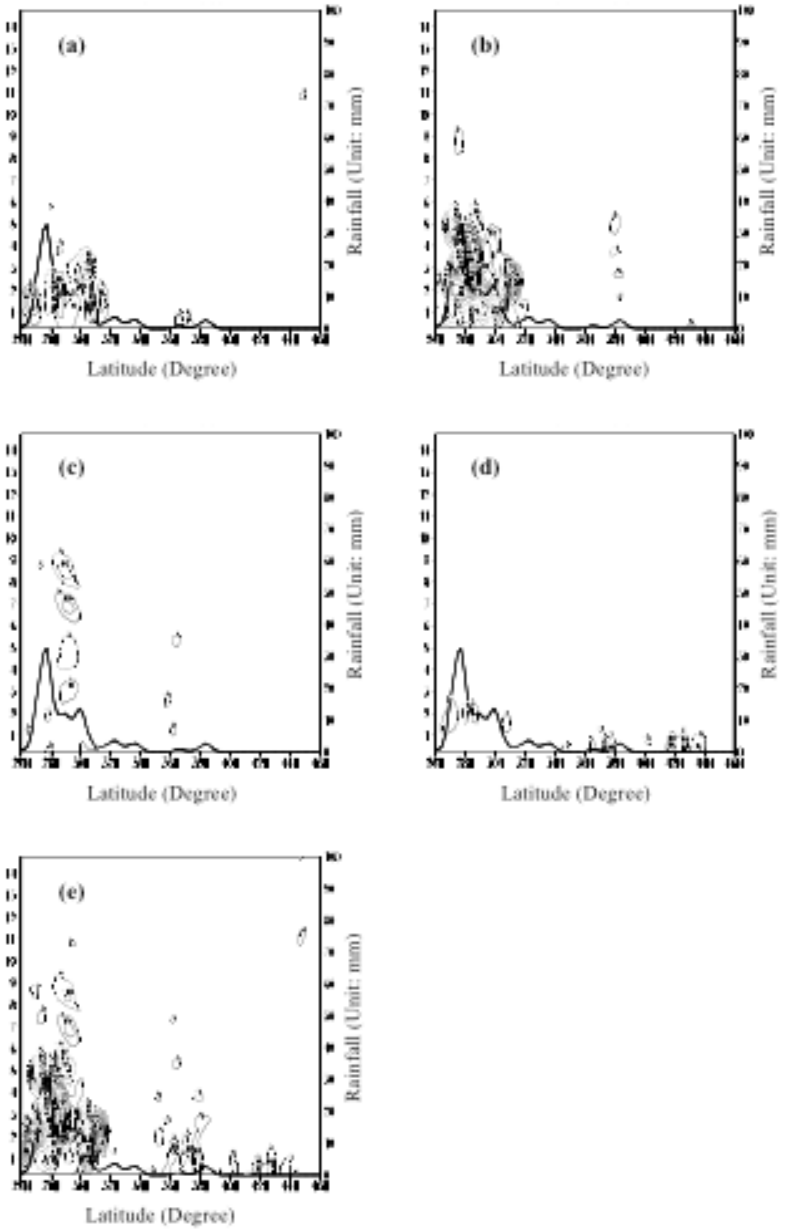

Figure 5: The vertical-latitudinal cross sections of (a) $\nabla \cdot \mathbf{F}_1$, (b) $\nabla \cdot \mathbf{F}_2$, (c) $\nabla \cdot \mathbf{F}_3$, (d) $\nabla \cdot \mathbf{F}_4$ and (e) $\nabla \cdot \mathbf{F}$ (all in unit: 10^{-12} K m^{-1} s^{-2}) averaged over the longitude belt of 116-119°E at 12 UTC 12 August 2004. The thick solid line denotes 6-h accumulated surface rainfall (Unit: mm).

Rainfall Reinforcement Associated with Landfalling Tropical Cyclones

Meiying Dong,[1, 2, 3] Lianshou Chen,[1] Ying, Li[1] and Chungu Lu[4]

[1.] State Key Laboratory of Severe Weather, Chinese Academy of Meteorological Sciences, Beijing 100081, China

[2.] Nanjing University of Information Science and Technology, Nanjing 210044, China

[3.] Zhejiang Meteorological Observatory, Hangzhou 310017, China

[4.] NOAA Earth System Research Laboratory, Boulder, Co. U.S.A

Extended Abstract

Usually, tropical cyclones (TCs) often bring about heavy rainfall during landfalling, which typically terminates with a demise of TCs over land. However, some TCs may suddenly produce even stronger rains than those during their landfalling. Such reinvigorating phenomena are known as Rainfall Reinforcement associated with Landfalling Tropical Cyclones (RRLTC). Because of its occurrence often under complex atmospheric environments, a prediction of RRLTC has always been a challenge to forecasters. Since RRLTC has characteristics of strong intensity and unexpectedness, it can induce tremendous disasters exceeding those during TC landfalling. For example, the rainfall reinforcement by Typhoon Nina (7503) (Chen and Ding 1979) occurred after it moved inland and downgraded into tropical depression (TD). The reinforcement of rainfall from this dissipating typhoon produced a record extreme precipitation in mainland China with a total of 1062 mm rainfall in 24 hours, which led to the well-known "75·8" severe flooding that killed tens of thousands of people. More recently, the severe tropical storm Bilis (0604) (Zhang and Kong 2007) reinforced rainfall after landfalling, and resulted in an extremely severe meteorological disaster in the forms of sustained torrential rains, flooding, landslide and mudslide in South China. Therefore, it is vitally important to study RRLTC for improved forecasting and disaster prevention and mitigation.

The data used in this study include those of National Center for Environmental Prediction (NCEP) and National Center for Atmospheric Research (NCAR) reanalysis data (2.5 ° × 2.5 ° horizontal grid spacing for four times a day), those from the "Typhoon Yearbook" for TC tracks (China Meteorological Administration, 1949-2006), daily TC precipitation data for the years from 1949 to 2006, and China nationwide 6 hourly precipitation data for the period of 1998-2006 (those in 2002 were removed from the data analyses due to evident errors detected, and those for Taiwan were not accounted for due to data incompleteness). The data used in the statistical calculations were the TC precipitation data of 24h, 12h and 6h, respectively. The 24h TC precipitation data were provided by the Shanghai Typhoon Institute, China Meteorological Administration. The 6h TC precipitation data were selected from China national precipitation dataset for the same stations and the same days as those of the 24 hours. The 12h TC precipitation data were accumulated from the 6h data.

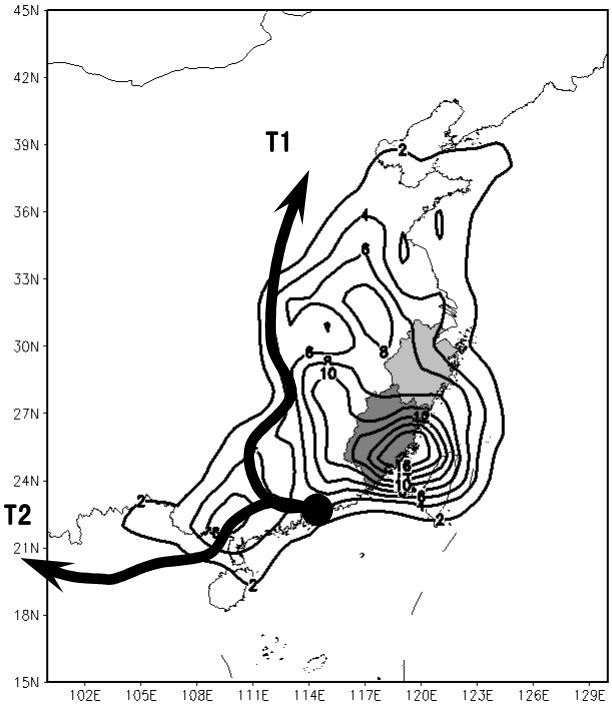

Fig. 1: Distribution of frequency of all TCs with rainfall reinforcement over land (unit: ‰, the thick solid lines with arrows display the two categories of northward and westward tracks represented by T1 and T2, respectively. The dark and light gray shading respectively denotes Fujian and Zhejiang province)

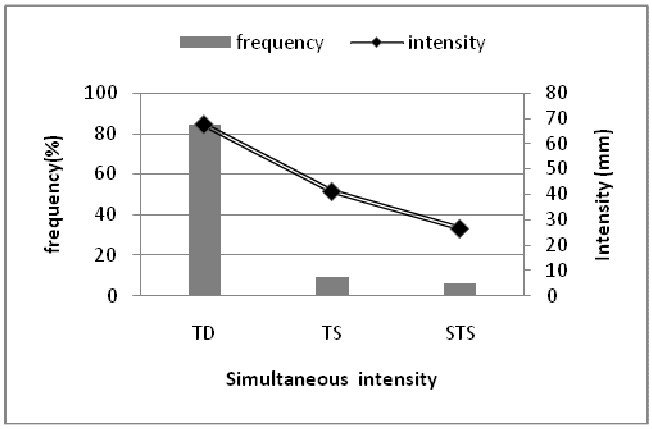

Fig. 2: Relationship between RRLTC occurrence frequency/intensity and TC category at the time of RRLTC occurrence.

According to the evolution of heavy rainfall intensity, a multi-scale criteria of RRLTC is put forward as 15mm, 12mm and 10mm for 24h, 12h and 6h accumulated rainfall respectively by using daily TC rainfall dataset. The TCs triggering rainfall reinforcement account for 9.7% of the total number of TCs that make landfall on China mainland, and often cause problems and surprises for forecasters. The TCs with rainfall reinforcement mostly make landfall in the east coast of China, and move primarily in two spreads of tracks, northward and westward, respectively (see Fig.1). RRLTC often occurs in the remnant of a tropical depression (see Fig.2), which has been downgraded from typhoon intensity, in particular in a period when the remnant is slowdown or even stagnated. The northeast and southwest quadrants of a TC are the two areas

with high occurrence frequency for rainfall reinforcement.

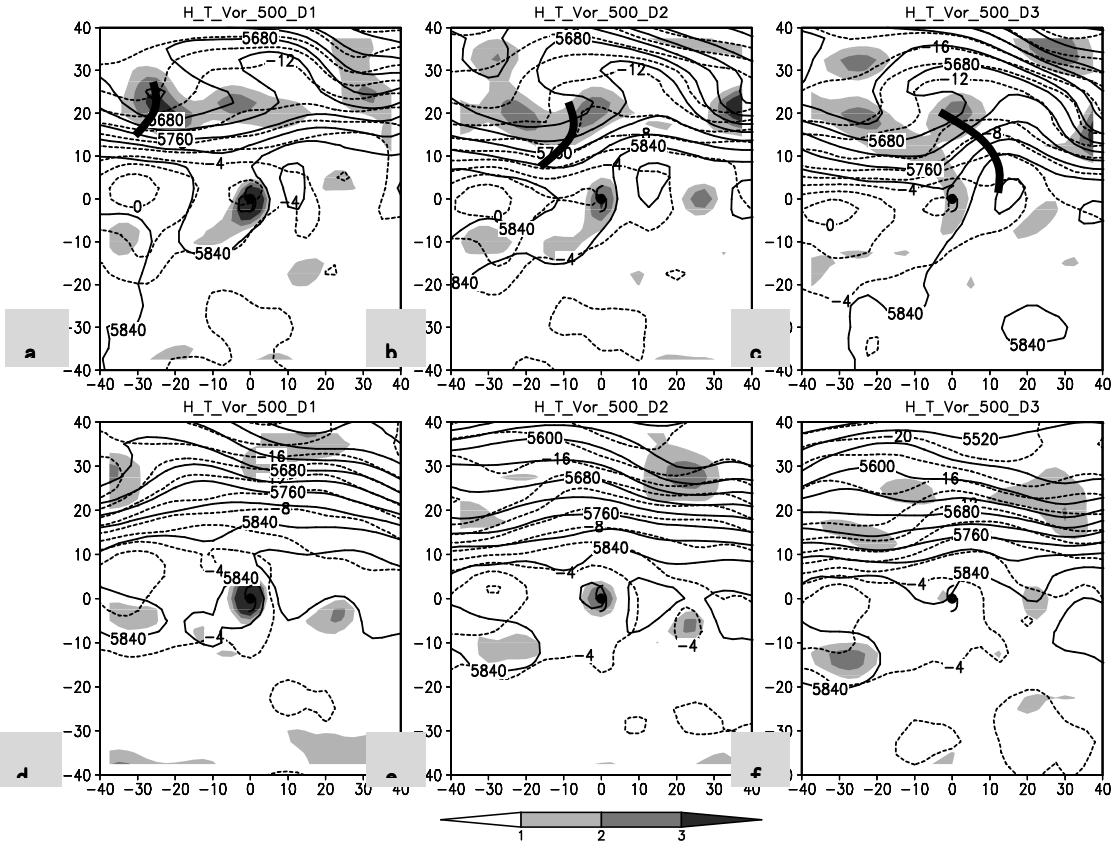

Fig. 3: Evolution of the geopotential height (solid curves, in unit: gpm), temperature (dash curves, in units: ℃), and vorticity (shaded, in units: 10-5•s-1) in days at 500hPa for (a) RTC (a - c), and (b) NRTC (d - f). The thick solid lines represent the westerly troughs. From left to right are circulation patterns from D1 to D3. The TC centers are located in the origin of the coordinates in longitudes and latitudes. The coordinates are positive in eastward and northward directions, negative in westward and southward directions..

The above analyses illustrated that RRLTC occurred mainly in the two lines of TC tracks, i.e., in the northward and westward tracks. Next we would like to examine characteristics of atmospheric circulation associated with these RRLTCs. A dynamic composite technique (Li 2004) was used for such an analysis. Based on similar TC tracks, similar rainfall reinforcement intensity, and similar quadrants for rainfall reinforcement (northward type in the northeast quadrant, and westward type in the southwest quadrant), samples of RRLTC categories (denoted as RTC) were selected. Four cases (6205, 6306, 8108, and 9417) were selected for northward type, and three cases (6120, 8107, and 0605) for westward type. Likewise, non-reinforcement category (denoted as NRTC) was sampled following the similar tracks as the above. Four cases (8209, 9418, 9504, 9909) for northward type and three cases (8404, 8817, and 9803) for westward type were selected. The duration of synthesis was chosen for three days, denoted as D1, D2 and D3 in the late text. For RTC category, the synthetic analysis is conducted for two days prior to reinforcement and one day during the reinforcement, and for the NRTC category, the synthetic analysis is done for the day at TC landfall and further two days afterward. Since precipitation is an accumulative value, the atmospheric circulation was taken as an average of the four observations of the day.

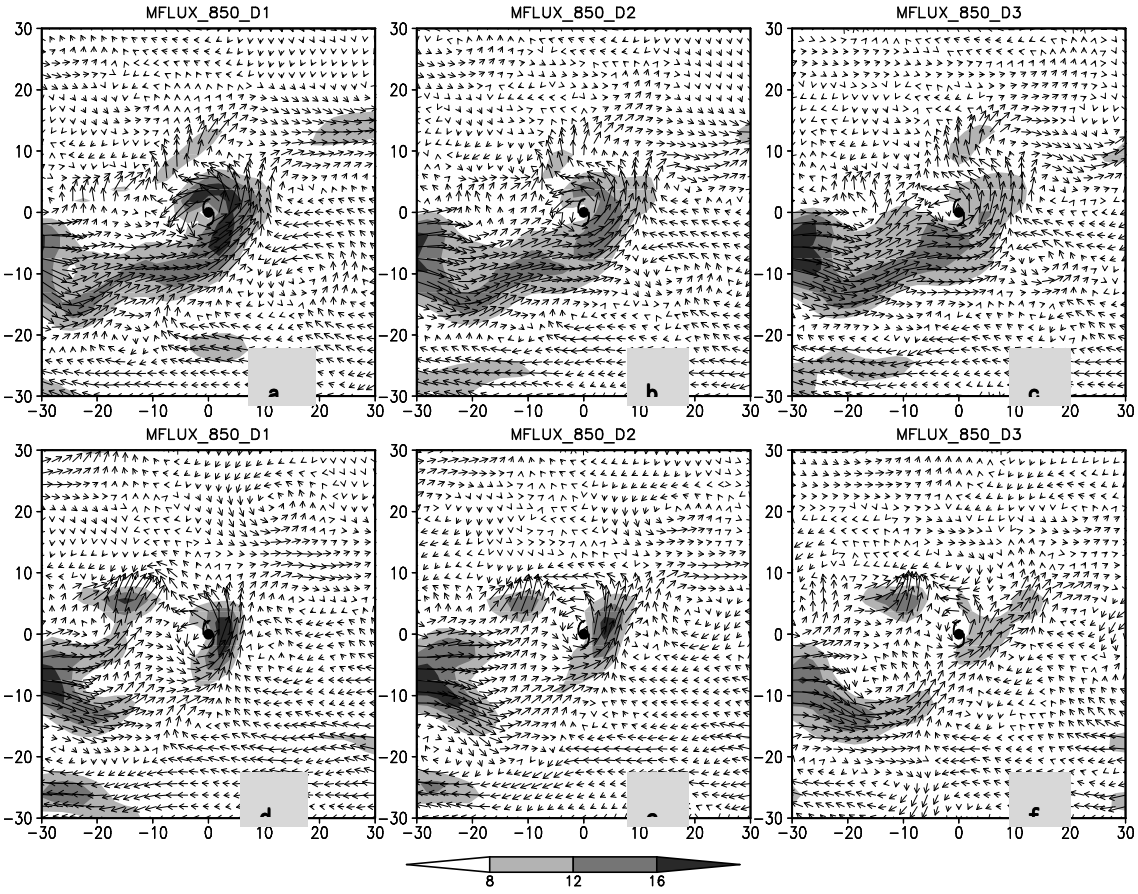

Fig. 4: Variations of moisture flux (vectors) and moisture content (shaded, in unit: g•hPa^{-1}•cm^{-1}•s^{-1}) at 850hPa for (a) RTC (a - c), and (b) NRTC (d - f). Others are the same as in Fig. 3, but for the westward track.

Diagnostic analyses show that the rainfall reinforcement for TCs with a northward track is mainly attributed to a superimposition of westerly troughs and the TCs (Fig.3) and their interactions. Such a superimposition is not present for northward tracking TCs without reinforcement. Rainfall reinforcement for the TCs with a westward track is mainly due to favorable moisture fluxes interacting with TC remnant cloud clusters (Fig.4). Analyses show that such moist transport is otherwise missing for westward moving TCs without reinforcement. RRLTCs require inputs from new energy sources. Results of the present study indicate that release of baroclinic potential energy and latent heat are the two major sources of energy, which trigger rainfall reinforcement of the remnants of the TCs with northward and westward tracks, respectively.

Key Words: Tropical cyclones, rainfall reinforcement, climatology characteristics, reinforcement energy source.

References

Bosart, L. F., and D. B. Dean, 1991: The Agnes rainstorm of June 1972: Surface feature evolution culminating

in inland storm redevelopment. *Weather and Forecasting*, **6**, 515-537.

Chen, L., 2006: Observations and Forecasts of Rainfall Distribution. Report on topic 0.3 in the Proceedings of Sixth International Workshop on Tropical Cyclones, 36-42.

Chen, L., and Y. Ding, 1979: *Introduction to Tropical Cyclones in the Western Pacific.* Science Press, Beijing, 440-473.

China Meteorological Administration, 1949-2006: *Typhoon Yearbook.*China Meteorological Press, Beijing, China.

Dimego, G. J., and L. F. Bosart, 1982b: The Transformation of Tropical Storm Agnes into an Extratropical Cyclone, Part II: Moisture, Vorticity and Kinetic Energy Budgets. *Mon. Wea. Rev.*, **110**, 412-433.

Dong, M., L. Chen, and P. Zheng, 2009: On Progress in research of extraordinary and sudden amplification of heavy rainfall associated with landfalling tropical cyclones. Journal of Tropical Meteorology. To be published.

Harr, P. A., and R. L. Elsberry, 2000: Extratropical transition of tropical cyclones over the western north Pacific, part II: the impact of midlatitude circulation characteristics. Mon. Wea. Rev., 128, 2634-2653.

Li, Y., 2004: An investigation on sustaining mechanism of Landfalling tropical cyclones. Ph.D. thesis of the joint Chinese Academy of Meteorological Sciences and Nanjing University of Information Science and Technology. 180pp.

Members of the National Research Project coded 85-906-07, 1996: Study on sciences, operational experiments and dynamic theories of typhoons. Series 4, China Meteorological Press, Beijing, 244pp.

Impact of Extratropically Transitioned Storms on Japanese Insured Losses

Peter J. Sousounis, Mélicie Desflots, and Jason Butke

AIR Worldwide Corp., Boston, MA

Japan experiences more extratropically transitioning storms, on average, than any other country because of the high tropical cyclone frequency and its northwestward location within the Northwest Pacific basin, as well as its orientation relative to the average storm track. These storms are meteorologically challenging as well as economically disrupting.

Transitioned storms are often characterized by reduced maximum wind speeds as compared to their former tropical-phase. However, the decrease in strength is also typically accompanied by significant increases in size to both the wind speed and precipitation footprints. The radius of maximum winds typically exceeds 100 or more kilometers and heavy rain can extend for hundreds of kilometers from the center of the storm.

The scientific challenges of forecasting these storms can be of secondary importance to the economic impacts they cause. For example, Typhoon Tokage (2004) transitioned shortly after landfall and resulted in insured losses of 88.5 Bn JPY. In contrast, Typhoon Etau (2003) took a very similar path, had very similar landfall characteristics, but transitioned over Hokkaido, and only resulted in 5.1 Bn JPY of insured losses.

The economic impacts in Japan from extratropical transitioning storms, from both wind and precipitation (flooding) perspectives, will be discussed via detailed analyses and modeling of the abovementioned storms.

Surface rainfall equation and modeling study of surface rainfall processes associated with a landfalling typhoon

Xiaopeng Cui*, and Shouting Gao

Laboratory of Cloud-Precipitation Physics and Severe Storms (LACS), Institute of Atmospheric Physics, Chinese Academy of Sciences, Beijing 100029, China

1. Introduction

China has a very long coast. In summers, many typhoons originating in the Western Pacific ocean make landfalls and bring torrential rainfalls and associated social and economical losses over the southeast coast of China and inland China. Thus typhoon-induced heavy rainfall is always one of the most important topics in the typhoon research community in China (Chen et al., 2004; Zhang et al., 2007; Zhao et al., 2008). Especially in 2009, a new National Basic Research Program of China (973 program) was carried out to mainly focus on the abnormal variations during landfalls of typhoons along the coast of China, and one of its main topics is the rainfall associated with landfalling typhoons.

To better understand surface rainfall processes, Gao et al. (2005) derived a diagnostic equation, named surface rainfall equation, in which surface rain rate is simply written as the sum of water vapor and cloud sources/sinks. Cui and Li (2006) further broke the water vapor source/sink term into local vapor change, vapor convergence, and surface evaporation. Further studies (Gao et al., 2006; Sui et al., 2007; Gao and Li, 2008; Cui, 2008; Gao et al., 2009; Cui, 2009) showed that the surface rainfall equation is a very useful research tool for analysis of surface rainfall processes.

In this study, the surface rainfall equation is described briefly in the next section. And a 2D Cloud-Resolving Model (CRM) is used to simulate a torrential rainfall event associated with the landfalling typhoon Kaemi (2006) over southeast coast of China. The simulation data are validated with rain gauge data and further used to analyze the surface rainfall processes associated with the landfall by using the surface rainfall equation.

2. Surface rainfall equation

The prognostic equations for mixing ratios of cloud water, raindrops, cloud ice, snow, and graupel in the CRM used in this study are

$$\frac{\partial q_c}{\partial t} = -\frac{\partial (u q_c)}{\partial x} - \frac{1}{\overline{\rho}} \frac{\partial (\overline{\rho} w q_c)}{\partial z} - P_{SACW} - P_{RAUT} - P_{RACW} - P_{SFW}(T < T_o) - P_{GACW} + P_{CND}$$

* Corresponding author address: Dr. Xiaopeng Cui, Laboratory of Cloud-Precipitation Physics and Severe Storms (LACS), Institute of Atmospheric Physics, Chinese Academy of Sciences, Beijing 100029, China.

E-mail: xpcui@mail.iap.ac.cn

$$- P_{IHOM}(T < T_{oo}) + P_{IMLT}(T > T_o) - P_{IDW}(T_{oo} < T < T_o), \quad (1)$$

$$\frac{\partial q_r}{\partial t} = -\frac{\partial (uq_r)}{\partial x} - \frac{1}{\bar{\rho}}\frac{\partial}{\partial z}\bar{\rho}(w - w_{Tr})q_r + P_{SACW}(T > T_o) + P_{RAUT} + P_{RACW} + P_{GACW}(T > T_o)$$

$$- P_{REVP} + P_{RACS}(T > T_o) - P_{IACR}(T < T_o) - P_{GACR}(T < T_o) - P_{SACR}(T < T_o) - P_{GFR}(T < T_o)$$

$$+ P_{SMLT}(T > T_o) + P_{GMLT}(T > T_o), \quad (2)$$

$$\frac{\partial q_i}{\partial t} = -\frac{\partial (uq_i)}{\partial x} - \frac{1}{\bar{\rho}}\frac{\partial (\bar{\rho} w q_i)}{\partial z} - P_{SAUT}(T < T_o) - P_{SACI}(T < T_o) - P_{RACI}(T < T_o)$$

$$- P_{SFI}(T < T_o) - P_{GACI}(T < T_o) + P_{IHOM}(T < T_{oo}) - P_{IMLT}(T > T_o) + P_{DEP}$$

$$+ P_{IDW}(T_{oo} < T < T_o), \quad (3)$$

$$\frac{\partial q_s}{\partial t} = -\frac{\partial (uq_s)}{\partial x} - \frac{1}{\bar{\rho}}\frac{\partial}{\partial z}\bar{\rho}(w - w_{Ts})q_s + P_{SAUT}(T < T_o) + P_{SACI}(T < T_o) + \delta_4 P_{SACW}(T < T_o)$$

$$+ P_{SFW}(T < T_o) + P_{SFI}(T < T_o) + \delta_3 P_{RACI}(T < T_o) - P_{RACS}(T > T_o) - P_{GACS} - P_{SMLT}(T > T_o)$$
$$- (1 - \delta_2) P_{RACS}(T < T_o) + \delta_2 P_{SACR}(T < T_o) + (1 - \delta_1) P_{SDEP}(T < T_o) - P_{MLTS}(T > T_o)$$

$$+ \delta_3 P_{IACR}(T < T_o) - (1 - \delta_4) P_{WACS}(T < T_o), \quad (4)$$

$$\frac{\partial q_g}{\partial t} = -\frac{\partial (uq_g)}{\partial x} - \frac{1}{\bar{\rho}}\frac{\partial}{\partial z}\bar{\rho}(w - w_{Tg})q_g + (1 - \delta_3) P_{RACI}(T < T_o) + P_{GACI}(T < T_o)$$

$$+ P_{GACW}(T < T_o) + P_{GACS} + (1 - \delta_4) P_{SACW}(T < T_o) + (1 - \delta_3) P_{IACR}(T < T_o) + P_{GACR}(T < T_o)$$
$$+ P_{GFR}(T < T_o) + (1 - \delta_2) P_{RACS}(T < T_o) + (1 - \delta_4) P_{WACS}(T < T_o) - P_{GMLT}(T > T_o)$$

$$+ (1 - \delta_1) P_{GDEP}(T < T_o) - P_{MLTG}(T > T_o) + (1 - \delta_2) P_{SACR}(T < T_o), \quad (5)$$

and,

$\delta_1 = 1$, only when $q_c + q_i > 10^{-8} g g^{-1}, T < T_o$,

$\delta_2 = 1$, only when $q_s + q_r < 10^{-4} g g^{-1}, T < T_o$,

$\delta_3 = 1$, only when $q_r > 10^{-4} g g^{-1}, T < T_o$,

$\delta_4 = 1$, only when $q_s \le 10^{-4} g g^{-1}, q_c > 5 \times 10^{-4} g g^{-1}, T < T_o$.

Where, q_c, q_r, q_i, q_s, q_g are mixing ratios of cloud water, raindrops, cloud ice, snow and graupel, respectively. w_{Tr}, w_{Ts}, and w_{Tg} are terminal fall velocities of raindrops, snow and graupel, respectively. T_o＝0℃， T_{oo}＝－35℃. Microphysical processes and their parameterization schemes in Eqs. (1-5) refer to Li et al. (1999).

By adding the above Eqs.(1-5) together and taking mass integration, we get

$$\frac{\partial}{\partial t}(L_{WP}+I_{WP})=C_{LWP+IWP}-P_{rain}-P_{snow}-P_{graupel}+C_{MP}, \tag{6}$$

and,

$$C_{LWP+IWP}=-[\frac{\partial}{\partial x}(q_5 u)]$$

$$P_{rain}=\overline{\rho}w_{Tr}q_r\,|_{z=0},$$

$$P_{snow}=\overline{\rho}w_{Ts}q_s\,|_{z=0},$$

$$P_{graupel}=\overline{\rho}w_{Tg}q_g\,|_{z=0},$$

$$C_{MP}=[P_{CND}]+[P_{DEP}]+[P_{SDEP}]+[P_{GDEP}]-[P_{REVP}]-[P_{MLTS}(T>T_o)]-P_{MLTG}(T>T_o)]$$

Where, $[(\ )]=\int_{z_b}^{z_t}\overline{\rho}(\ )dz$, z_t and z_b are the heights of the top and bottom of the model. $L_{WP}=[q_c+q_r]$, $I_{WP}=[q_i+q_s+q_g]$, and $q_5=q_c+q_r+q_i+q_s+q_g$. P_{rain}, P_{snow}, and $P_{graupel}$ are surface rain rate, snow rate and graupel rate, respectively.

The vapor equation in the CRM can be expressed as,

$$\frac{\partial q_v}{\partial t}=-\frac{\partial(u'q_v')}{\partial x}-\overline{u}^{o}\frac{\partial q_v'}{\partial x}-\frac{1}{\overline{\rho}}\frac{\partial(\overline{\rho}w'q_v')}{\partial z}-\overline{w}^{o}\frac{\partial q_v'}{\partial z}-w'\frac{\partial\overline{q}_v}{\partial z}-\overline{u}^{o}\frac{\partial\overline{q}_v^{o}}{\partial x}$$

$$-\overline{w}^{o}\frac{\partial\overline{q}_v}{\partial z}-P_{CND}-P_{DEP}-P_{SDEP}-P_{GDEP}+P_{REVP}+P_{MLTS}(T>T_o)+P_{MLTG}(T>T_o) \tag{7}$$

Where, "—" denotes a zonal mean, "′" denotes a perturbation from the zonal mean, and "^{o}" denotes imposed observed variables in the model.

（7）is mass integrated to yield,

$$\frac{\partial[q_v]}{\partial t}=Q_{WVF}+Q_{WVE}-C_{MP}, \tag{8}$$

Where,

$$Q_{WVF}=-[\frac{\partial(u'q_v')}{\partial x}]-[\overline{u}^{o}\frac{\partial q_v'}{\partial x}]-[\overline{w}^{o}\frac{\partial q_v'}{\partial z}]-[w'\frac{\partial\overline{q}_v}{\partial z}]-[\overline{u}^{o}\frac{\partial\overline{q}_v^{o}}{\partial x}]-[\overline{w}^{o}\frac{\partial\overline{q}_v}{\partial z}],$$

$$Q_{WVE}=\overline{\rho}(w'q_v')\,|_{z=0}.$$

Adding（6）to（8）, we get

$$P_s=Q_{WVT}+Q_{WVF}+Q_{WVE}+Q_{CM}, \tag{9}$$

Where,

$$P_s=P_{rain}+P_{snow}+P_{graupel},$$

$$Q_{WVT} = -\frac{\partial}{\partial t}[q_v],$$

$$Q_{CM} = -\frac{\partial}{\partial t}(L_{WP} + I_{WP}) + C_{LWP+IWP}.$$

Positive values of Q_{WVT}, Q_{WVF}, Q_{WVE} and Q_{CM} denote local vapor loss, vapor convergence, surface evaporation and local hydrometeor loss/ hydrometeor convergence, respectively, whereas negative Q_{WVT}, Q_{WVF}, and Q_{CM} denote local vapor gain, vapor divergence, and local hydrometeor gain/hydrometeor divergence, respectively. Surface rain rate is simply expressed as the sum of water vapor source/sink (Q_{WVT}, Q_{WVF}, and Q_{WVE}) and cloud source/sink (Q_{CM}).

3. Typhoon Kaemi (2006), Model, and Experiment

Typhoon Kaemi (2006) formed in the early morning on 18 July 2006 over the Northwest Pacific ocean and strengthened into a typhoon in around the early morning of 21 July and moved towards the northwest. Kaemi made its first landfall over Taidong of Taiwan province of China on 24 July 2006 with a maximum wind of 40 m s^{-1} and a minimum center surface pressure of 960 hPa, and made its second landfall over Jinjiang of Fujian province of China on 25 July 2006 with a maximum wind of 33 m s^{-1} and a minimum center surface pressure of 975 hPa. After that, Kaemi weakened quickly into a tropical storm and then a tropical depression. And after about 4-day staying over China mainland, Kaemi disappeared over the southern coast of Guangxi province on 29 July 2006. Since Kaemi moved very slowly over China mainland and stayed over China mainland for more than 4 days, Kaemi brought heavy rainfalls to most parts of south China, especially Guangdong, Guangxi, Fujian, and Hunan provinces, leading to a death of more than 60 persons and a direct economical loss of several thousand million RMBs (From the typhoon yearbook of 2006 of Shanghai Typhoon Institute of China Meteorological Administration).

At 0800 LST 24 July, Kaemi is still over the ocean to the southeast of Taiwan (Fig.1). Moist air is transferred continuously from the southwest and the Western Pacific ocean through the southern part of Kaemi's circulation and the passage between the typhoon and the subtropical high (Fig.1a). At 0800 LST 25 July, Kaemi finished its first landfall on Taidong and is facing the second (Fig.1b). The main part of the circulation of Kaemi has touched the mainland China and the cold air moves towards Kaemi, especially to the west of 110°E. And associated heavy rainfall occurred in the southeast coast of China and south China. At 0800 LST 26 July, Kaemi has finished its second landfall and weakened into a tropical depression. Its circulation covered most part of the south China (Fig.1c) and heavy rainfall mainly occurred in the southern part of the typhoon circulation. From 27 July, Kaemi turned anticlockwise and began to move to the southwest. Heavy rainfall still occurred in the southern part of the typhoon circulation since abundant water vapor is transferred from the summer monsoon circulation (Fig.1d). Heavy rainfall also occurred in the eastern part of the typhoon circulation since water vapor is also transferred from south to north there. On 28 and 29 July, Kaemi got weaker and moved near to the southern coast of Guangxi province. Heavy rainfall mainly occurred close to the coast of Guangxi, and there are also some heavy rainfalls in Guangdong, Fujian, Hunan, and Jiangxi provinces (Fig.1e,f) (from the typhoon yearbook of 2006).

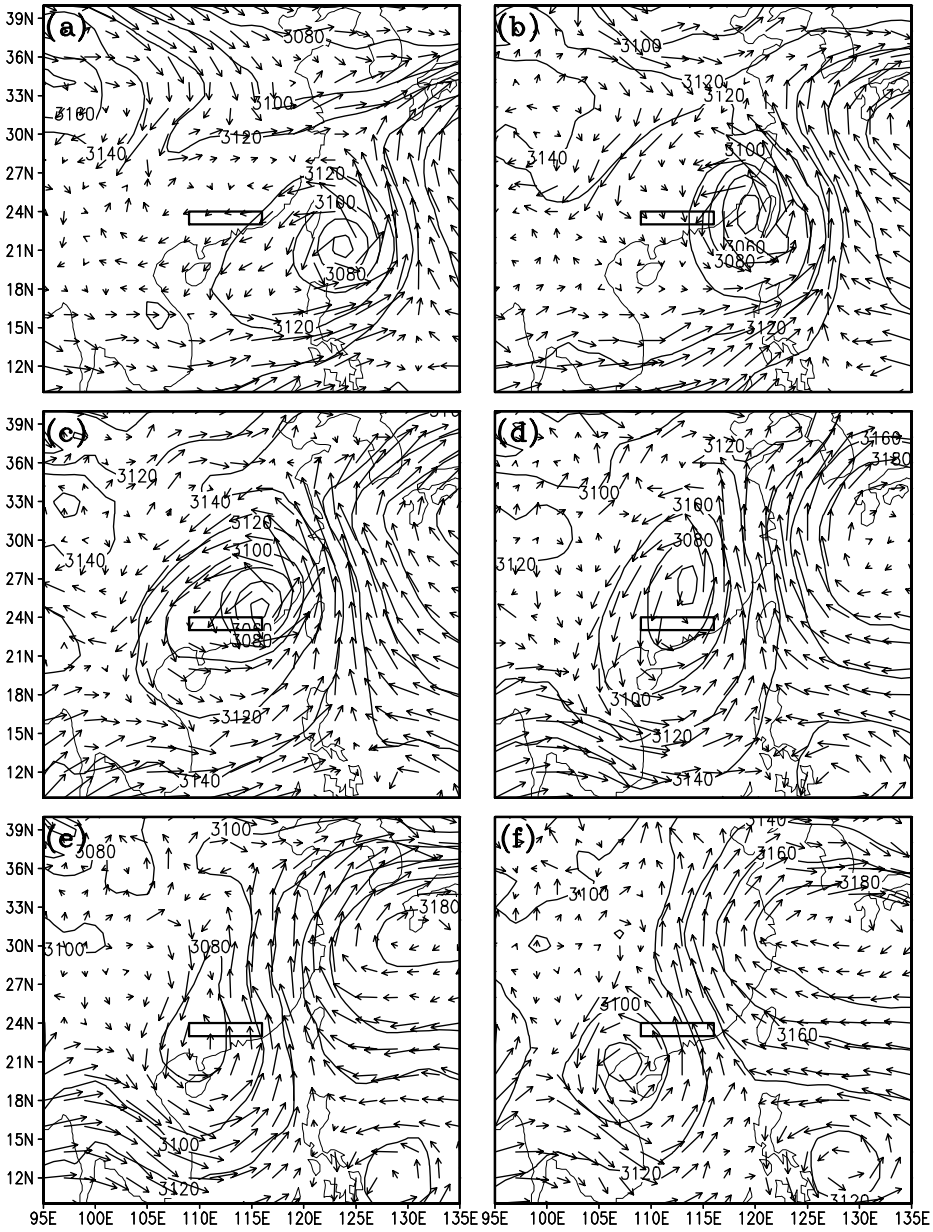

Fig. 1 Geopotential height(m) and wind vectors at 700 hPa on (a) 0800 LST 24 July, (b) 0800 LST 25 July, (c) 0800 LST 26 July, (d) 0800 LST 27 July, (e) 0800 LST 28 July, (f) 0800 LST 29 July

The cloud-resolving model used in this study was originally developed by Soong and Ogura, Soong and Tao in 1980. The 2D version of the model used by Sui et al. (1994,1998) and further modified by Li et al. (1999) is used in this study. The governing equations and model setup can be found in Li et al. (1999). The horizontal domain is 768 km with a horizontal grid resolution of 1.5 km. The top model level is 42 hPa. The model is forced by the imposed zonally-uniform vertical velocity, zonal wind, horizontal temperature and vapor advection from NCEP/GDAS data with a horizontal resolution of 1^{o}x1^{o} and a temporal resolution of 4 times per day. The model is integrated from 2000 LST 25 to 1900 LST 31 July 2006 (a total of 6 days) with the large-scale forcing data (Fig.2) averaged over 23-24^{o}N, 109-116^{o}E (The box in Fig.1).

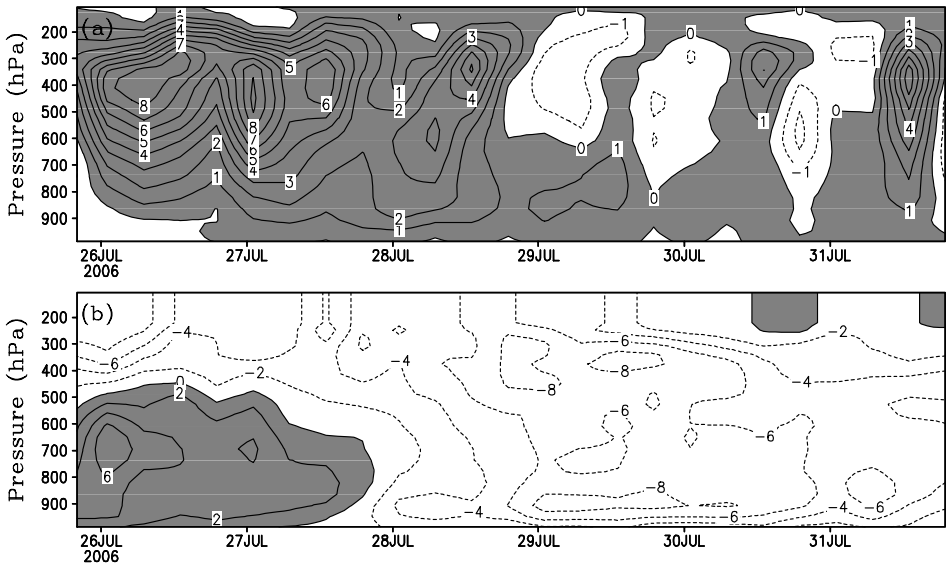

Fig. 2 Time-pressure cross sections of (a)vertical velocity (cm s^{-1}) and (b) zonal wind (m s^{-1}) from 2000 LST 25 July to 1900 LST 31 July 2006. The data are averaged in a rectangular box of 23-24°N, 109-116°E. Upward motion in (a) and westerly wind in (b) are shaded.

4. Comparison of simulations with observations

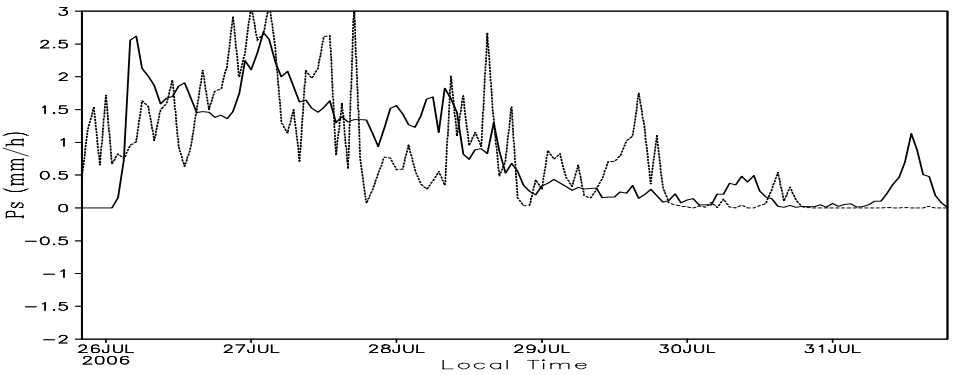

Fig. 3 Time series of domain-mean simulated P_s (solid) and observed P_s (dashed) calculated in the rectangular box of 23-24°N, 109-116°E as indicated in Fig.1. Unit is mm h^{-1}.

The time series of model domain-mean simulated surface rain rate is compared with that of the observed surface rain rate in Fig.3. The observed surface rain rate is calculated by using the rain gauge data in a rectangular box of 23-24°N, 109-116°E, which is the simulation domain and indicated in Fig.1. The time average of the observed surface rain rate is 0.800 mm h^{-1}, which is very close to the simulated one (0.813 mm h^{-1}). The Root-Mean-Squared (RMS) difference in surface rain rate between the simulation and the gauge observation is 0.660 mm h^{-1}, which is much smaller than the standard deviations of both simulated rain rate (0.753 mm h^{-1}) and observed rain rate (0.833 mm h^{-1}). Some differences between the simulation and observations may be caused by the spin-up of the model, partially due to the inconsistent calculations of phase and magnitude of the imposed vertical velocity from the NCEP/GDAS data and the sampling and accuracy of the observed rain gauge data.

5. Surface rainfall processes analysis

(1) Model domain mean analysis

Table 1 gives the time means of fractional coverage, P_s, Q_{WVT}, Q_{WVF}, Q_{WVE}, Q_{CM}, ice water path (*IWP*), and liquid water path (*LWP*), respectively. It shows that time averaged and model domain-mean P_s (0.813 mm h^{-1}) mainly comes from large-scale convergence (Q_{WVF}, 0.665 mm h^{-1}) and local vapor loss (Q_{WVT}, 0.115 mm h^{-1}). Large underestimation (about 15%) of P_s will occur if Q_{WVT} and Q_{CM} are not considered as contributors to P_s (As the methods used in Kuo (1965,1974)).

Table 1 Time means of fractional coverage (%), P_s, Q_{WVT}, Q_{WVF}, Q_{WVE}, Q_{CM} (mm h^{-1}), IWP, and LWP (g g^{-1}) over different regions and their sums(model domain-mean).

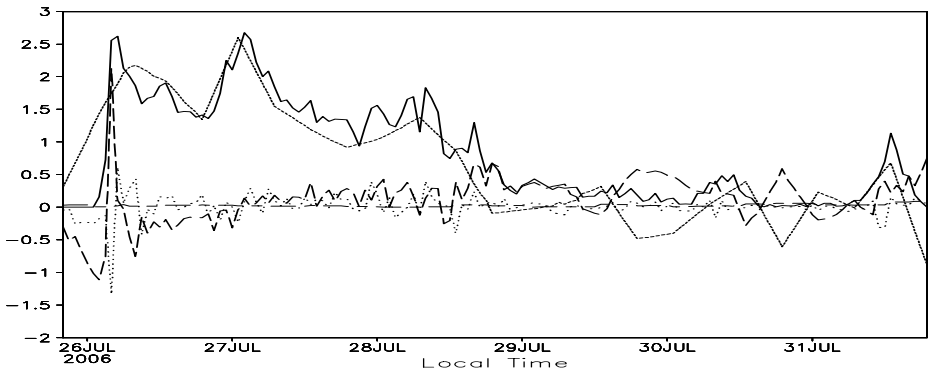

Fig. 4 Surface rainfall processes analysis using the surface rainfall equation. The solid, long dashed, dashed, long-short dashed, and dotted lines are referred to model-domain-mean P_s, Q_{WVT}, Q_{WVF}, Q_{WVE}, and Q_{CM} (mm h^{-1}), respectively.

Fig.4 shows the model domain-mean surface rainfall processes analysis by using the above mentioned surface rainfall equation. Some features are easy to be noted: (1) Water vapor convergence (Q_{WVF}) accounts for most of the variation of P_s during most of the integration time, while it is not always contributor to P_s, especially after the late night of 28 July, when local vapor loss (positive Q_{WVT}) could be another contributor while water vapor divergence (negative Q_{WVF}) restrains P_s. This reveals that surface rainfall could occur even when divergence is dominant; (2) Surface evaporation (Q_{WVE}) is not important to the

Clear-sk regions

Fractional **38.6**

surface rainfall in this case though it is always positive; (3) Surface rainfall is a result of multi-timescale interactions. Q_{WVE} possesses the longest time scale, and may exert impact on P_s in longer time scale, and Q_{WVF} possesses the second longest time scale and can explain most of the variation of P_s. While Q_{WVT} and Q_{CM} possess shorter time scales which can explain more detailed variations in P_s; (4) Water vapor source/sink (Q_{WVT}, Q_{WVF}, and Q_{WVE}) is the most important contributors to P_s, while sometimes cloud source/sink (Q_{CM}) can also exert important impact.

(2) Partitioning analysis

To further examine the surface rainfall processes in difference regions, the partitioning method proposed by Sui et al.(1994) is applied to each grid point to determine the type (clear sky, raining stratiform, convective, or non-raining stratiform regions) and the summations of quantities are taken and divided by the total zonal grid points (512) for the hourly simulation data.

Table 1 shows the partitioning analysis results. In the 6 days, more than one third (38.6%) of the domain is clear sky, and 45% is occupied by rainfall regions (raining stratiform (32.4%) and convective (12.6%) regions). More than 60% of the surface rain rate (0.813 mm h^{-1}) comes from raining stratiform region (0.492 mm h^{-1}). In raining stratiform region, both water vapor and cloud sources/sinks contribute to surface rain rate, about 78% of the surface rain rate (0.492 mm h^{-1}) comes from water vapor convergence (0.382 mm h^{-1}), and about 17% comes from cloud source/sink (cloud decay, 0.084 mm h^{-1}). In convective region, about one third of the surface rain rate (0.321 mm h^{-1}) comes from local vapor loss (The atmosphere gets drier. 0.103 mm h^{-1}), and water vapor convergence (0.289 mm h^{-1}) contributes to both the other two thirds of the surface rain rate and cloud development (-0.073 mm h^{-1}). This further enhances the important impact of cloud source/sink, and in this case, from the view of time mean and model domain mean, the clear sky and non-raining stratiform regions contribute less.

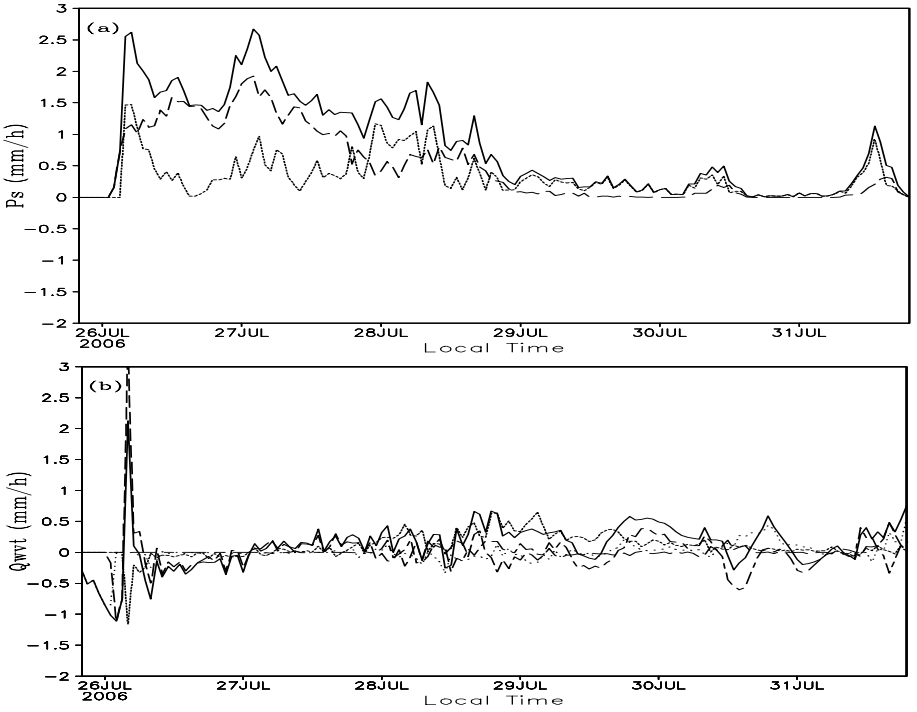

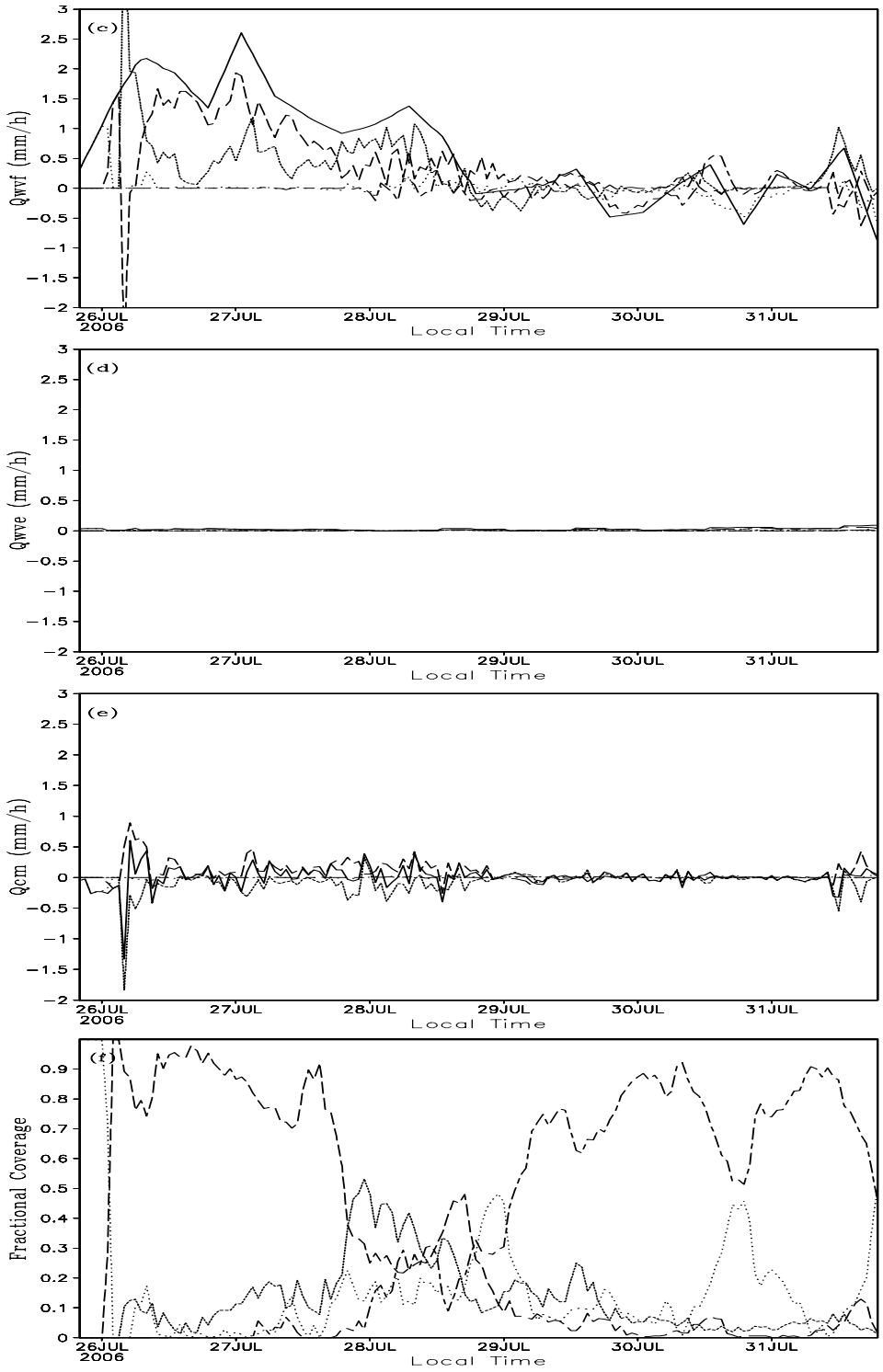

Fig. 5 Partitioning analysis. The solid, long-short dashed, long dashed, dashed, and dotted lines are referred to model domain mean, clear sky, raining stratiform, convective, and non-raining stratiform regions, respectively. (a) P_s, (b) Q_{WVT}, (c) Q_{WVF} ,(d) Q_{WVE} ,(e) Q_{CM} and (f)Fractional coverage. (Units for a-e: mm h^{-1})

Fig.5 shows P_s, Q_{WVT}, Q_{WVF}, Q_{WVE}, Q_{CM}, and fractional coverage in different regions. In Fig.5a, stratiform rainfall is dominant from the early morning of 26 July till the late night of 27 July. After that, convective rainfall dominates till about 1000 LST 28 July. Then stratiform rainfall re-dominates till late night of 28 July, and then convective rainfall dominates again till the end of the integration. The variations of Q_{WVT} and Q_{CM} are much complicated during the integration (Fig.5 b,e). Before 28 July, the variations of Q_{WVT} in clear sky and non-raining stratiform regions contribute less to that of the domain-mean Q_{WVT} while after that they contribute much (Fig.5b), especially the clear sky, which is consistent to the corresponding variations in their fractional coverage(Fig.5f) where before 28 July almost the whole domain is occupied by rainfall regions(raining stratiform and convective regions) while after that clear sky region becomes the main contributor and non-raining stratiform region also occupied much of the domain. As for Q_{CM} (Fig.5e), the variations of Q_{CM} in rainfall regions(raining stratiform and convective regions) are the main contributors to that of the model domain-mean Q_{CM} while the variations of Q_{CM} in rainfall-free regions(clear sky and non-raining stratiform regions) contribute less, especially before 29 July. In Fig.5d, Q_{WVE} are always positive and contribute to the model domain mean in all the four regions, while all Q_{WVE} are too small and contribute less to the surface rain rate. Q_{WVF} (Fig.5c) is the main contributor to P_s (Fig.4). The variations of Q_{WVF} in rainfall regions(raining stratiform and convective regions) are the two main contributors to the variations of the model domain-mean Q_{WVF}, then the main contributors to P_s before the afternoon of 28 July. After that, the contributions from the rainfall-free regions (clear sky and non-raining stratiform regions) get bigger.

6. Conclusion

Surface rainfall equation (Gao et al., 2005; Cui and Li, 2006; Cui, 2009) is a very useful research tool for surface rainfall process analysis, in which surface rain rate is simply expressed as the sum of water vapor source/sink (Q_{WVT}, Q_{WVF}, and Q_{WVE}) and cloud source/sink (Q_{CM}).

The detailed surface rainfall processes associated with Typhoon Kaemi(2006) are investigated based on hourly data from a 2D CRM simulation and the above surface rainfall equation. The model is integrated for 6 days with imposed large-scale forcing calculated from NCEP/GDAS data. The simulation data are validated with observations in terms of surface rain rates. The RMS difference between the simulation and observations is 0.660 mm h^{-1}, which is much smaller than the standard deviations of both the simulation (0.753 mm h^{-1}) and the observation (0.833 mm h^{-1}).

Time averaged and model domain-mean P_s mainly comes from large-scale convergence (Q_{WVF}) and local vapor loss (positive Q_{WVT}). Large underestimation (about 15%) of P_s will occur if Q_{WVT} and Q_{CM} are not considered as contributors to P_s. Q_{WVF} accounts for the variation of P_s during most of the integration time, while it is not always contributor to P_s, and surface rainfall could occur when divergence is dominant. Surface rainfall is a result of multi-timescale interactions.

Partitioning analysis tells that stratiform rainfall is dominant from the morning of 26 July till the late night of 27 July. After that, convective rainfall dominates till about 1000 LST 28 July. Before 28 July, the variations of Q_{WVT} in rainfall-free regions contribute less to that of the model domain mean while after that

they contribute much, which is consistent to the corresponding variations in their fractional coverage. The variations of Q_{WVF} in rainfall regions are the main contributors to the variations of the model domain-mean Q_{WVF}, then the main contributors to P_s before the afternoon of 28 July. After that, the contributions from the rainfall-free regions get bigger.

References

CHEN Lian-shou, LUO Zhe-xian, LI Ying. Research advances on tropical cyclone landfall process[J]. Acta Meteor. Sinica(in Chinese), 2004, 62(5): 541-549

CUI X P, LI X F. Role of surface evaporation in surface rainfall processes[J]. J. Geophys. Res., 2006, 111, D17112, doi: 10.1029/2005JD006876.

CUI X P. A Cloud-Resolving Modeling Study of Diurnal Variations of Tropical Convective and Stratiform Rainfall[J], J. Geophys. Res., 2008, 113, D02113, doi:10.1029/2007JD008990.

CUI Xiao-peng. Quantitative diagnostic analysis of surface rainfall processes by surface rainfall equation[J], Chinese Journal of Atmospheric Sciences(in Chinese), 2009, 33(2): 375-387.

GAO S T, CUI X P, ZHU Y S, et al. Surface rainfall processes as simulated in a cloud resolving model[J], J. Geophys. Res., 2005, 110, D10202, doi: 10.1029/2004JD005467.

GAO S T, PING F, CUI X P, et al. Short timescale air-sea coupling in the tropical deep convective regime[J]. Meteor. Atmos. Phys., 2006, 93: 37-44.

GAO S T, LI X F. Cloud-resolving modeling of convective processes[M]. 2008, Springer, Dordrecht. 206 pp.

GAO Shou-ting, CUI Xiao-peng, LI Xiao-fan. A modeling Study of Diurnal Rainfall Variations during the 21-Day Period of TOGA COARE[J], Advs Atmos Sci, 2009, accepted.

KUO H L. On formation and intensification of tropical cyclones through latent heat release by cumulus convection[J]. J. Atmos. Sci., 1965, 22(1): 40-63.

KUO H L. Further studies of the parameterization of the influence of cumulus convection on large-scale flow[J]. J. Atmos. Sci., 1974, 31(5): 1232-1240.

LI X F, SUI C H, LAU K M, et al. Large-scale forcing and cloud-radiation interaction in the tropical deep convective regime[J], J. Atmos. Sci., 1999, 56(17): 3028-3042.

SUI C H, LAU K M, TAO W K, et al. The tropical water and energy cycles in a cumulus ensemble model. Part I: Equilibrium climate[J], J. Atmos. Sci., 1994, 51(5): 711-728.

SUI C H, LI X F, LAU K M. Radiative-convective processes in simulated diurnal variations of tropical oceanic convection[J], J. Atmos. Sci., 1998, 55(13): 2345-2357.

SUI C H, LI X F, YANG M J. On the definition of precipitation efficiency[J]. J. Atmos. Sci., 2007, 64(12): 4506-4513.

ZHANG Hai-xia, CUI Xiao-peng, KANG Feng-qin, et al. Observational analysis for a torrential rain caused by a landfall typhoon[J]. Plateau Meteorology(in Chinese), 2007, 26(5): 980-991

ZHAO Yu, CUI Xiao-peng, WANG Jian-guo. A study on a heavy rainfall event triggered by inverted typhoon trough in Shandong province. Acta Meteor. Sinica(in Chinese), 2008, 66(3): 423-436

Observational Analysis of Heavy Rainfall Mechanisms Associated with Severe Tropical Storm Bilis (2006) after Its Landfall

Shuanzhu Gao

China National Meteorological Center, Beijing, China

Zhiyong Meng

Department of Atmospheric Sciences, School of Physics, Peking University, Beijing, China

Fuqing Zhang

Department of Meteorology, The Pennsylvania State University, University Park, Pennsylvania

Lance F. Bosart

Department of Atmospheric Sciences, University at Albany, State University of New York, Albany, New York

ABSTRACT: In July of 2006, Bilis, a severe tropical storm in the western North Pacific Ocean, made landfall on the coast of Fujian Province, China. Bilis was not particularly intense at landfall and further weakened gradually thereafter. Its track was well predicted by the China National Meteorological Center (CNMC), but the real-time forecast greatly underestimated the intensity of the heavy rainfall, which triggered large-area severe flooding after the storm moved inland. To explore possible contributors to the distribution of rainfall associated with Bilis at different times, the observed rainfall over land associated with Bilis is grouped into three stages based on the timing and location of their occurrence.

The first stage of the rainfall is defined for the rainfall appearing at the coastal area of Fujian and Zhejiang Provinces between 1200 UTC 13 July and 1200 UTC 14 July right before and after Bilis's second landfall. As a result of the inner-core circulation and the outer rainbands interacting with the coastal terrains, heavy rainfall began to fall at approximately 1200 UTC 13 July in the coastal area of northern Fujian Province and southern Zhejiang Province and later expanded to most part of Jiangxi and Fujian Provinces. During this stage, rainfall was generally within about 300 km of the storm center in all quarters but with the prevalence to the forward right. The magnitude of precipitation decreased gradually from the coastal area toward inland, coinciding with the weakening of Bilis. During this stage, the precipitation in the coastal areas of southern Zhejiang and northern Fujian Provinces was generally greater than 100 mm while in Jiangxi Province only 25–50 mm of rainfall were observed. This stage of rainfall was generally well predicted by the official forecast of CNMC.

The second stage of rainfall is defined for the rainfall observed from approximately 0600 UTC 14 July until approximately 1800 UTC 15 July along the border regions between Jiangxi, Hunan, and Guangdong Provinces. The rainfall between 1200 UTC 14 July and 1200 UTC 15 July is the most intense precipitation during this stage. The rainfall for this stage was apparently separated from the first stage, which can also be observed from satellite images (e.g., at 1200 and 1800 UTC 14 July. With a westward movement of the weakened TC and the gradual dissipation of the intense inner core, the cloud and rainfall patterns became more

and more widespread and asymmetric, with a significant enhancement to the west and south (forward and left) of the TC. The 24-h accumulated rainfall valid at 1200 UTC 15 July was greater than 100 mm in northern Guangdong, southern Jiangxi, and southern Hunan Provinces with a localized maximum of greater than 250 mm recorded in Hunan Province. A large area of intensive rainfall in this area persisted until 1200 UTC 15 July, with lingering moderate rainfall in Hunan and Guangdong Provinces thereafter.

The 24-h official rainfall forecast issued by CNMC for the period between 1200 UTC 13 July and 1200 UTC 14 July 2006 nearly completely missed the moderate rainfall observed between Hunan and Jiangxi Provinces. A subsequent 24-h forecast for the period between 1200 UTC 14 July and 1200 UTC 15 July 2006 was apparently improved but still underpredicted the observed rainfall along the border regions between Hunan, Jiangxi, and Guangdong Provinces. It will be of both operational and research interest to understand the heavy rainfall mechanisms for this stage that caused widespread catastrophic flooding and subsequent large loss of life and property.

Because the majority of the rainfall during the second stage occurred over mountainous regions, it is widely suspected that the Nanling Mountains, the mountain range between Hunan and Guangdong Provinces, and its interaction with the TC circulation could be important contributors to the excessive rainfall. In the meantime, the infrared satellite images from 1200 UTC 14 July to 1800 UTC 14 July 2006 show that the convection associated with this stage of rainfall is localized. The next section will demonstrate that the three ingredients of deep moist convection are all in place during this stage of rainfall. Widespread moist and unstable flow is observed. Several processes are likely contributing to lifting, such as vertical wind shear, warmair advection, frontogenesis, and/or topographic forcing.

The third stage of the rainfall is defined for the rainfall occurring along the coastal areas of Guangdong and Fujian Provinces during 0600 UTC 15 July–1200 UTC 16 July starting before the end of the second stage of the rainfall. The most intense precipitation during this stage fell between 1200 UTC 15 July and 1200 UTC 16 July. The strong southwesterly flow brought abundant moisture from the South China Sea to the rainfall area. The heavy-precipitation belt (>100 mm) extended 100 km inland from the coast, spanning nearly 700 km in length with the maximum rainfall rate at around 1800 UTC 15 July. Operational forecasting for this stage of rainfall was very successful. This stage of rainfall was likely caused by the interaction of the much-weakened Bilis circulation with the South China Sea monsoon along with lifting by the coastal topography.

Using the real-time observational data archive from CNMC and the FNL global gridded analysis fromNCEP, this study explores possible mechanisms of torrential rainfalls over large areas of southern China induced by Bilis, a western North Pacific severe tropical storm that made landfall on the southeastern coast of mainland China on 14 July 2006 and persisted over land until after 17 July 2006.

From the observational analyses, it is found that the heavy rainfall associated with Bilis can be roughly divided into three stages based on the timing and location. The first stage of the rainfall happened in Fujian and Zhejiang Provinces and could be directly induced by the inner-core circulation during Bilis's landfall. The second stage of rainfall caused the most catastrophic flooding and is the primary focus of the current study. It occurred inland near the border regions between Jiangxi, Hunan, and Guangdong Provinces. This stage of the rainfall could be attributed to moist and unstable flow along with lifting from vortex–shear interaction, warm-air advection, frontogenesis, and topography. The third stage of rainfall that occurred along the coastal areas of Guangdong and Fujian Provinces likely resulted from the interaction of Bilis circulation with the South China Sea monsoon enhanced by topographical lifting along the coast.

The mechanism of the second stage of rainfall was explored using an ingredients-based method. The result shows that the rainfall could be a result of all three ingredients of deep moist convection (moisture, instability, and lifting) getting together. Possible lifting mechanisms associated with the rainfall in the second stage were investigated in detail. Strong vertical shear is observed in this stage of rainfall. The rainfall is mainly located on

the downshear side of Bilis with a preference on down-tilt and downshear right. Impact of vertical shear on rainfall distribution may come from vortex tilting and the vorticity balance argument. Consistent with the vertical wind shear, widespread lowlevel warm-air advection is found in southeastern China, which may also contribute to low-level lifting through quasigeostrophic forcing. Furthermore, the low-level convergence together with flow (confluence) deformation produces significant frontogenesis that collocates well with the observed vertical motion and associated rainfall. Through numerical sensitivity experiments using WRF with and without the complex topography, it is found that the influence of complex topography is secondary for the second stage of the rainfall, despite some apparent local enhancement and redistribution of precipitation.

Since diagnosis of the omega equation, vertical shear, vortex tilting, and frontogenesis can be easily applied to any gridded observational analysis or forecast field in real time, they may be used as a guidance to forecast heavy rainfall events associated with TCs after they move inland. It is worth cautioning the generality of this single case to other landfalling TCs. In particular, our results are obviously limited by the quality and the resolution of the NCEP global analysis.

Trend Discrepancies in Western North Pacific Tropical Cyclones

Jin-Jie SONG[1], Yuan WANG[1] and Liguang Wu[2]

[1] Key Laboratory of Mesoscale Severe Weather /MOE, and School of Atmospheric Sciences, Nanjing University，P. R. China

[2] Key Laboratory of Meteorological Disaster of Ministry of Education, Nanjing University of Information Science and Technology, P. R. China

Abstract

In order to detect the possible differences of tropical cyclone (TC) position, frequency, intensity and the TC-related destruction, three TC best-track datasets over the western North Pacific from the Joint Typhoon Warning Center (JTWC), the Regional Specialized Meteorological Center (RSMC), and Shanghai Typhoon Institute (STI) are analyzed and compared for the period 1945 to 2007 in this paper. The main objective of this study is to answer two questions: Are the trends of annual number and potential destructiveness shown in different datasets still exist if only TCs recorded simultaneously in all the datasets are considered? And do the differences result from the TC intensity that is averaged over different time periods in different TC centers? To achieve it, TCs recorded simultaneously in all the three datasets are indentified and examined, which are called concurred-TCs in this study.

There exist several TC warning organizations in the western North Pacific (WNP) region to provide TC observations and forecasts operationally, including the Joint Typhoon Warning Center (JTWC) of U.S. Naval Pacific Meteorology Oceanography Center in Hawaii (in Guam before 1999), the Regional Specialized Meteorological Center (RSMC) of Japan Meteorological Agency in Tokyo, the Shanghai Typhoon Institute (STI) of China Meteorological Administration in Shanghai. So far, researches about the trends in TC activity over the WNP are primarily derived from the JTWC best-track dataset, but datasets from other organizations should not be neglected.

In the WNP basin, the observational data used to determine TC positions and intensities in the three organizations (JTWC, RSMC, and STI) are almost the same (for instance, taking aircraft reconnaissance before 1980s, and weather satellite monitoring after 1980s). It is found that the annual average position differences between any two of the datasets are less than 30 km, and the TC position differences decline with time. However, the algorithms to estimate intensity which is measured by maximum sustained wind (VMAX) are different for these organizations. The VMAX-estimating techniques are mainly dependent on the different time intervals used for averaging TC VMAX (1-min for JTWC, 2-min for STI, or 10-min for RSMC), and their diversity could lead to different VMAX estimates in different organizations.

Totally speaking, the absolute value of VMAX difference is increased between STI and JTWC and between RSMC and JTWC since 1977, indicating that the annual average TC intensities in the STI and RSMC datasets are increasingly weaker than in the JTWC dataset. The maximum intensity difference occurred in the mid-1990s, exceeding 10 m s^{-1}.

Although VMAX for an individual concurred-TC from one organization could be greater or smaller than VMAX in another dataset, some statistical relationships could be obtained by the least-square regression

fitting. It is shown by these relationships that: When the intensity of TCs surpasses the typhoon (TY) strength (VMAX≥ 32.6 $m \cdot s^{-1}$), $VMAX_{STI}$ is generally smaller than $VMAX_{JTWC}$ and greater than $VMAX_{RSMC}$, and there exists a statistic relationship of $VMAX_{JTWC} > VMAX_{STI} > VMAX_{RSMC}$. However, when TCs are at the tropical depression (TD) strength (VMAX< 17.2 $m \cdot s^{-1}$), $VMAX_{JTWC} < VMAX_{STI}$ and $VMAX_{JTWC} < VMAX_{RSMC}$ account for very great proportion, despite that the VMAX from STI and RSMC datasets are consistent. This phenomenon is different from the Atkinson's (1974) argument which suggests that the 10-min averaged wind speed to be approximately 88% of 1-min average (meaning $VMAX_{JTWC} = 0.88 \times VMAX_{RSMC}$).

When concurred-TCs are analyzed individually, it is found that: For intensive TCs (e.g. TY), the relationship $VMAX_{JTWC} > VMAX_{STI} > VMAX_{RSMC}$ is held in their mature stages. To the contrast, for weak TCs such as tropical storms (17.2 $m \cdot s^{-1} \leq$ VMAX< 32.6 $m \cdot s^{-1}$), VMAX in the three datasets is nearly the same.

Considering the minimum central pressure (MSLP) as another estimate of TC intensity, there exists $MSLP_{JTWC} < MSLP_{STI} \leq MSLP_{RSMC}$ for TYs, whereas $MSLP_{STI} < MSLP_{JTWC}$ and $MSLP_{RSMC} < MSLP_{JTWC}$ for TDs. These results are similar to them of VMAX.

The difference of VMAX could influence the trends related to concurred-TCs. Although the annual numbers of TS and category 1 TY from any two datasets are nearly the same, there are great differences in the annual number of TCs reaching category 2 or higher. In 1977-2007, there are more TCs reaching category 4 or higher in the JTWC dataset than in the STI (RSMC) dataset, which could be caused by the fact that some TCs of categories 2-3 in STI (RSMC) could be included in category 4 or higher in the JTWC dataset. On the other hand, the trend of the annual number of categories 2-3 TYs in the JTWC dataset is opposite to that in the STI (RSMC) dataset during 1977-2007, as well as that of category 4 or higher TYs. For JTWC, the annual number of category 4 or higher TYs generally increases by 0.16 per year with a decrease in the STI (0.10 y^{-1}) and RSMC (0.04 y^{-1}) datasets. To the contrast, the annual number of categories 2-3 TYs decreases in the JTWC dataset (0.10 y^{-1}) with a general increase in the STI (0.08 y^{-1}) and RSMC (0.08 y^{-1}) datasets.

The power dissipation index (PDI) used to indicate TC threat is also analyzed in this paper. In 1977-2007, the total PDI for concurred-TCs in the STI and RSMC datasets display slightly decreasing trends respectively by the magnitude 1.2×10^5 $m^3 \cdot s^{-3}$ and 0.6×10^5 $m^3 \cdot s^{-3}$, whereas a significant increase of concurred-TC total PDI by 4.8×10^5 $m^3 \cdot s^{-3}$ is shown in the JTWC datasets. This is caused by the great difference of PDI for categories 4-5 TYs. For categories 4-5 TYs, the JTWC PDI is significantly greater than that of STI (RSMC), and its trend in 1977-2007 is opposite to the other two. The former remarkably increased, whereas the latter slightly decreased.

The PDI could be influenced by the accumulated lifetime of TCs according to its definition. Although the trends of the accumulated lifetime for concurred-TCs in TS and categories 1-3 are similar from different datasets, there exist great differences in categories 4-5 TYs. A longer accumulated lifetime is shown in the JTWC dataset than the other two. The JTWC accumulated lifetime for categories 4-5 TYs shares the same trend with its total PDI, so do the STI and RSMC. Unlike the JTWC datasets, it is clear that neither RSMC nor STI dataset suggests an increase in WNP TC destructiveness.

The trends related to TCs for global-warming are still in debate. Given that there are significant differences in the estimated TC intensity in these main TC centers, we suggest that it's necessary to understand the underlying mechanisms responsible for TC intensity change and to further validate these datasets with observations.

Impact of Assimilating AMSU-A Radiance Data on Hurricane Katrina's Initialization

Dongliang Wang[1,2], Zhiquan Liu[2] and Dale Barker[2]

[1] Shanghai Typhoon Institute

[2] National Center for Atmospheric Research, Boulder, Colorado

1. WRF-3DVAR system and radiance data assimilation

The WRF-3DVAR adopts the incremental formulation (Courtier et al. 1994) and is a component of the WRF variational data assimilation (WRF-Var) system. It is originally based upon MM5 3DVAR system (Barker et al. 2004), but the basic software framework and coordination are fully updated for the ARW model. WRF-3DVAR assimilation system was designed for providing optimal initial and boundary conditions for the WRF model by using a variety of observations, containing both conventional data and a number of satellite retrieved data.

In the past four years, a generic radiance data assimilation capability has been developed in WRF-Var for regional and mesoscale applications. Radiance data interface has been implemented for National Centers for Environmental Prediction (NCEP) BUFR radiance data. As the core components of radiance assimilation, both the latest version 8 of RTTOV (Saunders et al. 1999) and the Community Radiative Tranfer Model (CRTM, Weng et al. 2007) are incorporated into WRF-Var as the observation operator of radiance data. Other important components include quality control for selected instruments (e.g., AMSU, SSMIS, AIRS), bias correction algorithm (Harris and Kelly 2002; Derber and Wu 1998), observation thinning and observation error tuning (Desroziers and Ivanov 2001).

2. Experimental design

The ARW model is used for numerical simulations in this study. Domain horizontal resolution is 12km. The grid's dimensions are 460X351X51 in east-west, north-south, and vertical directions. The model top is set to 10 hPa.

For each simulation, the model integrates 108 hours from 00 UTC 26 August. Besides a control experiment with an initial field interpolated from the NCEP GDAS at 00 UTC 26 August, four assimilation experiments are conducted. They are respectively corresponding to assimilating only conventional observations, only AMSU-A radiance data, conventional plus AMSU-A radiance data and AMSU-A radiance data plus a single MSLP observation. An ARW 6-hour forecast initialized from the GDAS analysis at 1800 UTC 25 August is used as the background field for these four assimilation experiments.

In this study, only AMSU-A radiance data is assimilated even though data from other instruments (e.g., AMSU-B, AIRS) can be also used in WRF-3DVAR. NOAA-15 satellite has good coverage over the experimental domain within the ±3h assimilation window centered at 00 UTC 26 August (Figure 1). Only channels 1~10 are used here. Channels 1~4 are used only over water and channels 5~10 are used over both land and water.

Other observations in our assimilation experiments come from National Center for Atmospheric Research

(NCAR) real time archives, including surface network (SYNOP, METAR, SHIP, BUOY) and upper-air network (RADIOSONDE, AIREP, PILOT, PROFILER) as well as some retrieved products (GPS precipitable water vapor, QuikSCAT sea surface winds). The assimilated single MSLP observation (25.9N/80.3W, 985hPa), which is at the same location as the best-track but 2hPa higher, is from the real-time advisory delivered by NHC.

3. Results and conclusion

Most data around TC vortex, where precipitation areas are very likely located, is rejected with quality control.

The observed brightness temperatures have an obvious cold bias of about 1.3K relative to those obtained by applying RTTOV to the background field. This bias is significantly reduced before assimilation.

Comparing with the CTRL initial fields, the intensity of vortex is strengthened in terms of maximum wind speed for all the 4 assimilation experiments. In particular, it is shown that merely assimilating AMSU-A radiances can obtain a similar maximum wind analysis to that from the assimilation of conventional observations. The vertical structure of the vortex is also largely changed. The warm core is enhanced, inflow in the lower levels and outflow in the higher levels are also strengthened to different extents. All of these features are critical to hurricane evolution. As a result, the simulated hurricane intensity and intensification rate are improved. Especially during the initial rapid intensification period, when AMSU-A radiance data and a single MSLP observation are assimilated, RMSE of simulated MSLP is reduced from 24 to 5 hPa, and RMSE of maximum 10-m wind speed from 15.9 to 6.2 m s^{-1}.

Assimilating AMSU-A data can improve the depiction of large-scale environmental flow in Katina's initial field, which subsequently causes positive impact on the track forecast of Katrina. When merely assimilating AMSU-A radiances or assimilating AMSU-A radiances plus a single MSLP observation, westward and southward components of environmental advection are enhanced, which results in a dramatic improvement of the simulated track. For the experiment AMSUA+SLP, the track errors for 24-, 48-, 72-, 96-h are reduced from 151, 246, 451, and 519 km to 129, 103, 110, and 94 km, respectively. However, the positive impact of AMSU-A radiance data seems to be reduced to a large extent when GTS data is added. The reason for that is unknown and needs to be further investigated. The background error covariance constraint should also play an important role to transfer direct temperature information in AMSU-A data to wind changes through mass-wind relation between analysis increments. Although the results presented in this study are based on one case only and it requires more case studies in order to draw more general conclusions, we do clearly demonstrate the benefit of radiance assimilation for improving hurricane analysis and forecast in terms of both track and intensity.

In the near future, information from other instruments should be also explored to improve hurricane initialization. For example, AMSU-B, which is sensitive to troposphere water vapor and has higher spatial resolution, has the potential to improve the depiction of the moisture field. Furthermore, the assimilation system can be better tuned for quality control, observation error specification, use of an advanced bias correction algorithm, and so on. From a longer-term perspective, more promising results are anticipated from assimilating radiance data using more advanced techniques, such as 4DVAR (Huang et al. 2008), ensemble Kalman filter (EnKF) and some hybrid variational/ensemble techniques (Wang et al. 2007). One more challenging problem is to assimilate radiance data under cloudy and precipitating conditions, which should be crucial to improve quantitative cloud and precipitation forecast.

References

Barker, D., W. Huang, Y. Guo, A. Bourgeois, and Q. Xiao, 2004: A three-dimensional variational (3DVAR) data assimilation system for MM5: Implementation and initial results. *Mon. Wea. Rev.,* **132,** 897–914.

Courtier, P., J.-N. Thépaut and A. Hollingsworth, 1994: A strategy for operational implementation of 4D-Var, using an incremental approach. *Quart. J. Roy. Meteor. Soc*., **120,** 1367-1388

Derber, J., and W. Wu, 1998: The use of TOVS cloud-cleared radiances in the NCEP SSI analysis system. *Mon. Wea. Rev.*, **126,** 2287–2299.

Desroziers, D. and S. Ivanov, 2001: Diagnosis and adaptive tuning of information error parameters in a variational assimilation. *Quart. J. Roy. Meteor. Soc.*, **127**, 1433-1452.

Harris, B. and G. Kelly, 2001: A satellite radiance-bias correction scheme for radiance assimilation. *Quart. J. Roy. Meteor. Soc.*, **127**, 1453-1468.

Saunders, R., M. Matricaedi, and P. Brunel, 1999: An improved radiative transfer model for assimilation of satellite radiance observations. *Quart. J. Roy. Meteor. Soc.*, **125**, 1407-1425.

Weng, F., T. Zhu, and B. Yan, 2007: Satellite Data Assimilation in Numerical Weather Prediction Models. Part II: Uses of Rain-Affected Radiances from Microwave Observations for Hurricane Vortex Analysis. *J. Atmos. Sci.*, **64**, 3910–3925.

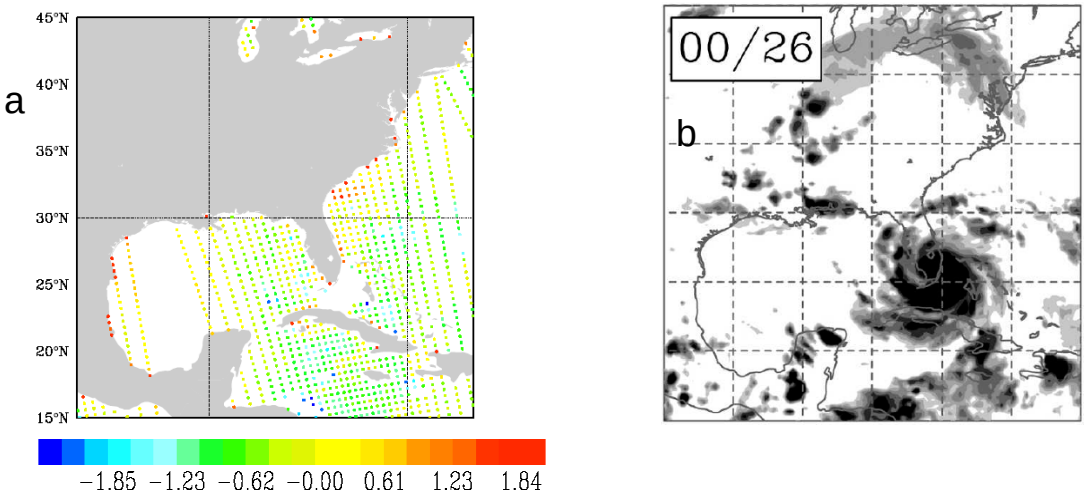

Fig. 1: (a) The innovation (observation minus background) of brightness temperature after bias correction and quality control for NOAA15 AMSU-A channel 4 within the assimilation window and (b) Infrared GOES satellite image at 0000 UTC 26 Aug.

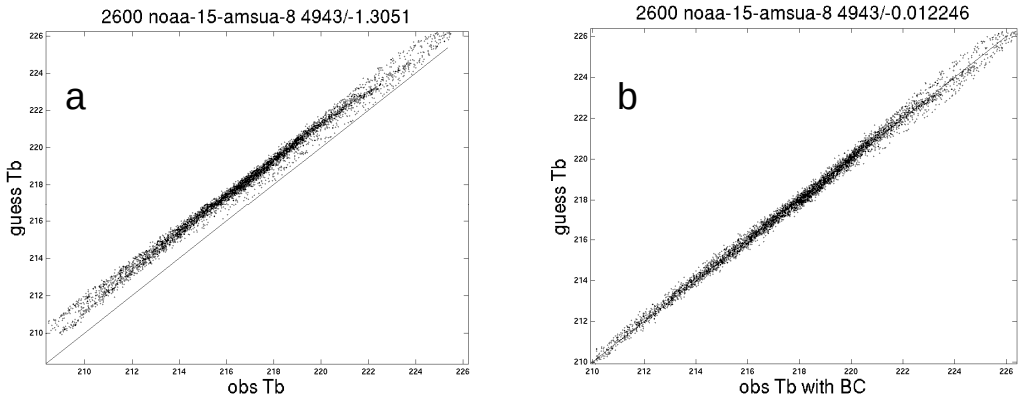

Fig. 2: Scatter plot of observed (a) before and (b) after bias correction versus computed brightness temperatures for NOAA15 AMSU-A channel 6.

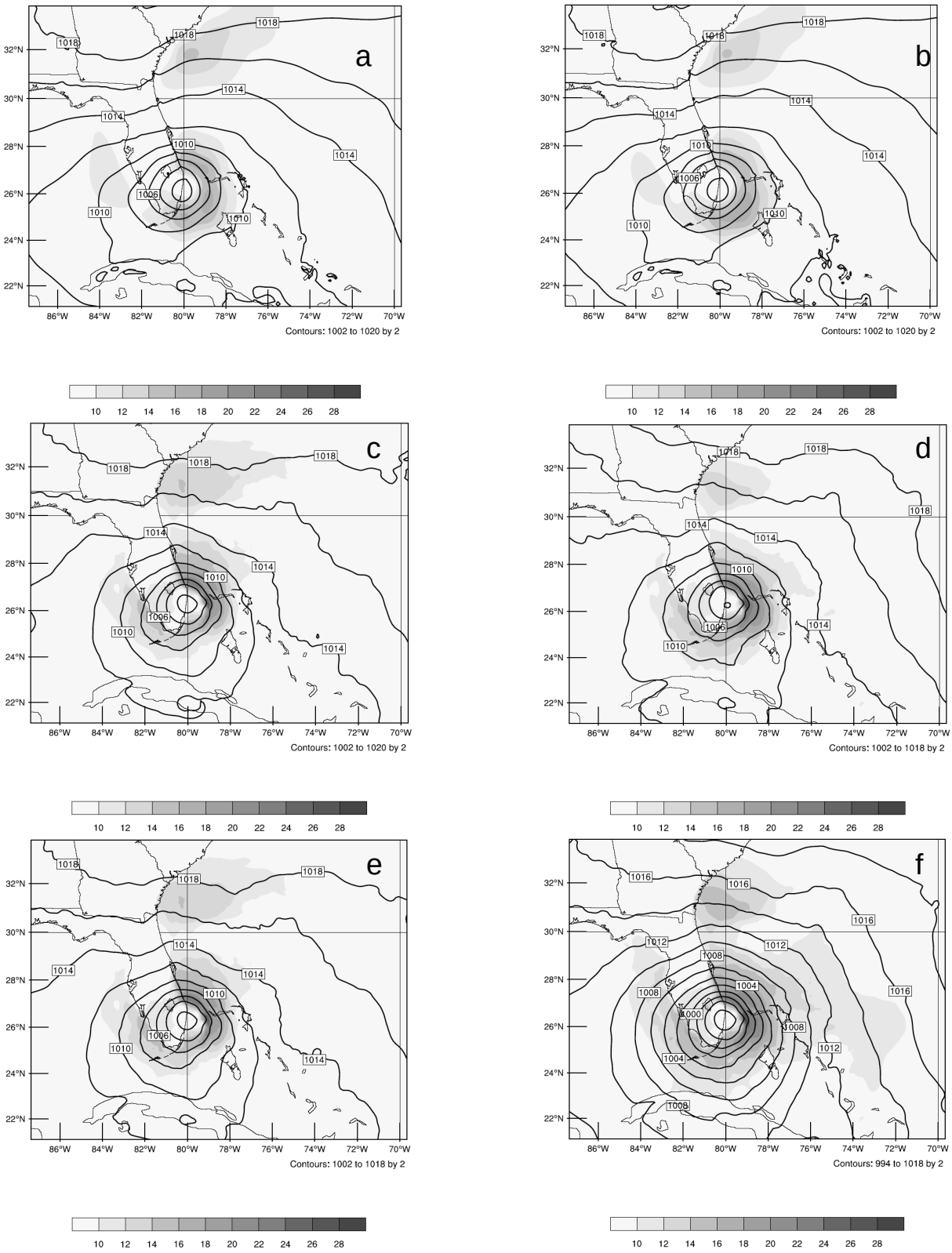

Fig. 3: The distributions of the initial SLP (hPa) and the lowest level wind speed (m s^{-1}) for (a) CTRL, (b) background, (c) GTS-only, (d) AMSUA-only, (e) AMSUA+GTS and (f) AMSUA+SLP.

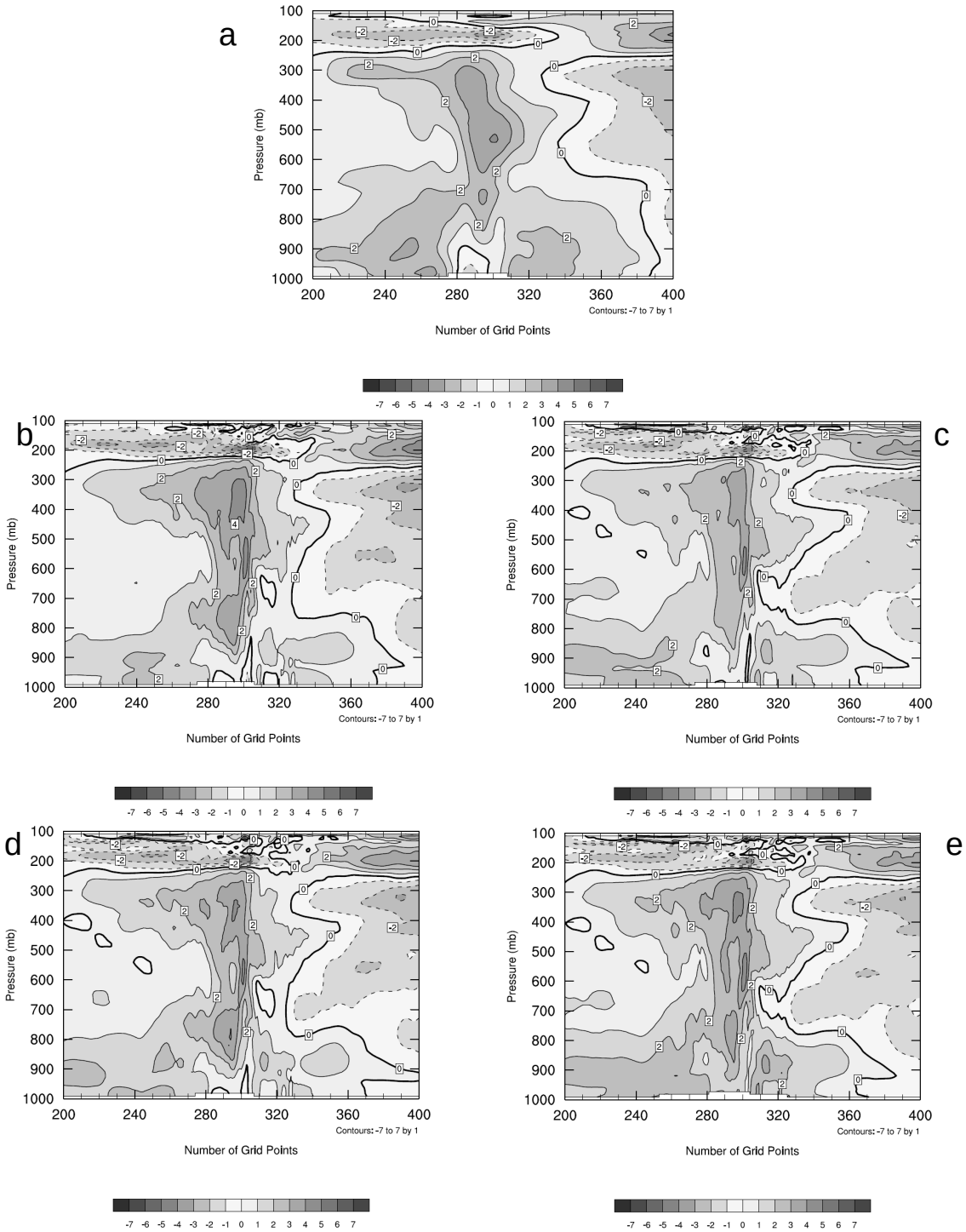

Fig. 4: Vertical cross sections through the hurricane center of the initial temperature deviation (K) for the experiments (a) CTRL, (b) GTS-only, (c) AMSUA-only, (d) AMSUA+GTS and (e) AMSUA+SLP.

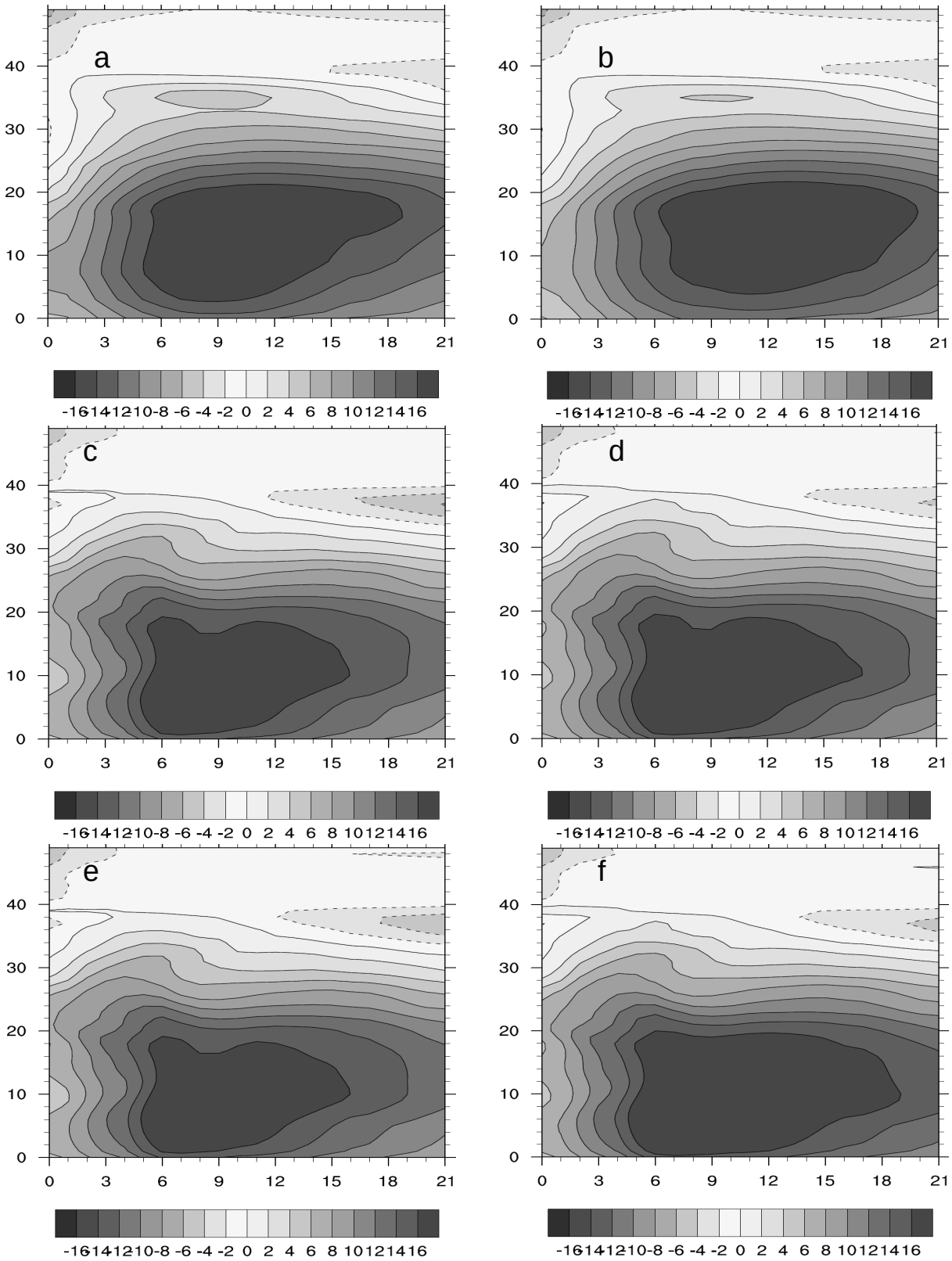
a
b
c
d
e
f
0 10 20 30 40
0 3 6 9 12 15 18 21
-16 -14 -12 -10 -8 -6 -4 -2 0 2 4 6 8 10 12 14 16

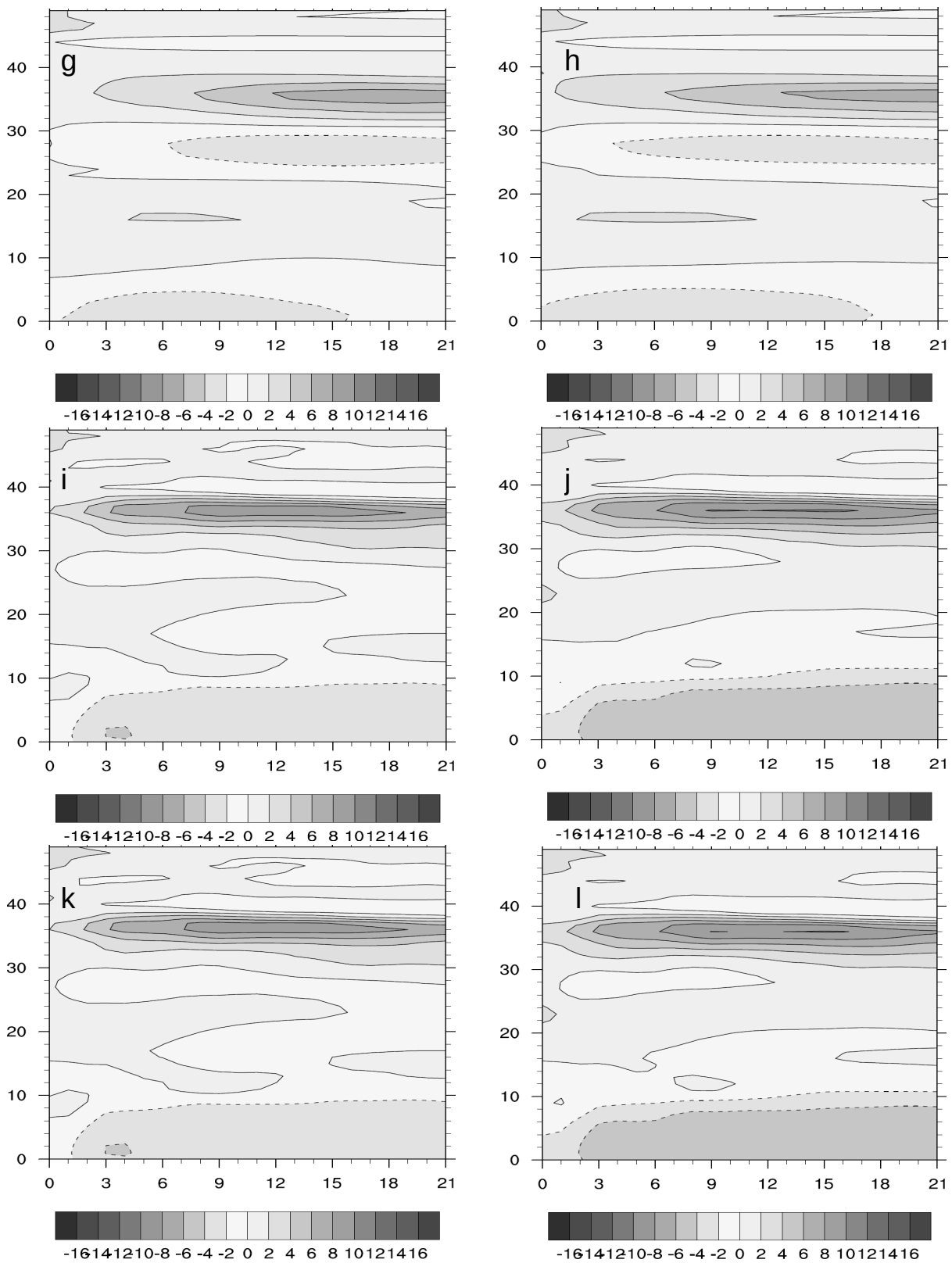

Fig. 5: Vertical cross sections of initial axisymmetric mean (a-f) tangential and (g-l) radial wind (m s^{-1}) for (a,g) CTRL, (b,h) background, (c,i) GTS-only, (d,j) AMSUA-only, (e,k) AMSUA+GTS and (f,l) AMSUA+SLP. X-axis is the number of grid point relative to the hurricane center and y-axis model's vertical level.

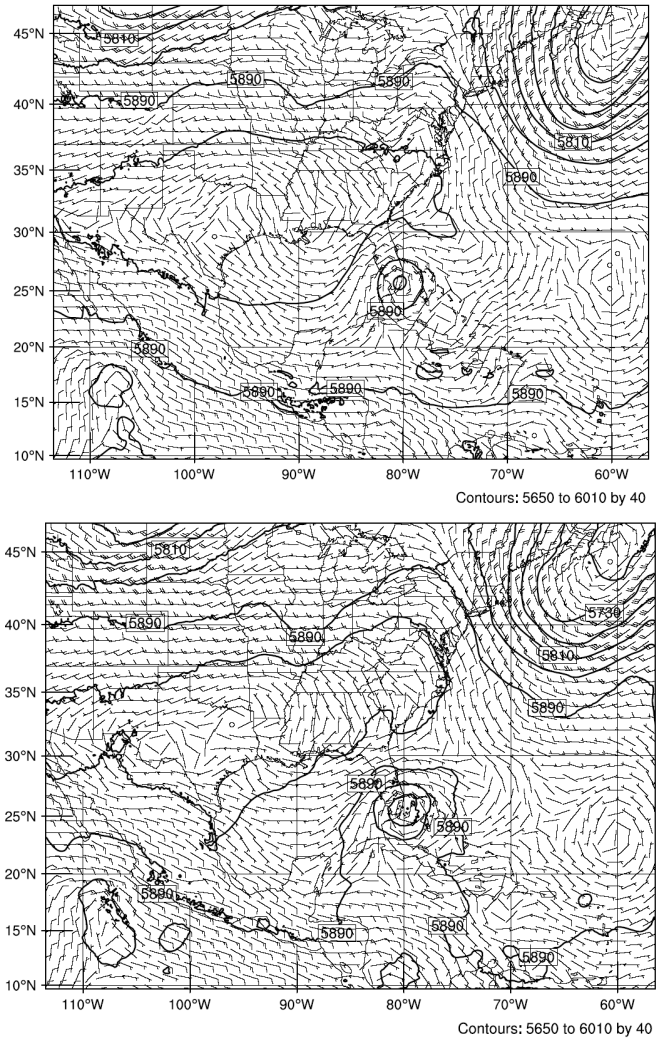

Fig. 6: The contours of geopotential height (m) and wind vector at 500 hPa for (a) CTRL and (b) AMSUA+SLP at initial time.

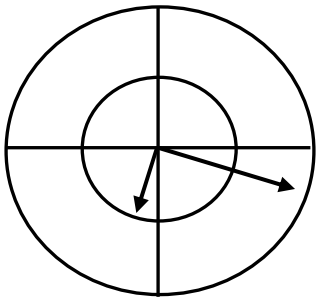

$V_{(AMSUA+SLP)——CTRL}$ **$V_{(AMSUA+GTS)——(AMSUA-only)}$**

Fig. 7: Differences of deep-layer mean flow averaged between 850 and 200 hPa at 2-7 degree radius from the cyclone center between AMSUA+SLP and CTRL, as well as between AMSUA+GTS and AMSUA-only. The circle shows the scale of every 0.45 m s^{-1}.

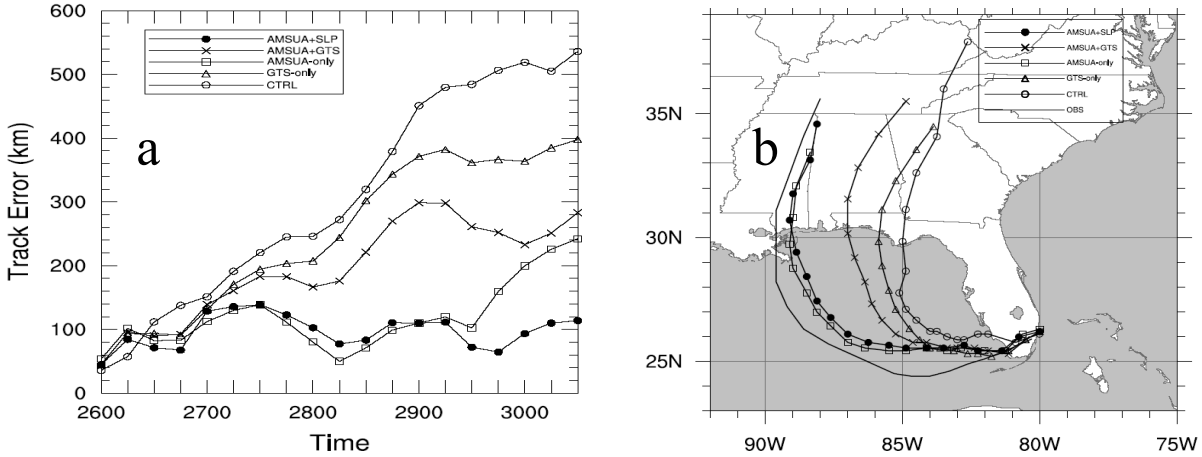

Fig. 8: (a) Time evolution of track forecast errors for CTRL and 4 assimilation experiments, and (b) simulated track.

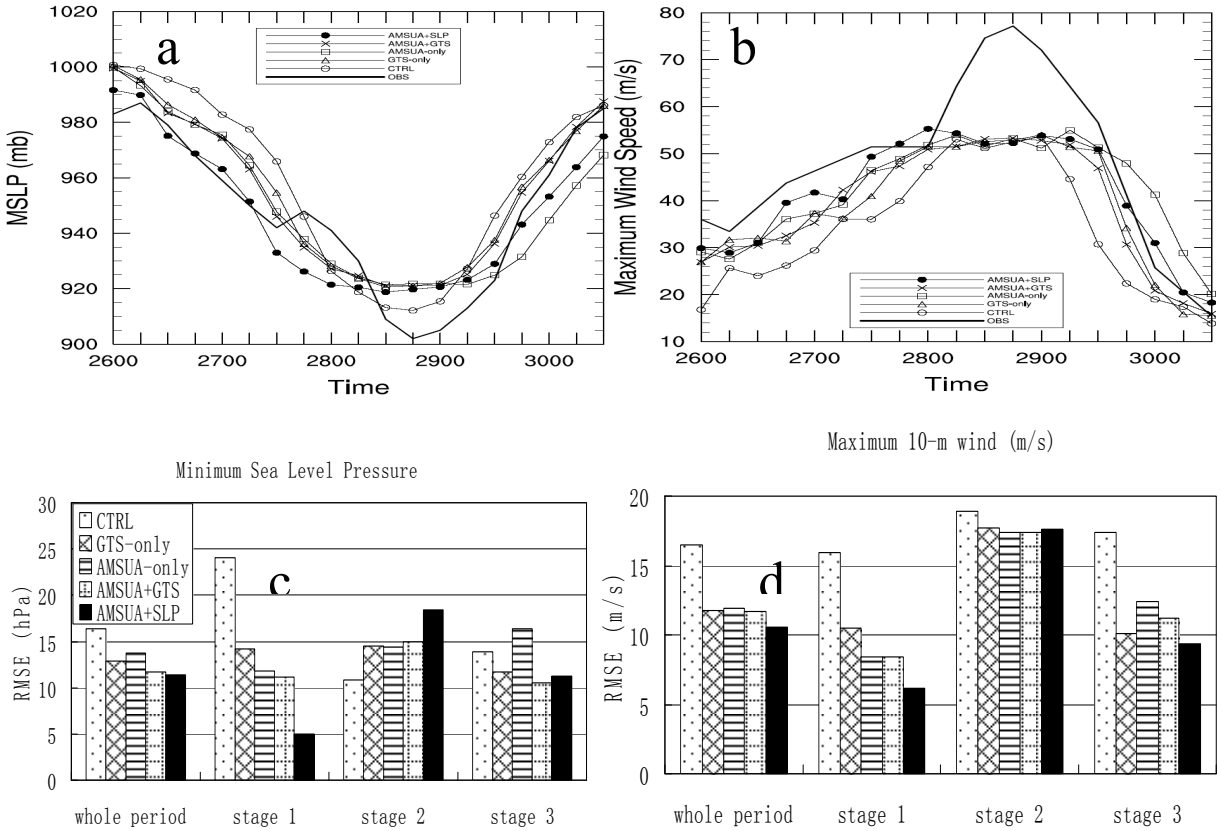

Fig. 9: Time evolution of simulated (a) Minimum Sea Level Pressure (MSLP, hPa), (b) maximum 10-m wind speed (m s^{-1}), (c) Root-mean-square error (RMSE) of MSLP (hPa) and (d) RMSE of maximum 10-m wind (m s^{-1}).

The Role of Low-Level Jet to The Development of Far Distance Tropical Cyclone Torrential Rainfalls Over North China*

YAO Xuexiang[1]，ZHANG Yingxin[2, 3]，LI Yunchuan[3]

[1)] Hebei Meteorological Bureau , Shijiazhuang, China, 050021；

[2)] Hebei Meteorological Observatory, Shijiazhuang, China,050021；

[3)] Hebei Provincial Key Lab for Meteorology and Eco-Environment,Shijiazhuang, China,050021.

Extended Abstract

Using data of precipitatíon in Hebei province, we got 24 cases of the far distance tropical cyclone torrential rainfall(≥50mm a day) between 1985 and 2005. Accounting for 17.3% of the total number of torrential rainfall cases in North China. It showed that the far distance tropical cyclone torrential rainfalls were one of the heavy rain type in North China.And it should be taken seriously. Using conventional meteorological observation data, typhoon yearbooks and NCEP/NCAR reanalysis data, the composing circumfluence of the torrential rainfalls in North China caused by remote tropical cyclones landing or activating on the coast of East China were counted and analyzed.

The synoptic model of the far distance tropical cyclone torrential rainfalls in Hebei province was established(Fig 1). Subtropical High ,westerly trough in middle latitude and tropical cyclone (or its depress) were main affected systems. There were south-east or southerly jets (or core) at the Low level of troposphere toward North of China between the tropical cyclone and subtropical High. Ahead the westerly trough were usually south-west jet(or core).

Studies have shown that the far distance tropical cyclone torrential rainfalls are closely related with the southeast jets , usually located between Subtropical High and tropical cyclone. The

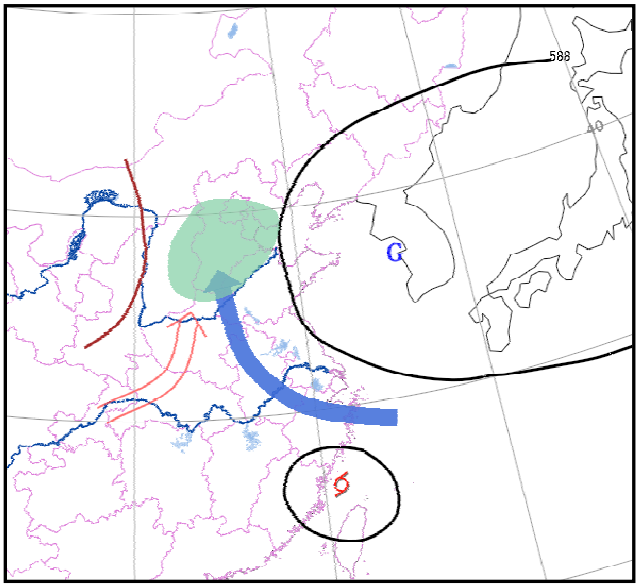

Fig.1synoptic modelof the torrential rainfalls in Hebei province caused by remote tropical cyclones

*Foundation item National Natural Science Foundation ect D2008001282、Hebei Science and Technology key project 052435183D and CMATG2009MS13、CMATG2009YB05

Corresponding author：Zhang yingxin, Hebei Meteorological Observatory,Email:zhangyx92005@yahoo.com.cn.

southeast jet (or core) at the Low level of troposphere played two role in the cases of heavy rain in North China.

In One hand, it could carry moisture air to North China.Take the heavy rain case occuried Jul,4-6,2000. for example. At 20:00(BJT) the 4th, the Subtropical High was located in the vicinity of the Korean Peninsula, while the tropical cyclone on the ocean of southeastern Taiwan. A Southeast Jet formed between Subtropical High and tropical cyclone. This jet was across about 500km long from south to north, the width of about 300km, Jet core, located in Zhengzhou (Figure omitted).Fig.2 was the water vapor flux at 700hPa and divergence of water vapor flux at 850hPa. With the south easterly jet, there were strong water vapor flux and convergence of water vapor flux at low level of troposphere. On the other hand ,.it was the source energy of heavy rain and strengthening the unstable condition of atmosphere. The tough of θse usually extended to North China(Figure omitted).

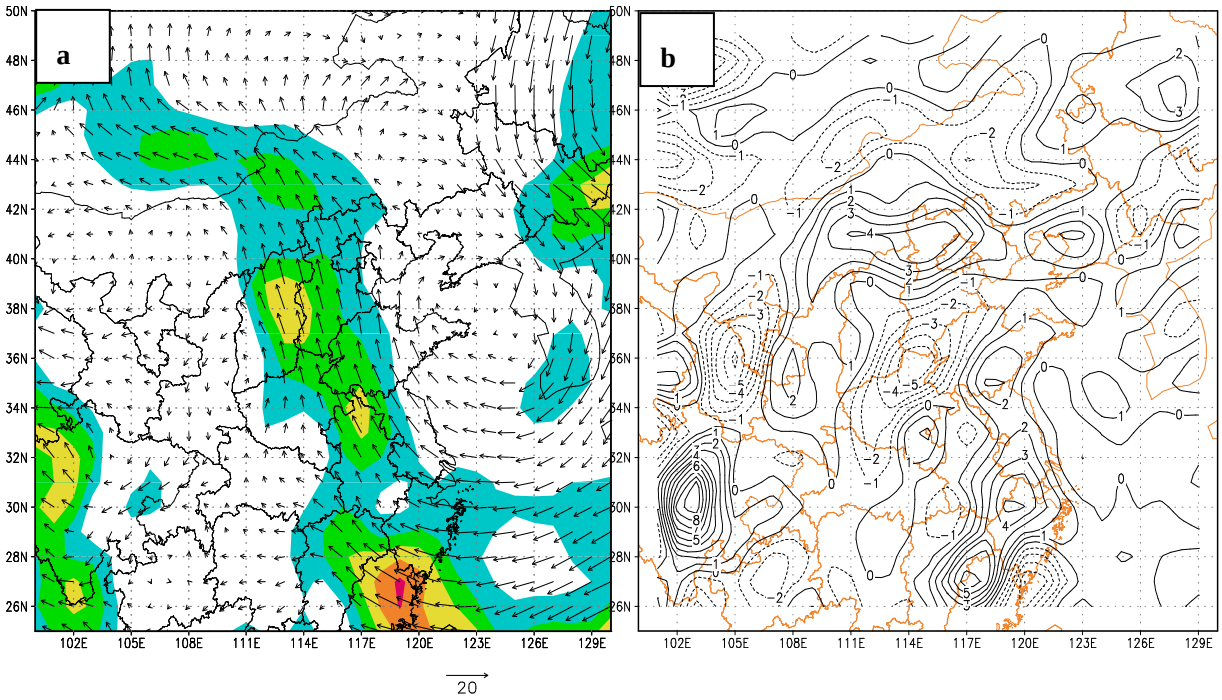

Fig.2 Water vapor flux at 700hPa(a) and divergence of water vapor flux at 850hPa(b) at

During the operational work.,we should pay more attention not only to the heavy rain aronud tropical cyclone,but also to the far distance tropical cyclone torrential rainfalls colsely related with the low-level jets(or cores).

Keywords: the far distance tropical cyclone torrential rainfall, low-level jet,North China

REFERENCES:

[1] Yang Xiaoxia, Chen Lianshou. Liu Shijun.et a1.2008. A study of the far distance tropical cyclone torrential rainfalls In Shandong Provinω• Acta Meteorologica sinica，66(2) :236 -250

[2] Chen Lianshou, Meng Zhiyong. 2001. An overview on tropical cyclone reserch progress in China during past ten years (in Chininese). Chinese J Atmos Sci, 25(3) :420-432

[3]Chen Lianshou. 2003. An overview of the impact of interaction between low-mid latitude circulation on rainfall and tropical cyclone behavior. Paper Presented at the 24th Conference on Hurricanes and Tropical Meteorology，29 May -2 June. Fort Lauderdale. FL. USA. 63.

[4] Chen Zhongming，Huang FuJun, He Guangbi. 2002. A case studyof interactions between the tropical cyclone and the souththwest vortex. Part 1: Diagnostíc analysis (in Chinines).Chínese J Atmos Sci, 26(3): 352-360

[5] Duan Yîhong, Yu Hui. 2005. Review of the reaserch in the intensity change of tropica1 cyc1one. Acta Meteorologica Sînaca(in Chinines)，62(5):636-645.

[6]Lei Xiaotu, Chen Lianshou. 2001.An overview on the interaction between tropica1 cyclone and mid-latitude western systerns. J Tropi-cal Metor(in Chinese), 25(3) :420-432.

[7]Lei Xiaotu, Chen Lianshou. 2001b. Tropica1 cyclone landfalling and its interaction with mid-latitude circu1ation systems. Acta Meteor Sinica (în Chininese)，59(5) :602-615.

[8] Li Ying, Chen Lianshou. 2005. Numerical study on impacts of boundary layer flux over wetland on sustention and rainfall of landfalling tropical cyclone. Acta Meteor Sinica (în Chininese)，62(5): 683-693.

Typhoon Vortex Self-Organization in Baroclinic Environment*

TENG Daigao (滕代高)[1], LUO Zhexian (罗哲贤)[2], YU Hui (余 晖)[3]

[1] Zhejiang Meteorological Observatory, Hangzhou 310017

[2] Key Laboratory of Meteorological Disater, NUIST, Nanjing 210044

[3] Shanghai Typhoon Institute, Laboratory of Typhoon Forecast Technique, CMA, Shanghai 200030

ABSTRACT

Self-organization of typhoon vortex in a baroclinic environment is studied based on eight numerical experiments with the fifth generation PSU/NCAR mesoscale numerical model MM5(V3). Results show that, when there are only two 400km-away meso-scale axisymmetric vortices with a radius of 500km in the initial field, the two vortices move away from each other during co-rotating till the distance between them greater than a critical distance named co-rotating critical distance. Then, they stop co-rotating. The situation is changed when a small vortex with a radius 80 km is introduced between two vortices in the initial field, with the two initially separated vortices approaching each other during their co-rotation, and finally self-organizing into a typhoon-like vortex consisting of an inner core and spiral bands. This result supports both Zhou Xiuji's view in 1994 and the studies in the barotropic framework concerning the interactions between vortices of the same and different scales. Otherwise, there are different for the development of typhoon vortex self-organized at various pressure level, i.e., the interaction between mesoscale vortices and small vortex being introduced into the double mesoscale vortices system can result in vortices system self-organizing into a new larger vortex similar to typhoon below 500 hPa, but with several discreting vorticity sheets at 300 hPa, which is resulted in the baroclinicity of weather system. Six other experiments are carried out to study the effects of initial vortex parameters, including initial position of the small scale vortex, distance and intensities of the initially axisymmetric binary meso-scale vortices. It is found that the distance between the initial axisymmetric meso-scale vortices is the most important one that influences the self-organizing process of the final typhoon-like vortex. This conclusion is similar to that achieved in barotropical model experiments such as Zhou et al. (2006) and Luo (2005, 2006).

The analysis in this paper just focuses on comparing the form difference of relative vorticity field without discussing the mechanism of vorticity change process in vortex self-organization. On the other hand, the vortices interaction is a very sophisticated problem. In this paper, only some preliminary results without environmental flow in baroclinic atmosphere is put forward, which is still in ideal conditions. In addition, the double typhoons' interaction is complicated, involving environmental flow change and multiple mesoscale vortices (Zhou et al., 2006a, b), which is a multi-scale sophisticated problem (Luo, 2005). Simulations for typical real cases are necessary. These all need further studies.

Key words: self-organization, small-scale vortex, meso-scale vortex, typhoon vortex, three-dimensional

* Supoorted by the key project of Science and Technology Department of Zhejiang Province under No. 2007C13G1610002.

vortex

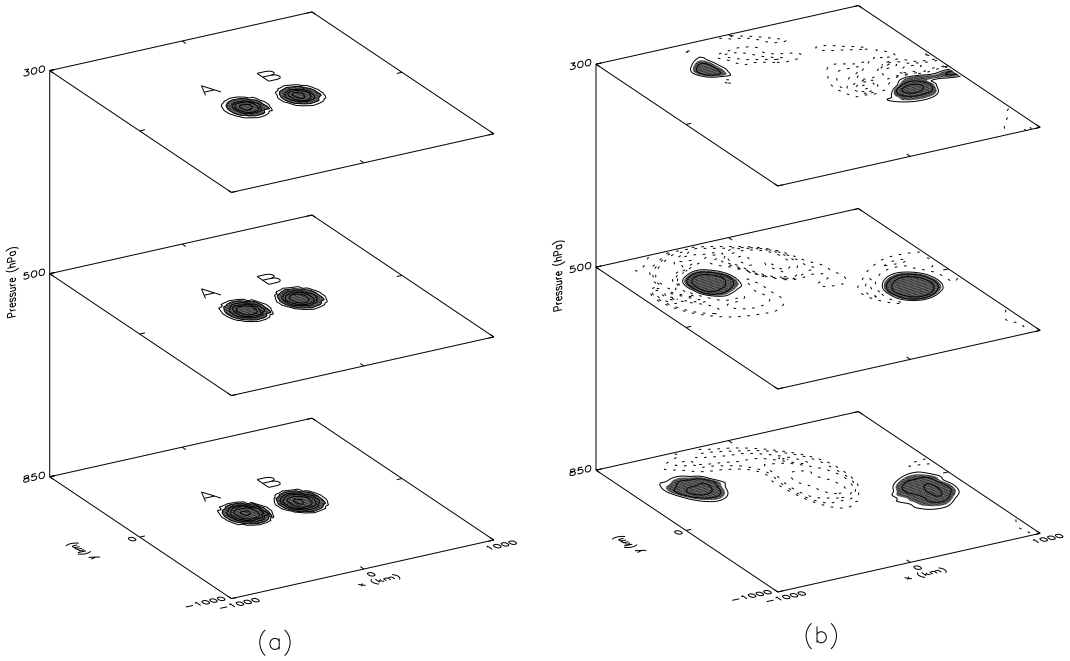

Fig.1. Relative vorticity distribution at 850, 500, and 300 hPa at t=0 and 120 h in Exp.1.
(a) t=0 h, (b) t=120 h, contours: -10e-05, -5e-05, -3e-05, -2e-05, -1e-05, 0, 1e-05, 2e-05, 3e-05, 5e-05, 1e-04, 5e-04, 10e-04, 20e-04, shaded value $\geq$2e-05, unit: s^{-1}.

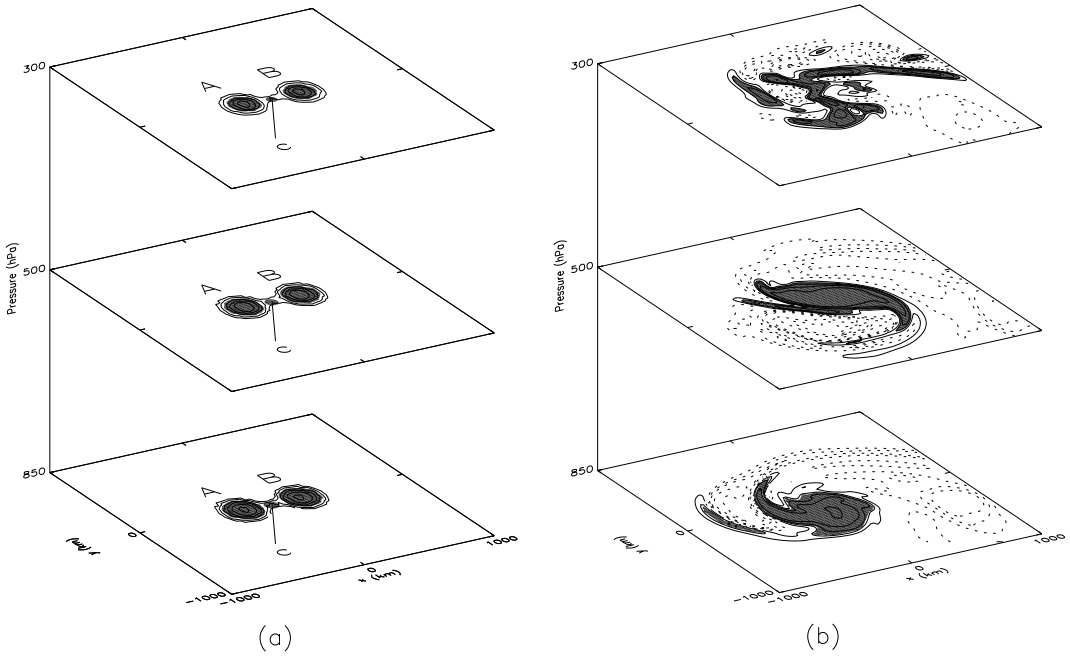

Fig.2 Relative vorticity distribution at 850, 500, and 300 hPa at t=0 and 96 h in Exp.2.
(a) t=0 h, b t=96 h, contours: -10e-05, -5e-05, -3e-05, -2e-05, -1e-05, 0, 1e-05, 2e-05, 3e-05,

5e-05, 1e-04, 5e-04, 10e-04, 20e-04, shaded value≥2e-05, unit: s^{-1}.

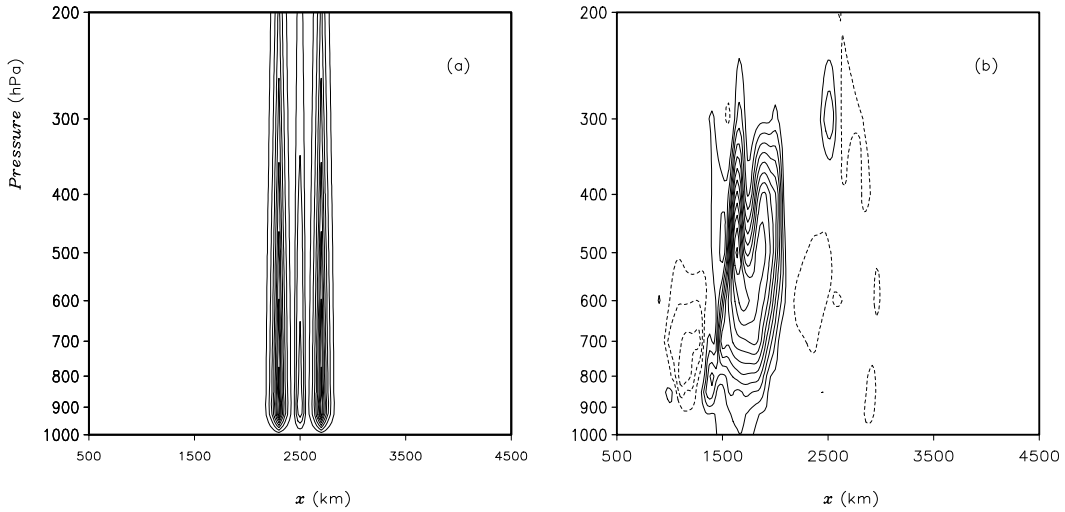

Fig.3. The latitude-vertical cross-section of Relative vorticity field in Exp.2 at t=0 and 96 h.
(a) t=0 h, (b) t=96 h, the contour interval is $2.0\times10^{-4}s^{-1}$ for meso-scale vortices and $0.5\times10^{-4}s^{-1}$ for small-scale vortex in (a) but $0.2\times10^{-4}s^{-1}$ in (b).

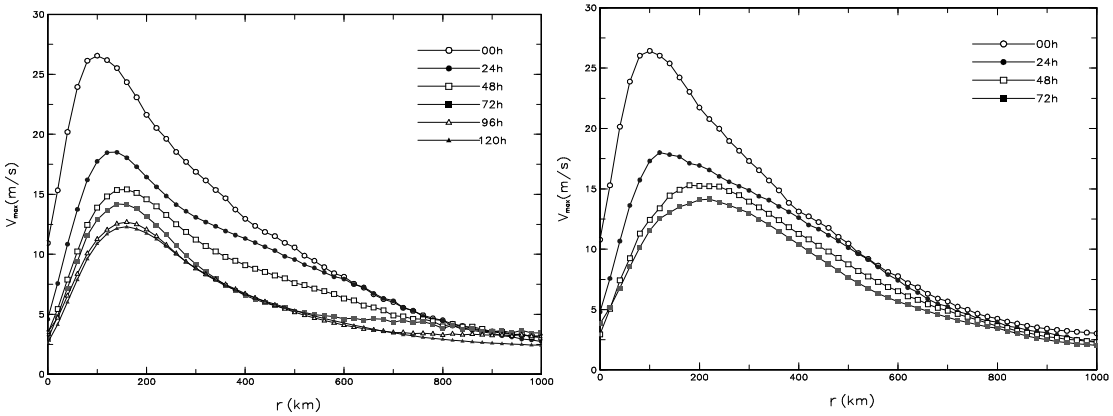

Fig.4. The radial distribution of azimuthal average maximum tangential wind velocity of vortex-A (a) at each 24 h at 700 hPa in Exp.1(a). The origin of coordinate is the center of vortex-A.
(b) for Exp.2

REFERENCES

Chen Lianshou, and Ding Yihui, 1979: Generality on Typhoon in Western Pacific. Since Press, Beijing, China. 156-157. (in Chinese)

Chen Y., and Yau M. K., 2001: Spiral bands in a simulated hurricane Part 1. vortex Rossby wave verification. J. Atmos. Sci., 58, 2128-2145.

Chuang H. Y., and Sousounis P. J., 2000: A technique for generating idealized initial and boundary conditions for the PSU-NCAR model MM5. Mon Wea Rev, 128, 2875-2882.

Duan Y. H., Wu R. S., Yu H., Liang X. D., and Johnny C. L. Chan, 2004: The role of $\beta-$ effect and a uniform current on tropical cyclone intensity. Adv. Atmos. Sci., 21(1), 75-86.

Duan Yuhong, Yu Hui, and Wu Rongsheng, 2005: Review of the research in the intensity change of tropical cyclone. Acta Meteor. Sinica, 63(5), 636-645. (in Chinese)

Grell G. A., Dudhia J., and Stauffer D. R., 1994: A description of the fifth-generation Penn State/NCAR Mesoscale Model(MM5). NCAR Tech. Note NCAR/TN-398+STR, 122pp.

Luo Zhexian, and Ma Jingxian, 2001: Binary tropical cyclone interaction the south of an idealized subtropical ridge. Acta Meteor. Sinica, 59(4), 450-458. (in Chinese)

Luo Zhexian, 2005: A Study on typhoon self-organization in a multi-scale coexisting system. Acta Meteor. Sinica, 63(5), 672-682. (in Chinese)

Luo, Z., and Liu, C., 2006: An investigation into the sensitivity of idealized vortex interactions to initial conditions and island topography. Geophys. Res. Letters., 33(1), L01807.

Montgomery M. T., and Enagonio J., 1998: Tropical cyclogenesis via convectively forced vortex Rossby waves in a three-dimensional quasi-geostrophic model. J. Atmos. Sci., 55, 3176-3207.

Wang Y. Q., and Holland G. J., 1996: The Beta drift of baroclinic vortices. Part I: Adiabatic vortices. J. Atmos. Sci., 53(3), 411-427.

Zängl G. A., 2004: reexamination of the valley wind system in the Alpine inn valley with numerical simulations. Meteorol. Atmos. Phys., 87, 241-256.

Zhou Jialing,, Ma Jingxian, Chen Lianshou, and Luo Zhexian, 2006: A preliminary study on the self-organization process of multi-vortices. Acta Meteor Sinica, 64(4): 464-43. (in Chinese)

Zhou Jialing, Ma Jingxian, Chen Lianshou, and Luo Zhexian. 2006: Influences of the initial structure and scale on the self–organization of vortices. Acta Meteor. Sinica, 64(5), 537-551. (in Chinese)

Zhou Xiuji, Luo Zhexian, and Gao Shouting., 2006: Two possible mechanisms for vortex self-organization. Science in China Ser. D, 36(2), 201-208. (in Chinese)

Zhou Xiuji, 1994: Atmospheric Sciences in 21th Century—in Memory of the 70th Anniversary of the Foundation of Chinese Meteorological Society. Acta Meteor. Sinica, 52(3), 257-260. (in Chinese)

Appendix: Model and initial and boundary conditions

MM5 (V3) (Grell et al., 1994) is a mesoscale numerical weather forecasting model that solves non-hydrostatic atmospheric motion equations in σ-coordinate with various parameterization schemes. In this paper, doubly nested experiments have been conducted in ideal conditions (without environmental flow) using the model. The spacing in inner and outer area is 20 and 60 km, respectively, and the corresponding grid points are 253×253 and 101×101. The vertical coordinate has 17 σ-levels, and the values of σ are as follows: 1.00, 0.99, 0.98, 0.96, 0.94, 0.91, 0.88, 0.85, 0.82, 0.77, 0.66, 0.55, 0.44, 0.33, 0.22, 0.11, and 0.00. The top pressure of model is 100 hPa. All experiments integrate for 120 h and export results per 6 h with a time step of 180 s. Grell cumulus parameterization scheme and Blanckard planetary boundary level scheme are used. The vertical velocity equals 0.0 on the top and surface boundary, lateral boundary condition are time-dependant (Grell et al., 1995).

When t=0, the velocity profile of mesoscale vortices is decided by (Wang et al., 1996):

$$V_M(r,\sigma)=\begin{cases} V_m(\frac{r}{r_m})\exp(1.0-(\frac{r}{r_m}))\times\sin(\frac{\pi}{2}\frac{\sigma+0.2}{1.2}) & r\le r_c, \\ 0 & r>r_c. \end{cases} \qquad (1)$$

the corresponding vortex structure is as follows:

$$\xi_M(r,\sigma)=\begin{cases}(\frac{2.0V_m}{r_m})(1.0-\frac{0.5r}{r_m})\exp(1.0-\frac{r}{r_m})\times\sin(\frac{\pi}{2}\frac{\sigma+0.2}{1.2}) & r\le r_c,\\ 0 & r>r_c.\end{cases} \quad (2)$$

where r is the distance to the vortex center, r_c is scale parameter of mesoscale vortex, V_m is maximum tangential wind velocity at surface, and r_m represents the distance where V_m appears.

$$\sigma=\frac{P-P_t}{P_s-P_t}. \quad (3)$$

where P is the reference-state pressure, P_t is a specified constant top pressure, and P_s is the reference-state surface pressure.

When $t=0$, let the small vortex structure as follows:

$$\xi_\gamma=\xi_{\max}\times\begin{cases}\sin^2(\frac{\pi(\delta r-\Delta)}{2\Delta})\times\sin(\frac{\pi}{2}\frac{\sigma+0.2}{1.2}) & \delta r\le\Delta,\\ 0 & \delta r>\Delta.\end{cases} \quad (4)$$

where $\xi_{\max}$ is the maximum relative vorticity at vortex center, δ_r is the distance to the vortex center with $\delta r=\sqrt{(x-x_c)^2+(y-y_c)^2}$, and Δ is the scale parameter of the small vortex. The values of parameters are: $V_m=32.0\ \mathrm{ms}^{-1}$, $r_m=100.0\ \mathrm{km}$, $r_c=500\ \mathrm{km}$, $P_s=1010\ \mathrm{hPa}$, $P_t=100\ \mathrm{hPa}$, $\xi_{\max}=1.74\times10^{-4}\ \mathrm{s}^{-1}$, $\Delta=80.0\ \mathrm{km}$.

Table 1 The setup for eight experiments

Exps	$V_m(\mathrm{ms}^{-1})$	$d_{AB}(\mathrm{km})$	$d_{oc}(\mathrm{km})$	$r_c(\mathrm{km})$	$\Delta(\mathrm{km})$
Exp.1	32.0	400.0		500.0	
Exp.2	32.0	400.0	0.0	500.0	80.0
Exp.3	32.0	400.0	500.0 (North)	500.0	80.0
Exp.4	32.0	400.0	500.0 (South)	500.0	80.0
Exp.5	32.0	360.0		500.0	
Exp.6	32.0	440.0		500.0	
Exp.7	36.0	400.0		500.0	
Exp.8	28.0	400.0		500.0	

d_{AB} is the distance between vortex- A and B. d_{oc} is the distance between small vortex-c and the middle point of centers of vortex-A and -B

Offshore TC Track Forecasting using Doppler Radar Velocity Field

Wu Chenfeng[1)], Wei Yingzhi[2)], Su Weidong[3)]

[1)] Meteorological Bureau of Xiamen, Xiamen 361012; [2)] (Meteorological Bureau of Fujian, Fuzhou 350001;
[3)] Meteorological Bureau of Putian, Putian 351100, China

Track forecasting of tropical cyclones (TC) has been greatly improved in recently years. Although most of the forecasts are based on numerical forecasting and analyses of satellite data, the problem is long prediction time and lacking effective ways for short-term forecasting of offshore TC's abnormal path.

1 Simulation of TC wind field

Most of the observations and research results have demonstrated that TC wind field is consisted of three different types of wind: cyclonic wind field which is circulating the TC centre, synoptic scale environmental wind which has influences on TC track and convergence (divergence) wind towards (away from) the TC centre.

1.1 Rankin model

Cyclonic-wind field of TC can be simulated by Rankine model[16]:

$$V_S = V_{\max} \bullet f(r) \qquad (1)$$

$$f(r) = \frac{r}{R_{\max}} \qquad r \le R_{\max}$$

$$f(r) = \frac{R_{\max}}{r} \qquad r > R_{\max}$$

Where $R_{\max}$ is radius of maximum wind velocity, $V_{\max}$ is the maximum wind velocity, and r is the distance towards the TC centre. The model assumes that TC wind field is concentric distribution around the TC centre and the tangential speed is the velocity on the concentric circles. The above equations show that the rotate speed V_S is directly proportional to the radius in the range from the TC centre to $R_{\max}$ and inversely proportional to the radius out of $R_{\max}$.

1.2 The characteristics of TC Doppler velocity

In our experiment, we made following assumption: TC is located at azimuth 135°, 80 km from the radar;

radius of maximum wind speed is 30 km, where maximum tangential speed is 60 m s^{-1} and environmental wind speed is 10 m s^{-1}.

According to equation (1), Doppler velocity map (Figure is not shown) simulated by only TC (without environmental wind field) appears to exist a pair of azimuthally symmetric positive and negative velocity core. The negative core is on the left side of direction of radar detection while the positive is on the right side, and the TC centre is on the zero velocity curve. Outside the eye region, the characteristics of speed map doesn't change much when there is convergence (divergence) wind towards (away from) the TC centre, which demonstrates that convergence (divergence) wind has little influence on the Doppler velocity.

The Doppler velocity map has clealy changed when the TC overlap with the environment wind field. When the environmental wind angle is 135°, the Doppler velocity field appears to be asymmetric and the velocity of the negative speed core is large than the positive one. The zero velocity curve away from the north (south) side of the radar bends towards the negative (positive) velocity field, especially when the TC centre is not on the zero velocity curve. When the environmental wind angle is 45°, the characteristics are very similar with TC simulation without environmental wind: TC centre is on the curve which is straight and the Doppler velocity field is asymmetric.

The above analyses show that TC's Doppler velocity field is going to change due to the variation of speed and direction of environmental flow. The zero speed curve bends in various degrees and extreme regions of both sides of the curve is asymmetric. The location of TC centre is away from the zero velocity curve and leans to the region which has large absolute value of extreme. Thus, according to the Doppler volecity of real TC and comparing the characteristics to the simulations, the environmental wind speed can be estimated and then the moving speed of TC can be estimated, too.

2 Applied study of TC Doppler velocity

2.1 Study of Typhoon Aere (2004)

After Typhoon Aere (2004) moving near Taiwan's northeast coast and entering Taiwan Strait, it moved from northwest to west firstly and suddently turn west-southwestward. This kind of TC track is very unusual in the TC history. Since Typhoon Aere turned left for the second time during 04:00-12:00 UTC, August 25, the observed velocity Figures are compared to simulated ones to define environmental steering flow and the reasons for second time turn-left will be discussed as follows. At 03:59 UTC, August 25, TC centre was located at north of Taiwan Strait, and the Doppler radial velocity map is shown in Figure 1a. When simulated environmental wind angle is 90º (Fig. 1b), TC centre leans to the negative velocity region, and the extreme of negative wind speed is much larger than the positive one; the zero velocity at north side of the station increases with the distance from the station and bend over to the negative velocity region, which is consist with observations. If the environmental wind angle is increasing (decreasing) (Fig. 1c,1d), the zero velocity curve at the north side is going to be over bending (extended) and positive velocity is going to be too small (large) in the close range of the TC circulation field. It is thus clear, when the environmental flow is due east with angle of 90º, the TC will move towards west by the eastly steering flow.

At 05:43 UTC, August 25, the typhoon made close approach to the mainland, and the Doppler radial velocity map is shown in Figure 2a. When the simulated environmental wind angle is 45º (Fig. 2b), TC centre is almost on the zero velocity curve with absolute value of negative wind speed a little larger than the positive

one; the zero velocity curve at the north side of the station increased with the distance from the station and bend a little towards the negative wind speed field. When the environmental wind angle is 70º (20º) (Fig. 2c,2d), the TC centre leans to negative (positive) velocity region, the zero velocity curve at the north side of the station bend over to the negative (positive) velocity region and the extreme value of negative wind speed is larger (smaller) than the positive one. As a result, the simulation with 45º environmental wind is most similar to the observations, which indicates that the environmental wind veered from east to northeast. However, the TC was still moving towards west at this time and turn southwest at 09:00 UTC, which means first the environmental wind changed then the moving direction of TC changed. The time gap is about 3 hours.

2.2 Analyses of Typhoon Nock-ten (2004)

According to the TC Warning Graphic at 2004-10-25 00:00 UTC of Joint Typhoon Warning Centre (JTWC) (Figure is not shown), Typhoon Nock-ten was going to move from towards northwest to towards northeast which means it wouldn't land on Taiwan. The truth is the typhoon moved accelerately towards northwest and landed on the north of Taiwan two and half an hour later, casuing huge damage. It changed its direction after 6 hours.

Figure 3a shows that the Doppler radial velocity of Typhoon Nock-ten observed by the Doppler radar in Jilong at 23:44 UTC, October 24. When the simulated environmental wind angle is 185º (Fig. 3c), the positive wind velocity near the station is a little small and the zero velocity curve is over bending at the north side of the station; when the simulated environmental wind angle is 135 º, the range of positive wind speed is too large and the zero velocity curve is over extended; when the simulated environmental wind angle is 160 º, the asymmetry of both positive and negative speed core, the degree of crook of the zero velocity curve at the north side of the station and curve's distribution in the positive and negative velocity regions are most similar to the observations which indicates the environmental wind direction is south-southeast and the typhoon is moving towards northwest. The observation shows that the actual typhoon track is towards north and 1 hour later the typhoon turned northeast, which indicates south-southeast environmental steering flow emerge about 1 hour early than the typhoon moving towards northeast.

3 Summary

Above studies shows, by comparing Doppler velocity images with simulated environmental wind with different wind direction, real-time environmental wind and its direction changes can be monitored, thus TC track can be monitored more accurately, which could hardly be done by large-scale meteorological data. The conclusion of the environmental wind changing before the changes of the TC track is very important to the short-term forecast for TC track.

Acknowledge: This paper is finished under the supervision of Profess Tang Dazhang and the academician Xu Jianming and with the help from Sun Xuguang and Wei Jingcheng. We are very appreciating of their help.

References:

[1] Vickery, P. J., 2005: Simple empirical models for estimating the increase in the central pressure of tropical cyclones after landfall along the coastline of the United States. J. Appl. Meteor., 44, 1807-1826.

[2] Roy Bhowmik, S. K., S. D. Kotal, and S. R. Kalsi, 2005: An empirical model for predicting the decay of

tropical cyclone wind speed after landfall over the Indian region. J. Appl. Meteor., 44, 179-185.

[3] Willoughby H. E., E. N. Rappaport, F. D. Marks, 2005: Hurricane Forecasting, the state of the art,paper submitted for the Hurricane Forecast socioeconomic working group, Pomona CA, 16-18February 2005.

[4] Chen L S, Luo Z L, Li Y.Research advances on tropical cyclone landfall process [J].ACTA METEOROLOGICA SINICA,2004,62(5):541-549.

[5] Lee W C. etc. Tropical cyclone kinematic structure retrieved from single-Doppler radar observations. Part Ⅰ:Interpolation of Doppler velocity patterns and the GBVTD technique[J]. Mon. Wea. Rev.,1999，127(10)：2419-2439.

[6] Lee W C.,F. D. Marks. Tropical cyclone kinematic structure retrieved from single-Doppler radar observations. Part II：The GBVTD-simplex centre finding algorithm[J]. Mon. Wea. Rev.，2000，128(6)，1925-1936.

[7] Micheal M. B，Wen-Chau Lee. Improved tropical cyclone circulation centres derived from the GBVTD-simpler algorithm[C]. 2003,31th International Conference on Radar Meteorology：Seattle, WA, Amer. Meteor. Soc.

[8] Wei Y Z et al,. The asymmetric wind structure of Typhoon Aera detected by doppler radar [J]. Journal of Applied Meteorolotical Science, 2007, 18(3): 285-294.

[9] Wang F Y, Wang Y X, Tao Z Y. The study of mesoscale wind field detection technique for single doppler weather radar [J]. Journal of Tropical Meteorology, 2003, 19(3): 291-298.

[10] Gu J F, Xue J S, Yan H. A summarization of the four-dimensional variational doppler radar analysis system [J]. Journal of Tropical Meteorology 2004, 20(1): 1-13.

[11] Wei Y Z et al,. Doppler radar echo characteristics for cold air intruding into Typhoon Changhu [J].Journal of Tropical Meteorology 2008, 24(6): 599-608.

[12] Chen L S et al,. Introduction to tropical cyclone dynamics [M].Beijing: China Meteorological Press，2002.17-36,78-81,248-252,300-304.

[13] Wang N et al,. Recognizing low-altitude wind shear and vonvergence line with doppler radar[J].Journal of Applied Meteorological Science, 2007, 18(3): 314-320.

[14] Chen D H, Wang S W, Wang H J.Performance of parameterization of sub-scale physical processes in numerical model and its effects on typhoon track forecastings [J].Journal of Applied Meteorological Science，1996,7(1).

[15] Ma S H, Qu A X, Zhang Y.Optimization and parallel of typhoon track prediction model in NMC and track error analyses [J].Journal of Applied Meteorological Science, 2004,15(3).

[16] Hu M B, Gao T C, Tang D Z. Analyses and usage of doppler weather radar data[M].Beijing:China PLA Press,2000,90-140.

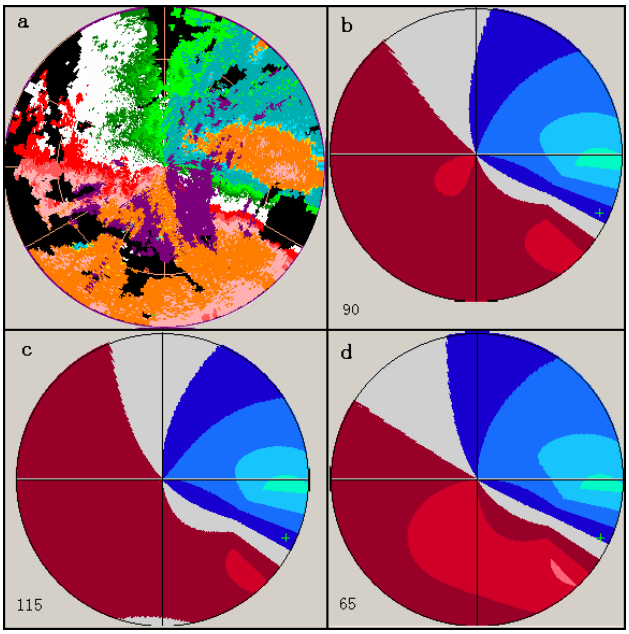

Figure 1 03:59 UTC, August 25,2004 a) Radar observation b) 90° c) 115° d) 65°
Location of TC 115°/127km, radius of maximum wind speed 50km, maximum wind speed 30m s^{-1}, environmental wind speed 10m s^{-1}

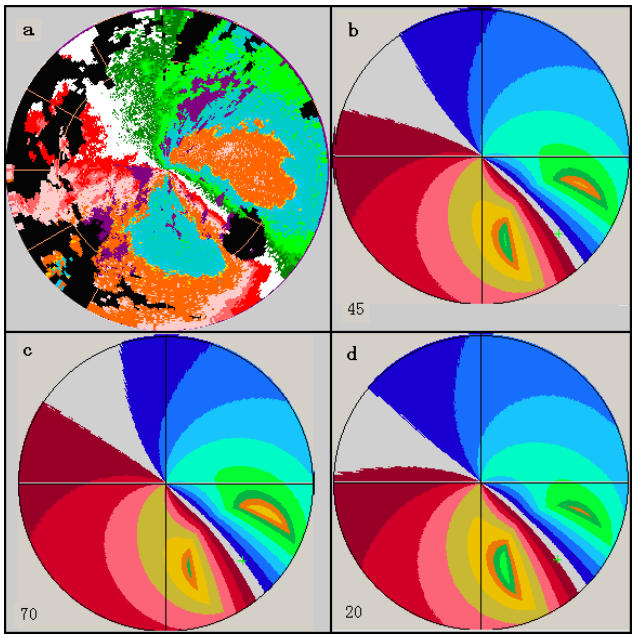

Figure 2 05:43 UTC, August 25,2004 a) Radar observation b) 40° c) 70° d) 20°
Location of TC 135°/100km, radius of maximum wind speed 50km, maximum wind speed 60m s^{-1}, environmental wind speed 10m s^{-1}

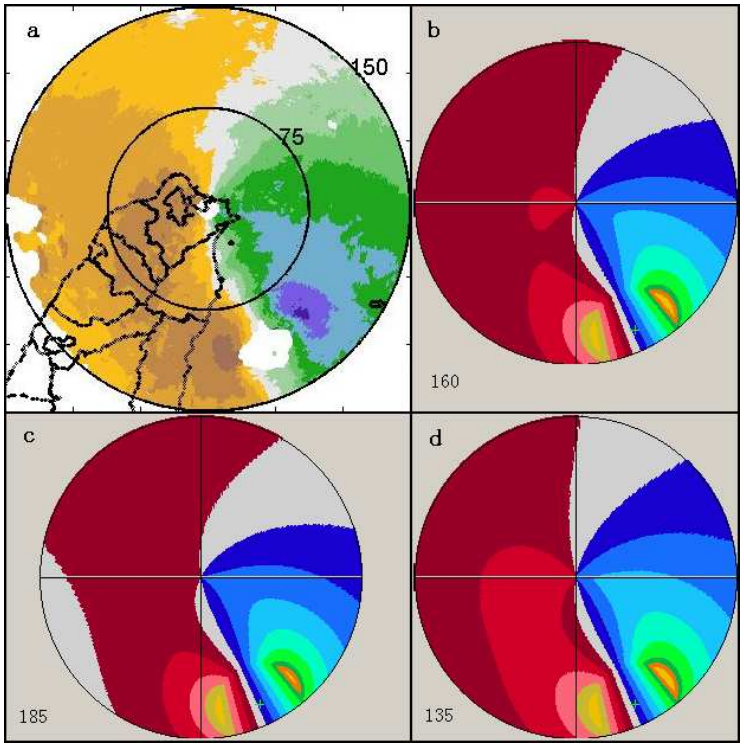

Figure 3 23:44 UTC, October 24,2004 a) Radar observation b) 160° c) 185° d) 135°
Location of TC 160° /118km, radius of maximum wind speed 35km, maximum wind speed 60m s^{-1}, environmental wind speed 10m s^{-1}

Doppler Radar Data Study of Structure and characteristic Associated with Landfalling Typhoons on Southeast Coast of ZheJiang Province in China

Chunxiao JI [1)] Fang ZHAO [2)]

[1)] Zhejiang Institute of Meteorological Sciences, Hangzhou 310017, China

[2)] Zhejiang Meteorological Observatory, Hangzhou 310017, China

1. Introduction

This study investigated temporal and spatial variations of reflectivity and precipitation structure within 300 km radius of typhoon center by using reflectivity data taken from Doppler radars located in ZheJiang Province. Three typhoons making landfall along southeast coast of ZheJiang Province in China have been selected to examine the changes of precipitation distribution from ~6h before landfall to ~7h after landfall. The three-dimensional wind fields are retrieved from Wenzhou Doppler radar data using 4D-var wind retrieval technology. The 3D structure of the mesoscale convective system producing the most severe heavy rainfall at Yunyan and Changchan is analyzed with single-Doppler radar retrieved wind and radar reflectivity observed by Wenzhou Doppler radar.

2. Results

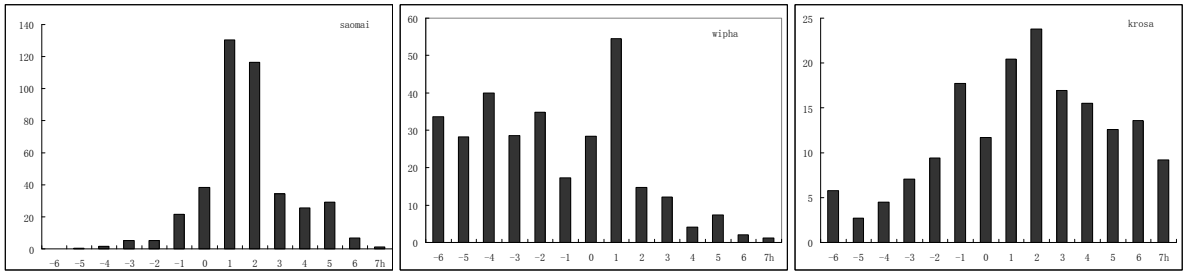

Fig. 1 The hourly precipitation of observation from ~6h before landfall to ~7h after landfall，horizontal coordinate indicates times(h), "-" before landfall, "+" after landfall, vertical coordinate indicates precipitation(mm), the typhoon Saomai is in Yunyan, the typhoon Wipha and krosa is in Changchan

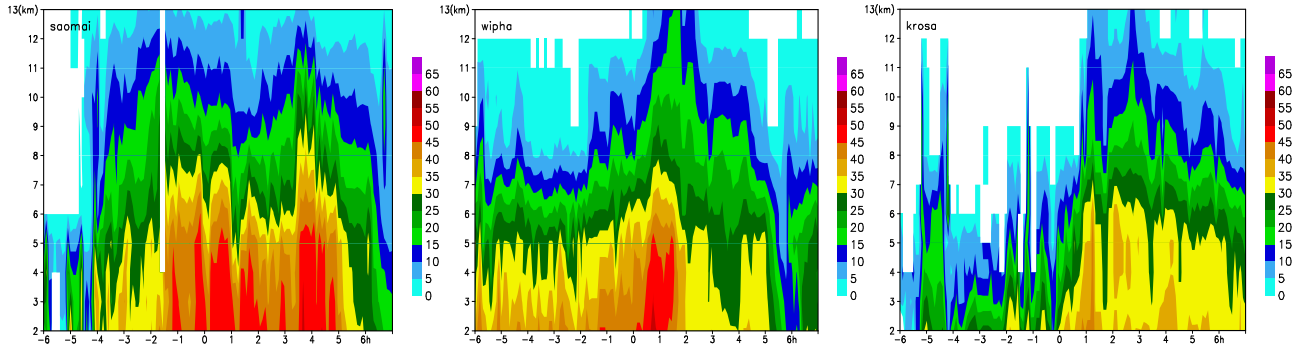

Fig. 2，as Fig. 1 but for the time-height cross sections reflectivity（shaded，dBz） observed by Wenzhou Radar，vertical coordinate indicates hight（km）

From fig. 1, we can see that, after 1h of landfalling, the maximum of hourly precipitation of the typhoon Saomai which was observed in Yunyan was 130.6mm, while the typhoon Wipha is 54.6mm and krosa is

23.8mm in Changchan. The difference of hourly precipitation was about five times between Saomai and krosa. Fig. 2 shows that, the stronger the typhoon intensity, the bigger the reflectivity of the middle and low levels, and the more severe the mesoscale convective system and the precipitation rate.

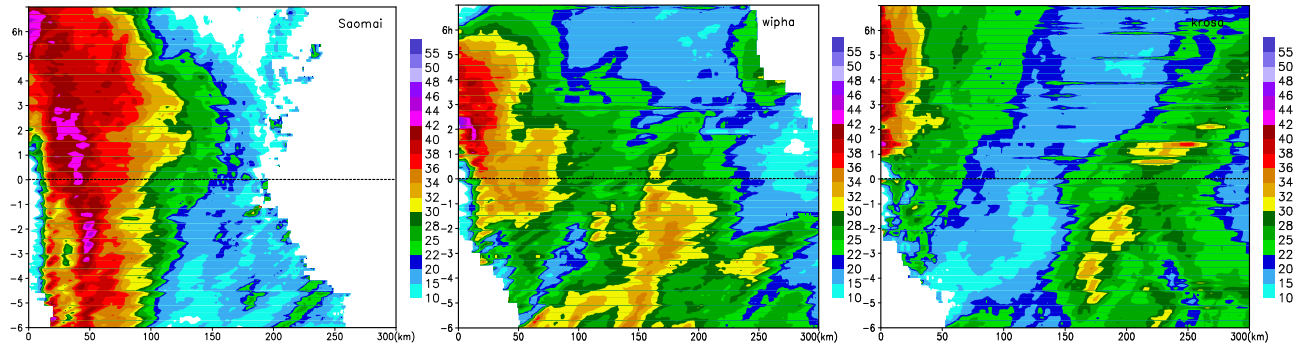

Fig. 3 the azimuthal mean reflectivity of different typhoon at 3km（shaded，dBz）, vertical coordinate indicates times(h), horizontal coordinate indicates distances from typhoon center (km),dashed line is landfalling time

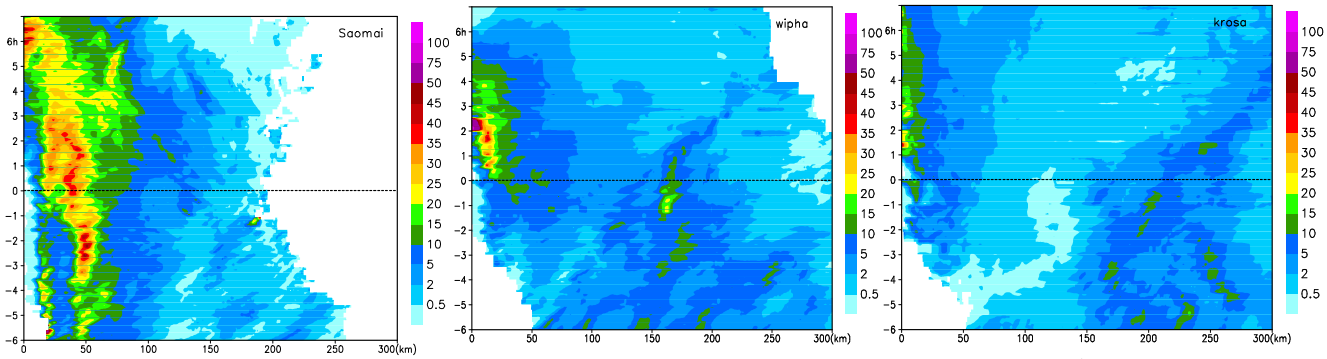

Fig. 4 as Fig. 3 but for the azimuthal mean hourly precipitation（shaded，mm）

The axisymmetric component of typhoon echo(rainfall), represented by the radial distribution of the azimuthal mean reflectivity, reveals that echo(rainfall) spreads from typhoon eyewall before landfallling. The mean echo(rainfall rate) in the inner-core region increases abruptly, accompanied with the rapid contraction of the precipitation toward typhoon center when typhoons are approaching the coast. the mean rainfall rate in the typhoon eyewall will intensified after landfall.

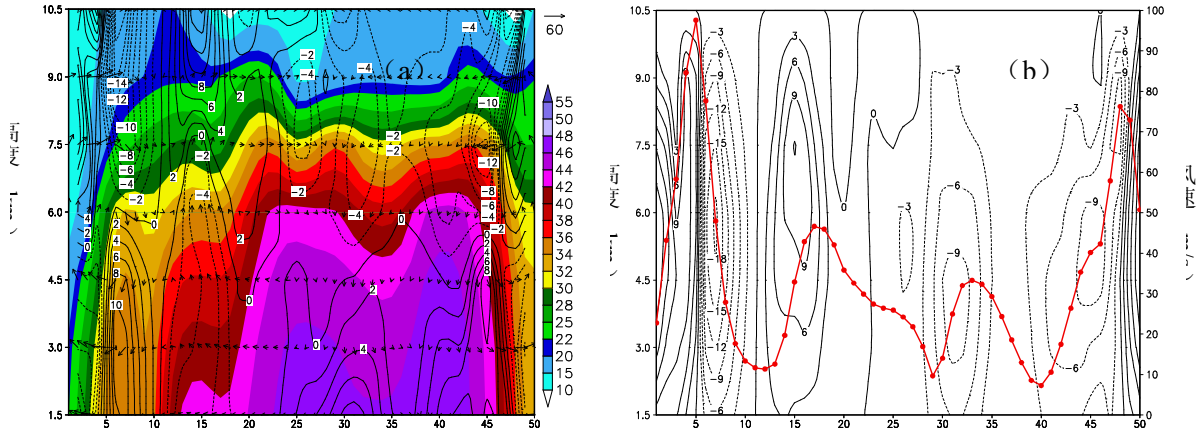

Fig. 5a the zonal vertical cross section of reflectivity of typhoon Saomai（shaded，dBz）, u-w

compose（arrow，ms^{-1}）, divergence（$\times 10^{-5}s^{-1}$，isoline）at 2006.8.10.08:32Z in Yunyan（white triangle）, vertical coordinate indicates hight(km), horizontal coordinate indicates the number of grid, solid(dashed) line for divergence(convergence)

Fig. 5b as Fig. 5a but for the vertical winds shear(ms^{-1}，red line), vertical velocity（ms^{-1}，isoline）, solid(dashed) line for ascent(descent)

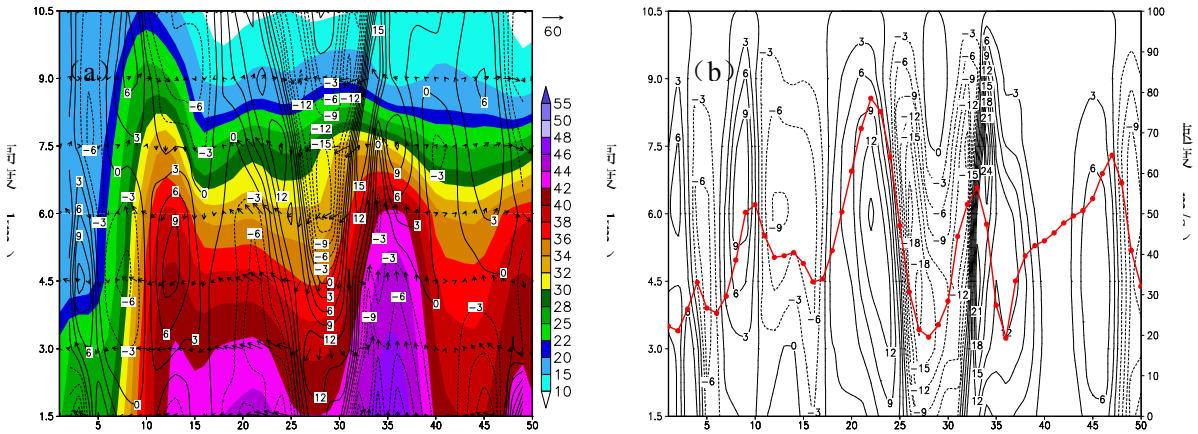

Fig. 6 as Fig. 5 but for 2006.8.10.10:33Z

The single-Doppler radar retrieved wind fields indicate that, before 1h of typhoon Saomai landfalling(Fig. 5) , divergence occurred in the lowand middle levels in Yunyan, the divergent maximum value was about $8\times10^{-5}s^{-1}$。the maximum descent velocity value was about -9 m/s. The upward movement (12 m/s) occurred in the west side of Yunyan. The vertical winds shear value is about 30m/s in Yunyan. But after 1h of typhoon Saomai landfalling(Fig. 6) , convergence occurred in the lowand middle levels in Yunyan, the convergent maximum value was about $-12\times10^{-5}s^{-1}$. the maximum ascent velocity value was about 24 m/s. The vertical winds shear value is about 60m/s in Yunyan.

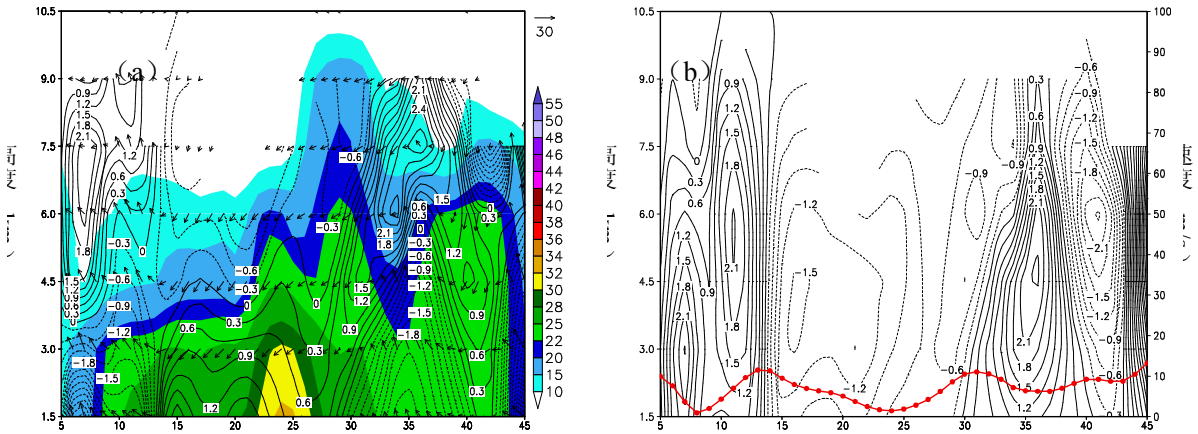

Fig. 7 as fig. 5 but for u-w×10 compose（arrow，ms^{-1}）typhoon Krosa at 2007.10.7.06:29Z in Changchan

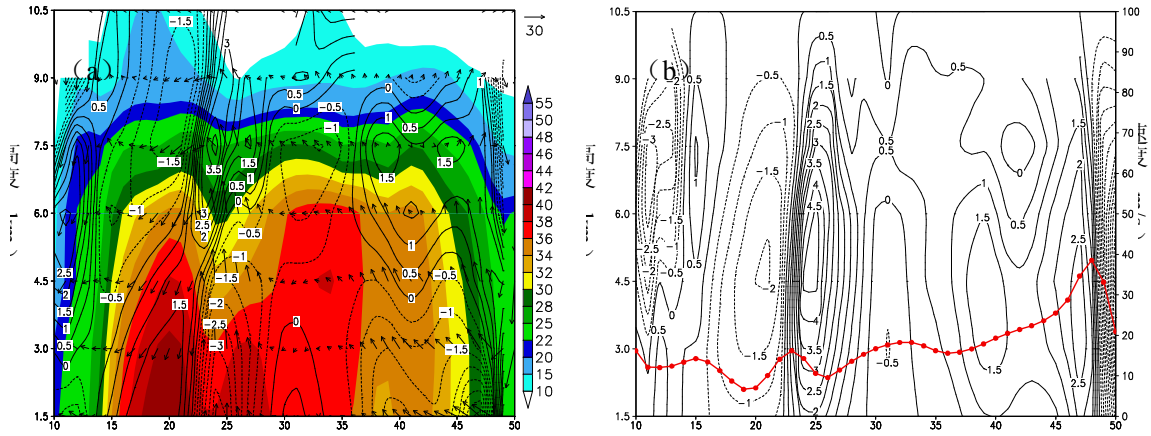

Fig. 8 as fig. 7 but for 2007.10.07.08:33Z

From Fig. 7, before 1h of typhoon Krosa landfalling , divergence occurred in the lowand middle levels in Changchan, the divergent maximum value, about $1.5\times10^{-5}s^{-1}$, was less than typhoon Saomai。 the maximum descent velocity value was about -1.5 m/s. The upward movement (2.4 m/s) occurred in the east and west sides of Changchan. The vertical winds shear value is about 4m/s in Changchan. But after 1h of typhoon Krosa landfalling(Fig. 8) , convergence occurred in the low and middle levels in Changchan, the convergent maximum value was about $-3.5\times10^{-5}s^{-1}$. the maximum ascent velocity value was about 4.5 m/s. The vertical winds shear value is about 10m/s in Changchan.

This study shows that, with the enhanced convergent(divergent) wind fields in the low(upper) levels, the tilted upward movement in the mesoscale convective system is severed and the precipitation rate is increased obviously. The typhoon intensity is proportion to the increases of the precipitation rate. The stronger the typhoon intensity, the bigger the vertical winds shear value. The area of the maximum vertical winds shear value is correspond to the most severe heavy rainfall. The obvious increase of the vertical winds shear value takes an important role in the enhancement and sustaining of the mesoscale convective system in spiral rain bands of typhoon landfalling.

Observation Error Statistics of Spaced-based GPS RO in WRF-Var system and Numerical Experiments for Tyhoon Dujuan

X.-X. Ma[1], Y.-R.Guo[2], Y.-H.Kuo[2], H.-C.Lin[2]

1 Shanghai Meteorological Center, Shanghai, China, 200030

2 National Center for Atmospheric Research, Boulder, CO, USA, 80301

1. Introduction

As one of the most catastrophic weather phenomenon in the nature, tropical cyclone (TC) has been invoked more attention to advance the understanding and prediction of it, especially for its track and intensity. During the past decade or so, many researchers have suggested that the buildup of greenhouse will likely result in a rise in sea surface temperature (SST), subsequently increasing both the number and maximum intensity of TCs（e.g.krishnamurit et al. 1998;Knutson and Kuroda. et. al. 1998）. With the help of data assimilation system, such as WRF-Var system, more and more unconventional data can be ingested into numerical weather prediction (NWP) to improve the initial field of NWP[Zou et al.1995;Kuo et al.1997;Healy et al.2005;Huang et al.2005].

Global positioning system (GPS) RO observations from low-earth-orbit (LEO) satellites have an advantage on the measurability of all weather conditions and no matter with day- or night- time. The Challenging Mini-satellite Payload for Geophysical Research and Application (CHAMP, Germany) and Satellite de Aplicaciones Cientifics–C (SAC-C, Argentina) can obtain about 350 occultation events daily. In the near future, six COSMIC LEO satellites (Taiwan & UCAR), which launched on 14th April 2006, will get about 2500-3000 daily measurements for real-time applications. It will be a great compensation for less available conventional data in data-sparse oceanic regions where is the most important area for TCs' formation and development.

GPS refractivity is derived from bending angles defined for each incident ray through its perigee point. In this study, based on one month CHAMP GPS RO data from UCAR/COSMIC Data Analysis and Archive Center (CDAAC), we attempt to improve the GPS RO observation error specification, and to compare two new refractivity error specifications with the old one and incorporate the best one into WRF-Var assimilation system for improving typhoon Dujuan forecast. In addition to GPS error specification, a series of numerical experiments have been performed to confirm the impacts of GPS, BOGUS, dropsonde and conventional data using WRF-Var and WRF system.

2.Methodology

2.1 Observation Pre-processing

Huang et al. (2005) defined the GPS refractivity error as below:

$$Error = N\_bottom \times e^{\left(\frac{p-p_0}{a}\right)} \quad [1]$$

$$a = \frac{p_t - p_0}{\log\left(\frac{N\_top}{N\_bottom}\right)} \quad [2]$$

where *N_bottom* = 10 and *N_top* = 3 are error of the refractivity N respectively at the bottom and top of the atmosphere. Refractivity error only depends on pressure, as shown in Figure 1a. However, Recent study by Kuo et al. (2004) indicates that refractivity error is related not only to the altitude also to the latitude and refractivity itself, thus based on one month

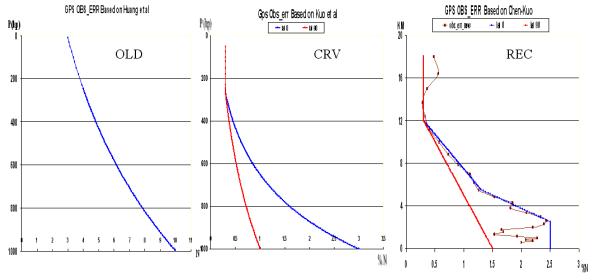

(a) (b) (c)

Figure 1. Error profiles. (a) OLD, based on Huang et al. (2005); (b) CRV (curves), based on Kuo et al. (2004); (c) REC (rectilinear lines) based on Chen-Kuo

data of Dec. 2001, two curves (CRV) were designed, as shown in Figure1b. Upper than 270hPa there is a static error percent (EP) of 0.3, and at the bottom level of 1000hPa, EP is defined as 3 for latitude 0° (blue line) and 1 for 90° (red line). Between 1000hPa and 270hPa, EP can be derived from the equations [1] and [2]. For other latitudes, the EPs are obtained by linear interpolation between latitude 0° and 90°. The CRV error is much smaller than the OLD one as shown in Figure 2.

Figure 2. The comparison of CRV and OLD profile

Another error specification is based on the statistics data from 15 Aug. to 15. Sep. 2003 that is coincident to typhoon Dujuan's period. As indicated in Figure1c, the profile of REC is very similar to that of CRV, but two rectilinear (REC) lines instead of the two curves. Above 12km, no matter with the latitude, there is only one EP value as 0.3. Below 12km, for latitude 0°, there are two vertical key points to separate the profile into three rectilinear lines: 0~2.5km, EP=2.5; 5.5km, EP= 1.3; for latitude 90°, EP is equal to 1.5 at 0km. For example, in the 6-hour observation window centered at 00UTC on 31 Aug. 2003, there were 8 GPS soundings in the Dujuan assimilation domain. The difference of REC minus OLD for sea level pressure (SLP) and surface temperature, after assimilation with WRF-Var, are shown in Figure 3. Since the GPS refractivity error of REC is smaller than that of OLD, the averaged difference is positive for SLP (Fig 3a) and is negative for temperature (Fig3.b). Like temperature, the wind velocity also becomes smaller (not shown). These indicate that two new GPS error specifications, CRV and REC, reduce to some extent the intensity of typhoon.

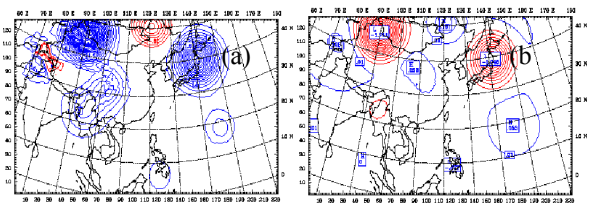

Figure 3. The difference of REC minus OLD for (a) SLP and (b) temperature

after assimilation with WRF-Var.

2.2 Quality Control

In WRR-Var, there are three steps in quality control procedure:

1) Innovation (O-B) check: the data will be discarded when O-B >5 $_o$ (observation error);

2) Relative error check: the relative error is defined as $R.E = \frac{|(O-B)|}{0.5\times(O+B)}$, when $h \le 7km,\quad R.E. > 5.0\%,$ or $7km < h < 25km,\quad R.E. > 4.0\%,$ or $h \ge 25km,\ RE. > 100\%.$ the data will be discarded;

3) Level data check: if the data at certain levels below 7 km fails to pass the relative error check, all data below that level will be discarded. Usually the data at the low levels has lower confidence (see Fig. 1c) due to the super-refractivity.

Figure 4a shows all 53 GPS RO soundings available during the Typhoon Dujuan period from 09UTC 28th to 15UTC 31st August 2003 from CHAMP data downloaded from COSMIC/CDAAC. Figure 4b gives the innovations (O-B) (red lines) after quality control and the observation errors (green lines) for all these GPS RO soundings with REC refractivity error specification. The background fields (B) are obtained from 6-hourly NCEP AVN analyses

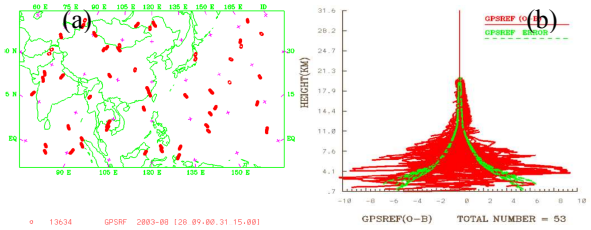

Figure4. (a). GPS RO soundings distribution; (b) innovations after quality control for the REC OBS error specification

Table 1 gives the results after assimilation of the GPS RO data for different observation error specifications. Still the "Chen-Kuo 2005" error specifications obtains a reasonable reduction of the analysis error with RMS(O-A)/RMS(O-B) =36.07%, close to e^{-1}.

Error specification	Huang et al (OLD)	Kuo et al (CRV)	Chen-Kuo (REC)	REC, Variable Perigee
(O-B) bias	0.076	0.013	-0.035	0.013
(O-A) bias	0.136	0.008	-0.003	0.000
(O-B) RMS	1.488	1.297	1.547	1.558
(O-A) RMS	1.038 (69.76%)	0.369 (28.45%)	0.558 (36.07%)	0.557 (35.75%)

Table 1. Averaged O-B and O-A of GPS refractivity for different observation error specifications.

3. Numerical Experiments Design

WRF V2.1 and WRF-Var 2.1 are used to simulate typhoon Dujuan , whose life period is from late August to early September 2003. It had a westward track and had been predicted to landfall in Taiwan, but finally it passed by near the South of Taiwan. To improve the prediction, some numerical experiments have been done to test the impact of different observation types assimilated into WRF-Var.

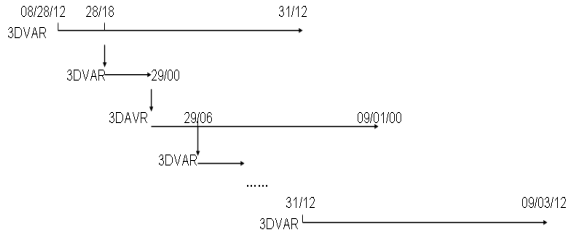

Figure 5. Flow chart for 6-hourly cycling run

The assimilation window is 6 hour. Within each window, there are only a few GPS soundings in the model domain, generally less than 10, cycling experiments (i.e., taking WRF 6-hour forecasts as the background of WRF-Var for current time) were set up in this study to accumulate the effects of GPS data. The cycling runs start from 12 UTC 28th Aug. and end at 12UTC 31st Sep. 2003 as illustrated in Figure 5. A long range forecast (72 hours) is done only at 00UTC and 12UTC. So the whole cycling run totally has seven 72-h forecasts and thirteen analyses. The cumulative numbers of GPS RO soundings used in the cycling run are shown in Figure 6, respectively for 3 hours (red line) and 6 hours (blue line) cycling interval. The case number sequentially represents seven analysis times when a 72-hour forecast is deduced.

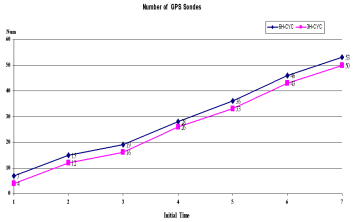

Figure 6. cumulative numbers of GPS RO soundings during experiment period.

The domain size is 228×128×31 with a horizontal resolution of 45-km and the tuned NCEP background error statistics (cv_options=3) are used in WRF-Var. The physics options chosen for the WRF model are listed in the table 2 below.

Micro_physics	WSM3(3)	**Sf_surface**	T-De(1)
Ra_longwave	RRTM(1)	**Bl_boundary**	YSU(1)
Ra_shortwave	Dudhia(1)	**CU**	K-F (1)
Sf_sfc_lay	M-O (1)	**Subgrid-turbdiffusion**	No

Table 2 the physics options used in WRF model

As a control experiment, Exp1 (NON) directly uses NCEP Aviation Model (AVN) global analysis as the initial field; Exp2 (CVN) assimilates conventional Global Telecommunications System (GTS) data; Exp3 (CVB) uses GTS data plus BOGUS (global bogus and typhoon bogus) data from Taiwan Central Weather Bureau (CWB); Exp4~Exp6, based on Exp3, but add GPS RO data with three different refractivity error specifications, respectively named as OLD, CRV and REC (ALL); Exp7 (DRP) further adds dropsondes to Exp6; Exp8 is the same as Exp6 but with cold start mode; Exp9 (CVBN) and Exp10 (ALLN) have two nested domains respectively at 45-km and 15-km resolutions to look into the fine structure of typhoon such as precipitation distribution. Exp9 is without GPS and Exp10 with GPS based on REC specification.

4. Results

One firstly examines the impact of the new GPS refractivity error specifications. The statistics of 72-h forecast track errors are plotted in Figure 7 for the 7 forecasts at initial time 00 UTC and 12 UTC. For the convenience of comparison, the difference of track error between experiments is shown in Figure 7. The blue line is the difference of OLD minus REC, and the red line OLD minus CRV. Both have positive average value: 12.25km for CRV and 11.7km for REC and indicate positive impact on track forecast with new specifications, particularly at the beginning times of cycling.

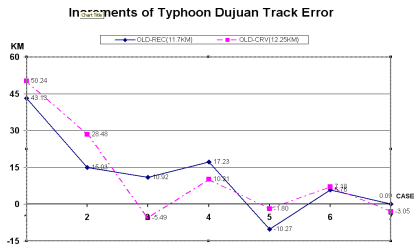

Figure7. Difference of Dujuan track error.

To compare the impact of assimilating BOGUS, GPS RO data as well as cycling run, the 72-h forecasts initialized at 00UTC 31st Aug. 2003 have been chosen to display the track, central SLP and track error of Dujuan (Figure 8). From Figure 8a, one can see that all assimilation experiments produce a better track forecast than the control experiment (red line, no assimilation). For intensity (Figure 8b), the experiments without assimilation (red line) and cold start (green line) fails to produce a similar tendency of central SLP to that of the best track (black line) at all; Cycling experiment with conventional data (blue line) results in some improvement; Adding BOGUS (light-blue line) and GPS RO (light-red line) results in further SLP intensification at initial time from 994hPa to 984hPa, but GPS RO causes SLP decreasing a little more quickly than that without GPS RO being assimilated. Figure 8c gives the averaged 72-h track errors for control experiment (Exp1, red line), BOGUS (Exp3, green line) and GPS (Exp6, blue line). The average values of track error for them are respectively 81.7km, 64.3km and 57.4km. In spite of less available GPS RO data used in Exp6, slight improvement by using GPS RO can be observed.

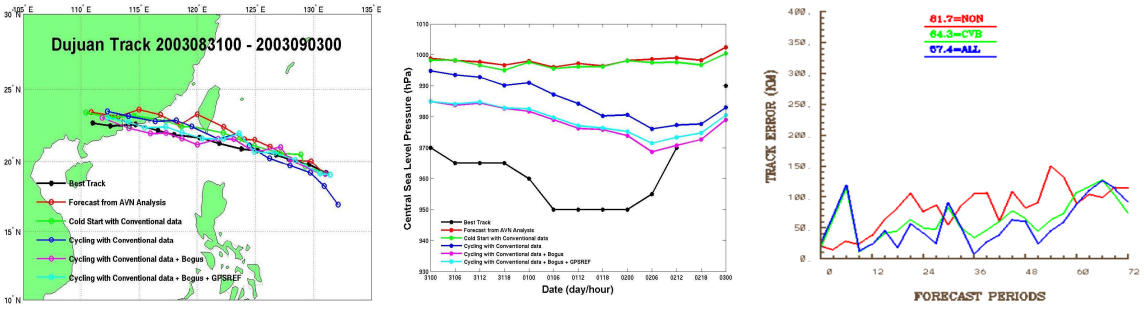

(a) **(b)** **(c)**

Figure 8 a） 72-h forecasts for Dujuan track； b） 72-h forecasts for Dujuan central SLP C） 72-h forecasts for Dujuan track error

GPS RO is expected to be able to improve humidity analysis and subsequently precipitation prediction. 12-h precipitation (12-24 UTC 1 September 2003) is shown in Figure 9. Figure 9a is the observed precipitation with a maximum value of 657.744mm. With the GPS RO (Figure 9c), derived from Exp10 (15km resolution), the maximum value and the corresponding location are much better than those of Exp9, which is without GPS RO (Figure 9b).

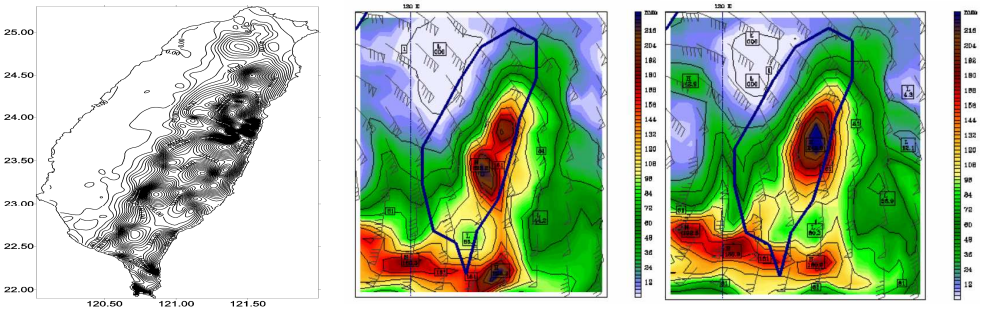

(a) **(b)** **(c)**

Figure 9: 12-h precipitation distribution (12-24 UTC 1 Sep. 2003). a) observational precipitation (657.744mm); b) Exp9, without GPS (223.2mm); c) Exp10, with GPS (242.6mm)

Finally, to clarify main factors to improve typhoon forecast, table 3 summarizes improvement of 72-h average track error and central SLP for each factor. Time period means number of cases (e.g., 7 x 72 h = 7 runs with 72-h forecast). The result indicates that the six factors all have positive impact for track forecast. BOGUS and WRF-Var take the first two places for both track and intensity; other four factors have slightly negative impact for pressure forecast.

Factors	Definition	Track (km)	Press. (mb)	Time period
TC Bogus	Exp2-Exp3	110.8	18.1	4x 72 h
GPS RO data	Exp3-Exp6	5.2	-0.25	5x 72 h
Dropsonde	Exp6-Exp7	4.2	-0.56	1 x 42 h
Cycling	Exp8-Exp6	17.8	-0.26	6 x 72 h
GPS Specification	Exp4-Exp6	11.7	-0.11	7 x 72 h
WRF-Var vs. AVN	Exp1-Exp8	47.5	18.0	4x 72 h

Table 3. Impact of six factors for track and SLP prediction.

5. Conclusions

New GPS RO refractivity error specifications, which take into account geographic- , altitude- and itself value- dependent observation error based on one month GPS data, reduce track forecast error of typhoon DUJUAN comparing to the old error specification scheme.

With GPS refractivity data, both domains respectively with a resolution of 45km and 45/15km nested, obtain positive result in terms of track and precipitation prediction, although less available GPS RO soundings over CWB domain during the whole cycling.

TC bogus data plays a substantial role for TC forecast. TC bogus also results in improved forecast with Global bogus than without it.

Since dropsonde captures the meteorological data from very close area to typhoon, they improve the initial field of forecast.

Warm-start (cycling) experiment reduces the track error obviously comparing to cold-start run due to accumulation of previous information.

WRF-Var with conventional data, BOGUS and GPS RO data can substantially improve the prediction for typhoon Dujuan both in terms of track and intensity comparing to the forecast initialized from AVN analysis.

FORECASTING SMALL/MIDGET TROPICAL CYCLONES IN THE DATA-SPARSE SOUTH-WEST PACIFIC REGION

A Waqaicelua

Regional Specialised Meteorological Centre Nadi-Tropical Cyclone Centre (RSMC Nadi-TCC)

Fiji Meteorological Service, Private Mail Bag NAP0351, Nadi Airport, Republic of Fiji Islands.

Tropical cyclone formation occurs mostly in data sparse oceanic regions, as in the Southwest Pacific basin, forcing heavy reliance on satellite and numerical weather prediction data to locate, analyse and forecast these processes. Subsequently, accurately forecasting tropical cyclone development and associated thermal structure in the lower region of the troposphere, becomes a very challenging task. Whenever rapid intensification occurs with strong vertical wind shear at lower levels, accompanied by intense heavy rain and high winds at the surface, impact on communities and the environment have been found to be severe. This always demands a lot from the severe weather and especially tropical cyclone early warning system, with the objective of ensuring safety of lives and property.

Introduction

The Southwest Pacific region consists of mostly under-developed island countries scattered in the tropical Pacific Ocean. With varying degrees of natural capacities and capabilities, they have to rely heavily on foreign aid, for sustainable development.

Subsequently, the national meteorological service's ability to maintain and sustain quality observations networks is usually relegated to the bottom of their national strategic plans. Quality of data is seriously affected when maintenance services are not carried out routinely. Upgrades and new installations are usually held back and/or forced to compete with other capital demands. High communications infrastructure costs restrict timely exchange of critical observations data to RMSC Nadi, as well as the region and beyond.

This has not helped mitigate the increasing vulnerability of island country communities to tropical cyclones and other high impact severe weather events during landfall. Leading up to actual landfall, the major damage (both wind and flooding) and losses tend to be in highly developed coastal zones, which continue to increase in value and complexity. However, the major loss of life in recent decades has been from inland rainfall and its associated flooding, and landslides.

To meet the early warning system demands, RSMC Nadi has to heavily depend on satellite and numerical output data in order to routinely provide timely and objective forecasts, warnings and advisories to the region. In this respect, the introduction of the Severe Weather Forecasting (Disaster Risk Reduction) Demonstration Project (SWFDDP) for the South Pacific islands is absolutely timely.

With young forecasters, the lack of experience (and thus skill) with, and appreciation of, small tropical cyclones (or midgets) has led to large errors in intensity forecasts and especially at landfall. This is also true with rapid or explosive developers. Accurately forecasting weather associated with these systems remains a huge challenge at RMSC Nadi.

In this report, a closer look at a midget system that affected Fiji in 2004, as well as some operational aspects of forecasting, are taken.

Tropical Depression TD 10F April 2004

A Tropical Disturbance (TD 10F) was first identified embedded in an active monsoon trough to the northeast of Vanuatu, on April 4th 2004. For three days, it remained weak and slow moving. On the afternoon of the 7th, it intensified into a tropical depression and began moving southeast about 10 knots. Overnight, very deep convection erupted about the low-level centre. As a consequence, the system was caught up in the prevailing strong (20 to 30 knots), low- to mid-level northwest steering field, thus the acceleration to about 15 knots towards the southeast. Vertical shear over the depression was quite significant (25 to 30 knots) but this was neutralised, effectively, by the rapidly increasing translational speed.

This was a small system and it proved quite difficult to track until it moved within the range of the Nadi radar. Minimum pressure recorded was 990hPa and one of the synoptic stations in Fiji (Yasawa-i-rara WMO Station No: 91660) reported sustained winds of 43 knots before it stopped transmitting.

Numerical forecast models failed to forecast the development of this system. The microwave sequence (Figure 1) clearly showed the rapid intensification of this system whilst located northwest of Nadi. The EIR sequence (Figure 2) indicated the rapid increase in convection up to 1125UTC when, in retrospect, it would needed to have been named to provide any useful warning.

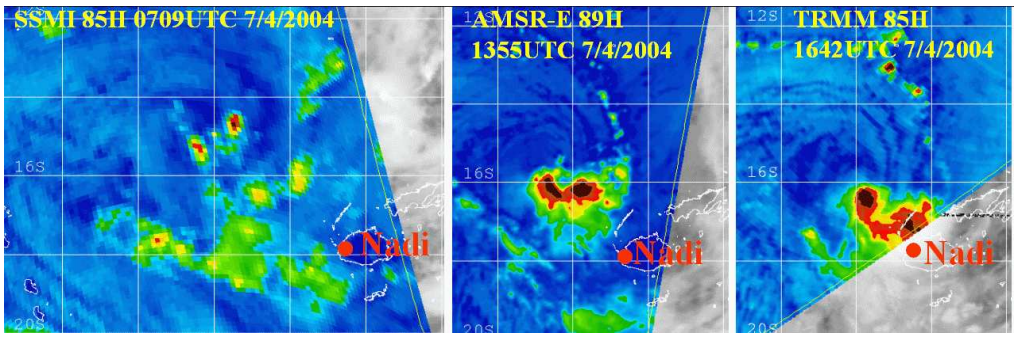

Figure 1. Rapid intensification of TD 10F April 2004 from microwave data.

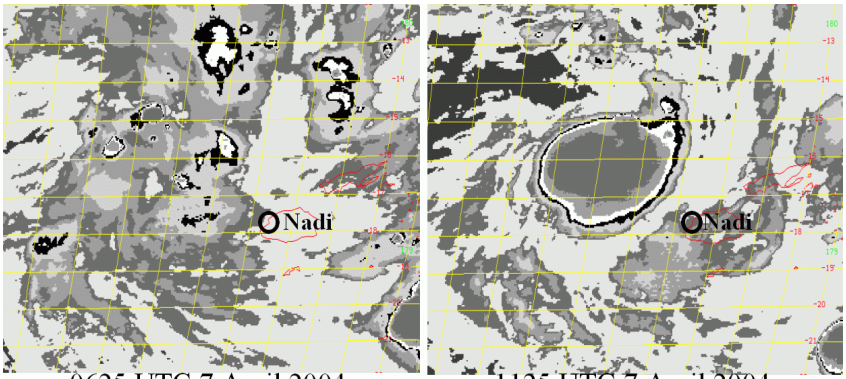

Figure 2. Enhanced Infrared satellite imagery shows rapid increase in cold cloud over a period of 5 hours.

The 700hPa sequence (Figure 3) has been reconstructed from the sparse actual data and a re adjustment of the NCEP/NCAR reanalyses which had the low level vortex in the wrong area. The intensification is associated with a thermal trough moving up towards Fiji, by following the 434 decametre contour at 00Z on the 7th in a trough over Vanuatu and at 12Z on the 7th the trough moves up towards Fiji. The red streamlines represent flow from warm to cool, or isentropic uplift, which releases convection. The trough relaxes by 00Z on the 8th which is perfect for development as the shear which stimulated the convective blow up then weakens, thus putting the developing system in a lower shear environment (the red

plots are 850/500 shears).

The 200hPa winds show a diffluent pattern over Fiji during the intensification.

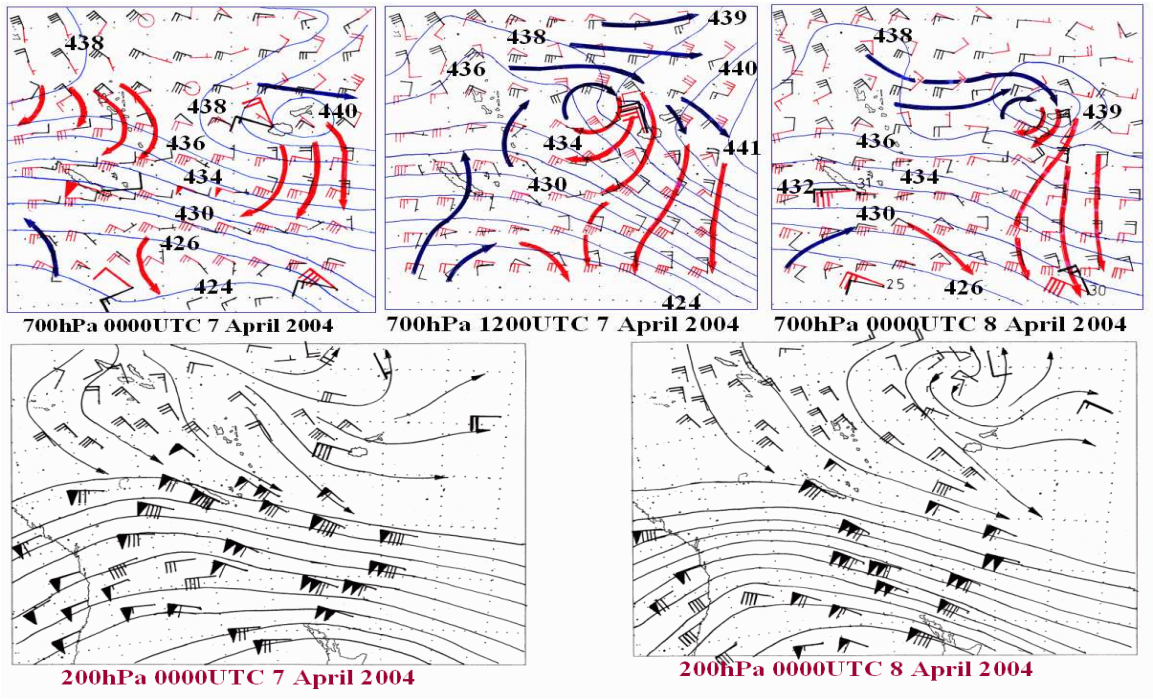

Figure 3. 700hpa and 200hpa analyses (red plots are 500/850 shear values)

Effects

Damage wreaked by TD10F was severe and confined to a thin strip along the path of the system (refer to Figure 4). At least 11 people were confirmed dead, and 9 still missing. Most fatalities were through drowning. Damage to infrastructure and public utilities, particularly roads and bridges was severe, due mainly to flooding and landslides. Root crops, suffered severely. Other root- and fruit crops were destroyed or severely damaged. Most family homes were severely damaged or destroyed (blown or washed away). The business community also suffered severely mostly through flooding. The Kings Road especially the sector along the northeast coast of Viti Levu (largest island in Fiji) was closed for all traffic for several days as parts of the road were washed away. Communications into or out of this affected area was severed particularly during the height of the storm. Damage costs were confirmed at F$5.6 million (inclusive of damage costs to a different flooding incident in other parts of Viti Levu a week later).

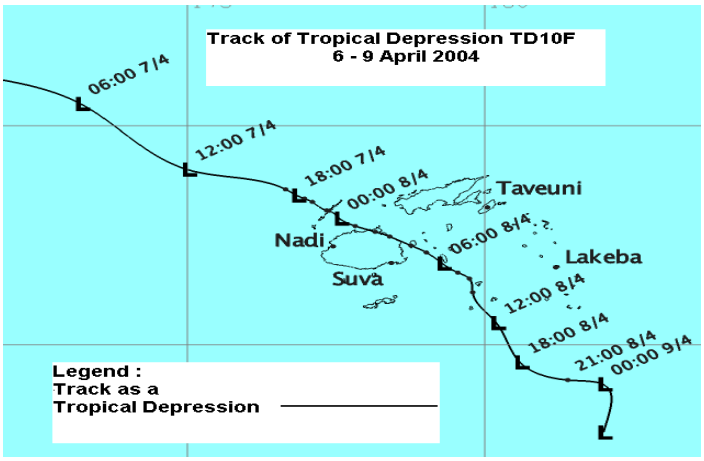

Figure 4. RSMC Nadi's Best Track of TD 10F.

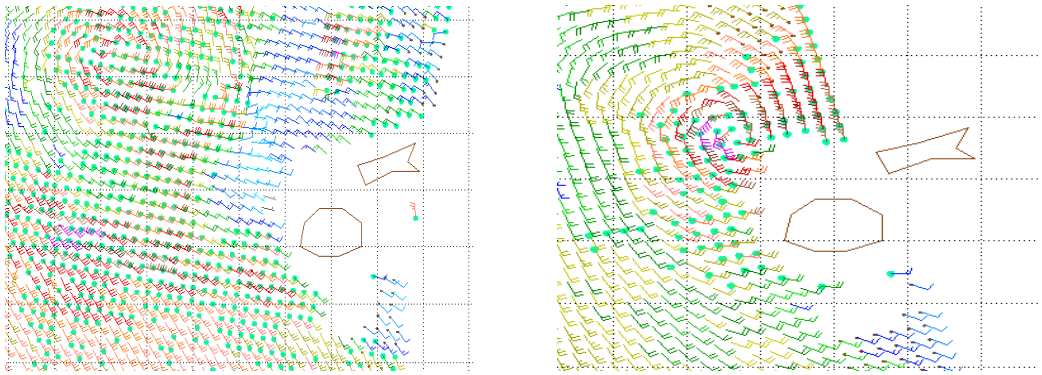

Figure 5: Quikscat passes at 0618Z (left) and 1844Z on 7th April 2004

Operational Aspects

TD 10F was a very small and compact system, even smaller than "normal" midgets. At the Joint Typhoon Warning Centre, guidance to forecasters indicate that midget cyclones (radius of gales of 111 km or less) can sustain hurricane force winds with central pressures 20 to 25 hPa higher than larger storms. The lack of knowledge and skills in forecasting these systems was notable. The absence of critical surface observations along its path made the situation at the forecast room a lot worse. Subsequently, validation of satellite and radar observations could not be conducted objectively. Further, the failure of the global models to capture this rapid intensification exerted pressure on forecasters

In retrospect, TD 10F should have been named, though possibly for a mere 6 to 9 hours. Had it been so, the warnings would have been more meaningful for the affected communities.

Summary

Forecasters' operational knowledge and skill in forecasting rapidly developing small systems as well as landfall processes is crucial to an effective early warning system. Numerical models at times can provide excellent forecasts of the formation of tropical cyclones. Associated with these correct forecasts are similarly accurate forecasts of the thermal structure of tropical cyclones indicating that these structures are important to the intensification mechanism. A good knowledge of the model performance in tropical cyclone basins can alert forecasters to increase the monitoring of likely cyclogenesis.

Bibliography

Callaghan, J. J. 2004: Tropical Cyclone Intensification, Preprints, The International Conference on Storms Brisbane Queensland Australia July 2004.

Callaghan, J. J. 2008: Operational Forecasting of Tropical Cyclone Formation, The Sixth International Conference on Tropical Cyclones, Costa Rica 2008.

Holland G. J. 2002: Tropical Cyclone Landfall Processes, The fifth International Conference on Tropical Cyclones, Townsville, Australia 2002.

Callaghan J and Smith R.K. 1998: The relationship between maximum surface winds and central pressure in tropical cyclones.
AMM 47, 191-202.

An Ensemble Forecast Experiment of Landing Typhoon

TAN Yan

Shanghai Typhoon Institute，Laboratory of Typhoon Forecast Technique/CMA，Shanghai 200030

1 Introduction

The regional typhoon ensemble prediction system is based on GRAPES_TCM model, which consists of three parts, the initialization of typhoon vortex, the initial ensemble perturbation and the post-process. This ensemble prediction system is implemented operational since 2006, and providing the ensemble products for 72 hours, such as ensemble tracks, strike probability and the distribution of typhoon positions, as well as the probability distribution of some synoptic fields.

The system produces 9 members from GRAPES_TCM model. AVN data are adopted as the initial and lateral boundary data for the following ensemble forecast. The model domain covers 0-45° N, 90−160° E. Resolution is about 0.5 degree. Another model configuration is the same as operational work..

2 Experiment design

Schematic diagram of perturbation using BGM method is in Fig.1, One assumption that the small initial perturbation is coming to saturation for 36 hours. The scaling factor is defined by each variable which is used to control the perturbation magnitude to be reasonable for each 12 hour breeding cycle.

12 hours forecast data from AVN model is adopted as the initial data(A), After the vortex relocation, reference to the errors of observation, random errors with the normal distribution are added to ensemble members(R) , For each scaling process(f), the output of the model should be filtered into two parts, the environment field and vortex itself. According to the expressions (1) and (2), different scaling factors are applicable to different parts. And a pairs of new perturbations, including the environment and vortex itself(P/N) could be added to the initial data for the next breeding cycle till the whole process of breed.

$$f = C \times \Delta P \qquad (1)$$

$$f = C \times (X_{pi} - X_{ni}) \times \| X_c \| / \| X_{pi} - X_{ni} \| \qquad (2)$$

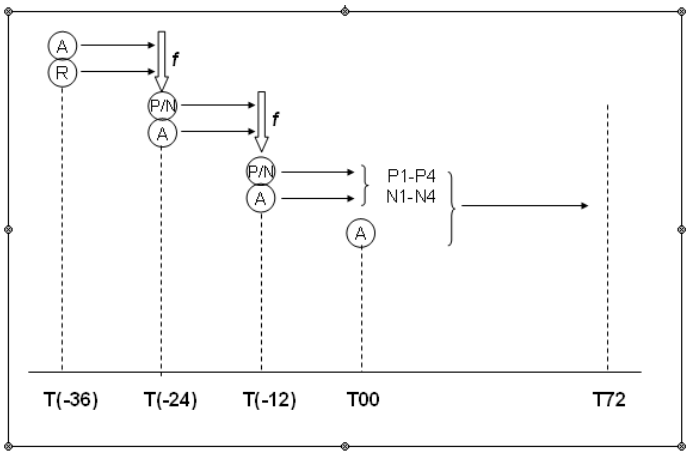

Fig. 1 Schematic diagram of perturbation using BGM method.

3 Result analysis

Ensemble mean and spread is a good indicating for the forecast uncertainties. At the initial time, the spatial distribution of spread is asymmetry. There is a maximum region near the typhoon vortex clearly, the

vertical attribute is keep the same, from the low level to high level of troposphere, the maximum region is still kept near vortex with the magnitude around 40gpm. Other variables such as wind, temperature are not showed here, but there is not such an obvious maximum region. Some scattered high region and low region are located between vortex region and others.

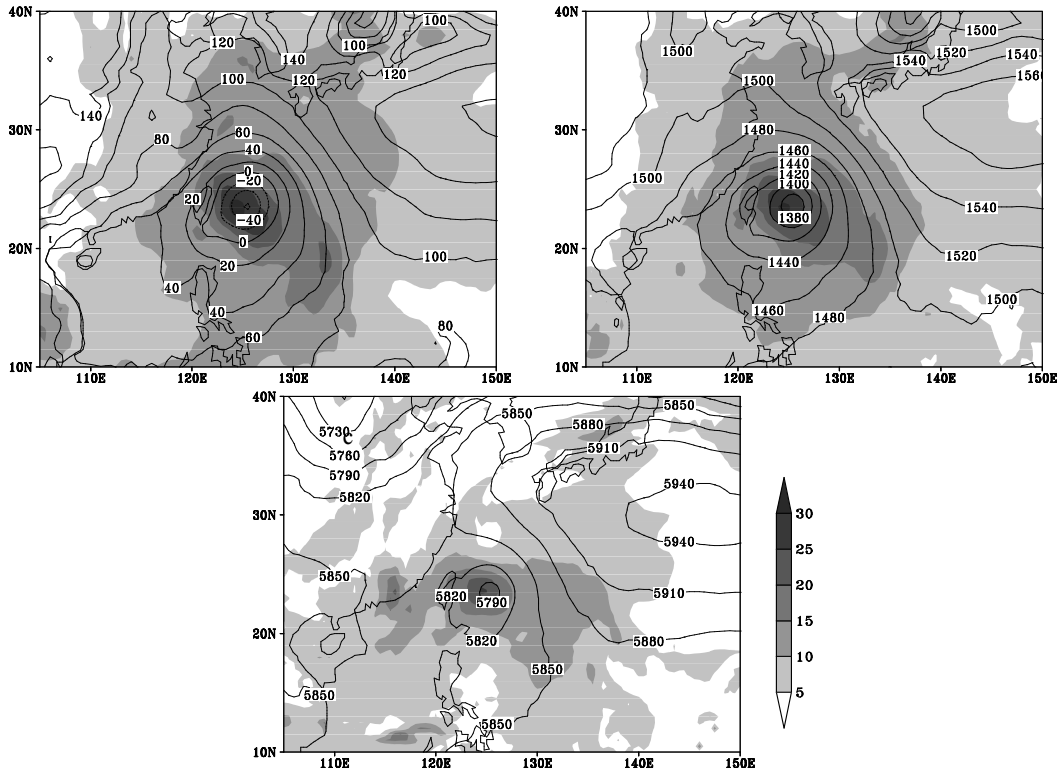

Fig.2 Mean (shaded) and spread of different levels at initial time
left:1000hPa, middle:850hPa, right:500hPa（unit：gpm）

In order to research the time series of ensemble spread, 1000hPa, 850hPa and 500hPa are selected to express as the different levels of troposphere. The latitude wind (U) and geopotential height are showed in fig.3, others variables nearly have the same developmental tendency. From the left diagram of latitude wind, the small differences are existent at the beginning of model integral, that's the result of BGM processes. The differences at 500hPa are much more obvious than the low level of troposphere. The spread of members enlarged with the time and the development speed are increased especially below mid-level. From the left diagram of geopotential height, the ensemble spread at low level of troposphere is larger than mid-level, even high level. There is an obvious change of ensemble spread when WHIPA made landfall at 1900UTC Sept. 2007，this change are reflected to the whole troposphere. After the landing process, the ensemble spread is increased and the forecast uncertainty is increased accordingly.

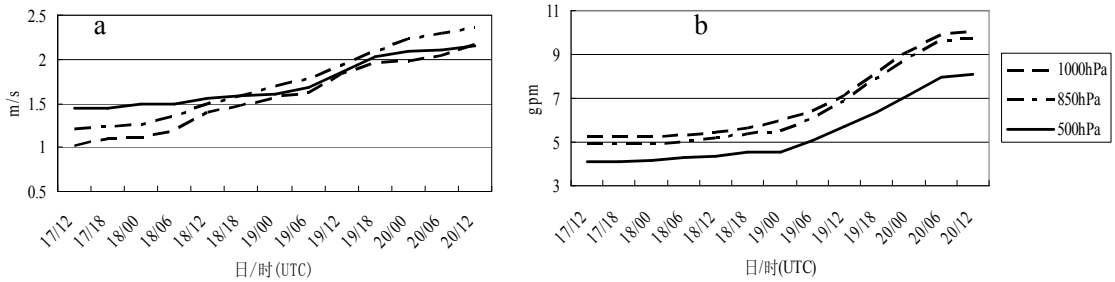

Fig.3 Time series of ensemble spread.

Fig.4 illustrate the track forecast and the strike probability in the next 72 hours. After WHIPA made landfall at Fujian province, it kept moving into the inland of China, Finally, turn southeast and left the mainland of China, dissipated on the sea. Black line is control run, it seems more northward than

observation during the whole life time of WHIPA. The landing point is located in Zhejiang province and there is a large possible that impact Shanghai. But there is large spread of ensemble members, blue line are members forecast, Totally, the main two s are nearly opposite. One of the scenario is that WHIPA could made landfall in Fujian province and kept moving into then inland, with the slow moving speed and finally dissipated. Another is moving northward and made landfall at Zhejiang province, mainly affecting the coast land of east China, then further affected Korea peninsula.

Produce the strike probability from large numbers of ensemble information, from the point of view of probability forecast, strike probability chart could give us the forecast uncertainty quantificationally. Before WHIPA made landfall, forecasts of members are consistent basically, about 70% probability seems to make landfall at the coastland in Fujian province, the most likely place is the boundary place between Fujian and Zhejiang province. But the different is increased after TC made landfall, the strike probability of regions affected by TC is decreased. More members tend to move northward and enter to sea later.

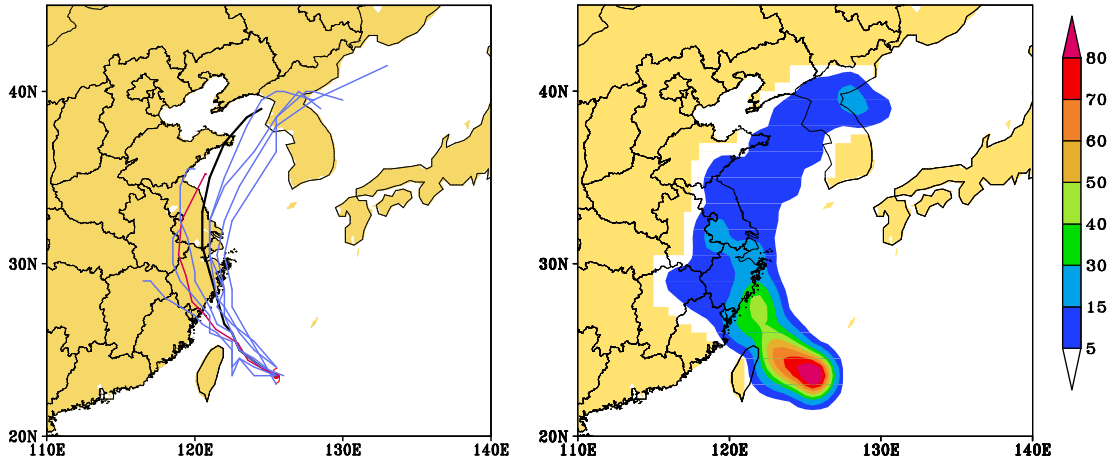

Fig.4 Track forecast，red line is observation, black line is control run, blue lines are ensemble members (left) and the strike probability in the next 72 hours (right).

Track error diagram in Fig. 5 contain different errors of members, which including control run, arithmetic average of all members and such one of the best forecast, even different types of forecast scenarios by cluster analysis. Only for 60 hours at 00UTC 20 Sept. because of the TC disappear. Ward cluster are adopted to classify members into twp types, one type is characterized by the TC disappeared inland, this type contain member 2,3,6 and 8, another one is characterized by the TC moving recurvated, containing member 1,4,5 and 7. For control forecast, errors are 68km (24hours) , 316km (48hours) and 230km (60 hours). For the ensemble mean of all members, errors are 89km (24hours), 300km (48hours) and 250km (60 hours). It seems that forecast only at 48 hours is better than that of control run. Totally, there is no advantage for ensemble forecasts. But the ensemble mean after cluster analysis is different. Type one has smaller error than control run during the time, with 34kn (24 hours), 153km (48 hours) and 191km (60 hours). Type two has negative effect for computing members track error. It has larger errors all the time. Member 3 is the best one with smallest error in all members during the time. How to do the post-process of ensemble forecast is so important to improving the forecast ability and application for ensemble forecast.

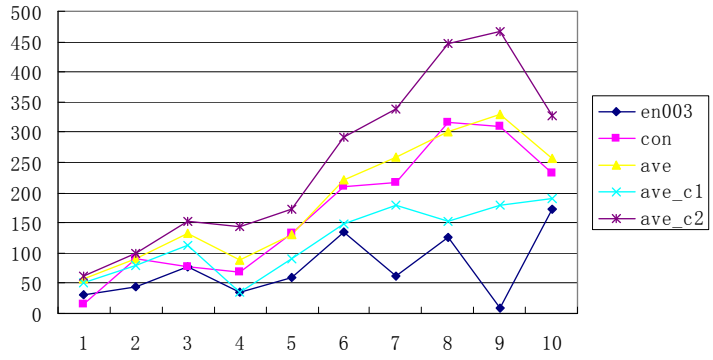

Fig.5 Track error with interval 6h. x-axis is forecast times(6h/time)，y-axis is track error (unit：km)
('en003' is one of the ensemble member；'con' is control run；'ave' is the ensemble mean;
'ave_c1' is mean of cluster one；'ave_c 2 ' is mean of cluster two)

Forecast Demonstration Project on Landfalling Tropical Cyclones over the Bay of Bengal : Pre-pilot Phase 2008

M. MOHAPATRA, AJIT TYAGI AND B. K. BANDYOPADHYAY

India Meteorological DepartmentMausam Bhavan, Lodi Road, New Delhi-1100 03.

Ph. 91-11-24652484, Fax-91-11-24643128
E-Mail : ajit.tyagi@gmail.com

ABSTRACT

The extensive coastal belts of India, Bangladesh and Myanmar are exposed to tropical cyclones (TCs) developing over the Bay of Bengal and hence suffer from loss of lives and properties due to impact of landfall events including heavy rain, gales and storm surges. India Meteorological Department (IMD) acts as Regional Specialized Meteorological Centre (RSMC) for TCs for this region. It uses various numerical weather prediction (NWP) models including global (T-254), regional (LAM and QLM), and meso-scale (MM5, WRF) models apart from various international global models for prediction of TC genesis, intensification, movement and landfall characteristics. However, extensive performance evaluation and numerical experimentation studies on TC forecasting over the region conclude that the large errors in 48 hour TC intensity and landfall forecasts are due to lack of critical observations from the cyclone core environment. Hence a forecast demonstration project (FDP) on landfalling TCs over the Bay of Bengal has been taken up to demonstrate and modify the ability of the NWP models using enhanced observation over the region including the measurements from the dropsonde over the periphery of the TC and hence to assess improvement in forecast accuracy. The programme consists of pre-pilot phase (15 Oct.–30 Nov. 2008, 2009), Pilot Phase (15 Oct.–30 Nov 2010, 2011) and final phase (15 Oct.– 30 Nov. 2012). The period of 15 October to 30 November is considered for FDP as on an average 2-3 TCs develop during this period out of about 4 TCs developing during the year as a whole over the Bay of Bengal.

The pre-pilot phase of FDP was conducted during 2008 and objectives of the pre-pilot phase programme were met by conducting a joint observational, communicational and NWP efforts by several national and international agencies during the period 15 Oct.-30 Nov. 2008. There were three be Intensive Observational Phases (IOP) within this period tuning three actual cyclones, viz. Rashmi (25-27 October 2008), Khai-Muk (13-16 November 2008) and Nisha (25-27 November 2008). The results of the experiments alongwith the problems and prospective are presented and analysed.

Forecast Techniques and Early Warning System for Landfalling Tropical Cyclones over the North Indian Ocean

AJIT TYAGI, M. MOHAPATRA AND B. K. BANDYOPADHYAY

India Meteorological DepartmentMausam Bhavan, Lodi Road, New Delhi-1100 03.

Ph. 91-11-24652484, Fax-91-11-24643128
E-Mail : ajit.tyagi@gmail.com

ABSTRACT

India Meteorological Department (IMD) monitors and predicts Tropical cyclones (TC) over north Indian Ocean (NIO) and provides early warning services to national agencies for management of the cyclone. It also provides TC advisories to World Meteorological Organisation (WMO)/ Economic and Social Cooperation for Asia and the Pacific (ESCAP) Panel member countries as one of the Regional Specialised Meteorological Centre (RSMC) for TCs. The average operational forecast errors of IMD in recent five years for 24 hrs track and landfall forecasts are about 140 km and 90 km respectively indicating improvement in landfall forecast. The forecast techniques used by IMD for intensity and track forecast and strategies adopted for early warning of landfalling TCs have been analysed and discussed.

Scientific and technological advances in TC forecasting are translated into effectiveness of TC warning in IMD. The forecast and warning operations and decision-making process is made by blending scientifically based conceptual models, meteorological datasets, technology and expertise.

The design of a TC warning system in IMD takes into consideration of the prevailing state of the meteorological science, the available technological means of communication, the built-up environment such as dwellings, socio-economic conditions, appropriateness of protective actions as well as the expectations of the society. To maximise relevance and effectiveness of the TC warning, strategies are formulated in respect of the design, products generation, presentation & dissemination of the warning, coordination with disaster management agencies and public awareness.

The problems and perspective of existing Forecasting techniques and early warning system are also analysed. IMD has taken up various technological upgradation measures with respect to TC forecasting and its early warning in its ongoing modernization programme, which will eventually help in addressing the thrust areas and requirements.

Interaction between Landfalling Tropical Cyclone and Summer Monsoon

CHENG Zhengquan1), Chen Lianshou2), LI Ying2)

1) Guangdong Meteorological Observatory, Guangzhou, 510080

2) Chinese Academy of Meteorological Sciences, Beijing, 100081

Abstract

Tropical cyclones would decay and the caused rain becomes weakened because of land friction. But some encounter the onset or strengthening of summer monsoon, which causes extra-heavy rain and lead to serious disasters. No. 0604 typhoon *BILIS* is such a typical case. *BILIS* made landfall at the southeastern coastal areas of China as severe tropical cyclone and soon decayed to tropical depression, when the southwestern monsoon became active. The remnant of *BILIS* moved into the inland and endured several days, and led to a large range of heavy rainfall. The caused flood, landslide and debris flow produced a calamity. More than 800 people died and over 100 disappeared. Based on two groups of typhoons with distinct rainfall and dynamic composite analysis, a case diagnosis and several groups of numerical experiments, the interaction between landfalling tropical cyclones and summer monsoon is analyzed. Results are listed as follows.

The dynamic composite analysis shows that, the low-level southwestern jet is crucial to the intensity and duration of heavy rain for the landfalling tropical cyclones. Those typhoons with strong rainfall always link with strong low-level southwestern jets for a long time even after landfall. Once the link breaks, tropical cyclones always decay soon and the induced rainfall becomes weakened consequently.

Strong summer monsoon surge transfers sufficient water vapor and instable energy, which is favorable to the maintenance of cyclones and the intensification of rainfall. Numerical experiments reveal that, the water vapor transfer has an important impact on the structure and the heavy rain events of landfalling tropical cyclones. Transfer from the outer environment is favorable to a longer duration of the tropical cyclone over land. Without the water vapor transfer, the warm core structure of the typhoon collapses soon and the rainfall is obviously weakened.

The change of water vapor flux in monsoon jet could impact the coverage and intensity of heavy rainfall. The sensibility experiments show that, stronger monsoons(jets) strengthens the water vapor flux transferred to the landfalling tropical cyclone, and stronger rain covers wider area. Vice versa.

Summer monsoon itself is an important system for heavy rain processes. When a tropical cyclone moves into the monsoon channel, the coverage and the intensity of heavy rain change a lot. Experiments reveal that, the typhoon not only converges the water vapor and instable energy because of its unique dynamic structure, but also changes the distribution of water vapor and instable energy fields with its movement, which leads to the change of the intensity and distribution of heavy rainfall.

WMO 2nd International Workshop on Tropical Cyclone Landfall Processes (IWTCLP-II)
(19-23 October, 2009)

Meeting Program

Sunday, 18 October 2009

0800-2000 Registration

Monday, 19 October 2009

0800 Registration
0900 Opening Ceremony
Chair: Dr. Renhe Zhang
Chairman of LOC, President of CAMS

Welcome Speech	Guoguang Zheng Administrator of CMA, PR of China with WMO, Honorary Chair of the Meeting
Welcome Speech	Dinghua Yang Vice Chairman of Shanghai Municipal People's Congress
Opening Address	Prof. Lianshou Chen Chair of the Meeting
Opening Address	Prof. Russell Elsberry Chair of the Meeting
Opening Address	Mr. Koji Kuroiwa Representative of WMO
	Dr. Xu Tang Chairman of LOC, Director General of SMB
	Prof. Zhenquan Cao Vice Chair of Shanghai Association for Science and Technology
	Mrs. Nanette Lomarda Representative of WMO

0945 Photo
1000 Break

Session 1a Tropical cyclone impacts
(Chair: Prof. Russell Elsberry, Dr. Xiaotu Lei)

1020 An overview on the study of Tropical Cyclone Rainfall and Intensity Change in Different Phases (Prof. Lianshou Chen)

1050 Practices and Experiences on Multi-hazard Early Warning System:

---With Emphasis on Typhoon Early Warning (Dr. Xu Tang)

1120 Changes in track and structure associated with tropical cyclone landfall (Prof. Johnny Chan)

1150 Unusual Variation of Landfall Tropical Cyclone Behavior and Associated Physical Mechanism (Dr. Yihong Duan and Dr. Hui Yu)

1220 Lunch

Session 1b Tropical cyclone impacts
(Chair: Dr. Yihong Duan)

1345 Terrain effects on the tropical cyclone rainfall over Taiwan (Dr. Tian-Chiang Yeh and Prof. Chih-Pei Chang)

1415 Hydrological Perspective on Tropical Cyclone Forecasts (Dr. Jinping Liu)

1445 Forecasting surface impacts of wind, wave, and storm surge (Dr. Bruce Harper)

1515 Break

Session 1c Tropical cyclone impacts
(Chair: Prof. Johnny Chan)

1535 Air-sea interactions in tropical cyclones (Prof. Nick Shay)

1605 WWRP Support to Multi-hazard Early Warning System (Ms. Nanette Lomarda)

1635 A Statistical analysis of unusual track characteristics of tropical cyclones close to Taiwan Island (A.-M. Liu, Y. Lin, X.-Y. Wu, and Z.-G. Huang)

1705 Discussion of tropical cyclone impacts

1720 End of session

1800 Reception

Tuesday, 20 October 2009

Session 2: Panel discussion on forecasting tropical cyclone landfall
(Chair: Prof. Russell Elsberry)

0900 Research needs and opportunities for improved forecasting of U.S. landfalling tropical cyclones (Dr. Robert Rogers)

0920 Tropical cyclone information and products at the JMA—Present status and challenges for the future (Dr. Kiichi Sasaki)

0940 A brief overview of operational tropical cyclone forecasting in Taiwan (Dr. T.–C Yeh)

1000 Tropical cyclone landfall forecasting at Queensland Tropical Warning Center (Dr, Jim Davidson)

1020 Tropical cyclone landfall forecasting at Philippine PAGASA (Dr. Prisco Nilo)

1040 Discussion

1120 Break

Session 3a: Research advances related to landfall
(Chair: Prof. Lianshou Chen, Dr. Ying Li)

1140 Targeted observations of tropical cyclones (Prof. C.-C. Wu)

1210 Lunch

Session 3b: Research advances related to landfall
(Chair: Dr. Bruce Harper)

1345 Some recent studies related to tropical cyclone wind structure changes (Prof. Russell Elsberry)

1415 Airborne deployment of GPS dropsondes from high altitude for diagnosis of tropical cyclone genesis: Examples from T-PARC/ TCS08 (Dr. Peter Black)

1430 Airborne deployment of expendable platforms for mitigation of tropical cyclone landfall impacts: Examples from T-PARC/ TCS08 (Dr. Peter Black)

1445 Transition of the inflow boundary layer of landfalling tropical cyclones (Prof. Yuqing Wang and Jing Xu)

1515 Break

Session 4: Opportunities for improved guidance products
(Chair: Dr. Kiichi Sasaki, Dr. Sung-Dae Kang)

1535 Satellite digital data and products for tropical cyclone studies (Dr. Tetsuo Nakazawa, with Jeff Hawkins and Chris Velden)

1605 Tropical cyclones landfalling in the mainland, Hainan and Taiwan of China and their interrelations (Fumin Ren, S.-L. Wang, and Lianshou Chen)

1635 Landfalling tropical cyclone: Forecasting system of the future (Dr. Robert Rogers)

1705 Discussion
1730 End of session

Wednesday, 21 October

Session 5: Shanghai Expo 2010 and potential related programs
(Chair: Dr. Koji Kuroiwa, Dr.Tetsuo Nakazawa)

0900 Practices in Public Weather Service Typhoon Early Warnings and Disaster Mitigation (Jonathan Wakrat)
0930 Landfall Typhoon Forecast Evaluation and Assessment Demonstration Project (Yu Hui)
1000 Tropical Cyclone Structure (TCS10) and other 2010 Field Experiments (Prof. Russell Elsberry)
1030 Break

Session 6: FDP and Contributed papers on forecasting
(Chair: Ms. Nanette Lomarda, Dr. T.-C. Yeh)

1050 Proposed Forecast Demonstration Project (Dr.Gong-CMA NMC)
1120 Recent improvements of forecasting and early warning system for landfall of tropical cyclones (Siriranjith Jayasekera)
1140 Cuban Experience in Tropical Cyclone Landfall Forecast for an Effective Warning System (Jose Rubiera)
1200 Experiments on a Statistical Prediction Scheme of Tropical Cyclone Intensity Forecast in Western North Pacific Based on Partial Least Square Regression (Li-na Bai, Jin-jie Song, Yuan Wang, Lianshou Chen, Pei-yan Chen)
1220 Lunch

Session 7: Contributed papers on impacts
(Chair: Dr. Jim Davidson, Dr. Peter Black)

1345 Diagnostic methods for evaluating forecasts for landfalling tropical cyclones (Dr. Barbara Brown)
1415 Study on the impact of Landfall Typhoon Cyclone in China (Qinghong Zhang and Qing Wei)
1435 Tropical Cyclone Landfall Processes (Evan Thompson)
1455 The effects of the vortex intensity to the forecast tracks of typhoon “Fengshen” (Suhong Ma and Anxiang Qu)
1515 Break

Session 8: Contributed papers on research advances
(Chair: Dr. Robert Rogers)

1535 Adiabatic rearrangements of potential vorticity hollow towers (Dr. Eric Hendricks and Prof. Wayne Schubert)
1555 Primary analyses on structure and evolution of Typhoon Khanun (2005) during its later period from land into sea (Gang Fu, Na Wei, Qian Wang, and Xiaolan Li)
1615 Eyewall evolution of Typhoon Aere (2004) (Qingqing Li)
1635 Gradient-wind Momentum Approximation and Dynamics of Boundary Layer in Tropical Cyclone (Yuan Wang, Yunwu Zhao, and Jin-jie Song)
1655 The Mechanism of High Precipitation of Morakot : A Preliminary Numerical Test Study (Jie Tang)
1715 End of session

Thursday, 22 October

Session 9: Contributed papers on observations
(Chair: Prof. Yuan Wang)

0900 Climatic Trend of the Tropical Cyclones' Influences on China's Mainland as Revealed by the Wind and Precipitation Observations (Ming Ying and Baode Chen)
0920 Moist Frontogenesis Evolution during the Extratropical Transition (ET) process of the typhoon landfalled at China mainland (Jie Tang)
0940 Targeting Studies for Extra-tropical Transition of Hurricane Fabian: Signal Propagation, the Interaction between Fabian and Midlatitude Flow, and Observation Strategy (Hua Chen and Weiyu Pan)
1000 An Overview on Study in Tropical Cyclone Remote Rainfall (Chunhua Cong Lianshou Chen, Xiaotu Lei, and Ying Li)
1020 Break

Session 10: Contributed papers on modeling
(Chair: Prof. Yuqing Wang)

1040 A Numerical Study of "The Perfect Flood" of Hurricane Floyd 1999 (Lian Xie and Qianhong Tang)
1100 Performance of a Modified Kain-Fritsch Convection Trigger Scheme in Rainfall Simulation during Typhoon Landfall (Lei-Ming Ma and Zhe-Min Tan)
1120 Convective Asymmetries Associated with Tropical Cyclone Landfall: β-Plane Simulations (Wei Huang and Xudong Liang)

1140 A Study on Formation and Development of Mesoscale Convergence Line within Typhoon Circulation ((Ying Li, Lianshou Chen, and Chuanhai Qian)
1200 Effect of tropical SST forcing on the regional circulation in East Asia (Sung-dae Kang, Seong-Hee Won, Tae-Ryong Kim)

1220 Lunch

1400 Excursion

1830 Banquet

Friday, 23 October

Parallel Session :Working Group on Tropical Meteorology Research meeting
(Chair: Prof. Lianshou Chen)

0900 Work Review and Future Plans (Profs. Lianshou Chen, Russell Elsberry, Chih-pei Chang)
1030 Break
1100 Discussion and Recommendation
1200 Closing
1220 Lunch

Session 11: Contributed papers on rainfall and ET
(Chair: Prof. Qinghong Zhang)

0900 Wave activity associated with a landfalling typhoon (Lingkun Ren and Chungu Lu)
0920 Rainfall Reinforcement Associated with Landfalling Tropical Cyclones (Meiying Dong, Lianshou Chen, Ying Li, and Chungu Lu)
0940 Surface rainfall equation and modeling study of surface rainfall processes associated with a landfalling typhoon (Xiaopeng Cui, Shouting Gao)
1000 Observational Analysis of Heavy Rainfall Mechanisms Associated with Severe Tropical Storm Bilis (2006) after Its Landfall (Shuanzhu Gao, Zhiyong Meng, Fuqing Zhang, and Lance Bosart)
1020 Trend Discrepancies in Western North Pacific Tropical Cyclones (Jin-Jie Song, Yuan Wang, and Liquang Wu)

1040 Break

Session 12: Contributed papers on different topics
(Chair: Prof. Gang Fu)

1100 The Role of Low-Level Jet to The Development of Far Distance Tropical Cyclone Torrential Rainfalls Over North China （YAO Xuexiang，ZHANG Yingxin，LI Yunchuan）

1120 Typhoon Vortex Self-Organization in Baroclinic Environment (TENG Daigao, LUO Zhexian, YU Hui)

1140 Offshore TC Track Forecasting using Doppler Radar Velocity Field (Wu Chenfeng, Wei Yingzhi, Su Weidong）

1200 Doppler Radar Data Study of Structure and characteristic Associated with Landfalling Typhoons on Southeast Coast of ZheJiang Province in China (Chunxiao JI, Fang Zhao)

1220 Lunch

1400 Closing ceremony

The Framework of WMO 2nd International Workshop on Tropical Cyclone Landfall Processes (IWTCLP-II)
19-23 October 2009, Shanghai, China

	19 Oct.（Mon）	20 Oct.（Tue）	21 Oct.（Wed）	22 Oct.（Thu）	23 Oct.（Fri）	
08:00	08:00-Registration					
09:00-12:20	09:00-Opening 09:45-Photo 10:00-10:20 Break 10:20-12:20 **Session 1a** Chair: Prof. Russell Elsberry	09:00-11:20 **Session 2** ***Panel discussion*** on Forecasting tropical Cyclone landfall Chair: Prof. Russ Elsberry 11:20-11:40 Break 11:40-12:10 **Session 3a** Chair: Prof. Lianshou Chen Dr. Ying Li	09:00-10:30 **Session 5** Shanghai EXPO 2010 and potential related programs Chair: Dr.Koji Kuroiwa Dr. Tetsuo Nakazawa 10:30-10:50 Break 10:50-12:20 **Session 6** Chair:Ms.NanetteLomarda Dr. T.-C. Yeh	09:00-10:20 **Session 9** Chair: Prof. Yuan Wang 10:20-10:40 Break 10:40-12:20 **Session 10** Chair:Prof.Yuqing Wang	WGTMR Meeting	09:00-10:40 **Session 11** Chair: Prof. Qinghong Zhang 10:40-11:00 Break 10:10-12:20 **Session 12** Chair: Prof. Gang Fu
			12:20-13:45 Lunch			
13:45-17:20	13:45-15:15 **Session 1b** Chair: Dr. Yihong Duan Dr. Xiaotu Lei 15:15-15:35 Break 15:35-17:20 **Session 1c** Chair: Prof. Johnny Chan	13:45-15:15 **Session 3b** Chair: Dr. Bruce Harper 15:15-15:35Break 15:35-17:30 **Session 4** Chair: Dr. Kiichi Sasaki Dr. Sung-Dae Kang	13:45-15:15 **Session 7** Chair: Dr. Jim Davidson Dr. Peter Black 15:15-15:35 Break 15:35-17:15 **Session 8** Chair: Dr. Robert Rogers	14:00 Excursion	14:00 Closing of the Meeting	
	Reception（**18:00-20:00**）			Banquet**(18:30-20:30**）		

Session 1 (a,b,c): Tropical cyclone impacts
Session 2: Panel discussion on forecasting tropical cyclone landfall
Session 3(a, b): Research advances related to landfall
Session 4: Opportunities for improved guidance products
Session 5: Shanghai Expo 2010 and potential related programs
Session 6: FDP and Contributed papers on forecasting
Session 7: Contributed papers on impacts
Session 8: Contributed papers on research advances
Session 9: Contributed papers on observations
Session 10: Contributed papers on modeling
Session 11: Contributed papers on rainfall and ET
Session 12: Contributed papers on different topics

Ceremony
Presentation (Invited & contributed)
Panel discussion
Shanghai EXPO 2010 & discussion
WGTMR Meeting
Poster Session

World Weather Research Programme (WWRP)
Report Series

Sixth WMO International Workshop on Tropical Cyclones (IWTC-VI), San Jose, Costa Rica, 21-30 November 2006 (WMO TD No. 1383) (WWRP 2007 - 1).

Third WMO International Verification Workshop Emphasizing Training Aspects, ECMWF, Reading, UK, 29 January - 2 February 2007) (WMO TD No. 1391) (WWRP 2007 - 2).

WMO International Training Workshop on Tropical Cyclone Disaster Reduction (Guangzhou, China, 26 - 31 March 2007) (WMO TD No. 1392) (WWRP 2007 - 3).

Report of the WMO/CAS Working Group on Tropical Meteorology Research (Guangzhou, China, 22-24 March 2007) (WMO TD No. 1393) (WWRP 2007 - 4).

Report of the First Session of the Joint Scientific Committee (JSC) for the World Weather Research Programme (WWRP), (Geneva, Switzerland, 23-25 April 2007) (WMO TD No. 1412) (WWRP 2007 – 5).

Report of the CAS Working Group on Tropical Meteorology Research (Shenzhen, China, 12-16 December 2005) (WMO TD No. 1414) (WWRP 2007 – 6).

Preprints of Abstracts of Papers for the Fourth WMO International Workshop on Monsoons (IWM-IV) (Beijing, China, 20-25 October 2008) (WMO TD No. 1446) (WWRP 2008 – 1).

Proceedings of the Fourth WMO International Workshop on Monsoons (IWM-IV) (Beijing, China, 20-25 October 2008) (WMO TD No. 1447) (WWRP 2008 – 2).

WMO Training Workshop on Operational Monsoon Research and Forecast Issues – Lecture Notes, Beijing, China, 24-25 October 2008 (WMO TD No. 1453) (WWRP 2008 – 3).

Expert Meeting to Evaluate Skill of Tropical Cyclone Seasonal Forecasts (Boulder, Colorado, USA, 24-25 April 2008) (WMO TD No. 1455) (WWRP 2008 – 4).

Recommendations for the Verification and Intercomparison of QPFS and PQPFS from Operational NWP Models – Revision 2 - October 2008 (WMO TD No. 1485) (WWRP 2009 - 1).

Strategic Plan for the Implementation of WMO's World Weather Research Programme (WWRP): 2009-2017 (WMO TD No. 1505) (WWRP 2009 – 2).

4th WMO International Verification Methods Workshop, Helsinki, Finland, 8-10 June 2009 (WMO TD No. 1540) (WWRP 2010 - 1).

1st WMO International Conference on Indian Ocean Tropical Cyclones and Climate Change, Muscat, Sultanate of Oman, 8-11 March 2009 (WMO TD No. 1541) (WWRP 2010 - 2).

Training Workshop on Tropical Cyclone Forecasting WMO Typhoon Landfall Forecast Demonstration Project, Shanghai, China, 24-28 May 2010 (WMO TD No. 1547) (WWRP 2010 - 3).